



Accurate structural determination of biomolecules via single-molecule high-precision FRET measurements

Inaugural dissertation

for the attainment of the title of doctor
in the Faculty of Mathematics and Natural Sciences
at the Heinrich Heine University Düsseldorf

presented by

Olga Doroshenko

From Khalymonovo, Ukraine

Düsseldorf, August 2019

from the institute for Physical Chemistry II
at the Heinrich Heine University Düsseldorf

Published by permission of the
Faculty of Mathematics and Natural Sciences at
Heinrich Heine University Düsseldorf

Supervisor: Prof. Dr. Claus A. M. Seidel
Co-supervisor: apl. Prof. Dr. Ing. Gerhard Steger

Date of the oral examination: 19.12.2019

Scientific Meetings

13th International Workshop on “Single Molecule Spectroscopy and Ultrasensitive Analysis in the Life Sciences” September 4-6, 2013 in Berlin (Poster)

12th Greta Pifat Mrzljak international School of Biophysics, September 27-October 6, 2014 in Primosten, Croatia (Poster and Oral contribution)

10th European Biophysics Congress July 18-22, 2015 in Dresden (Poster)

7th Nucleinsäurechemie Treffen September 17-18, 2015 in Berlin (Poster)

60th Annual Biophysical Society Meeting February 27-March 2, 2016 in Los Angeles, USA (Poster)

2nd FRET meeting April 3-6, 2016 in Göttingen (Poster)

61th Annual Biophysical Society Meeting February 11-15, 2017 in New Orleans, USA (Poster)

Biennial meeting of the German Biophysical Society September 16-19, 2018 in Düsseldorf (Poster)

63th Annual Biophysical Society Meeting March 2-6, 2019 in Baltimore, USA (Poster and Oral contribution)

Abstract

Förster resonance energy transfer (FRET) is a rising tool to determine structure and dynamics by structural heterogeneities and underlying kinetics at single molecule (sm) and ensemble level. It is one of few methods that can resolve distances at the nm scale both *in vitro* and *in vivo*. The method employs donor (D) and acceptor (A) fluorophores tethered to the macromolecule of interest and measures the radiationless energy transfer from the excited D to A. FRET has a very broad spectrum of applications, as it can cover a wide range of spatial and temporal resolution. It is suitable to study protein folding¹⁻³, recover conformational changes of polypeptides⁴ up to ribosomal subunits⁵. Also FRET measurements are useful for formulating kinetic schemes⁶⁻⁸ and in combination of different approaches can even reveal dynamics across five orders of magnitude in time (**Chapter 4**).

Yet, it has been challenging to verify and compare experimental results from different labs, as a common protocol for measurements and analysis was missing. Another obstacle is the wide usage of the home-build microscopes and in-house software, implemented individually in many labs. To resolve this issue, my group together with 20 groups from all over the world participated in the blind study to measure FRET distances on the common samples, compare the results and issue the guideline with methodological recommendation (**Chapter 2**). We demonstrated that FRET Efficiency could be obtained with st.dev. up to ± 0.02 with the suggested method. In addition to that I provide the explicit characterization of the dyes properties that are essential for fluorescence spectroscopy with nucleic acids.

In my dissertation I combined experimental data obtained from sm-FRET studies with computer simulations to resolve spatial structures: (i) RNA three-way junctions (RNA 3WJs) and (ii) a 12-mer chromatin array.

(i) RNA three-way junctions

Chapter 3 involved three RNA 3WJ with different sequence at the junction in order to study the effect of this parameter on the structural conformation. To resolve RNA 3WJ 3D structures with high accuracy and precision 42-45 sm-FRET measurements are performed for each structure. The analysis include the studies of the sequence dependent conformations, different way of alignment and formulating a common representative structure for all RNA 3WJ. I found a unique solution for each studied RNA 3WJ. The findings also revealed that all obtained structural models of the RNA 3WJ are close to be planar but exhibit distinct coaxial stacking. Helix *a* with G-C pair at the junction never participates in the stacking interaction, indicating a specific spatial orientation of the helices that is coded by their sequence at the intersection. Also representing common structure appears to be not symmetrical and with inequivalent helical positions. Thorough analysis of experimental and modeling errors allowed us to determine the precision of $\sim 2 \text{ \AA}$.

(ii) 12-mer chromatin array

In **Chapter 4** two sm-FRET approaches are utilized: (i) confocal microscopy with Multiparameter Fluorescence Detection (MFD) of freely diffusing molecules and (ii) Total Internal Reflection Fluorescence (TIRF) microscope of the surface-immobilized molecules. Two major conformers of 12-mer chromatin array with a distinct stacking regime are resolved and dynamic-register model with at least eight states is formulated. Moreover, insights on register exchange dynamics are provided, reporting interchange between registers in millisecond time regime and local interaction between neighboring tetranucleosomes on microsecond time scale. This work also demonstrates that the chromatin effector heterochromatin protein 1 α (HP1 α) affects conformational changes of the chromatin fiber inducing its compactization. The binding mechanism of HP1 α and chromatin fibers is formulated and suggests rapid exchange dynamics on hundreds of millisecond to second timescale.

Lastly, resolved structural models for RNA 3WJ and 12-mer chromatin array together with their detailed documentation are ready for deposition to PDB-Dev archive.

Papers and Manuscript

Chapter 2 Precision and accuracy of single-molecule FRET measurements – a multi-laboratory benchmark study

Current status: published in *Nature Methods*, 2018, **15**, 669-676

Björn Hellenkamp, Sonja Schmid, **Olga Doroshenko**, Oleg Opanasyuk, Ralf Kühnemuth, Soheila Rezaei Adariani, Anders Barth, Victoria Birkedal, Mark E. Bowen, Hongtao Chen, Thorben Cordes, Tobias Eilert, Carel Fijen, Markus Götz, Giorgos Gouridis, Enrico Gratton, Taekjip Ha, Christian A. Hanke, Andreas Hartmann, Jelle Hendrix, Lasse L. Hildebrandt, Johannes Hohlbein, Christian G. Hübner, Eleni Kallis, Achillefs N. Kapanidis, Jae-Yeol Kim, Georg Krainer, Don C. Lamb, Nam Ki Lee, Edward A. Lemke, Brié Levesque, Marcia Levitus, James J. McCann, Nikolaus Naredi-Rainer, Daniel Nettels, Thuy Ngo, Ruoyi Qiu, Carlheinz Röcker, Hugo Sanabria, Michael Schlierf, Benjamin Schuler, Henning Seidel, Lisa Streit, Philip Tinnefeld, Swati Tyagi, Niels Vandenberk, Keith R. Weninger, Bettina Wünsch, Inna S. Yanez-Orozco, Jens Michaelis, Claus A.M. Seidel, Timothy D. Craggs, Thorsten Hugel

Authors contributions:

- B.H., T.H., J.M., C.S. designed the research;
- B.H., S.S., O.D., O.O., R.K., S.R.A., B.A., A.B., T.E., C.F., B.S., V.F., G.G., C.A.H., A.H., J.H., L.L.H., E.K., G.K., B.L., J.J.M., N.N., D.N., R.Q., C.R., B.S., H.S., L.S., S.T., N.V., B.W., I.S.Y. and T.D.C., T.C., C.G., M.A., P.H., V.H., B.H., N.C.R., T.S., A.M.V. performed measurements;
- B.H., S.S. and T.H. compared the measurements;
- all authors contributed to the analysis of the data and commented on the manuscript;
- B.H., S.S., T.D.C., J.M., C.S. and T.H. wrote the manuscript in consultation with O.D. and O.O.
- O.D. performed the model calculations.

Chapter 3 Accurate determination of the RNA three-way junctions via single-molecule high-precision FRET measurements

Current status: manuscript in preparation

Author contributions (O.D.):

- Experiment design: e.g. choosing optimal fluorescence labeling positions;
- Optimization of the sample preparation protocol;
- Sample and buffer preparation for single-molecule and eTCSPC measurements;
- Alignment of the single-molecule setup;
- Conduction of the single molecule and eTCSPC experiments;

- Analysis of all ensemble and single-molecule fluorescence data;
- Error estimation analysis;
- Generation of the structural models via Rigid Body Docking method;
- Estimation of model precision;
- Writing the dissertation chapter.

Chapter 4 Single-molecule FRET reveals multiscale chromatin dynamics modulated by HP1 α

Current status: published in *Nature Communications*, 2018, **9**, 235

Sinan Kilic, Suren Felekyan, **Olga Doroshenko**, Iuliia Boichenko, Mykola Dimura, Hayk Vardanyan, Louise C. Bryan, Gaurav Arya, Claus A.M. Seidel & Beat Fierz

Author contributions:

- B.F. coordinated the project;
- B.F., S.K. and C.A.M.S. conceived and designed the studies;
- B.F. supervised chromatin synthesis and reconstitution, and smTIRF studies;
- C.A.M.S. supervised the confocal smFRET studies and quantitative FRET analysis;
- S.K. synthesized labeled chromatin fibers, modified histones and performed smTIRF experiments;
- I.B. produced phosphorylated HP1 α and performed TIRF experiments;
- L.B. produced synthetic histones;
- S.F., O.D., S.K. and H.V. performed and analyzed confocal FRET experiments;
- S.F., C.A.M.S. and B.F. performed kinetic modeling;
- S.F. performed PDA;
- G.A. performed coarse-grained simulations;
- G.A. and B.F. generated chromatin models;
- O.D and M.D. performed FPS analysis with chromatin models;
- All authors were involved in data analysis and interpretation;
- All coauthors wrote the manuscript.

Contents

CHAPTER 1 GENERAL INTRODUCTION	1
1.1 Hierarchy of the nucleic acid structures	1
1.2 Methods in structural biology	2
1.3 Outline of the thesis.....	3
CHAPTER 2 PRECISION AND ACCURACY OF SINGLE-MOLECULE FRET MEASUREMENTS – A MULTI-LABORATORY BENCHMARK STUDY	6
2.1 Introduction.....	8
2.2 Results	10
2.2.1 Procedure to determine the experimental FRET efficiency $\langle E \rangle$	12
2.2.2 Distance determination.....	16
2.2.3 Distance uncertainties.....	18
2.3 Discussion	20
2.4 Online Methods	22
2.4.1 Samples	25
2.4.2 General correction procedure.....	26
2.4.3 Data acquisition.....	26
2.4.4 Uncertainty in distance due to R_0	30
2.5 Supplementary Material:	34
2.6 Appendix with my measurements and analysis	62
2.6.1 Material and methods.....	62
2.6.1.1 Setups and correction factors for given samples at given setups.....	62
<i>Single molecule Molecule Multiparameter Fluorescence Detection (MFD)</i>	62
<i>Ensemble Time Correlated Single Photon Counting (eTCSPC) setup</i>	64
2.6.1.2 Photon distribution analysis (PDA)	64
2.6.1.3 Gaussian distributed distance R_{DA} fitting of the time resolved fluorescence data	64
2.6.1.4 Global fit of the time-resolved polarized and magic angle fluorescence data	65
2.6.2 Results	67
2.6.2.1 MFD plots.....	67
2.6.2.3 PDA results.....	73
2.6.2.4 Ensemble Time Correlated Single Photon Counting (eTCSPC) results	77
<i>Fitting results of the Gaussian distributed distances R_{DA}</i>	78
<i>eTCSPC fluorescent decay measurement of donor only samples under magic angle condition</i>	80

<i>eTCSPC fluorescent polarized decay measurement of FRET samples</i>	82
<i>Anisotropy results</i>	85
2.6.3 Joint table of the results of all experimental methods	85
CHAPTER 3 ACCURATE STRUCTURAL DETERMINATION OF THE RNA THREE-WAY JUNCTIONS VIA SINGLE-MOLECULE HIGH-PRECISION FRET MEASUREMENTS	87
3.1 Introduction	87
3.2 Materials and Methods	88
3.2.1 System of study and nomenclature	88
3.2.2 Oligonucleotides	90
3.2.3 Hybridization procedure	91
3.2.4 Measurement buffer	92
3.2.5 Instrumentation and calibration measurements	92
<i>Ensemble Time Correlated Single Photon Counting (eTCSPC)</i>	92
<i>Confocal microscope setups</i>	93
3.2.6 Calibration measurements	94
<i>Single-molecule data calibration with standard protocol with ds DNA and determination of detection efficiency</i> <i>g_G/g_R</i>	95
3.2.7 Data analysis	96
<i>Multi-parameter Fluorescence Detection (MFD)</i>	96
3.2.7.1 Fluorescence signals	97
3.2.7.2 Fluorescence lifetime	98
3.2.7.3 Steady state fluorescence anisotropy	98
3.2.7.4 1D and 2D histograms	99
3.2.7.5 Time-resolved experiments	101
<i>Fluorescence lifetime determination</i>	101
<i>Fluorescence quantum yield determination</i>	102
<i>Time-resolved fluorescence anisotropy</i>	102
3.2.7.6 Photon distribution analysis (PDA)	103
3.2.8 Error propagation	105
3.2.8.1 Confidence intervals for fit parameters in PDA	108
3.2.8.2 Uncertainties due to the orientation factor κ^2	108
3.2.9 FRET position and screening (FPS) calculation	110
3.2.9.1 Accessible Volume simulation	110
3.2.9.2 R_{MP} to $\langle R_{DA} \rangle_E$ conversion function	112
3.2.9.3 Rigid Body Docking	112
3.2.10 Cluster analysis of RNA 3WJ	116
3.2.11 Precision of the RBD structures via bootstrapping	117
3.3 Results and discussions	118
3.3.1 Position dependency of fluorescent dyes	118
3.3.1.1 Acceptor fluorescence lifetime and fluorescence quantum yield	118
<i>End-labeled molecules</i>	119
<i>Labels at the junction region</i>	119

<i>Labels in the internal helical part</i>	120
3.3.1.2 Donor fluorescence lifetime and quantum yield	122
3.3.1.3 Fluorescence residual anisotropy	124
<i>Acceptor residual anisotropy</i>	124
<i>Donor residual anisotropy</i>	127
3.3.2 2D MFD plots.....	132
3.3.3 PDA analysis	133
3.3.4 Error estimation analysis.....	134
3.3.4.1 Calibration factors.....	134
3.3.4.2 κ^2 estimation.....	135
3.3.4.3 All uncertainties	140
3.3.5 Model selection.....	148
3.3.6 Visual representation and comparison of RNA 3WJ	149
3.3.7 Cluster analysis of the rigid body docking (RBD) results	151
3.3.7.1 Model assessment	153
3.3.8 Conformational space for RBD structures.....	156
3.3.8.1 Mutual angles	158
3.3.8.2 Rotation angles	160
3.3.8.3 Structural planarity	163
3.3.8.4 Alignment via sequence.....	165
3.3.8.5 Comparison of two alignment methods	171
3.4 Conclusions and future directions	176
3.5 Supporting information.....	179
3.5.1 eTCSPC fluorescence decay measurements of single labeled RNA 3WJ	179
3.5.1.1 Donor only lifetime measurements	179
3.5.1.2 Acceptor only lifetime measurements.....	182
3.5.2 eTCSPC polarized fluorescence decay measurements of acceptor labeled RNA3WJ	187
3.5.3 Additional 2D MFD histograms and static FRET lines.....	192
3.5.3.1 2D MFD histograms	192
3.5.3.2 Static FRET lines	208
3.5.4 PDA analysis	214
3.5.4.1 Additional S_g/S_r histograms.....	214
<i>Measurements of $J(acd)$</i>	214
<i>Measurements of $J(abd)$</i>	219
<i>Measurements of $J(bcd)$</i>	223
3.5.4.2 Tables with fitting parameters.....	227
CHAPTER 4 SINGLE-MOLECULE FRET REVEALS MULTISCALE CHROMATIN DYNAMICS MODULATED BY HP1A.....	234
4.1 Introduction.....	235
4.2 Results	235

4.3 Conclusions	242
CHAPTER 5 CONCLUSIONS	244
ABBREVIATIONS AND NOMENCLATURE	245
ACKNOWLEDGEMENT	248
CHAPTER 6 REFERENCES.....	250

Published Papers

- Publication I** **Precision and accuracy of single-molecule FRET measurements
– a multi-laboratory benchmark study**
- Publication II** **Single molecule FRET reveals multiscale chromatin dynamics
modulated by HP1 α**

Chapter 1 General Introduction

1.1 Hierarchy of the nucleic acid structures

Nucleic acids are very important biomolecules and essential to all living forms, from complex organisms with eukaryotic cells to more primitive prokaryotes. Eukaryotic cells locate their DNA in the nucleus, mitochondria and chloroplasts, while RNA can be found in the nucleus and cytoplasm. However, prokaryotes do not have a nucleus, and thus contain their DNA and RNA in the cytoplasm. DNA and RNA perform different functions in cells. DNA encodes genetic information and stores it as genes, while RNA converts the code into new proteins that catalyzes chemical reactions in living organisms.

Structurally, DNA and RNA consist of only 4 building blocks called nucleotides. DNA and RNA share adenine (A), cytosine (C) and guanine (G), while thymine (T) occurs only in DNA and uracil (U) only in RNA. Sequence of nucleotides are linked by phosphodiester bonds into very diverse nucleotide strings and present the lowest level in nucleic acid complexity, the so called primary structure (Figure 1.1). Next step of organization is the secondary structure. It features DNA or RNA strands associated through their nucleotides specifically via hydrogen bonds. Complementary bases are connected in a specific manner, forming so called Watson-Crick base pairs, namely C-G in DNA and RNA, A-T in DNA and A-U in RNA. Complementary strands run in opposite directions and generate a helical shape that is fundamental component of the secondary and tertiary structure. Helices of different lengths are present in diverse and complex biomolecules, linked together in various junctions, connected via single strands, bulges, or decomposed into loops^{9 10-13}. And finally, in eukaryotic cells DNA can be bound to eight proteins called histones to form nucleosomes that consequently pack into higher-order chromatin fiber^{14 15}, forming DNA quaternary structures.

Such gradation allows addressing the problem at different levels of nucleic acid complexity, aimed at resolving 3D structure of macromolecule, taking into account the steric constrains, geometrical parametrization of the molecular subunits and their tertiary contacts and interaction with the environment. Also it is crucial to recognize structural heterogeneities and determine their stability. Macromolecule can be functional in some predominant state or during interstate transition^{15,16}. So revealing the kinetic scheme of the conformational changes will throw light on the underlying mechanism of binding with diverse partners or local interaction that resolves in folding.

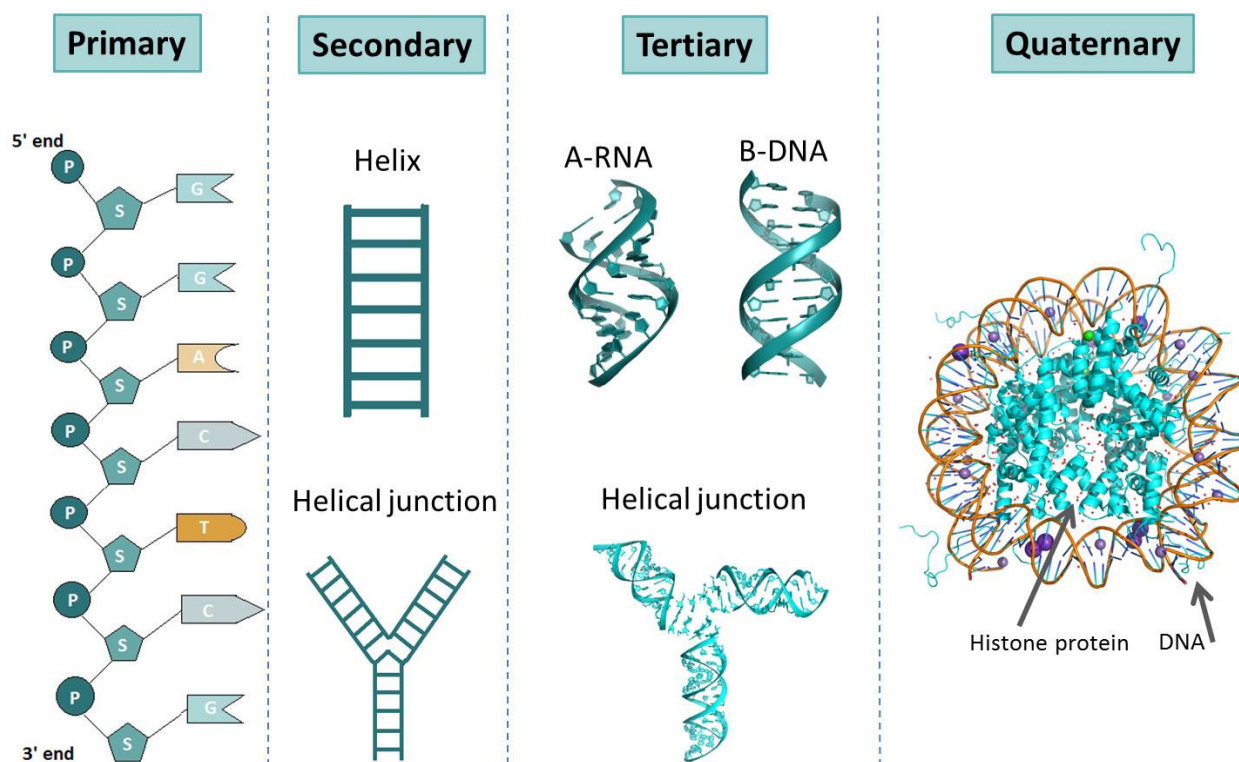


Figure 1.1. Schematic representation of the structural levels of nucleic acids. Primary level is presented with DNA sequence; Secondary level is presented with double helix and helical three –way junction; Tertiary level: A- form RNA (PDB: ADNA), B-form DNA (PDB: 1BNA) and RNA 3WJ J(acd) studied in this work; Quaternary level: nucleosome (PDB: 1EQZ)

1.2 Methods in structural biology

Over the past few decades a lot of effort was invested in methodologies in order to resolve biomolecular structures and link them with their functionality. Fluorescence based techniques, cryogenic electron microscopy (cryo-EM), double electron-electron resonance (DEER) techniques were revolutionized to become complementary tools to the well-established x-ray crystallography, electron microscopy, and NMR spectroscopy. Each of these techniques has its own advantages and limitations, so in order to address a biological question correctly, an appropriate method or combination of methods have to be employed. Important factors to consider are the size of molecule, its primary or secondary structure, expected timescale of conformational transition, resolution and *in vitro* or *in vivo* application. One of the most recognized methods, X-ray crystallography, is a powerful tool to obtain sub-Å resolution in structure^{17,18}, however it reports only the average conformation, struggling to disassemble states of dynamic molecules. Another established tool, NMR, has an advantage to study molecules in solution and to recover structural ensembles and conformational flexibility of different regions of the studied object^{19,20}. However, the method is limited to proteins smaller than 35 kDa and requires a large amount of the sample. Electron microscopy and cryo-

EM are used for large structural assemblies, but provides only nm resolution. In light of these facts, Förster Resonance Energy Transfer (FRET) is an optimal method that does not require molecules of particular size and can be employed both *in vitro* and *in vivo*. The macromolecule is required to be labeled with two fluorescence dyes, a donor-acceptor pair, where non-radiative energy transfers occurs from excited donor to acceptor. This approach allows detecting of structural heterogeneities as well as conformational changes or interaction between molecules with spatial resolution of 2 Å²¹.

1.3 Outline of the thesis

In this thesis, I present a study on the nucleic acid systems with increasing complexity, starting with probing single-molecule FRET method and working towards establishing a worldwide recognized protocol with robust double stranded DNA (dsDNA) (**Chapter 2**). Systems like these are well studied and described²²⁻²³⁻²⁶ and widely used in method probing²⁷, DNA nanotechnology²⁸ or as molecular diagnostic agent²⁹. In case of this work dsDNA was used to demonstrate the comparability of the FRET measurements among the scientists worldwide. To diversify the experiment and to probe whether the fluorescence properties of the dyes can affect the distance calculation, four different dye pairs were selected as labels. Next challenge that was addressed was how to compare acquired FRET distances from different labs as different data acquisition and analysis require home-built microscopes and in-house written software. Until this study, there was no common language and many terms were introduced in the groups individually, requiring deep understanding of the terminology of the particular community. Thus, unified nomenclature was suggested. Also detailed methodological description of measurements and data analysis were absent, to guide through the major problems of the method and enable the researches to validate and compare their results within the community. In the main text we focus on the most common, used in the community, intensity based method, where signals in the green (“donor”) and red (“acceptor”) channels are recorded and used to calculate interdye distance. Careful estimation of the distance uncertainties is a prerequisite for reporting the distances with high accuracy and precision. Furthermore, there are many other fluorescence methods that are widely used³⁰⁻³³ and can be advantageous if temporal resolution is of interest. Thus, complementary to the intensity-based method, we report results from ensemble lifetime, single molecule lifetime and phasor approach methods. My measurement and analysis for this paper are presented in **Chapter 2.5**.

Chapter 3 deals with the nucleic acid systems of higher complexity. In this section I present how single molecule high precision FRET measurements can accurately define 3D structures of RNA three-way junction systems and present the structural variation due to the change in sequence. Helical junctions are among many structural motifs that are responsible for RNA tertiary arrangements. Conformational behavior can be strongly affected by helical stacking interactions, helical rotation and their relative orientation, or interaction with the solvent that increases the rate of binding sites for ions.

Recovering the fully structural information will link the 3D structures to understand their fundamental functions in the cells³⁴⁻³⁷. Despite the great effort in understanding junctional motifs^{38 39 40 9,41,42}, accurate structural definition of the junctions without bulges remain poorly understood.

In this work I determine the structures of the three different RNA 3WJ by performing more than 40 single-molecule FRET experiments on each of the construct. Recovered distance set is used to reconstruct structural model. To summarize I report the experimental and modeling uncertainties, accounting for daily calibration procedure, reference sample and dye behavior.

Finally, **Chapter 3.3.1** is dedicated to the fluorescence properties of dyes. Quality of the reported interdye distance and its uncertainties is strongly dependent on the proper account of the photophysical properties of the dyes. For example, fluorescence quantum yield of the acceptor strongly contributes to the observed apparent FRET efficiency distribution broadening⁴³ and should not be confused with conformational exchanges. Also careful analysis of the donor and acceptor residual anisotropies is needed to rationalize dye motion and account for the relative orientation of the transition dipole of the dyes⁴⁴. Therefore I present the systematic ensemble analysis of the fluorescent quantum yield and anisotropy of the donor Alexa488 and acceptor Cy5 dyes and demonstrate that these characteristics strongly depend on the microenvironment of the dye and are position dependent.

Chapter 4 provides insights into organization of nucleosome units into higher-order chromatin fiber, determines heterogeneities and reveals its dynamics on a timescale from microsecond to second.

Efficient packaging DNA into chromatin allows fitting and storing DNA sequence into the nucleus. Unraveling how mononucleosomes rearrange into chromatin fiber is key to understanding how it prevents DNA damage, regulates DNA replication and gene expression.

Early works employing electron microscopy^{45 46} suggested chromatin folding in zig-zag ribbon that minimizes contacts between the nucleosomes or solenoid-type arrangement, depending on linker DNA length. Other techniques that address structural analysis like x-ray crystallography and neutron scattering^{14,47,48} support this models as well.

Unfortunately, these methods cannot provide any insights on the dynamical nature of the chromatin fibers or their subunits, although there is sufficient evidence in the literature on the existence dynamic rearrangements^{8,49-52}.

Also we investigated whether chromatin fiber can be modulated by protein factors. For this study we chose heterochromatin 1 α (HP1 α) that is known to bind histone H3K9Me3 in multivalent fashion. Being highly dynamic itself^{53,54}, chromatin effector HP1 α involved in chromatin compaction and enables gene silencing⁵³⁻

⁵⁵. However, there is no evidence on structural information of chromatin-effector complex and how HP1 α controls chromatin motion. Also information about dynamics of such association remains unclear.

In this section I present the study on 12-mer nucleosome array, labeled with two different FRET pairs with diverse Förster radii. This enables us to register wide range of interdye distances and probe distinct contacts and motions. To recover structural states and dynamic on timescale from microseconds to seconds, we combine two smFRET methods: confocal microscopy of freely diffusing molecules in solution and total internal reflection fluorescence (TIRF). Together with computational structural modeling method FPS²¹ we were able to present chromatin fiber as two distinct stacking registers and reveal their multiscale dynamics on micro- to millisecond timescale.

Chapter 2 Precision and accuracy of single-molecule FRET measurements – a multi-laboratory benchmark study

Björn Hellenkamp^{1,°}, Sonja Schmid^{1,°}, **Olga Doroshenko**²⁰, Oleg Opanasyuk²⁰, Ralf Kühnemuth²⁰, Soheila Rezaei Adariani¹⁵, Anders Barth²¹, Victoria Birkedal⁹, Mark E. Bowen¹¹, Hongtao Chen²⁶, Thorben Cordes^{14,25}, Tobias Eilert¹⁹, Carel Fijen⁷, Markus Götz¹, Giorgos Gouridis^{14,25}, Enrico Gratton²⁶, Taekjip Ha²², Christian A. Hanke²⁰, Andreas Hartmann¹⁷, Jelle Hendrix^{5,6}, Lasse L. Hildebrandt⁹, Johannes Hohlbein^{7,8}, Christian G. Hübner¹⁶, Eleni Kallis¹⁹, Achillefs N. Kapanidis¹⁰, Jae-Yeol Kim²³, Georg Krainer^{17,18}, Don C. Lamb²¹, Nam Ki Lee²³, Edward A. Lemke³, Brié Levesque¹¹, Marcia Levitus²⁴, James J. McCann¹¹, Nikolaus Naredi-Rainer²¹, Daniel Nettels⁴, Thuy Ngo²², Ruoyi Qiu¹², Carlheinz Röcker¹⁹, Hugo Sanabria¹⁵, Michael Schlierf¹⁷, Benjamin Schuler⁴, Henning Seidel¹⁶, Lisa Streit¹⁹, Philip Tinnefeld^{13,27}, Swati Tyagi³, Niels Vandenberk⁵, Keith R. Weninger¹², Bettina Wünsch¹³, Inna S. Yanez-Orozco¹⁵, Jens Michaelis^{19,*}, Claus A.M. Seidel²⁰, Timothy D. Craggs^{2,10}, Thorsten Hugel¹

¹Institute of Physical Chemistry, University of Freiburg, Germany

²Department of Chemistry, University of Sheffield, S3 7HF, UK

³Structural and Computational Biology Unit, EMBL Heidelberg, Germany

⁴Department of Biochemistry, University of Zurich, Switzerland

⁵Laboratory for Photochemistry and Spectroscopy, Department of Chemistry, University of Leuven, B-3001 Leuven, Belgium

⁶Present address: Hasselt University, Faculty of Medicine and Life Sciences and Biomedical Research Institute, B-3590 Hasselt, Belgium

⁷Laboratory of Biophysics, Wageningen University & Research, 6708 WE, Wageningen, NL

⁸Microspectroscopy Research Facility Wageningen, Wageningen University & Research, 6708 WE, Wageningen, NL

⁹Interdisciplinary Nanoscience Center and Department of Chemistry, Aarhus University, 8000 Aarhus C, Denmark

¹⁰Gene Machines group, Clarendon Laboratory, Department of Physics, University of Oxford, Parks Road, OX1 3PU, Oxford, UK

¹¹Department of Physiology & Biophysics, Stony Brook University, Stony Brook, NY 11794, USA

¹²Department of Physics, North Carolina State University, Raleigh, NC 27695 USA

¹³Institute of Physical & Theoretical Chemistry, and Braunschweig Integrated Centre of Systems Biology (BRICS), and Laboratory for Emerging Nanometrology (LENA), Braunschweig University of Technology, Rebenring 56, 38106 Braunschweig, Germany

¹⁴Molecular Microscopy Research Group, Zernike Institute for Advanced Materials, University of Groningen, Nijenborgh 4, 9747 AG Groningen, The Netherlands

¹⁵Department of Physics and Astronomy, Clemson University, 29634 Clemson, SC, USA

¹⁶Institute of Physics, University of Lübeck, Germany

¹⁷B CUBE – Center for Molecular Bioengineering, TU Dresden, Arnoldstr. 18, 01307 Dresden, Germany

¹⁸Molecular Biophysics, University of Kaiserslautern, Erwin-Schrödinger-Str. 13, 67663 Kaiserslautern, Germany.

¹⁹Institute for Biophysics, Ulm University, Albert-Einstein-Allee 11, 89081 Ulm, Germany

²⁰Chair for Molecular Physical Chemistry, Heinrich-Heine-Universität Düsseldorf, 40225 Düsseldorf, Germany

²¹Lamb lab, Department of Chemistry, LMU München, Butenandtstrasse 5-13, 81377 Germany

²²Ha lab, Department of Biomedical Engineering, John Hopkins University, USA

²³School of Chemistry, Seoul National University, Seoul, South Korea

²⁴School of Molecular Sciences and The Biodesign Institute, Arizona State University, USA

²⁵Physical and Synthetic Biology, Faculty of Biology, Ludwig Maximilians-Universität München, Großhadernerstr. 2-4, 82152 Planegg-Martinsried, Germany

²⁶Department of Biomedical Engineering, University of California, Irvine, Irvine, California, USA

²⁷ Department of Chemistry, Ludwig-Maximilians-Universitaet Muenchen, Butenandtstr. 5-13, 81377 München, Germany.

° these authors contributed equally

2.1 Introduction

Förster Resonance Energy Transfer (FRET)⁵⁶, also sometimes termed Fluorescence Resonance Energy Transfer, has become a well-established method for studying biomolecular conformations and dynamics at both the ensemble⁵⁷⁻⁵⁹ and the single-molecule (sm) level^{4,21,60-63}. In such experiments, the energy transfer between a donor and an acceptor fluorophore pair is quantified with respect to their proximity⁵⁶. The fluorophores are usually attached via flexible linkers to defined positions of the system under investigation. Amongst other factors, the transfer efficiency depends on the inter-dye distance, which is well described by Förster's theory for distances $> 30 \text{ \AA}$ ^{64,65}. Accordingly, FRET has been termed a 'spectroscopic ruler' on the molecular scale⁵⁷. Such a ruler is an important tool to determine distances *in vitro*, and even in cells⁶⁶, with potentially Ångström accuracy and precision. In its single-molecule implementation, FRET largely overcomes ensemble- and time-averaging and can uncover individual species within heterogeneous and dynamic biomolecular complexes, as well as transient intermediates⁶⁰.

The two most popular smFRET approaches to determine distances are confocal microscopy on freely diffusing molecules, and total internal reflection fluorescence (TIRF) microscopy on surface-attached molecules. Here, we focus on intensity-based measurements, in which the FRET efficiency, E , is determined from donor and acceptor photon counts, and then subsequently used to calculate the inter-fluorophore distance according to Förster's theory.

The vast majority of intensity-based smFRET studies to date rely on characterizing relative changes in FRET efficiency. This ratiometric approach is often sufficient to distinguish different conformations of a biomolecule (e.g. an open conformation with low FRET efficiency vs. a closed conformation with high FRET efficiency), and to determine their interconversion kinetics. Yet, determining distances provides additional information that can be used, for example, to compare with known structures, or assign conformations to different structural states. In combination with prior structural knowledge and computer simulations, FRET-derived distances are increasingly being used to generate novel biomolecular structural models using hybrid structural tools^{21,61,62,67-70}.

However, comparing and validating distance measurements from different labs are difficult, especially given the lack of detailed methodological descriptions in many publications. In addition, different methods for data acquisition and analysis, often using home-built microscopes with in-house software, can have very different uncertainties and specific pitfalls. To overcome these issues, we have developed general methodological recommendations and well-characterized FRET-standard samples to enable the validation of results and the estimation of distance accuracy and precision. This approach should allow the scientific community to confirm consistency of smFRET-derived distances and structural models. To

facilitate data validation across the field, we recommend the reporting of specific FRET-related parameters with a unified nomenclature.

Various fluorescence intensity- and lifetime-based procedures have been proposed with the aim of determining FRET efficiencies^{63,71-76}. Here, we present a general methodological guide based on some of these procedures that allows us to obtain quantitative and reliable smFRET data. The step-by-step procedure results in a consistent determination of FRET efficiencies that corrects for dye and setup characteristics and is independent of the software used. It includes deconvolution of the underlying uncertainties involved in the determination of the necessary correction factors, enabling scientists to specify the overall uncertainty of the determined FRET efficiency. These steps are tested in a worldwide, comparative, blind study by 20 participating labs. For standardized FRET samples, we show that FRET efficiencies can be determined with a standard deviation $E < \pm 0.05$.

In order to convert the measured smFRET efficiency to a distance, the Förster equation is used (Table 2.1, eq. (III)), which critically depends on the dye-pair-specific Förster radius, R_0 . We discuss the measurements required to determine R_0 and the associated uncertainties. Another uncertainty arises from the fact that many positions are being sampled by the dye relative to the biomolecule to which it is attached. Therefore, specific models are used to describe the dynamic movement of the dye molecule, during the recording of each FRET-efficiency measurement^{68,69}. In summary, the investigation of the underlying error sources enables us to specify uncertainties for individual FRET-derived distances. We anticipate that the investigated samples and the presented procedure will help unify the research field, serving as a standard for future publications and benchmarking the use of smFRET as an accurate spectroscopic ruler.

2.2 Results

We have chosen double-stranded DNA as a FRET standard for the following reasons: any DNA sequence can be synthesized; FRET dyes can be specifically tethered at desired positions; the structure of B-form DNA is well characterized; and the samples are stable at room temperature for a time window that is large enough for shipping to labs around the world. The donor and acceptor dyes are attached via C2- or C6-amino-linkers to thymidines of opposite strands (see Figure 2.6). These thymidines were separated either by 15 or by 23 base pairs (Figure 2.1 and *Online Methods section 1*). The attachment positions were known only to the reference lab that designed the samples. Based on the resulting high-efficiency and low-efficiency samples we were able to determine all correction parameters and to perform a self-consistency test (see below).

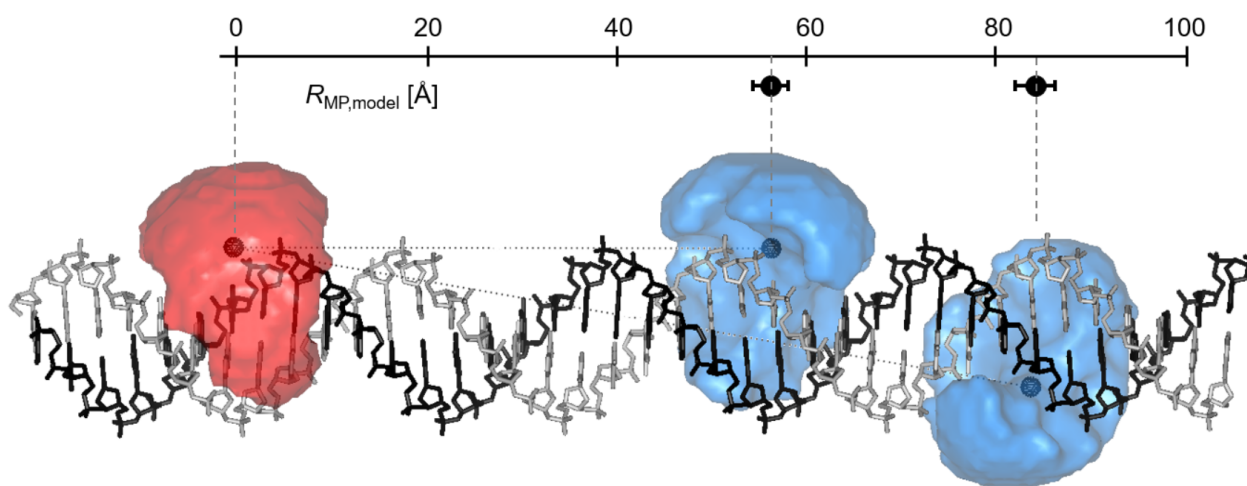


Figure 2.1 Schematic of the FRET standard molecules. Double-stranded DNA is labeled with a FRET pair at 15 or 23 base-pair separation (for sequences see Online Methods). One DNA strand labeled with an acceptor dye (red) and the complementary strand labeled with a donor dye (blue) at one of two positions were annealed to generate the FRET standards. The accessible volumes (AVs) of the dyes are illustrated as semi-transparent surfaces and were calculated using freely available software²¹. The mean dye positions are indicated by darker spheres (assuming homogeneously distributed dye positions, see Supplementary Note 2). The distance between the mean dye positions is defined as $R_{MP,model}$. Calculated values for $R_{MP,model}$ together with error bars obtained by varying parameters of the AV model are displayed (see Supplementary Note 2). The B-DNA model was generated using the Nucleic Acid Builder version 04/17/2017 for Amber⁷⁷.

A wide variety of dyes are used in smFRET studies. Here we used Alexa and Atto dyes (Figure 2.6) due to their high quantum yields and well-studied characteristics. Eight hybridized double-stranded FRET samples were shipped to all participating labs. In the main text, we focus on four FRET samples that were measured by most labs in our study (see *Online Methods section 1* for details):

1-1o: Atto550/Atto647N, 23 bp-separation.

1-hi: Atto550/Atto647N, 15 bp-separation.

2-lo: Atto550/Alexa647, 23 bp-separation.

2-hi: Atto550/Alexa647, 15 bp-separation.

In this nomenclature, the number refers to the dye pair and the last two letters indicate either the low-efficiency (lo) or high-efficiency (hi) configurations. The results with other FRET pairs (Alexa488/Alexa594 and Alexa488/Atto647N) at these positions are reported in Figure 2.7 and *Supplementary Note 1*. As a first test for the suitability of the labels, we checked the fluorescence lifetimes and time-resolved anisotropies (Table 2.6) of all donor-only and acceptor-only samples. The results indicate that there is no significant quenching and that all dyes are sufficiently mobile at these positions (see *Supplementary Note 1*).

There are two main routes to measuring accurate distances by FRET: fluorescence intensity-based and fluorescence lifetime-based measurements. In this study, we focus on the intensity-based methods, because they are easier to implement and were performed by more labs in our blind study. Specifically, we discuss solution-based measurements collected using a confocal microscope, and surface-based measurements collected using a TIRF microscope. In the framework of this study, other measurements were also performed using different fluorophores (samples 3 and 4) and different FRET methods (ensemble lifetime³³, single-molecule lifetime⁷³, and a phasor approach⁶²; for these results, see Figure 2.7 and *Supplementary Note 1 and 5*).

Most intensity-based FRET measurements are performed on custom-built setups for single-molecule detection featuring at least two separate spectral detection channels for donor and acceptor emission (Figure 2.8 and Figure 2.9). Here, the main challenge is the measurement of absolute corrected fluorescence intensities. The ideal solution is a ratiometric approach which for intensity-based confocal FRET measurements was pioneered by Weiss and coworkers using alternating two color laser excitation (ALEX) with microsecond pulses^{74,78}. In this approach the total fluorescence signal (donor and acceptor emission) after donor excitation is normalized to the acceptor fluorescence after acceptor excitation, to correct for dye and instrumental properties⁷⁴. The ALEX approach was also adapted for TIRF measurements⁷⁶. To increase time resolution and to enable time-resolved spectroscopy, Lamb and coworkers introduced pulsed interleaved excitation (PIE) with picosecond pulses⁷⁹.

In both confocal and TIRF microscopy, the corrected FRET efficiency histogram is determined first, from which the expectation value of the FRET efficiency $\langle E \rangle$ is computed. Subsequently, the distance is calculated, assuming a suitable model for the inter-dye distance distribution and dynamics^{4,27,64}. Below, we describe a concise and robust procedure that is suitable for both confocal and TIRF-based

measurements. The results of our blind study underline the robustness and precision of this method. Further, we derive self-consistency arguments and comparisons to structural models and thereby confirm the accuracy of this method.

2.2.1 Procedure to determine the experimental FRET efficiency $\langle E \rangle$

Our general procedure is largely based on the Lee et al. approach⁷⁴, with modifications to establish a robust workflow and standardize the nomenclature. Intensity-based determination of FRET efficiencies requires the consideration of certain correction factors (see Table 2.1): Background signal correction (BG) from donor and acceptor channels; factor for spectral crosstalk (α), arising from donor fluorescence leakage in the acceptor channel; factor for direct excitation (δ) of the acceptor with the donor laser; detection correction factor (γ). The optimal way to determine these factors is by alternating the excitation between two colors, which allows for the determination of the FRET efficiency (E) and the relative stoichiometry (S) of donor and acceptor dyes, for each single-molecule event. This introduces the additional excitation correction factor (β) to normalize to equal excitation rates (see *Online Methods section 2.6*).

The following step-by-step guide for intensity-based FRET data analysis is subdivided for the type of FRET experiment (confocal and TIRF); notably, the order of the steps is crucial for the correct application of this procedure.

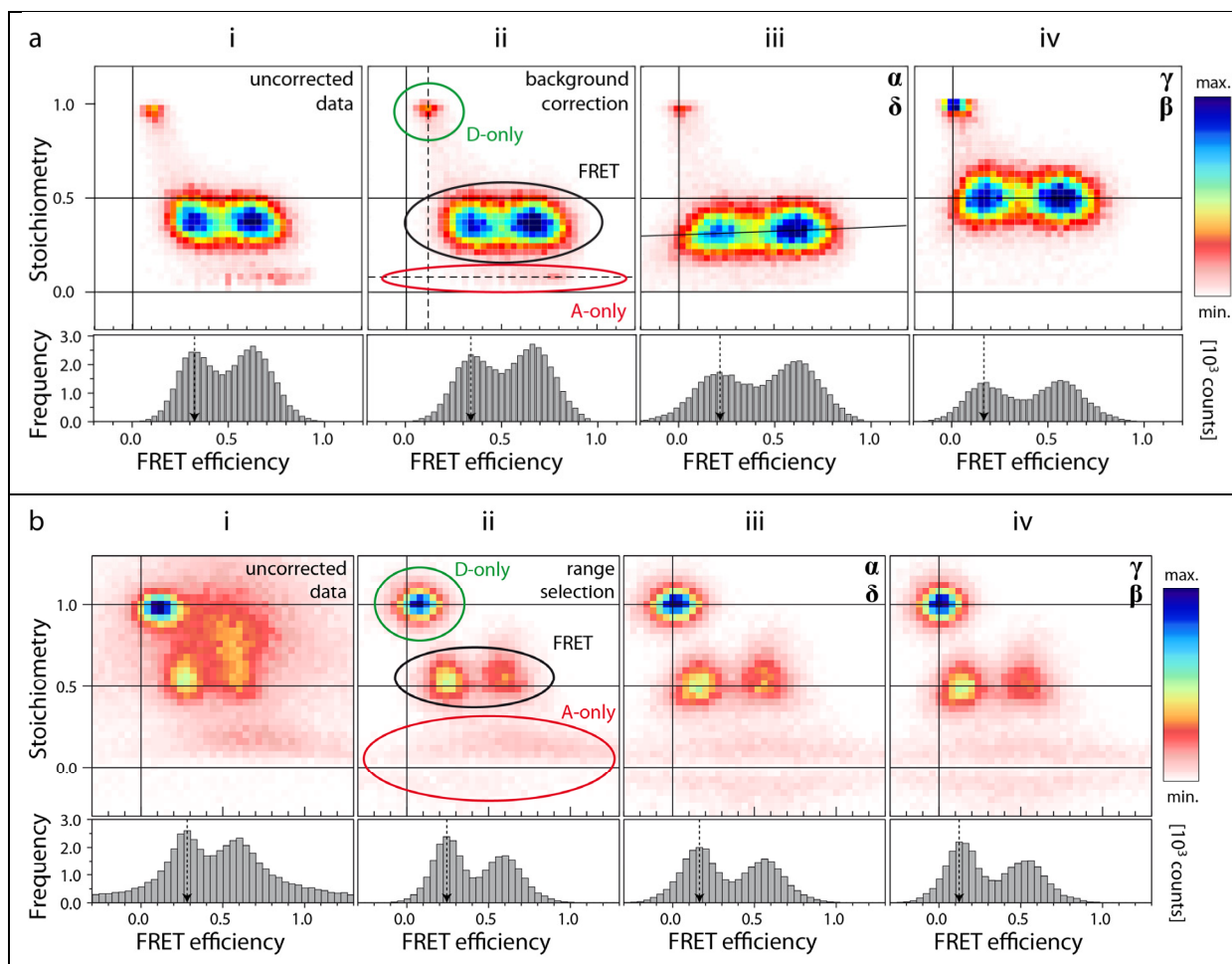


Figure 2.2 Stepwise correction of confocal (a) or TIRF (b) data, shown for the combination of sample 1-lo and 1-hi. The general terms stoichiometry S and FRET efficiency E are used here in place of the corresponding specific terms for each correction step (see Online Methods – section 2). (i) ${}^iS_{app}$ vs ${}^iE_{app}$, (ii) ${}^{ii}S_{app}$ vs ${}^{ii}E_{app}$, (iii) ${}^{iii}S_{app}$ vs ${}^{iii}E_{app}$, (iv) S vs E . (a) Workflow for correcting the confocal data for background (i->ii), leakage (factor α) and direct excitation (δ) (ii->iii), excitation and detection factors (β, γ) (iii->iv). (b) Workflow for correcting the TIRF data for background and photo-bleaching by selection of the pre-bleached range (i->ii), leakage and direct excitation (ii->iii), detection and excitation factors (iii->iv). The efficiency histograms below show a projection of the data with a stoichiometry between 0.3 and 0.7. Note the significant shift of the FRET efficiency peak positions, especially for the low FRET efficiency peak ($E \sim 0.25$ uncorrected to $E \sim 0.15$ fully corrected). Donor only (D-only), FRET and acceptor only (A-only) populations are specified.

Diffusing molecules: Confocal Microscopy

In confocal-based smFRET experiments with alternating excitation, photon bursts from individual molecules freely diffusing through the laser focus of a confocal microscope are collected and analyzed. From the data, first a 2D histogram of the uncorrected FRET efficiency (${}^iE_{app}$) versus uncorrected stoichiometry (${}^iS_{app}$) is calculated (Figure 2.2a(i)). See *Online Methods (section 2.0)* for the detailed procedure. Then, the average number of background photons is subtracted for each channel separately (Figure 2.2a(ii)). Next, to obtain the FRET sensitized acceptor signal (F_{AD}), donor leakage (α) ${}^{ii}I_{Dem|Dex}$

and direct excitation ($\delta^{ii}I_{Aem|Aex}$) must be subtracted from the acceptor signal after donor excitation. As samples never contain 100% photoactive donor and acceptor dyes, the donor- and acceptor-only populations are selected from the measurement and used to determine the leakage and direct excitation (Figure 2.2a(iii)). After this correction step, the donor-only population should have an average FRET efficiency of 0 and the acceptor-only population should have an average stoichiometry of 0.

The last step deals with the detection correction factor γ and the excitation correction factor β . If at least two species (two different samples or two populations within a sample) with different inter-dye distances are present, they can be used to obtain the “*global γ -correction*”. If one species with significant distance fluctuations, e.g. through intrinsic conformational changes, is present a “*single-species γ -correction*” may be possible. Both correction schemes assume that the fluorescence quantum yields and extinction coefficients of the dyes are independent of the attachment point (see *Online Methods section 2.6*). The correction factors obtained by the reference lab are compiled in Table 2.2. The final corrected FRET efficiency histograms are shown in Figure 2.2a(iv). The expected efficiencies $\langle E \rangle$ are obtained as the mean of a Gaussian fit to the respective efficiency distributions (see *Online Methods section 2.7*).

Surface-attached molecules: TIRF Microscopy

The correction procedure for TIRF-based smFRET experiments is similar to the procedure for confocal-based experiments. In the procedure used for ALEX data⁷⁶, a 2D histogram of the uncorrected FRET efficiency (iE_{app}) versus uncorrected stoichiometry (iS_{app}) is first generated (Figure 2.2b(i)). The background subtraction is critical in TIRF microscopy as it can contribute significantly to the measured signal. Different approaches can be used to accurately determine the background signal (see *Online Methods section 2.3*), such as measuring the background in the vicinity of the selected particle or measuring the intensity after photobleaching (Figure 2.2b(ii)). After background correction, the leakage and direct excitation can be calculated from the ALEX data as for confocal microscopy (Figure 2.2b(iii)).

Again, determination of the correction factors β and γ are critical⁷². As in confocal microscopy, one can use the stoichiometry information available from ALEX when multiple populations are present to determine an average detection correction factor (*global γ -correction*). In TIRF microscopy, the detection correction factor can also be determined on a molecule-by-molecule basis, provided the acceptor photobleaches before the donor (*individual γ -correction*). In this case, the increase in the fluorescence of the donor can be directly compared to the intensity of the acceptor before photobleaching. A 2D histogram of the corrected FRET efficiency versus the corrected stoichiometry is shown in Figure 2.2b(iv).

In the absence of alternating excitation, the following problems were occasionally encountered during this study: (i) the low-FRET efficiency values were shifted systematically to higher efficiencies, because FRET efficiency values at the lower edge are overlooked due to noise; (ii) the direct excitation was difficult to detect and correct for, due to its small signal to noise ratio; (iii) the acceptor bleaching was difficult to detect for low FRET efficiencies. Therefore, implementation of ALEX is strongly recommended for obtaining accurate FRET data.

Nine of the twenty participating labs determined FRET efficiencies by confocal methods for sample 1 and 2 (Figure 2.3a). Seven of the twenty participating labs determined FRET efficiencies by TIRF-based methods and these are summarized in Figure 2.3b. The combined data from all labs measuring samples 1 and 2 agree very well, with a standard deviation for the complete data set of $\Delta E < \pm 0.05$. This is a remarkable result, considering that different setup types were used (confocal- and TIRF-based setups) and different correction procedures were applied (e.g. individual, global or single species γ -correction).

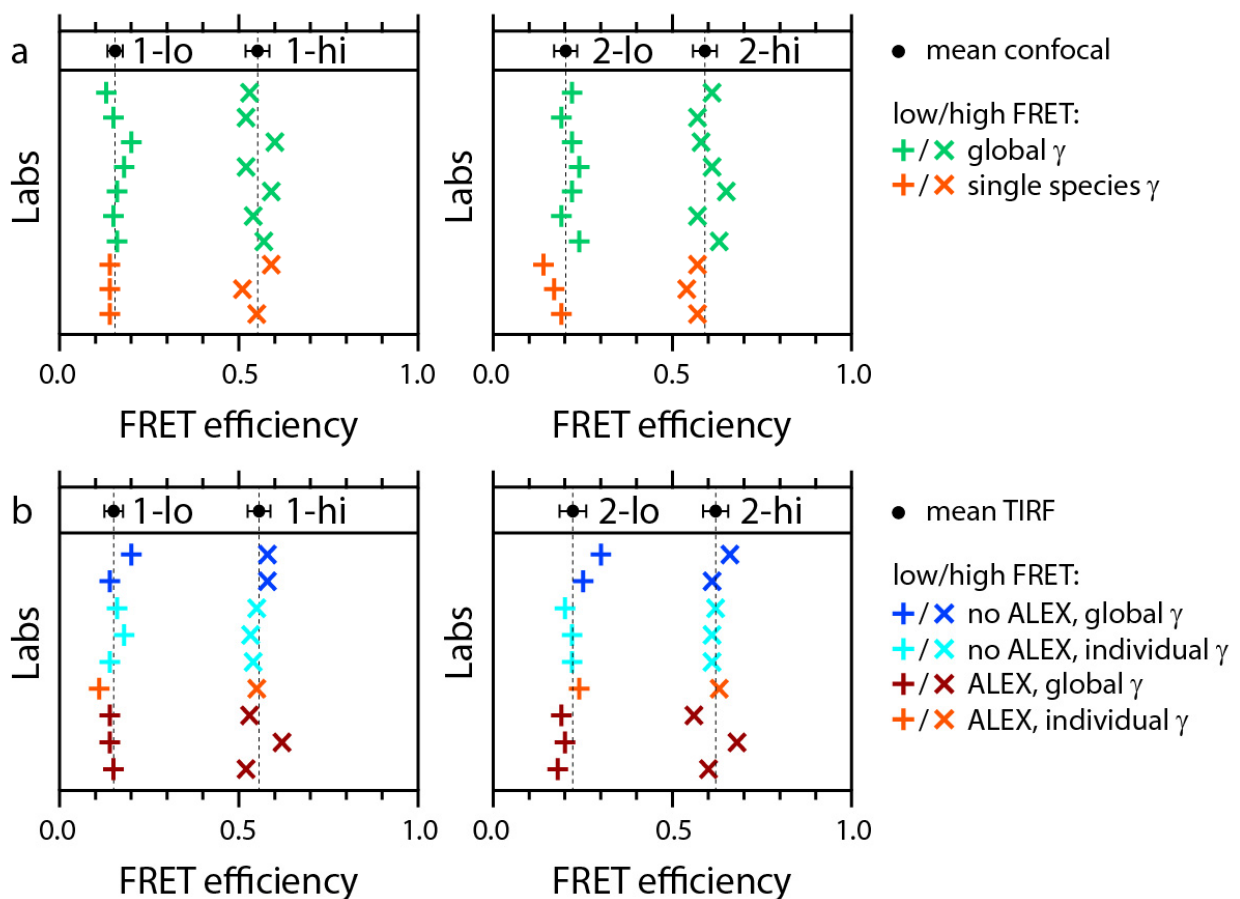


Figure 2.3 Summary of the results of the intensity-based methods. (a) Confocal measurements. (b) TIRF measurements. Note that some laboratories performed measurement with both methods. In the top panel of each

plot, the mean and standard deviations are depicted. Dashed lines indicate the means, their values are summarized in Table 2.4. Example correction factors are given in Table 2.2.

2.2.2 Distance determination

The reported intensity-based FRET efficiencies are consistent throughout the labs, despite using different setup types and procedures. However, the ultimate goal is to derive distances from the FRET efficiencies. The efficiency-distance conversion requires both the knowledge of the Förster radius, R_0 , for the specific FRET pair used, and a specific dye model, describing the behavior of the dye attached to the macromolecule. In the following, we describe (i) how R_0 can be determined and (ii) how to use a specific dye model to calculate the $R(\langle E \rangle)$ referred to as $R_{\langle E \rangle}$ and the R_{MP} . $R_{\langle E \rangle}$ is the apparent donor-acceptor distance, which is directly related to the experimental FRET efficiency $\langle E \rangle$ (eq. V), but it is not a physical distance. R_{MP} is the distance between the mean positions of the dyes, which is not directly measured in the experiment, but is a real distance. R_{MP} is important, for example, for mapping the physical distances required for rigid body structural modeling.

For computing R_0 , the following parameters need to be determined or estimated (eq. VII): the index of refraction of the medium between the two fluorophores (n), the spectral overlap integral (J), the fluorescence quantum yield of the donor ($\Phi_{F,D}$), and the relative dipole orientation factor (κ^2) (see *Online Methods* for an estimate of their uncertainties). The overlap integral, the donor fluorescence quantum yield and the time-resolved fluorescence anisotropies of the donor-only and acceptor-only samples were measured by some of the participating labs (see Table 2.3 and Table 2.6). The dyes are attached via flexible linkers to the DNA, enabling rotation and translation within the accessible volume. The steady state anisotropies r_s and residual anisotropies r_∞ indicate that all used dyes are sufficiently mobile for dynamic averaging of the orientation factor, so that the average orientation factor $\langle \kappa^2 \rangle = 2/3$ can be assumed (the uncertainty in the exact average in κ^2 and the propagation of this error are further discussed in the *Online Methods Equation 21-22*). In short, this assumption is valid as long as the FRET rate (k_{FRET}) is much slower than the rotational relaxation rate (k_{rot}) of the dye. Our model assumptions also include that the dye with the translational diffusion rate (k_{diff}) samples the overall accessible volume within the experimental integration time ($1/k_{int}$), i.e. $k_{rot} \gg k_{FRET} \gg k_{diff} \gg k_{int}$. The validity of these assumptions is justified by experimental observables discussed in the *Online Methods, Section 3.4*.

The determined Förster radii for sample 1 and sample 2 are given in Table 2.4. Literature values differ mainly because the refractive index of water is often assumed, while we used $n_{im} = 1.40$ here (see *Online Methods, Section 3.1*). Note that our careful error analysis led to an error estimate of 7% for the determined R_0 , which is relatively large (mainly due to the uncertainty in κ^2). Thus, a rigorous error analysis for R_0 should be performed whenever distance information is needed (see the *Online Methods*).

Next, we used the measured smFRET efficiencies and the calculated Förster radii to compute the apparent distance $R_{(E)}$ from each lab's data (eq. V) under the assumption $k_{rot} \gg k_{FRET} \gg k_{diff} \gg k_{int}$. Figure 2.4a+b shows the calculated values for these apparent distances for sample 1 and 2 for every data point in Figure 2.3. The average values for all labs are given in Table 2.4. Note that these errors only include the statistical variations of the FRET efficiencies, but do not include the error in the Förster radii, thus these errors represent the precision of the measurement, but not the accuracy. Including the knowledge of the dye attachment positions, a static structure of the DNA and this particular dye model, we computed also model values as described in *Supplementary Note 2*, which are also given in Table 2.4. Considering the error ranges, the experimental and model values agree very well with each other (the deviations range between 0 and 8 %).

The real distance between the center points (mean position) of the accessible volumes R_{MP} deviates from the experimentally observed $R_{(E)}$, because of the different averaging in distance and efficiency space. $R_{(E)}$ corresponds to the real distance R_{MP} only in the hypothetical case in which both dyes are unpolarized point sources, where the AVs have zero volume. In all other cases, R_{MP} is the only physical distance. It can be calculated by one of the following two strategies: (i) If the dye model and the local environment of the dye is known (see Figure 2.1), simulation tools such as the FPS²¹ can be used to compute the R_{MP} from $R_{(E)}$ for a given pair of AVs. (ii) If the structure of the investigated molecule is unknown *a priori*, a sphere is a useful assumption for the AV. A lookup table with polynomial conversion functions can then be calculated for defined AVs and Förster radii in order to relate $R_{(E)}$ to R_{MP} (*Supplementary Note 3*). The results, given as distances determined using the latter approach, are shown in Figure 2.4c+d and Table 2.4. The respective model values are based on the center points of the AVs depicted in Figure 2.1 and given in Table 2.4 (see *Supplementary Note 2* for details).

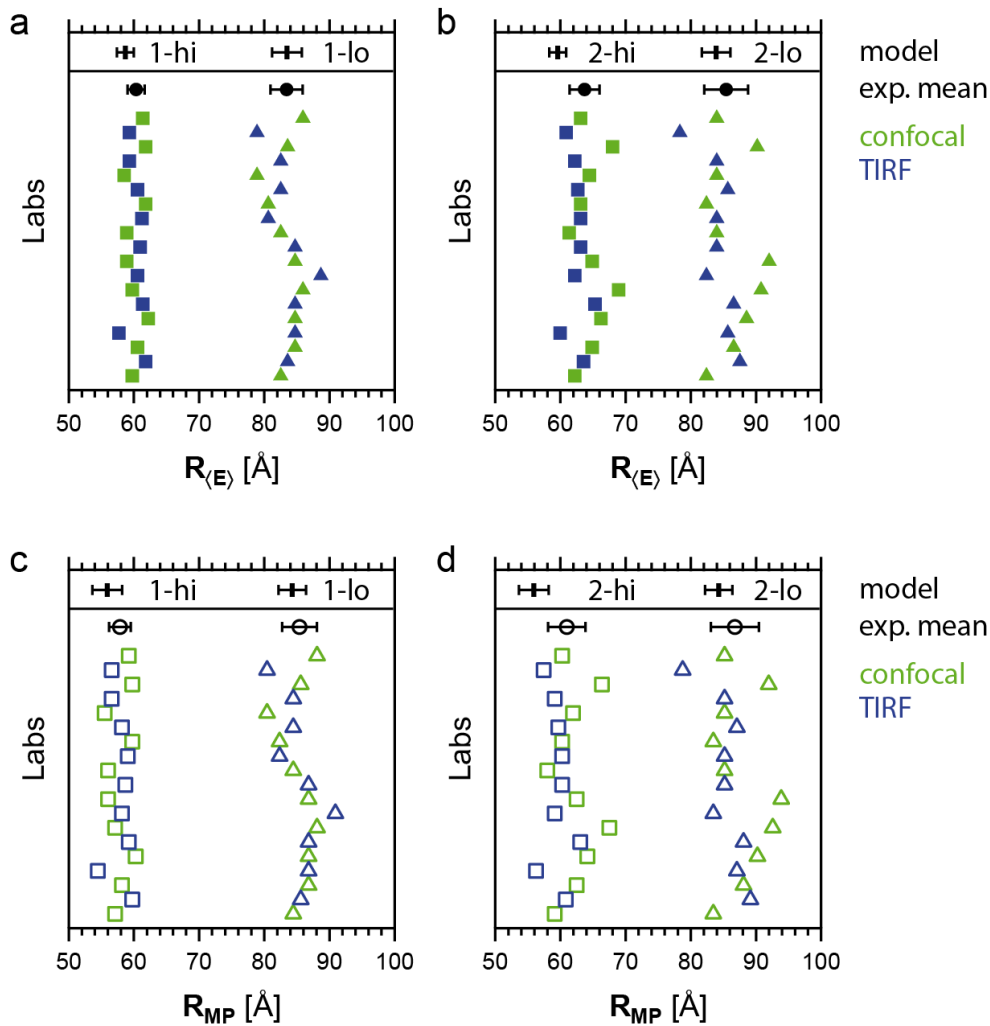


Figure 2.4 Mean inter-dye distances determined from the nineteen $\langle E \rangle$ values measured in sixteen different labs. **(a)** $R_{\langle E \rangle}$ for sample 1; **(b)** $R_{\langle E \rangle}$ for sample 2; **(c)** R_{MP} for sample 1; **(d)** R_{MP} for sample 2. The black dots (exp. mean) indicate the means and the error bars the statistical error (standard deviation) assuming $R_0=62.6$ Å and $R_0=68.0$ Å for sample 1 and 2, respectively). The black bars indicate the model values and their error (determined by variation of model parameters), see main text for details and Table 2.4 for values.

2.2.3 Distance uncertainties

To understand the precision and accuracy of distance determination by smFRET, we estimated all uncertainty sources and propagated them into distance uncertainties. First, we discuss the error in determining the distance between two freely rotating but spatially fixed dipoles, R_{DA} , with the Förster equation (eq. III). Figure 2.5a shows how uncertainties in each of the correction factors (α , γ , δ) and the background signals (BG_D , BG_A) translate into the uncertainty of R_{DA} (see *Supplementary Note 4* for all equations). The solid gray line shows the sum of these efficiency-dependent uncertainties, which are mainly setup-specific quantities. For the extremes of the distances the largest contribution to the

uncertainty in R_{DA} arises from background photons in the donor and acceptor channels. In the presented example with $R_0 = 62.6 \text{ \AA}$ the total uncertainty ΔR_{DA} based on the *setup-specific uncertainties* is less than 4 \AA for $35 \text{ \AA} < R_{DA} < 90 \text{ \AA}$. Notably, in confocal measurements, larger intensity thresholds can decrease this uncertainty. The uncertainty in R_{DA} arising from errors in R_0 (blue line in Figure 2.5b) is added to the efficiency-related uncertainty in R_{DA} (bold grey line) to estimate the total experimental uncertainty in R_{DA} ($\Delta R_{DA, total}$, black line). The underlying uncertainties for determining R_0 are dominated by the dipole orientation factor κ^2 and the refractive index n_{im} , and are further discussed in the *Online Methods, Section 3.0*. Including the uncertainty in R_0 , the error $\Delta R_{DA, total}$ for a single smFRET-based distance between two freely rotating point dipoles is less than 6 \AA for $35 \text{ \AA} < R_{DA} < 80 \text{ \AA}$. It is worth mentioning that this uncertainty might be considerably reduced when multiple distances are calculated within a structure as the self-consistency in such a network enforces more precise localization⁶². In addition to the background issues, an R_{DA} shorter than 30 \AA may be prone to larger errors due to: (i) potential dye-dye interactions and (ii) the dynamic averaging of the dipole orientations being reduced due to an increased FRET rate.

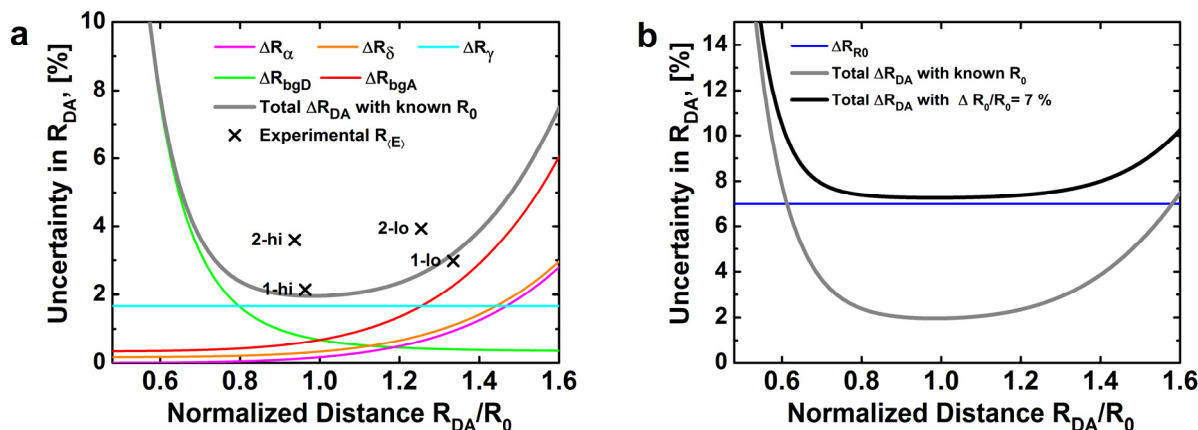


Figure 2.5 Error propagation of experimental uncertainties. (a) R_{DA} uncertainty contributions from the experimental correction factors: ΔR_{γ} (gamma factor), ΔR_{bgD} and ΔR_{bgA} (background), ΔR_{α} (leakage), ΔR_{δ} (direct excitation), total uncertainty with known R_0 ; crosses indicate uncertainty of experimental values of $R_{(E)}$ across the labs. See Supplementary Note 4 for details on the error propagation. (b) Uncertainty in R_{DA} (black line) based on the efficiency-related uncertainty (bold grey line) and the uncertainty for determining R_0 (blue line). See main text for details. Here we use the following uncertainties, which were determined for the confocal based measurements on sample 1: $\Delta R_0/R_0=7\%$, $\Delta\gamma/\gamma=10\%$, $\Delta I^{(BG)}/I=2\%$, $\Delta\alpha=0.01$ and $\Delta\delta=0.01$. For absolute values see Table 2.2.

It is important to verify the model assumption of a freely rotating and diffusing dye. Even though time-resolved fluorescence anisotropy can monitor whether dye rotation is fast, the possibility of dyes interacting with the DNA cannot be fully excluded. Thus, it is not clear if the dye molecule is completely free to sample the computed AV (free diffusion), or whether there are sites of attraction (preferred regions) or sites of repulsion (disallowed regions). In order to validate the dye model, we developed a

self-consistency argument that bypasses several experimental uncertainties. The samples 1 and 2 were designed such that the ratio, R_{rel} , of their respective $R_{(E)}$ values is (quasi) independent of R_0 :

$$\begin{aligned}
 R_{rel} &= \frac{R_{(E),lo}}{R_{(E),hi}} = \frac{R_{0,lo}}{R_{0,hi}} \sqrt{\frac{1/E_{lo} - 1}{1/E_{hi} - 1}} = \sqrt{\frac{\kappa_{lo}^2 \Phi_{D,lo} J_{lo} n_{hi}^4}{\kappa_{hi}^2 \Phi_{D,hi} J_{hi} n_{lo}^4}} \sqrt{\frac{1/E_{lo} - 1}{1/E_{hi} - 1}} \\
 &= f \cdot \sqrt{\frac{1/E_{lo} - 1}{1/E_{hi} - 1}}
 \end{aligned} \tag{1}$$

The pre-factor, f , should be approximately the same for all measured dye combinations, for several reasons. First, the donor positions are identical for all lo- and hi-samples, respectively. Therefore, the following assumptions can be made: (i) the ratio of the donor quantum yields are identical; (ii) the ratio of the spectral overlaps J for the lo- and hi- sample of one and the same dye pair should be the same; (iii) for the given geometry (see Figure 2.1) the refractive indices n_{im} of the medium between the dyes should also be very similar; (iv) the ratio of the orientation factors κ^2 should be nearly equal as the measured donor anisotropies are low for the lo- and hi- positions. Second, the acceptor extinction coefficients eliminate each other as the acceptor is at the same position for the lo- and hi-samples. Thus, the different dye pairs and the model used in this study should all give similar values for R_{rel} . Table 2.4 indeed shows that the relative $R_{(E)}$ ratios are very similar and the deviations from the corresponding model values are less than 5% for sample 1 and 2, which is well within the experimental error. This further demonstrates the validity of the assumptions for the dye model and averaging regime used here.

While the analysis in this paper used a static model for the DNA structure, DNA is known not to be completely rigid⁸⁰. We tested our DNA model by performing MD simulations of the DNA molecule (without attached dye molecules, see *Supplementary Note 6*) and found that the averaged expected FRET efficiency using the computed dynamically-varying DNA structure leads to comparable but slightly longer distances than for the static model. The deviations between the models and data are reduced (Table 2.4) for those cases where larger deviations were observed using static models.

2.3 Discussion

The aim of this blind study was to assess the consistency of FRET measurements from different labs around the world using various DNA FRET standards, without prior knowledge of the distance between the FRET pairs. The reported FRET efficiencies for the intensity-based measurements were consistent, with an overall standard deviation $\Delta E < \pm 0.05$ for each sample. This remarkable consistency was achieved by applying the same step-by-step procedure to perform the experiment and analyze the data.

We also showed that the factors required for correcting the FRET efficiency can be determined with high precision, independent of the different setup types and acquisition software used. Together the measurement errors in the correction factors cause an uncertainty in R_{DA} of less than 5 %, which agrees well with the variations observed between the reported results from the different labs. Ultimately, we are interested in the absolute distances derived from these FRET measurements. Figure 2.5b shows good precision in the range from $0.6 R_0$ to $1.6 R_0$, which corresponds to an uncertainty of less than $\pm 6 \text{ \AA}$ in the distance range from 35 to 80 \AA for sample 1. This estimation is valid if the dyes are sufficiently mobile which has been supported by time-resolved anisotropy measurements and further confirmed by a self-consistency argument. For sample 2 the standard deviation is slightly larger than for sample 1 (see Figure 2.5a), which could be explained by dye specific photophysical properties. Interestingly for this case, the local gamma correction in the TIRF experiments yields data with a comparatively small standard deviation, while the global gamma correction data shows a comparatively large standard deviation (Figure 2.3b). The values for samples 3 and 4 (Table 2.4) show similar precision, considering the smaller number of measurements (N).

In addition to the achievable precision, we also tested the accuracy of the experimentally derived distances by comparing them with model distances. We found an excellent agreement within 2 \AA for sample 1 and within 7 \AA for sample 2. Both results are within the estimated theoretical distance uncertainty. For sample 2, which had the cyanine based dye Alexa647 instead of the carbopyronine based dye Atto647N as an acceptor, the lower accuracy could be explained by an imperfect sampling of the full AV or dye specific photophysical properties. Previously it has been shown that cyanine dyes are sensitive to their local environment ⁸¹ and therefore require especially careful characterization for each new labelled biomolecule.

The mean values of sample 3 and 4 are also within the error of the model values (for details see Table 2.4 and *Supplementary Note 5*). This suggests that none of the four FRET pairs explored in this study exhibit significant dye artefacts. For future work, it will be very powerful to complement intensity-based high-precision smFRET studies with sm-lifetime studies because the picosecond time resolution can provide additional information on calibration and fast dynamic averaging.

The results from different labs and the successful self-consistency test clearly show the great potential of absolute smFRET-based distances for investigating biomolecular conformations and dynamics, as well as for integrative structural modeling. While R_{MP} can be used to explore the real distance space in biomolecules, $R_{(E)}$ can be used to directly compare the observables in FRET experiments with structural models. The ability to accurately determine distances on the molecular scale with smFRET experiments and to estimate the uncertainty of the measurements, provides the groundwork for smFRET-based

structural and hybrid approaches. Together with the automated selection of the most informative pairwise labeling positions⁶⁹, and fast analysis procedures^{21,62,63} we anticipate smFRET-based structural methods to become an important tool for *de novo* structural determination and structure validation, especially for large and flexible structures where other structural biology methods are difficult to apply.

2.4 Online Methods

Table 2.1 Nomenclature. Since the nomenclature for FRET-based experiments is not consistent, we propose and use the following terms in this manuscript.

<i>Central Definitions:</i>		
$E = \frac{F_{A D}}{F_{D D} + F_{A D}}$	FRET efficiency	(I)
$S = \frac{F_{D D} + F_{A D}}{F_{D D} + F_{A D} + F_{A A}}$	Stoichiometry	(II)
$E = \frac{1}{1 + R_{DA}^6/R_0^6}$	FRET efficiency for a single donor acceptor distance R_{DA}	(III)
$\langle E \rangle = \frac{1}{nm} \sum_{i=1}^n \sum_{j=1}^m \frac{1}{1 + \mathbf{R}_{A(j)} - \mathbf{R}_{D(i)} ^6/R_0^6}$	Mean FRET efficiency for a discrete distribution of donor acceptor distances with the position vectors $\mathbf{R}_{D(i)}$ and $\mathbf{R}_{A(j)}$	(IV)
$R_{\langle E \rangle} \equiv R(\langle E \rangle) = R_0(\langle E \rangle^{-1} - 1)^{1/6}$	The apparent donor acceptor distance is computed from the average FRET efficiency for a distance distribution. It is a FRET averaged quantity which was also referred to as FRET-averaged distance $\langle R_{DA} \rangle_E$ (ref ³²).	(V)
$R_{MP} = \left \langle \mathbf{R}_{D(i)} \rangle - \langle \mathbf{R}_{A(j)} \rangle \right $ $= \left \frac{1}{n} \sum_{i=1}^n \mathbf{R}_{D(i)} - \frac{1}{m} \sum_{j=1}^m \mathbf{R}_{A(j)} \right $	Distance between the mean dye positions with the position vectors $\langle \mathbf{R}_{D(i)} \rangle$ and $\langle \mathbf{R}_{A(j)} \rangle$	(VI)
<i>Subscripts:</i>		
D or A	Concerning donor or acceptor	
A D	Acceptor fluorescence given donor excitation, $D D, A A$ accordingly	
Aem Dex	Intensity in the acceptor channel given donor excitation, $Dem Dex, Aem Aex$, accordingly	
app	apparent, i.e. including systematic, experimental offsets	
<i>Superscripts:</i>		
BG	Background	
DO/ AO	Donor-only species/ Acceptor-only species	
DA	FRET species	
<i>i -iii</i>	Indicates (i) the uncorrected intensity; (ii) intensity after BG correction; (iii) intensity after BG, alpha and delta corrections	

Correction Factors:	
$\alpha = \frac{g_{R D}}{g_{G D}} = \frac{\langle iiE_{app}^{(DO)} \rangle}{1 - \langle iiE_{app}^{(DO)} \rangle}$	Leakage of D fluorescence into A channel
$\beta = \frac{\sigma_{A R} I_{Aex}}{\sigma_{D G} I_{Dex}}$	Normalization of excitation intensities, I , and cross-sections, σ , of A and D
$\gamma = \frac{g_{R A} \Phi_{F,A}}{g_{G D} \Phi_{F,D}}$	Normalization of fluorescence quantum yields, Φ_F , and detection efficiencies, g , of A and D
$\delta = \frac{\sigma_{A G} I_{Dex}}{\sigma_{A R} I_{Aex}} = \frac{\langle iiS_{app}^{(AO)} \rangle}{1 - \langle iiS_{app}^{(AO)} \rangle}$	Direct acceptor excitation by the donor excitation laser (lower wavelength)
Primary Quantities:	
I	Experimentally observed intensity
F	Corrected fluorescence intensity
τ	Fluorescence lifetime [ns]
$\Phi_{F,A}$ or $\Phi_{F,D}$	Fluorescence quantum yield of A and D, respectively
r	Fluorescence anisotropy
R	Inter-dye distance [Å]
$\frac{R_0}{\text{Å}} = 0.2108 \sqrt[6]{\left(\frac{\Phi_{F,D} \kappa^2}{n_{im}^4}\right) \frac{J}{\text{M}^{-1} \text{cm}^{-1} \text{nm}^4}}$	Förster radius [Å], for a given J in units below (VII)
$\kappa^2 = (\cos \theta_{AD} - 3 \cos \theta_D \cos \theta_A)^2$	Dipole orientation factor
$J = \int_0^\infty \bar{F}_D(\lambda) \varepsilon_A(\lambda) \lambda^4 d\lambda$	Spectral overlap integral [$\text{cm}^{-1} \text{M}^{-1} \text{nm}^4$] (see Figure 2.11)
$\bar{F}_D(\lambda)$ with $\int_0^\infty \bar{F}_D(\lambda) d\lambda = 1$	Normalized spectral radiant intensity of the excited donor [nm^{-1}], defined as the derivative of the emission intensity F with respect to the wavelength.
$\varepsilon_A(\lambda)$	Extinction coefficient of A [$\text{M}^{-1} \text{cm}^{-1}$]
n_{im}	Refractive index of the medium in-between the dyes
Further Quantities	
$g_{R A}$ or $g_{G D}$	Detection efficiency of the red detector (R) if only acceptor was excited or green detector (G) if donor was excited. Analogous for others.
$\sigma_{A/G}$	Excitation cross-section for acceptor when excited with green laser. Analogous for the others.
Abbreviations:	
1-lo	dsDNA oligo with Atto550 and Atto647N 23 basepairs apart
1-hi	dsDNA oligo with Atto550 and Atto647N 23 basepairs apart
2-lo	dsDNA oligo with Atto550 and Atto647N 15 basepairs apart
2-hi	dsDNA oligo with Atto550 and Alexa647 15 basepairs apart

Table 2.2 Typical correction factors for sample 1 (Atto550-Atto647N) at given setups (reference lab). For the instrumental details of the setups see Figure 2.8 and Figure 2.9.

Factor	Experiment type	
	confocal	TIRF
α	0.11	0.07
β	1.80	0.85
γ	1.20	1.14
δ	0.11	0.065

Table 2.3 Typical parameters for sample 1 and sample 2 that define R_0 (Seidel lab). For their determination see Online Methods section 3.0.

dye pairs	κ^2	n_{im}	$\Phi_{F,D}$	ϵ_A [$M^{-1}cm^{-1}$]	J [$cm^{-1}M^{-1}nm^4$]	R_0 [\AA]
Atto550-Atto647N	2/3	1.40	0.765	150000	$5.180 \cdot 10^{15}$	62.6
Atto550-Alexa647	2/3	1.40	0.765	270000	$8.502 \cdot 10^{15}$	68.0

Table 2.4 Summary of resulting mean efficiencies $\langle E \rangle$, apparent distance $R_{(E)}$, mean position distance R_{MP} and corresponding model distances $R_{(E)}^{(model)}$ (Supplementary Note 2) and dynamic model distances $R_{(E)}^{(dynamic\ model)}$ (Supplementary Note 6) and the experimental ratio $R_{rel} = R_{(E)}^{(lo)}/R_{(E)}^{(hi)}$ and the model $R_{rel}^{(model)} = R_{(E)}^{(model,lo)} / R_{(E)}^{(model,hi)}$ for all intensity based measurements. The errors (standard deviations) report on the precision of the measurements and not their accuracy.

Sample	N	$\langle E \rangle$	R_0 [\AA]	$R_{(E)}$ [\AA]	$R_{(E)}^{(model)}$ [\AA]	$R_{(E)}^{(dynamic\ model)}$ [\AA]	R_{rel}	$R_{rel}^{(model)}$	R_{MP} [\AA]	$R_{MP}^{(model)}$ [\AA]
1-lo	19	0.15±0.02	62.6±4.0	83.4±2.5	83.5±2.3	83.9	1.38	1.42	85.4±2.7	84.3±2.1
1-hi	19	0.56±0.03		60.3±1.3	58.7±1.3	60.3			57.9±1.7	55.9±2.3
2-lo	19	0.21±0.04	68.0±5.0	85.4±3.4	83.9±2.2	84.2	1.34	1.41	86.8±3.7	84.3±2.1
2-hi	19	0.60±0.05		63.7±2.3	59.6±1.3	61.0			61.0±2.9	55.9±2.3
3-lo	7	0.04±0.02	49.3[a]	89.5±12.3	82.4±2.6	83.1	1.49	1.46	85.7±5.3	86.1±2.3
3-hi	7	0.24±0.04		60.1±2.3	56.4±1.9	58.4			61.1±2.9	57.1±2.3
4-lo	4	0.13±0.06	57.0[a]	79.6±6.2	82.6±2.5	83.5	1.31	1.43	82.9±6.8	86.3±2.3
4-hi	4	0.41±0.04		60.7±1.7	57.6±1.5	59.5			60.4±2.3	58.7±2.3

[a] The R_0 for these samples have been taken from the literature and converted from a refractive index of $n_{im} = 1.33$ to $n_{im} = 1.40$:

Sample 3: $R_0 = 49.3 \text{ \AA}$ from ref.⁸²

Sample 4: $R_0 = 57.0 \text{ \AA}$ from ref.⁷⁶

2.4.1 Samples

Altogether, 8 different FRET-samples were designed with the acceptor dyes positioned 15 or 23 base pairs away from the donor dyes (see Table 2.5 and *Supplementary Note 5*). IBA GmbH (Göttingen) synthesized and labeled the single DNA strands followed by HPLC purification. Here the dyes were attached to a thymidine (dT), which is known to cause the least fluorescence quenching of all nucleotides³³.

Most labs measured the following four DNA samples listed in Table 2.5. Therefore, we focus on these four samples in the main text of this manuscript. The additional samples and the corresponding measurements can be found in *Supplementary Note 5* and Figure 2.7 and Table 2.4. The following buffer was requested for all measurements: 20 mM MgCl₂, 5 mM NaCl, 5 mM Tris, at pH 7.5, degassing just before the measurement at room temperature.

The linker lengths were chosen in a way that all dyes had about the same number of flexible bonds between the dipole axis and the DNA. The Atto550, Alexa647 and Atto647N already have an intrinsic flexible part before the C-linker starts (Figure 2.6). In addition, the DNAs were designed such that the distance ratio between the high FRET efficiency and low FRET efficiency sample should be the same for all samples, largely independent of R_0 .

Table 2.5 The main focus in the manuscript are the 1-lo, 1-hi, 2-lo, 2-hi samples. The so called donor strand (D-strand) is labeled with donor dye and acceptor strand (A-strand) with acceptor dye. The labeling sites of the donor and acceptor are shown in green and in red on the sequence respectively

Name	Base position (Linker), strand	Dyes (Donor/Acceptor)	Sequence
1-lo	T 31(C2), D-strand T 31(C2), A-strand	Atto550 NHS Ester/ Atto647N NHS	5' - GAG CTG AAA GTG TCG AGT TTG TTT GAG TGT TTG TCT GG - 3' 3' - CTC GAC TTT CAC AGC TCA AAC AAA CTC ACA AAC AGA CC - 5' - biotin
1-hi	T 23(C2), D-strand T 31(C2), A-strand	Atto550 NHS Ester/ Atto647N NHS	5' - GAG CTG AAA GTG TCG AGT TTG TTT GAG TGT TTG TCT GG - 3' 3' - CTC GAC TTT CAC AGC TCA AAC AAA CTC ACA AAC AGA CC - 5' - biotin
2-lo:	T 31(C2), D-strand T 31(C2), A-strand	Atto550 NHS Ester/ Alexa647 NHS Ester	5' - GAG CTG AAA GTG TCG AGT TTG TTT GAG TGT TTG TCT GG - 3' 3' - CTC GAC TTT CAC AGC TCA AAC AAA CTC ACA AAC AGA CC - 5' - biotin
2-hi:	T 23(C2), D-strand T 31(C2), A-strand	Atto550 NHS Ester/ Alexa647 NHS Ester	5' - GAG CTG AAA GTG TCG AGT TTG TTT GAG TGT TTG TCT GG - 3' 3' - CTC GAC TTT CAC AGC TCA AAC AAA CTC ACA AAC AGA CC - 5' - biotin

2.4.2 General correction procedure

Efficiency E and Stoichiometry S are defined in Table 2.1. Determination of the corrected FRET E and S is largely based on the Lee et al. approach⁷⁴ and consists of the following steps: (1) data acquisition; (2) generation of uncorrected E vs S 2D histograms; (3) background subtraction; (4) correction for the position-specific excitation in TIRF experiment; (5) correction for leakage and direct acceptor excitation; (6) correction for excitation intensities and absorption cross-sections, quantum yields and detection efficiencies.

2.4.3 Data acquisition

The sample with both dyes is measured and the three intensity time traces are extracted: acceptor emission upon donor excitation ($I_{Aem|Dex}$), donor-emission upon donor excitation ($I_{Dem|Dex}$), and acceptor-emission upon acceptor excitation ($I_{Aem|Aex}$).

For the confocal setups a straight forward burst identification is performed by binning the trace into 1 ms bins. Usually a minimum threshold (e.g. 50 photons) is applied to the sum of the donor and acceptor signals upon donor excitation for each bin. This threshold is used again in every step, such that the number of utilized bursts may change from step to step (if the γ correction factor is not equal to one). Some labs use sophisticated burst-search algorithms. For example, the dual channel burst search^{83,84} recognizes the potential bleaching of each dye within bursts. Note that the choice of the burst-search algorithm can have an influence on the γ correction factor. For standard applications, the simple binning method is often sufficient, especially for well-characterized dyes and low laser powers. This study shows that the results do not significantly depend on these conditions (if applied properly), as every lab used its own setup and procedure at this stage.

For the TIRF setups, traces with one acceptor and one donor are selected, defined by a bleaching step. In addition, only the relevant *range* of each trajectory – i.e. prior to photo-bleaching of either dye - is included in all further steps.

2D histogram: A 2D histogram (Figure 2.2a,b) of the apparent stoichiometry, ${}^iS_{app}$, vs. apparent FRET efficiency, ${}^iE_{app}$, defined by Equations 2 and 3 is generated, where

$${}^iS_{app} = (I_{Aem|Dex} + I_{Dem|Dex}) / (I_{Aem|Dex} + I_{Dem|Dex} + I_{Aem|Aex}) \quad (2)$$

$${}^iE_{app} = I_{Aem|Dex} / (I_{Aem|Dex} + I_{Dem|Dex}) \quad (3)$$

Background correction: Background $I^{(BG)}$ is removed from each uncorrected intensity iI separately, leading to the background corrected intensities ${}^{ii}I$, ${}^{ii}S_{app}$, ${}^{ii}E_{app}$:

$$\begin{aligned}
ii I_{Dem|Dex} &= i I_{Dem|Dex} - I_{Dem|Dex}^{(BG)} \\
ii I_{Aem|Aex} &= i I_{Aem|Aex} - I_{Aem|Aex}^{(BG)} \\
ii I_{Aem|Dex} &= i I_{Aem|Dex} - I_{Aem|Dex}^{(BG)}
\end{aligned} \tag{4}$$

For *confocal measurements*, the background is determined by averaging the photon count rate for all time bins that are below a threshold, which is e.g. defined by the maximum in the frequency vs intensity plot (density of bursts should not be too high). Note, that a previous measurement of the buffer only, can uncover potential fluorescent contaminants, but it can differ significantly from the background of the actual measurement. The background intensity is then subtracted from the intensity of each burst in each channel (Eq. 4). Typical background values are 0.5-1 photon / ms (Figure 2.1a).

For *TIRF measurements*, various trace-wise or global background corrections can be applied. The most common method defines background as the individual offset (time average) after photo-bleaching of both dyes in each trace. Another possibility is to select the darkest spots in the illuminated area and to subtract an average background time trace from the data or to use a local background, e.g. with a mask around the particle. The latter two have the advantage that possible (exponential) background bleaching is also corrected for. We have not investigated the influence of the kind of background correction during this study, but a recent study has shown that not all background estimators are suitable for samples with a high molecule surface coverage⁸⁵.

Overall, a correction of the background is very important, but can be done very well in different ways.

The position specific excitation correction (optional for TIRF): The concurrent excitation profiles of both lasers are key for accurate measurements (see Figure 2.11). Experimental variations across the field of view are accounted for using a position-specific normalization:

$${}_{(profile)} ii I_{Aem|Aex} = ii I_{Aem|Aex} \frac{I_D(x', y')}{I_A(x, y)} \tag{5}$$

where $I_D(x', y')$ and $I_A(x, y)$ denote the excitation intensities at corresponding positions in the donor or acceptor image, respectively. Individual excitation profiles are determined as the mean image of a stack of images recorded while moving across a sample chamber with dense dye coverage.

Leakage (α) and direct excitation (δ): After the background correction, the leakage fraction of the donor emission into the acceptor detection channel and the fraction of the direct excitation of the acceptor by the donor-excitation laser are determined. The correction factor for leakage (α) is determined by Equation 6 using the FRET efficiency of the donor-only population (D-only in Figure 2.2a,b(ii)). The

correction factor for direct excitation (δ) is determined by Equation 7 from the stoichiometry of the acceptor-only population (A-only in Figure 2.2a,b(ii)).

$$\alpha = \frac{\langle {}^{ii}E_{app}^{(DO)} \rangle}{1 - \langle {}^{ii}E_{app}^{(DO)} \rangle} \quad (6)$$

$$\delta = \frac{\langle {}^{ii}S_{app}^{(AO)} \rangle}{1 - \langle {}^{ii}S_{app}^{(AO)} \rangle} \quad (7)$$

where ${}^{ii}E_{app}^{(DO)}$ and ${}^{ii}S_{app}^{(AO)}$ are calculated from the background-corrected intensities ${}^{ii}I$ of the corresponding population, i.e. donor-only or acceptor-only, respectively. This correction together with the previous background correction results in the donor-only population being located at $\langle E \rangle = 0, \langle S \rangle = 1$ and acceptor-only population at $\langle S \rangle = 0, \langle E \rangle = 0 \dots 1$. The corrected acceptor fluorescence after donor excitation $F_{A|D}$ is given by Equation 8, which yields the updated expressions for the FRET efficiency and stoichiometry, Equations 9 and 10, respectively.

$$F_{A|D} = {}^{ii}I_{Aem|Dex} - \alpha {}^{ii}I_{Dem|Dex} - \delta {}^{ii}I_{Aem|Aex} \quad (8)$$

$${}^{iii}E_{app} = F_{A|D} / (F_{A|D} + {}^{ii}I_{Dem|Dex}) \quad (9)$$

$${}^{iii}S_{app} = (F_{A|D} + {}^{ii}I_{Dem|Dex}) / (F_{A|D} + {}^{ii}I_{Dem|Dex} + {}^{ii}I_{Aem|Aex}) \quad (10)$$

In principle, the leaked donor signal could be added back to the donor emission channel³⁷. However, this requires precise knowledge about spectral detection efficiencies, which is not otherwise required, and has no effect on the final accuracy of the measurement. As the determination of α and δ influences the γ and β correction in the next step, both correction steps can be repeated in an iterative manner if required (e.g. if the γ and β factors deviate largely from one).

γ and β correction factors: Differences in the excitation intensities and cross-section, as well as, quantum yields and detection efficiencies are accounted for by using the correction factors γ and β , respectively. If the fluorescence quantum yields do not depend on efficiencies or such dependence is negligible (*homogenous approximation*), mean values of efficiencies $\langle {}^{iii}E_{app}^{(DA)} \rangle$ and of stoichiometries $\langle {}^{iii}S_{app}^{(DA)} \rangle$ are related by equation 11:

$$\langle iii S_{app}^{(DA)} \rangle = \left(1 + \gamma \beta + (1 - \gamma) \beta \langle iii E_{app}^{(DA)} \rangle \right)^{-1} \quad (11)$$

So, in the homogeneous approximation, γ and β correction factors can be determined by fitting FRET populations to the $iii S_{app}^{(DA)}$ vs. $iii E_{app}^{(DA)}$ histogram with the line defined by Equation 11. As this method relies on the analysis of $iii S_{app}^{(DA)}$, $iii E_{app}^{(DA)}$ values obtained from multiple species, we term this method, *global* γ -correction. Such a fit can be performed for all FRET populations together, for any of their subsets, and in principle, for each single-species population separately (see below). Alternatively, a linear fit of inverse $\langle iii S_{app}^{(DA)} \rangle$ vs. $\langle iii E_{app}^{(DA)} \rangle$ with y-intercept a and slope b can be performed.

In this case, $\beta = a + b - 1$ and $\gamma = (a - 1)/(a + b - 1)$.

Error propagation, however, is more straightforward if Equation 11 is used. If there is a complex dependence between properties of dyes and efficiencies, the homogeneous approximation is no longer applicable. In this case, the relationship between $iii S_{app}^{(DA)}$, $iii E_{app}^{(DA)}$ for different populations (or even subpopulations for the same single-species) cannot be described by Equation 11 with a single γ correction factor. Here, β and γ can be determined for a single species. We call this “*single-species* γ -correction”. This works only if the efficiency broadening is dominated by distance fluctuations. The reason for this assumption is the dependency of these corrections factors on both the stoichiometry and the distance-dependent efficiency. In our study, global and local γ -correction yielded similar results. Therefore, the homogenous approximation and distance fluctuations as the main cause for efficiency broadening can be assumed for sample 1 and 2. Systematic variation of the γ -correction factor yields an error of about 10%.

Alternatively, determination of γ , β factors can be done trace-wise, e.g. as in msALEX experiments⁸⁶ where the γ factor is determined as the ratio of the decrease in acceptor signal and the increase in donor signal upon acceptor bleaching. We call such an alternative correction, *individual* γ -correction. The analysis of local distributions can provide valuable insights about properties of the studied system.

After γ and β correction, the corrected donor (acceptor) fluorescence after donor (acceptor) excitation $F_{D|D}$ ($F_{A|A}$) amounts to:

$$F_{D|D} = \gamma \ ii I_{Dem|Dex} \quad (12)$$

$$F_{A|A} = \frac{1}{\beta} \ ii I_{Aem|Aex} \quad (13)$$

Fully corrected values: Application of all corrections leads to the estimates of real FRET efficiencies, E , and stoichiometries, S , from the background corrected intensities, ^{ii}I . The explicit expressions of fully corrected FRET efficiency and stoichiometry are:

$$E = \frac{[^{ii}I_{Aem|Dex} - \alpha ^{ii}I_{Dem|Dex} - \delta ^{ii}I_{Aem|Dex}]}{\gamma [^{ii}I_{Dem|Dex}] + [^{ii}I_{Aem|Dex} - \alpha ^{ii}I_{Dem|Dex} - \delta ^{ii}I_{Aem|Dex}]} \quad (14)$$

$$S = \frac{\gamma [^{ii}I_{Dem|Dex}] + [^{ii}I_{Aem|Dex} - \alpha ^{ii}I_{Dem|Dex} - \delta ^{ii}I_{Aem|Dex}]}{\gamma [^{ii}I_{Dem|Dex}] + [^{ii}I_{Aem|Dex} - \alpha ^{ii}I_{Dem|Dex} - \delta ^{ii}I_{Aem|Dex}] + \frac{1}{\beta} [^{ii}I_{Aem|Aex}]} \quad (15)$$

Plots of the E vs. S histogram are shown in Figure 2.2a(iv) and Figure 2.2b(iv). Now, the FRET population should be symmetric to the $S = 0.5$ line. The donor-only population should still be located at $E = 0$ and the acceptor-only population at $S = 0$. Finally, the corrected FRET efficiency histogram is generated using events with a stoichiometry of $0.3 < S < 0.7$ (see Figure 2.2a,b bottom). The expected value of the corrected FRET efficiencies $\langle E \rangle$ is deduced as the center of a Gaussian fit to the efficiency histogram. This is a good approximation for FRET efficiencies in the range between about 0.1 and 0.9. In theory, the shot-noise limited efficiencies follow a binomial distribution if the photon number per burst is constant. For extreme efficiencies or data with a small average number of photons per burst, the efficiency distribution can no longer be approximated with a Gaussian. In this case and also in the case of efficiency broadening due to distance fluctuations, a detailed analysis of the photon statistics can be useful^{83,87-89}.

2.4.4 Uncertainty in distance due to R_0 :

According to Förster theory⁵⁶, the FRET efficiency, E , and the distance, R , are related by equation III in Table 2.1. In this study, we focused on comparing E in a blind study across different labs. The Seidel lab determined an R_0 for this system to convert efficiencies to distances. There are many excellent reviews on how to determine the Förster radius R_0 ^{73,90,91} and a complete discussion would be beyond the scope of this experimental comparison study. In the following, we estimate and discuss the different sources of uncertainty in R_0 , by utilizing standard error propagation (see also *Supplementary Note 4*). R_0 is given by equation VII, Table 2.1.

The 6th power of the Förster radius is proportional to the relative dipole orientation factor κ^2 , the donor quantum yield $\Phi_{F,D}$, the overlap integral J , as well as n^{-4} , where n is the refractive index of the medium:

$$R_0^6 \sim \kappa^2 \cdot \Phi_{F,D} \cdot J \cdot n^{-4} \quad (16)$$

For Table 2.5b, we use a total Förster radius related distance uncertainty of 7 %, which is justified by the following estimate. Please note that the error in the dipole orientation factor is always very specific for the investigated system, while the errors in the donor quantum yield, overlap integral and refractive index are more general, but their mean values do also depend on the environment.

The refractive index. Different values for the refractive index in FRET systems have been used historically, but ideally the refractive index of the donor-acceptor intervening medium n_{im} should be used, though some experimental studies suggest that the use of the refractive index of the solvent may be appropriate, but this is still open for discussion (see e. g. discussion in⁹²).

$$R_0^6(n) \sim n_{im}^{-4} R_0^6 \sim \kappa^2 \cdot \Phi_{F,D} \cdot J \cdot n^{-4} \quad (17)$$

In the worst case, this value n_{im} might be anywhere in-between the refractive index of the solvent ($n_{water} = 1.33$) and a refractive index for the dissolved molecule ($n < n_{oil} = 1.52$)⁹³, i.e. $n_{water} < n_{im} < n_{oil}$. This would result in a maximum uncertainty of $\Delta n_{im} < 0.085$. As recommended by Clegg, we used $n_{im} = 1.40$ to minimize this uncertainty⁹⁴ (see Table 2.3). The distance uncertainty propagated from the uncertainty of the refractive indices can then be assumed to be:

$$\Delta R_0(n) \approx \frac{4}{6} R_0 \frac{\Delta n_{im}}{n} < 0.04 \cdot R_0 \quad (18)$$

The donor quantum yield $\Phi_{F,D}$ is position dependent, therefore we measured the fluorescence lifetimes and quantum yields of the free dye Atto550 and the 1-hi and 1-lo(Atto550) (see Table 2.6).

In agreement with Sindbert et al.⁴⁴, the uncertainty of the quantum yield is estimated at $\Delta \Phi_{F,D} = 5$ % arising from the uncertainties of the $\Phi_{F,D}$ values reference dyes and the precision of the absorption and fluorescence measurements. Thus, the distance uncertainty owing to the quantum yield is estimated at:

$$\Delta R_0(\Phi_{F,D}) \approx \frac{R_0}{6} \frac{\Delta \Phi_{F,D}}{\Phi_{F,D}} = 0.01 \cdot R_0 \quad (19)$$

The overlap integral J was measured for the unbound dyes in solution (Atto550 and Atto647N), as well as for samples 1-lo and 1-hi. This resulted in a deviation of about 10 % for J using the literature values for the extinction coefficients. All single stranded labeled DNA samples used in this study were purified with HPLC columns providing a labelling efficiency of at least 95 %. The label efficiencies of the single

stranded singly-labeled DNA and of the double stranded singly-labeled DNA samples were determined by the ratio of the absorption maxima of the dye and the DNA and were all above 97 %. This indicates an error of the assumed extinction coefficient of less than 3 %. Thus, the distance uncertainty due to the overlap spectra and a correct absolute acceptor extinction coefficient can be estimated by Equation 20. However, the uncertainty in the acceptor extinction coefficient might be larger for other environments, such as when bound to a protein.

$$\Delta R_0(J) \approx \frac{R_0 \Delta J}{6 J} = 0.025 \cdot R_0 \quad (20)$$

In addition to the above uncertainty estimation, the J -related uncertainty can also be obtained by verifying the self-consistency of a β -factor network⁶². Finally, we found little uncertainty by using the well tested dye Atto647N. Fluorescence spectra were measured on a Fluoromax4 spectrofluorimeter (Horiba, Germany). Absorbance spectra were recorded on a Cary5000 UV/VIS spectrometer (Agilent, USA). See Figure 2.11.

The κ^2 factor and model assumptions: The uncertainty in the distance depends on the dye model used⁶⁸. Several factors need to be considered, given the model assumptions of unrestricted dye rotation, equal sampling of the entire accessible volume, and the following rate inequality $k_{rot} \gg k_{FRET} \gg k_{diff} \gg k_{int}$.

First, the use of $\langle \kappa^2 \rangle = 2/3$ is justified if $k_{rot} \gg k_{FRET}$, because then there is rotational averaging of the dipole orientation during energy transfer. k_{rot} is determined from the rotational correlation time $\rho_1 < 1$ ns and k_{FRET} is determined from the fluorescence lifetimes $1 \text{ ns} < \tau_f < 5$ ns. Hence the condition $k_{rot} \gg k_{FRET}$ is not strictly fulfilled. We estimate the error this introduces into κ^2 from the time-resolved anisotropies of donor and acceptor dyes. If the transfer rate is smaller than the fast component of the anisotropy decay (rotational correlation time) of donor and acceptor. Then, the combined anisotropy, r_C , is given by the residual donor and acceptor anisotropies ($r_{D,\infty}$ and $r_{A,\infty}$, respectively):

$$r_C = \sqrt{r_{A,\infty}} \sqrt{r_{D,\infty}} \quad (21)$$

In theory, the donor and the acceptor anisotropy should be determined at the time of energy transfer. If the transfer rate is much slower than the fast component of the anisotropy decay of donor and acceptor, the residual anisotropy can be used (Figure 2.13)⁶². Also, the steady state anisotropy values can give an indication of the rotational freedom of the dyes on the relevant time scales, if the inherent effect by the fluorescence lifetimes is taken into account (see Perrin equation, Table 2.6 and Figure 2.12).

If the steady-state anisotropy and r_C are low (< 0.2), one can assume (but not prove) sufficient isotropic coupling (rotational averaging), i.e. $\langle \kappa^2 \rangle = 2/3$, with an uncertainty of about 5 %⁶²:

$$\Delta R_0(\kappa^2, r_C < 0.2) \approx 0.05 \cdot R_0 \quad (22)$$

Spatial sampling. In addition, it is assumed that both dyes remain in a fixed location for the duration of the donor lifetime, i.e. $k_{FRET} \gg k_{diff}$, where k_{diff} is defined as the inverse of the diffusion time through the complete AV. Recently the diffusion coefficient for a tethered Alexa488 dye was determined to be $D=10 \text{ \AA}^2/\text{ns}$ (ref. ³³). Therefore, k_{diff} is smaller than the k_{FRET} . For short distances ($< 5 \text{ \AA}$) the rates become comparable, but the effect on the inter dye distance distribution within the donor lifetime is small, as has been observed in time resolved experiments. We also assumed that, in the experiment, the efficiencies are averaged for all possible inter-dye positions. This is the case when $k_{diff} \gg k_{int}$, which is a very good assumption for TIRF experiment with $k_{int} > 100 \text{ ms}$ and also for confocal experiments with k_{int} around 1 ms.

Overall uncertainty in R_0 . Time-resolved anisotropy measurements of samples 1 and 2 resulted in combined anisotropies below 0.1. Therefore we assumed isotropic coupling to obtain R_{MP} . The R_{MP} match the model distances very well, further supporting these assumptions. Finally, an experimental study on κ^2 distributions also obtained typical errors of 5 %⁴⁴.

The overall uncertainty for the Förster radius would then result in:

$$\begin{aligned} \Delta R_0(n^{-4}, \Phi_{F,D}, J, \kappa^2) &= \sqrt{\Delta R_0(n)^2 + \Delta R_0(\Phi_{F,D})^2 + \Delta R_0(J)^2 + \Delta R_0(\kappa^2)^2} \\ &\lesssim 0.07 \cdot R_0 \Delta R_0(\kappa^2, r_C < 0.2) \approx 0.05 \cdot R_0 \end{aligned} \quad (23)$$

The absolute values determined for this study are summarized in Table 2.3. Please note that the photophysical properties of dyes vary in different buffers and when attached to different biomolecules. Therefore, all four quantities contributing to the uncertainty in R_0 should be measured for the system under investigation. When supplier values or values from other studies are applied, the uncertainty can be much larger. The values specified here could be further evaluated and tested in another blind study.

2.5 Supplementary Material:

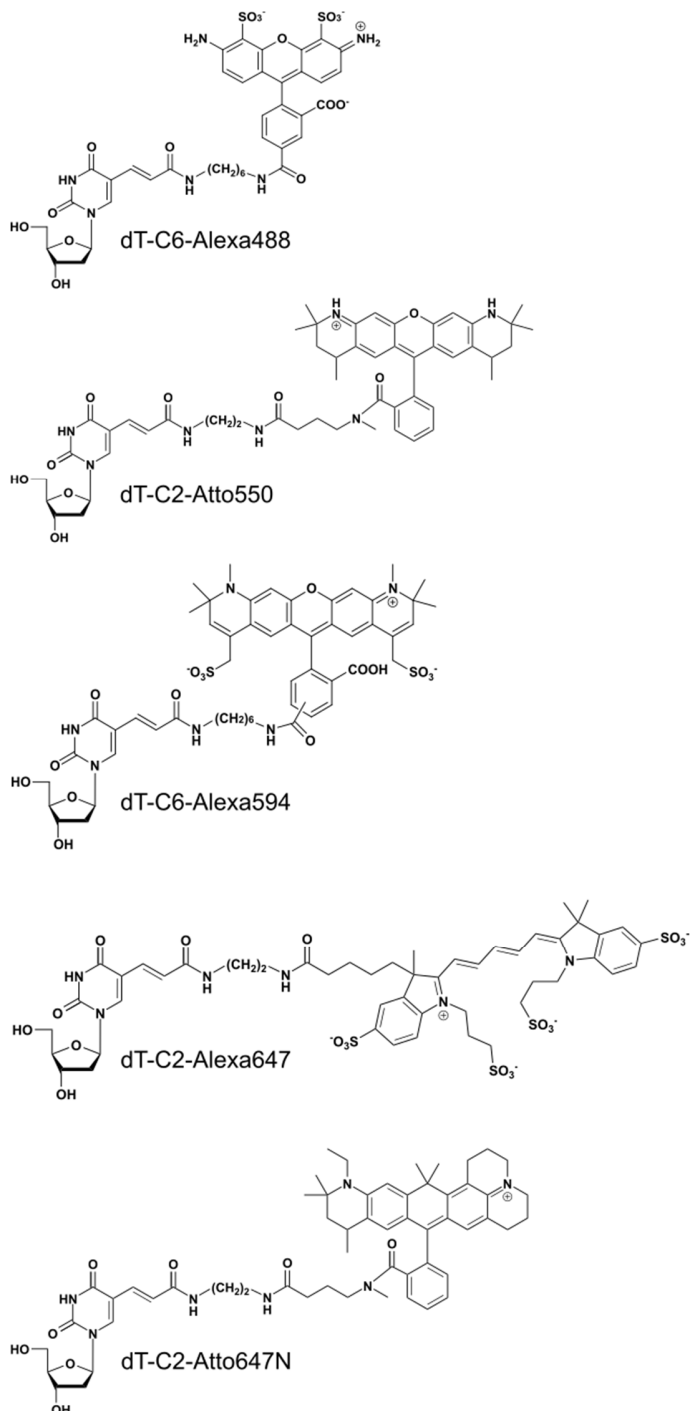


Figure 2.6 Structural formula of the dyes used in this study.

Based on dyes from Molecular Probes / Thermo Fisher Scientific (Waltham, USA) and Atto-tec (Siegen, D).

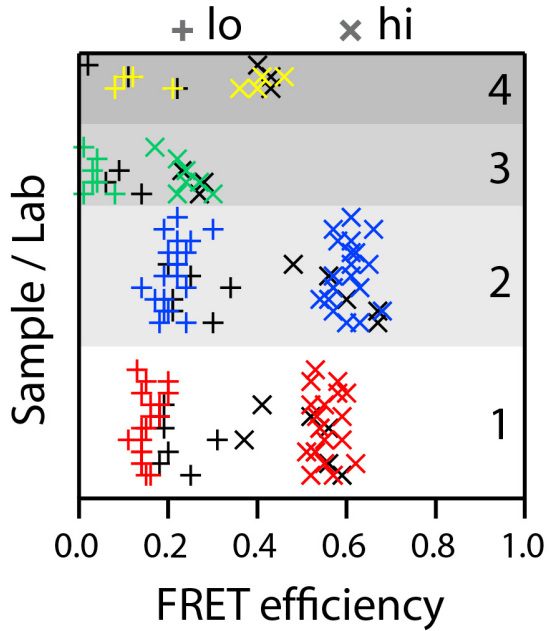


Figure 2.7 FRET efficiencies of all labs for all measured samples as indicated. Sample 1 to 4 (see Table 2.5 and Supplementary Note 5) are color coded (red, blue, green, yellow) for all data points from intensity-based techniques. For a table of $R_{(E)}$ and R_{MP} see Table 2.4 (main text). Ensemble lifetime, single molecule lifetime and phasor approach derived data is shown in black. The FRET efficiencies (means and s.d.) for these measurements (depicted in black) are: $E_{1a}=0.21\pm0.05$; $E_{1b}=0.51\pm0.08$; $E_{2a}=0.25\pm0.06$; $E_{2b}=0.59\pm0.07$; $E_{3a}=0.10\pm0.04$; $E_{3b}=0.26\pm0.03$; $E_{4a}=0.12\pm0.10$; $E_{4b}=0.42\pm0.02$.

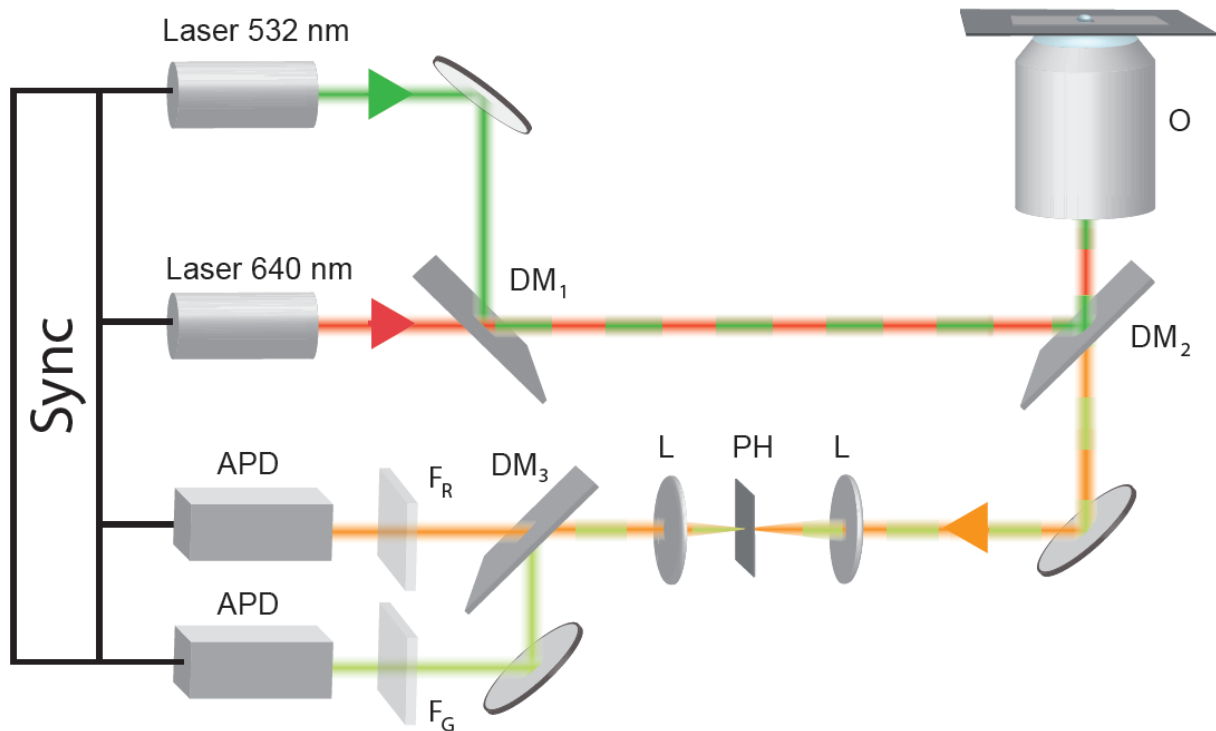


Figure 2.8 Schematics of a typical confocal setup with alternating laser excitation / pulsed interleaved excitation and color-sensitive detection. The most important elements are specified: Objective (O), dichroic mirror (DM), pinhole (P), spectral filter (F), avalanche photo diode (APD) and electronic micro- or picosecond synchronization of laser pulses and single photon counting (Sync).

Elements used for the correction factors in Table 2.2 (main text) were: F34-641 Laser clean-up filter z 640/10 (right after Laser 640 nm); DM₁: F43-537 laser beam splitter z 532 RDC ; DM₂: F53-534 Dual Line beam splitter z 532/633; DM₃: F33-647 laser beam splitter 640 DCXR; F_G: F37-582 Brightline HC 582/75; F_R: F47-700 ET Bandpass 700/75; Objective: Cfi plan apo VC 60xWI, NA1.2; Detectors: MPD Picoquant (green), tau-SPAD, Picoquant (red); Pinholes: 100 μm ; Laser power at sample: $\approx 100 \mu\text{W}$; Beam diameter $\approx 2\text{mm}$; Diffusion time of Atto550 and Atto647N around 0.42 ms and 0.50 ms, respectively.

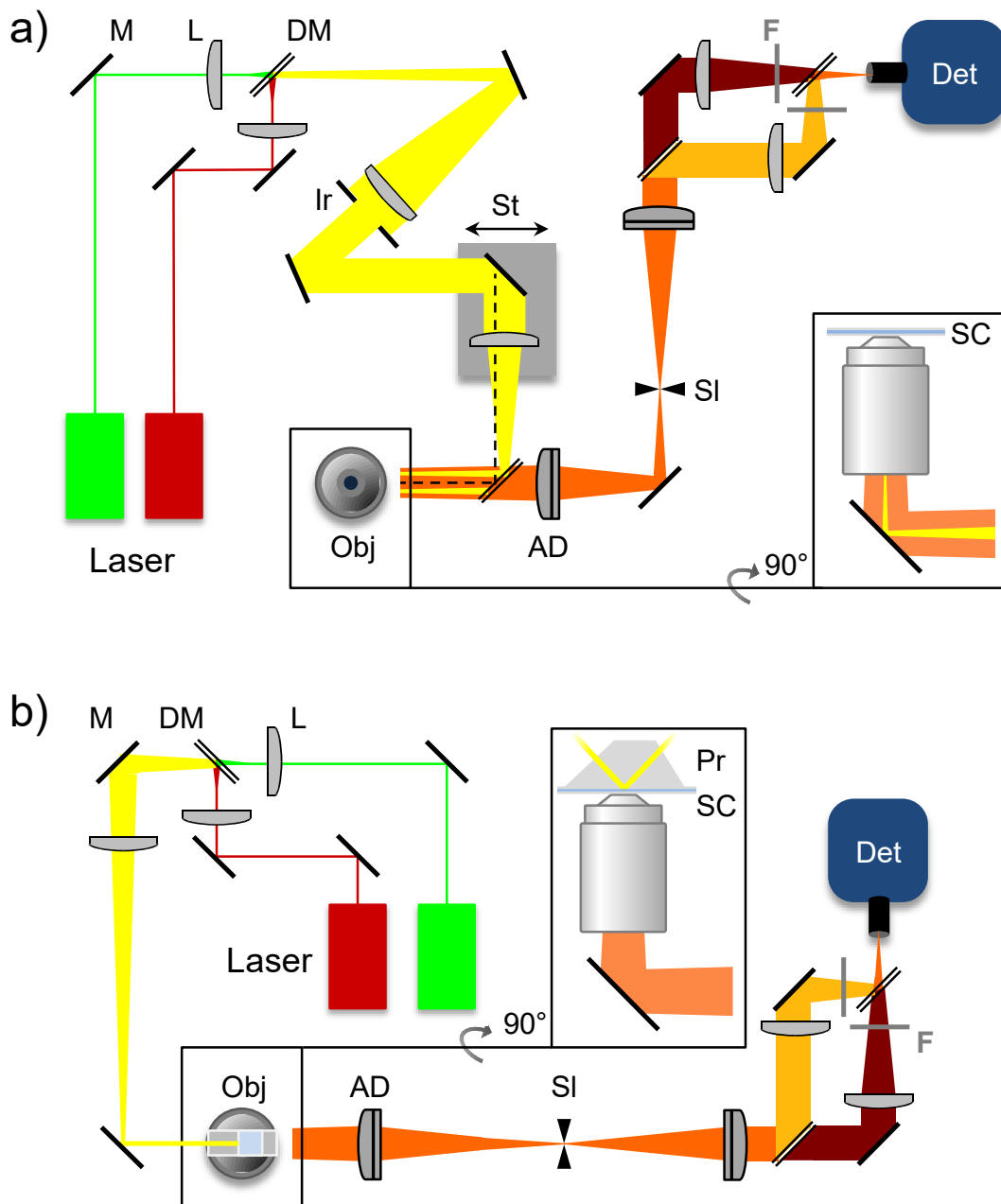


Figure 2.9 Schematic designs of an objective-type (a) and a prism-type TIRF setup (b). Green and red lasers are used to excite donor and acceptor dyes, respectively. M, mirror. L, lens. DM, dichroic mirror. Obj, objective. AD, achromatic doublet lens. SI, tunable slit. F, filters. Det, detector (e.g. electron multiplying charge-coupled device camera, EMCCD). The inset shows a side view of the objective with the out-of-plane (45°) mirror below. SC, sample chamber. Ir, iris. St, translation stage, Pr, prism. The dashed black line in (a) indicates the *on-axis* path to the objective, in contrast to the displayed *off-axis* path for TIR illumination. Elements used for the correction factors in Table 2.2 (main text) were: Dichroic before objective: F53-534 (AHF), Dichroics in detection: F33-726 and F33-644 (AHF). Band pass filters in detection: BP F39-572 and BP F37-677 (AHF). SI: SP40 (Owis), Objective: CFI Apo TIRF 100x, NA 1.49 (Nikon). Camera: EMCCD, iXonUltra, Andor. Lasers: 532nm, Compass 215M (Coherent) and 635nm, Lasiris (Stoker Yale).

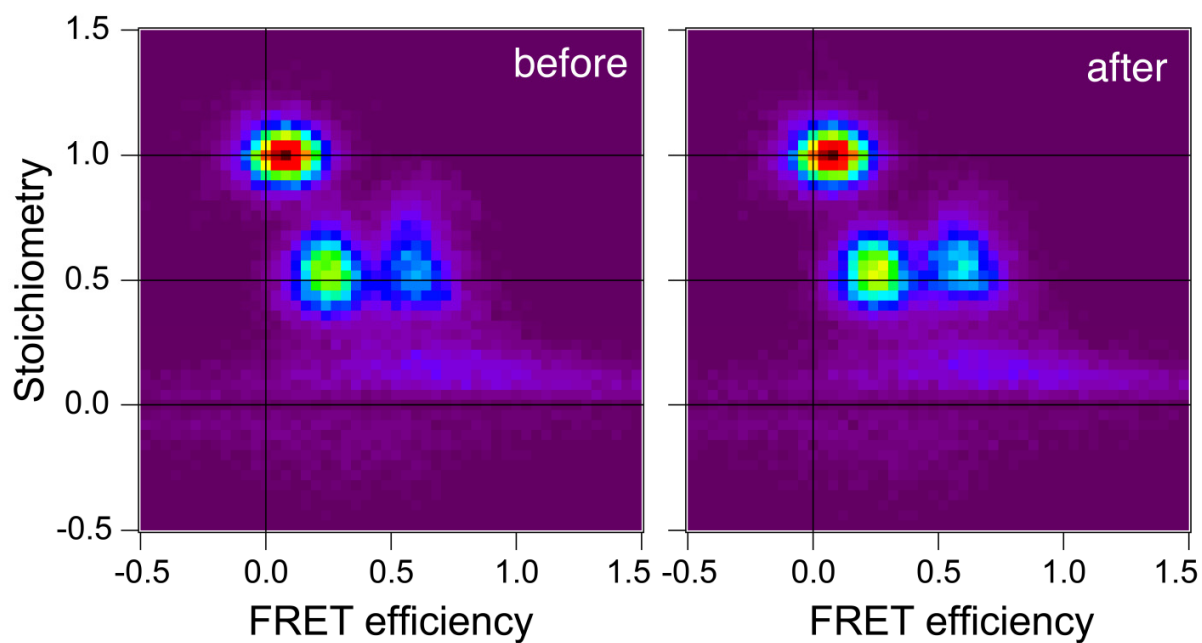


Figure 2.10 Accounting for the differences in the excitation intensity profiles of the green and red laser across the field of view. The individual excitation profiles are determined as the mean image of a stack of images recorded while moving across a dense layer of dyes. In contrast to the uncorrected case (“before”), a position specific normalization creates narrower and more symmetric SE-populations (“after”). The standard corrections described in the main text are performed subsequently.

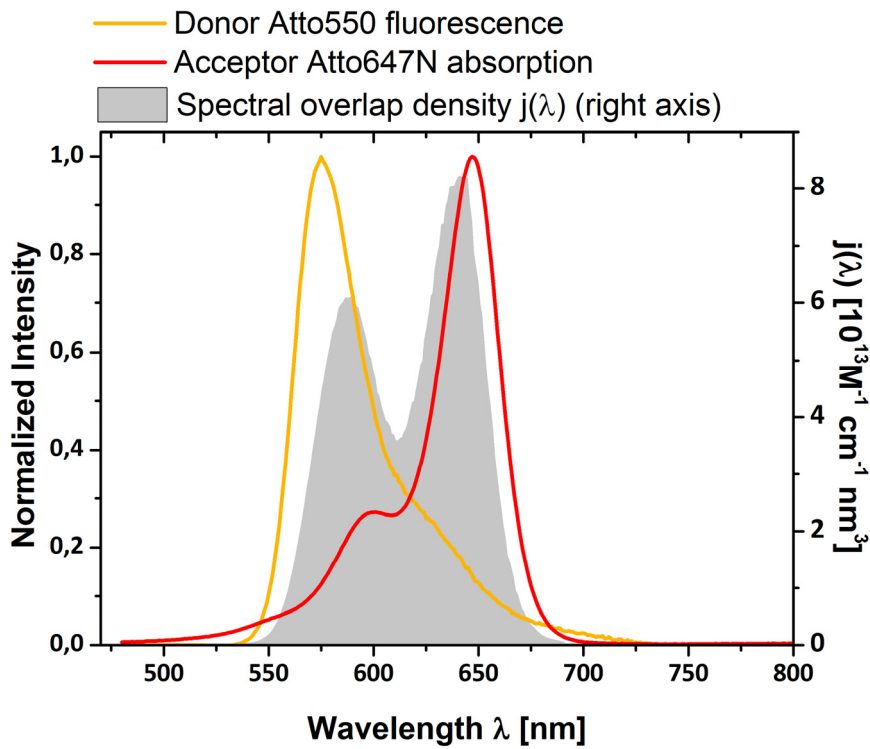


Figure 2.11 Computation of the spectral overlap integral J for the FRET pair Atto550-Atto647N in sample 1. Normalized donor fluorescence and acceptor absorption spectra normalized to the maximum (left scale). Spectral overlap density $j(\lambda)$ (right scale) to compute the spectral overlap integral J [$\text{cm}^{-1}\text{M}^{-1}\text{nm}^4$] with $J = \int_0^{\infty} j(\lambda) d\lambda$ and $j(\lambda) = \bar{F}_D(\lambda)\varepsilon_A(\lambda)\lambda^4$. The extinction coefficient ε_A of Atto647N was assumed to be $150000 \text{ M}^{-1}\text{cm}^{-1}$ at the maximum as provided by the manufacturer.

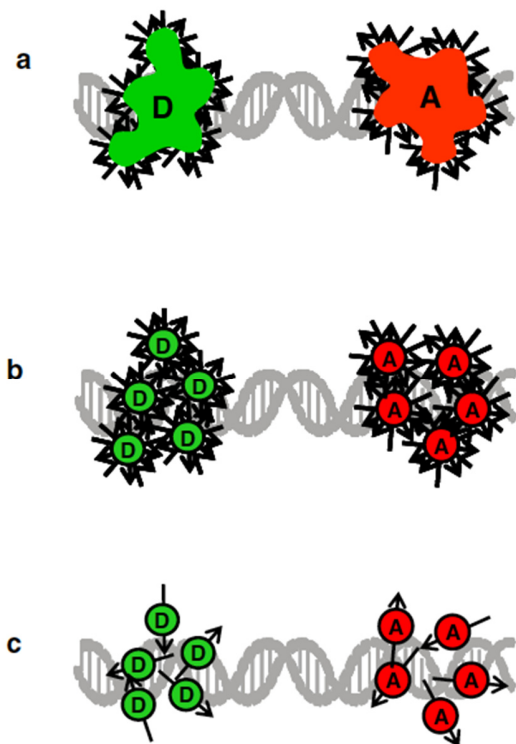


Figure 2.12 Visualizations of different averages for efficiencies according to different fluorophore dynamics. (a) Dynamic average, which applies in the case of the fluorophore movements being faster than the rate of energy transfer. There the rate of energy transfer has to be calculated taking into account the average over all possible distances and orientations. (b) Intermediate case, called the isotropic average, where the orientational variation of the fluorophores is faster than the rate of energy transfer while the positional variation is slower (c) Static case, where the fluorophore movements are much slower than the rate of energy transfer. In this case each distance and respective fluorophore orientation has to be taken into account with its individual transfer efficiency. These efficiencies then are averaged by the measurement process. (Figure from ref. ²⁷).

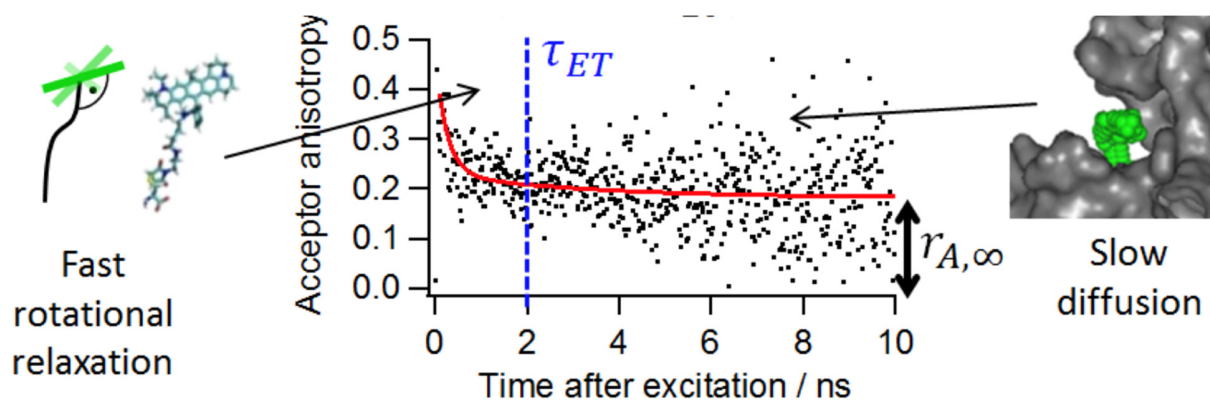


Figure 2.13 Time-resolved anisotropies and FRET. The time-resolved anisotropies of dyes bound to a larger object (e.g. DNA or protein) normally consist of a fast decay from rotational relaxation of the dipole (left) and of a slow decay from translational relaxation (right). $\tau_{ET} = 1/k_{FRET}$: time of energy transfer; $r_{A,\infty}$: residual anisotropy of dye A. (Figure from ref. ⁶²)

Table 2.6 Spectroscopic parameters of the dyes in samples 1 and 2. Residual anisotropy r_{∞} , combined anisotropy r_c , fluorescence quantum yields of donor and acceptor $\Phi_{F,D}$ and $\Phi_{F,A}$, respectively (determined according to the procedure detailed in the online methods), and species average fluorescence lifetimes $\langle \tau \rangle_x$ for the samples 1 (Atto550 /Atto647N) and the samples 2 (Atto550 /Alexa647). All measurements were done in 20mM MgCl₂,5mM NaCl,5mM TRIS at pH 7.5 measurement buffer.

Sample 1	1-lo(Atto550)	1-lo (Atto647N)	1-hi (Atto550)	1-hi (Atto647N)
Base position (Linker), strand	T 31, (C2), D-strand	T 31(C2), A-strand	T 23(C2), D-strand	T 31(C2), A-strand
Residual anisotropy $r_{A,\infty}$ or $r_{D,\infty}$ [a]	0.08	0.07	0.11	0.07
Combined anisotropy r_c	0.07		0.09	
Steady state anisotropy r_s	0.11	0.09	0.13	0.09
Lifetime $\langle \tau \rangle_x$ / ns (SD: 2%) [b]	3.76	3.62	3.81	3.62
Fluorescence quantum yield $\Phi_{F,D}$ or $\Phi_{F,A}$	0.77±0.015[c]	0.65 [d]	0.77±0.015[c]	0.65 [d]
R_0 [Å] [e]	62.6			
$\langle \Phi_{F,D} \rangle$ [e]	0.765			
ϵ_A [M ⁻¹ cm ⁻¹]	150000			
J [cm ⁻¹ nm ⁴ M ⁻¹]	5.180·10 ¹⁵			
n_{im}	1.40			
κ^2	2/3			
Sample 2	2-lo(Atto550)	2-lo (Alexa647)	2-hi (Atto550)	2-hi (Alexa647)
Base position (Linker), strand	T 31, (C2), D-strand	T 31(C2), A-strand	T 23(C2), D-strand	T 31(C2), A-strand
Residual anisotropy $r_{A,\infty}$ or $r_{D,\infty}$ [a]	0.08	0.05	0.11	0.05
Combined anisotropy r_c	0.06		0.07	
Steady state anisotropy r_s	0.11	0.15	0.14	0.14
Lifetime $\langle \tau \rangle_x$ /ns (SD: 2%) [b]	3.76	1.19	3.81	1.19
Fluorescence quantum yield $\Phi_{F,D}$ or $\Phi_{F,A}$ [c]	0.77±0.015[c]	0.35	0.77±0.015[c]	0.35
R_0 [Å] [e]	68.0			
$\langle \Phi_{F,D} \rangle$ [e]	0.765			
ϵ_A [M ⁻¹ cm ⁻¹]	270000			
J [cm ⁻¹ nm ⁴ M ⁻¹]	8.502·10 ¹⁵			
n_{im}	1.40			
κ^2	2/3			

[a] The depolarization time of all species are given together with their amplitudes in Table 2.8

[b] The fluorescence lifetimes of all species are given together with their species fractions in Table 2.7

[c] Measured relative to Rhodamine 6G in air-saturated Ethanol with $\Phi_{F,Rh6G}=0.95$. In the same measurement we obtained for the free dye $\Phi_{F,Atto550} = 0.8 \pm 0.014$ and $\tau_{Atto550} = 3.60 \text{ ns} \pm 2\%$, which corresponds to the values given by the manufacturer.

[d] The following reference values for the free dyes in solution were used from the manufacturers to scale the fluorescence quantum via the fluorescence lifetime of the free dye:

$\Phi_{F,Atto647N} = 0.65$; $\Phi_{F,Alexa647} = 0.33$; $\tau_{Atto647N} = 3.5 \text{ ns}$; $\tau_{Alexa647} = 1.0 \text{ ns}$.

A fluorescence lifetime analysis to relate the quantum yield Φ'_F and lifetime τ' specified by the manufacturer to the measured lifetime τ and quantum yield Φ_F :

$$\Phi_F = \Phi'_F \cdot \tau / \tau'$$

Here, we assume that the manufacturer Φ'_F is correct, that the radiative constant is unchanged and that the lifetime decay is monoexponential. For many dyes in distinct environments, this might not be the case.

Supplementary Note 1: Time-resolved experiments

Global fit of the time-resolved polarized and magic angle fluorescence ensemble data

All polarization resolved fluorescence decay curves ($F_{VV}(t), F_{VH}(t)$) with the Polarizer / Analyzer settings (Vertical, V / Horizontal, H) of singly labeled molecules were studied in ensemble experiments in the Seidel lab by high-precision time correlated single-photon counting and were fitted jointly with corresponding magic angle (M) fluorescence decay $f_{VM}(t) = f(t)$. To reduce the number of parameters in the fits we used the so called homogenous approximation³³. We assumed that de-excitation and depolarization of dyes are independent, i.e. in each donor de-excitation state dyes are characterized by the same set of depolarization times. For this case we can write model functions for the decay of the excited state population $f(t)$ and the fluorescence anisotropy $r(t)$:

$$f_{VV}(t) = f(t)[1 + 2r(t)] \quad (24)$$

$$f_{VH}(t) = f(t)[1 - r(t)] \quad (25)$$

$$\text{with } f(t) = \sum_i x_i e^{-t/\tau_i} \quad \text{and } r(t) = \sum_j b^{(j)} e^{-t/\rho_j}$$

Here, τ is the fluorescence lifetime and ρ is the depolarization times. x_i is (with $\sum_i x^{(i)} = 1$) the species fraction of molecules having the lifetime τ_i and the factor b_j is fraction of molecules having the depolarization time ρ_j where the fundamental anisotropy r_0 is given by $\sum_j b^{(j)} = r_0$ and the residual anisotropy is given by $b^{(3)} = r_\infty$. A maximum of three species for i and j were necessary to obtain satisfactory fits judged by χ^2_r .

To fit real experimental decays IRF, background and amplitudes of the VV , VH signals are accounted as:

$$F_{VV}(t) = F_0 \cdot IRF_{VV}(t) \otimes f_{VV}(t) + B_{VV} \quad (26)$$

$$F_{VH}(t) = g_{VV/VH} F_0 \cdot IRF_{VH}(t) \otimes f_{VH}(t) + B_{VH} \quad (27)$$

Where g_{VVVH} is a correction factor for a polarization dependent detection efficiency, F_0 - amplitude scaling factor, $IRF_{VV}(t)$, $IRF_{VH}(t)$ - instrument response functions and B_{VV} , B_{HV} - background values. The “ \otimes ” sign designates circular convolution.

The fit results for fluorescent signal in parallel and perpendicular polarization planes with respect to the vertically polarized excitation light with their rotation correlation times and amplitudes for D-only and A-only labeled DNA are presented in Table 2.7 and Table 2.8. The measured data and fitted curves with their weighted residuals are presented in the first column of the Figure 2.14. Typical magic angle fluorescence decays are shown in the right column of the Figure 2.14.

As expected ⁴, the amplitude b_l for the fast depolarization motion with ρ_l is approximately a factor 2 larger for dyes where the transition dipole moment is more perpendicular to the linker (disc case: Alexa 488 and Alexa594) than for dyes with a more parallel the transition dipole moment (cone case: Atto550, Atto647N and Alexa647) (compare Figure 2.6 and Table 2.8). Note that some dyes (e.g. Alexa488 and Alexa594) depolarize especially fast, because they have a large fraction of the fastest depolarization time such that $k_{rot} \gg k_{FRET}$ might be satisfied for even higher FRET efficiencies. The depolarization of these dyes is best described by a disc model ².

Table 2.7 Fluorescence lifetimes τ_i and their amplitudes x_i for all studied Donor-only (DO) and Acceptor-only samples (AO). The quality of the fits was judged by χ_r^2 [a,b]

Base position (Linker), strand	Dye [c]	Sample (DO or AO)	τ_1 [ns] (x_1)	τ_2 [ns] (x_2)	τ_3 [ns] (x_3)	$\langle \tau \rangle_x$ [ns]	χ_r^2
T 31(C2), D-strand	Atto550	1-lo (DO), 2-lo (DO)	0.74 (0.03)	3.47 (0.59)	4.44 (0.38)	3.76	1.03
T 23(C2), D-strand	Atto550	1-hi (DO), 2-hi (DO)	0.86 (0.03)	3.54 (0.63)	4.59 (0.34)	3.81	1.02
T 31(C2), A-strand	Atto647N	1-(AO), 3-(AO)	0.24 (0.04)	3.40 (0.52)	4.19 (0.44)	3.62	1.03
T 31 (C2), A-strand	Alexa647	2 -(AO)	0.66 (0.05)	1.18 (0.90)	1.90 (0.05)	1.19	1.00
T 31(C6), D-strand	Alexa488	3-lo (DO)	0.36 (0.03)	2.37 (0.05)	4.11 (0.92)	3.91	1.03
T 23(C6), D-strand	Alexa488	3-hi (DO)	0.37 (0.04)	2.70 (0.04)	4.13 (0.92)	3.92	1.08
T 31 (C6), A-strand	Alexa594	4-(AO)	0.31 (0.03)	3.76 (0.64)	4.55 (0.33)	3.91	0.99

[a] in 20mM MgCl₂, 5mM NaCl, 5mM TRIS at pH 7.5 measurement buffer.

[b] typical errors: average lifetime: $\tau \pm 0.02$ ns. Three lifetime: shortest lifetime $\tau_1 \pm 20\%$ (with $x_1 \sim 15\%$), $\tau_2 \pm 10\%$ (with $x_2 \sim 25\%$), $\tau_3 \pm 3\%$ (with $x_3 \sim 15\%$).

[c] Spectral settings:

Atto550 (fluor. max 574 nm): excitation wavelength 552 nm, emission wavelength 580 nm (bandpass 5.4 nm).

Atto647N (fluor. max 664 nm): excitation wavelength 635 nm, emission wavelength 665 nm (bandpass 9.2 nm).

Alexa647 (fluor. max 665 nm): excitation wavelength 635 nm, emission wavelength 665 nm (bandpass 8.1 nm).

Alexa488 (fluor. max 525 nm): excitation wavelength 485 nm, emission wavelength 520 nm (bandpass 9.2 nm).

Alexa594 (fluor. max 617 nm): excitation wavelength 590 nm, emission wavelength 617 nm (bandpass 8.1 nm).

Note that the fluorescence lifetime analysis exhibited signatures of solvent relaxation. Therefore we use wide bandpasses.

Table 2.8 Rotation correlation times ρ_i with correspondent amplitudes b_i for Donor-only (DO) ($r_0 = 0.38$) and Acceptor-only (AO) ($r_0 = 0.38$) samples. The 1σ confidence range for the longest correlation time is indicated in square brackets. The fit model is described by Eqs. 26-27 with the model functions Eqs. 26-27. The quality of the fits was judged by χ_r^2

Base position (Linker),strand	dye	Sample (DO or AO)	ρ_1 [ns] (b_1)	ρ_2 [ns] (b_2)	ρ_3 [ns] (1σ conf.) ($b_3 = r_\infty$) [b]	χ_r^2
T 31(C2), D-strand	Atto550	1-lo (DO), 2-lo (DO)	0.63 (0.14)	3.08 (0.16)	174 [97-540] (0.08)	1.04
T 23(C2), D-strand	Atto550	1-hi (DO), 2-hi (DO)	0.58 (0.12)	2.76 (0.15)	63 [50-86] (0.11)	1.01
T 31(C2), A-strand	Atto647N	1-(AO), 3-(AO)	0.41 (0.14)	2.05 (0.17)	46 [37-62] (0.07)	1.01
T 31 (C2), A-strand	Alexa647 [a]	2 -(AO)	0.32 (0.09)	1.14 (0.23)	1e5 [125- ∞] (0.06)	0.99
T 31(C6), D-strand	Alexa488	3-lo (DO)	0.25 (0.22)	1.31 (0.12)	31 [24-42] (0.04)	1.03
T 23(C6), D-strand	Alexa488	3-hi (DO)	0.26 (0.22)	1.43 (0.12)	37 [31-46] (0.04)	1.04
T 31 (C6), D-strand	Alexa594	4-(AO)	0.46 (0.22)	1.88 (0.09)	77 [58-121] (0.07)	1.02

[a] Only VV, VH depolarization curves used for fitting in this case.

[b] Due to fluctuations in the G-factor determinations we have small systematic errors; i.e. $\rho_3 > 20$ ns and not the fitted value

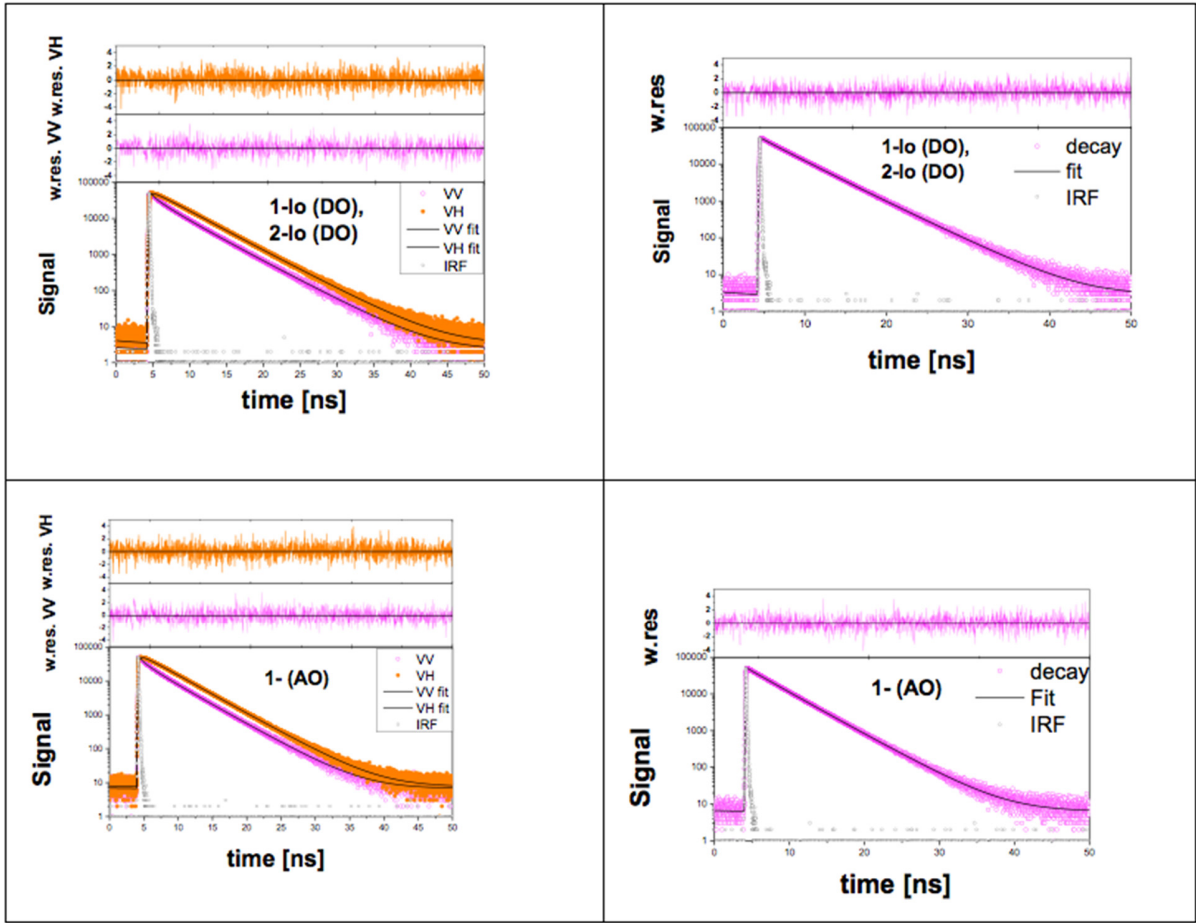


Figure 2.14 Left panels: Typical fluorescent signal in parallel and perpendicular polarization channels (magenta and orange) with the corresponding fits (black) for 1-lo (DO), 2-lo (DO), 1-(AO) samples with weighted residuals on the top. Right panels: the corresponding magic angle fluorescence decay curves with weighted residuals on the top. The fit results are displayed in Table 2.7 and Table 2.8 using fit procedure described by Eqs.24-25 with the model functions eqs 1.3-1.4. The quality of the fits was judged by χ_r^2

Species average lifetime determination

Magic angle fluorescence decays were described with three fluorescence lifetimes τ_i and the species fractions x_i and thus species averaged lifetime $\langle \tau \rangle_x$ was calculated as:

$$\langle \tau \rangle_x = x_1 \tau_1 + x_2 \tau_2 + x_3 \tau_3 \quad (28)$$

Experimental deviations obtained during lifetime-based experiments

The lifetime-based measurements had a significantly lower precision and accuracy than intensity-based measurements. The following factors might be responsible for the observed deviations in the fluorescence lifetime-based FRET experiments:

1. The precision propagates differently for intensity based and time-resolved techniques. In intensity-based FRET measurements the relative error of a normalized donor-acceptor distance changes less with increasing distance. The precision of time-resolved FRET measurements is highest for small DA distances (the minimum is $R_{DA}/R_0 \approx 0.7$) which were not the focus of this study²⁷.
2. Time-resolved techniques strongly depend on a representative (chemically equivalent) Donor-only reference sample that is crucial for resolving large distances accurately.
3. If in the ensemble measurements the FRET sample contains also molecules which are labeled with a donor, it becomes very difficult to resolve species with low FRET efficiencies.
4. The accuracy of time-resolved FRET measurements depends on an appropriate fit model. It is crucial to consider the heterogeneity of the donor lifetimes and dye-linker distributions (eq. 27 in ref.³³). Moreover, the analysis model should allow fitting a variable fraction of donor-only species, which was needed for all provided samples. Altogether, this results in complex fit models which are not widely used in the FRET community because they are difficult to implement in commercial software. In contrast, some groups analyzed the donor decays by a simple series of exponentials, which results in a systematic shift of the obtained FRET parameters.

Thus all four effects in time-resolved FRET measurements contributed to the fact that the precision and accuracy of the distances recovered especially for all lo-samples was markedly lower than that of intensity-based methods.

Supplementary Note 2: AV simulations to compute donor acceptor distances

The model for the double-stranded B-DNA is generated using the Nucleic Acid Builder version 04/17/2017 for Amber⁷⁷ (see Figure 2.1, main text). For modeling the dye molecule, we use a geometrical approach that considers sterically allowed dye positions within the linker length from the attachment point with equal probability. This defines the accessible volume (AV)⁶⁷. The dye molecules are modeled as ellipsoids (approximated by three radii; AV3-Model) and AVs are generated using the FPS software²¹. For the distance computation a dye pair specific Förster Radius is used; i.e., it is assumed that within the AV the dye molecule samples all positions isotropically, however, for a single excitation it is at a fixed position. Moreover, it is assumed that dye rotation is so fast, that all possible orientations are sampled during the fluorescence lifetime and thus the factor $\langle \kappa^2 \rangle = 2/3$ (isotropic coupling).

The boundary tolerance (called ‘allowed sphere’ in the FPS software) is used to ignore small residues that are fixed in the PDB-model, but flexible in solution. The larger this value, the larger the structural parts that are ignored for the AV generation. The labelling position is the C7 of the thymine (the C-atom of the thymine’s methyl group). All mean geometric dyes parameters are estimated with ChemDraw software (see Table 2.9). Further used parameters are: Boundary tolerance 0.5, accessible volume grid (rel.) 0.2; Min. grid [Å] 0.4, Search nodes: 3 and E samples: 200.

Table 2.9 Recommended dye parameters for the AV simulations with AV3-model.

	linker length [Å]	linker width [Å]	R1 [Å]	R2 [Å]	R3 [Å]
dT-C6-Alexa488	20.5	4.5	5.0	4.5	1.5
dT-C2-Atto550	20.4	4.5	7.1	5.0	1.5
dT-C6-Alexa594	20.0	4.5	8.1	3.2	2.6
dT-C2-Alexa647	21.0	4.5	11.0	4.7	1.5
dt-C2-Atto647N	20.4	4.5	7.2	4.5	1.5

Error estimation. For each sample the distances between mean dye positions (R_{MP}^{model}) and expected experimentally observed apparent distance $R_{(E)}^{model}$ are calculated (see Table 2.4, main text). The error for the model distances is estimated by varying the linker lengths (from 10 to 21 Å), linker width (from 4.0 to 5.0 Å), the dye model (single sphere with the radius 6 Å (AV1 model) and ellipsoid with three radii

$R_1=7.1 \text{ \AA}$, $R_2=4.5 \text{ \AA}$ and $R_3=1.8 \text{ \AA}$ (AV3 model) and the boundary tolerance between dye and DNA (0.5 and 1.5 \AA). The standard deviation of all DA distances computed by FPS was used as error.

Supplementary Note 3: $R_{(E)}$ to R_{MP} conversion

For the conversion between $R_{(E)}$ and R_{MP} we distinguish two cases, a known and unknown environment of the dye molecule:

Case 1, the local environment of the dye molecule is known. Here, we use average (apparent) distances from different data-sources, i.e., $R_{(E)}$ from experiment, and R_{MP} from coarse-grained-structural modeling to generate conversion functions. Typically, we use coarse-grained simulations to approximate accessible volumes (AVs) for biomolecules ²¹. These AVs are translated / rotated and the average apparent DA distance ($R_{(E)}$) and the distance R_{MP} are calculated, which introduces noise. The resulting conversion tables are approximated by third order polynomials. Here we used the AVs for the samples 1,2,3,4 low and high FRET correspondingly. For the polynomial $R_{MP} = (a_0 + a_1 R_{(E)} + a_2 R_{(E)}^2 + a_3 R_{(E)}^3)$ the coefficients are given in the Table 2.10 for all FRET pairs.

Note that the conversion functions are specific for the chosen dye pair because they depend on the Förster Radius of the FRET pair and the used dye parameters for the AV simulation. The differences between AVs in different molecular environments (DNA or protein) become smaller the less restricted the dye is. The offset of the conversion function depends on the size of the dye spheres and the linker lengths.

Table 2.10 Conversion polynomial for $R_{MP} = (a_0 + a_1 R_{(E)} + a_2 R_{(E)}^2 + a_3 R_{(E)}^3)$ using the dye pair specific R_0 and specific AVs of the samples 1, 2, 3 and 4, respectively. Note that these polynomials are only valid for this specific geometry and dyes

FRET pair	$R_0 [\text{\AA}]$	$a_0 [\text{\AA}]$	a_1	$a_2 [\text{\AA}]^{-1}$	$a_3 [\text{\AA}]^{-2}$
Atto550-Atto647N	62.6	-41.8	2.13	$-0.92 \cdot 10^{-2}$	$2.40 \cdot 10^{-5}$
Atto550-Alexa647	68.0	-40.3	1.99	$-0.74 \cdot 10^{-2}$	$1.67 \cdot 10^{-5}$
Alexa488-Atto647N	49.3	-53.8	2.83	$-1.89 \cdot 10^{-2}$	$6.17 \cdot 10^{-5}$
Alexa488-Alexa594	57.0	-43.9	2.24	$-1.02 \cdot 10^{-2}$	$2.48 \cdot 10^{-5}$

Case 2, the local environment of the dye molecule is not known. Here, we make the most general assumption that the AV can be approximated by a sphere with its radius estimated from the size of the dye and linker length (slightly smaller than the dye and linker length). This allows us to estimate the

conversion of $R_{(E)}$ to R_{MP} by performing Monte Carlo simulations⁶³. In the Monte Carlo simulation, we place 10,000 positions uniformly distributed within a sphere of 18 Å radius for both dyes. For a given distance of the mean position of these spheres (R_{MP}) we calculate the respective FRET efficiencies via the Förster formula with an orientation factor of $\kappa^2 = 2/3$. The mean of these values is an unbiased estimate for the expected value of the FRET efficiency. We vary the mean position distance from 0.5 R_0 to 1.5 R_0 and fit the resulting means with a third order polynomial (coefficients a_0 , a_1 , a_2 and a_3). For convenience the conversion coefficients for a large range of used Förster radii were determined and given here in Table 2.11.

The equivalence of both approaches is demonstrated in Table 2.10 for the dye pair Atto550-Atto647N.

Table 2.11 Coefficients for the conversion polynomials $R_{(E)}$ to R_{MP} for case 2. These are valid for the specified Förster radius R_0 .

R_0 [Å]	a_0 [Å]	a_1	a_2 [Å] ⁻¹	a_3 [Å] ⁻²
50	-33.6	1.65	$3.25 \cdot 10^{-3}$	$-7.26 \cdot 10^{-5}$
51	-34.0	1.70	$1.55 \cdot 10^{-3}$	$-5.68 \cdot 10^{-5}$
52	-33.0	1.64	$2.25 \cdot 10^{-3}$	$-5.85 \cdot 10^{-5}$
53	-31.7	1.57	$2.93 \cdot 10^{-3}$	$-5.91 \cdot 10^{-5}$
54	-32.8	1.64	$1.27 \cdot 10^{-3}$	$-4.65 \cdot 10^{-5}$
55	-32.0	1.61	$1.43 \cdot 10^{-3}$	$-4.46 \cdot 10^{-5}$
56	-30.0	1.51	$2.78 \cdot 10^{-3}$	$-4.98 \cdot 10^{-5}$
57	-30.0	1.51	$2.19 \cdot 10^{-3}$	$-4.39 \cdot 10^{-5}$
58	-30.0	1.52	$1.73 \cdot 10^{-3}$	$-3.91 \cdot 10^{-5}$
59	-27.7	1.42	$3.03 \cdot 10^{-3}$	$-4.37 \cdot 10^{-5}$
60	-29.1	1.49	$1.55 \cdot 10^{-3}$	$-3.42 \cdot 10^{-5}$
61	-27.5	1.42	$2.36 \cdot 10^{-3}$	$-3.67 \cdot 10^{-5}$
62	-26.5	1.37	$2.77 \cdot 10^{-3}$	$-3.74 \cdot 10^{-5}$
63	-27.3	1.42	$1.67 \cdot 10^{-3}$	$-2.99 \cdot 10^{-5}$
64	-25.6	1.35	$2.56 \cdot 10^{-3}$	$-3.28 \cdot 10^{-5}$
65	-26.1	1.38	$1.88 \cdot 10^{-3}$	$-2.83 \cdot 10^{-5}$
66	-26.4	1.39	$1.42 \cdot 10^{-3}$	$-2.50 \cdot 10^{-5}$
67	-24.9	1.33	$2.07 \cdot 10^{-3}$	$-2.69 \cdot 10^{-5}$
68	-24.1	1.30	$2.27 \cdot 10^{-3}$	$-2.68 \cdot 10^{-5}$
69	-24.2	1.31	$1.90 \cdot 10^{-3}$	$-2.39 \cdot 10^{-5}$
70	-23.3	1.28	$2.29 \cdot 10^{-3}$	$-2.49 \cdot 10^{-5}$
71	-24.4	1.33	$1.30 \cdot 10^{-3}$	$-1.95 \cdot 10^{-5}$
72	-23.4	1.29	$1.80 \cdot 10^{-3}$	$-2.11 \cdot 10^{-5}$
73	-22.6	1.27	$1.86 \cdot 10^{-3}$	$-2.04 \cdot 10^{-5}$

R_0 [Å]	a_0 [Å]	a_1	a_2 [Å] ⁻¹	a_3 [Å] ⁻²
74	-23.0	1.28	$1.53 \cdot 10^{-3}$	$-1.84 \cdot 10^{-5}$
75	-22.4	1.26	$1.62 \cdot 10^{-3}$	$-1.80 \cdot 10^{-5}$
76	-21.8	1.24	$1.70 \cdot 10^{-3}$	$-1.77 \cdot 10^{-5}$
77	-21.6	1.24	$1.58 \cdot 10^{-3}$	$-1.66 \cdot 10^{-5}$
78	-21.8	1.25	$1.28 \cdot 10^{-3}$	$-1.47 \cdot 10^{-5}$
79	-21.2	1.23	$1.44 \cdot 10^{-3}$	$-1.49 \cdot 10^{-5}$
80	-21.2	1.24	$1.32 \cdot 10^{-3}$	$-1.41 \cdot 10^{-5}$
81	-20.5	1.22	$1.43 \cdot 10^{-3}$	$-1.39 \cdot 10^{-5}$
82	-20.3	1.21	$1.40 \cdot 10^{-3}$	$-1.34 \cdot 10^{-5}$
83	-20.5	1.22	$1.17 \cdot 10^{-3}$	$-1.20 \cdot 10^{-5}$
84	-19.8	1.20	$1.36 \cdot 10^{-3}$	$-1.24 \cdot 10^{-5}$
85	-20.3	1.22	$0.96 \cdot 10^{-3}$	$-1.05 \cdot 10^{-5}$
86	-19.5	1.19	$1.20 \cdot 10^{-3}$	$-1.10 \cdot 10^{-5}$
87	-19.1	1.18	$1.22 \cdot 10^{-3}$	$-1.08 \cdot 10^{-5}$
88	-19.0	1.18	$1.15 \cdot 10^{-3}$	$-1.02 \cdot 10^{-5}$
89	-19.0	1.18	$1.04 \cdot 10^{-3}$	$-0.95 \cdot 10^{-5}$
90	-18.8	1.18	$0.99 \cdot 10^{-3}$	$-0.91 \cdot 10^{-5}$

We tested that the polynomials derived using case 1 or case 2 generally yield almost identical conversion functions (Figure 2.15).

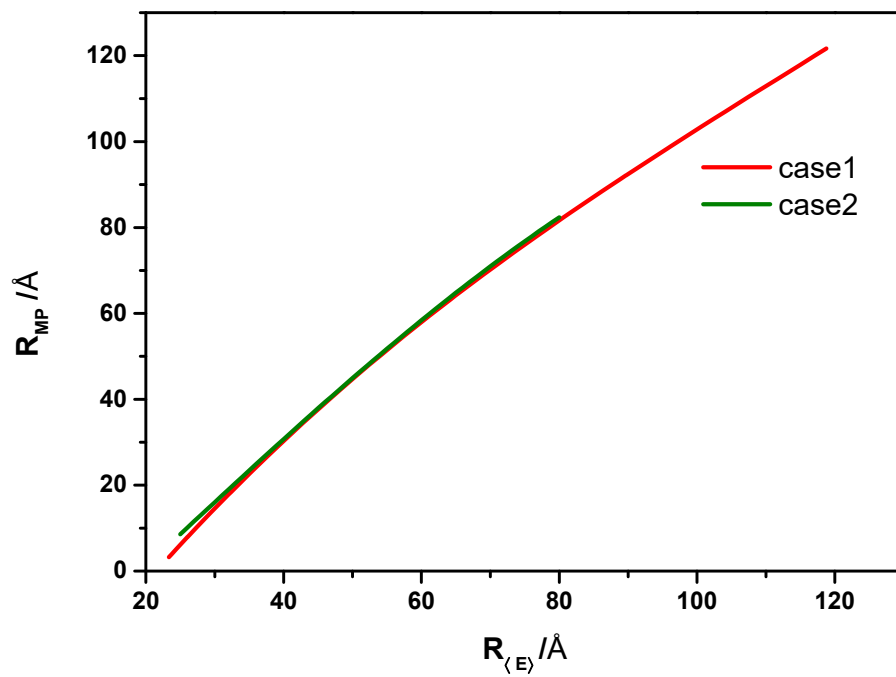


Figure 2.15 Polynomial $R_{MP} = a_0 + a_1 R_{(E)} + a_2 R_{(E)}^2 + a_3 R_{(E)}^3$ for the dye pair Atto550-Atto647N with AVs for DNA (case 1: $R_0 = 62.6 \text{ Å}$) and with the approximation by a sphere (case 2: $R_0 = 62.0 \text{ Å}$). Interpolated points in steps of 1 Å .

Supplementary Note 4: Error propagation

Based on the measurements of sample 1-lo and 1-hi, we performed an error propagation using $\Delta E = 0.033$ (which was the precision for these two best investigated samples). Figure 2.5 follows from the following distance uncertainty:

$$\begin{aligned}\Delta R(R_0, \Delta R_0, \Delta E | R) &= \sqrt{\left(\frac{\partial R(R_0, E)}{\partial R_0} \cdot \Delta R_0\right)^2 + \left(\frac{\partial R(R_0, E)}{\partial E} \cdot \Delta E\right)^2} \\ &= \sqrt{\left(\frac{R}{R_0} \cdot \Delta R_0\right)^2 + \left(\frac{1}{6} \left(1 + \left(\frac{R}{R_0}\right)^6\right)^2 \left(\frac{R}{R_0}\right)^{-5} R_0 \cdot \Delta E\right)^2}\end{aligned}\quad (29)$$

In the following, we performed more detailed error propagation with disentangled error sources. We estimate the uncertainties of all quantities separately and propagate them towards an uncertainty in the distance. The overall uncertainty in the distance is given by:

$$\begin{aligned}\Delta R\left(R_0, \Delta R_0, \gamma, \Delta\gamma, \langle F \rangle, \Delta I_{Dem|Dex}^{(BG)}, \Delta I_{Aem|Dex}^{(BG)}, \Delta\beta, \Delta\alpha | R\right) \\ = \sqrt{\Delta R_{R_0}^2 + \Delta R_{\gamma}^2 + \Delta R_{bgD}^2 + \Delta R_{bgA}^2 + \Delta R_{\alpha}^2 + \Delta R_{\delta}^2}\end{aligned}\quad (30)$$

with the following error contribution for the Förster radius:

$$\Delta R_{R_0}(R) = R \frac{\Delta R_0}{R_0}\quad (31)$$

And the following error contribution for the gamma factor:

$$\Delta R_{\gamma}(R) = \frac{R}{6} \cdot \frac{\Delta\gamma}{\gamma}\quad (32)$$

And the following error contribution for the background in the donor channel after donor excitation:

$$\Delta R_{bgD}(R) = \frac{R}{6} \left[\gamma \left(1 + \left(\frac{R_0}{R}\right)^6\right) + \alpha \left(1 + \left(\frac{R}{R_0}\right)^6\right) \right] \cdot \frac{\Delta I_{Dem|Dex}^{(BG)}}{\langle F \rangle}\quad (33)$$

And the following error contribution for the background in the acceptor channel after donor:

$$\Delta R_{bgA}(r) = -\frac{R}{6} \left(1 + \left(\frac{R}{R_0} \right)^6 \right) \cdot \frac{\Delta I_{Aem|Dex}^{(BG)}}{\langle F \rangle} \quad (34)$$

And the following error contribution for the direct excitation factor of the acceptor with the green laser:

$$\Delta R_{\delta}(R) = -\frac{R}{6} \beta \left(1 + \left(\frac{R}{R_0} \right)^6 \right) \cdot \Delta \delta \quad (35)$$

And the following error contribution for the leakage factor of donor fluorescence in the acceptor channel:

$$\Delta R_{\alpha}(R) = -\frac{R}{6} \frac{1}{\gamma} \left(\frac{R}{R_0} \right)^6 \cdot \Delta \alpha \quad (36)$$

Please note that for determination of background we set $\gamma=\beta=1$ and $\alpha = \delta = 0$. This represents the ideal values. Further parameters and uncertainties are taken from the reference lab: $\Delta\gamma/\gamma = 0.1$, $\langle F \rangle = 50$, $\Delta I_{Dem|Dex}^{(BG)}=1$, $\Delta I_{Aem|Dex}^{(BG)} = 1$, $\Delta\delta/\delta= 0.1$, $\frac{\Delta\alpha}{\alpha} = 0.1$, $\Delta R_0 = 0.07$. See *Online Methods, Section 2 and 3* for the nomenclature and details on the Förster radius. $\langle F \rangle$ is the average sum of the corrected donor and acceptor fluorescence.

The above error analysis is based on R_{DA} and may be further propagated to the apparent donor-acceptor distance $R_{(E)}$ and the distance between the mean positions of the dyes, R_{MP} , when the above model assumption of a freely rotating and diffusing dye is applied. This becomes very involved and does not show significant deviations from Figure 2.5 in the main text.

Supplementary Note 5: Further samples

Table 2.12 Further samples that being studied

Name	Base position (Linker), strand	Dyes (Donor/ Acceptor)	Sequence
3-lo	T 31(C6), D-strand	Alexa488 Tetrafluorophenyl Ester/	5' - GAG CTG AAA GTG TCG AGT TTG TTT GAG TGT T TG TCT GG-3'
	T 31(C2), A-strand	Atto647N NHS	3' - CTC GAC T T T CAC AGC TCA AAC AAA CTC ACA AAC AGA CC-5' - biotin
3-hi	T 23(C6), D-strand	Alexa488 Tetrafluorophenyl Ester/	5' - GAG CTG AAA GTG TCG AGT TTG T T T GAG TGT TTG TCT GG-3'
	T 31(C2), A-strand	Atto647N NHS	3' - CTC GAC T T T CAC AGC TCA AAC AAA CTC ACA AAC AGA CC-5' -biotin
4-lo	T 31(C6), D-strand	Alexa488 Tetrafluorophenyl Ester/	5' - GAG CTG AAA GTG TCG AGT TTG TTT GAG TGT T TG TCT GG-3'
	T 31(C6), A-strand	Alexa594 Tetrafluorophenyl Ester	3' - CTC GAC T T T CAC AGC TCA AAC AAA CTC ACA AAC AGA CC-5' - biotin
4-hi	T 23(C6), D-strand	Alexa488 Tetrafluorophenyl Ester/	5' - GAG CTG AAA GTG TCG AGT TTG T T T GAG TGT TTG TCT GG-3'
	T 31(C6), A-strand	Alexa594 Tetrafluorophenyl Ester	3' - CTC GAC T T T CAC AGC TCA AAC AAA CTC ACA AAC AGA CC-5' - biotin

Even for samples 3 and 4 the precision of the hi-samples, where all individual FRET efficiencies were in a sensitive range of the specific dye pairs, is very good (2 - 4 %). Moreover, the experimental and model values of the low- and hi-samples agree very well with each other (the deviations range between 2 and 10 %). This suggests that we do not have dye artifacts for all four FRET pairs. The results obtained for the different FRET pairs will be important in the future to judge key aspects of different fluorophore properties.

Supplementary Note 6: MD simulations

While the analysis in this paper used a static model for the double-stranded DNA structure, DNA is known to not be completely rigid⁸⁰. Therefore, we performed Molecular dynamics (MD) simulations of the DNA molecule to explore its rigidity using the latest force fields which were reported to be consistent with experimental observables of the conformational flexibility of dsDNA.

The all-atom MD simulations were performed with the Amber16 suite of programs⁹⁵ using the bsc1 force field⁷⁷. The initial structure of the B-DNA molecule, which was generated by 3D-DART (see main text), was placed in an octahedral box of TIP3P water molecules⁹⁶, such that the distance between the edge of the water box and the closest DNA atom was at least 11 Å. MgCl₂ and NaCl were added to achieve concentrations of 20 mM and 10 mM, respectively. For Na⁺ and Cl⁻, the parameters by Joung and Cheatham⁹⁷ were used, while for Mg²⁺ the parameters by Li et al.⁹⁸ were used.

Each system was then prepared based on a protocol used earlier⁹⁹. The simulation system was minimized by 200 steps of steepest descent and subsequently 50 steps of conjugate gradient minimization. The minimized system was heated from 100 to 300 K over 50 ps, and subsequently the solvent density was adjusted for 150 ps by NPT-MD simulation. During the previous two steps, harmonic force restraints were applied on all solute atoms with force constants of 5 kcal mol⁻¹ Å⁻². These harmonic force restraints were gradually reduced to 1 kcal mol⁻¹ Å⁻² during 250 ps of NVT-MD simulation. This step was followed by 50 ps of NVT-MD simulation without positional restraints.

The time step for all MD simulations was 2 fs. Subsequently, we performed five independent MD simulations of 250 ns length each. Coordinates were extracted from the simulations every 20 ps. We used the FPS program²¹ to calculate FRET efficiencies for the structural ensemble of the MD simulation, i.e. for each structure the AVs with the spatial dye (D and A) distributions is calculated and the average FRET efficiency is computed.

The ensembles from the MD simulations suggest that the DNA is not completely rigid, but exhibits some bending motion (Figure 2.16). The obtained distributions of FRET efficiencies show that the ensembles from the MD simulations yield comparable, but slightly lower mean FRET efficiencies and thus longer distances than for the static model (Figure 2.17, Table 2.13).

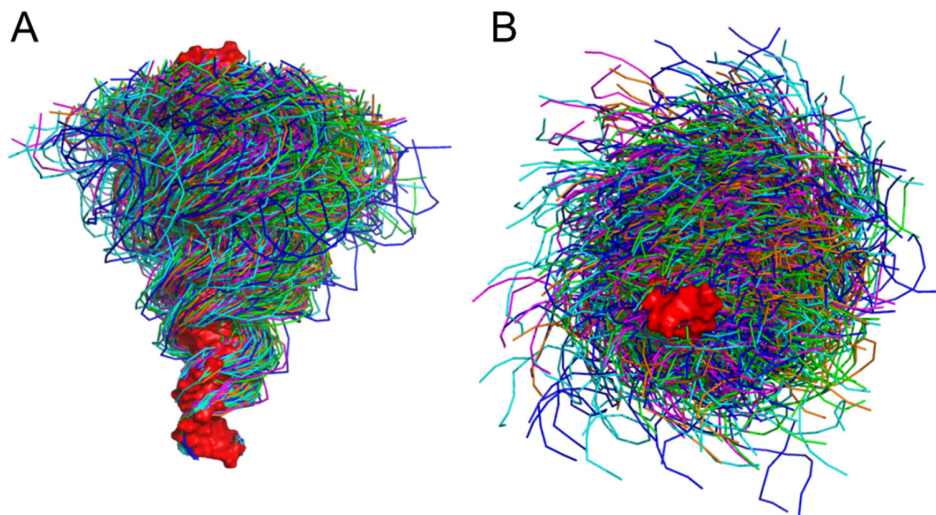


Figure 2.16: Structural ensembles from the MD simulations. The starting structure (red surface representation) was overlaid with conformations extracted from the MD simulations using the first 5 base pairs of the DNA. The five independent MD simulations are shown as differently colored ribbons (green, blue, orange, magenta, and cyan). For visibility, snapshots extracted every 2 ns were used for this representation. A: Side view; B: Top view.

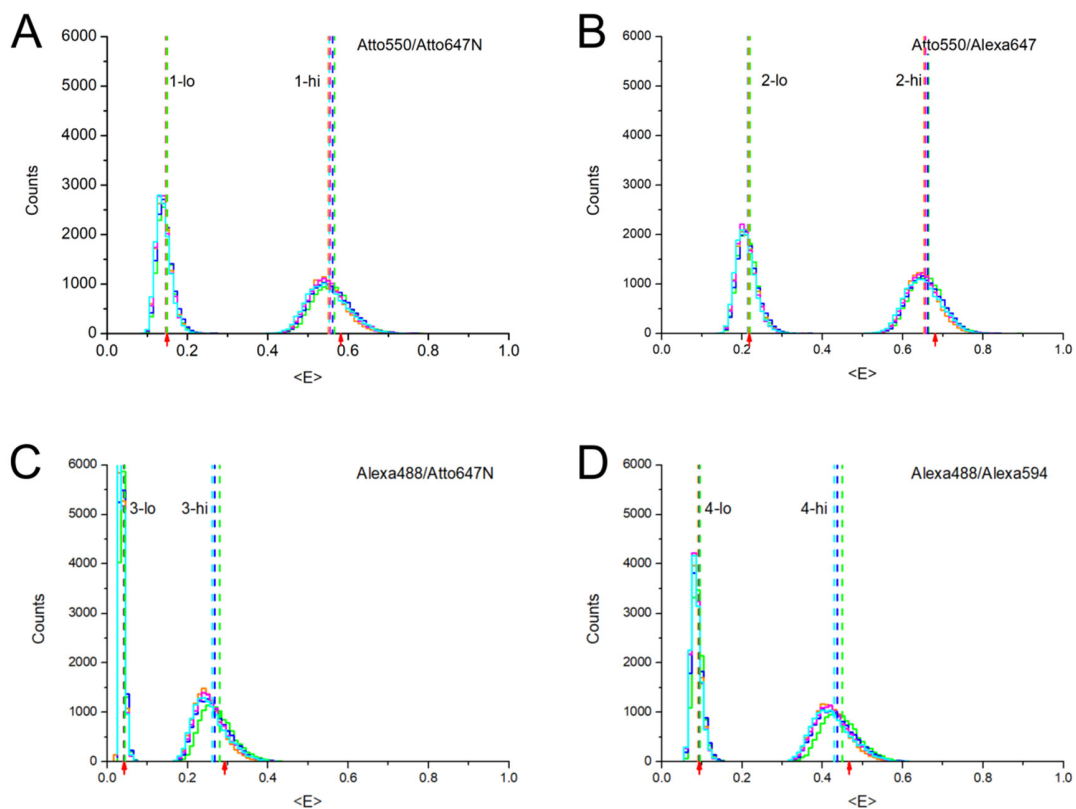


Figure 2.17 Distribution of FRET efficiencies calculated for the conformation extracted from the MD simulations for the four samples (A: Atto550/Atto647N, B: Atto550/Alexa647, C: Alexa488/Atto647N, D: Alexa488/Alexa594). The

five colors (green, blue, orange, magenta, and cyan) correspond to the five independent MD simulations performed. Vertical dashed lines indicate the mean of the distribution, while the red arrows below the X-axis indicate the values calculated for the starting structure.

Table 2.13 Comparison of FRET efficiencies $\langle E \rangle_{dyn}$ and corresponding DA distances $R_{\langle E \rangle}^{(dyn)}$ calculated from the five MD simulations to the values from experiments ($\langle E \rangle_{exp}$, $R_{\langle E \rangle}^{(exp)}$) and the static model with $\langle E \rangle_{static}$.

Sample	$\langle E \rangle_{dyn}^{[a]}$	$\langle E \rangle_{static}^{[b]}$	$\langle E \rangle_{exp}^{[c]}$	$R_{\langle E \rangle}^{(dyn)} [\text{Å}]^{[d]}$	$R_{\langle E \rangle}^{(exp)} [\text{Å}]^{[e]}$
Atto550/Atto647N					
1-lo	0.15	0.15	0.15 ± 0.02	83.9	83.4 ± 2.5
1-hi	0.56	0.58	0.56 ± 0.03	60.3	60.3 ± 1.3
Atto550/Alexa647					
2-lo	0.22	0.22	0.21 ± 0.04	84.2	85.4 ± 3.4
2-hi	0.66	0.68	0.60 ± 0.05	61.0	63.7 ± 2.3
Alexa488/Atto647N					
3-lo	0.04	0.04	0.04 ± 0.02	83.1	89.5 ± 12.3
3-hi	0.27	0.29	0.24 ± 0.04	58.4	60.1 ± 2.3
Alexa488/Alexa594					
4-lo	0.09	0.09	0.13 ± 0.06	83.5	79.6 ± 6.2
4-hi	0.44	0.47	0.41 ± 0.04	59.5	60.7 ± 1.7

[a] Calculated as average over the five simulations (the standard deviation is in all cases below 0.008).

[b] Calculated for the static starting structure.

[c] From measurements (cf. main text, Table 2.4).

[d] Calculated from $\langle E \rangle_{dyn}$ using Formula (V) from Table 2.1 in the main text.

[e] Calculated from experiments (cf. main text; Table 2.4).

2.6 Appendix with my measurements and analysis

2.6.1 Material and methods

2.6.1.1 Setups and correction factors for given samples at given setups

Single molecule Molecule Multiparameter Fluorescence Detection (MFD)

All single-molecule experiments were conducted on three confocal setups with different modifications of particular elements. The general scheme of the setup is illustrated on Figure 2.18. All samples were measured in NUNC chambers (Lab-Tek, Thermo Scientific, Germany) with 300 μ L sample volume.

Confocal 1 for measurements of the samples with Alexa488-Atto647N

The fluorescent donor molecules (Alexa 488) are excited by 485 nm pulsed diode laser (LDH-D-C 485, PicoQuant), operated at 64 MHz, 110 μ W in the sample in one color excitation experiment or at 32 MHz in PIE experiment, 110 μ W in the sample. The laser light is guided into the epi-illuminated confocal microscope (Olympus IX71, Hamburg, Germany) with a 60x/1.2 water immersion objective (UPlanSApo 60x/1.2w, Olympus Hamburg, Germany) and is reflected by dichroic beamsplitter FF500/646-Di01 (Semrock, USA). Additionally in the PIE experiment the fluorescent acceptor molecules (Atto647N) are excited by 635 nm pulsed diode laser (LDH-D-C 640, PicoQuant). The emitted fluorescence from the labeled molecules is collected through the objective and spatially filtered using a pinhole with typical diameter of 100 μ m. Then, the signal is split into parallel and perpendicular components via polarizing beam splitter and then at two different spectral windows (e.g. “green” and “red”) and then split again using 50/50 beam splitters resulting in a total of eight detection channels.

Additionally green (HQ 520/35 nm for Alexa488) from AHF, Tübingen, Germany and red (HQ 720/150 nm for Atto647N) bandpass filters (AHF, Tübingen, Germany) are placed in front of the detectors to provide the registration only of the fluorescence photons coming from the acceptor and donor molecules. Detection is performed using eight avalanche photodiodes (4 green channels: τ -SPAD (PicoQuant, Germany) and 4 red channels: AQR 14 (Perkin Elmer). The detector outputs were recorded by a TCSPC module (HydraHarp 400, PicoQuant).

Confocal 2 for measurements of the samples with Atto550-Atto647N

Confocal setup 2 is similar to the one described above. The differences are described below: Confocal microscope: Olympus IX71 (Hamburg, Germany); Objective: Olympus UPlanSApo 60x/1.2w (Hamburg, Germany); Dichroic Beamsplitter: F68-532_zt532/640NIRrpo (AHF, Tübingen, Germany); Fluorescence dichroic beamsplitter: T640lpxr (AHF, Tübingen, Germany); Diode lasers: 530nm (LDH-P-FA 530B, PicoQuant) and 640nm (LDH-D-C 640, PicoQuant), both with repetition rate 32MHz and with power

75.5 μ W and 16.7 μ W in the sample respectively; Bandpass filters: green ET595/50 and red HQ730/140; 2 green and 2 red detectors: both SPCM-AQRH 14 (Excelitas, USA).

Confocal 3 for measurements of the samples with Alexa488-Alexa594

Confocal setup 3 is similar to the confocal setup 1. The differences are described below: Confocal microscope (Olympus IX70, Hamburg, Germany); Dichroic beam splitter: Q505LP (AHF, Tübingen, Germany); Fluorescence dichroic beamsplitter: 595 LP DCXR (AHF, Tübingen, Germany); Diode lasers: 495nm (PicoQuant, Germany) with repetition rate 32MHz and with power in the sample 110 μ W; Bandpass filters: green HQ520/66, red HQ630/60; 2 green and 2 red detectors: SPCM-AQRH 14 (Perkin Elmer); TCSPC module SPC 132 (Becker&Hickl, Germany).

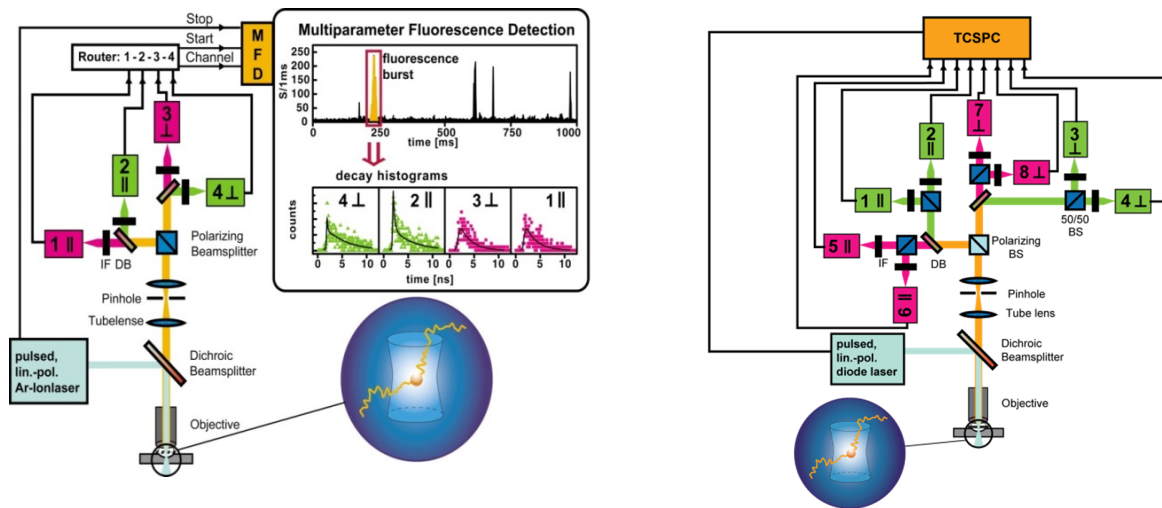


Figure 2.18 Schematic experimental confocal setup 3 and data acquisition (left) and confocal setup 1,2 (right)

Parameters used for studied FRET pairs for given experimental setups are collected in the Table 2.14

Table 2.14 Typical correction factors for sample 1 (Atto550-Atto647N), sample2 (Atto550-Alexa647), sample 3(Alexa488-Atto647N) and sample 4(Alexa488-Alexa594) for the SMD experiment

Parameter name	Dye pair			
	Atto550-Atto647N	Atto550-Alexa647	Alexa488-Atto647N	Alexa488-Alexa594
α	0.062	0.062	0.01	0.052
δ	0.15	0.19	n.a	0.06
$g_{G D}/g_{R A}$	2.10	1.60	0.80	1.02
$\Phi_{F,D(0)}$	0.77	0.77	0.80	0.80
$\Phi_{F,A}$	0.74[b]	0.350 (2-lo),0.405 (2-mid),0.409(2-hi) [a]	0.65	0.70
γ	0.46	0.28 (2-lo), 0.33 (2-	1.02	1.09

		mid), 0.33(2-hi)		
--	--	------------------	--	--

[a] accounting for effective acceptor brightness: $B_A = a_{\text{trans}} * \Phi_{F,A}$, where $\Phi_{F,A} = 0.476$ (from the reference Cy5 with $\tau = 1.0\text{ns}$ and $\Phi_{F,A} = 0.4$). Here $a_{\text{trans}}(2a) = 0.75$, $a_{\text{trans}}(2b) = 0.85$, $a_{\text{trans}}(2c) = 0.86^{100}$

[b] This value was obtained by calibrating the setup with estimated detection efficiency ratio $g_{G|D}/g_{R|A}$ and FRET Efficiency, obtained from studied 1a-1b samples from round 1 in the paper.

Ensemble Time Correlated Single Photon Counting (eTCSPC) setup

Fluorescence lifetime decays were recorded by using FT300 setup (PicoQuant, Germany) with white light laser from NKT Photonics (Germany) with repetition rate 20 MHz. All samples were measured in Quartz Ultra-Micro-cuvettes (Helma #105.252.85.40), with total sample volume 20 μl . Ludox scattering solution was used to record instrument response function (IRF). The detailed measurement conditions for the experiments are provided below in the Table 2.15

Table 2.15 Settings for Picoquant FT300 setup

	Atto 550	Alexa 488	Atto 647N	Alexa647	Alexa 594
Excitation, nm	552	485	635	635	590
Emission, nm	580	520	665	665	617
Bandpass, nm	5.4	9.2	9.2	8.1	8.1
Excitation filter	none	ZET 488/10x	ZET 635/20x	ZET 635/20x	none
Emission filter	FGL 570	FGL 515	FGL 645	FGL 645	FGL 610

2.6.1.2 Photon distribution analysis (PDA)

The analysis procedure and chosen model as described in Chapter 3.3.3.

2.6.1.3 Gaussian distributed distance R_{DA} fitting of the time resolved fluorescence data

The specific fluorescence decays were analyzed by a fit model described previously¹⁰¹. Due to local quenching the fluorescence decay of the donor in the absence of FRET is already often multi-exponential

$$F_{D(0)}(t) = \sum_i x_D^{(i)} \exp(-t / \tau_{D(0)}^{(i)}) \quad (37)$$

The time resolved fluorescence intensity decays of FRET-samples were fitted globally with the decays of the donor only sample. We assume that quenching the donor radiative lifetime is not changed by quenching. Hence, the FRET-rate (k_{FRET}) is only determined by the donor-acceptor distance and their

relative orientation. In the presence of FRET, the donor fluorescence decay can be expressed using the donor-acceptor distance distribution $p(R_{DA})$

$$F_{(D)}(t) = \sum_i x_D^{(i)} \int_{R_{DA}} p(R_{DA}) \exp\left(-\frac{t}{\tau_{D(0)}^{(i)}} [1 + (R_0/R_{DA})^6]\right) dR_{DA} \quad (38)$$

Here we assumed Gaussian distribution of donor-acceptor distances ($p(R_{DA})$) with a mean of $\langle R_{DA} \rangle$ and a half-width of σ_{DA} which is expressed as

$$p(R_{DA}) = \frac{1}{\sqrt{2\pi}\sigma_{DA}} \exp\left(-\frac{(R_{DA} - \langle R_{DA} \rangle_{exp})^2}{2\sigma_{DA,exp}^2}\right) \quad (39)$$

In addition, a fraction of Donor only molecules (x_{Donly}) and a constant offset c was considered to describe the experimentally observed fluorescence decay $F(t)$

$$F(t) = (1 - x_{Donly})F_D(t) + x_{Donly}F_{D(0)} + c \quad (40)$$

Fitting results of the fluorescence decays of FRET-samples are demonstrated in Figure 2.24 and in Table 2.20. The results of the donor only fluorescence decays are in Figure 2.25 and in the Table 2.21.

2.6.1.4 Global fit of the time-resolved polarized and magic angle fluorescence data

All fluorescence depolarization decay curves ($F_{VV}(t), F_{VH}(t)$) of single labeled molecules were fitted jointly with corresponding magic angle fluorescence decay $F_D(t)$. The corresponding expectations for the delta excitation pulse can be written as

$$f_{VV}(t) = \sum_j \sum_i x^{(i,j)} e^{-k_d^{(t)} t} [1 + 2e^{-k_r^{(t)} t}]; \sum_j \sum_i x^{(i,j)} = r_0 \quad (41)$$

$$f_{VH}(t) = \sum_j \sum_i x^{(i,j)} e^{-k_d^{(t)} t} [1 - 2e^{-k_r^{(t)} t}] \quad (42)$$

$$f_{VV}(t) = \sum_j \sum_i x^{(i,j)} e^{-k_d^{(t)} t} [1 + 2e^{-k_r^{(t)} t}]; \sum_j \sum_i x^{(i,j)} = r_0 \quad (43)$$

$$f_D(t) = \sum_i x_d^{(i)} e^{-k_d^{(i)} t}; \sum_i x_d^{(i)} = 1 \quad (44)$$

$$r(t) = \sum_j x_r^{(j)} e^{-k_r^{(j)} t} ; \sum_j x_r^{(j)} = r_0 \quad (45)$$

Where, the element of matrix $x^{(i,j)}$ is a fraction of molecules having the donor de-excitation rate constant $k_d^{(i)}$ and the depolarization rate constant $k_r^{(j)}$, the element of vector $x_d^{(i)}$ is fraction of molecules having the donor de-excitation rate constant $k_d^{(i)}$ and the element of vector $x_r^{(j)}$ is fraction of molecules having the depolarization rate constant $k_r^{(j)}$.

It should be noted that in general matrix $[x^{(i,j)}]$ is independent of vectors $x_d^{(i)}$ and $x_r^{(j)}$. So if N_d is the number of donor states, N_r is the number of depolarization states, then such model would require to fit $N_d + N_r + N_d \cdot N_r$ independent fractions.

To reduce the number of parameters we used so called homogenous approximation. We assumed that de-excitation and depolarization of dyes are independent, i.e. in each donor de-excitation states dyes characterized by the same set of depolarization rate constants. In this case $x^{(i,j)} = x_d^{(i)} x_r^{(j)}$, and we can write

$$f_{VV}(t) = \sum_j \sum_i x_d^{(i)} x_r^{(j)} e^{-k_d^{(i)} t} [1 + 2e^{-k_r^{(j)} t}] = f_D(t)[1 + 2r(t)] \quad (46)$$

And

$$f_{VH}(t) = \sum_j \sum_i x_d^{(i)} x_r^{(j)} e^{-k_d^{(i)} t} [1 - e^{-k_r^{(j)} t}] = f_D(t)[1 - r(t)] \quad (47)$$

So we have the same expression as in case of simple mono-exponential donor and acceptor decays and the number of fraction values is reduced to $N_d + N_r$. In this work the best fit results were achieved with $N_d = N_r = 3$.

To fit real experimental decays IRF, background and amplitudes of the VV, VH signals are accounted as

$$F_{VV}(t) = F_0 \cdot IRF_{VV}(t) \otimes f_{VV}(t) + B_{VV} \quad (48)$$

$$F_{VH}(t) = g_{VV/VH} \cdot F_0 \cdot IRF_{VH}(t) \otimes f_{VH}(t) + B_{VH} \quad (49)$$

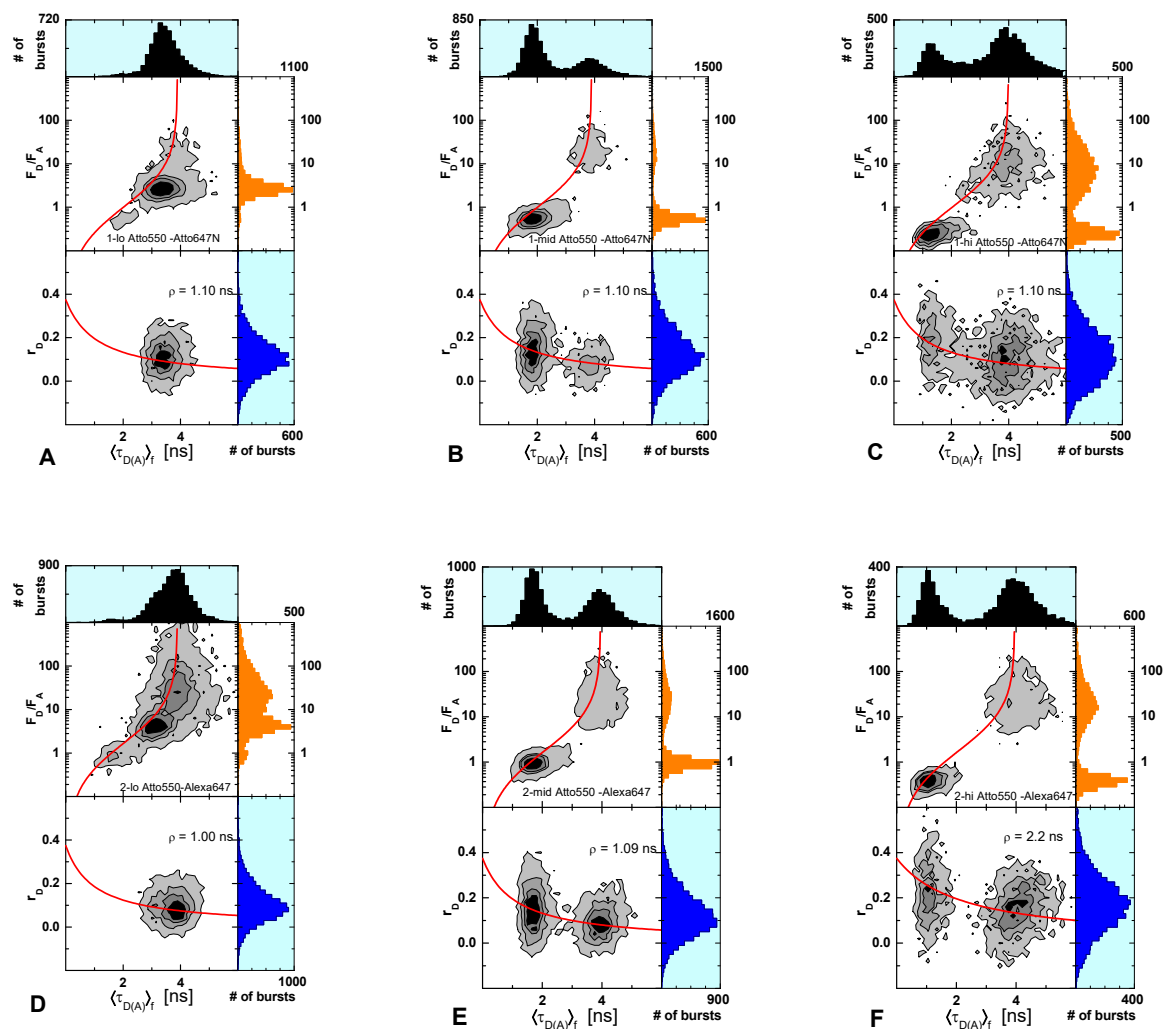
Where $g_{VV/VH}$ is g-factor, F_0 - amplitude scaling factor, $IRF_{VV}(t)$, $IRF_{VH}(t)$ - instrument response functions and B_{VV} , B_{VH} - background values. The “ \otimes ” sign designates circular convolution.

Fitting results for fluorescent signal in parallel and perpendicular polarization planes with respect to the vertically polarized excitation light with their rotation correlation times and amplitudes for donor only and acceptor only labeled DNA are presented in Table 2.22. The measured data and fitted curves with their weighted residuals are presented in the left column of the Figure 2.26. Typical magic angle fluorescence decays are shown in the right column of the Figure 2.26 and extracted fitting parameters are in the Table 2.23. The fit quality is judged by χ^2_r .

2.6.2 Results

2.6.2.1 MFD plots

Joint Figure of all one color excitation (OCE) MFD plots



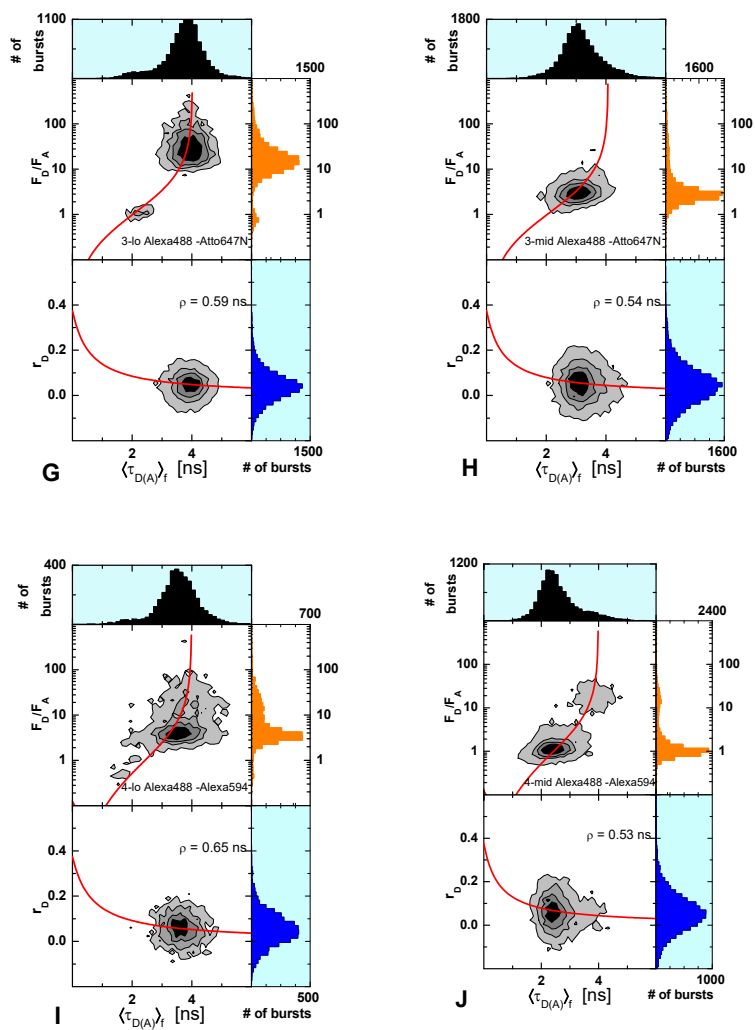


Figure 2.19 2D probability probability histogram of fluorescence green to red signal ratio F_D/F_A vs fluorescence lifetime of donor in presence of acceptor $\langle \tau_{D(A)} \rangle_f$ and static FRET line (red) (upper panel) and donor fluorescence anisotropy r_D vs $\langle \tau_{D(A)} \rangle_f$ with Perrin equation (red line) (lower panel) generated from OCE experiment for studied samples. The correspondent 1D projections are also shown. Static FRET lines are collected in the Table 2.16 and correction parameters are in the Table 2.18.

Table 2.16 Static FRET lines used to describe relationship between efficiency F_D/F_A and $\langle \tau_{D(A)} \rangle_f$ for OCE on Figure 2.19.

sample	Static FRET line
1-lo	$(0.7232/0.6500)/((3.8895/((-0.0429*x^3)+(0.2911*x^2)+0.5283*x-0.0472))-1)$
1-mid	$(0.7232/0.6500)/((3.8895/((-0.0429*x^3)+(0.2911*x^2)+0.5283*x-0.0472))-1)$
1-hi	$(0.7258/0.6500)/((3.9798/((-0.0414*x^3)+(0.2794*x^2)+0.5548*x-0.0508))-1)$
2-lo	$(0.7232/0.3900)/((3.8895/((-0.0429*x^3)+(0.2911*x^2)+0.5283*x-0.0472))-1)$
2-mid	$(0.7347/0.3900)/((3.9512/((-0.0417*x^3)+(0.2866*x^2)+0.5299*x-0.0477))-1)$
2-hi	$(0.7347/0.3900)/((3.9512/((-0.0417*x^3)+(0.2866*x^2)+0.5299*x-0.0477))-1)$
3-lo	$(0.7780/0.6500)/((4.0150/((-0.0383*x^3)+(0.2727*x^2)+0.5335*x-0.0483))-1)$
3-mid	$(0.7875/0.6500)/((4.0649/((-0.0373*x^3)+(0.2685*x^2)+0.5352*x-0.0487))-1)$
4-lo	$(0.7701/0.7000)/((3.9864/((-0.1161*x^3)+(0.9267*x^2)-0.9493*x+0.3973))-1)$
4-mid	$(0.7701/0.7000)/((3.9864/((-0.1161*x^3)+(0.9267*x^2)-0.9493*x+0.3973))-1)$

Joint Figure of all pulsed interleaved excitation (PIE) MFD plots

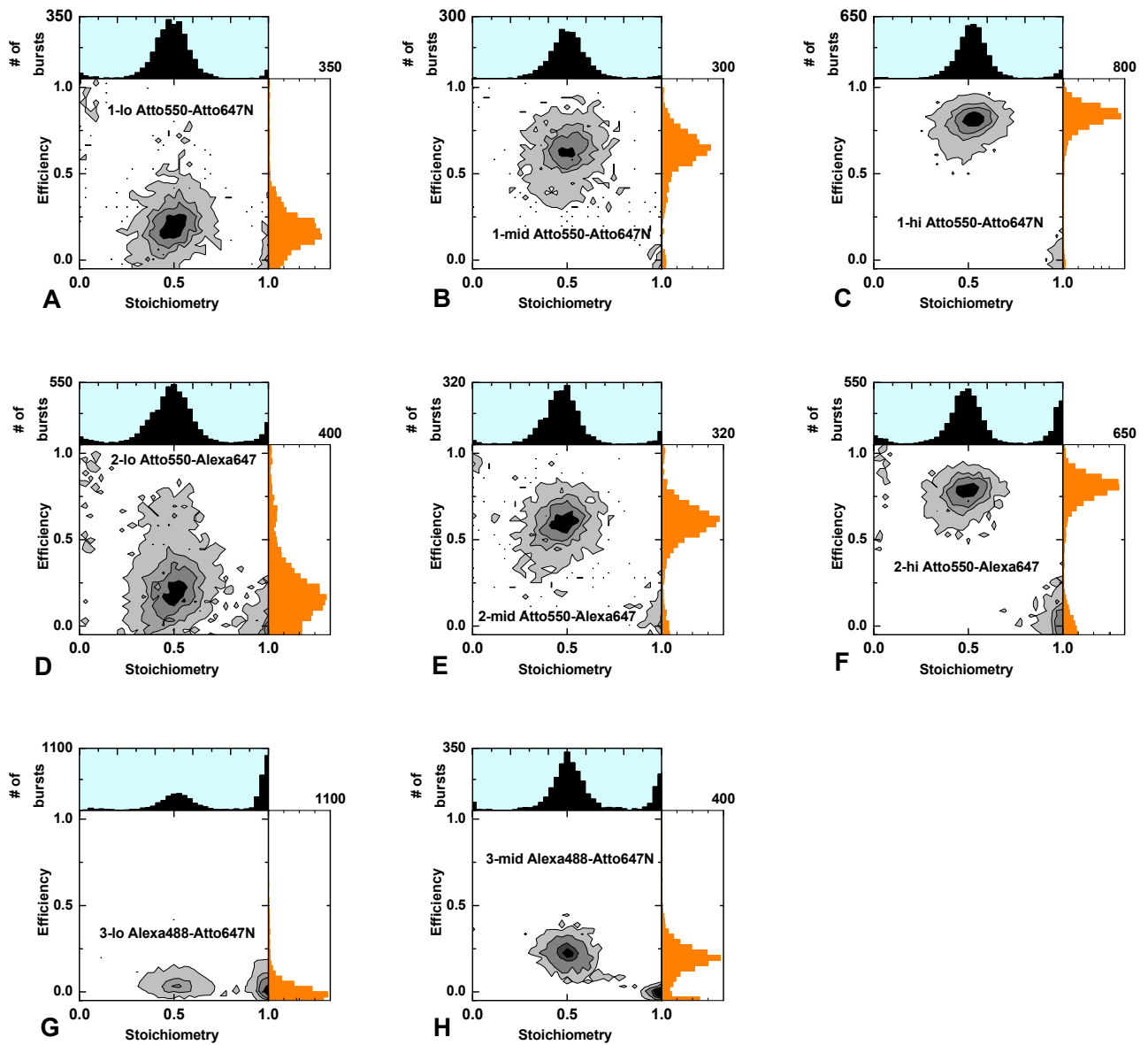


Figure 2.20 2D probability histogram of FRET efficiency E versus Stoichiometry S generated from PIE experiment for studied samples. The correspondent 1D projection is also shown. Correction factors used to generate histograms and FRET lines are in the Table 2.14 and Table 2.19.

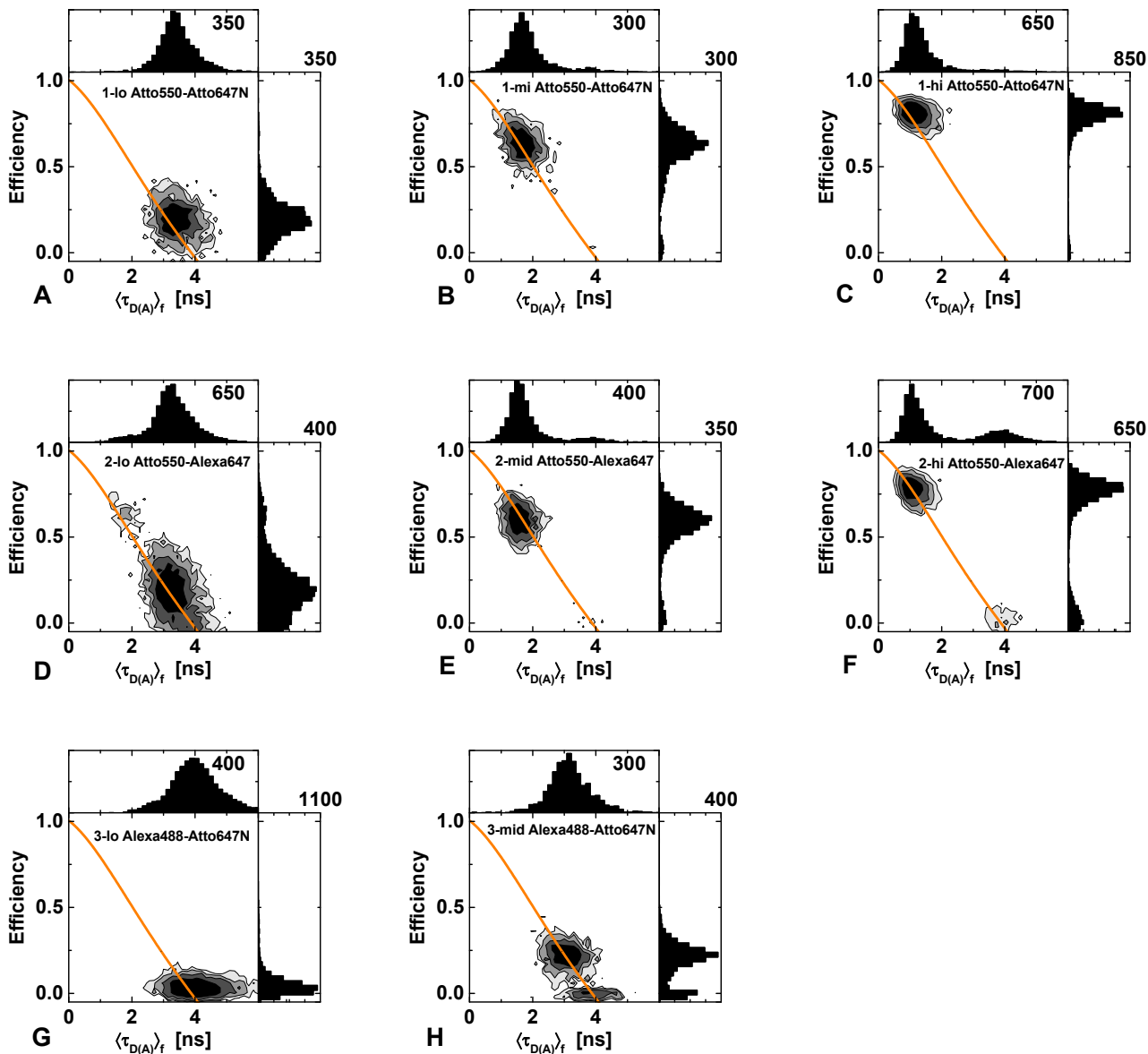


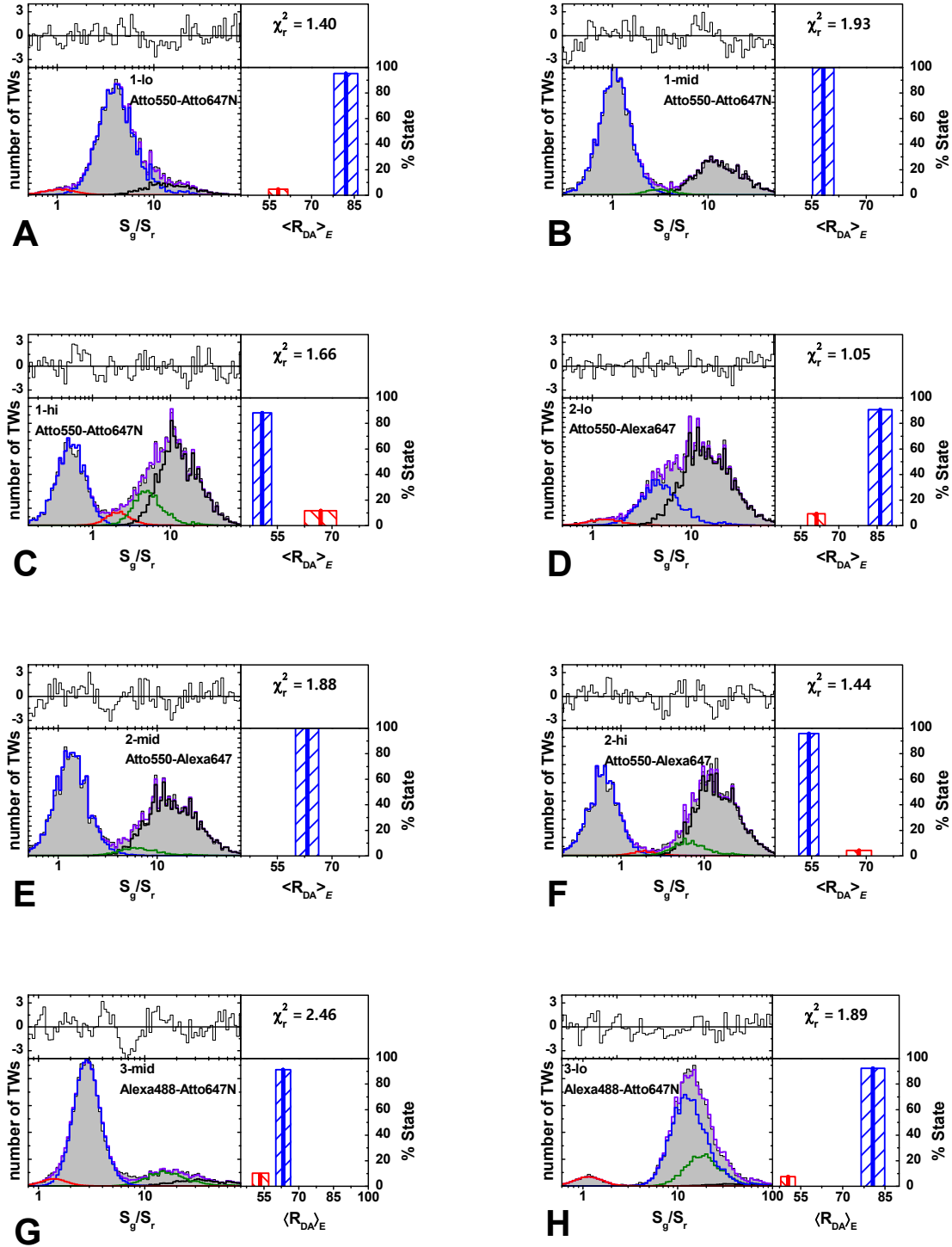
Figure 2.21 2D probability histogram of FRET efficiency E vs fluorescence lifetime of donor in presence of acceptor $\langle \tau_{D(A)} \rangle_f$ with static FRET line (orange) generated from PIE experiment for studied samples. The correspondent 1D projections are also shown. Correction parameters used to generate histograms and FRET lines are in the Table 2.14 and Table 2.18. Static FRET lines are combined in the Table 2.17.

Table 2.17 Static FRET lines used to describe relationship between efficiency E and $\langle \tau_{D(A)} \rangle_f$ in PIE experiment on Figure 2.21

sample	Static FRET line
1-lo	$1 - (((0.0079 * x^4) + (-0.0952 * x^3) + (0.3691 * x^2) + 0.5466 * x - 0.0169) / 3.8895)$
1-mid	$1 - (((0.0079 * x^4) + (-0.0952 * x^3) + (0.3691 * x^2) + 0.5466 * x - 0.0169) / 3.8895)$
1-hi	$1 - (((0.0079 * x^4) + (-0.0952 * x^3) + (0.3691 * x^2) + 0.5466 * x - 0.0169) / 3.8895)$
2-lo	$1 - (((0.0079 * x^4) + (-0.0952 * x^3) + (0.3691 * x^2) + 0.5466 * x - 0.0169) / 3.8895)$
2-mid	$1 - (((0.0079 * x^4) + (-0.0952 * x^3) + (0.3691 * x^2) + 0.5466 * x - 0.0169) / 3.8895)$
2-hi	$1 - (((0.0080 * x^4) + (-0.0965 * x^3) + (0.3728 * x^2) + 0.5464 * x - 0.0169) / 3.8895)$
3-lo	$1 - (((0.0079 * x^4) + (-0.0952 * x^3) + (0.3691 * x^2) + 0.5466 * x - 0.0169) / 3.8895)$
3-mid	$1 - (((0.0079 * x^4) + (-0.0952 * x^3) + (0.3691 * x^2) + 0.5466 * x - 0.0169) / 3.8895)$

2.6.2.3 PDA results

Joint Figure of all OCE PDA plots



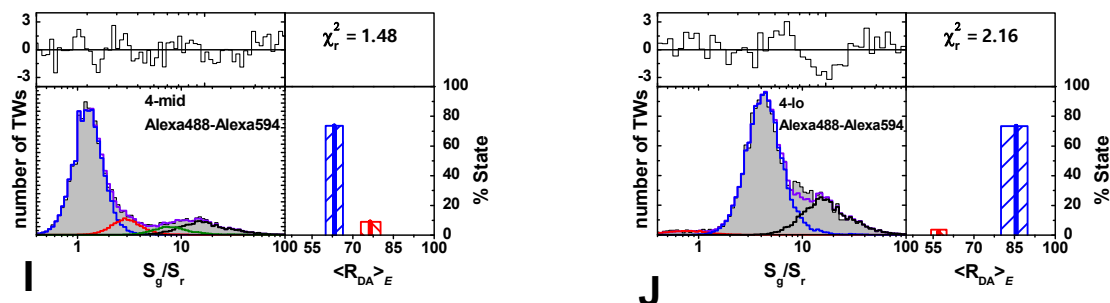


Figure 2.22 Results of PDA analysis of OCE data. S_g/S_r histogram of experimental data (gray area) is fitted (purple solid line). The right panel shows the distances and relative amplitudes (solid blue and red lines) and the overall confidence intervals for the distances (striped boxes) of the FRET state. Weighted residuals are shown in the upper plot. Correction parameters used to generate histograms are in the Table 2.18.

Table 2.18 Fit parameters for the PDA fits of the OCE experiment: experimental distances $\langle R_{DA} \rangle_E$ with corresponding fractions x_i and half-width σ , donor only fraction x_{DO} and impurity. Correction factors: background signal in the green $\langle B_G \rangle$ and red channels $\langle B_R \rangle$, leakage of D into A channel α , direct acceptor excitation δ and detection efficiency ratio $g_{G|D}/g_{R|A}$

Sample	$\langle R_{DA} \rangle_{E1}, \text{\AA}(x_1),$ $\langle R_{DA} \rangle_{E2}, \text{\AA}(x_2)$	$\sigma_1, \text{\AA}$ $\sigma_2, \text{\AA}$	$x_{DO}, \%$	Impurity, %	$\langle B_G \rangle, \text{kHz}$	$\langle B_R \rangle, \text{kHz}$	α	δ	$g_{G D}/g_{R A}$	χ_r^2
1-lo	81.9 (83.9%), 58.2 (4.0%)	5.3, 2.8	12.2	-	0.662	0.409	0.062	0.15	2.1	1.40
1-mid	58.3 (67.6%)	2.34	29.7	2.7	0.662	0.409	0.062	0.15	2.1	1.94
1-hi	51.0 (34.0%), 68.0 (4.5%)	2.46, 2.0	47.8	13.7	0.662	0.409	0.062	0.15	2.1	1.66
2-lo	86.8 (27.0%), 61.6 (3.0%)	7.5, 3.0	70.0	-	0.662	0.409	0.062	0.19	1.6	1.28
2-mid	63.2 (48.7%)	2.6	44.2	7.1	0.662	0.409	0.062	0.19	1.6	2.46
2-hi	54.3 (38.5%), 68 (1.6%)	2.56, 2.0	52.8	7.0	0.662	0.409	0.062	0.19	1.6	1.44
3-lo	80.7 (68.3%), 50.5 (5.6%)	4.0, 2.5	2.4	23.7	1.026	0.550	0.010	-	0.8	1.89
3-hi	59.5 (76.1%), 52.3 (4.1%)	2.1, 1.8	7.8	12.1	1.114	0.653	0.010	-	0.8	2.46
4-lo	79.9 (74%), 56.5 (2.6%)	5.7, 4.0	23.4	-	0.551	0.339	0.052	0.06	0.8	2.16
4-mid	59.6(72.9%), 71.1 (9.9%)	2.1, 2.5	12.6	4.6	0.551	0.339	0.052	0.06	0.8	1.48

Joint Figure of all PIE PDA plots

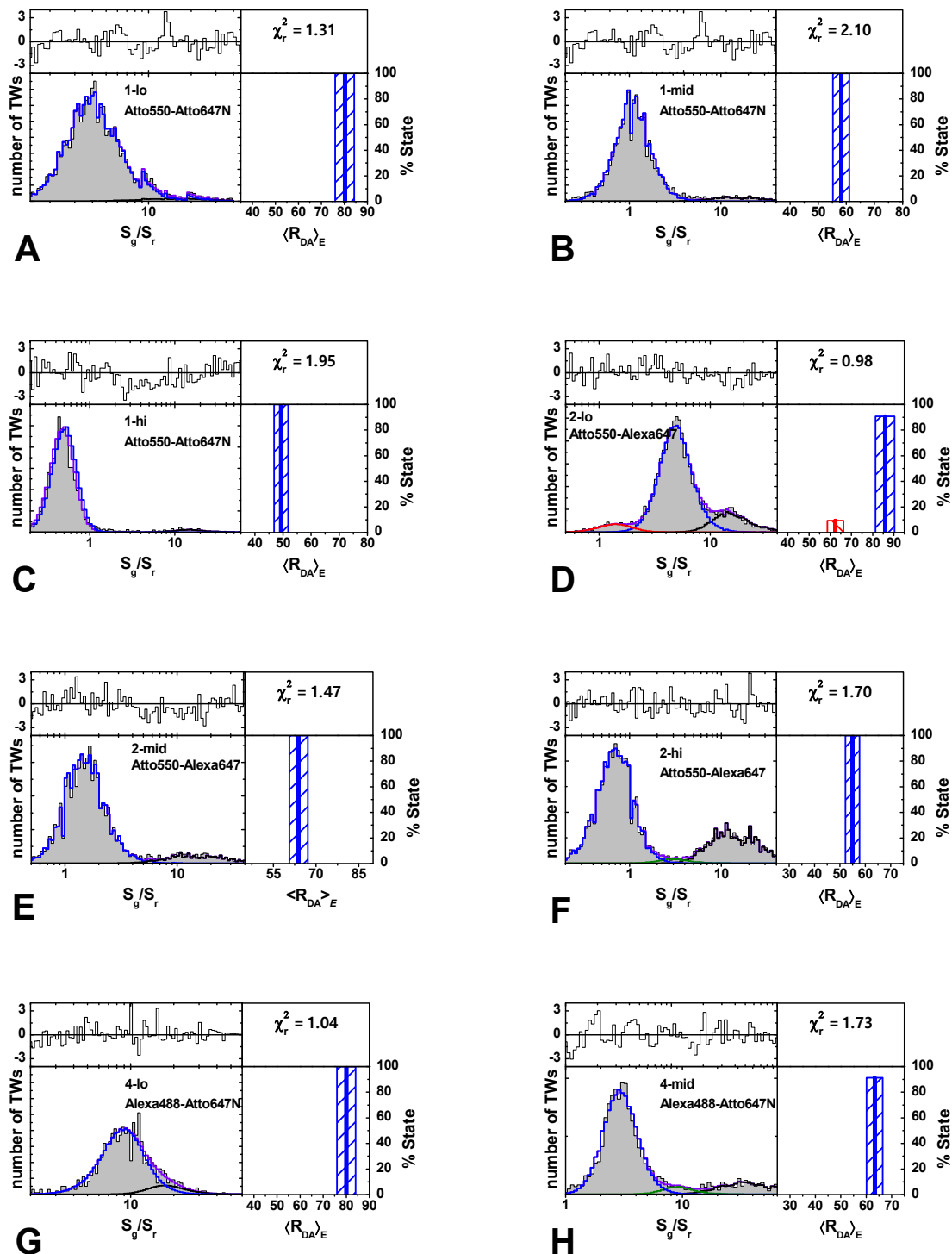


Figure 2.23 Results of PDA analysis of PIE data. S_g/S_r histogram of experimental data (gray area) is fitted (purple solid line). The right panel shows the distances and relative amplitudes (solid blue and red lines) and the overall

confidence intervals for the distances (striped boxes) of the FRET state. Weighted residuals are shown in the upper plot. Correction parameters used to generate histograms are in the Table 2.19.

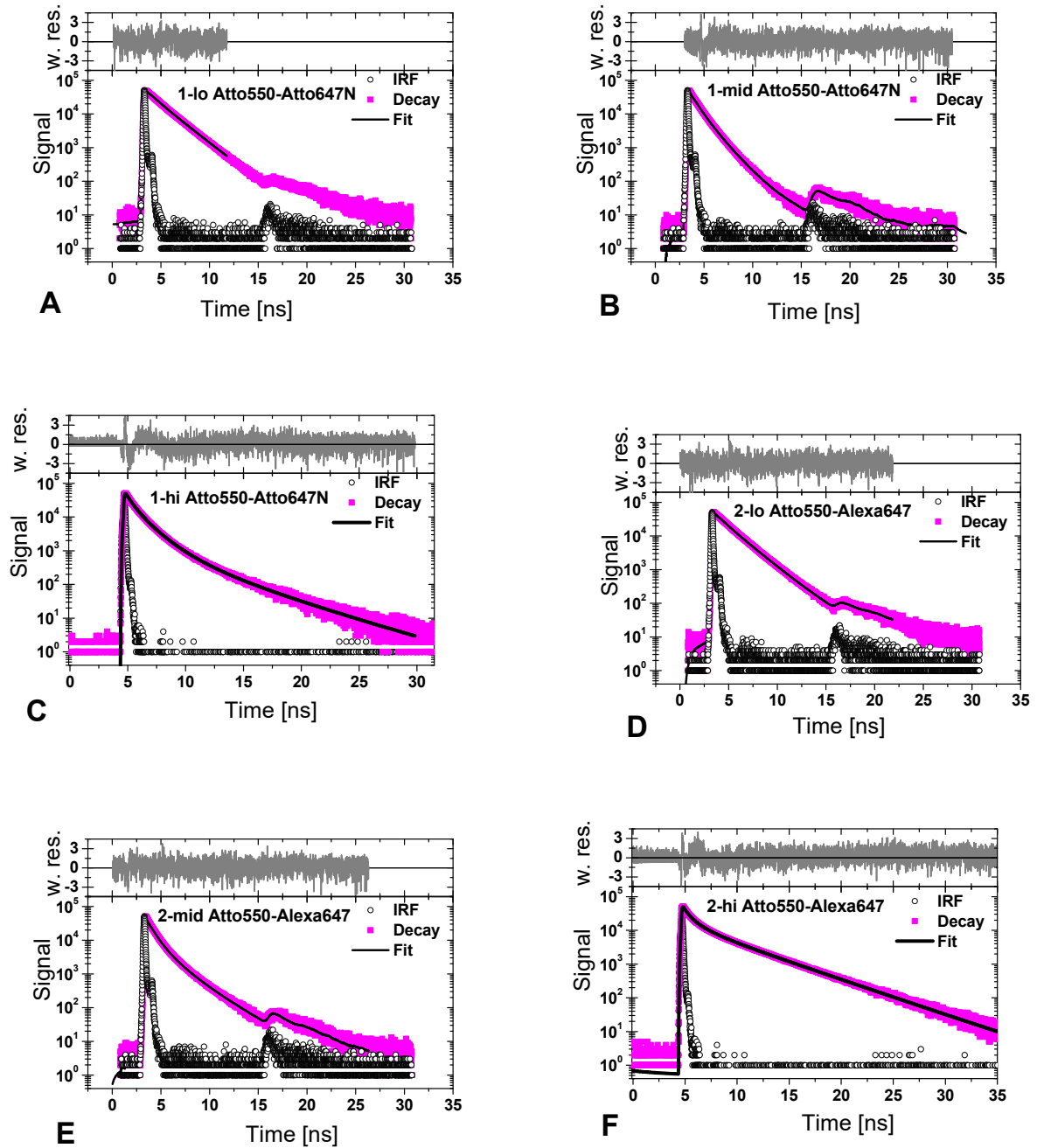
Table 2.19 Fit parameters for the PDA fits of the PIE experiment: experimental distances $\langle R_{DA} \rangle_E$ with corresponding fractions x_i and half-width σ , donor only fraction x_{DO} and impurity. Correction factors: background signal in the green $\langle B_G \rangle$ and red channels $\langle B_R \rangle$, leakage of D into A channel α , direct acceptor excitation δ and detection efficiency ratio $g_{G|D}/g_{R|A}$.

sample	$\langle R_{DA} \rangle_{E1}, \text{\AA}(x_1),$ $\langle R_{DA} \rangle_{E2}, \text{\AA}(x_2)$	$\sigma_1, \text{\AA}$ $\sigma_2, \text{\AA}$	$x_{DO}, \%$	Impurity, %	$\langle B_G \rangle,$ kHz	$\langle B_R \rangle,$ kHz	α	δ	$g_{G D}/g_{R A}$	χ_r^2
1-lo	80.3 (96.7%)	5.0	3.3	-	1.004	0.180	0.062	0.15	2.1	1.1
1-mid	58.0 (94.3%)	3.2	5.7	-	1.004	0.180	0.062	0.15	2.1	2.1
1-hi	49.3 (94.3%)	2.4	3.8	1.9	0.747	0.179	0.062	0.15	2.1	1.9
2-lo	85.5(78.0%), 61.3(6.3%)	7.1, 3.5	15.7	-	0.662	0.409	0.062	0.19	1.6	0.9
2-mid	63.9 (89.3%)	2.7	10.7	-	1.004	0.180	0.062	0.19	1.6	1.5
2-hi	55.0 (69.2%)	2.6	28.8	2.0	0.747	0.179	0.062	0.19	1.6	1.7
3-lo	80.0(89.7%)	7.1	10.3		1.036	0.65	0.017	-	0.8	1.0
3-hi	59.8 (79.5%)	2.8	15.4	5.1	1.026	0.397	0.017	-	0.8	1.7

2.6.2.4 Ensemble Time Correlated Single Photon Counting (eTCSPC) results

eTCSPC fluorescent decay measurement of FRET samples under magic angle condition

Presentation of the fluorescence decays of the FRET samples are in Figure 2.24. Fit results and calculated FRET efficiency are in the Table 2.20.



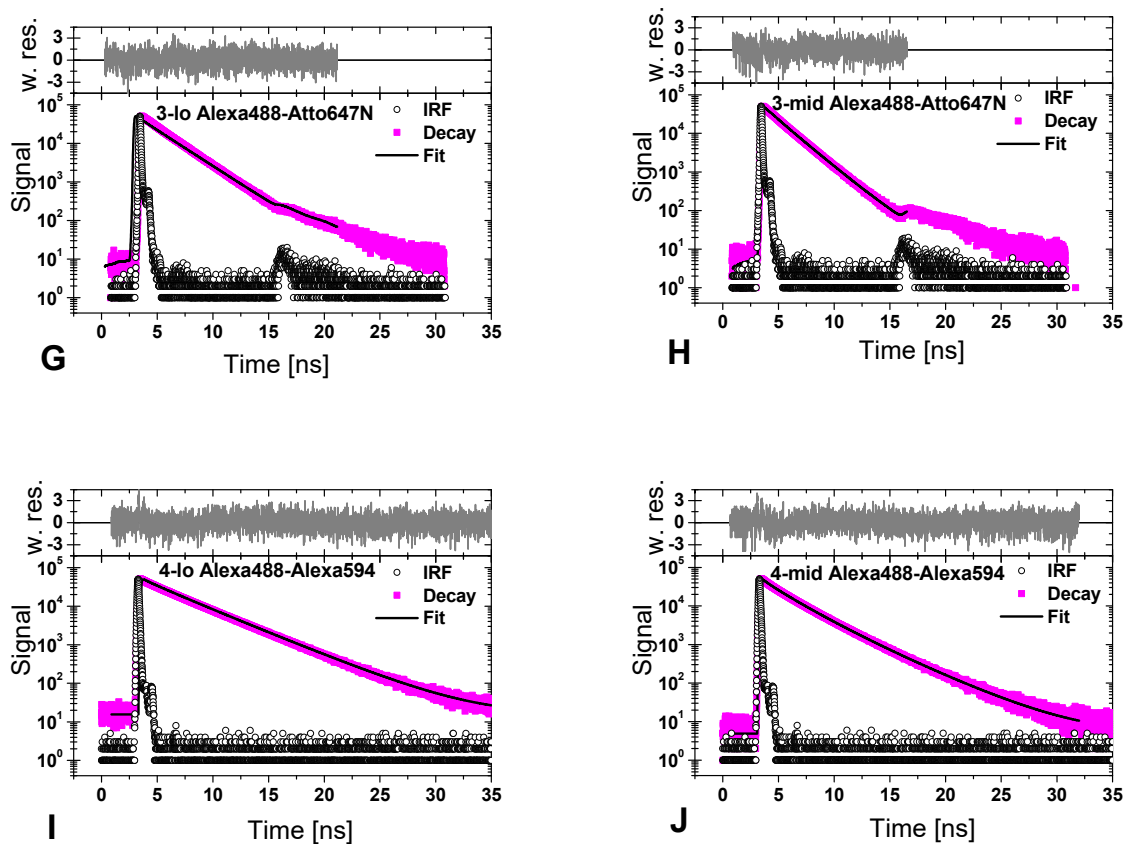


Figure 2.24 Fluorescent decays of the measured FRET samples. Experimental data is shown as magenta dots, instrument response function as white dots, and fit is a black curve. Weighted residuals are shown in the upper block.

Fitting results of the Gaussian distributed distances R_{DA}

The results of the global fits of FRET samples together with the correspondent donor only samples are presented in the Table 2.20 and Table 2.21. Fluorescence lifetimes τ_i and corresponding fractions x_i are global parameters.

Table 2.20 Fit results of Gaussian distributed distance R_{DA} with half-width σ_{DA} , donor only fraction x_{DO} and recalculated mean FRET Efficiency $\langle E \rangle$. Quality of the fits are judged by χ_r^2 .

Sample	$\langle E \rangle$	$\langle R_{DA} \rangle, \text{\AA}$	$\sigma_{RDA}, \text{\AA}$	x_{DO}	χ_r^2
1-lo	0.17	83.1	11.9	0.00	1.13
1-mid	0.54	61.1	7.3	0.02	1.21
1-hi	0.81	48.5	6.3	0.02	1.08
2-lo	0.23	84.0	10.0	0.08	1.10
2-mid	0.67	60.1	5.8	0.10	1.10
2-hi	0.85	49.9	5.9	0.26	1.02
3-lo	0.06	82.4	13.9	0.38	1.04
3-hi	0.26	59.1	6.0	0.10	1.24
4-lo	0.11	85.5	15.8	0.02	1.09
4-mid	0.41	60.9	7.0	0.08	1.12

eTCSPC fluorescent decay measurement of donor only samples under magic angle condition

Presentation of the magic angle fluorescence decays of the donor only samples are in Figure 2.25. Fit results of donor only decays from the global fits are combined in the Table 2.21.

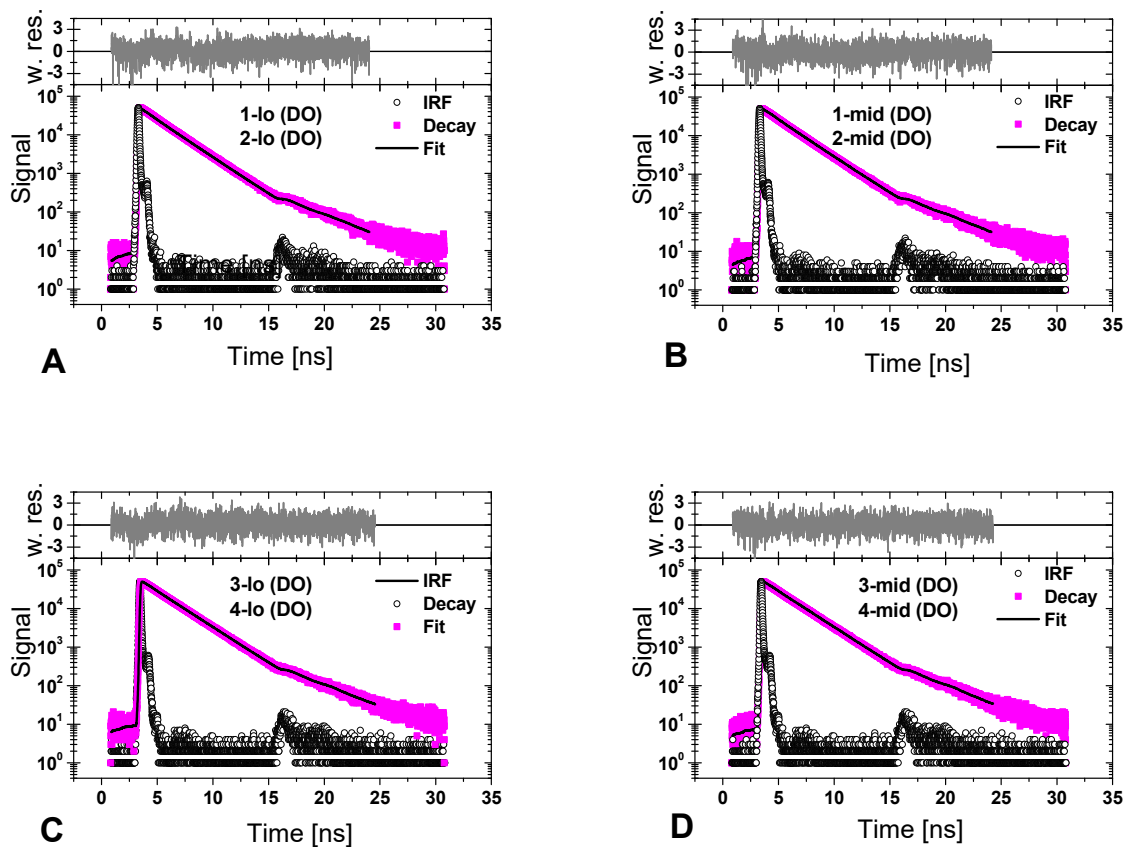


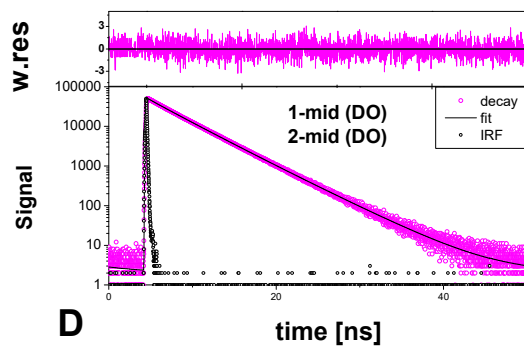
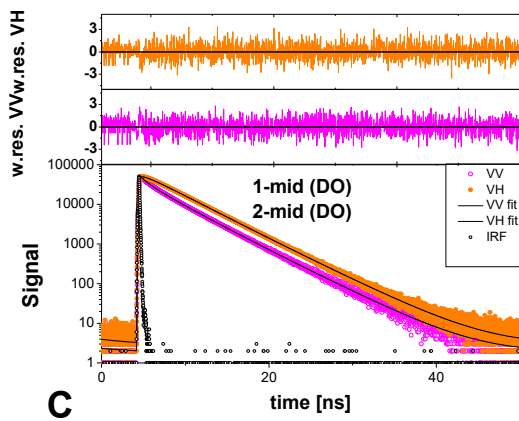
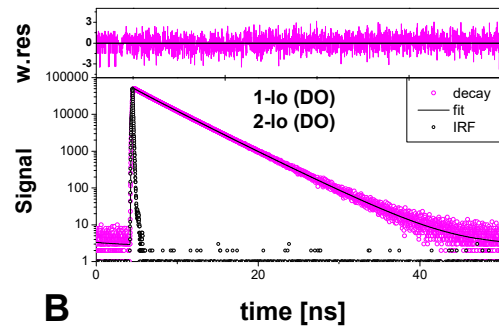
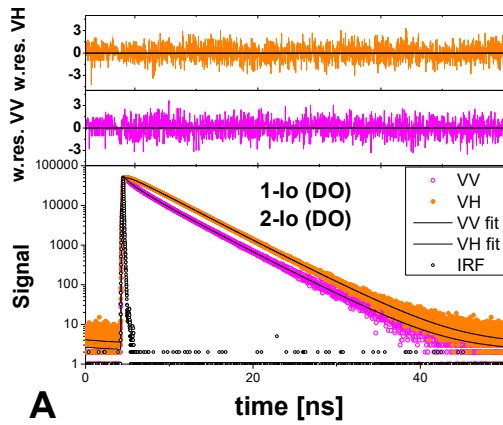
Figure 2.25 Fluorescent decays of the measured donor only samples. Experimental data is shown as magenta dots, instrument response function as white dots, and fit is a black curve. Weighted residuals are shown in the upper block.

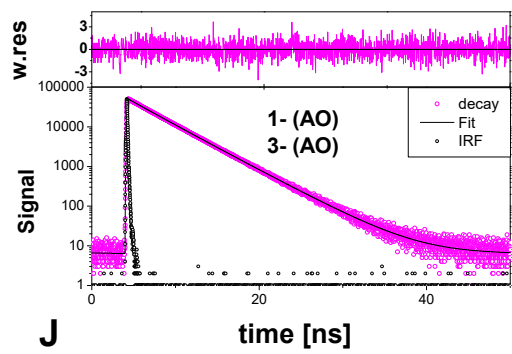
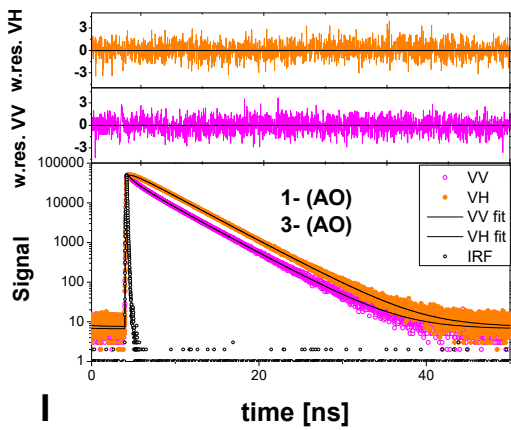
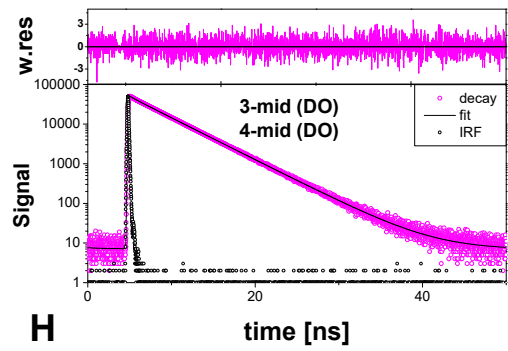
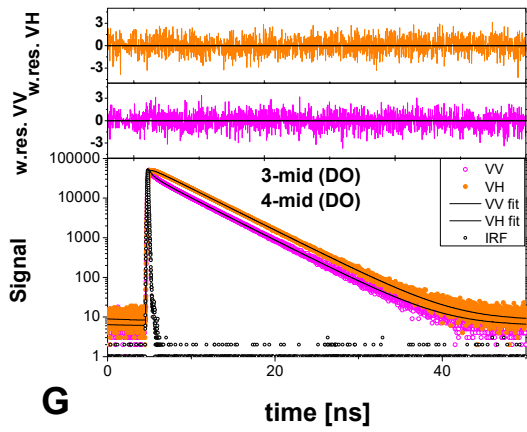
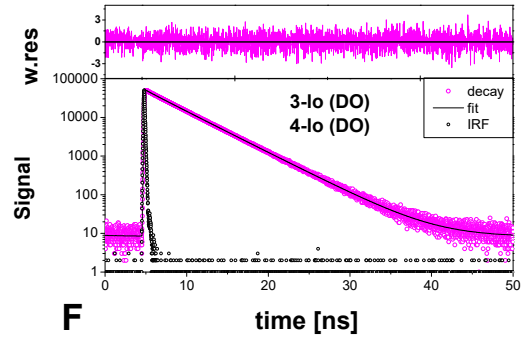
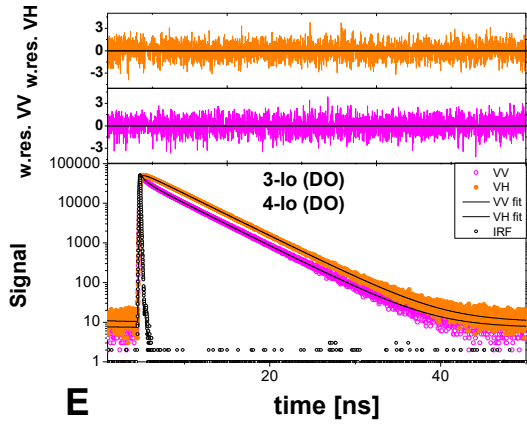
Table 2.21 Fluorescence lifetimes τ_i and their amplitudes x_i for all studied donor only (DO) samples. Here $\langle \tau \rangle_x$ is the species weighted fluorescence lifetime. Quality of the fits are judged by χ_r^2 .

Base position (Linker), strand	Dye	Sample (DO)	τ_1 , [ns] (x_1)	τ_2 , [ns] (x_2)	$\langle \tau \rangle_x$, [ns]	χ_r^2
T 31(C2), D-strand	Atto550	1-lo (DO),	1.87 (0.12)	4.01 (0.88)	3.75	1.08
T 23(C2), D-strand	Atto550	1-mid (DO),	2.52 (0.20)	4.15 (0.80)	3.82	1.05
T 19(C2), D-strand	Atto550	1-hi (DO),	2.26 (0.19)	4.16 (0.81)	3.79	1.07
T 31(C2), D-strand	Atto550	2-lo (DO),	1.91 (0.12)	4.02 (0.88)	3.77	1.13
T 23(C2), D-strand	Atto550	2-mid (DO),	2.32 (0.17)	4.11 (0.83)	3.81	1.10
T 19(C2), D-strand	Atto550	2-hi (DO),	2.30 (0.20)	4.18 (0.80)	3.80	1.02
T 31(C2), D-strand	Alexa488	3- lo (DO),	1.21 (0.08)	4.06 (0.92)	3.83	1.15
T 23(C2), D-strand	Alexa488	3-mid (DO),	1.01 (0.06)	4.10 (0.94)	3.91	1.19
T 31(C2), D-strand	Alexa488	4- lo (DO),	0.96 (0.06)	4.08 (0.94)	3.89	1.04
T 23(C2), D-strand	Alexa488	4-mid (DO),	0.93 (0.06)	4.08 (0.94)	3.89	1.08

eTCSPC fluorescent polarized decay measurement of FRET samples

Presentation of fluorescence polarized decays of the donor only and acceptor only samples are in Figure 2.26. Fit results from the global fits are combined in the Table 2.22 and Table 2.23.





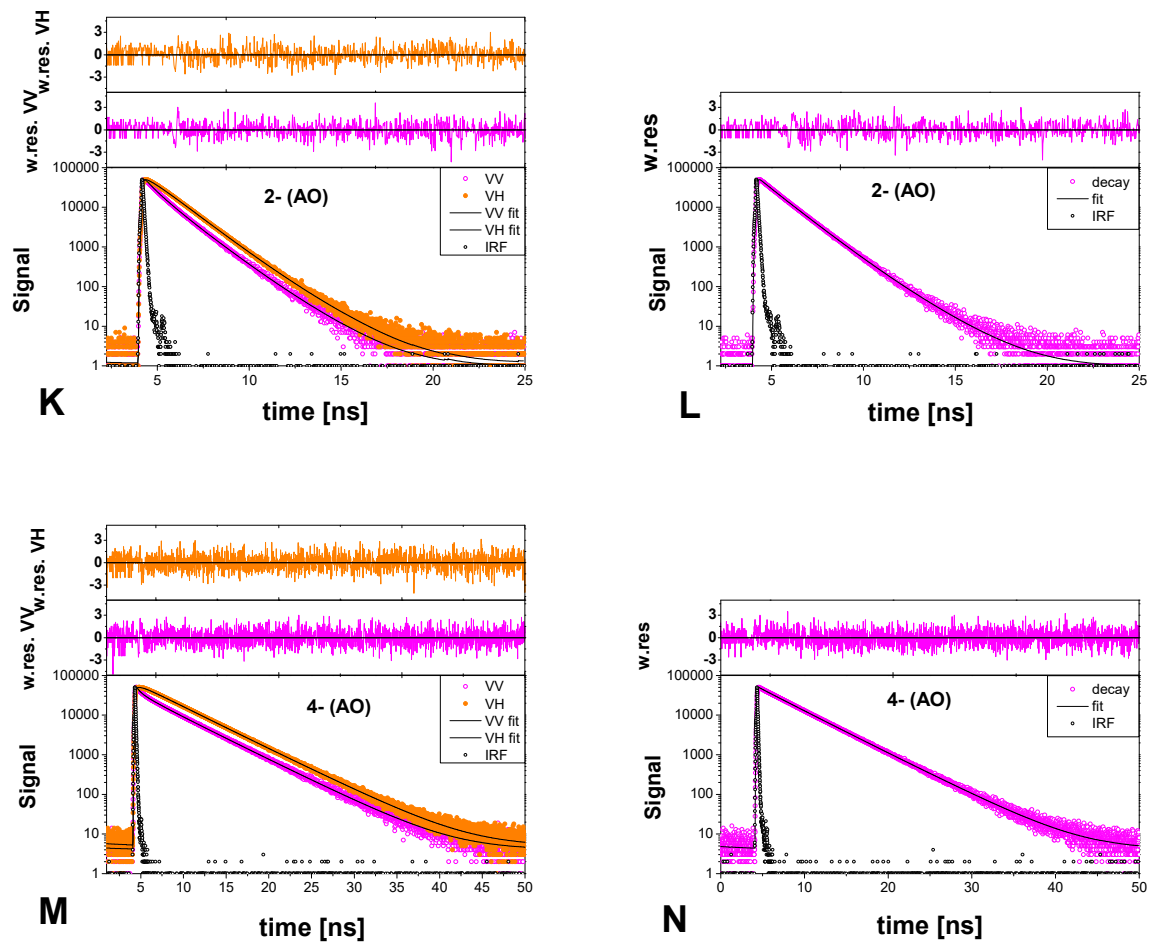


Figure 2.26 Left pannels: Fluorescent signal in parallel and perpendicular polarization channels (magenta and orange) with the corresponding fits (black) for 1-lo (DO), 2-lo (DO), 1-hi(DO), 2-hi (DO) and 1-(AO) samples with weighted residuals on the top. Right panels: the corresponding magic angle fluorescence decay curves with weighted residuals on the top.

Anisotropy results

The results of the global fit of fluorescence polarized decays together with the magic angle fluorescence decays are presented in the Table 2.22 and Table 2.23. Fluorescence lifetimes τ_i and corresponding fractions x_i are global parameters.

Table 2.22 Rotation correlation times ρ_i with correspondent amplitudes b_i for donor only (DO) ($r_0 = 0.38$) and acceptor only (AO) ($r_0 = 0.38$) samples. The 1σ confidence range for the longest correlation time is indicated in square brackets. Quality of the fits is judged with χ_r^2 .

Base/position(Linker)	dye	Sample (DO or AO)	$\rho_1(b_1)$	$\rho_2(b_2)$	$\rho_\infty [1\sigma \text{ conf.}] (b_3) [b]$	χ_r^2
T 31(C2)	Atto550	1-lo (DO), 2-lo (DO)	0.63(0.14)	3.08(0.16)	174[97÷540](0.08)	1.04
T 23(C2)	Atto550	1-mid (DO), 2-mid (DO)	0.58 (0.12)	2.76(0.15)	63[50÷86](0.11)	1.01
T 31(C2)	Atto647N	1-(AO), 4-(AO)	0.41(0.14)	2.05(0.17)	46[37÷62](0.07)	1.01
T 31 (C2)	Alexa647[a]	2 -(AO)	0.32(0.09)	1.14(0.23)	1e5[125÷∞](0.06)	0.99
T 31(C6)	Alexa488	4-lo (DO)	0.25(0.22)	1.31(0.12)	31[24÷42](0.04)	1.03
T 23(C6)	Alexa488	4-mid (DO)	0.26(0.22)	1.43(0.12)	37[31÷46](0.04)	1.04
T 31 (C6)	Alexa594	5-(AO)	0.46(0.22)	1.88(0.09)	77[58÷121](0.07)	1.02

[a] Only VV, VH depolarization curves used for fitting in this case

[b] due to fluctuations in the G-factor determinations we have small systematic errors; i.e. $\rho_3 > 20$ ns and not the fitted value

Table 2.23 Fluorescence lifetimes τ_i and their amplitudes x_i for all studied donor only (DO) and acceptor only (AO) samples. Here $\langle \tau \rangle_x$ is the species weighted fluorescence lifetime. Quality of the fits is judged with χ_r^2 .

Base/position(Linker)	sample	Sample (DO or AO)	$\tau_1(x_1)$	$\tau_2(x_2)$	$\tau_3(x_3)$	$\langle \tau \rangle_x$	χ_r^2
T 31(C2)	Atto550	1-lo (DO), 2-lo (DO)	0.74(0.03)	3.47(0.59)	4.44(0.38)	3.76	1.03
T 23(C2)	Atto550	1-mid (DO), 2-mid (DO)	0.86(0.03)	3.54(0.63)	4.59(0.34)	3.81	1.02
T 31(C2)	Atto647N	1-(AO), 4-(AO)	0.24(0.04)	3.40(0.52)	4.19(0.44)	3.62	1.03
T 31 (C2)	Alexa647	2 -(AO)	0.66(0.05)	1.18(0.90)	1.90(0.05)	1.19	1.00
T 31(C6)	Alexa488	4-lo (DO) 3-lo (DO)	0.36(0.03)	2.37(0.05)	4.11(0.92)	3.91	1.03
T 23(C6)	Alexa488	4-mid (DO) 3-mid (DO)	0.37(0.04)	2.70(0.04)	4.13(0.92)	3.92	1.08
T 31 (C6)	Alexa594	5-(AO)	0.31(0.03)	3.76(0.64)	4.55(0.33)	3.91	0.99

2.6.3 Joint table of the results of all experimental methods

The results of all measured samples with all available techniques are combined in the Table 2.24

Table 2.24 Summary of the experimental mean efficiencies $\langle E \rangle$ and experimental distances resulting from eTCSPC and single molecule experiments (OCE and PIE), compared with model distances $R_{\langle E \rangle}^{(model)}$ and $R_{MP}^{(model)}$

R ₀ , nm	Sample name	eTCSPC experiment		Single molecules experiment				Modeling	
		$\langle R_{DA} \rangle$, [Å]	$\langle E \rangle$	OCE		PIE		$R_{\langle E \rangle}^{(model)}$, [Å]	$R_{MP}^{(model)}$, [Å]
				$\langle R_{DA} \rangle_{E_f}$, [Å]	$\langle E \rangle$	$\langle R_{DA} \rangle_{E_f}$, [Å]	$\langle E \rangle$		
6.26±0.4	1-lo Atto550-Atto647N	83.1	0.17	81.9	0.17	80.3	0.19	83.5±2.4	84.2±2.1
6.26±0.4	1-mid Atto550-Atto647N	61.1	0.54	58.3	0.61	58.0	0.61	58.7±1.6	55.8±2.3
6.26±0.4	1-hi Atto550-Atto647N	48.5	0.81	51.0	0.77	49.3	0.80	51.6±2.9	46.6 ±3.2
6.8±0.5	2-lo Atto550-Alexa647	84.0	0.23	86.8	0.20	85.5	0.21	83.9±2.2	84.2±2.4
6.8±0.5	2-mid Atto550-Alexa647	60.1	0.67	63.2	0.61	63.9	0.59	59.6±1.3	55.8±2.6
6.8±0.5	2-hi Atto550-Alexa647	49.9	0.85	54.3	0.79	55.0	0.78	52.3±1.9	46.6±1.8
4.93	3-lo Alexa488-Atto647N	82.4	0.06	80.7	0.05	80.0	0.06	82.4±2.4	84.0±2.1
4.93	3-mid Alexa488-Atto647N	59.1	0.26	59.5	0.25	59.8	0.24	56.4±1.6	55.7±2.3
5.7	4-lo Alexa488-Alexa594	85.5	0.11	79.9	0.12	n.a	n.a	82.6±2.4	83.8±2.1
5.7	4-mid Alexa488-Alexa594	60.9	0.41	59.6	0.43	n.a	n.a	57.6±1.6	55.5±2.3

Chapter 3 Accurate structural determination of the RNA three-way junctions via single-molecule high-precision FRET measurements

3.1 Introduction

Protein-coding RNA and non-coding RNA play an important biological role in essential cellular processes. Essentially it is composed only of four building blocks that predominantly combine in A-form helices of various lengths and are linked by various junctions, bulges or single-stranded loops. These secondary structural elements are connected by tertiary interactions and assemble into intricate 3D structures. Alone or in protein complexes, often modulated by metal ion-media or stereochemical effects, precise RNA structures create an environment for performing various functions¹⁰² and perform complicated movements on large time scales ranging from picoseconds to seconds. They translate genetic information into molecular machines, catalyze chemical reactions, actively participate in DNA replication and even activate an opportunity for mutations that cause disease¹⁰³⁻¹⁰⁸.

Helical junctions are one of the most critical structural motifs and prominent examples can be found in wide range of RNA structures: from small nuclear (sn)-RNA species to large ribosomal subunits¹⁰⁹⁻¹¹³. Helical junctions determine stability, control folding and the overall RNA architecture¹¹⁴ whereas their exact sequence ensures binding to the partner molecules¹¹⁵.

In this study, Watson-Crick base paired derivative of the core unit of the hairpin ribozyme¹¹⁶ was modified from four-way junction into four different three-way junctions (3WJ). This area of investigation raises a great interest as there has been little systematic study about the conformation of 3WJ in RNA without bulges.

It has been shown^{40,42,114} that changing the junction's topology influences the dynamics and stability of the conformers, but the importance of the sequence variation on the junction remains poorly understood.

To uncover the fundamental behavior of helical motifs and to compare topology of RNA 3WJ we employ high precision single molecule Förster Resonance energy transfer (sm-FRET) method. Briefly, the macromolecule is labeled with two fluorophores: donor and red-shifted acceptor that mediate by dipole-dipole interaction⁵⁶. The excited donor radiationlessly transfers energy to an excited acceptor. The registered efficiency is related to inter-dye distance as $\sim \frac{1}{R^6}$ and also depends on mutual dye orientation. Typically fluorophores are coupled to the macromolecule with long flexible linkers and can detect inter-dye in the wide range from 20-120 Å. There are two possible approaches of utilizing FRET as a "spectroscopic ruler": 1) confocal setup, where freely diffusing molecules are observed in femtoliter (10^{-15} l) volume or 2)

surface-immobilized molecule measured by camera based on total internal reflection fluorescence (TIRF). Combination of fluorophores with high photostability and quantum yield¹¹⁷⁻¹²¹, sensitive detectors¹²² with high efficiency and picosecond resolution reflects in the possibility to perform experiments on timescales from seconds up to hours¹¹⁸ and investigate different molecular conformations and detect possible dynamics between them in real time. This work is based on the employment of the first method and provides the opportunity to observe and characterize separate molecules close to the physiological conditions^{123,124} with high sensitivity and in great detail.

Multiparameter fluorescence detection (MFD) toolkit^{21,73} was utilized to analyze experimental data and together with the modeling approach²¹, FRET-restrained 3D structures were resolved. Also in order to deliver highly precise and accurate structures, statistical and systematic errors were studied. The importance of the daily calibration measurements were indicated as the calibration factors strongly affect the quality of the data analysis.

3.2 Materials and Methods

3.2.1 System of study and nomenclature

Studied RNA three-way junction structures are derived from the RNA four-way junction (RNA 4WJ) (Figure 3.1B)¹²⁵ consequently omitting one of the helix in each structure (Figure 3.1C-F). RNA 4WJ molecule was in turn derived from the hairpin ribozyme¹¹⁶ (PDB-ID: 1M5K) (Figure 3.1 A), preserving the junction and introducing perfect Watson-Crick base pairing throughout the helices. Various uracils and guanines were chosen as labeling sites for Alexa488 as donor and Cy5 as acceptor (green and red circles on Figure 3.1). Throughout this work, 42 FRET pairs were measured and analyzed for J(bcd) and J(abd) constructs (Figure 3.1D-E) and 45 FRET pairs for J(acd) (Figure 3.1F).

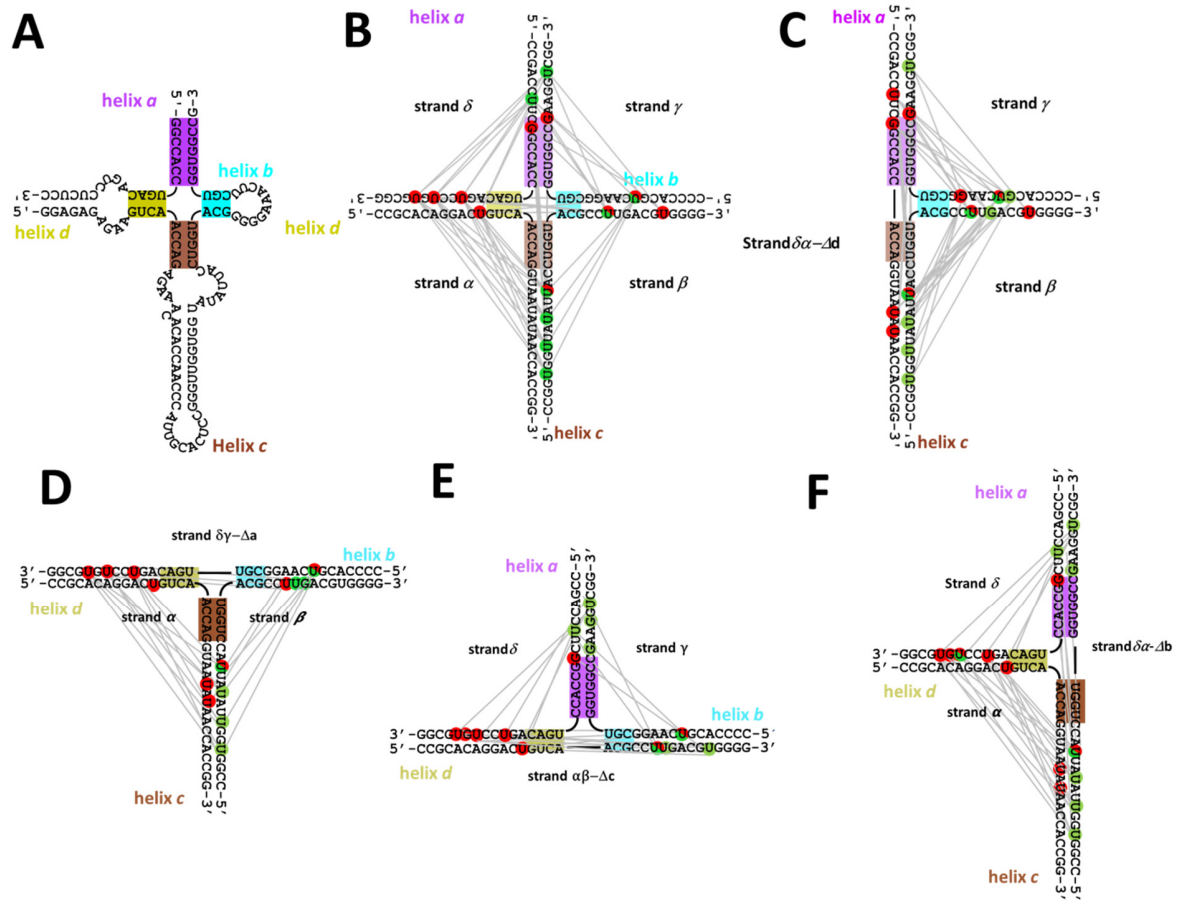


Figure 3.1 Secondary structure of (A) hairpin ribozyme; (B) RNA 4WJ J(abcd); (C) RNA 3WJ J(abc) studied by H. Vardanyan and used for comparison in this study¹²⁶; (D) RNA 3WJ J(bcd); (E) RNA 3WJ J(abd); (F) RNA 3WJ J(acd). Green and red circles represent labeling sites for donor and acceptor and each grey line depicts connection between FRET labels in the pair.

It is important to indicate the origin of the name formation of the constructs and their labels. RNA 3WJ is formed from the combination of three different helices thus the name reflects them. For example, J(bcd) (Figure 3.1D) is constructed of helices *b*, *c* and *d*. Dye type (donor or acceptor), strand and helix name and number of the base starting from the 5'-end form the label name. For example label on J(acd) junction: (A) δ 10a name indicates that this is acceptor label (A) on strand δ and helix *a*, position 10 from 5'-end. Another example of the donor label on J(acd): (D) $\delta\alpha$ - Δ b14c. Here (D) indicates donor label on $\delta\alpha$ - Δ b strand and on helix *c* on position 14. Consequently, names of the molecules form as combination of labeled and unlabeled strands, separated by “/”. For example, J(acd) molecule with acceptor on helix *a*, strand δ , position 10 and donor on helix *c*, strand $\delta\alpha$ - Δ b, position 14 is named as (A) δ 10a/(D) $\delta\alpha$ - Δ b14c/ α .

3.2.2 Oligonucleotides

Highly pure, labeled and unlabeled RNA oligonucleotides with HPLC and premium PAGE cleaning were purchased from PURIMEX and IBA companies (Germany). Ordered oligonucleotides were lyophilized and desalted, and delivered in defined aliquots. The purity documentation was controlled with analytical PAGE run by manufacturers. Chemical structures of the modified uracil and guanine with linker and dyes are depicted in Figure 3.2.

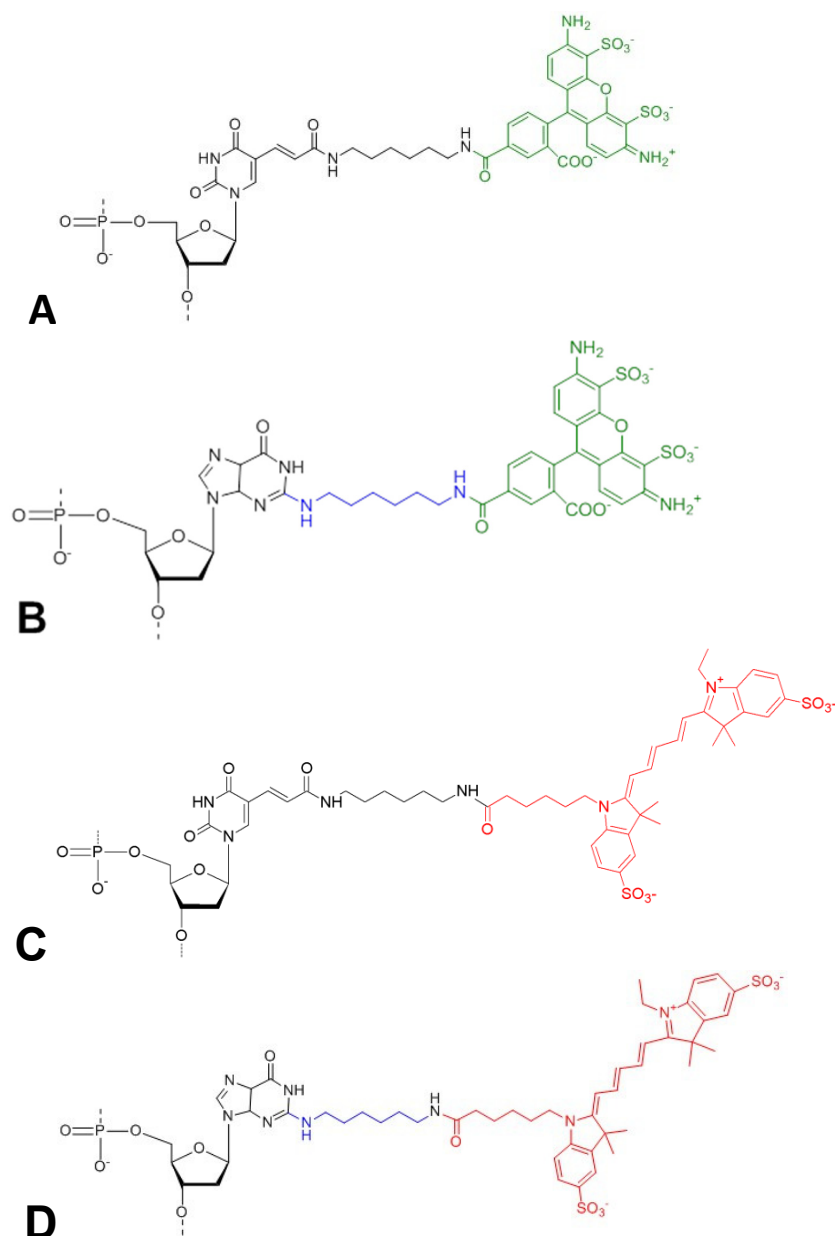


Figure 3.2 (A) Chemical structures of modified uracil with Alexa-TPF-ester; (B) modified guanine with Alexa-TPF-ester; (C) modified uracil with Cy5-NHS; (D) modified guanine with Cy5-NHS.

3.2.3 Hybridization procedure

Two different hybridization methods were used in RNA study. First protocol was successfully used by S.Sindbert¹²⁵ and H.Vardanyan¹²⁶ (Protocol 1). Later studies by J.-P. Sobczak et al¹²⁷ demonstrated more cooperative folding of DNA at constant temperature into complex nanoscale objects (Protocol 2). This protocol was adapted for RNA studies and allowed to improve the hybridization yield almost 2 times (Figure 3.3) and to significantly decrease the preparation time. To verify this, pulsed interleaved excitation (PIE) single molecule experiment¹²⁸ was conducted on the samples hybridized with Protocol 1 and 2 and 2D histograms of intensity green to red signal ratio S_G/S_R vs Stoichiometry were plotted. Shortly, this representation identifies separately populations with acceptor only, donor only and double labeled species. Data based on the sample preparation with Protocol 2 reveals more FRET active bursts than the other method (blue boxes on Figure 3.3). In both methods RNA single strands were mixed in the following proportions: Donor only labeled strand/ Acceptor only labeled strand/ unlabeled strand =1/3/4. Hybridization buffer contained 20 mM $\text{KH}_2\text{PO}_4/\text{K}_2\text{HPO}_4$, 100 mM KCl, and 20 mM MgCl_2 , pH 6.5.

Protocol 1:

The solution was quickly heating up to 85°C inside a thermo-cycler (primus 96 advanced, peqLab, Erlangen, Germany) with 0.1°C/s and then slowly cooling to 4°C with 2°C/h. Total time was 32 hours.

Protocol 2:

The solution was quickly heated up to 85°C inside a thermo-cycler (primus 96 advanced, peqLab, Erlangen, Germany) with 0.1°C/s and then fast cooled up to 52°C. The solution was kept at this condition for 2 hours and afterwards quickly cooled down to 4°C. Total time of the procedure is 2 hours.

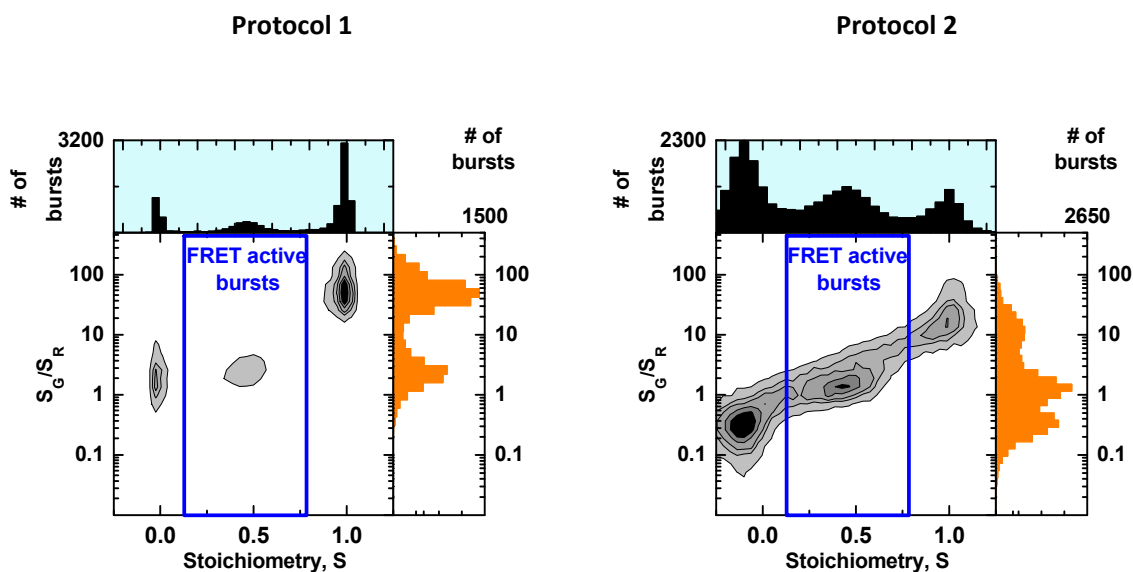


Figure 3.3 2D histogram of green to red signal ratio S_G/S_R vs Stoichiometry for two measurements of (A) $\alpha 26c/(D)\delta\gamma$ - $\Delta a8b/\beta$, prepared according Protocol 1 (left panel) and Protocol 2 (right panel). FRET active bursts are in the blue box. Sample prepared accordingly to Protocol 1 acquires 26% FRET bursts and accordingly Protocol 2 - 43%.

3.2.4 Measurement buffer

The measurement buffer contained 20 mM $\text{KH}_2\text{PO}_4/\text{K}_2\text{HPO}_4$, 100 mM KCl and 20 mM MgCl_2 at pH 6.5. Additionally, 0.5 mM of Trolox¹²⁹ was added to decrease the bleaching of Cy5 in the single molecule experiments.

3.2.5 Instrumentation and calibration measurements

Ensemble Time Correlated Single Photon Counting (eTCSPC)

Fluorescence lifetime decays were recorded by using IBH-5000U (IBH Scotland) setup with repetition rate 10MHz and diode laser LDH-P-C-470 (PicoQuant, Germany) for the green dye or diode laser LDH-8-1-126 (PicoQuant, Germany) for the red dye or FT300 setup (PicoQuant, Germany) with white light laser from NKT Photonics (Germany) with repetition rate 20 MHz. Cutoff filters were used to reduce the contribution of the scattered light (Table 3.1). All samples were measured in Quartz Ultra-Micro-cuvettes (Helma #105.252.85.40), total volume of 20 μl . Ludox scattering solution was used to record instrument response function (IRF). Excitation and emission wavelength were set as the excitation wavelength of the sample. The maximum counts in the peak for the fluorescence decay was set to 50000 counts.

Table 3.1 Settings for the IBH-5000U and PicoQuant FT300 setups

For Alexa488	IBH-5000U	PicoQuant FT300
Excitation, [nm]	470	485
Emission, [nm]	520	520
Excitation slits, [nm]	4	none
Emission slits, [nm]	32	8-16.2
Filter	OG 500	FGL515
For Cy5		
Excitation, [nm]	635	635
Emission, [nm]	665	665
Excitation slits, [nm]	4	none
Emission slits, [nm]	32	8-16.2
Filter	OG 640	FGL 645

Confocal microscope setups

Single molecule experiments were performed on two home-built Multiparameter Fluorescence Detection (MFD) microscopes. The general scheme of the setups is illustrated on Figure 3.4.

The first setup is four-channel MFD setup and has epi-illuminated confocal microscope (IX70, Olympus, Hamburg, Germany) with a 60x/1.2 water immersion objective (UPLSAPO 60x/1.2w, Olympus Hamburg, Germany). The fluorescent donor molecules (Alexa 488) are excited by a linearly polarized, active-mode-locked Argon-ion laser (Innova Saber, Coherent, Santa Clara, CA, USA, 496.5 nm, 73.5 MHz, ~ 300 ps, 110 μ W in the sample) or by a 485 nm diode laser (LDH-D-C 485, PicoQuant, Berlin, Germany, 110 μ W in the sample) operating at 64 MHz. In typical smFRET experiments fluorescence sample is diluted into picomolar concentration (pM) and placed in a confocal microscope where a sub-nanosecond laser pulse excites labeled molecules freely diffusing through a detection volume. A typical confocal volume is a femtoliter (fl). This concentration allows detection of only single molecule event at a time. The emitted fluorescence from the labeled molecules is collected through the objective and spatially filtered using a pinhole with typical diameter of 100 μ m. Then, the signal is split into parallel and perpendicular components via polarizing beam splitter and then at two different spectral windows (e.g. “green” and “red”). Additionally

green (HQ 533/46 nm for Alexa488 and Rh110) (AHF, Tubingen, Germany) and red (HQ 720/150 nm for Cy5) bandpass filters (AHF, Tubingen, Germany) are placed in front of the detectors to provide the registration only of the fluorescence photons coming from the acceptor and donor molecules. Detection on the first setup is performed using four avalanche photodiodes (green channels: τ -SPAD-100, PicoQuant; red channels: SPCM-AQR-14, Perkin Elmer). Each photon detector channel is then coupled to time correlated single photon counting (SPC 132, Becker and Hickl, Berlin, Germany)

The second set up is similar to the one described above. Excitation is achieved using 485 nm pulsed diode lasers (LDH-D-C 485, PicoQuant, operated at 64 MHz) on an Olympus IX71 microscope. Laser power in the sample is 110 μ W. Detection on the second setup is performed using eight avalanche photodiodes. After separating the fluorescence signal according to polarization and color, each of the four channels was split again using 50/50 beam splitters resulting in a total of eight detection channels ((4 green channels: τ -SPAD (PicoQuant, Germany) and 4 red channels: APD (Perkin Elmer)). This assures dead time free detection of the photons. Bandpass filters were HQ 520/35 and HQ 720/150 (both AHF) for green and red channels, respectively. The detector outputs were recorded by a TCSPC module (HydraHarp 400, PicoQuant).

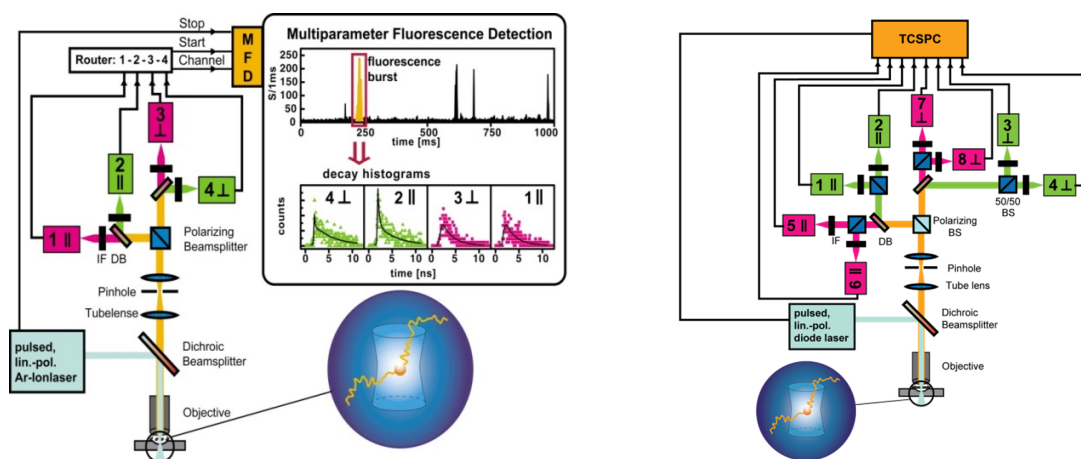


Figure 3.4 Experimental setup for smMFD setup and data acquisition: setup 1 – left panel and setup2 – right panel.

3.2.6 Calibration measurements

Accurate FRET Efficiency and distance determination requires close attention to the setup alignment and estimation of correction parameters that can distort detected fluorescence signal. For example, the detectors and laser (of the setup 1) alignment and the control measurements of possible setup “drifts” were performed every measurement day. The monitor includes measurements of the reference Rh110 and Rh101 dyes (nM concentration) for diffusion time and for g-factor estimation (Chapter 3.2.7) and water for IRF and buffer for background estimation. Detection efficiency ratio g_G/g_R was estimated by measuring the mixture of the

labeled DNA with Alexa488 and Cy5 with different inter-dye distances (section below). To confirm the proper alignment of the setup freely diffusing Rho110 dye of pM concentration is used where obtained fluorescence lifetime and anisotropy were controlled. All reference measurements were performed on the microscope coverglass in 50 μ l volume, whereas studied samples were measured in NUNC chambers (Lab-Tek, Thermo Scientific, Germany), total volume 300 μ l.

Single-molecule data calibration with standard protocol with ds DNA and determination of detection efficiency g_G/g_R

Detection efficiency ratio g_G/g_R is an essential part of the calibration process and an important factor in accurate FRET Efficiency and distance determination. Due to possible misalignment of the detector channels or temperature fluctuations in the room, this value has to be controlled at every measurement session. Thus mixture of two double-stranded DNA with known fluorescence characteristics and FRET efficiencies were chosen (Figure 3.5). Single strands labeled with C6- linkers and Alexa488 (or Cy5) were purchased from Purimex (Germany). See Figure 3.5 for chemical structures.

A

5'-d(GCA ATA CTT GGA CTA GTC TAG GCG AAC GTT TAA GGC GAT CTC TGT TTA CAA CTC CGA AAT AGG CCG)
 3'-d(CGT TAT GAA CCT GAT CAG ATC CGC TTG CAA ATT CCG CTA GAG ACA AAT GTT GAG GCT TTA TCC GGC)

B

5'-d(GCA ATA CTT GGA CTA GTC TAG GCG AAC GTT TAA GGC GAT CTC TGT TTA CAA CTC CGA AAT AGG CCG)
 3'-d(CGT TAT GAA CCT GAT CAG ATC CGC TTG CAA ATT CCG CTA GAG ACA AAT GTT GAG GCT TTA TCC GGC)

C

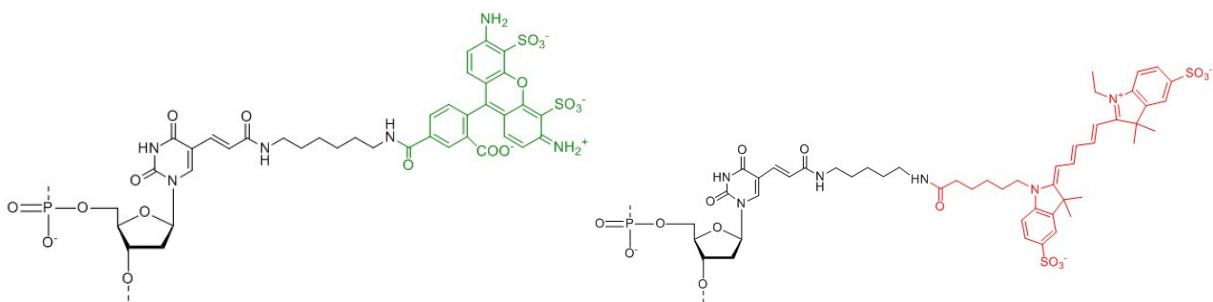


Figure 3.5 A-B): Sequence and labeling positions (green for donor Alexa488 and red for acceptor Cy5) for calibration samples ds DNA. C) Structural formula of the modified dT and fluorescence dyes Alexa488 (left) and Cy5 (right).

We assume that chosen system does not undergo any dynamic processes and observed FRET populations should be located on the FRET line as it is demonstrated on Figure 3.6 (more about analysis is in Chapter 3.3.2). With known mixture of two dsDNA with 9 and 15 base pair separation and expected $\langle R_{DA} \rangle_E$ 44.7 Å and 59.1 Å, background in green and red channel, fluorescence quantum yield of donor and acceptor, g_G/g_R could be estimated.

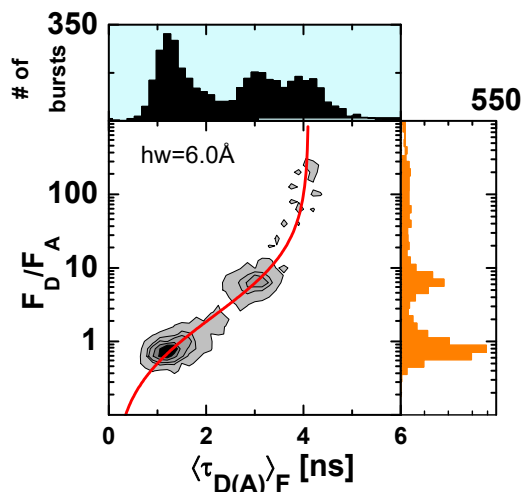


Figure 3.6 Typical 2D histogram of fluorescence green to red intensities F_D/F_A vs fluorescence lifetime of donor in presence of acceptor $\langle \tau_{D(A)} \rangle_F$ of the mixture of two labeled ds DNA with 9 and 15 base pairs separation. The static FRET line is built based on following parameters: $\sigma_{DA}=6$ Å, $\tau_{D(0)}=4.1$ ns, $\Phi_{FD(0)}=0.8$ and $\Phi_{FA(0)}=0.32$.

3.2.7 Data analysis

Multi-parameter Fluorescence Detection (MFD)

Various fluorescence dimensions can be exploited in MFD experiment, such as spectral properties of absorption and fluorescence, fluorescence anisotropy, fluorescence lifetime, intensity indicators and distance between fluorophores. The proper usage of these characteristics within the method allows resolving unique information about the heterogeneities and possible interconversion between the states.

In single-molecule (sm-) confocal experiment, single molecules are detected during their free diffusion through a confocal volume. Detected photons are registered as fluorescence bursts of certain intensity and duration. To remove the background, the threshold for the maximum inter-photon time and a minimum photon number within a burst (typically 60-80 photons) is applied.

The most informative plots can be constructed of the following fluorescence indicators: fluorescence signals of the donor F_D and acceptor F_A , fluorescence anisotropy r_D and fluorescence average donor lifetime in presence of acceptor $\langle \tau_{D(A)} \rangle_F$.

3.2.7.1 Fluorescence signals

Fluorescence signal $F_{\lambda_{em}|\lambda_{ex}}$ refer to the number of photons, detected in the green (G) and red (R) channels respectively and calculated from the total corrected signal S corrected by non-fluorescence background and dark counts with factors $\langle B \rangle$ in each channel correspondingly. Here the indices should be read as following: ($D|D$) is donor intensity if donor was excited and ($A|A$) is the acceptor intensity if the acceptor was excited.

$$F_{G|G} = S_{G|G} - \langle B_{G|G} \rangle \quad (50)$$

$$F_{R|G} = S_{R|G} - \alpha F_{G|G} - \langle B_{R|G} \rangle \quad (51)$$

$F_{R|G}$ signal consists of not only the acceptor signal but also of the “leakage” of the donor fluorophore into the red channel, which is called emission crosstalk α and could be expressed as the ratio of donor fluorescence recorded by red detectors to the donor fluorescence recorded by green fluorescence.

Afterwards the fluorescence signal has to be corrected by the properties of the setup with known green and red detection efficiencies $g_{G|D}$ and $g_{R|D}$ as only the fraction is transmitted through the optical elements of the setup

$$F_{D|D} = \frac{S_{G|G} - \langle B_{G|G} \rangle}{g_{G|D}} \quad (52)$$

$$F_{A|D} = \frac{S_{R|R} - \alpha F_{G|G} - \langle B_{R|R} \rangle}{g_{R|D}} \quad (53)$$

Note that detection efficiencies are functions of many device parameters (e.g. time of measurement, fluorescence filters, and efficiencies of the detectors) and can be expressed as

$$g_{R|D} = \int_{\lambda_{em}} g_R(\lambda_{em}) \varepsilon_{R|D}(\lambda_{em}) d\lambda_{em} \quad (54)$$

$$g_{G|D} = \int_{\lambda_{em}} g_G(\lambda_{em}) \varepsilon_{G|D}(\lambda_{em}) d\lambda_{em} \quad (55)$$

$g_R(\lambda_{em})$ and $g_G(\lambda_{em})$ are the shape functions of the detection efficiencies that take into account wavelength dependent sensitivities and performance of the devices elements and $\varepsilon_{R|D}(\lambda_{em})$ and $\varepsilon_{G|D}(\lambda_{em})$ are emission spectral coefficients.

Further in the manuscript shortened symbols will be used: $F_{D|D} = F_D$ and $F_{A|D} = F_A$; $g_{G|D} = g_G$ and $g_{R|D} = g_R$; $S_{G|G} = S_G$ and $S_{R|R} = S_R$.

3.2.7.2 Fluorescence lifetime

In typical sm-experiment the fluorescence burst contains approximately 100 photons and thus it is impossible to determine $\langle \tau \rangle_x$ that characterizes presence of multiple species. Hence, maximum likelihood estimator (MLE)^{89,130,131} is employed to calculate fluorescence averaged lifetime $\langle \tau \rangle_F$ for single molecule bursts. It could be expressed by the individual components $\tau_{D(A)}^{(i)}$ and their corresponding fractions $x^{(i)}$

$$\langle \tau_{D(A)} \rangle_F = \frac{\sum_i x^{(i)} \tau_{D(A)}^{(i)2}}{\sum_i x^{(i)} \tau_{D(A)}^{(i)}} \quad (56)$$

As it is impossible to calculate the conversion function $\langle \tau \rangle_F$ to $\langle \tau \rangle_x$ analytically, the empirical dependence is provided:

$$\langle \tau \rangle_x = \sum_{i=0}^n c_i (\langle \tau \rangle_F)^i \quad (57)$$

Here c_i are polynomial coefficients obtained by numerical simulations⁴⁴ and calculated assuming that R_{DA} is Gaussian distributed⁸⁹.

3.2.7.3 Steady state fluorescence anisotropy

Fluorescence anisotropy of the donor r_D can be determined as¹³².

$$r_D = \frac{gF_{||} - F_{\perp}}{(1 - 3l_2)gF_{||} + (2 - 3l_1)F_{\perp}} \quad (58)$$

Where $F_{||}$ and F_{\perp} are fluorescence signals of the donor with parallel and perpendicular polarization, g (sometimes is called *g-Factor*) is the ratio of the detection efficiencies of the perpendicular to parallel polarized light and l_1 and l_2 are the factors that compensate for the signal depolarization by the objective due to the high numerical aperture. In this work $l_1 = 0.0308$ and $l_2 = 0.0368$ are used for setup 1 and $l_1 =$

0.0175 and $l_2 = 0.0526$ for setup 2. The g -Factor was determined experimentally every measurement day using reference dyes Rhodamine 110 and Rhodamine 101.

$$F_{||}(t) = \frac{1}{3}F(t)[1 + 2r(t)] \quad (59)$$

$$F_{\perp}(t) = \frac{1}{3}F(t)[1 - r(t)] \quad (60)$$

In this work anisotropy was modeled as bi-exponential decay with fundamental anisotropy r_0 and rotation correlation time ρ .

$$r(t) = r_0 \sum_i e^{-t/\rho_i} \quad (61)$$

3.2.7.4 1D and 2D histograms

Using three above mentioned independent fluorescence parameters it is possible to construct 1D histograms of fluorescence green to red signal ratio F_D/F_A , fluorescence average donor lifetime in presence of acceptor $\langle \tau_{D(A)} \rangle_F$ and donor fluorescence anisotropy r_D (Figure 3.7A-C). The combinations of 1D histograms into 2D histograms (Figure 3.7D) reveals more detailed information on the heterogeneities, can better separate states that lead to further analysis of the individually selected states.

Selected bursts are represented on a 2D frequency histogram of fluorescence green to red signal ratio F_D/F_A against fluorescence average donor lifetime in presence of acceptor $\langle \tau_{D(A)} \rangle_F$ (upper panel of Figure 3.7D) with corresponding 1D plots. Here the number of molecules (fluorescent bursts) in each bin is colored in gray scale from white (lowest) to black (highest).

The theoretical relationship between F_D/F_A (or equivalent FRET Efficiency E) and $\langle \tau_{D(A)} \rangle_F$ is demonstrated via linker-corrected static FRET line (red curve) and described as Eq.62. This relation depends on various experimental parameters: fluorescence quantum yields of the donor alone $\Phi_{F,D}$ and of the acceptor in the presence of the donor $\Phi_{F,A}$; background corrections in green and red channels $\langle B_{G|G} \rangle$ and $\langle B_{R|G} \rangle$, emission crosstalk α and detection efficiency ratio g_G/g_R . Any deviation from the line would indicate dynamical process on ms-timescale or additional photophysical processes.

$$F_D / F_A = \frac{\Phi_{F,D}}{\Phi_{F,A}} \left/ \left(\frac{\langle \tau_{D(0)} \rangle_x}{c_3 \langle \tau_{D(A)} \rangle_F^3 + c_2 \langle \tau_{D(A)} \rangle_F^2 + c_1 \langle \tau_{D(A)} \rangle_F + c_0} - 1 \right) \right. \quad (62)$$

The lower panel of Figure 3.7D demonstrates the relationship between donor anisotropy versus $\langle \tau_{D(A)} \rangle_F$ on 2D histogram. The steady-state anisotropy of donor r_D is linked with donor lifetime $\tau_{D(A)}$, rotation correlation time ρ_D with anisotropy r_0 at time zero via Perrin equation

$$r_D = \frac{r_0}{1 + \tau_{D(A)}/\rho_D} \quad (63)$$

In order to resolve donor residual anisotropy it is not enough to assume model with single rotation correlation time and thus Perrin equation had to be modified. Here bi-exponential solution for intensity decay (Eq.64) is assumed, where each species has τ_i and ρ_i and is weighted (fraction x).

Here the longest rotation correlation time ($\rho_1 \sim 20ns$) would reflect the global motion of the molecule with the dye on the linker and the fastest motion is the rotation of the dye itself ($\rho_2 \sim 0.4ns$).

$$r_D = r_0 \cdot \left(\frac{x}{1 + \frac{\tau_1}{\rho_1}} + \frac{1-x}{1 + \frac{\tau_2}{\rho_2}} \right) \quad (64)$$

Solving the Eq.64 for fraction x one could define the residual anisotropy as

$$r_\infty = x * r_0 = \frac{(\rho_1 + \tau) * \left(\frac{r}{r_0} * \rho_2 + \frac{r}{r_0} * \tau - \rho_2 \right)}{\rho_1 * \tau - \rho_2 * \tau} * r_0 \quad (65)$$

Here fraction x corresponds to the fraction of the trapped state of the dye $x = S_{trap}$.

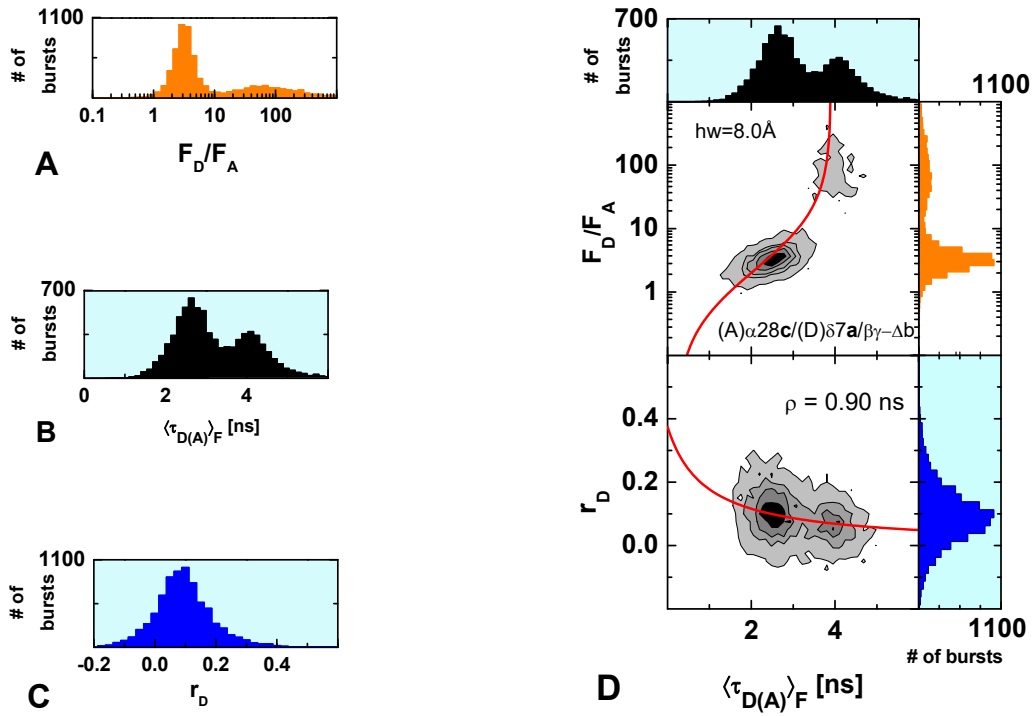


Figure 3.7 (A) typical 1D histograms of F_D/F_A intensity ratio; (B) fluorescence average donor lifetime in presence of acceptor $\langle \tau_{D(A)F} \rangle$; (C) fluorescence anisotropy of the donor; (D) typical 2D histogram of F_D/F_A vs $\langle \tau_{D(A)F} \rangle$ (upper plot) and r_D vs $\langle \tau_{D(A)F} \rangle$ (lower plot) for J(acd)_(A)α28c/(D)δ7a/βγ-Δb. Static FRET line and Perrin equation are shown as red curves (upper plot and lower plots correspondingly).

3.2.7.5 Time-resolved experiments

Fluorescence lifetime determination

To define the fluorescence lifetime of the donor-only and acceptor-only samples TCSPC measurement were performed (see Chapter 3.3.1). Due to the local quenching and steric effects the fluorescence decay of the donor-only (similarly acceptor-only) RNA 3WJ sample was always multi-exponential

$$F_0(t) = \sum_i x_i \exp(-t/\tau_i) \quad (66)$$

Where species weighted average lifetime can be expressed as

$$\langle \tau \rangle_x = \sum_i x_i \tau_i \quad (67)$$

and fluorescence weighted average lifetime can be expressed as

$$\langle \tau \rangle_F = \frac{\sum_i x_i \tau_i^2}{\sum_i x_i \tau_i} \quad (68)$$

Where x_i is the fraction and τ_i is the lifetime of the i^{th} component. Donor-only decays were always fitted either with two or three species, while for acceptor-only decays two species were sufficient. Fit quality is evaluated with χ_r^2 . The recorded decays are in Chapter 3.5.1.1.

Fluorescence quantum yield determination

Fluorescence quantum yield plays a crucial role in the distance R_{DA} (Eq. 79) and static FRET line determination. It is known¹³³⁻¹³⁵ that fluorescence properties of the dyes might be affected by local environment. Thus this factor must be considered carefully and all labeling positions that are used for the FRET samples must be reviewed. To determine $\Phi_{F,D}$ and $\Phi_{F,A}$ for each labeling cite, eTCSPC measurements for single labeled molecules were performed. Both donor Alexa488 and acceptor Cy5 dyes were described by multi-exponential decays (Chapter 3.3.1). Fluorescence quantum yield of the bright species is related to the species average lifetime $\langle \tau \rangle_x$ and the fluorescence quantum yield $\Phi_{F,ref}$ and the lifetime of the reference sample $\tau_{F,ref}$

$$\Phi_{F,D} = \Phi_{F,ref} \cdot \frac{\langle \tau \rangle_x}{\langle \tau \rangle_{x,ref}} \quad (69)$$

For the reference we used free dyes in solution Alexa488 with $\langle \tau \rangle_x = 4.1\text{ns}$ and $\Phi_{F,D} = 0.8$ and Cy5 with $\langle \tau \rangle_x = 1.16\text{ ns}$ and $\Phi_{F,A} = 0.32$ due to the presence of $\sim 20\%$ cis-trans isomerization under single-molecule conditions (instead of $\Phi_{F,A} = 0.4$ expected for ensemble measurements)⁴⁴. Here, we assume only dynamic quenching and that the lifetime decay of the reference sample is monoexponential.

Fitting results for fluorescence decays and calculated values for species weighted lifetime $\langle \tau \rangle_x$, fluorescence weighted average lifetime $\langle \tau \rangle_F$ and fluorescence quantum yield for donor-only and acceptor-only molecules are compiled in the Table 3.5-3.7.

Time-resolved fluorescence anisotropy

All fluorescence depolarization decay curves ($F_{VV}(t)$, $F_{VH}(t)$) with the Polarizer/Detector settings (V -Vertical, H - Horizontal) of single labeled molecules were measured by eTCSPC and fitted jointly with corresponding magic angle (M) fluorescence decay $f_{VM}(t) = f(t)$. To reduce the number of parameters so called homogenous approximation is done³³. It's assumed that de-excitation and depolarization of dyes are

independent, i.e. in each donor de-excitation states dyes characterized by the same set of depolarization rate constants.

$$f_{VV}(t) = \sum_j \sum_i x_d^{(i)} x_r^{(j)} e^{-k_d^{(i)}t} [1 + 2e^{-k_r^{(j)}t}] = f_D(t)[1 + 2r(t)] \quad (70)$$

$$f_{VH}(t) = \sum_j \sum_i x_d^{(i)} x_r^{(j)} e^{-k_d^{(i)}t} [1 - e^{-k_r^{(j)}t}] = f_D(t)[1 - r(t)] \quad (71)$$

Here $k_d^{(i)}$ is donor de-excitation rate constant, $k_r^{(j)}$ is the depolarization rate constant, $x_d^{(i)}$ is the fraction of molecules having the donor de-excitation rate constant $k_d^{(i)}$ and $x_r^{(j)}$ is the fraction of molecules having the depolarization rate constant $k_r^{(j)}$.

$$f_D(t) = \sum_i x_i e^{-t/\tau_i} \text{ and } r(t) = \sum_i b^{(j)} e^{-t/\rho_j}$$

Note that $\sum_i b^{(j)} = r_0$ and $b^l = r_\infty$

So we have the same expression as in case of simple mono-exponential donor and acceptor decays and the number of fraction values is reduced to $N_d + N_r$. In this work the best fit results were achieved with $N_d = N_r = 3$.

To fit real experimental decays IRF, background and amplitudes of the VV, VH signals are accounted next way:

$$F_{VV}(t) = F_0 \cdot IRF_{VV}(t) \otimes f_{VV}(t) + B_{VV} \quad (72)$$

$$F_{VH}(t) = g_{VV/VH} F_0 \cdot IRF_{VH}(t) \otimes f_{VH}(t) + B_{VH} \quad (73)$$

Where $g_{VV/VH}$ is g-factor, F_0 - amplitude scaling factor, $IRF_{VV}(t)$, $IRF_{VH}(t)$ - instrument response functions and B_{VV} , B_{VH} - background values. The “ \otimes ” sign designates circular convolution.

3.2.7.6 Photon distribution analysis (PDA)

PDA accurately predicts the shape of one-dimensional S_G/S_R (or equivalently F_D/F_A) histograms in the presence of FRET. It accounts for shot noise, background contributions and additional broadening due to complex acceptor photophysics^{43,89,136} and indicate whether an observed distribution is due to shot noise only or whether there is a real distribution of the parameter of interest (e.g. distance).

In single molecule measurement low number of molecules is detected per observation time and thus low signal. Therefore the background has to be considered. The measured signal S is a mixture of

fluorescence signal F and background B . The values of S , F , and B are expressed in photon counts per time window of a fixed length (TW). During the experiment the signal is measured by single-photon counting detectors and divided into green (G) and red (R) components.

The PDA method starts from the calculation of the probability of observing a certain combination of photon counts in green and red detection channels. As different combinations of F_G , F_R , B_G , B_R could result in the same value of S_G/S_R therefore the sum of all combinations is calculated

$$P(S_G, S_R) = \sum_{F_G+B_G=S_G; F_R+B_R=S_R} P(F)P(F_G, F_R|F)P(B_G)P(B_R) \quad (74)$$

$P(F)$ is the probability to observe F fluorescence photons per time window and

is obtained by deconvolution from the total signal intensity distribution $P(S)^{137}$, which is given as

$$P(S) = P(F) \otimes P(B) \quad (75)$$

Assuming that data is binned into equal time bins, the probability to detect a background photon follows a Poisson distribution with known mean intensities $\langle B_G \rangle$ and $\langle B_R \rangle$

$$P_{B_i}(B_i) = \frac{\langle B_i \rangle^{B_i}}{B_i!} \cdot e^{-\langle B_i \rangle} \quad (76)$$

$P(F_G, F_R|F)$ represents the conditional probability of observing a particular combination of green and red fluorescence photons, F_G and F_R , provided the total number of registered fluorescence photons is F , and can be expressed as a binomial distribution

$$P(F_G, F_R|F) = \frac{F!}{F_G! (F - F_G)!} p_G^{F_G} (1 - p_G)^{F - F_G} \quad (77)$$

Here p_G is the probability a detected photon is registered by in the green detection channel. The relation between p_G and FRET efficiency E is described as following:

$$p_G = \left(1 + \alpha + \gamma \cdot \frac{E}{(1 - E)}\right)^{-1} \quad (78)$$

Where $\gamma = \frac{\Phi_{F,A}}{\Phi_{F,D}} \cdot \frac{g_R}{g_G}$ and α is emission crosstalk.

To convert the signal intensity ratio S_G/S_R (or fluorescence ratio F_D/F_A) into an inter-dye distance R_{DA}^j

$$R_{DA}^j = R_{0r} \cdot \left[\Phi_{F,A} \cdot \frac{F_D^{(j)}}{F_A^{(j)}} \right]^{1/6} = R_{0r} \cdot \left[\Phi_{F,A} \cdot \frac{1 - E^{(j)}}{E^{(j)}} \right]^{1/6} \quad (79)$$

Here $\Phi_{F,A}$ is the position-dependent acceptor fluorescence quantum yield and R_{0r} is the "reduced" Förster radius⁷³.

The distribution $P(S_G, S_R)$ is typically used to generate one-dimensional (1D) histograms of green to red signal intensity ratio S_G/S_R and fitted to experimental data.

In this work the signals of the selected FRET bursts were split into equal time windows (TW=3ms). Note, that only full length time windows were used and incomplete pieces at the end of bursts were excluded. For each PDA fit bursts were identified and selected from MFD data set using $|T_G - T_R| < 1$ ms macrotime filter to remove contributions from photophysical processes¹²⁸. Model that accounts for one or two FRET states (Gaussian distributed distances) and a donor only contribution was used. Broadening of FRET states was accounted by a global parameter σ^{43} . In some cases an impurity with an apparent distance of typically 70 – 100 Å had to be taken into account. Thus, for n FRET states $2n + 1$ to $2n + 3$ fit parameters were required depending on whether the impurity state was considered. The fit goodness was determined by χ^2 maximum likelihood test.

3.2.8 Error propagation

In this section error types that influence R_{DA} determination are discussed: systematic error that affect accuracy, random errors that affect precision of the desired value and modeling errors introduced by the model that characterizes experimental data. Typical sources of the systematic errors could be faulty daily calibration procedure or improper reference sample for the analysis. The random error originates from the photon noise or random errors of the operator.

In this study, we consider the following experimental factors that could contribute to the final error propagation of R_{DA} :

1. Errors in Förster Radius calculation: refractive index n , orientation factor κ^2 and overlap integral J
2. Background contributions $\langle B_G \rangle, \langle B_R \rangle$
3. Detection efficiency ratio g_G/g_R
4. Emission crosstalk α
5. Acceptor fluorescence quantum yield $\Phi_{F,A}$
6. Random errors $R_{DA,random}$ in PDA analysis.

There are different possible error sources: error contributions due to the sample feature $\Delta R_{DA}^2(R_0)$ (resolved in R_0 experiments) and setup calibration and measurement error $\Delta R_{DA}^2(meas)$.

So final error could be rewritten as

$$\Delta R_{DA}(total) = \sqrt{\Delta R_{DA}^2(R_0) + \Delta R_{DA}^2(meas)} \quad (80)$$

$\Delta R_{DA}(R_0)$ is calculated as:

$$\Delta R_{DA}(R_0) = 0.37 \cdot R \cdot \delta R'_{DA}(R_0) = 0.37 \cdot R \cdot \sqrt{\delta R_{DA}^2(J) + \delta R_{DA}^2(n) + \delta R_{DA}^2(\kappa^2)} \quad (81)$$

The weighting factor 0.37 for $\Delta R_{DA}(R_0)$ in Eq.81 is obtained from reference samples dsRNA¹²⁵ assuming no dynamical processes and completely rigid helix. In order to obtain high precision of the experimental distance, calibration against the reference dsRNA sample is needed. Parameters that contribute to $\Delta R_{DA}(R_0)$ are not determined daily, thus their error could be overestimated. Weighting factor compensates error overestimation and results in the final $\chi_r^2=1$ for ds RNA.

The following error contribution for the overlap integral J

$$\delta R_{DA}(J) = \frac{R_0}{R} \cdot \Delta J \quad (82)$$

and for the refractive index:

$$\delta R_{DA}(n) = \frac{R_0}{R} \cdot \Delta n \quad (83)$$

Here $\Delta J = 0.025$,¹³⁸ $\Delta n = 0.04$ (based on varying $n= 1.33$ - 1.50 for different media), $\delta R_{DA}^2(\kappa^2)$ is the uncertainty from the mutual orientation of donor and acceptor and is described in detail in the Chapter 3.2.8.2.

$$\delta R_{DA}(\kappa^2) = \frac{R_0}{R} \cdot \Delta \kappa^2 \quad (84)$$

ΔR_{meas}^2 is determined for each measurement individually.

ΔR_{meas}^2 error could be expressed as

$$\Delta R_{meas}^2 = \Delta R_{DA}^2(BG) + \Delta R_{DA}^2(\gamma) + \Delta R_{DA}^2(\alpha) + \Delta R_{DA}^2(random) \quad (85)$$

Where $\gamma = \frac{g_G}{g_R} \cdot \frac{\Phi_{F,A}}{\Phi_{F,D}} = \gamma' \cdot \frac{\Phi_{F,A}}{\Phi_{F,D}}$

Background contribution is expressed as

$$\Delta R_{DA}(BG) = \delta R_{DA}(BG) \cdot R \quad (86)$$

where

$$\delta R_{DA}(BG) = \frac{1}{6 \cdot \Phi_{FA}} \left[\left(\frac{\Delta B_G}{F_0 \frac{1}{1 + \left(\frac{R}{R_0}\right)^6}} \right)^2 + \left(\frac{\Delta B_R}{\gamma \cdot F_0 \left(1 + \left(\frac{R}{R_0}\right)^6\right)^{-1}} \right)^2 \right] \quad (87)$$

And count rate of the donor in absence of FRET $F_0=40$ kHz.

The following error contribution for the gamma factor:

$$\Delta R_{DA}(\gamma) = \delta R_{DA}(\gamma) \cdot R \quad (88)$$

and

$$\delta R_{DA}(\gamma) = \frac{R}{6} \cdot \frac{\Delta \gamma}{\gamma} = \frac{R}{6} \cdot \sqrt{\left(\frac{\Delta \gamma'}{\gamma'}\right)^2 + \left(\frac{\Delta \Phi_{FA}}{\Phi_{FA}}\right)^2} \quad (89)$$

Here, the following error contribution for the background in the donor channel after donor excitation

$$\Delta R_{DA}(\alpha) = \delta R_{DA}(\alpha) \cdot R \quad (90)$$

and

$$\delta R_{DA}(\alpha) = -\frac{R}{6} \frac{1}{\gamma} \left(\frac{R}{R_0}\right)^6 \cdot \Delta \alpha \quad (91)$$

Setup-related calibration parameters (α, γ, B_G, B_R) account for the measurement sensitivity and vary for different setups. Thus relative error contributions for these parameters for each experiment should be setup-specific.

The PDA error $\Delta R_{DA}(random)$ is described in detail in Chapter 3.2.8.1.

3.2.8.1 Confidence intervals for fit parameters in PDA

The relative random error contribution $\delta R_{DA}(random)$ was determined by scanning the χ^2 -surface (also known as support plane analysis¹³⁹) of the data using knowledge of the data-noise. One of the free fit parameters (normally $R_{DA}^{(i)}$, their corresponding fractions $x^{(i)}$ and width of the distribution σ) is varied from the value where $\chi_{r,min}^2$ is minimum, then rerun the least-squares fit with the new value as a constant, while other free parameters are tuned in order to minimize χ_r^2 . If new χ_r^2 is reduced, then the revised parameter is consistent with experimental data. Then the selected value is changed again until it crosses the acceptable value as judged by F_χ statistics¹⁴⁰. Normally 100000 iterations are applied with acceptance threshold $\chi_{r,min}^2 + (2/N_{bins})^2$, where N_{bins} is the number of histogram bins. Selected threshold displays the range of parameters that are consistent with experimental data within 1σ confidence interval.

A minimal bounding box encloses all error surface points (gray area in Figure 3.8) whereas the points under the threshold are depicted in black (Figure 3.8).

The uncertainty $\delta R_{DA}(random)$ of the PDA fit has to be determined individually for each FRET data. All values are presented in Table 3.16-3.18.

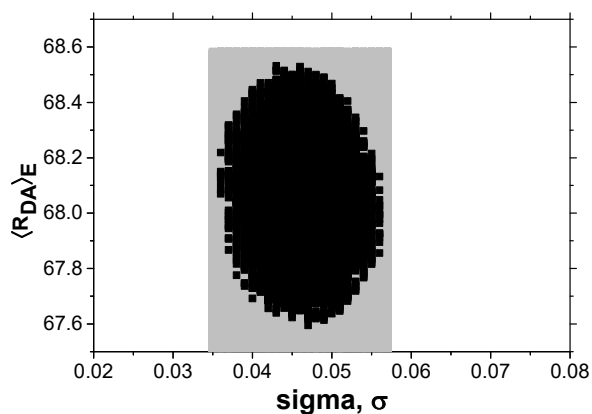


Figure 3.8 Confidence intervals for measured distances $\langle R_{DA} \rangle_E$ vs sigma. Bounding box is presented as gray area, points under acceptance threshold are marked in black.

3.2.8.2 Uncertainties due to the orientation factor κ^2

Determination of $\langle \kappa^2 \rangle$ gets difficult as the relative orientation of the donor and acceptor dipole moments to the distance vector remains unknown. However an estimation of the minimum and maximum values of κ^2 can be obtained from the anisotropy measurements¹⁴¹. To rationalize dye motion a few models have been

suggested and discussed^{44,141,142} and Kalinin *et al* (in preparation). In this study we used the so called diffusion with traps model (DWT) developed by Kalinin and co-authors. Briefly, suggested model accounts for random orientation of transition dipoles of trapped populations(not averaged) and compute the overall FRET efficiency limits assuming 4 cases for FRET between donor and acceptor: 1) $D_{free} \rightarrow A_{free}$, 2) $D_{free} \rightarrow A_{trapped}$, 3) $D_{trapped} \rightarrow A_{free}$, and 4) $D_{trapped} \rightarrow A_{trapped}$.

$$\begin{aligned}
E = & (1 - s_D)(1 - s_A)E(D_{free} \rightarrow A_{free}) + s_D s_A E(D_{trapped} \rightarrow A_{trapped}) \\
& + (1 - s_D)s_A E(D_{free} \rightarrow A_{trapped}) \\
& + (1 - s_A)s_D E(D_{trapped} \rightarrow A_{free})
\end{aligned} \tag{92}$$

Here s_D and s_A are the trapped donor and acceptor fractions and they are related to the residual anisotropy as (Eq. 65). Note, in the beginning a FRET efficiency $E_{2/3}$ has to be defined by choosing a certain donor acceptor distance R_{DA} for $\langle \kappa^2 \rangle = 2/3$.

One could calculate E_{min} and E_{max} :

$$\begin{aligned}
E_{min} = & (1 - S_D)(1 - S_A)E(\kappa^2 = 2/3) + s_D s_A E(\kappa^2 = 0) \\
& + (s_D + s_A - 2s_D s_A)E(\kappa^2 = 1/3)
\end{aligned} \tag{93}$$

$$\begin{aligned}
E_{max} = & (1 - S_D)(1 - S_A)E(\kappa^2 = 2/3) + s_D s_A E(\kappa^2 = 4) \\
& + (s_D + s_A - 2s_D s_A)E(\kappa^2 = 4/3)
\end{aligned} \tag{94}$$

The observed experimental distance distribution is characterized by a distribution of apparent distances R_{DA} , which can be described as effective dynamically averaged with $\langle \kappa^2 \rangle_{eff}$ (Figure 3.9)

$$\langle \kappa^2 \rangle_{eff} = 2/3 \left(\frac{R_{DA}}{R_0} \right)^6 / (1/E - 1) \tag{95}$$

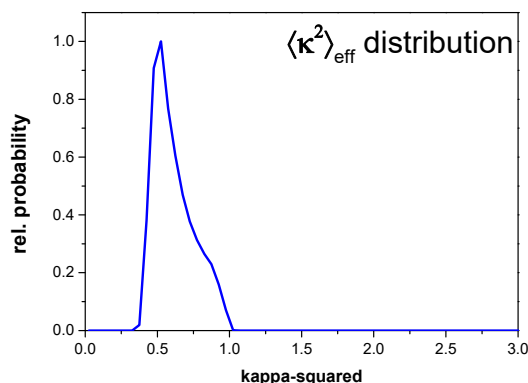


Figure 3.9 Typical representation of $\langle \kappa^2 \rangle_{eff}$ for the DWT model. The data is obtained for (D) γ 8b_(A) δ 10a_ $\alpha\beta$ - Δ c sample

The difference between extreme cases in E (or $\langle \kappa^2 \rangle_{eff}$) allows us to calculate standard deviation

$$\Delta \kappa^2 = \langle \kappa^2 \rangle_{eff,max} - \langle \kappa^2 \rangle_{eff,min} \quad (96)$$

The relative error is calculated as

$$\delta R_{DA}(\kappa^2) = \frac{R_0}{R} \cdot \Delta \kappa^2 \quad (97)$$

And the absolute error

$$\Delta R_{DA}(\kappa^2) = \delta R_{DA}(\kappa^2) \cdot R \quad (98)$$

3.2.9 FRET position and screening (FPS) calculation

3.2.9.1 Accessible Volume simulation

The prediction of the FRET labels positions with respect to the macromolecule is crucial for quantitative FRET analysis and particularly FRET distance calculation. In this study we model dye distribution by the accessible volume (AV) approach as described in ^{67,143}. The model for double-stranded RNA is generated using Nucleic Acid Builder for Amber (online version: <http://structure.usc.edu/make-na/server.html>).

For modeling the dye molecule, we use a geometrical approach that considers sterically allowed dye positions within the linker length from the attachment point with equal probability. This defines the accessible volume (AV)^{67,138}. Both donor and acceptor dyes are modeled as ellipsoids (approximated by three radii; in the software- AV3-Model) and AVs are generated using the FPS software²¹ (Figure 3.10).

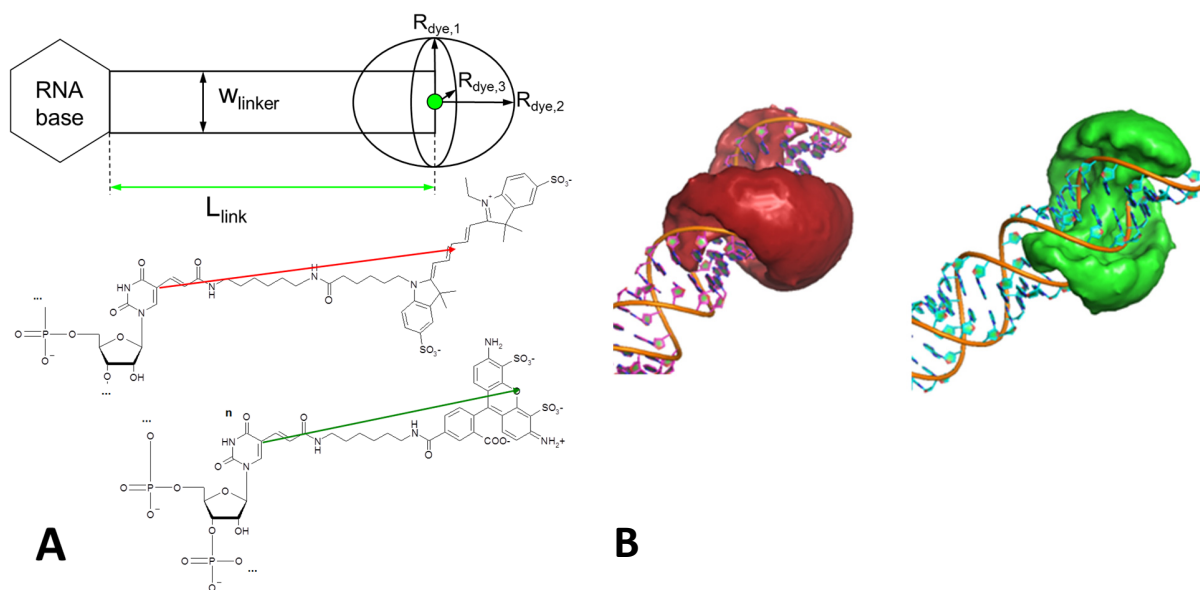


Figure 3.10 Schematic representation of the dye modeling with AV. A) Fluorophores are approximated by an ellipsoid with defined radii $R_{dye,1}$, $R_{dye,2}$ and $R_{dye,3}$ and connected with a linker with length L_{link} and width w_{link} . Structures of Cy5 (middle) and Alexa488 (bottom) coupled to dsRNA. Red and green arrows indicate the definition of the L_{link} . (B) AV clouds for Cy5 on position $\delta\gamma\text{-}\Delta a28d$ on J(bcd) (left) and Alexa488 on position $\beta 5c$ (right).

The attachment points are atom C5 for the uracils and atom N2 (or C2 depending on pdb file) for guanines. All geometric dyes parameters are estimated using the ChemDraw software (see Table 3.2 below). Further used FPS parameters are: Boundary tolerance 0.5, Accessible volume grid (rel.) 0.2; Min. grid [Å] 0.4, Search nodes: 3 and E samples: 200. The boundary tolerance (called ‘allowed sphere’ in the FPS software) is used to ignore small residues that are fixed in the PDB-model, but flexible in solution. The larger this value, the larger the structural parts that are ignored for the AV generation.

Table 3.2 Dye parameters for the AV simulations with donor Alexa488 and acceptor Cy5.

Dye	Linker length L_{link} , [Å]	Linker width W_{link} , [Å]	$R_{dye(1)}$, [Å]	$R_{dye(2)}$, [Å]	$R_{dye(3)}$, [Å]
Alexa488 (D)	20	4.5	5.0	4.5	1.5
Cy5 (A)	22	4.5	11.0	3.0	1.5

3.2.9.2 R_{MP} to $\langle R_{DA} \rangle_E$ conversion function

The distance between mean positions of the dyes, R_{MP} , is derived from geometrical consideration and cannot be obtained experimentally

$$R_{MP} = \left| \langle \overrightarrow{R_D} \rangle - \langle \overrightarrow{R_A} \rangle \right| = \left| \frac{1}{n} \sum_{i=1}^n \overrightarrow{R_D}^{(i)} - \frac{1}{m} \sum_{j=1}^m \overrightarrow{R_A}^{(j)} \right| \quad (99)$$

In this study we consider the case when environment of the dye molecule is known¹³⁸. R_{MP} can be approximated from experimentally obtained $\langle R_{DA} \rangle_E$ using the conversion function based on the set of calculated dye distributions on known structures²¹. The relationship is the third order polynomial $R_{MP} = -50.26 + 2.59 \cdot \langle R_{DA} \rangle_E - 0.014 \cdot \langle R_{DA} \rangle_E^2 + 0.00004 \cdot \langle R_{DA} \rangle_E^3$

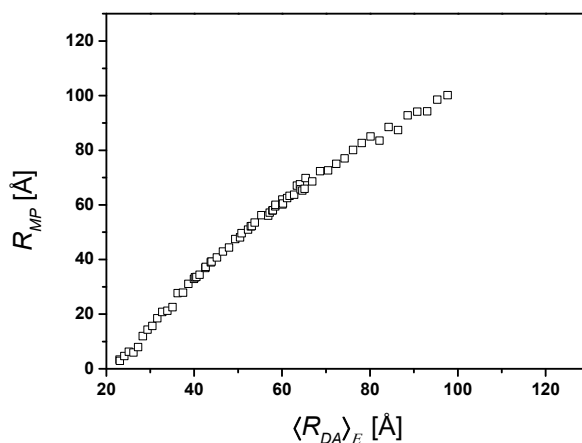


Figure 3.11 $\langle R_{DA} \rangle_E$ to R_{MP} conversion function for dsRNA with the dyes Alexa488 and Cy5 with $R_0=52\text{\AA}$.

3.2.9.3 Rigid Body Docking

The rigid body docking approach is used to find three dimensional 3WJ structural model based on sm-FRET-derived distances. Here we assume each helix is a rigid rod that can be flexible only within two (or less) base pairs to the junction. Each nucleotide of this area is treated as independent unit, resulting in maximal flexibility of the resulting 3WJ junction construct. As shown by Toulmin¹⁴⁴ and Boerner *et al* (in preparation) GC-rich construct adopt a fully paired conformation whereas AU base pairing in the junction is not possible or very unstable. Thus the following model (Table 3.3: Model 2 „GC-rigid AU-soft“) suggests rigid hydrogen bonds between GC bases and flexible bonds between AU bases in the junction. Also all units are connected with their neighboring nucleotides with O3'-P backbone bonds and by artificial bonds for additional stacking stabilization as it is shown in the Figure 3.12A.

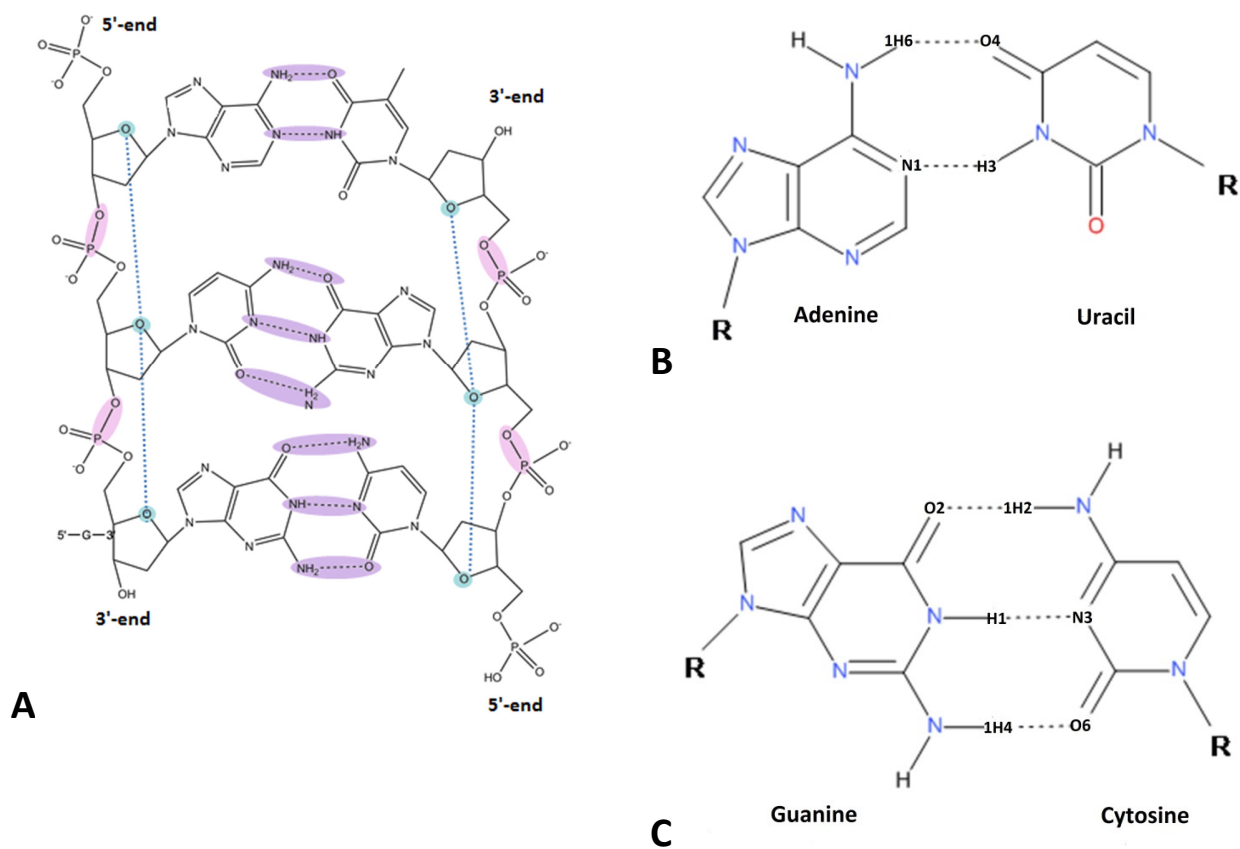


Figure 3.12 (A) Schematic view of the RNA base pairs and their connecting bonds used in RBD. Separate bodies were connected via O3'-P bonds within sugar phosphate backbone (magenta sections) and via hydrogen bonds between the bases that considered as separate bodies (violet sections). Note, that there are three hydrogen bonds between C-G bases (PDB names: O2-1H2, N3-H1, 1H4-O6) and two between U-A bases (PDB names: 1H6-O4 and N1-H3). Additional stability is facilitated by artificial bond O5'- O5' between two consequent nucleotides within a strand (blue dashed lines); (B) U-A bases with 1H6-O4 and N1-H3 bonds; (C) C-G bases with O2-1H2, N3-H1, 1H4-O6 bonds.

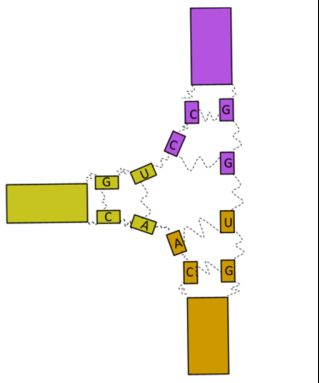
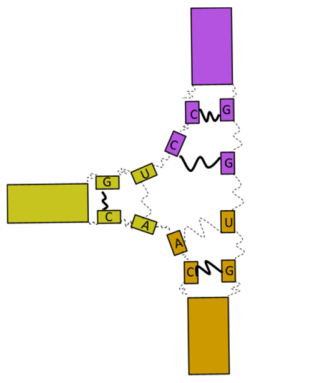
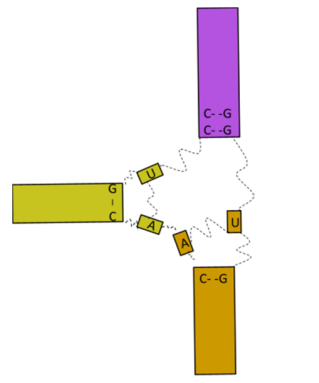
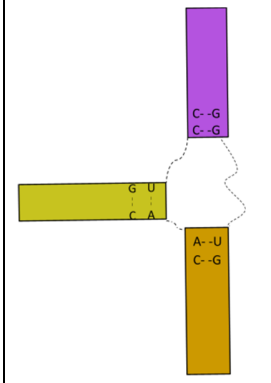
The full description of the bond's length and their errors are described in Table 3.3. Here atoms names are presented as they appear in the .pdb files.

Table 3.3 Bond parameters, used in the rigid body docking modeling.

	Base pair bonding		Model 1	Model 2	Model 3	Model 4
Bond type	GC	AU	GC-soft, AU-soft	GC-stiff, AU-soft	GC- rigid, AU-soft	GC-rigid, AU-rigid
			bond length [-error;+error]			
Hydrogen	O2-1H2, N3-H1, 1H4-O6	1H6-O4 N1-H3	GC: 1.8 [-1.0;+20] AU: 1.8 [-1.0;+20]	GC: 1.8 [-0.2;+0.2] AU: 1.8 [-1.0;+20]	AU: 1.8 [-1.0;+20]	Watson-Crick
Covalent	O3'-P		2.0 [-1.0;+20]	2.0 [-1.0;+20]	2.0 [-1.0;+20]	2.0 [-1.0;+20]
Stacking	O5'- O5'		5.9 [-1.0;+20]	5.9 [-1.0;+20]	5.9 [-1.0;+20]	5.9 [-1.0;+20]

Three alternative models were formulated and tested based on hydrogen bond's flexibility (Table 3.3-Table 3.4). **Model 1** has identically flexible hydrogen bonds for GC and AU bases that provide more junction flexibility in comparison to **Model 2**. To the contrary, **Model 3** restricts hydrogen bonds between GC bases even more than **Model 1** such that Guanines and Cytocines are not treated as independent units and become part of the helix. And lastly, **Model 4** has very rigid junction (Table 3.4).

Table 3.4 Schematic representation of the modeling units and bonds between them for all tested models for J(acd) construct

Model 1: GC-soft, AU-soft	Model 2: GC-stiff, AU-soft	Model 3: GC-rigid, AU-soft	Model 4: GC-rigid, AU-rigid
Hydrogen bond length [-errors;+errors]			
GC: 1.8[-1.0;+10] AU: 1.8[-1.0;+20]	GC: 1.8[-0.2;+0.2] AU: 1.8[-1.0;+20]	AU: 1.8[-1.0;+20]	Watson-Crick
			

For the docking procedure, the coordinates of the mean dye position are obtained by AV simulations and then fixed with respect to the rigid body. Then all mean dye position are connected with n springs with length R_{DA} (major population from PDA analysis, see Chapter 3.3.3) and corresponding spring constant ΔR_{DA} that reflect experimental errors (see Table 3.16-3.18).

To test whether given experimental data is well described by the suggested model, the χ^2 quantity is commonly used. Such determination is called a chi-square test for goodness of fit. The weighted data-model deviation has to be minimized for the set of n measured distances

$$\chi_{FRET}^2 = \sum_{i=1}^n \frac{(R_{DA(i)} - R_{model(i)})^2}{\Delta R_{DA(i)}^2} \quad (100)$$

In addition to FRET restrains, clashes between single bodies also contribute to the total energy of the system

$$\chi_{clash}^2 = \sum_{i,j} \begin{cases} 0 & , r_{ij} \geq r_{wi} + r_{wj} \\ \frac{(r_{wi} + r_{wj} + r_{ij})^2}{r_{ctol}^2} & , r_{ij} < r_{wi} + r_{wj} \end{cases} \quad (101)$$

Where r_{ij} is the distance between atoms i and j , r_{wi} and r_{wj} are correspondent van der Waals radii and r_{ctol} is the pre-defined clash tolerance.

As each of the rigid bodies has $p=6$ degrees of freedom, the reduced number of degrees of freedom will be $n-p$, where n is the number of FRET restrains. Thus the resulting χ_r^2 parameter can be calculated as

$$\chi_r^2 = (\chi_{FRET}^2 + \chi_{clash}^2)/(n - p) \quad (102)$$

Typically 1000 trials with randomly assigned initial helical orientation are performed and each resulting model is characterized by χ_r^2 . The derived models are further refined in order to optimize local interaction i.e removal of steric clashes between fluorophores and other helices they are not attached to. All structures are optimized again with new AVs. The solutions of the docking simulations are sorted by χ_r^2 in increasing order (Figure 3.23).

Note, that J(abd) RBD ensemble has a structure with lower χ_{FRET}^2 than the best RBD structure. This is due to the fact that when the best structure is selected, χ_{clash}^2 contribution is taken into account as well.

3.2.10 Cluster analysis of RNA 3WJ

χ_r^2 and root-mean-squared-deviation (RMSD) are used to distinguish between clusters of solutions. Solutions are considered ambiguous if the respective χ_r^2 values do not differ significantly. For this, a threshold indicating 95% confidence was applied, calculated as the inverse of the left-tailed probability of the chi-square distribution ¹⁴⁵

$$f(x; N_{dof}) = \frac{2^{-N_{dof}/2}}{\Gamma(N_{dof}/2)} x^{-N_{dof}/2-1} e^{-1/(2x)} \quad (103)$$

where $x>0$ and N_{dof} denotes the degrees of freedom and is calculated as $N_{dof} = N_{measurements} - N_{fit.param}$.

For the RBD model $N_{fit.param} = (6 + 6) - (3 * 2) = 6$. Here (6+6) represents rotational and translation motions for two big bodies (truncated helices) with respect to a third one and (3 * 2) stand for the O-P bond between the bodies. As in the modeling only one O-P bond was used, the second bond represents a phase space restriction due to clashes. However these extra 3 bonds don't dramatically change the final χ_r^2 (e.g. for J(bcd): $\chi_r^2 = \frac{37.9}{42-6} = 1.05$ and $\chi_r^2 = \frac{37.9}{42-9} = 1.1$).

So finally with $N_{fit.param} = 6$ we obtain: $N_{dof} = 42 - 6 = 36$ for J(bcd), $N_{dof} = 45 - 6 = 39$ for J(acd), $N_{dof} = 42 - 6 = 36$ for J(abd) and $N_{dof} = 44 - 6 = 38$ for J(abc). Solutions below the threshold and with good configuration represent the family of best structures and selected for further analysis. Good configuration is considered if there is no strong violation of the bonds between the docked bodies.

The degree of similarity of two three-dimensional nucleic structures can be measured by the root-mean-square deviation (RMSD) between equivalent atom pairs following optimal structural alignment. In nucleic acid structures often the backbone phosphorous atoms are used.

$$RMSD = \sqrt{\frac{1}{N} \sum_{i=1}^N d_i^2} \quad (104)$$

where d_i is the distance between equivalent atoms i of the structure and reference structure. The smaller the value, the more identical the structures are. The primary cut-off criterion is 2 Å RMSD and it is considered that thermal fluctuations alone lead to the deviations in RMSD of 1-1.5 Å¹⁴⁶.

3.2.11 Precision of the RBD structures via bootstrapping

In order to estimate the precision of the RBD structures a bootstrapping procedure is performed. Shortly, bootstrapping is random sampling of the conformations with their replacement¹⁴⁷ that allows to define precision of the sample distribution. The known sample (distance set of the RBD structures) is repeatedly sampled with replacement 1000 times and all these new samples are used to calculate the sampling distribution. Assuming that the original sample is representative, the resampling from that sample should be close to drawing a new sample. At the end an ensemble of structures with perturbed distances and with 1 Å clash tolerance is presented and used for further analysis (Figure 3.30B, Figure 3.31).

3.3 Results and discussions

3.3.1 Position dependency of fluorescent dyes

To characterize the position dependent fluorescent properties of coupled fluorescence dyes, we employed 58 single labeled (28 acceptor only labeled and 30 donor only labeled) molecules that fully cover all possible dye-local environment interaction on studied RNA systems. Donor-only and acceptor-only fluorescence decays were measured (Figure 3.13 and Figure 3.41-3.46) and fitted with two or three fluorescence lifetimes (Eq. 66). In this work we consider local dye motion at three different RNA microenvironments: at the end of the helix, internal helical part and the junction.

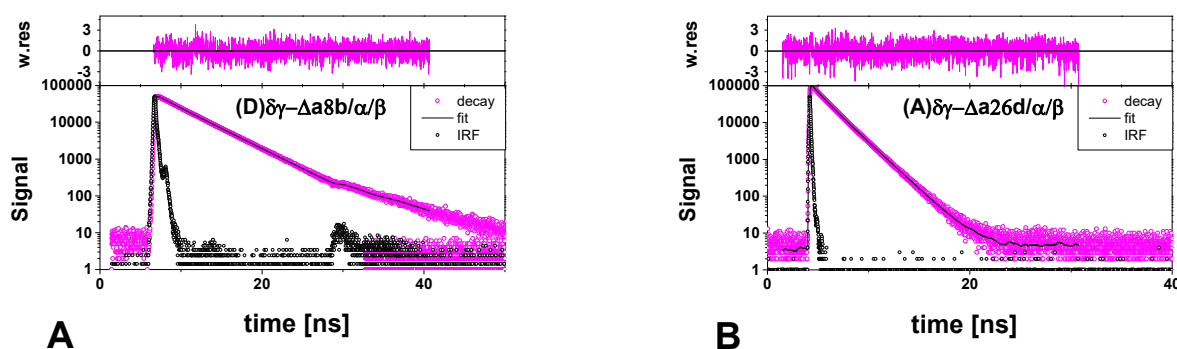


Figure 3.13 eTCSPC measurements of (A) fluorescence donor only decay for J(bcd) construct labeled with Alexa488 and (B) fluorescence acceptor only decay for J(bcd) construct labeled with Cy5. Experimental data (purple circles), fits (black curve) and IRF (black open circles) are shown. Weighted residuals are presented above each plot (magenta solid lines). See Table 3.5 for fitting parameters

3.3.1.1 Acceptor fluorescence lifetime and fluorescence quantum yield

The fluorescence properties of Cy5 are affected strongly by the local environment¹⁴⁸. In this study we differentiate three local environments: internal helical part, end of the helix and the junction. To demonstrate position dependent fluorescent properties of Cy5 we overlaid the secondary structure of all three RNA 3WJ and assigned labeling positions to the specific category: magenta –helical terminus, cyan – internal part of the helix, blue – junction area (Figure 3.14). Note that in this study long linkers (~20 Å) are used. Kalinin and co-authors (manuscript in preparation) demonstrated that the dye is displaced towards 3'-end and thus some acceptors on helix *d* can easily reach the helical terminus.

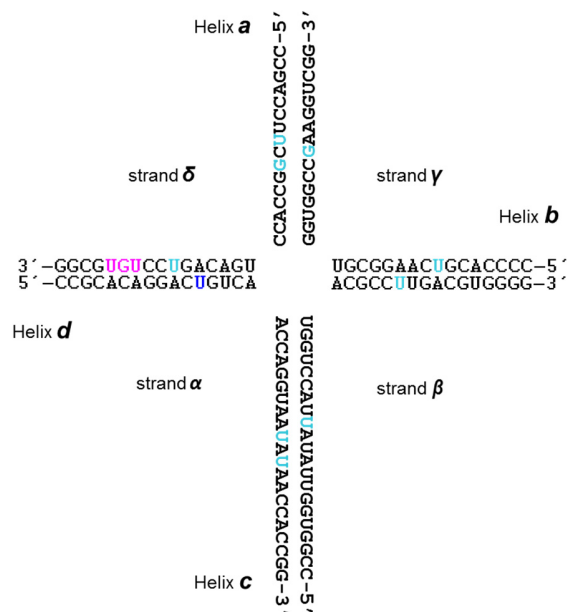


Figure 3.14 Overlay of all three RNA 3WJ secondary structures. All acceptor labeling positions are colored: magenta – helical end, cyan – internal part of the helix, blue – junction area.

End-labeled molecules

It is known that cyanine dye that is labeled close to the helical terminus stacks onto the end of helix in the manner of an additional base pair¹⁴⁹⁻¹⁵¹. In such a case, cis-trans photo-isomerization is disturbed and fluorescence lifetime and quantum yield differ from the one on internal labels. In contrast to Uracil labeled dyes that point into major groove, Guanine labeled fluorophores point into minor groove and are more displaced from the helix¹²⁵. Thus “end effect” for positions (A) $\delta 27d/\gamma/\alpha\beta-\Delta c$ on J(acd) and (A) $\delta 27d/\alpha/\beta\gamma-\Delta b$ on J(abd) are less pronounced. The fluorescence lifetimes and quantum yields of Cy5 at this position are similar to the one in the internal helical part (Table 3.5), indicating sufficient displacement of the fluorophore from the helical terminus.

Labels at the junction region

Acceptors coupled to sites (A) $\alpha\beta-\Delta c12d/\delta/\gamma$ on J(abd) and (A) $\alpha 12d/\delta/\beta\gamma-\Delta b$ on J(acd) and (A) $\alpha 12d/\beta/\delta\gamma-\Delta a$ on J(bcd) demonstrate also that Cy5 strongly interacts with junction area (higher $\Phi_{F,A}$ values in the Table 3.5). The junction sites could be quite narrow for free dye, wobbling on the linker, and thus Cy5 could be locked in some particular conformation^{134,152}.

Labels in the internal helical part

Values in Table 3.5 demonstrate that the labeling sites in the internal part of the helix and G-labeled helical ends are the safest positions for acceptor labeling. Their fluorescence quantum yield values are close to the reference value of free dye $\Phi_F = 0.32 \pm 0.015$ ⁴⁴.

Fluorescence quantum yield of acceptor is an essential part of distance calculation (Eq. 79) and static FRET lines (Eq. 62). As all studied structures share particular microenvironment, fluorescence properties for some labels were not measured and could be adopted from other structures. Some values were adopted from previous studies on J(abcd)¹²⁵ and are indicated in the Table 3.5 with asterisk and blue color.

Table 3.5 Fitting results of fluorescence lifetime of J(abd), J(acd), J(bcd) acceptor only samples. $\langle\tau\rangle_F$ is fluorescence weighted averaged lifetime, $\langle\tau\rangle_x$ - species weighted lifetime and $\Phi_{F,A}$ is corresponding fluorescence quantum yield. Fit quality is judged with χ_r^2 . Values marked with asterisk are adopted from previous studies on RNA 4WJ.

Construct	Sample name	x_1	τ_1 [ns]	x_2	τ_2 [ns]	χ_r^2	$\langle\tau\rangle_x$ [ns]	$\langle\tau\rangle_F$ [ns]	$\Phi_{F,A}$
J(abd)*	(A) γ 8b/ $\delta/\alpha\beta$ - Δc	0.74	1.02	0.26	1.79	1.12	1.22	1.32	0.335
J(abd)*	(A) δ 23d/ $\alpha/\alpha\beta$ - Δc	0.76	0.99	0.24	1.63	1.12	1.14	1.21	0.312
J(abd)	(A) δ 28d/ $\gamma/\alpha\beta$ - Δc	0.67	1.88	0.33	0.93	1.12	1.56	1.69	0.428
J(abd)	(A) δ 26d/ $\alpha/\alpha\beta$ - Δc	0.66	1.72	0.34	1.06	1.12	1.50	1.56	0.409
J(abd)*	(A) γ 24a/ $\delta/\alpha\beta$ - Δc	0.42	1.52	0.58	0.93	1.09	1.17	1.25	0.321
J(abd)	(A) $\alpha\beta$ - Δc 12d/ δ/γ	0.38	2.05	0.62	1.04	0.98	1.42	1.59	0.389
J(abd)	(A) $\alpha\beta$ - Δc 22b/ δ/γ	0.22	1.74	0.78	1.02	1.09	1.17	1.25	0.321
J(abd)	(A) δ 10a/ $\gamma/\alpha\beta$ - Δc	0.36	1.50	0.64	0.89	1.08	1.11	1.18	0.303
J(abd)	(A) δ 27d/ $\gamma/\alpha\beta$ - Δc	0.39	1.56	0.6	0.62	1.03	0.98	1.20	0.268
J(abd)	(A) δ 8a/ $\gamma/\alpha\beta$ - Δc	0.32	1.20	0.68	0.92	0.73	1.01	1.03	0.276
J(bcd)	(A) $\delta\gamma$ - Δa 28d/ α/β	0.86	1.93	0.14	1.00	0.97	1.80	1.86	0.492
J(bcd)	(A) $\delta\gamma$ - Δa 26d/ α/β	0.77	1.73	0.23	0.97	0.96	1.56	1.63	0.426
J(bcd)	(A) $\delta\gamma$ - Δa 23d/ α/β	0.2	1.59	0.80	1.03	1.13	1.14	1.19	0.313
J(bcd)	(A) $\delta\gamma$ - Δa 8b/ α/β	0.37	1.79	0.627	1.03	1.02	1.32	1.42	0.359

Construct	Sample name	x_1	τ_1 [ns]	x_2	τ_2 [ns]	χ_r^2	$\langle\tau\rangle_x$ [ns]	$\langle\tau\rangle_F$ [ns]	$\Phi_{F,A}$
J(bcd)	(A) $\alpha 12d/\beta/\delta\gamma$ - Δa	0.38	2.05	0.62	1.00	1.07	1.39	1.58	0.381
J(bcd)	(A) $a 28c/\beta/\delta\gamma$ - Δa	0.22	1.47	0.78	0.89	1.02	1.02	1.08	0.279
J(bcd)	(A) $a 26c/\beta/\delta\gamma$ - Δa	0.25	1.46	0.75	0.9	1.04	1.04	1.09	0.284
J(bcd)	(A) $\beta 14c/\alpha/\delta\gamma$ - Δa	0.17	1.89	0.83	1.01	1.11	1.16	1.25	0.317
J(acd)*	(A) $\beta\gamma$ - $\Delta b 14c/\alpha/\delta$	0.25	1.71	0.75	0.92	1.54	1.12	1.22	0.305
J(acd)	(A) $\alpha 12d/\delta/\beta\gamma$ - Δb	0.35	2.02	0.65	1.00	1.12	1.35	1.53	0.370
J(acd)	(A) $\delta 10a/\alpha/\beta\gamma$ - Δb	0.35	1.50	0.65	0.89	1.00	1.10	1.18	0.301
J(acd)	(A) $\alpha 28c/\beta\gamma$ - $\Delta b/\delta$	0.28	1.44	0.72	0.92	1.08	1.06	1.12	0.291
J(acd)	(A) $\alpha 26c/\beta\gamma$ - $\Delta b/\delta$	0.23	1.49	0.77	0.91	1.05	1.05	1.10	0.286
J(acd)	(A) $\delta 26d/\alpha/\beta\gamma$ - Δb	0.68	1.72	0.32	0.96	1.12	1.47	1.56	0.403
J(acd)	(A) $\delta 28d/\alpha/\beta\gamma$ - Δb	0.66	1.88	0.34	0.96	1.08	1.57	1.69	0.429
J(acd)	(A) $\delta 27d/\alpha/\beta\gamma$ - Δb	0.38	1.56	0.73	0.62	1.09	1.05	1.15	0.286
J(acd)*	(A) $\delta 23d/\alpha/\beta\gamma$ - Δb	0.76	0.99	0.24	1.63	1.12	1.14	1.21	0.312

3.3.1.2 Donor fluorescence lifetime and quantum yield

As previously with acceptor, donor labeling sites were categorized into groups: helical end (magenta labels in Figure 3.15) and internal part of the helix (cyan labels in Figure 3.15).

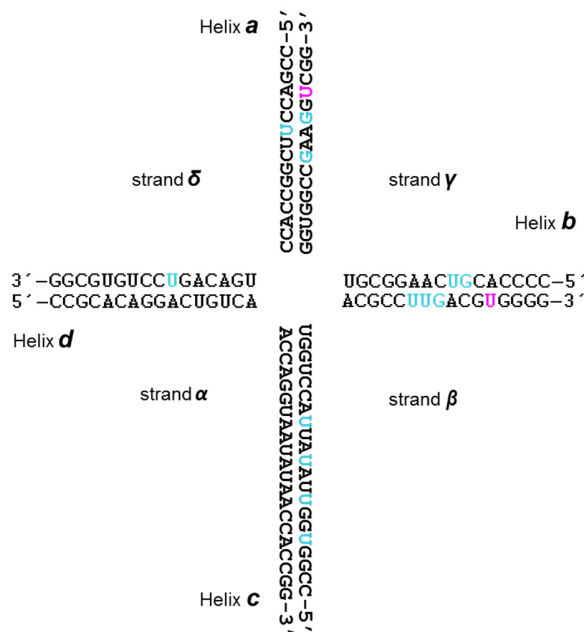


Figure 3.15 overlay of all three RNA 3WJ secondary structures. All donor labeling positions are colored: magenta-helical end, cyan – internal helical labels.

The difference in the fluorescence lifetime and quantum yield for the internally- and end- labeled dyes indicate different dye-guanine interactions. This assumption is based on the previous literature reports where due to the fraying of the terminal base pairs, GC base pair exhibited opening and closing dynamics¹⁵³⁻¹⁵⁶. Others^{133,134} report Rhodamine dye preferably stacking on the terminal pair. In this case there have been reports, proposing different possible conformers due to Rhodamine dye-Guanine interactions and possible quenching by Guanine via photo-induced electron transfer (PET)¹⁵⁷. This effect manifests clearly on (D) $\beta\gamma$ - Δ b34a/ α/δ on J(acd), (D) γ 29a/ α/β - Δ c and (D) $\alpha\beta$ - Δ c28b/ γ/δ on J(abd) and demonstrate weak fluorescent RNA-dye complex (Table 3.6-3.7).

Fluorescence quantum yield of donor is an essential part of static FRET line determination. The summarized fit values for measured donor only samples are collected in the Table 3.6-3.7. As all studied structures share particular microenvironment, fluorescence properties for some labels were not measured and could be adopted from other structures. Some values were adopted from previous studies on J(abcd)¹²⁵, J(abd) and J(bcd) are indicated in the Table 3.6 with asterisk.

Table 3.6 Fitting results of fluorescence lifetime of J(abd), J(acd), J(bcd) donor only samples with two species. $\langle\tau\rangle_F$ is fluorescence weighted averaged lifetime, $\langle\tau\rangle_x$ is species weighted lifetime and $\Phi_{F,D}$ is corresponding fluorescence quantum yield. Fit quality is judged with χ^2_r . Values marked with asterisk are adopted from J(abd), J(bcd) and previous studies on RNA 4WJ

Construct	Sample name	x_1	τ_1 [ns]	x_2	τ_2 [ns]	χ^2_r	$\langle\tau\rangle_x$ [ns]	$\langle\tau\rangle_F$ [ns]	$\Phi_{F,D}$
J(bcd)	(D) $\delta\gamma$ - $\Delta a8b$ / α/β	0.90	3.95	0.10	0.98	1.08	3.64	3.87	0.711
J(bcd)	(D) $\beta28b$ / $\alpha/\delta\gamma$ - Δa	0.79	3.92	0.13	1.87	0.08	3.34	3.85	0.652
J(bcd)	(D) $\beta29b$ / $\alpha/\delta\gamma$ - Δa	0.93	4.02	0.07	1.05	1.08	3.82	3.96	0.745
J(bcd)* from J(abcd)	(D) $\beta8c$ / $\alpha/\delta\gamma$ - Δa	0.84	3.99	0.16	0.71	1.33	3.47	3.88	0.676
J(bcd)* from J(abcd)	(D) $\beta11c$ / $\alpha/\delta\gamma$ - Δa	0.90	3.98	0.10	0.56	1.17	3.64	3.93	0.710
J(bcd)* from J(abcd)	(D) $\beta14c$ / $\alpha/\delta\gamma$ - Δa	0.93	4.12	0.07	0.61	1.10	3.86	4.08	0.753
J(bcd)* from J(abcd)	(D) $\beta27b$ / $\alpha/\delta\gamma$ - Δa	0.79	3.87	0.21	0.40	1.44	3.15	3.77	0.614
J(bcd)* from J(abcd)	(D) $\beta5c$ / $\alpha/\delta\gamma$ - Δa	0.93	4.08	0.07	1.42	1.10	3.91	4.02	0.762
J(acd)	(D) $\delta7a$ / $\gamma/\beta\gamma$ - Δb	0.88	4.03	0.12	1.03	1.13	3.67	3.93	0.716
J(acd)	(D) $\delta23d$ / $\alpha/\beta\gamma$ - Δb	0.88	3.91	0.11	1.33	1.12	3.59	3.80	0.700
J(acd)	(D) $\beta\gamma$ - $\Delta b5c$ / α/δ	0.93	4.08	0.07	0.91	1.02	3.87	4.03	0.754
J(acd)	(D) $\beta\gamma$ - $\Delta b8c$ / α/δ	0.90	4.05	0.11	0.84	1.08	3.71	3.97	0.724
J(acd)	(D) $\beta\gamma$ - $\Delta b11c$ / α/δ	0.94	4.01	0.06	0.71	1.07	3.82	3.97	0.746
J(acd)	(D) $\beta\gamma$ - $\Delta b14c$ / α/δ	0.96	4.10	0.04	0.64	1.13	3.97	4.08	0.774
J(acd)	(D) $\beta\gamma$ - $\Delta b29a$ / α/δ	0.90	4.03	0.10	0.54	1.09	3.68	3.98	0.718
J(abd)	(D) $\gamma24a$ / $\alpha\beta$ - $\Delta c/\delta$	0.88	4.01	0.12	0.63	1.01	3.60	3.94	0.703
J(abd)	(D) $\gamma27a$ / $\delta/\alpha\beta$ - Δc	0.94	4.07	0.06	1.10	1.03	3.90	4.02	0.761
J(abd)	(D) $\delta7a$ / $\gamma/\alpha\beta$ - Δc	0.86	4.02	0.14	1.01	1.12	3.60	5.08	0.703
J(abd)	(D) $\delta23d$ / $\alpha/\alpha\beta$ - Δc	0.87	3.91	0.11	1.41	1.10	3.56	3.80	0.694
J(abd)	(D) $\alpha\beta$ - $\Delta c22b$ / γ/δ	0.89	3.93	0.11	0.97	1.09	3.61	3.85	0.705
J(abd)	(D) $\alpha\beta$ - $\Delta c23b$ / γ/δ	0.77	3.94	0.13	2.21	0.11	3.32	3.85	0.735
J(abd)* from J(abcd)	(D) $\gamma29a$ / $\alpha/\alpha\beta$ - Δc	0.70	3.56	0.30	0.58	1.57	2.67	3.37	0.520
J(abd)* from J(abcd)	(D) $\gamma7b$ / $\delta/\alpha\beta$ - Δc	0.88	3.92	0.12	1.22	1.20	3.60	3.81	0.703

Table 3.7 Fitting results of fluorescence lifetime of J(abd), J(acd), J(bcd) donor only samples with three species. $\langle\tau\rangle_F$ is fluorescence weighted averaged lifetime, $\langle\tau\rangle_x$ is species weighted lifetime and $\Phi_{F,D}$ is corresponding fluorescence quantum yield. Fit quality is judged with χ_r^2

construct	Sample name	x_1	τ_1 [ns]	x_2	τ_2 [ns]	x_3	τ_3 [ns]	χ_r^2	$\langle\tau\rangle_x$ [ns]	$\langle\tau\rangle_F$ [ns]	$\Phi_{F,D}$
J(bcd)	(D) $\delta\gamma$ - $\Delta a7b/\alpha/\beta$	0.82	4.05	0.09	1.72	0.08	0.28	1.05	3.51	3.92	0.684
J(acd)	(D) $\beta\gamma$ - $\Delta b34a/\alpha/\delta$	0.72	3.69	0.16	0.54	0.12	2.04	1.10	2.99	3.46	0.584
J(abd)	(D) $\gamma8b/\delta/\alpha\beta$ - Δc	0.74	3.93	0.16	1.87	0.11	0.27	1.07	3.24	3.71	0.632
J(abd)	(D) $\alpha\beta$ - $\Delta c28b/\gamma/\delta$	0.59	3.48	0.13	0.98	0.28	0.19	1.17	2.23	3.26	0.436

3.3.1.3 Fluorescence residual anisotropy

Acceptor residual anisotropy

For all FRET samples, corresponding reference acceptor only samples were prepared. In a few cases FRET samples were used, and in this case acceptor dye was directly excited. Note that studied molecules J(abd), J(acd) and J(bcd) share the labeling sites as they have the common helices (for example J(abd) and J(acd) structurally share helices *a* and *d*), so the reference construct of one RNA 3WJ could be used for others, fully accounting for the local environment. Overall, the results suggest a good agreement within the same labeling cite for different junction constructs (Table 3.8).

In order to retrieve fluorescence anisotropies, time resolved ensemble experiments were performed (Figure 3.16). Fluorescence anisotropy decays could be characterized with two rotation correlation times ρ_j and corresponding amplitudes $b^{(j)}$ (Chapter 3.2.7.3). The longest correlation time represents global motion of the molecule and its amplitude $b_2=r_\infty$. As the polarized decays were fitted jointly with their corresponding magic angle decays, the fluorescence lifetime information could be obtained. The fitting results are summarized in the Table 3.8).

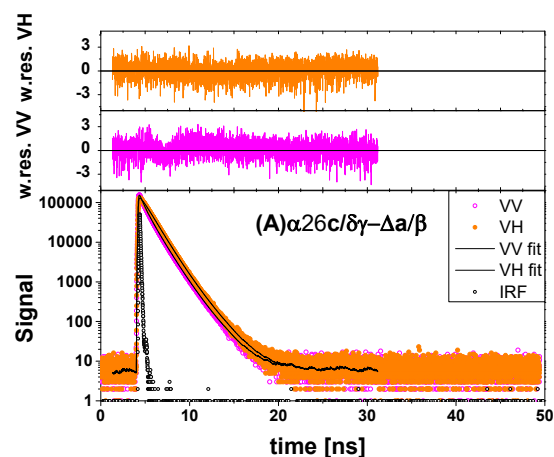


Figure 3.16 Typical fluorescence signal in parallel and perpendicular polarization channels (magenta and orange) with the corresponding fits (black) for $J(bcd)$ structures labeled with acceptor Cy5 with weighted residuals on the top. The fit results are presented in the Table 3.8. The fit quality was judged by χ_r^2 .

The results demonstrate higher residual anisotropies r_∞ for acceptors that are labeled at least 4 base pairs away from the 3'-end on d helix (e.g. (A) $\delta 28d/\gamma b/\alpha\beta-\Delta c$) in contrast to the labels on the 5'-end or in the internal helix. This can be explained by displacement of the mean dye position towards the 3'-end strand (Kalinin *et al* in preparation) and the resulting of dye-helix interaction^{135,158}. Recent studies^{149,151,152} demonstrate that cyanine dyes interact with the macromolecule and prefer to stick on the terminal bases. Any obstruction by local environment in fluorophore movement could affect cis–trans photoisomerization. This can be detected in fluorescence quantum yield and anisotropy changes.

Table 3.8 Fitting parameters for the fluorescence time-resolved anisotropy decays of the acceptor. Acceptor only samples are marked with (A), FRET samples have (A)/(D) indicators. Structures with missing reference samples adopted values from the construct with similar microenvironment. Those values are marked with asterisk (indicated below). Rotation correlation time ρ_i with amplitudes b_i with corresponding lifetimes τ_i and fraction x_i . The fit quality is judged by χ_r^2 . Values marked with asterisk are adopted from other molecules (indicated below).

Construct	Sample name	b_1	ρ_1	b_2	ρ_2	x_1	τ_1	x_2	τ_2	x_3	τ_3	χ_r^2
J(bcd)	(A) $\delta\gamma$ - Δa 28d/ (D) β 5d/ α	0.050	0.300	0.275	14.2	0.05	0.098	0.15	0.97	0.80	1.93	1.11
J(bcd)	(A) $\delta\gamma$ - Δa 26d/ β / α	0.113	0.577	0.282	18.90	0.21	0.87	0.79	1.71			1.06
J(bcd)* from J(acd)	(A) $\delta\gamma$ - Δa 23d/ β / α	0.224	0.671	0.156	2E+0	0.05	0.38	0.79	1.04	0.16	1.67	1.12
J(bcd)	(A) $\delta\gamma$ - Δa 8b/ (D) β 14c/ α	0.219	0.762	0.161	92.51	0.18	1.85	0.76	1.10	0.06	0.32	1.03
J(bcd)	(A) α 12d/ $\delta\gamma$ - Δa / β	0.168	0.638	0.203	139.2	0.65	1.07	0.31	1.91	0.04	0.30	1.03
J(bcd)	(A) α 28c/ β / $\delta\gamma$ - Δa	0.220	0.603	0.111	10.45	0.52	0.91	0.48	1.51			1.27
J(bcd)	(A) α 26c/ β / $\delta\gamma$ - Δa	0.257	0.705	0.115	182.2	0.68	0.97	0.26	1.49	0.06	0.06	0.97
J(bcd)	(A) β 14c/ (D) $\delta\gamma$ - Δa 7b/ α	0.220	0.590	0.160	1E+9	0.82	1.02	0.18	1.89			1.32
J(acd)* from J(bcd)	(A) $\beta\gamma$ - Δb 14c/ α / δ	0.220	0.590	0.160	1E+9	0.82	1.02	0.18	1.89			1.32
J(acd)* from J(bcd)	(A) α 12d/ δ / $\beta\gamma$ - Δb	0.168	0.638	0.203	139.25	0.65	1.07	0.31	1.91	0.04	0.30	1.03
J(acd)	(A) δ 10a/ (D) $\beta\gamma$ - Δb 5c/ α	0.212	0.669	0.168	21.56	0.26	1.72	0.68	1.05	0.06	0.24	1.14
J(acd)	(A) α 28c/ $\beta\gamma$ - Δb / δ	0.252	0.699	0.120	30.04	0.73	0.99	0.03	0.19	0.25	1.49	1.02
J(acd)	(A) α 26c/ $\beta\gamma$ - Δb / δ	0.243	0.612	0.137	20.00	0.07	0.46	0.80	1.06	0.13	1.71	1.11
J(acd)	(A) δ 26d/ α / $\beta\gamma$ - Δb	0.134	0.611	0.246	14.98	0.08	0.37	0.45	1.15	0.48	1.79	1.07
J(acd)	(A) δ 28d/ α / $\beta\gamma$ - Δb	0.127	0.421	0.250	20	0.06	0.29	0.39	1.09	0.56	1.91	1.15
J(acd)	(A) δ 27d/ α / $\beta\gamma$ - Δb	0.213	0.693	0.156	39.19	0.68	1.02	0.28	1.61	0.03	0.27	1.11
J(abd)	(A) δ 23d/ (D) $5\beta\gamma$ - Δb / α	0.224	0.671	0.156	2E+01	0.05	0.38	0.79	1.04	0.16	1.67	1.12
J(abd)	(A) γ 8b/ δ / $\alpha\beta$ - Δc	0.202	0.587	0.178	20	0.09	0.40	0.71	1.11	0.19	1.87	1.02

Construct	Sample name	b_1	ρ_1	b_2	ρ_2	x_1	τ_1	x_2	τ_2	x_3	τ_3	χ_r^2
J(abd)* from J(acd)	(A) $\delta 23d/\alpha/\alpha\beta-\Delta c$	0.224	0.671	0.156	2E+01	0.05	0.38	0.79	1.04	0.16	1.67	1.12
J(abd)	(A) $\delta 28d/\gamma/\alpha\beta-\Delta c$	0.115	0.560	0.259	37.00	0.62	1.90	0.33	1.03	0.05	0.13	1.1
J(abd)	(A) $\delta 26d/\alpha/\alpha\beta-\Delta c$	0.118	0.606	0.256	26.32	0.31	1.02	0.66	1.74	0.04	0.14	1.47
J(abd)	(A) $\gamma 24a/$ (D) $\alpha\beta-\Delta c 28b/\delta$	0.217	0.687	0.163	27.40	0.26	1.62	0.66	1.00	0.09	0.07	1.10
J(abd)	(A) $\alpha\beta-\Delta c 12d/$ δ/γ	0.150	0.522	0.212	9559.37	0.57	1.08	0.37	2.02	0.06	0.26	1.04
J(abd)	(A) $\alpha\beta-\Delta c 22b/$ (D) $\delta 7a/\gamma$	0.236	0.768	0.145	1116.00	0.09	0.40	0.78	1.09	0.12	1.85	0.85
J(abd)* from J(acd)	(A) $\delta 10a/\gamma/$ $\alpha\beta-\Delta c$	0.212	0.669	0.168	21.56	0.26	1.72	0.68	1.05	0.06	0.24	1.14
J(abd)	(A) $\delta 27d/$ (D) $\alpha\beta-\Delta c 27a/\gamma$	0.218	0.639	0.162	20.0	0.65	0.95	0.35	1.59			1.05
J(abd)	(A) $\delta 8a/$ (D) $\alpha\beta-\Delta c 28b/\gamma$	0.238	0.763	0.142	225.3	0.11	1.83	0.77	1.12	0.12	0.62	1.04

Donor residual anisotropy

The donor mobility at all labeling positions that are used in FRET study could be retrieved from FRET samples. To define donor residual anisotropy, we analyzed 2D plots of the fluorescence anisotropy r_D vs fluorescence average donor lifetime in presence of acceptor $\langle \tau_{D(A)} \rangle_F$ (Figure 3.17).

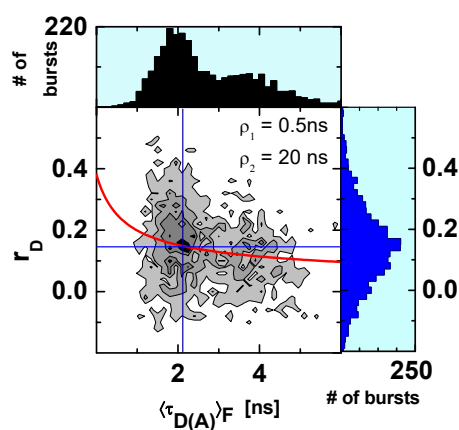


Figure 3.17 Typical representation of the fluorescence anisotropy r_D vs fluorescence average donor lifetime in presence of acceptor $\langle \tau_{D(A)} \rangle_F$. Red line represents the relationship as described in Eq. 64 and blue lines correspond to

the values of the major population r_D and $\langle \tau_{major} \rangle_F$ (Table 3.9-3.11). This demonstration is done on (A) $\delta 10a$ / (D) $\beta\gamma$ - $\Delta b11c/\alpha$ on J(abc) construct.

The relationship was fitted as described in Chapter 3.2.7.4 with Eq.64-65. Note that fraction x equals to the trapped fraction of the dye $x = s_{trap}$.

Table 3.9 Measured steady state polarized anisotropy r_D with correspondent fluorescence average lifetime of the major population $\langle \tau_{major} \rangle_F$ and calculated dye trapped fraction s_{trap} and corresponding donor residual anisotropy r_∞ for donors on J(bcd) construct.

FRET sample name	r_D	$\langle \tau_{major} \rangle_F$	s_{trap}	r_∞
(D) $\beta 11c$ /(A) $\alpha 12d/\delta\gamma$ - Δa	0.15	1.61	0.27	0.10
(D) $\beta 11c$ /(A) $\delta\gamma$ - $\Delta a23d/\alpha$	0.11	2.77	0.22	0.08
(D) $\beta 11c$ /(A) $\delta\gamma$ - $\Delta a26d/\alpha$	0.10	3.58	0.22	0.08
(D) $\beta 14c$ /(A) $\delta\gamma$ - $\Delta a28d/\alpha$	0.10	3.77	0.18	0.07
(D) $\beta 11c$ /(A) $\delta\gamma$ - $\Delta a8b/\alpha$	0.14	1.71	0.22	0.09
(D) $\beta 14c$ /(A) $\alpha 12d/\delta\gamma$ - Δa	0.14	1.34	0.20	0.07
(D) $\beta 14c$ /(A) $\delta\gamma$ - $\Delta a23d/\alpha$	0.12	1.96	0.20	0.08
(D) $\beta 14c$ /(A) $\delta\gamma$ - $\Delta a26d/\alpha$	0.09	3.37	0.17	0.07
(D) $\beta 11c$ /(A) $\delta\gamma$ - $\Delta a28d/\alpha$	0.09	3.42	0.22	0.09
(D) $\beta 14c$ /(A) $\delta\gamma$ - $\Delta a8b/\alpha$	0.13	1.83	0.22	0.08
(A) $\alpha 12d$ /(D) $\beta 27b/\delta\gamma$ - Δa	0.14	1.45	0.21	0.08
(D) $\beta 27b$ /(A) $\alpha 26c/\delta\gamma$ - Δa	0.11	2.99	0.22	0.08
(D) $\beta 27b$ /(A) $\alpha 28c/\delta\gamma$ - Δa	0.09	2.85	0.14	0.06
(D) $\beta 27b$ /(A) $\delta\gamma$ - $\Delta a23d/\alpha$	0.10	2.54	0.18	0.07
(D) $\beta 27b$ /(A) $\delta\gamma$ - $\Delta a26d/\alpha$	0.10	3.34	0.20	0.08
(D) $\beta 27b$ /(A) $\delta\gamma$ - $\Delta a28d/\alpha$	0.10	3.06	0.19	0.07
(A) $\alpha 12d$ /(D) $\beta 28b/\delta\gamma$ - Δa	0.15	1.45	0.26	0.10
(D) $\beta 28b$ /(A) $\alpha 26c/\delta\gamma$ - Δa	0.10	2.97	0.19	0.07
(A) $\alpha 28c$ /(D) $\beta 28b/\delta\gamma$ - Δa	0.10	2.93	0.20	0.08
(D) $\beta 28b$ /(A) $\delta\gamma$ - $\Delta a23d/\alpha$	0.11	2.93	0.21	0.08
(D) $\beta 28b$ /(A) $\delta\gamma$ - $\Delta a26d/\alpha$	0.09	3.11	0.17	0.06
(D) $\beta 28b$ /(A) $\delta\gamma$ - $\Delta a28d/\alpha$	0.12	3.11	0.27	0.10
(A) $\alpha 12d$ /(D) $\beta 29b/\delta\gamma$ - Δa	0.15	1.67	0.28	0.10
(D) $\beta 29b$ /(A) $\delta\gamma$ - $\Delta a23d/\alpha$	0.12	2.71	0.25	0.09
(D) $\beta 29b$ /(A) $\delta\gamma$ - $\Delta a26d/\alpha$	0.11	2.85	0.22	0.08
(D) $\beta 29b$ /(A) $\delta\gamma$ - $\Delta a28d/\alpha$	0.11	3.04	0.23	0.09
(D) $\beta 5c$ /(A) $\alpha 12d/\delta\gamma$ - Δa	0.09	2.54	0.13	0.05
(D) $\beta 5c$ /(A) $\delta\gamma$ - $\Delta a23d/\alpha$	0.08	2.97	0.13	0.05
(D) $\beta 5c$ /(A) $\delta\gamma$ - $\Delta a26d/\alpha$	0.06	3.78	0.09	0.03
(D) $\beta 5c$ /(A) $\delta\gamma$ - $\Delta a28d/\alpha$	0.07	3.56	0.13	0.05

FRET sample name	r_D	$\langle \tau_{major} \rangle_F$	s_{trap}	r_∞
(D) $\beta 5c/(A)\delta\gamma-\Delta a8b/\alpha$	0.08	2.61	0.11	0.04
(D) $\beta 8c/(A)\alpha 12d/\delta\gamma-\Delta a$	0.09	1.96	0.10	0.04
(D) $\beta 8c/(A)\delta\gamma-\Delta a23d/\alpha$	0.09	2.69	0.14	0.05
(D) $\beta 8c/(A)\delta\gamma-\Delta a26d/\alpha$	0.09	3.55	0.18	0.07
(D) $\beta 8c/(A)\delta\gamma-\Delta a28d/\alpha$	0.08	3.60	0.15	0.06
(D) $\beta 8c/(A)\delta\gamma-\Delta a8b/\alpha$	0.11	1.98	0.15	0.06
(A) $\alpha 12d/(D)\delta\gamma-\Delta a7b/\beta$	0.07	1.67	0.03	0.01
(A) $\alpha 26c/(D)\delta\gamma-\Delta a7b/\beta$	0.06	2.56	0.03	0.01
(A) $\beta 14c/(D)\delta\gamma-\Delta a14b/\alpha$	0.11	2.32	0.03	0.01
(A) $\alpha 12d/(D)\delta\gamma-\Delta a8b/\beta$	0.13	1.17	0.13	0.05
(D) $\delta\gamma-\Delta a8b/(A)\alpha 26c/\beta$	0.10	2.25	0.14	0.05

Table 3.10 measured steady state polarized anisotropy r_D with correspondent fluorescence average lifetime of the major population $\langle \tau_{major} \rangle_F$ and calculated dye trapped fraction s_{trap} and corresponding donor residual anisotropy r_∞ for donors on J(abd) construct.

FRET sample name	r_D	$\langle \tau_{major} \rangle_F$	s_{trap}	r_∞
(D) $\gamma 8b/(A)\delta 10a/\alpha\beta-\Delta c$	0.12	1.78	0.18	0.07
(D) $\gamma 8b/(A)\delta 26d/\alpha\beta-\Delta c$	0.09	3.13	0.16	0.06
(D) $\gamma 8b/(A)\delta 28d/\alpha\beta-\Delta c$	0.11	3.03	0.23	0.09
(D) $\gamma 8b/(A)\delta 23d/\alpha\beta-\Delta c$	0.13	2.11	0.25	0.09
(D) $\gamma 8b/(A)\alpha\beta-\Delta c12d/\delta$	0.14	1.28	0.19	0.07
(A) $\delta 10a/(D)\alpha\beta-\Delta c28b/\gamma$	0.09	2.59	0.15	0.06
(A) $\delta 28d/(D)\alpha\beta-\Delta c28b/\gamma$	0.09	2.97	0.15	0.06
(A) $\delta 26d/(D)\alpha\beta-\Delta c28b/\gamma$	0.04	3.01	0.07	0.03
(A) $\delta 23d/(D)\alpha\beta-\Delta c28b/\gamma$	0.08	3.01	0.11	0.04
(D) $\delta 7d/(A)\alpha\beta-\Delta c22b/\gamma$	0.13	1.62	0.18	0.07
(D) $\delta 7d/(A)\alpha\beta-\Delta c12b/\gamma$	0.14	1.21	0.18	0.07
(A) $\gamma 8b/(D)\delta 7a/\alpha\beta-\Delta c$	0.13	1.88	0.23	0.09
(D) $\gamma 29a/(A)\alpha\beta-\Delta c12d/\delta$	0.06	3.36	0.07	0.03
(D) $\gamma 29a/(A)\delta 28d/\alpha\beta-\Delta c$	0.07	3.39	0.09	0.03
(D) $\gamma 29a/(A)\delta 26d/\alpha\beta-\Delta c$	0.07	3.30	0.10	0.04
(D) $\gamma 29a/(A)\delta 23d/\alpha\beta-\Delta c$	0.07	3.10	0.11	0.04
(D) $\gamma 29a/(A)\alpha\beta-\Delta c22b/\delta$	0.56	1.35	0.14	0.05

FRET sample name	r_D	$\langle \tau_{major} \rangle_F$	S_{trap}	r_{∞}
(A) $\delta 10\mathbf{a}/(\mathbf{D})\alpha\beta-\Delta\mathbf{c}23\mathbf{b}/\gamma$	0.14	1.88	0.28	0.10
(D) $\gamma 24\mathbf{a}/(\mathbf{A})\delta 23\mathbf{d}/\alpha\beta-\Delta\mathbf{c}$	0.08	2.48	0.10	0.04
(D) $\gamma 24\mathbf{a}/(\mathbf{A})\delta 26\mathbf{d}/\alpha\beta-\Delta\mathbf{c}$	0.10	2.38	0.16	0.06
(D) $\gamma 24\mathbf{a}/(\mathbf{A})\delta 28\mathbf{d}/\alpha\beta-\Delta\mathbf{c}$	0.08	2.68	0.12	0.05
(D) $\gamma 24\mathbf{a}/(\mathbf{A})\alpha\beta-\Delta\mathbf{c}22\mathbf{b}/\delta$	0.09	1.69	0.07	0.03
(D) $\gamma 24\mathbf{a}/(\mathbf{A})\alpha\beta-\Delta\mathbf{c}12\mathbf{d}/\delta$	0.11	1.26	0.05	0.02
(A) $\delta 10\mathbf{a}/(\mathbf{D})\alpha\beta-\Delta\mathbf{c}22\mathbf{b}/\gamma$	0.13	1.95	0.23	0.09
(A) $\delta 26\mathbf{d}/(\mathbf{D})\alpha\beta-\Delta\mathbf{c}22\mathbf{b}/\gamma$	0.10	3.13	0.20	0.08
(A) $\delta 28\mathbf{d}/(\mathbf{D})\alpha\beta-\Delta\mathbf{c}22\mathbf{b}/\gamma$	0.10	3.36	0.20	0.08
(D) $\gamma 29\mathbf{a}/(\mathbf{A})\delta 27\mathbf{d}/\alpha\beta-\Delta\mathbf{c}$	0.06	3.29	0.05	0.02
(A) $\delta 27\mathbf{d}/(\mathbf{D})\alpha\beta-\Delta\mathbf{c}22\mathbf{b}/\gamma$	0.10	3.18	0.20	0.08
(A) $\delta 27\mathbf{d}/(\mathbf{D})\alpha\beta-\Delta\mathbf{c}23\mathbf{b}/\gamma$	0.11	3.29	0.24	0.09
(D) $\gamma 24\mathbf{a}/(\mathbf{A})\delta 27\mathbf{d}/\alpha\beta-\Delta\mathbf{c}$	0.10	2.38	0.16	0.09
(D) $\gamma 8\mathbf{b}/(\mathbf{A})\delta 27\mathbf{d}/\alpha\beta-\Delta\mathbf{c}$	0.12	2.38	0.23	0.08
(D) $\delta 23\mathbf{d}/(\mathbf{A})\alpha\beta-\Delta\mathbf{c}22\mathbf{b}/\gamma$	0.11	2.78	0.21	0.08
(A) $\gamma 24\mathbf{a}/(\mathbf{D})\delta 23\mathbf{d}/\alpha\beta-\Delta\mathbf{c}$	0.11	2.66	0.21	0.08
(A) $\delta 26\mathbf{d}/(\mathbf{D})\alpha\beta-\Delta\mathbf{c}23\mathbf{b}/\gamma$	0.12	3.41	0.28	0.10
(D) $\gamma 27\mathbf{b}/(\mathbf{A})\delta 27\mathbf{d}/\alpha\beta-\Delta\mathbf{c}$	0.10	2.38	0.16	0.06
(A) $\delta 27\mathbf{d}/(\mathbf{D})\alpha\beta-\Delta\mathbf{c}28\mathbf{b}/\gamma$	0.07	2.85	0.08	0.03
(A) $\delta 28\mathbf{d}/(\mathbf{D})\alpha\beta-\Delta\mathbf{c}23\mathbf{b}/\gamma$	0.11	3.34	0.24	0.09
(A) $\delta 23\mathbf{d}/(\mathbf{D})\alpha\beta-\Delta\mathbf{c}23\mathbf{b}/\gamma$	0.12	2.77	0.24	0.09
(A) $\delta 8\mathbf{a}/(\mathbf{D})\alpha\beta-\Delta\mathbf{c}22\mathbf{b}/\gamma$	0.11	1.59	0.12	0.05
(A) $\delta 8\mathbf{a}/(\mathbf{D})\alpha\beta-\Delta\mathbf{c}23\mathbf{b}/\gamma$	0.12	1.74	0.17	0.07
(A) $\delta 8\mathbf{a}/(\mathbf{D})\alpha\beta-\Delta\mathbf{c}28\mathbf{b}/\gamma$	0.12	1.74	0.17	0.07
(D) $\gamma 27\mathbf{a}/(\mathbf{A})\alpha\beta-\Delta\mathbf{c}12\mathbf{d}/\delta$	0.07	1.67	0.01	0.004

Table 3.11 Measured steady state polarized anisotropy r_D with correspondent fluorescence average lifetime of the major population $\langle\tau_{major}\rangle_F$ and calculated dye trapped fraction s_{trap} and corresponding donor residual anisotropy r_∞ for donors on J(acd) construct.

FRET sample name	r_D	$\langle\tau_{major}\rangle_F$	s_{trap}	r_∞
(A) $\delta 10a$ /(D) $\beta\gamma$ - $\Delta b 14c/\alpha$	0.11	2.09	0.17	0.07
(A) $\delta 10a$ /(D) $\beta\gamma$ - $\Delta b 11c/\alpha$	0.15	2.11	0.30	0.11
(A) $\delta 28d$ /(D) $\beta\gamma$ - $\Delta b 14c/\alpha$	0.10	3.32	0.19	0.07
(A) $\delta 28d$ /(D) $\beta\gamma$ - $\Delta b 34a/\alpha$	0.05	3.29	0.02	0.01
(A) $\delta 26d$ /(D) $\beta\gamma$ - $\Delta b 34a/\alpha$	0.06	3.2	0.07	0.03
(A) $\delta 23d$ /(D) $\beta\gamma$ - $\Delta b 34a/\alpha$	0.06	3.11	0.07	0.03
(A) $\delta 23d$ /(D) $\beta\gamma$ - $\Delta b 14a/\alpha$	0.11	1.93	0.16	0.06
(A) $\delta 23d$ /(D) $\beta\gamma$ - $\Delta b 11a/\alpha$	0.14	2.71	0.30	0.11
(A) $\delta 23d$ /(D) $\beta\gamma$ - $\Delta b 8a/\alpha$	0.09	2.64	0.13	0.05
(A) $\delta 28d$ /(D) $\beta\gamma$ - $\Delta b 11a/\alpha$	0.11	3.79	0.25	0.10
(A) $\delta 28d$ /(D) $\beta\gamma$ - $\Delta b 8a/\alpha$	0.08	3.49	0.14	0.05
(A) $\delta 28d$ /(D) $\beta\gamma$ - $\Delta b 5a/\alpha$	0.06	3.44	0.08	0.03
(A) $\alpha 28c$ /(D) $\beta\gamma$ - $\Delta b 34a/\delta$	0.06	2.69	0.05	0.02
(A) $\delta 10d$ /(D) $\beta\gamma$ - $\Delta b 8c/\alpha$	0.07	2.73	0.08	0.03
(A) $\alpha 28c$ /(D) $\delta 7a/\beta\gamma$ - Δb	0.10	2.39	0.15	0.06
(A) $\delta 26d$ /(D) $\beta\gamma$ - $\Delta b 14a/\alpha$	0.08	3.15	0.14	0.05
(A) $\delta 26d$ /(D) $\beta\gamma$ - $\Delta b 11a/\alpha$	0.03	3.81	0.13	0.05
(A) $\delta 26d$ /(D) $\beta\gamma$ - $\Delta b 8a/\alpha$	0.07	3.09	0.08	0.03
(A) $\delta 26d$ /(D) $\beta\gamma$ - $\Delta b 5a/\alpha$	0.06	3.86	0.10	0.04
(D) $\delta 7a$ /(A) $\beta\gamma$ - $\Delta b 14c/\alpha$	0.11	1.50	0.11	0.04
(A) $\delta 10a$ /(D) $\beta\gamma$ - $\Delta b 5c/\alpha$	0.06	3.60	0.07	0.03
(A) $\alpha 12d$ /(D) $\delta 7d/\beta\gamma$ - Δb	0.11	1.22	0.06	0.02
(A) $\alpha 12d$ /(D) $\beta\gamma$ - $\Delta b 14a/\delta$	0.15	1.45	0.24	0.10
(A) $\alpha 12d$ /(D) $\beta\gamma$ - $\Delta b 29a/\delta$	0.10	1.24	0.03	0.01
(A) $\alpha 26d$ /(D) $\beta\gamma$ - $\Delta b 29a/\delta$	0.08	2.99	0.13	0.05
(A) $\alpha 28d$ /(D) $\beta\gamma$ - $\Delta b 29a/\delta$	0.08	3.28	0.12	0.05
(A) $\delta 23d$ /(D) $\beta\gamma$ - $\Delta b 29a/\alpha$	0.08	2.52	0.09	0.03
(A) $\delta 26d$ /(D) $\beta\gamma$ - $\Delta b 29a/\alpha$	0.09	2.47	0.13	0.05
(A) $\delta 28d$ /(D) $\beta\gamma$ - $\Delta b 29a/\alpha$	0.08	2.85	0.12	0.05
(A) $\alpha 26d$ /(D) $\beta\gamma$ - $\Delta b 34a/\delta$	0.07	2.58	0.05	0.02
(A) $\alpha 26c$ /(D) $\delta 7a/\beta\gamma$ - Δb	0.08	2.42	0.07	0.03
(A) $\alpha 12d$ /(D) $\beta\gamma$ - $\Delta b 11a/\delta$	0.16	1.64	0.31	0.12
(A) $\alpha 12d$ /(D) $\beta\gamma$ - $\Delta b 8a/\delta$	0.11	2.02	0.16	0.06
(A) $\alpha 12d$ /(D) $\beta\gamma$ - $\Delta b 5a/\delta$	0.09	2.11	0.10	0.05

FRET sample name	r_D	$\langle \tau_{major} \rangle_F$	S_{trap}	r_{∞}
(A) $\alpha 12d/(D)\beta\gamma-\Delta b34a/\delta$	0.07	2.18	0.05	0.02
(D) $\delta 23d/(A)\beta\gamma-\Delta b14c/\alpha$	0.09	1.79	0.17	0.07
(A) $\alpha 26c/(D)\delta 23a/\beta\gamma-\Delta b$	0.08	2.64	0.12	0.05
(A) $\alpha 28c/(D)\delta 23a/\beta\gamma-\Delta b$	0.14	2.95	0.33	0.13
(A) $\delta 27d/(D)\beta\gamma-\Delta b34a/\alpha$	0.03	3.81	0.05	0.02
(A) $\delta 27d/(D)\beta\gamma-\Delta b29a/\alpha$	0.08	2.44	0.10	0.04
(A) $\delta 27d/(D)\beta\gamma-\Delta b14c/\alpha$	0.09	2.35	0.12	0.05
(A) $\delta 27d/(D)\beta\gamma-\Delta b11c/\alpha$	0.11	3.16	0.24	0.10
(A) $\delta 27d/(D)\beta\gamma-\Delta b8c/\alpha$	0.06	3.27	0.05	0.02
(A) $\delta 27d/(D)\beta\gamma-\Delta b5c/\alpha$	0.03	3.34	0.08	0.03
(A) $\delta 23d/(D)\beta\gamma-\Delta b5c/\alpha$	0.06	3.12	0.05	0.02

3.3.2 2D MFD plots

MFD was applied to describe fluorescence bursts of single diffusing RNAs and to recover whether the molecule exhibits dynamics on the millisecond time scale. Collected 2D plots (Figure 3.18 and Chapter 3.2.7) demonstrate that donor only population (high F_D/F_A values, fluorescence lifetime of donor on presence of acceptor $\langle \tau_{D(A)} \rangle_F$ is around 4 ns) is linked with FRET populations (lower F_D/F_A values) via static FRET line (red curve) (Eq. (62)) indicating the absence of dynamic on ms-time scale. The connection between fluorescence anisotropy and fluorescence lifetime of donor in presence of acceptor $\langle \tau_{D(A)} \rangle_F$ can be linked via Perrin equation, assuming single exponential solution one rotation correlation time (see legend Figure 3.18).

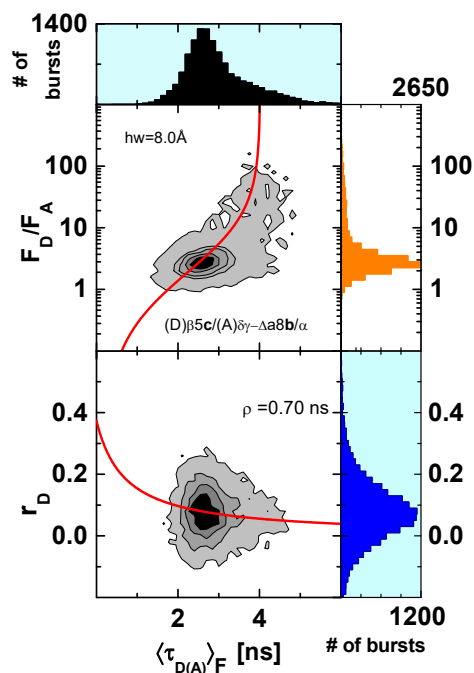


Figure 3.18 2D histogram of F_D/F_A vs $\langle \tau_{D(A)} \rangle$ (upper plot) and r_D vs $\langle \tau_{D(A)} \rangle$ (lower plot) for (D) β 5c/(A) $\delta\gamma$ - Δ a8b/ α on J(bcd) construct. Static FRET line and Perrin equation are shown as red curves (upper plot and lower plot correspondingly).

3.3.3 PDA analysis

PDA was used to separate shot noise from inhomogeneous broadening and calculate FRET-averaged distances $\langle R_{DA} \rangle_E$ (see Chapter 3.2.7.6). As an example, smFRET S_g/S_r histogram of (D) δ 7a/(A) $\beta\gamma$ - Δ b14c/ α on J(acd) is plotted (Figure 3.19). To satisfy the experimental data, a model with two-FRET states, a donor only fraction and an impurity fraction was introduced. PDA analysis demonstrates that all FRET samples have one major population (up to 85%) and often one minor (2-30%) due to the incompletely hybridized variants of RNA 3WJ or acceptor photophysics (for details see ¹²⁶). For further modeling distances obtained from the major population are used. Histograms and the fitting results for all J(abd), J(abc) and J(bcd) RNA 3WJ constructs are collected in Chapter 3.5.4.

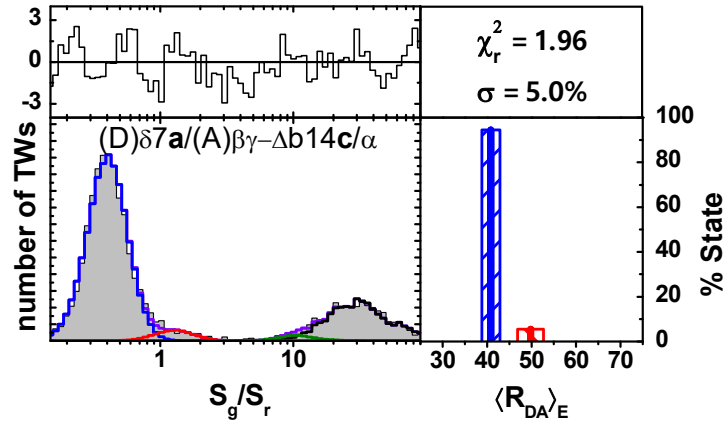


Figure 3.19 Results of PDA analysis for the sample (D) $\delta 7a/(A)\beta\gamma-\Delta b14c/\alpha$ on J(acd). Left panel: S_g/S_r histogram of experimental data (gray area) is fitted (purple solid line) using following parameters: 70.8% of $\langle R_{DA} \rangle_{E1}=40.8\text{\AA}$ (blue, 4% of $\langle R_{DA} \rangle_{E1}=50.1\text{\AA}$ (red), donor only fraction of 23.3% (black) and 1.9% of impurity (green) with global apparent width $\sigma=5.0$. Goodness of the fit is judged with weighted residuals (upper left panel). Right panel: Fitted distances for the major (blue) and minor (red) states with their relative amplitudes and confidence intervals (stripped boxes).

3.3.4 Error estimation analysis

3.3.4.1 Calibration factors

As described in Chapter 3.2.7, green B_G and red B_R background, emission crosstalk α , and γ calibration parameters were estimated from daily measurements.

Relative error $\frac{\Delta\gamma}{\gamma}$ was estimated by standard deviation over average value for multiple measurements within the same setup

$$\frac{\Delta\gamma}{\gamma} = \frac{st.dev(\gamma)}{average(\gamma)} \quad (105)$$

As Φ_{FA} was measured once, its error was not accounted for $\Delta R_{DA}(\gamma)$ (Eq. 89).

$\Delta\alpha$ was estimated by standard deviation for multiple measurements within the particular setup

$$\Delta\alpha = \frac{st.dev(\alpha)}{average(\alpha)} \cdot \alpha \quad (106)$$

where α is a daily measured parameter on particular setup.

ΔB_G , and ΔB_R were calculated in the same manner as $\Delta\alpha$.

Calculated uncertainties for calibration parameters on different setups are provided in Table 3.12.

Table 3.12 Absolute errors of the calibration parameters: green background B_G , red background B_R , emission crosstalk α and γ . For each uncertainty two values are given: for sample measured on setup 1 (first value) and samples measured on setup 2 (second value after slash) for structures J(bcd), J(abd) and J(acd). Values for J(abc) structures are added for comparison (obtained by H. Vardanyan).

	Setup 1/setup2			
Structure	(ΔB_G)	(ΔB_R)	$\Delta\alpha$	$\Delta\gamma$
J(bcd)	0.18/0.33	0.22/0.17	0.18/0.14	0.21/0.13
J(abd)	0.41/0.32	0.48/0.31	0.18/0.35	0.22/0.19
J(acd)	0.31/0.22	0.27/0.21	0.17/0.08	0.19/0.17
	Setup 3/setup4			
J(abc)	0.49/0.19	0.72/0.20	0.18/0.32	0.19/0.16

3.3.4.2 κ^2 estimation

Error contribution due to the orientation factor κ^2 , $\Delta R_{DA}(\kappa^2)$ was calculated assuming diffusion with traps model (Chapter 3.2.8.2). Here the residual anisotropy for donor and acceptor was used as described (Eq. 92) and average FRET efficiency is calculated via Förster formula (Eq. 107). Here we used the distance of the major peak obtained from PDA fitting.

$$E = \frac{1}{1 + (R_{DA}/R_0)^6} \quad (107)$$

Obtained results for $\Delta\kappa^2$ and $\delta R_{DA}(\kappa^2)$ are presented in Table 3.13-15 for the structures J(bcd), J(acd) and J(abd) correspondingly.

Table 3.13 Uncertainties due to the orientation factor k^2 and residual donor $r_{D,\infty}$ and acceptor $r_{A,\infty}$ anisotropies and experimental FRET efficiencies $\langle E \rangle$ used for the calculations in the studies system J(bcd).

FRET pair	$r_{D,\infty}$	$r_{A,\infty}$	E	$\Delta\kappa^2$	$\delta R_{DA}(\kappa^2)$
(D) $\beta 11\mathbf{c}/(\mathbf{A})\delta\gamma\text{-}\Delta\mathbf{a}28\mathbf{d}/\alpha$	0.085	0.275	0.1	0.057	0.040
(D) $\beta 11\mathbf{c}/(\mathbf{A})\delta\gamma\text{-}\Delta\mathbf{a}26\mathbf{d}/\alpha$	0.083	0.282	0.17	0.058	0.044
(D) $\beta 11\mathbf{c}/(\mathbf{A})\delta\gamma\text{-}\Delta\mathbf{a}23\mathbf{d}/\alpha$	0.082	0.156	0.37	0.034	0.031
(D) $\beta 11\mathbf{c}/(\mathbf{A})\delta\gamma\text{-}\Delta\mathbf{a}8\mathbf{b}/\alpha$	0.086	0.161	0.81	0.044	0.056
(D) $\beta 11\mathbf{c}/(\mathbf{A})\alpha 12\mathbf{d}/\delta\gamma\text{-}\Delta\mathbf{a}$	0.102	0.203	0.77	0.054	0.066
(D) $\beta 14\mathbf{c}/(\mathbf{A})\delta\gamma\text{-}\Delta\mathbf{a}28\mathbf{d}/\alpha$	0.067	0.275	0.19	0.054	0.042
(D) $\beta 14\mathbf{c}/(\mathbf{A})\delta\gamma\text{-}\Delta\mathbf{a}26\mathbf{d}/\alpha$	0.066	0.282	0.23	0.056	0.046
(D) $\beta 14\mathbf{c}/(\mathbf{A})\delta\gamma\text{-}\Delta\mathbf{a}23\mathbf{d}/\alpha$	0.075	0.156	0.65	0.035	0.039
(D) $\beta 14\mathbf{c}/(\mathbf{A})\delta\gamma\text{-}\Delta\mathbf{a}8\mathbf{b}/\alpha$	0.086	0.161	0.81	0.044	0.052
(D) $\beta 14\mathbf{c}/(\mathbf{A})\alpha 12\mathbf{d}/\delta\gamma\text{-}\Delta\mathbf{a}$	0.074	0.203	0.86	0.054	0.073
(D) $\beta 27\mathbf{b}/(\mathbf{A})\delta\gamma\text{-}\Delta\mathbf{a}28\mathbf{d}/\alpha$	0.072	0.275	0.26	0.055	0.046
(D) $\beta 27\mathbf{b}/(\mathbf{A})\delta\gamma\text{-}\Delta\mathbf{a}26\mathbf{d}/\alpha$	0.077	0.282	0.3	0.057	0.050
(D) $\beta 27\mathbf{b}/(\mathbf{A})\alpha 26\mathbf{c}/\delta\gamma\text{-}\Delta\mathbf{a}$	0.083	0.115	0.34	0.026	0.023
(D) $\beta 27\mathbf{b}/(\mathbf{A})\alpha 28\mathbf{c}/\delta\gamma\text{-}\Delta\mathbf{a}$	0.055	0.111	0.38	0.023	0.021
(A) $\alpha 12\mathbf{d}/(\mathbf{D})\beta 27\mathbf{b}/\delta\gamma\text{-}\Delta\mathbf{a}$	0.078	0.203	0.83	0.053	0.069
(D) $\beta 27\mathbf{b}/(\mathbf{A})\delta\gamma\text{-}\Delta\mathbf{a}23\mathbf{d}/\alpha$	0.068	0.156	0.41	0.032	0.030
(D) $\beta 28\mathbf{b}/(\mathbf{A})\delta\gamma\text{-}\Delta\mathbf{a}23\mathbf{d}/\alpha$	0.079	0.156	0.35	0.033	0.030
(D) $\beta 28\mathbf{b}/(\mathbf{A})\delta\gamma\text{-}\Delta\mathbf{a}26\mathbf{d}/\alpha$	0.063	0.282	0.28	0.056	0.048
(D) $\beta 28\mathbf{b}/(\mathbf{A})\delta\gamma\text{-}\Delta\mathbf{a}28\mathbf{d}/\alpha$	0.102	0.275	0.24	0.059	0.049
(A) $\alpha 26\mathbf{c}/(\mathbf{D})\beta 28\mathbf{b}/\delta\gamma\text{-}\Delta\mathbf{a}$	0.073	0.115	0.29	0.025	0.022
(A) $\alpha 12\mathbf{d}/(\mathbf{D})\beta 28\mathbf{b}/\delta\gamma\text{-}\Delta\mathbf{a}$	0.100	0.203	0.79	0.055	0.069
(A) $\alpha 28\mathbf{c}/(\mathbf{D})\beta 28\mathbf{b}/\delta\gamma\text{-}\Delta\mathbf{a}$	0.076	0.111	0.27	0.025	0.021
(D) $\beta 29\mathbf{b}/(\mathbf{A})\delta\gamma\text{-}\Delta\mathbf{a}28\mathbf{d}/\alpha$	0.088	0.275	0.3	0.057	0.050
(D) $\beta 29\mathbf{b}/(\mathbf{A})\delta\gamma\text{-}\Delta\mathbf{a}26\mathbf{d}/\alpha$	0.084	0.282	0.35	0.058	0.054
(D) $\beta 29\mathbf{b}/(\mathbf{A})\delta\gamma\text{-}\Delta\mathbf{a}23\mathbf{d}/\alpha$	0.095	0.156	0.36	0.035	0.033
(A) $\alpha 12\mathbf{d}/(\mathbf{D})\beta 29\mathbf{b}/\delta\gamma\text{-}\Delta\mathbf{a}$	0.105	0.203	0.75	0.054	0.066
(D) $\beta 5\mathbf{c}/(\mathbf{A})\delta\gamma\text{-}\Delta\mathbf{a}28\mathbf{d}/\alpha$	0.049	0.275	0.08	0.053	0.035
(D) $\beta 5\mathbf{c}/(\mathbf{A})\delta\gamma\text{-}\Delta\mathbf{a}26\mathbf{d}/\alpha$	0.033	0.0282	0.1	0.054	0.037
(D) $\beta 5\mathbf{c}/(\mathbf{A})\delta\gamma\text{-}\Delta\mathbf{a}23\mathbf{d}/\alpha$	0.049	0.156	0.33	0.03	0.027
(D) $\beta 5\mathbf{c}/(\mathbf{A})\delta\gamma\text{-}\Delta\mathbf{a}8\mathbf{b}/\alpha$	0.042	0.0161	0.43	0.031	0.030
(D) $\beta 5\mathbf{c}/(\mathbf{A})\alpha 12\mathbf{d}/\delta\gamma\text{-}\Delta\mathbf{a}$	0.049	0.203	0.50	0.040	0.040
(D) $\beta 8\mathbf{c}/(\mathbf{A})\delta\gamma\text{-}\Delta\mathbf{a}28\mathbf{d}/\alpha$	0.056	0.275	0.24	0.053	0.035
(D) $\beta 8\mathbf{c}/(\mathbf{A})\delta\gamma\text{-}\Delta\mathbf{a}26\mathbf{d}/\alpha$	0.067	0.282	0.16	0.056	0.042
(D) $\beta 8\mathbf{c}/(\mathbf{A})\delta\gamma\text{-}\Delta\mathbf{a}23\mathbf{d}/\alpha$	0.053	0.156	0.38	0.031	0.028
(D) $\beta 14\mathbf{c}/(\mathbf{A})\delta\gamma\text{-}\Delta\mathbf{a}8\mathbf{b}/\alpha$	0.066	0.16	0.70	0.035	0.052
(A) $\alpha 12\mathbf{d}/(\mathbf{D})\beta 8\mathbf{c}/\delta\gamma\text{-}\Delta\mathbf{a}$	0.036	0.203	0.62	0.039	0.042
(A) $\beta 8\mathbf{c}/(\mathbf{D})\delta\gamma\text{-}\Delta\mathbf{a}8\mathbf{b}/\alpha$	0.058	0.161	0.51	0.033	0.033
(A) $\alpha 26\mathbf{c}/(\mathbf{D})\delta\gamma\text{-}\Delta\mathbf{a}7\mathbf{b}/\beta$	0.012	0.115	0.52	0.022	0.022

FRET pair	$r_{D,\infty}$	$r_{A,\infty}$	E	$\Delta\kappa^2$	$\delta R_{DA}(\kappa^2)$
(A) α 12d/(D) $\delta\gamma$ - Δ a7b/ β	0.01	0.203	0.77	0.020	0.024
(D) $\delta\gamma$ - Δ a8b/(A) α 28c/ β	0.054	0.111	0.54	0.023	0.024
(D) $\delta\gamma$ - Δ a8b/(A) α 26c/ β	0.051	0.115	0.56	0.024	0.025
(A) α 12d/(D) $\delta\gamma$ - Δ a8b/ β	0.048	0.203	0.89	0.049	0.070

Table 3.14 Uncertainties due to the orientation factor k^2 and residual donor $r_{D,\infty}$ and acceptor $r_{A,\infty}$ anisotropies and experimental FRET efficiencies $\langle E \rangle$ used for the calculations in the studies system J(acd).

FRET pair	$r_{D,\infty}$	$r_{A,\infty}$	E	$\Delta\kappa^2$	$\delta R_{DA}(\kappa^2)$
(A) α 26c/(D) δ 23a/ $\beta\gamma$ - Δ b	0.045	0.137	0.36	0.027	0.025
(A) α 28c/(D) δ 23a/ $\beta\gamma$ - Δ b	0.126	0.12	0.24	0.033	0.027
(A) δ 23d/(D) $\beta\gamma$ - Δ b14a/ α	0.06	0.156	0.62	0.033	0.036
(A) α 12d/(D) δ 7d/ $\beta\gamma$ - Δ b	0.023	0.203	0.84	0.041	0.054
(A) α 26c/(D) δ 7a/ $\beta\gamma$ - Δ b	0.028	0.137	0.44	0.026	0.026
(A) α 28c/(D) δ 7a/ $\beta\gamma$ - Δ b	0.055	0.12	0.24	0.024	0.023
(D) δ 7a/(A) $\beta\gamma$ - Δ b14c/ α	0.041	0.16	0.81	0.034	0.043
(A) α 12d/(D) $\beta\gamma$ - Δ b11a/ δ	0.118	0.156	0.74	0.046	0.075
(A) δ 10a/(D) $\beta\gamma$ - Δ b11c/ α	0.115	0.168	0.66	0.045	0.050
(A) δ 23d/(D) $\beta\gamma$ - Δ b11a/ α	0.115	0.156	0.33	0.037	0.033
(A) δ 26d/(D) $\beta\gamma$ - Δ b11a/ α	0.050	0.25	0.22	0.047	0.033
(A) δ 27d/(D) $\beta\gamma$ - Δ b11c/ α	0.090	0.156	0.26	0.034	0.029
(A) δ 28d/(D) $\beta\gamma$ - Δ b11a/ α	0.095	0.25	0.11	0.052	0.036
(A) α 12d/(D) $\beta\gamma$ - Δ b14a/ δ	0.090	0.203	0.87	0.04	0.075
(A) δ 10a/(D) $\beta\gamma$ - Δ b14c/ α	0.065	0.168	0.58	0.035	0.037
(A) δ 23d/(D) $\beta\gamma$ - Δ b14a/ α	0.030	0.160	0.61	0.031	0.036
(A) δ 26d/(D) $\beta\gamma$ - Δ b14a/ α	0.052	0.246	0.25	0.048	0.040
(A) δ 27d/(D) $\beta\gamma$ - Δ b14c/ α	0.045	0.156	0.59	0.031	0.033
(A) δ 28d/(D) $\beta\gamma$ - Δ b14c/ α	0.073	0.25	0.23	0.05	0.041
(A) α 12d/(D) $\beta\gamma$ - Δ b29a/ δ	0.010	0.203	0.87	0.040	0.055
(A) α 26d/(D) $\beta\gamma$ - Δ b29a/ δ	0.049	0.137	0.36	0.027	0.025
(A) α 28d/(D) $\beta\gamma$ - Δ b29a/ δ	0.045	0.12	0.26	0.024	0.020
(A) δ 23d/(D) $\beta\gamma$ - Δ b29a/ α	0.033	0.156	0.49	0.030	0.030
(A) δ 26d/(D) $\beta\gamma$ - Δ b29a/ α	0.049	0.246	0.51	0.048	0.048
(A) δ 27d/(D) $\beta\gamma$ - Δ b29a/ α	0.038	0.156	0.54	0.03	0.031
(A) δ 28d/(D) $\beta\gamma$ - Δ b29a/ α	0.040	0.25	0.52	0.048	0.046
(A) α 12d/(D) $\beta\gamma$ - Δ b34a/ δ	0.018	0.156	0.74	0.046	0.039
(A) α 26d/(D) $\beta\gamma$ - Δ b34a/ δ	0.019	0.137	0.44	0.026	0.024
(A) α 28c/(D) $\beta\gamma$ - Δ b34a/ δ	0.019	0.12	0.30	0.023	0.020
(A) δ 23d/(D) $\beta\gamma$ - Δ b34a/ α	0.026	0.156	0.20	0.029	0.023
(A) δ 26d/(D) $\beta\gamma$ - Δ b34a/ α	0.025	0.246	0.13	0.046	0.034

FRET pair	$r_{D,\infty}$	$r_{A,\infty}$	E	$\Delta\kappa^2$	$\delta R_{DA}(\kappa^2)$
(A) $\delta 28\mathbf{d}/(\mathbf{D})\beta\gamma\text{-}\Delta\mathbf{b}34\mathbf{a}/\alpha$	0.008	0.25	0.12	0.047	0.034
(A) $\delta 27\mathbf{d}/(\mathbf{D})\beta\gamma\text{-}\Delta\mathbf{b}34\mathbf{a}/\alpha$	0.018	0.156	0.21	0.029	0.023
(A) $\delta 23\mathbf{d}/(\mathbf{D})\beta\gamma\text{-}\Delta\mathbf{b}5\mathbf{c}/\alpha$	0.021	0.156	0.32	0.029	0.026
(A) $\alpha 12\mathbf{d}/(\mathbf{D})\beta\gamma\text{-}\Delta\mathbf{b}5\mathbf{a}/\delta$	0.038	0.203	0.64	0.04	0.044
(A) $\delta 10\mathbf{a}/(\mathbf{D})\beta\gamma\text{-}\Delta\mathbf{b}5\mathbf{c}/\alpha$	0.025	0.168	0.18	0.032	0.025
(A) $\delta 26\mathbf{d}/(\mathbf{D})\beta\gamma\text{-}\Delta\mathbf{b}5\mathbf{a}/\alpha$	0.037	0.246	0.07	0.047	0.030
(A) $\delta 27\mathbf{d}/(\mathbf{D})\beta\gamma\text{-}\Delta\mathbf{b}5\mathbf{c}/\alpha$	0.030	0.156	0.16	0.03	0.023
(A) $\delta 28\mathbf{d}/(\mathbf{D})\beta\gamma\text{-}\Delta\mathbf{b}5\mathbf{a}/\alpha$	0.029	0.25	0.07	0.048	0.031
(A) $\alpha 12\mathbf{d}/(\mathbf{D})\beta\gamma\text{-}\Delta\mathbf{b}8\mathbf{a}/\delta$	0.059	0.203	0.61	0.041	0.044
(A) $\delta 10\mathbf{d}/(\mathbf{D})\beta\gamma\text{-}\Delta\mathbf{b}8\mathbf{c}/\alpha$	0.029	0.168	0.49	0.032	0.029
(A) $\delta 23\mathbf{d}/(\mathbf{D})\beta\gamma\text{-}\Delta\mathbf{b}8\mathbf{a}/\alpha$	0.049	0.156	0.40	0.030	0.028
(A) $\delta 26\mathbf{d}/(\mathbf{D})\beta\gamma\text{-}\Delta\mathbf{b}8\mathbf{a}/\alpha$	0.029	0.246	0.12	0.047	0.034
(A) $\delta 27\mathbf{d}/(\mathbf{D})\beta\gamma\text{-}\Delta\mathbf{b}8\mathbf{c}/\alpha$	0.019	0.156	0.16	0.029	0.022
(A) $\delta 28\mathbf{d}/(\mathbf{D})\beta\gamma\text{-}\Delta\mathbf{b}8\mathbf{a}/\alpha$	0.054	0.25	0.07	0.048	0.033

Table 3.15 Uncertainties due to the orientation factor k^2 and residual donor $r_{D,\infty}$ and acceptor $r_{A,\infty}$ anisotropies and experimental FRET efficiencies $\langle E \rangle$ used for the calculations in the studies system J(abd).

FRET pair	$r_{D,\infty}$	$r_{A,\infty}$	E	$\Delta\kappa^2$	$\delta R_{DA}(\kappa^2)$
(D) $\gamma 24\mathbf{a}/(\mathbf{A})\delta 23\mathbf{d}/\alpha\beta\text{-}\Delta\mathbf{c}$	0.039	0.156	0.512	0.03	0.049
(D) $\gamma 24\mathbf{a}/(\mathbf{A})\delta 26\mathbf{d}/\alpha\beta\text{-}\Delta\mathbf{c}$	0.06	0.256	0.538	0.05	0.052
(D) $\gamma 24\mathbf{a}/(\mathbf{A})\delta 28\mathbf{d}/\alpha\beta\text{-}\Delta\mathbf{c}$	0.046	0.259	0.471	0.05	0.049
(D) $\gamma 24\mathbf{a}/(\mathbf{A})\alpha\beta\text{-}\Delta\mathbf{c}22\mathbf{b}/\delta$	0.025	0.145	0.768	0.03	0.035
(D) $\gamma 24\mathbf{a}/(\mathbf{A})\alpha\beta\text{-}\Delta\mathbf{c}12\mathbf{d}/\delta$	0.019	0.212	0.868	0.04	0.057
(D) $\gamma 24\mathbf{a}/(\mathbf{A})\delta 27\mathbf{d}/\alpha\beta\text{-}\Delta\mathbf{c}$	0.060	0.162	0.535	0.03	0.034
(D) $\gamma 27\mathbf{b}/(\mathbf{A})\delta 27\mathbf{d}/\alpha\beta\text{-}\Delta\mathbf{c}$	0.06	0.162	0.381	0.03	0.029
(D) $\gamma 27\mathbf{a}/(\mathbf{A})\alpha\beta\text{-}\Delta\mathbf{c}12\mathbf{d}/\delta$	0.004	0.212	0.737	0.04	0.050
(D) $\gamma 29\mathbf{a}/(\mathbf{A})\alpha\beta\text{-}\Delta\mathbf{c}12\mathbf{d}/\delta$	0.027	0.212	0.491	0.04	0.040
(D) $\gamma 29\mathbf{a}/(\mathbf{A})\delta 28\mathbf{d}/\alpha\beta\text{-}\Delta\mathbf{c}$	0.034	0.259	0.084	0.05	0.034
(D) $\gamma 29\mathbf{a}/(\mathbf{A})\delta 26\mathbf{d}/\alpha\beta\text{-}\Delta\mathbf{c}$	0.039	0.256	0.1488	0.05	0.037
(D) $\gamma 29\mathbf{a}/(\mathbf{A})\delta 23\mathbf{d}/\alpha\beta\text{-}\Delta\mathbf{c}$	0.042	0.156	0.162	0.03	0.023
(D) $\gamma 29\mathbf{a}/(\mathbf{A})\alpha\beta\text{-}\Delta\mathbf{c}22\mathbf{b}/\delta$	0.052	0.145	0.635	0.03	0.033
(D) $\gamma 29\mathbf{a}/(\mathbf{A})\delta 27\mathbf{d}/\alpha\beta\text{-}\Delta\mathbf{c}$	0.020	0.162	0.223	0.03	0.024
(D) $\gamma 8\mathbf{b}/(\mathbf{A})\delta 10\mathbf{a}/\alpha\beta\text{-}\Delta\mathbf{c}$	0.068	0.168	0.633	0.036	0.039
(D) $\gamma 8\mathbf{b}/(\mathbf{A})\delta 26\mathbf{d}/\alpha\beta\text{-}\Delta\mathbf{c}$	0.062	0.256	0.178	0.051	0.040
(D) $\gamma 8\mathbf{b}/(\mathbf{A})\delta 28\mathbf{d}/\alpha\beta\text{-}\Delta\mathbf{c}$	0.087	0.259	0.139	0.053	0.039
(D) $\gamma 8\mathbf{b}/(\mathbf{A})\delta 23\mathbf{d}/\alpha\beta\text{-}\Delta\mathbf{c}$	0.093	0.156	0.529	0.036	0.037
(D) $\gamma 8\mathbf{b}/(\mathbf{A})\alpha\beta\text{-}\Delta\mathbf{c}12\mathbf{d}/\delta$	0.071	0.212	0.822	0.052	0.067
(D) $\gamma 8\mathbf{b}/(\mathbf{A})\delta 27\mathbf{d}/\alpha\beta\text{-}\Delta\mathbf{c}$	0.087	0.162	0.489	0.036	0.036
(D) $\delta 23\mathbf{d}/(\mathbf{A})\alpha\beta\text{-}\Delta\mathbf{c}22\mathbf{b}/\gamma$	0.079	0.145	0.361	0.031	0.028
(A) $\gamma 24\mathbf{a}/(\mathbf{D})\delta 23\mathbf{d}/\alpha\beta\text{-}\Delta\mathbf{c}$	0.080	0.163	0.373	0.035	0.032

FRET pair	$r_{D,\infty}$	$r_{A,\infty}$	E	$\Delta\kappa^2$	$\delta R_{DA}(\kappa^2)$
(D) $\delta 7\mathbf{d}/(\mathbf{A})\alpha\beta-\Delta\mathbf{c}22\mathbf{b}/\gamma$	0.070	0.145	0.804	0.036	0.046
(D) $\delta 7\mathbf{d}/(\mathbf{A})\alpha\beta-\Delta\mathbf{c}12\mathbf{b}/\gamma$	0.068	0.212	0.835	0.052	0.068
(A) $\gamma 8\mathbf{b}/(\mathbf{D})\delta 7\mathbf{a}/\alpha\beta-\Delta\mathbf{c}$	0.087	0.178	0.833	0.05	0.065
(A) $\delta 10\mathbf{a}/(\mathbf{D})\alpha\beta-\Delta\mathbf{c}22\mathbf{b}/\gamma$	0.088	0.168	0.701	0.041	0.046
(A) $\delta 26\mathbf{d}/(\mathbf{D})\alpha\beta-\Delta\mathbf{c}22\mathbf{b}/\gamma$	0.076	0.256	0.199	0.051	0.040
(A) $\delta 28\mathbf{d}/(\mathbf{D})\alpha\beta-\Delta\mathbf{c}22\mathbf{b}/\gamma$	0.077	0.259	0.131	0.052	0.037
(A) $\delta 27\mathbf{d}/(\mathbf{D})\alpha\beta-\Delta\mathbf{c}22\mathbf{b}/\gamma$	0.077	0.162	0.302	0.034	0.030
(A) $\delta 8\mathbf{a}/(\mathbf{D})\alpha\beta-\Delta\mathbf{c}22\mathbf{b}/\gamma$	0.046	0.142	0.905	0.037	0.054
(A) $\delta 10\mathbf{a}/(\mathbf{D})\alpha\beta-\Delta\mathbf{c}23\mathbf{b}/\gamma$	0.105	0.168	0.635	0.042	0.046
(A) $\delta 27\mathbf{d}/(\mathbf{D})\alpha\beta-\Delta\mathbf{c}23\mathbf{b}/\gamma$	0.092	0.162	0.232	0.035	0.029
(A) $\delta 26\mathbf{d}/(\mathbf{D})\alpha\beta-\Delta\mathbf{c}23\mathbf{b}/\gamma$	0.105	0.256	0.153	0.055	0.040
(A) $\delta 28\mathbf{d}/(\mathbf{D})\alpha\beta-\Delta\mathbf{c}23\mathbf{b}/\gamma$	0.092	0.259	0.156	0.054	0.041
(A) $\delta 23\mathbf{d}/(\mathbf{D})\alpha\beta-\Delta\mathbf{c}23\mathbf{b}/\gamma$	0.091	0.156	0.354	0.034	0.031
(A) $\delta 8\mathbf{a}/(\mathbf{D})\alpha\beta-\Delta\mathbf{c}23\mathbf{b}/\gamma$	0.065	0.142	0.847	0.037	0.049
(A) $\delta 10\mathbf{a}/(\mathbf{D})\alpha\beta-\Delta\mathbf{c}28\mathbf{b}/\gamma$	0.056	0.168	0.199	0.033	0.026
(A) $\delta 28\mathbf{d}/(\mathbf{D})\alpha\beta-\Delta\mathbf{c}28\mathbf{b}/\gamma$	0.055	0.259	0.062	0.051	0.032
(A) $\delta 26\mathbf{d}/(\mathbf{D})\alpha\beta-\Delta\mathbf{c}28\mathbf{b}/\gamma$	0.003	0.0256	0.068	0.048	0.031
(A) $\delta 23\mathbf{d}/(\mathbf{D})\alpha\beta-\Delta\mathbf{c}28\mathbf{b}/\gamma$	0.043	0.156	0.283	0.03	0.026
(A) $\delta 27\mathbf{d}/(\mathbf{D})\alpha\beta-\Delta\mathbf{c}28\mathbf{b}/\gamma$	0.031	0.162	0.144	0.031	0.023
(A) $\delta 8\mathbf{a}/(\mathbf{D})\alpha\beta-\Delta\mathbf{c}28\mathbf{b}/\gamma$	0.065	0.142	0.847	0.037	0.040

3.3.4.3 All uncertainties

In this section calculated values for various relative distance errors and absolute distance error $\Delta R_{DA}(total)$ are provided (see Chapter 3.2.8 for calculations).

Table 3.16 Experimentally obtained distances R_{DA} from PDA with corresponding relative error from PDA $\delta R_{DA}(random)$, relative errors for Förster radius $\delta R'_{DA}(R_0)$, relative errors for backgrounds $\delta R_{DA}(BG)$, relative error for emission crosstalk $\delta R_{DA}(\alpha)$, and relative error for gamma $\delta R_{DA}(\gamma)$. Absolute distance error is $\Delta R_{DA}(total)$ for J(bcd) structure

FRET pair	R_{DA}	$\delta R_{DA}(random)$	$\delta R'_{DA}(R_0)$	$\delta R_{DA}(BG)$	$\delta R_{DA}(\alpha)$	$\delta R_{DA}(\gamma)$	$\Delta R_{DA}(total)$, [Å]
(D) $\beta 11c$ / (A) $\delta\gamma$ - $\Delta a28d/\alpha$	74.4	0.007	0.05	0.006	0.003	0.034	3.0
(D) $\beta 11c$ / (A) $\delta\gamma$ - $\Delta a26d/\alpha$	68.0	0.008	0.06	0.005	0.001	0.034	2.8
(D) $\beta 11c$ / (A) $\delta\gamma$ - $\Delta a23d/\alpha$	57.0	0.005	0.05	0.005	0.001	0.034	2.2
(D) $\beta 11c$ / (A) $\delta\gamma$ - $\Delta a8b/\alpha$	40.9	0.008	0.08	0.018	0.0005	0.022	1.7
(D) $\beta 11c$ / (A) $\alpha 12d/\delta\gamma$ - Δa	42.6	0.008	0.09	0.007	0.0005	0.034	2.0
(D) $\beta 14c$ / (A) $\delta\gamma$ - $\Delta a28d/\alpha$	66.4	0.011	0.06	0.006	0.003	0.034	2.8
(D) $\beta 14c$ / (A) $\delta\gamma$ - $\Delta a26d/\alpha$	63.5	0.01	0.06	0.005	0.001	0.022	2.1
(D) $\beta 14c$ / (A) $\delta\gamma$ - $\Delta a23d/\alpha$	46.9	0.005	0.07	0.007	0.0005	0.034	2.2
(D) $\beta 14c$ / (A) $\delta\gamma$ - $\Delta a8b/\alpha$	41.9	0.017	0.08	0.013	0.0005	0.022	1.8
(D) $\beta 14c$ / (A) $\alpha 12d/\delta\gamma$ - Δa	38.4	0.010	0.10	0.015	0.0005	0.034	2.0
(D) $\beta 27b$ / (A) $\delta\gamma$ - $\Delta a28d/\alpha$	62.0	0.011	0.06	0.004	0.002	0.034	2.6

FRET pair	R_{DA}	δR_{DA} (<i>random</i>)	$\delta R'_{DA}(R_0)$	$\delta R_{DA}(BG)$	$\delta R_{DA}(\alpha)$	$\delta R_{DA}(\gamma)$	ΔR_{DA} (<i>total</i>), [Å]
(D) $\beta 27b$ / (A) $\delta\gamma$ - $\Delta a 26d/\alpha$	59.7	0.014	0.06	0.004	0.001	0.034	2.6
(D) $\beta 27b$ / (A) $\alpha 26c/\delta\gamma$ - Δa	58.2	0.007	0.05	0.007	0.0005	0.022	1.8
(D) $\beta 27b$ / (A) $\alpha 28c/\delta\gamma$ - Δa	56.6	0.005	0.05	0.007	0.0005	0.022	1.7
(A) $\alpha 12d$ / (D) $\beta 27b/\delta\gamma$ - Δa	40.1	0.009	0.09	0.007	0.0005	0.022	2.0
(D) $\beta 27b$ / (A) $\delta\gamma$ - $\Delta a 23d/\alpha$	55.2	0.011	0.05	0.004	0.0005	0.022	1.8
(D) $\beta 28b$ / (A) $\delta\gamma$ - $\Delta a 23d/\alpha$	57.8	0.005	0.05	0.005	0.0005	0.022	1.7
(D) $\beta 28b$ / (A) $\delta\gamma$ - $\Delta a 26d/\alpha$	60.8	0.011	0.06	0.005	0.001	0.022	2.1
(D) $\beta 28b$ / (A) $\delta\gamma$ - $\Delta a 28d/\alpha$	63.0	0.004	0.06	0.007	0.001	0.034	2.6
(A) $\alpha 26c$ / (D) $\beta 28b/\delta\gamma$ - Δa	60.3	0.005	0.05	0.007	0.001	0.034	2.3
(A) $\alpha 12d$ / (D) $\beta 28b/\delta\gamma$ - Δa	41.6	0.003	0.09	0.013	0.0005	0.034	2.0
(A) $\alpha 28c$ / (D) $\beta 28b/\delta\gamma$ - Δa	61.4	0.005	0.05	0.008	0.001	0.034	2.4
(D) $\beta 29b$ / (A) $\delta\gamma$ - $\Delta a 28d/\alpha$	58.7	0.014	0.07	0.003	0.001	0.022	2.1
(D) $\beta 29b$ / (A) $\delta\gamma$ - $\Delta a 26d/\alpha$	56.3	0.012	0.07	0.003	0.001	0.022	2.0
(D) $\beta 29b$ / (A) $\delta\gamma$ - $\Delta a 23d/\alpha$	55.5	0.008	0.06	0.004	0.0005	0.022	1.7
(A) $\alpha 12d$ / (D) $\beta 29b/\delta\gamma$ - Δa	42.4	0.009	0.09	0.008	0.0005	0.022	1.8

FRET pair	R_{DA}	δR_{DA} (<i>random</i>)	$\delta R'_{DA}(R_0)$	$\delta R_{DA}(BG)$	$\delta R_{DA}(\alpha)$	$\delta R_{DA}(\gamma)$	ΔR_{DA} (<i>total</i>), [Å]
(D) $\beta 5c$ / (A) $\delta\gamma$ - $\Delta a28d/\alpha$	78.7	0.023	0.05	0.005	0.0005	0.022	3.6
(D) $\beta 5c$ / (A) $\delta\gamma$ - $\Delta a26d/\alpha$	75.7	0.015	0.05	0.008	0.004	0.034	3.2
(D) $\beta 5c$ / (A) $\delta\gamma$ - $\Delta a23d/\alpha$	58.3	0.008	0.05	0.004	0.001	0.034	2.3
(D) $\beta 5c$ / (A) $\delta\gamma$ - $\Delta a8b/\alpha$	54.5	0.074	0.05	0.005	0.0005	0.022	4.4
(D) $\beta 5c$ / (A) $\alpha 12d/\delta\gamma$ - Δa	51.9	0.005	0.06	0.004	0.0005	0.034	2.1
(D) $\beta 8c$ / (A) $\delta\gamma$ - $\Delta a28d/\alpha$	78.0	0.047	0.05	0.014	0.007	0.034	4.9
(D) $\beta 8c$ / (A) $\delta\gamma$ - $\Delta a26d/\alpha$	68.7	0.012	0.06	0.006	0.001	0.034	2.9
(D) $\beta 8c$ / (A) $\delta\gamma$ - $\Delta a23d/\alpha$	56.6	0.006	0.05	0.005	0.001	0.034	2.2
(D) $\beta 14c$ / (A) $\delta\gamma$ - $\Delta a8b/\alpha$	41.9	0.016	0.08	0.013	0.0005	0.022	1.8
(A) $\alpha 12d$ / (D) $\beta 8c/\delta\gamma$ - Δa	48.0	0.004	0.07	0.005	0.0005	0.034	2.0
(A) $\beta 8c$ / (D) $\delta\gamma$ - $\Delta a8b/\alpha$	51.9	0.023	0.06	0.012	0.0005	0.022	2.1
(A) $\alpha 26c$ / (D) $\delta\gamma$ - $\Delta a7b/\beta$	51.2	0.008	0.05	0.009	0.0005	0.022	1.6
(A) $\alpha 12d$ / (D) $\delta\gamma$ - $\Delta a7b/\beta$	42.5	0.009	0.06	0.014	0.0005	0.022	1.5
(D) $\delta\gamma$ - $\Delta a8b$ / (A) $\alpha 28c/\beta$	50.6	0.020	0.05	0.007	0.0005	0.034	2.2
(D) $\delta\gamma$ - $\Delta a8b$ / (A) $\alpha 26c/\beta$	50.1	0.010	0.05	0.006	0.0005	0.034	2.0
(A) $\alpha 12d$ / (D) $\delta\gamma$ - $\Delta a8b/\beta$	36.6	0.010	0.10	0.013	0.0005	0.034	1.9

Table 3.17 Experimentally obtained distances R_{DA} from PDA with corresponding relative error from PDA $\delta R_{DA}(\text{random})$, relative errors for Förster radius $\delta R'_{DA}(R_0)$, relative errors for backgrounds $\delta R_{DA}(BG)$, relative error for emission crosstalk $\delta R_{DA}(\alpha)$, and relative error for gamma $\delta R_{DA}(\gamma)$. Absolute distance error is $\Delta R_{DA}(\text{total})$ for J(acd) structure.

FRET pair	R_{DA}	$\delta R_{DA}(\text{random})$	$\delta R'_{DA}(R_0)$	$\delta R_{DA}(BG)$	$\delta R_{DA}(\alpha)$	$\delta R_{DA}(\gamma)$	$\Delta R_{DA}(\text{total})$, [Å]
(A) $\delta 10a/$ (D) $\beta\gamma\text{-}\Delta b14c/\alpha$	49.4	0.009	0.062	0.009	0.0001	0.030	2.1
(A) $\delta 10a/$ (D) $\beta\gamma\text{-}\Delta b11c/\alpha$	46.6	0.004	0.073	0.011	0.0001	0.030	2.1
(A) $\delta 28d/$ (D) $\beta\gamma\text{-}\Delta b14c/\alpha$	63.9	0.012	0.056	0.006	0.0003	0.030	2.6
(A) $\delta 28d/$ (D) $\beta\gamma\text{-}\Delta b34a/\alpha$	72.3	0.003	0.048	0.005	0.0029	0.030	2.7
(A) $\delta 26d/$ (D) $\beta\gamma\text{-}\Delta b34a/\alpha$	70.9	0.025	0.048	0.010	0.0027	0.030	3.2
(A) $\delta 23d/$ (D) $\beta\gamma\text{-}\Delta b34a/\alpha$	65.6	0.049	0.044	0.009	0.0015	0.030	4.0
(A) $\delta 23d/$ (D) $\beta\gamma\text{-}\Delta b14a/\alpha$	47.9	0.010	0.062	0.010	0.0002	0.030	2.1
(A) $\delta 23d/$ (D) $\beta\gamma\text{-}\Delta b11a/\alpha$	58.5	0.012	0.053	0.006	0.0006	0.030	2.4
(A) $\delta 23d/$ (D) $\beta\gamma\text{-}\Delta b8a/\alpha$	55.6	0.007	0.052	0.007	0.0005	0.030	2.2
(A) $\delta 28d/$ (D) $\beta\gamma\text{-}\Delta b11a/\alpha$	74.2	0.020	0.049	0.009	0.0037	0.030	3.2
(A) $\delta 28d/$ (D) $\beta\gamma\text{-}\Delta b8a/\alpha$	75.3	0.023	0.046	0.010	0.0041	0.030	3.3
(A) $\delta 28d/$ (D) $\beta\gamma\text{-}\Delta b5a/\alpha$	80.3	0.048	0.044	0.013	0.0058	0.030	4.9
(A) $\alpha 28c/$ (D) $\beta\gamma\text{-}\Delta b34a/\delta$	60.1	0.010	0.045	0.006	0.0011	0.030	2.3
(A) $\delta 10d/$ (D) $\beta\gamma\text{-}\Delta b8c/\alpha$	56.8	0.006	0.052	0.006	0.0005	0.030	2.2
(A) $\alpha 28c/$ (D) $\delta 7a/\beta\gamma\text{-}\Delta b$	53.7	0.006	0.051	0.006	0.0004	0.030	2.1
(A) $\delta 26d/$ (D) $\beta\gamma\text{-}\Delta b14a/\alpha$	62.7	0.006	0.056	0.008	0.0013	0.030	2.5

FRET pair	R_{DA}	δR_{DA} (<i>random</i>)	$\delta R'_{DA}(R_0)$	$\delta R_{DA}(BG)$	$\delta R_{DA}(\alpha)$	$\delta R_{DA}(\gamma)$	ΔR_{DA} (<i>total</i>), [Å]
(A) $\delta 26d$ / (D) $\beta\gamma$ - $\Delta b11a/\alpha$	74.9	0.027	0.046	0.016	0.0039	0.030	3.6
(A) $\delta 26d$ / (D) $\beta\gamma$ - $\Delta b8a/\alpha$	72.1	0.006	0.048	0.009	0.0033	0.030	2.8
(A) $\delta 26d$ / (D) $\beta\gamma$ - $\Delta b5a/\alpha$	80.5	0.013	0.043	0.015	0.0061	0.030	3.3
(D) $\delta 7a$ / (A) $\beta\gamma$ - $\Delta b14c/\alpha$	40.8	0.004	0.074	0.016	0.0001	0.030	1.9
(A) $\delta 10a$ / (D) $\beta\gamma$ - $\Delta b5c/\alpha$	67.3	0.025	0.044	0.005	0.0007	0.030	3.0
(A) $\alpha 12d$ / (D) $\delta 7d/\beta\gamma$ - Δb	39.3	0.006	0.083	0.019	0.0001	0.030	2.0
(A) $\alpha 12d$ / (D) $\beta\gamma$ - $\Delta b14a/\delta$	39.6	0.006	0.097	0.018	0.0001	0.030	2.2
(A) $\alpha 12d$ / (D) $\beta\gamma$ - $\Delta b29a/\delta$	37.6	0.005	0.086	0.017	0.0001	0.030	1.9
(A) $\alpha 26d$ / (D) $\beta\gamma$ - $\Delta b29a/\delta$	57.2	0.007	0.049	0.005	0.0006	0.030	2.2
(A) $\alpha 28d$ / (D) $\beta\gamma$ - $\Delta b29a/\delta$	62	0.005	0.044	0.005	0.0008	0.030	2.3
(A) $\delta 23d$ / (D) $\beta\gamma$ - $\Delta b29a/\alpha$	52.5	0.009	0.055	0.005	0.0003	0.030	2.1
(A) $\delta 26d$ / (D) $\beta\gamma$ - $\Delta b29a/\alpha$	51.5	0.006	0.068	0.004	0.0004	0.030	2.2
(A) $\delta 28d$ / (D) $\beta\gamma$ - $\Delta b29a/\alpha$	54.1	0.018	0.065	0.004	0.0007	0.030	2.5
(A) $\alpha 26d$ / (D) $\beta\gamma$ - $\Delta b34a/\delta$	56.2	0.006	0.050	0.015	0.0005	0.030	2.3
(A) $\alpha 26c$ / (D) $\delta 7a/\beta\gamma$ - Δb	52.6	0.027	0.053	0.006	0.0001	0.030	2.5
(A) $\alpha 12d$ / (D) $\beta\gamma$ - $\Delta b11a/\delta$	43.5	0.006	0.079	0.012	0.0001	0.030	2.1
(A) $\alpha 12d$ / (D) $\beta\gamma$ - $\Delta b8a/\delta$	48.2	0.003	0.067	0.008	0.0002	0.030	2.1
(A) $\alpha 12d$ / (D) $\beta\gamma$ - $\Delta b11a/\delta$	47.4	0.010	0.068	0.008	0.0002	0.030	2.1
(A) $\alpha 12d$ / (D) $\beta\gamma$ - $\Delta b34a/\delta$	51.5	0.011	0.062	0.007	0.0005	0.030	2.2

FRET pair	R_{DA}	δR_{DA} (<i>random</i>)	$\delta R'_{DA}(R_0)$	$\delta R_{DA}(BG)$	$\delta R_{DA}(\alpha)$	$\delta R_{DA}(\gamma)$	ΔR_{DA} (<i>total</i>), [Å]
(D) $\delta 23d$ / (A) $\beta\gamma$ - $\Delta b14c/\alpha$	48.1	0.026	0.061	0.008	0.0001	0.030	2.3
(A) $\alpha 26c$ / (D) $\delta 23a/\beta\gamma$ - Δb	57.2	0.008	0.049	0.006	0.0002	0.030	2.2
(A) $\alpha 28c$ /(D) $\delta 23a/\beta\gamma$ - Δb	63.0	0.011	0.048	0.005	0.0003	0.030	2.4
(A) $\delta 27d$ / (D) $\beta\gamma$ - $\Delta b34a/\alpha$	64.7	0.027	0.045	0.008	0.0005	0.030	2.9
(A) $\delta 27d$ / (D) $\beta\gamma$ - $\Delta b29a/\alpha$	50.5	0.020	0.058	0.008	0.0001	0.030	2.3
(A) $\delta 27d$ / (D) $\beta\gamma$ - $\Delta b14c/\alpha$	48.9	0.006	0.060	0.006	0.0001	0.030	2.0
(A) $\delta 27d$ / (D) $\beta\gamma$ - $\Delta b11c/\alpha$	62.0	0.005	0.049	0.007	0.0003	0.030	2.3
(A) $\delta 27d$ / (D) $\beta\gamma$ - $\Delta b8c/\alpha$	68.3	0.007	0.042	0.008	0.0006	0.030	2.5
(A) $\delta 27d$ / (D) $\beta\gamma$ - $\Delta b5c/\alpha$	68.2	0.009	0.043	0.008	0.0005	0.030	2.6
(A) $\delta 23d$ /(D) $\beta\gamma$ - $\Delta b5c/\alpha$	59.1	0.010	0.049	0.004	0.0003	0.030	2.3

Table 3.18 Experimentally obtained distances R_{DA} from PDA with corresponding relative error from PDA $\delta R_{DA}(\text{random})$, relative errors for Förster radius $\delta R'_{DA}(R_0)$, relative errors for backgrounds $\delta R_{DA}(BG)$, relative error for emission crosstalk $\delta R_{DA}(\alpha)$, and relative error for gamma $\delta R_{DA}(\gamma)$. Absolute distance error is $\Delta R_{DA}(\text{total})$ for J(abd) structure.

FRET pair	R_{DA}	$\delta R_{DA}(\text{random})$	$\delta R'_{DA}(R_0)$	$\delta R_{DA}(BG)$	$\delta R_{DA}(\alpha)$	$\delta R_{DA}(\gamma)$	$\Delta R_{DA}(\text{total})$, [Å]
(D)Y8b/(A) $\delta 10a/\alpha\beta\text{-}\Delta c$	47.5	0.004	0.065	0.018	0.0003	0.032	2.2
(D)Y8b/(A) $\delta 26d/\alpha\beta\text{-}\Delta c$	66.4	0.010	0.054	0.010	0.0034	0.032	2.8
(D)Y8b/(A) $\delta 28d/\alpha\beta\text{-}\Delta c$	70.5	0.008	0.052	0.010	0.0053	0.032	2.9
(D)Y8b/(A) $\delta 23d/\alpha\beta\text{-}\Delta c$	51.0	0.051	0.061	0.010	0.0006	0.032	3.4
(D)Y8b/(A) $\alpha\beta\text{-}\Delta c12d/\delta$	40.3	0.008	0.091	0.041	0.0001	0.038	2.8
(A) $\delta 10a$ / (D) $\alpha\beta\text{-}\Delta c28b/\gamma$	65.6	0.008	0.046	0.027	0.0017	0.038	3.4
(A) $\delta 28d$ / (D) $\alpha\beta\text{-}\Delta c28b/\gamma$	81.7	0.030	0.044	0.077	0.0090	0.038	7.7
(A) $\delta 26d$ / (D) $\alpha\beta\text{-}\Delta c28b/\gamma$	80.4	0.023	0.044	0.028	0.0083	0.038	4.5
(A) $\delta 23d$ / (D) $\alpha\beta\text{-}\Delta c28b/\gamma$	60.7	0.014	0.048	0.021	0.0013	0.038	3.1
(D) $\delta 7d$ / (A) $\alpha\beta\text{-}\Delta c22b/\gamma$	41.1	0.007	0.075	0.034	0.0001	0.032	2.4
(D) $\delta 7d$ / (A) $\alpha\beta\text{-}\Delta c12b/\gamma$	39.7	0.004	0.092	0.033	0.0001	0.032	2.4
(A)Y8b/ (D) $\delta 7a/\alpha\beta\text{-}\Delta c$	39.8	0.006	0.090	0.024	0.0001	0.032	2.3
(D)Y29a/ (A) $\alpha\beta\text{-}\Delta c12d/\delta$	52.3	0.015	0.061	0.012	0.0006	0.038	2.7
(D)Y29a/ (A) $\delta 28d/\alpha\beta\text{-}\Delta c$	76.6	0.037	0.047	0.026	0.0113	0.032	4.6
(D)Y29a/ (A) $\delta 26d/\alpha\beta\text{-}\Delta c$	69.6	0.061	0.051	0.016	0.0051	0.032	5.1
(D)Y29a/ (A) $\delta 23d/\alpha\beta\text{-}\Delta c$	68.4	0.030	0.042	0.018	0.0027	0.038	3.8

FRET pair	R_{DA}	δR_{DA} (<i>random</i>)	$\delta R'_{DA}(R_0)$	$\delta R_{DA}(BG)$	$\delta R_{DA}(\alpha)$	$\delta R_{DA}(\gamma)$	ΔR_{DA} (<i>total</i>), [Å]
(D)Y29a/ (A) $\alpha\beta$ - $\Delta c22b/\delta$	47.4	0.014	0.061	0.011	0.0010	0.032	2.1
(A) $\delta 10a$ / (D) $\alpha\beta$ - $\Delta c23b/\gamma$	47.4	0.004	0.069	0.021	0.0002	0.038	2.5
(D)Y24a/ (A) $\delta 23d/\alpha\beta$ - Δc	51.6	0.009	0.056	0.008	0.0003	0.038	2.4
(D)Y24a/ (A) $\delta 26d/\alpha\beta$ - Δc	50.7	0.004	0.071	0.007	0.0004	0.038	2.5
(D)Y24a/ (A) $\delta 28d/\alpha\beta$ - Δc	53.0	0.006	0.067	0.006	0.0005	0.038	2.6
(D)Y24a/ (A) $\alpha\beta$ - $\Delta c22b/\delta$	42.6	0.005	0.068	0.020	0.0001	0.038	2.2
(D)Y24a/ (A) $\alpha\beta$ - $\Delta c12d/\delta$	38.0	0.008	0.086	0.029	0.0001	0.038	2.3
(A) $\delta 10a$ / (D) $\alpha\beta$ - $\Delta c22b/\gamma$	46.2	0.003	0.070	0.012	0.0003	0.038	2.3
(A) $\delta 26d$ / (D) $\alpha\beta$ - $\Delta c22b/\gamma$	66.2	0.007	0.055	0.008	0.0021	0.038	3.1
(A) $\delta 28d$ / (D) $\alpha\beta$ - $\Delta c22b/\gamma$	72.9	0.014	0.050	0.013	0.0044	0.038	3.5
(D)Y29a/ (A) $\delta 27d/\alpha\beta$ - Δc	64.0	0.009	0.045	0.011	0.0032	0.032	2.6
(A) $\delta 27d$ / (D) $\alpha\beta$ - $\Delta c22b/\gamma$	59.8	0.008	0.051	0.008	0.0011	0.032	2.4
(A) $\delta 27d$ / (D) $\alpha\beta$ - $\Delta c23b/\gamma$	63.5	0.009	0.048	0.009	0.0024	0.032	2.6
(D)Y24a/ (A) $\delta 27d/\alpha\beta$ - Δc	50.8	0.006	0.059	0.013	0.0003	0.032	2.2
(D)Y8b/ (A) $\delta 27d/\alpha\beta$ - Δc	52.4	0.004	0.059	0.012	0.0004	0.032	2.2
(D) $\delta 23d$ / (A) $\alpha\beta$ - $\Delta c22b/\gamma$	57.2	0.008	0.051	0.012	0.0008	0.032	2.4
(A)Y24a/ (D) $\delta 23d/\alpha\beta$ - Δc	56.7	0.006	0.054	0.008	0.0010	0.032	2.3
(A) $\delta 26d$ / (D) $\alpha\beta$ - $\Delta c23b/\gamma$	70.8	0.004	0.053	0.015	0.0030	0.038	3.4
(D)Y27b/ (A) $\delta 27d/\alpha\beta$ - Δc	57.9	0.017	0.051	0.007	0.0019	0.032	2.5

FRET pair	R_{DA}	δR_{DA} (<i>random</i>)	$\delta R'_{DA}(R_0)$	$\delta R_{DA}(BG)$	$\delta R_{DA}(\alpha)$	$\delta R_{DA}(\gamma)$	ΔR_{DA} (<i>total</i>), [Å]
(A) $\delta 27d$ / (D) $\alpha\beta$ - $\Delta c28b$ / γ	70.0	0.030	0.042	0.028	0.0046	0.032	3.9
(A) $\delta 28d$ / (D) $\alpha\beta$ - $\Delta c23b$ / γ	68.9	0.004	0.054	0.013	0.0020	0.038	3.3
(A) $\delta 23d$ / (D) $\alpha\beta$ - $\Delta c23b$ / γ	57.5	0.010	0.053	0.005	0.0009	0.038	2.7
(A) $\delta 8a$ / (D) $\alpha\beta$ - $\Delta c22b$ / γ	35.7	0.010	0.087	0.039	0.0000	0.038	2.4
(A) $\delta 8a$ / (D) $\alpha\beta$ - $\Delta c23b$ / γ	39.1	0.008	0.080	0.028	0.0001	0.038	2.3
(A) $\delta 8a$ / (D) $\alpha\beta$ - $\Delta c28b$ / γ	48.4	0.009	0.064	0.010	0.0003	0.038	2.4
(D) $\gamma 27a$ / (A) $\alpha\beta$ - $\Delta c12d$ / δ	43.8	0.008	0.075	0.012	0.0001	0.038	2.3
(D) $\gamma 8b$ / (A) $\delta 10a$ / $\alpha\beta$ - Δc	47.5	0.004	0.065	0.018	0.0003	0.032	2.2

3.3.5 Model selection

Four different RBD models were generated based on the distinct bond criteria for the junction (Table 3.3). Models were evaluated quantitatively by χ_r^2 , RMSD and visual inspection of the Watson-Crick base pairing (Table 3.19, Figure 3.20-3.22). Structures modeled with „GC-rigid, AU-rigid“ have the highest χ_r^2 , and thus were discarded for further analysis. The structures obtained with „GC-rigid, AU-soft“ violate FRET restraints and hence χ_r^2 is still high (Table 3.19).

Next, still accounting for Watson –Crick bases pairing, I explore „GC-stiff AU-soft“ model (Table 3.3 and Table 3.4). Overall comparison of the „GC-stiff AU-soft“ model with „GC-rigid, AU-soft“ reveals decreasing in χ_r^2 (Table 3.19).

The previously used model „GC-soft AU-soft“ for RNA 3WJ studies¹²⁶ does not account for differences in the bond rigidity in Watson –Crick bases pairing, however the structural differences between this model and model „GC-stiff AU-soft“ results in a similar χ_r^2 (Table 3.19). The biggest discrepancy is observed in the junction area, whereas helices are perfectly aligned for J(abd), J(bcd) and slightly misaligned for J(acd). As RNA constructs do not have fluorescence labels in the junction area, this FRET study cannot resolve junction and support structural configuration of any model.

Table 3.19 Trial models and goodness of the fit for the best RBD models. All RNA 3WJ are simulated with models with particular bond-error configuration (Table 3.3). The fit quality are judged with χ_r^2 .

System of study	Base pairs in the junction	Model			
		GC-soft AU-soft	GC-stiff, AU-soft	GC-rigid, AU-soft	GC-rigid, AU-rigid
		χ_r^2			
J(abd)	2 AU+1 GC	1.22	1.24	1.22	3.00
J(bcd)	3 AU	1.04	1.05	1.36	1.88
J(acd)	2 AU+1 GC	1.30	1.32	1.64	2.08
J(abc)	2 AU+1 GC	1.91	1.97	2.11	5.17

In conclusion it is proposed to use „GC-stiff AU-soft“ model as it optimizes hydrogen bond’s flexibility for Watson-Crick base pairs, provides enough flexibility due to the junction fragmentation into 12 pieces and finally optimally low χ_r^2 .

3.3.6 Visual representation and comparison of RNA 3WJ

Three dimensional RNA structures were obtained using Rigid Body Docking approach (Chapter 3.2.9.3) and visualized with Pymol 2.3¹⁵⁹. Selected model “GC-stiff AU-soft” was compared visually with complementary models “GC-soft AU-soft” and “GC-rigid AU-soft” (Table 3.4). For all studied structures model “GC-stiff AU-soft” and model “GC-soft AU-soft” provide very similar structures with RMSD below 2 Å (Figure 3.20-3.22B) and very similar χ_r^2 (Table 3.19). Comparison of the structures obtained with model “GC-stiff AU-soft” and model “GC-rigid AU-soft” gives diverse results for different structures. J(abd) (Figure 3.20A) shows that model “GC-rigid AU-soft” (in red) differs from model “GC-stiff AU-soft” (gray) in the junction and in one of the helical orientation. This difference is registered with RMSD=5.04.

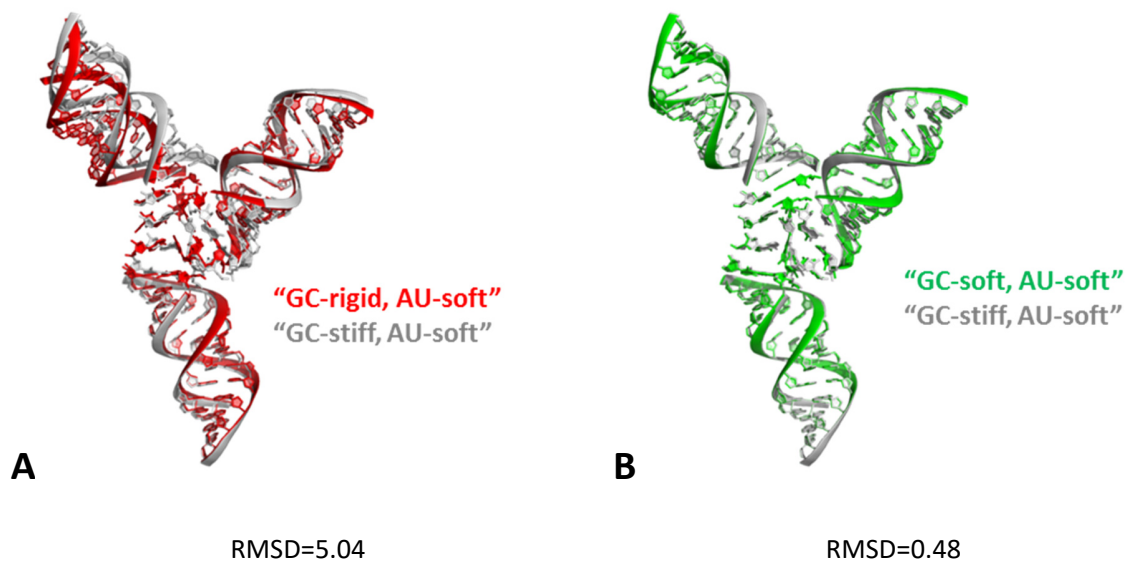


Figure 3.20 Visual representation of the simulated J(abd) structure, using different models: model "GC-rigid, AU-soft" in red, model "GC-soft, AU-soft" in green, model "GC-stiff, AU-soft" in gray. RMSD between P atoms of different structures indicates the structural similarity.

The discrepancy between "GC-rigid AU-soft" and "GC-stiff AU-soft" for J(acd) is less pronounced and resulted in RMSD=1.90

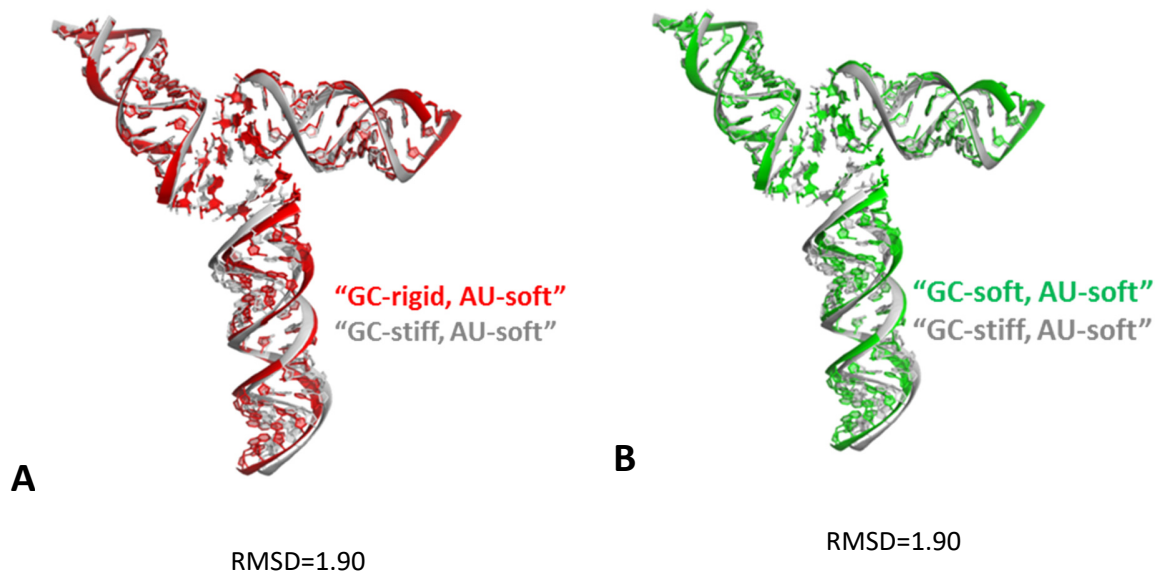


Figure 3.21 Visual representation of the simulated J(acd) structure, using different models: model "GC-rigid, AU-soft" in red, model "GC-soft, AU-soft" in green, model "GC-stiff, AU-soft" in gray. RMSD between P atoms of different structures indicates the structural similarity.

The model comparison for structure J(bcd) shows that model “GC-stiff AU-soft” and model “GC-rigid AU-soft” gives similar results (RMSD=1.47, Figure 3.22A) whereas the discrepancy between model “GC-stiff AU-soft” and model “GC-soft AU-soft” is even smaller (RMSD=0.57, Figure 3.22B).

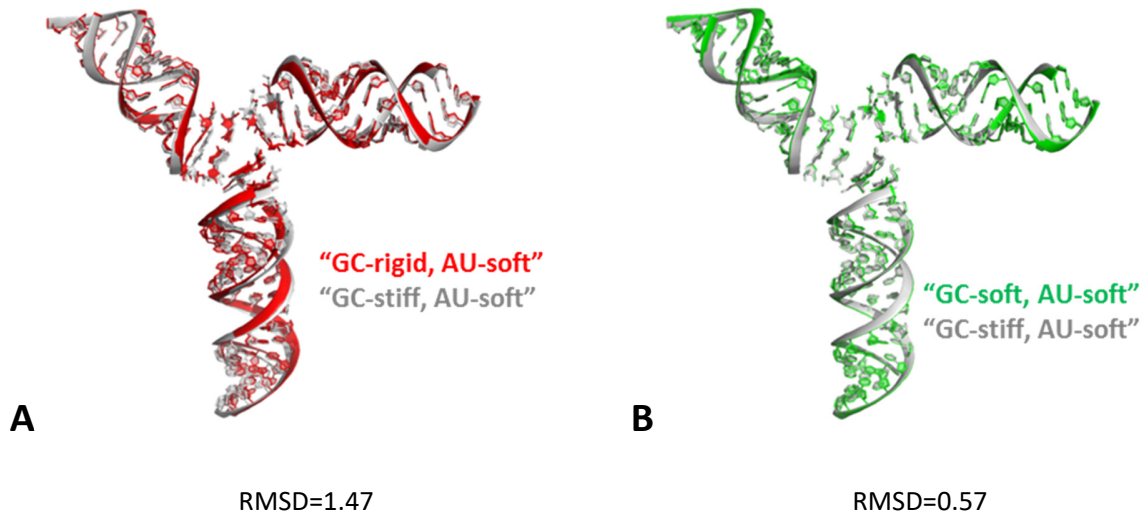


Figure 3.22 Visual representation of the simulated J(bcd) structure, using different models: model “GC-rigid, AU-soft” in red, model “GC-soft, AU-soft” in green, model “GC-stiff, AU-soft” in gray. RMSD between P atoms of different structures indicates the structural similarity.

3.3.7 Cluster analysis of the rigid body docking (RBD) results

Discrimination of the family of the best structures for selected “GC-stiff, AU-soft” model was done by cluster analysis (Figure 3.23). The reduced $\chi_{r,FRET}^2$ of the docked structures is plotted versus RMSD with respect to the best docked structure (Figure 3.24). Note, that J(abd) RBD ensemble has structures with lower χ_{FRET}^2 than the best RBD structure (green star in Figure 3.23B). This is due to the fact that when the best structure is selected, χ_{clash}^2 contribution is taken into account as well (Eq.102). The best structure for each RNA3WJ construct is depicted with green star in the Figure 3.23 and its three-dimensional structure used for structural comparison within all RNA 3WJ constructs (Chapter 3.3.8). 95% confidence interval is shaded with green and depends on the number of degrees of freedom of the model. Here $N_{dof} = 36$ for J(bcd), $N_{dof} = 39$ for J(acd) and $N_{dof} = 36$ for J(abd) and $N_{dof} = 38$ for J(abc) (see Chapter 3.2.10). Also the visual inspection of the Figure 3.23 indicates that there is always a family of structures with RMSD < 2 Å for every construct, indicating several unique solutions. The best structures within corresponding family are visualized in Figure 3.24.

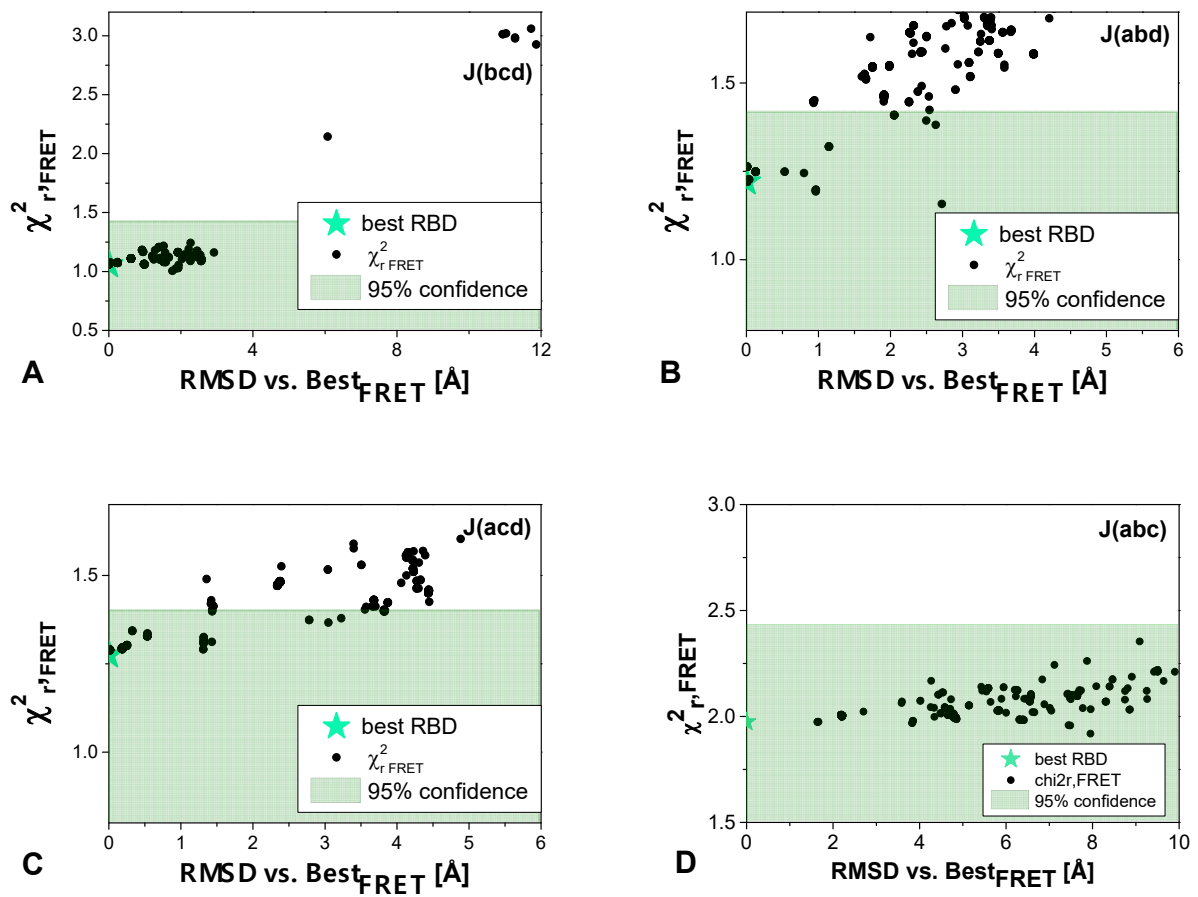


Figure 3.23 Model discrimination with cluster analysis (black points) of (A) J(bcd) structure; (B) J(abd) structure; (C) J(acd) structure; (D) J(abc) structure. Green area represents 95% confident interval, the best RBD solution is shown with green star.

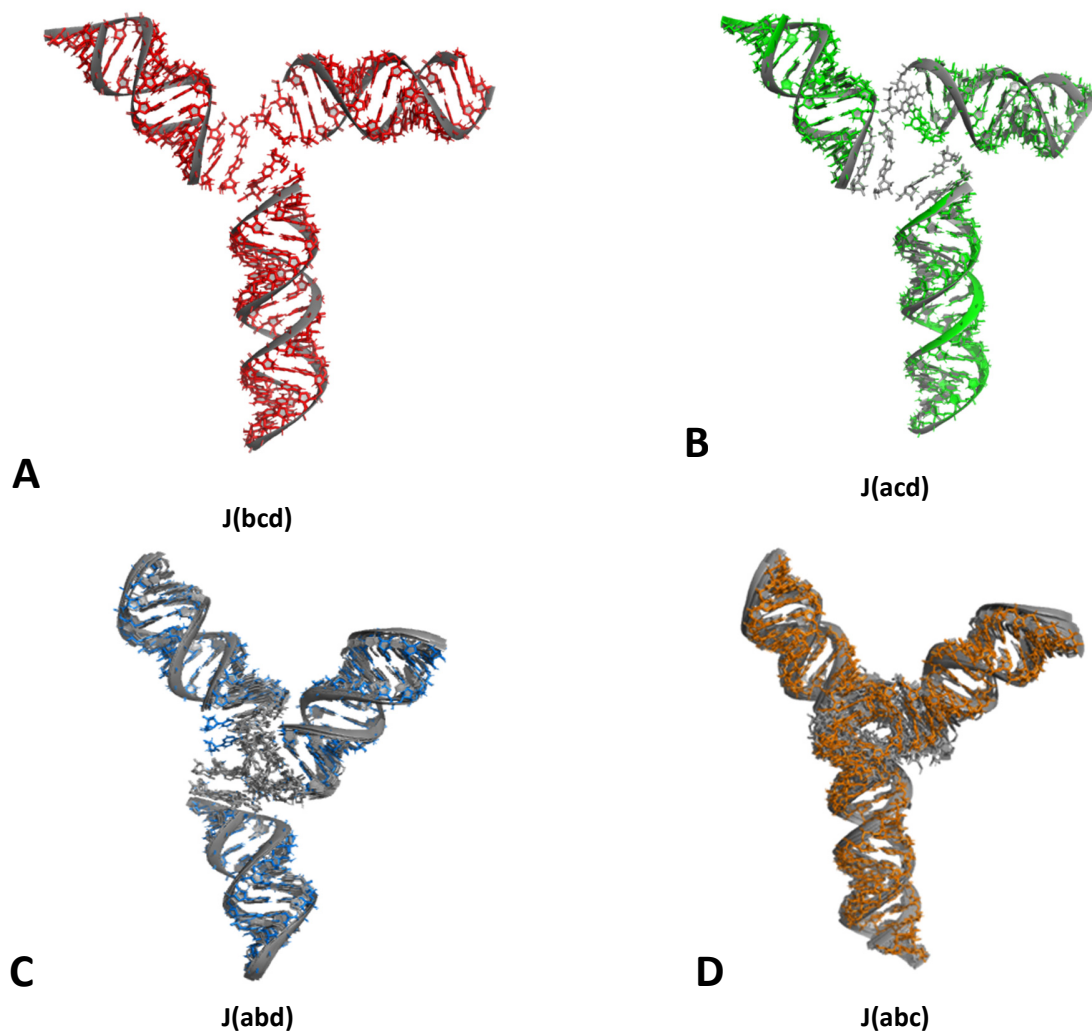


Figure 3.24 Visualization of the selected best structures from Figure 3.24. Colored sticks represent structure with the lowest $\chi^2_{r,FRET}$ (green star in Figure 3.23) whereas cartoon represent the best family within 95% confidence interval and $RMSD < 2 \text{ \AA}$. (A) J(bcd) structure; (B) J(bcd); (C) J(acd); (D) J(abc).

3.3.7.1 Model assessment

To test the accuracy of the selected model, deviations between the best RBD model distances R_{model} and the experimental distances $\langle R_{DA} \rangle_E$, weighted by experimental error ΔR_{DA} are plotted (Figure 3.25). Individual deviations are shown as weighted residuals in the bottom part of each plot. All deviations are assembled in histograms (upper plot) and fitted with Gaussian (magenta curve) distribution. This analysis allows detecting systematic errors if there is any.

For J(bcd) structure the center of the Gaussian fit of the weighted distance deviation is around zero ($x_{center} = -0.05$, $\sigma = 0.53$), indicating that there are no systematic deviations of the model. Model distances are slightly

larger than experimental distances for other structures ($J(\text{abd})= x_{\text{center}}= -0.5, \sigma=0.60$; $J(\text{acd}): x_{\text{center}}= -0.5, \sigma=0.58$; $J(\text{abc}): x_{\text{center}}= -0.5, \sigma=1.12$). This might indicate possible outliers in measured distances $\langle R_{DA} \rangle_E$ in RNA constructs with helix a . One of the possible reason could be quenching processes (Chapter 3.3.1) on the end labeled donor (position (D) γ 29a ($J(\text{abd}), J(\text{abc})$) or equivalent (D) $\beta\gamma$ - Δ b34a ($J(\text{acd})$) that strongly affects distance determination.

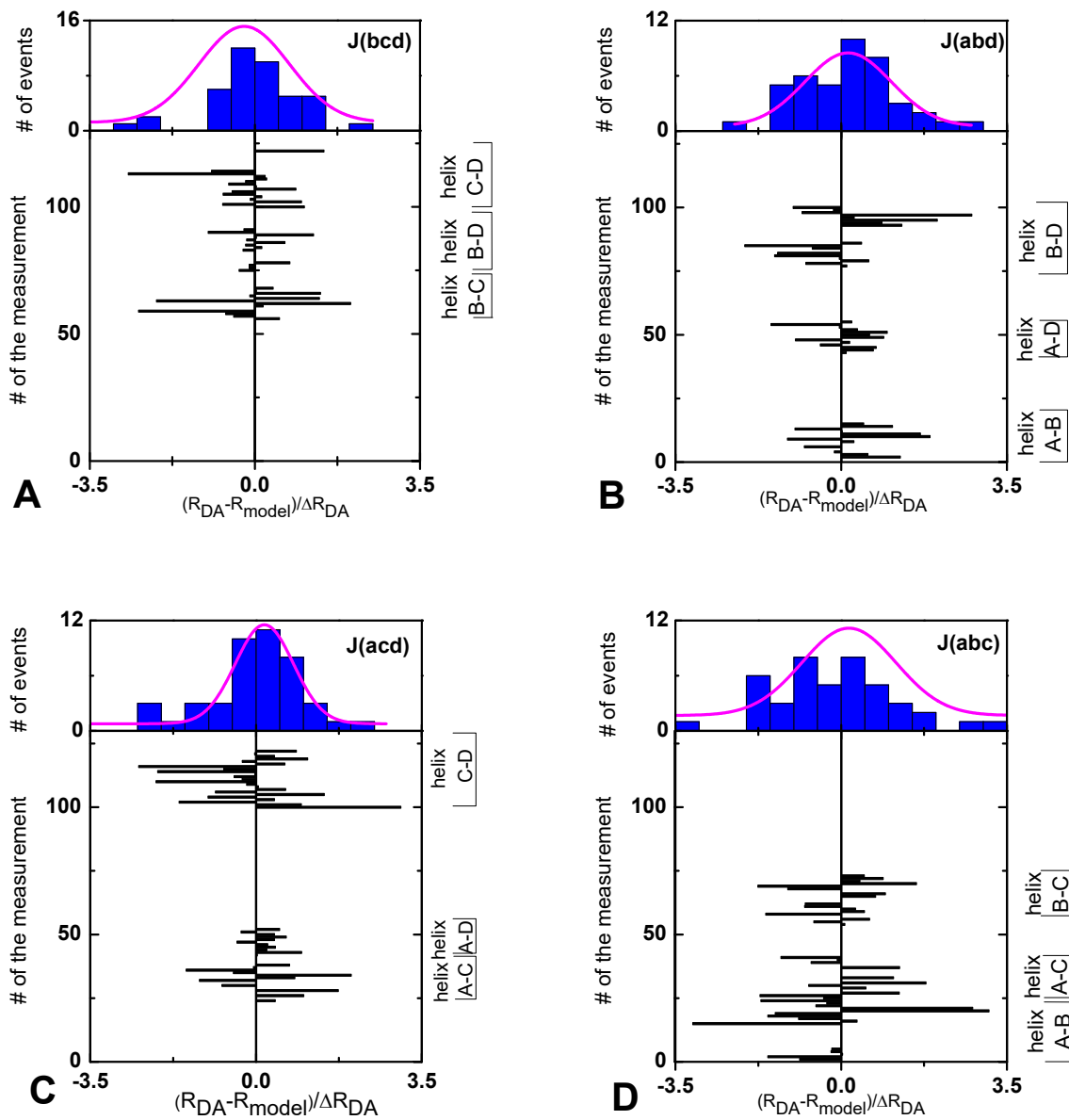


Figure 3.25 Frequency histograms of all experimental deviations $\langle R_{DA} \rangle_E$ from model distances R_{model} weighted by experimental error ΔR_{DA} (upper plots) with Gaussian fit (magenta curve). Correspondent residuals are depicted on the

bottom part. All residual plots share the same order of the interhelical FRET distances, right y-axis indicate the pair of helices interconnected by FRET distance, empty line indicate that particular FRET pair was not measured for specific molecule. (A) structure J(bcd); (B) structure J(abd); (C) structure J(acd); (D) structure J(abc).

Another way of approaching this problem is plotting the scatter plots of experimental $\langle R_{DA} \rangle_E$ distances versus model distances R_{model} (Figure 3.26). Additionally, experimental errors (Chapter 3.2.8) are also shown. In the absence of the systematic errors, points should be scattered around 1:1 line. Linear regression (red line) indicates almost no significant systematic deviations and follows nearly 1:1 line (gray line) for J(bcd), J(abd) and J(acd) with slight tendency of overestimating experimental distances. The deviations are even bigger for J(abc) construct.

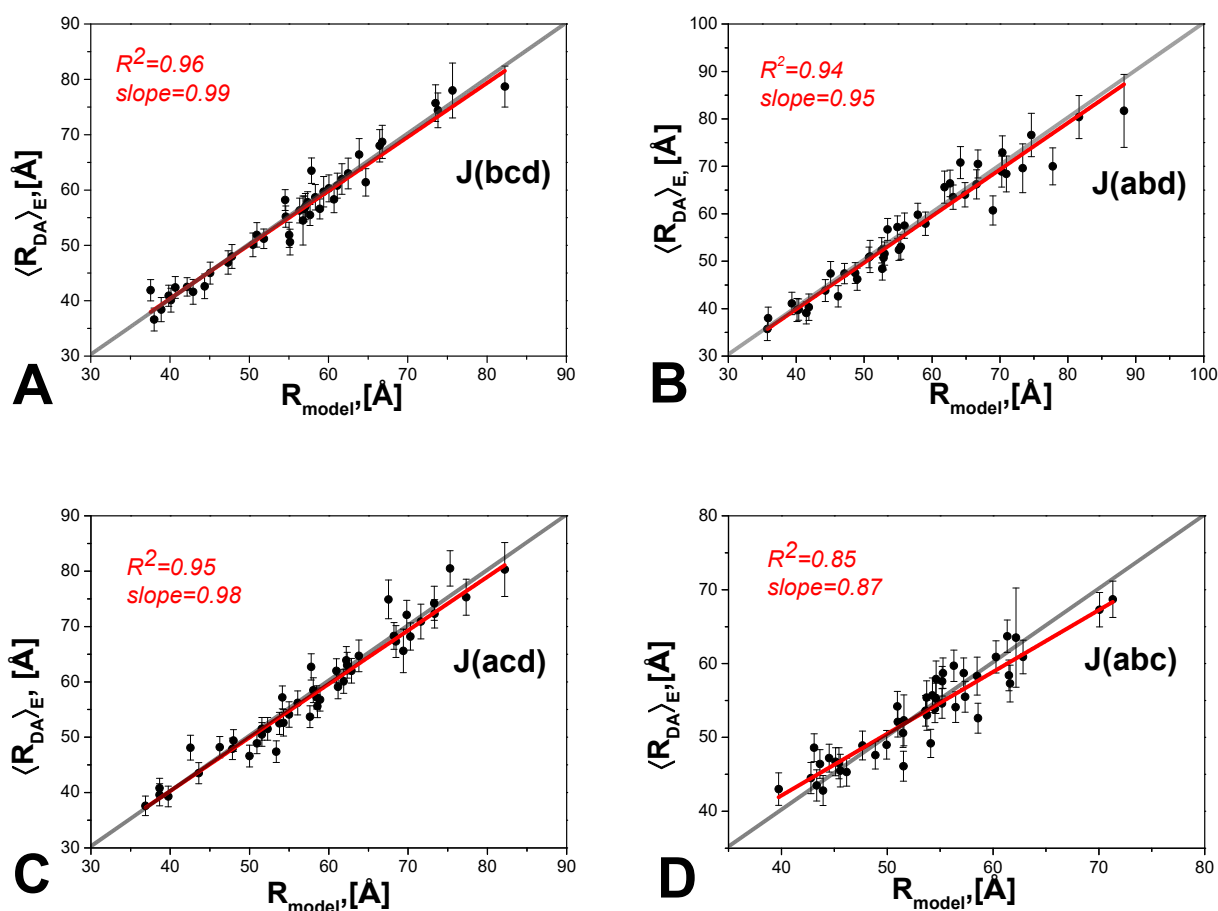


Figure 3.26 The experimental distances $\langle R_{DA} \rangle_E$ obtained from PDA analysis with experimental errors are plotted against model distances R_{model} for the collection of RNA 3WJ constructs. Red line is the linear regression and black line is 1:1 line. (A) structure J(bcd); (B) structure J(abd); (C) structure J(acd); (D) structure J(abc).

3.3.8 Conformational space for RBD structures

This chapter presents the study of the structural similarity based on different alignment methods and comparison of the geometrical parameters. Based on selected criteria (Chapter 3.3.6), structures modeled with “GC-stiff, AU-soft” model are chosen for further analysis (Figure 3.27).

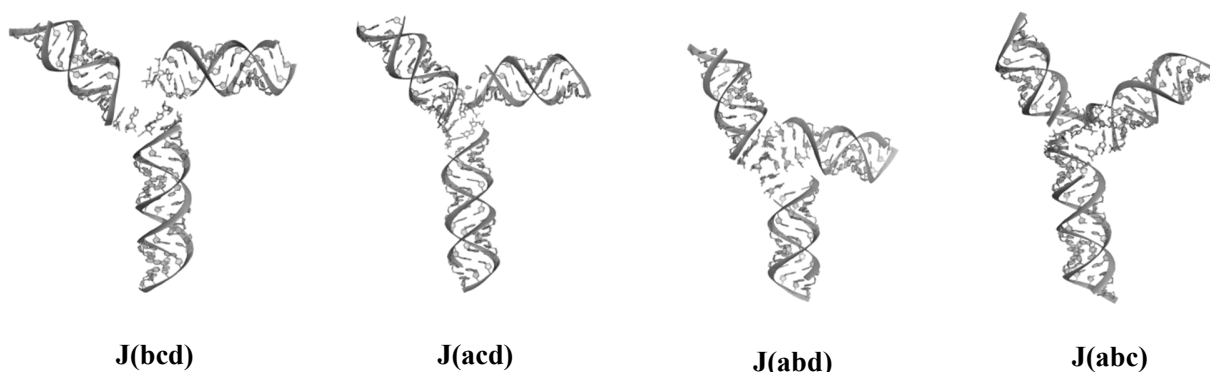


Figure 3.27 Best RNA 3WJ structures with the lowest χ_r^2

RNA 3WJ conformations can be designated through Euler angles that characterize the orientation of the helices with respect to each other^{160,161}. This information is a key to understanding whether the studied RNA3WJ molecules are structurally similar. Here, two strategies of structural comparison based on Euler angles are proposed.

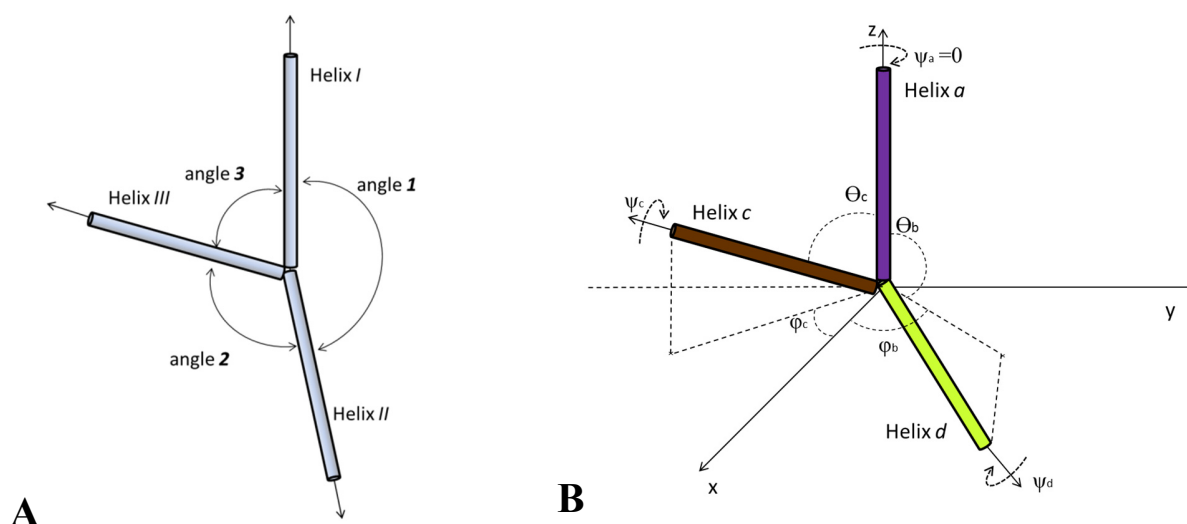


Figure 3.28 Schematic representation of mutual (A) and Euler (B) angles describing the steric helical orientation demonstrated on the J(acd) structure.

First, the structures are compared by their shape. In this case, the individual sequence information is ignored and the RNA 3WJ constructs are compared via mutual angles according to an established routine. Note that each RNA 3WJ has an individual set of three helices out of four possible (Figure 3.1) and thus, within the given naming system, it is impossible to compare the structures even in pairs as they share only two out of three helices, e.g. J(abd) and J(acd). Therefore, to be able to compare structures with different helical names, a different naming convention is needed.

Mutual angles were calculated for each structure and the helix names were assigned such that the largest mutual angle (*angle 1*) is always between Helix *I* and Helix *II*, second largest angle (*angle 2*) is between Helix *II* and Helix *III* and the smallest angle (*angle 3*) is between Helix *III* and Helix *I* (Figure 3.28A, Table 3.20). This transition from the letters *a, b, c, d* to roman numbers *I, II, III* distinguishes sequence-based alignment from structural alignment and helps to compare RNA 3WJ with different sequences.

Table 3.20 Reassignment of the helical names. Letters *a, b, c, d* change from sequence-based naming to the shape-base nomenclature of the roman numbers.

Structure	Helix <i>I</i>	Helix <i>II</i>	Helix <i>III</i>
J(abc)	Helix b	Helix c	Helix a
J(abd)	Helix b	Helix d	Helix a
J(acd)	Helix c	Helix d	Helix a
J(bcd)	Helix c	Helix d	Helix b

For a comprehensive description of the obtained 3D structures, such as exact orientation and helical rotation, complete set of Euler angles can be calculated for each construct and compared between all RNA systems. In this approach the shape-based naming is used. The coordinate system is chosen such that the rotation matrix of helix *I* is always an identity matrix. That means that helix *I* lies along z-axis, its Euler angles equals zero ($\varphi_I, \theta_I, \psi_I = 0$) and the first P-atom of the first nucleotide on the 5'-end serves as the rotation pivot point with rotation angle $\psi_{P_atom} = -50.86^\circ$.

Alignment is always done via helix *I* for each structure. The mutual angle θ between helix pairs indicates the general shape and the angles φ and ψ define the twist of helices and the planarity of the junction in a given coordinate system (Figure 3.28B).

3.3.8.1 Mutual angles

The best structure after docking (structure with the lowest χ_r^2) for each RNA 3WJ was bootstrapped 10000 times and the structures within the 68%, 87% and 95% confidence levels were selected for display (Figure 3.30B). Figure 3.29A demonstrates mutual angle *I* vs mutual angle *II* for selected bootstrapped J(abd) structures. The inner light blue contour corresponds to the 1 σ (68%), the middle blue contour to 1.5 σ (87%), and outer dark blue to the 2 σ (95%) confidence interval. Such analysis was carried out for all combinations of mutual angles for all RNA 3WJ structures and the result is displayed in Figure 3.30B. The results demonstrate a wide angular distribution for bootstrapped structures. For J(acd) and J(abd) angle *I* can reach up to 180°, indicating approximate coaxial helical stacking of helices C-D and helices B-D (Figure 3.30B). The largest angle *I* is similar for structures J(bcd) and J(abc) within the 1.5 σ confidence interval, but unlike other two structures does not reach 180° and thus coaxial helical stacking is not observed for J(bcd) and J(abc). In conclusion, due to the high overlap of the distributions, the shapes of the studied RNA 3WJ as indicated by the mutual angles, are not distinguishable within given confidence intervals.

Data for J(abc) structures has been measured in the previous work and provided by H. Vardanyan.

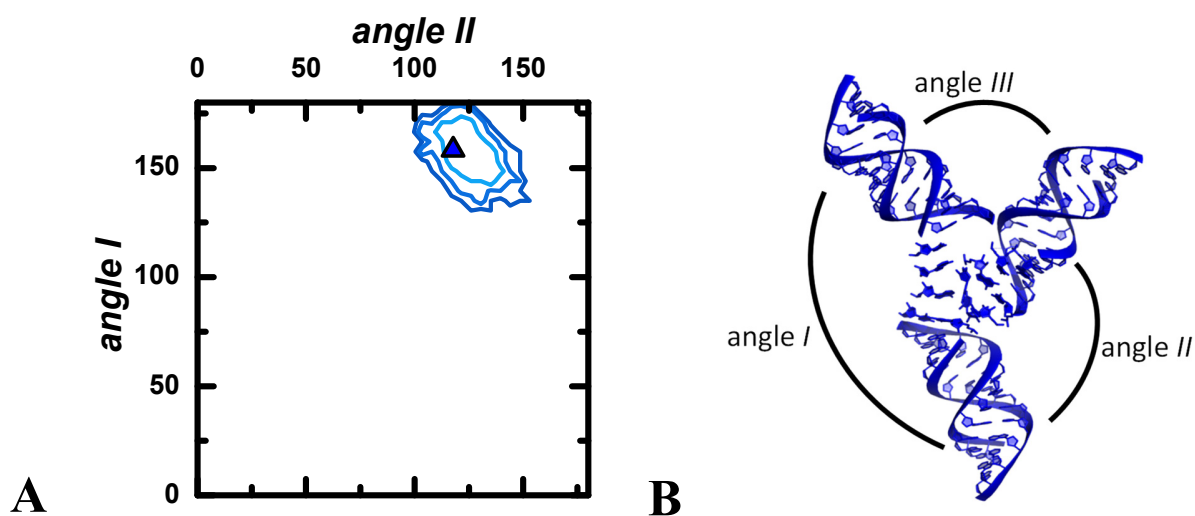


Figure 3.29 (A) Visual representation of the biggest mutual angle *I* vs second biggest angle *II* for bootstrapped J(abd) structures with 68%, 87% and 95% confidence intervals, represented by light blue, blue and dark blue respectively. The blue triangle indicates the structure with the lowest χ_r^2 . (the best structure); (B) The best J(abd) structure after Rigid Body Docking modeling. All mutual angles are shown schematically: the largest angle (angle *I*), the second large (angle *II*) and the smallest angle (angle *III*).

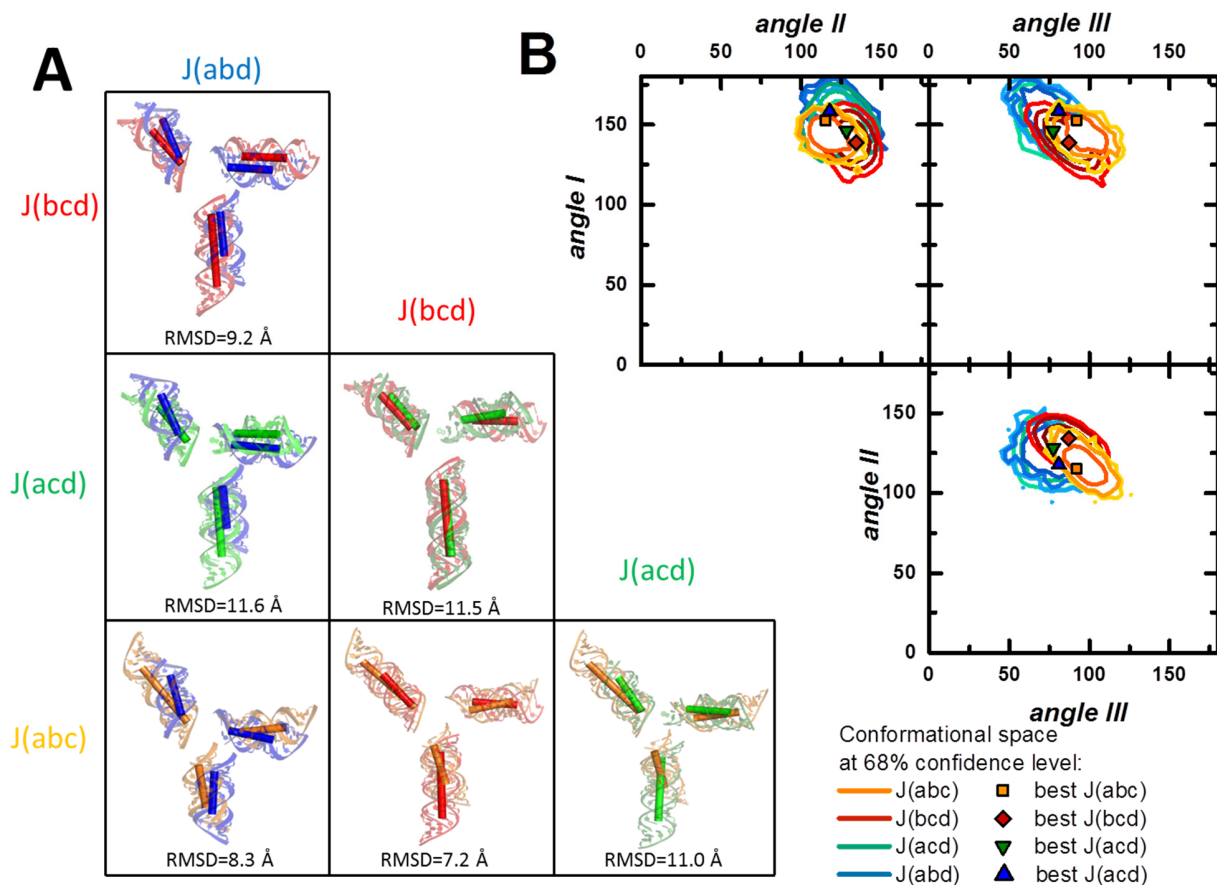


Figure 3.30 (A) Visual representation of the RNA 3WJs with the lowest χ_r^2 (the best structures) aligned via mutual angles pairwise in all possible combinations. Alignment is carried out only via helices, while the junctions are not considered. This plot should be read as a matrix, e.g. the first column represents the overlay of J(abd) with all other possible structures, whereas second row represents alignment with J(acd). Then, the cross-section of the first column and second row shows the overlay between J(abd) and J(acd). The RMSD values between phosphorous atoms are shown below each overlay. Large values indicate that even though helices have similar mutual angles, they differ in their rotation; (B) The best structures are shown with symbols and in the same colors as in (A): J(abd) in blue up-triangle, J(acd) in green down-triangle, J(bcd) in red diamond and J(abc) in orange square. Exact values for mutual angles for the best structures are presented in Table 3.21. Visual representation of the mutual angles for bootstrapped structures with 68%, 87% and 95% confidence intervals are shown as contours. J(abd) in blue hues, J(acd)-in green hues, J(bcd) – in red hues and J(abc) –orange hues.

Visual representation of the best docked structures is shown in Figure 3.30. Alignment is done only via helices, omitting first two base-pairs in the junction. The RMSD between P atoms is reported based on given alignment.

Mutual angles values for the best docked structures (structures with the lowest χ_r^2) after Rigid Body Docking modeling are provided in the Table 3.21.

Table 3.21 Mutual angles values for the best RBD structures with the lowest χ_r^2 for studied RNA 3WJ and J(abc) for comparison. Helices that form the angle are shown in brackets.

Structure	Angle I (helical pair)	Angle II (helical pair)	Angle III (helical pair)
J(abd)	158.3° (d-b)	117.8°(a-d)	80.9°(a-b)
J(acd)	146.1° (d-c)	128.2°(a-d)	77.4°(a-c)
J(bcd)	138.8° (d-c)	134.1°(b-d)	87.0°(c-b)
J(abc)	152.6° (c-b)	115.3°(a-c)	92.1°(a-b)

3.3.8.2 Rotation angles

The global conformation of RNA 3WJ is defined not only by the mutual arrangement but also by helical rotation. A full description of the helical orientation can be extracted from the calculation of Euler angles (Figure 3.28B) with respect to a fixed coordinate system. Here, the previously discussed mutual angle is denoted as θ , rotation around the helical axis ψ is given, and ϕ indicates the angle between helical projection and the axis. Subscripts indicate the helical number according to the established designation in Figure 3.28A and at the beginning of the chapter. As mentioned above, all angles of the helix I are zero and thus not further discussed. Euler angles of the helices II and III are illustrated in Figure 3.31. The reassignment from roman numbers to Latin letters for the helix names is provided in Table 3.20. Topological confinement for selected structures is illustrated within 68%, 87% and 95% confidence levels. Figure 3.31A illustrates the orientation map for helix II. The rotation of helix ψ_{II} is widely distributed for all structures, indicating diverse rotational conformation for the particular helices in RNA 3WJ. Interestingly, ψ_{II} for J(abd) (in blue) covers $[-\pi;\pi]$ space, indicating loss of this degree of freedom, or so-called gimbal lock. The same observation is valid for the ϕ_{II} angle for J(abd). ϕ_{II} for J(acd) (green) structure is also widely distributed and aligns with J(bcd) within all three suggested confidence intervals and only within 2σ with J(abc) (orange).

Analysis of angles of the helix *III* (Figure 3.31B) reveals that for φ_{III} the different structures prefer to cluster in groups by J(abd) with J(abc) and another group J(bcd) with J(acd). These groups do not overlay within 95% confidence interval. All four studied RNA 3WJ have similar ψ_{III} angle within all suggested confidence intervals.

In summary, the data suggests that topologically allowed range of helical rotation can be slightly modulated by sequence variation.

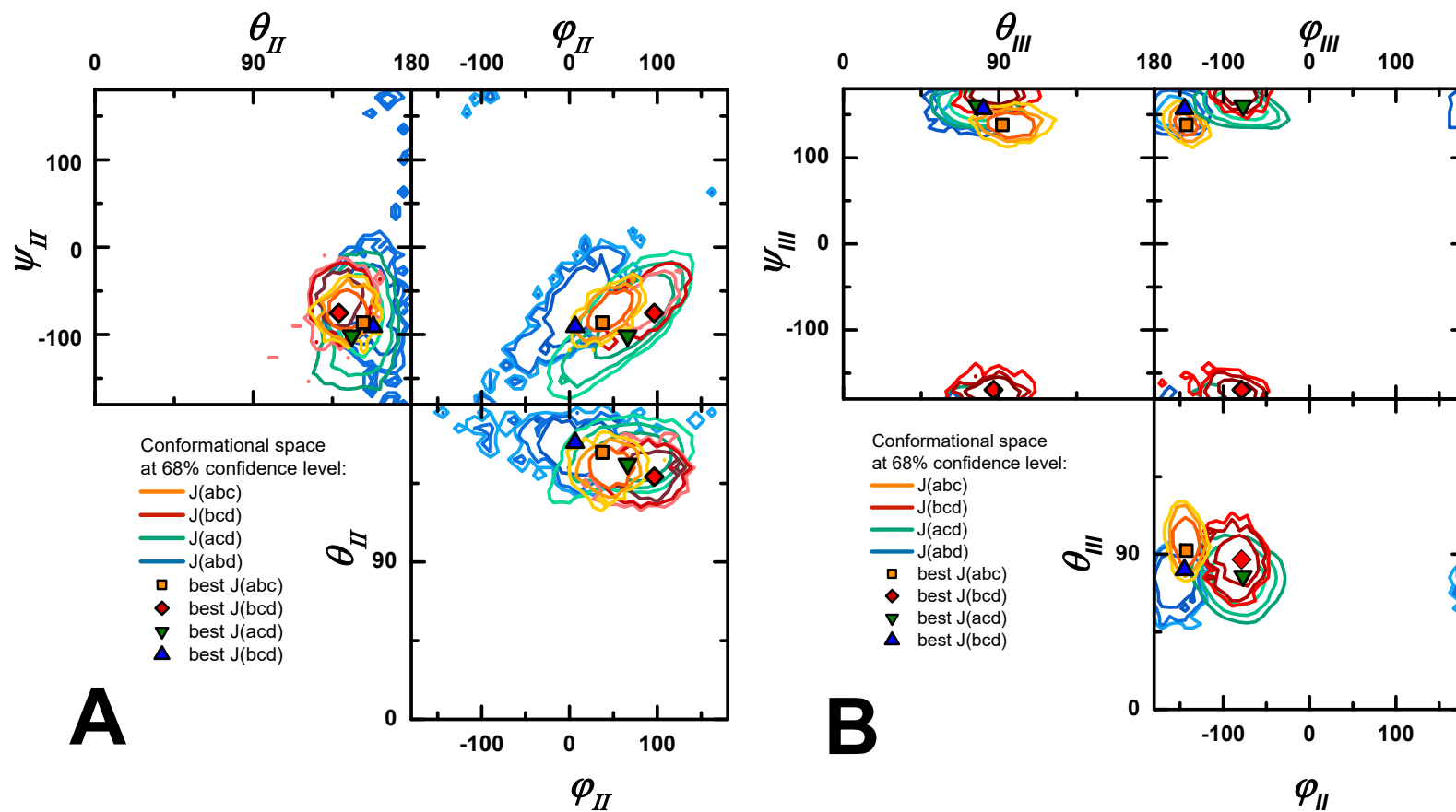


Figure 3.31 Error range for orientation of helices: (A) helices forming the angle II and (B) helices forming the angle III in terms of Euler angles with 68%, 87% and 95% confidence interval. Here, bootstrapped structure s are depicted as: J(bcd) in red hues, J(acd) in green hues, J(abd) in blue hues and J(abc) in orange hues. The best structures are shown with symbols and in the same colors as contours: J(abd) in blue up-triangle, J(acd) in green down-triangle, J(bcd) in red diamond and J(abc) in orange square.

3.3.8.3 Structural planarity

In order to investigate the structural planarity of RNA 3WJ, the coplanarity score can be calculated. A set of vectors are coplanar if they have the same initial point and lie in the same plane. Geometrically, the absolute value of the triple product defines the volume V of the parallelepiped with sides represented as three vectors (Figure 3.32). So, if these three vectors are coplanar, then the triple product of these three 3-dimensional vectors \vec{a} , \vec{b} and \vec{c} equals zero¹⁶² (Eq. 108), meaning that the parallelepiped defined by them is flat and has no volume.

$$V = \vec{a} \cdot (\vec{b} \times \vec{c}) \quad (108)$$

Swapping any two of the three operands gives the negative value of the triple product and is called left-handed triple.

$$V = \vec{a} \cdot (\vec{b} \times \vec{c}) = -\vec{a} \cdot (\vec{c} \times \vec{b}) \quad (109)$$

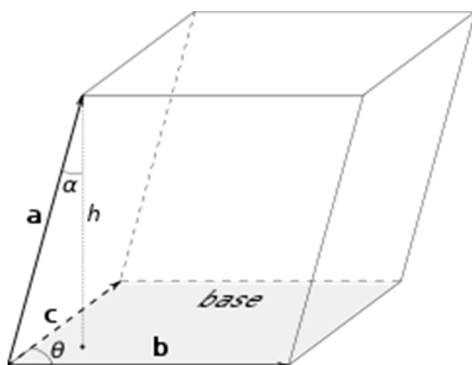


Figure 3.32 Three vectors \vec{a} , \vec{b} , \vec{c} defining a parallelepiped. Figure is taken from Wikipedia.

I analyzed all structures within 95% confidence interval. For each RNA configuration within the collected ensemble, each helix was represented by a vector and then the triple product was calculated for each 3WJ. The coplanarity distribution is shown in Figure 3.33.

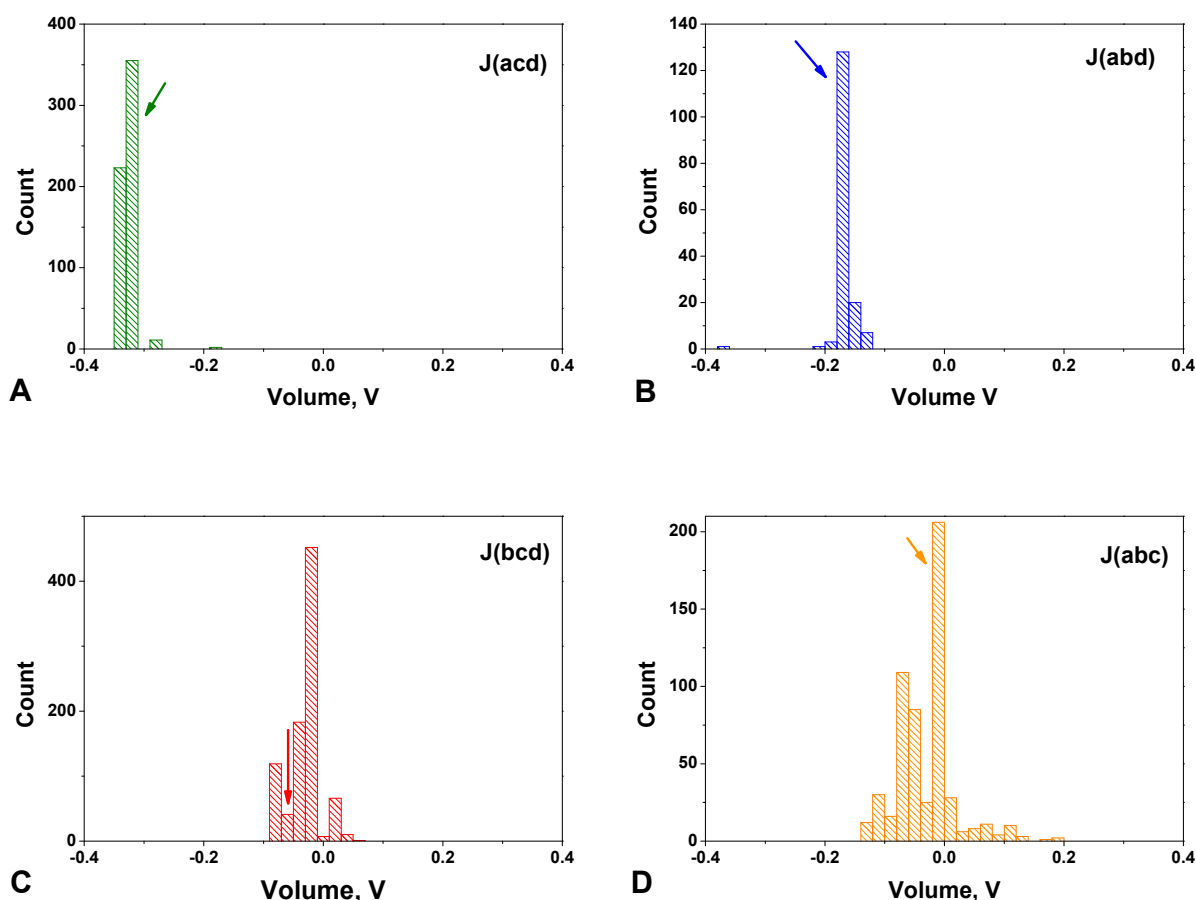


Figure 3.33 Coplanarity distribution within 95% confidence interval for structures (A): J(acd) in green; (B) J(abd) in blue; (C) J(bcd) in red; (D) J(abc) in orange. J(abc) structures within 95% confidence interval were estimated as suggested in ¹²⁶, as obtained χ_r^2 for the best structures with current method is higher than 95% threshold. The y-axis indicates the number of the structures in the bin; the x-axis is vector triple product, V , as described in equation 108. Arrows indicate the bin containing the best RBD structure (with the lowest χ_r^2).

The distributions in Figure 3.33 demonstrate that J(acd) and J(abd) ensembles are not planar and have narrow distributions, although each of them has a specific outlier (J(acd) at $V = -0.18$ and J(abd) at $V = -0.36$). The J(bcd) ensemble is broader and the triple product V covers the range from -0.09 to 0.05, meaning that it includes planar structures. Figure 3.33C shows that most of the structures are close to planar with $V = -0.013$ although the conformer with the lowest χ_r^2 is tripod-like with $V = -0.053$ (indicated with red arrow). The J(abc) best structure is planar (orange arrow, Figure 3.33D), although this family has the broadest distribution. Triple products, V , for the best structures and the standard deviation of the distribution are collected in Table 3.22.

Table 3.22 Coplanarity characteristics for the best RBD structures of the studied RNA 3WJ systems (with the lowest χ_r^2 as indicated with arrows in (A)-(D)) and the standard deviation of the distributions in Figure 3.33.

Structure	Coplanarity, V	St.dev
J(abd)	-0.175	0.019
J(acd)	-0.326	0.011
J(bcd)	-0.053	0.027
J(abc)	-0.002	0.050

Data for J(abc) construct is added for comparison (previously studied by H. Vardanyan¹²⁶).

3.3.8.4 Alignment via sequence

The RNA sequence plays an important role in the formation of tertiary structures^{160,163} and specific binding of ribosomal proteins that stabilize the RNA structure (e.g. S15)^{164,165}. Thus it is crucial to understand the link between sequence variation and the conformational space of RNA.

In this chapter, comparison of the studied RNA 3D structures based on sequence alignment is discussed. As before (Figure 3.31) I will consider mutual angles for comparison.

Alignment via a particular helix (e.g. helix a) makes the comparison of all four RNA 3WJ impossible, as they do not share all the same helix. Only three structures out of four have at least one helix in common and thus can be compared (Figure 3.34-3.37). Figure 3.34 demonstrates all possible combinations of the mutual angles for structures that contain helix a within 68%, 87% and 95% confidence levels. For this representation all structures are aligned via helix A and mutual angles are calculated as discussed above (see also Figure 3.28). In this depiction J(abd) (in blue) and J(acd) (in green) are highly similar within the chosen confidence levels. Additionally, Figure 3.34A also demonstrates that some structures in the selected ensemble reveal stacking interaction between helix b and d for J(abd) and c and d for J(acd). At the same time confidence intervals of J(acd) does not overlap with those of J(abc) (in orange) within any considered confidence interval (Figure 3.34B). Figure 3.34C demonstrates the comparison of J(abd) and J(abc). The plot suggests that these structures are similar within 87% and 95% confidence levels.

Now let us consider alignment via helix b (Figure 3.35). Comparison of J(abd) and J(bcd) shows similarity only within 87% and 95% confidence levels (Figure 3.35A), J(abc) and J(bcd) demonstrate strong topological diversity and are not comparable even within 95% confidence interval (Figure 3.35B). Figure 3.35C shows that J(abc) and J(abd) are similar within 68%, 87% and 95% confidence levels.

Alignment via helix c reveals the following features (Figure 3.36): Comparison of J(abc) in orange with J(acd) in green (Figure 3.36A) demonstrates a slight overlap within the 95% confidence level suggesting diversity of the constructs. Figure 3.36B demonstrates that J(bcd) and J(abc) are significantly different. Finally, alignment of J(acd) in green with J(bcd) in red on Figure 3.36C shows that selected structures are similar already within 68% confidence interval. Note that the mutual angles on the Figure 3.35B are identical as the same structures are compared.

Lastly, the alignment via helix d is presented in Figure 3.37. All possible RNA 3WJ combinations have been previously discussed separately on different Figures but are collected in one plot for systematic analysis. Figure 3.37A shows the comparison of the J(abd) and J(acd) as discussed above in alignment via helix a; Figure 3.37B is J(abd) and J(bcd) (discussed above in alignment via helix b); Figure 3.37C is J(bcd) and J(acd) and discussed in helix c alignment part.

To conclude, the comparison via sequence reveals that the studied RNA 3WJs show various three-dimensional global conformations and indicate orientation differences between the structures, depending on the alignment. From the above results, a common feature is that helix a is never involved in stacking interaction, supposable due to absence of the adenine-uracil bases in the junction.

Alignment via helix A

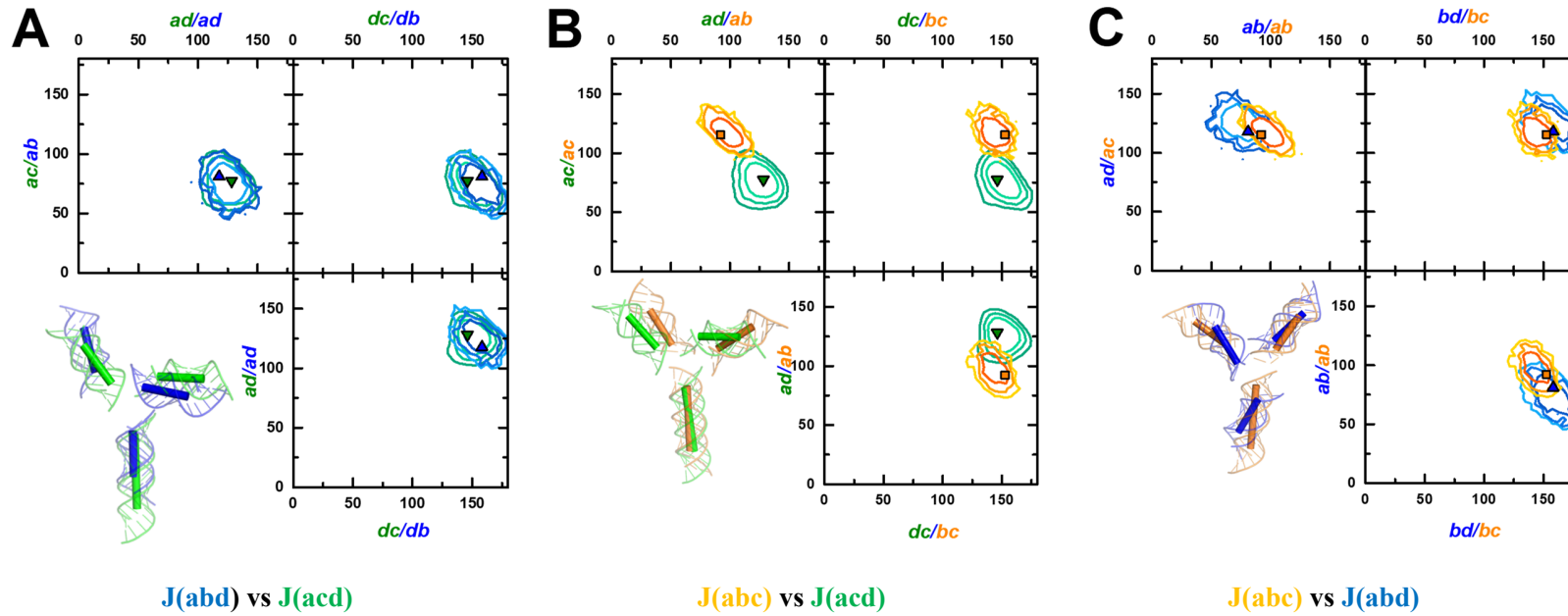


Figure 3.34 Topological confinement of the structures, that contain helix A: $J(\text{abd})$ in blue, $J(\text{acd})$ in green and $J(\text{abc})$ in orange in terms of mutual angles. Structures with the lowest χ_r^2 are indicated with triangles or square in corresponding color. Alignment is carried out via helix A: (A) comparison of $J(\text{abd})$ and $J(\text{acd})$; (B) comparison of $J(\text{abc})$ and $J(\text{acd})$; (C) comparison of $J(\text{abc})$ and $J(\text{abd})$. 3D structures with the lowest χ_r^2 are aligned and presented in the insets of every figure.

Alignment via helix B

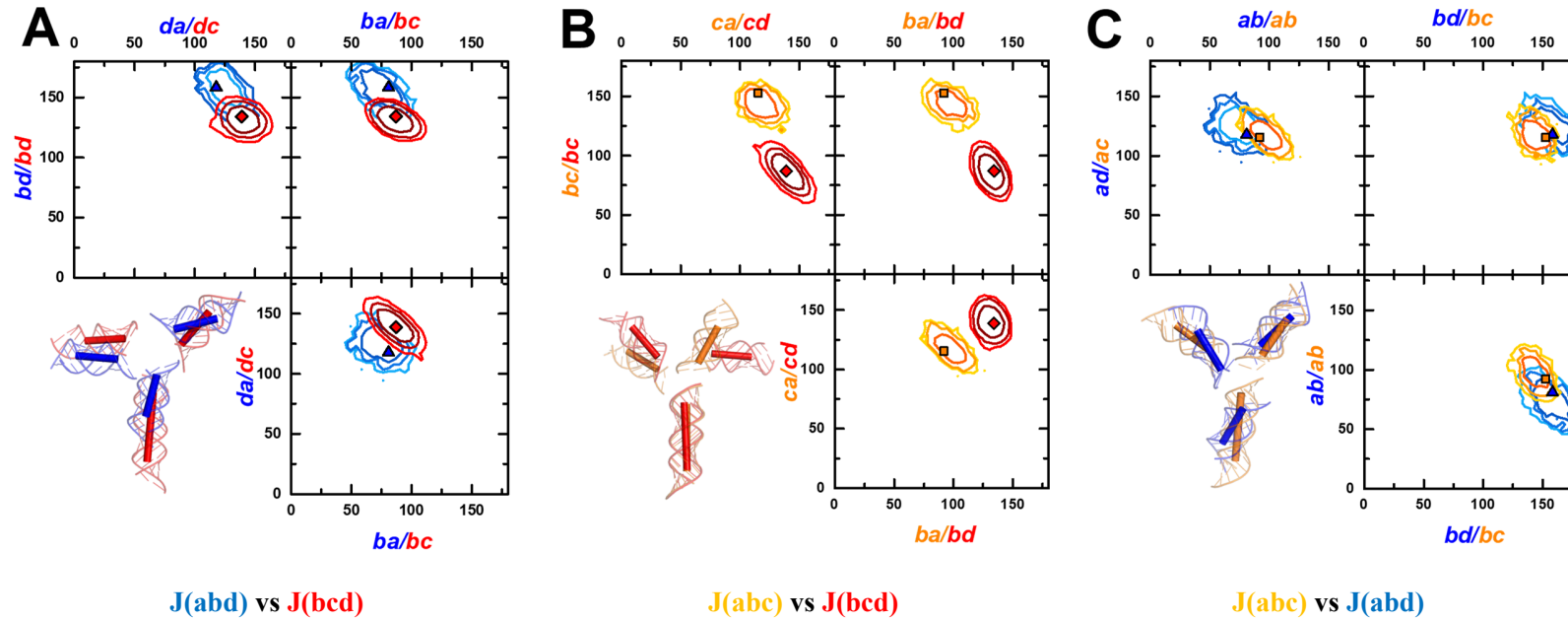


Figure 3.35 Topological confinement of structures, that contain helix B: $J(abd)$ in blue, $J(bcd)$ in red and $J(abc)$ in orange in terms of mutual angles. Structures with the lowest χ_r^2 are indicated with triangles, diamonds or square in corresponding color. Alignment is carried out via helix B: (A) comparison of $J(abd)$ and $J(bcd)$; (B) comparison of $J(abc)$ and $J(bcd)$; (C) comparison of $J(abc)$ and $J(abd)$. 3D structures with the lowest χ_r^2 are aligned and presented in the insets of every figure.

Alignment via helix C

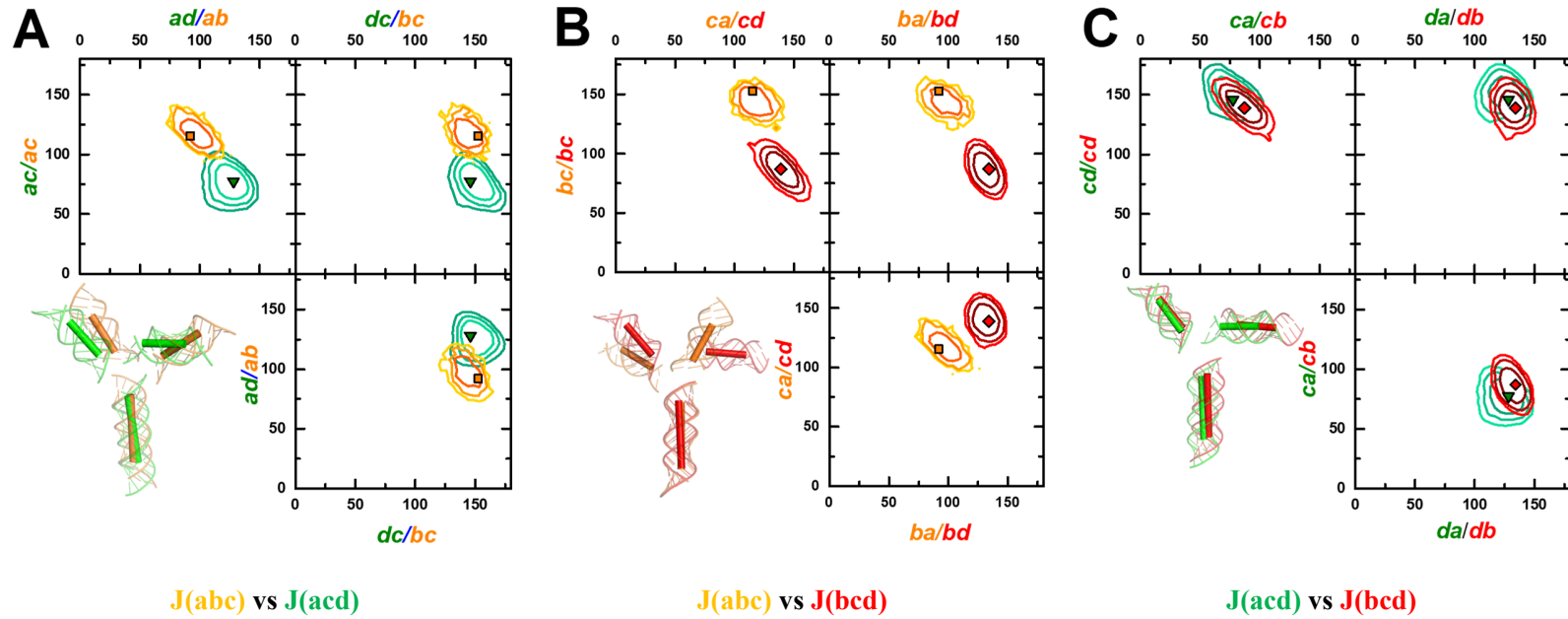


Figure 3.36 Topological confinement of structures, that contain helix C: $J(acd)$ in green, $J(bcd)$ in red and $J(abc)$ in orange in terms of mutual angles. Structures with the lowest χ_r^2 are indicated with triangles, diamonds or square in corresponding color. Alignment is carried out via helix C: (A) comparison of $J(abc)$ and $J(acd)$; (B): comparison of $J(abc)$ and $J(bcd)$; (C) comparison of $J(bcd)$ and $J(acd)$. 3D structures with the lowest χ_r^2 are aligned and presented in the insets of every figure. Alignment is carried via helix C: (A) comparison of $J(abc)$ and $J(acd)$; (B): comparison of $J(abc)$ and $J(bcd)$; (C) comparison of $J(bcd)$ and $J(acd)$.

Alignment via helix D

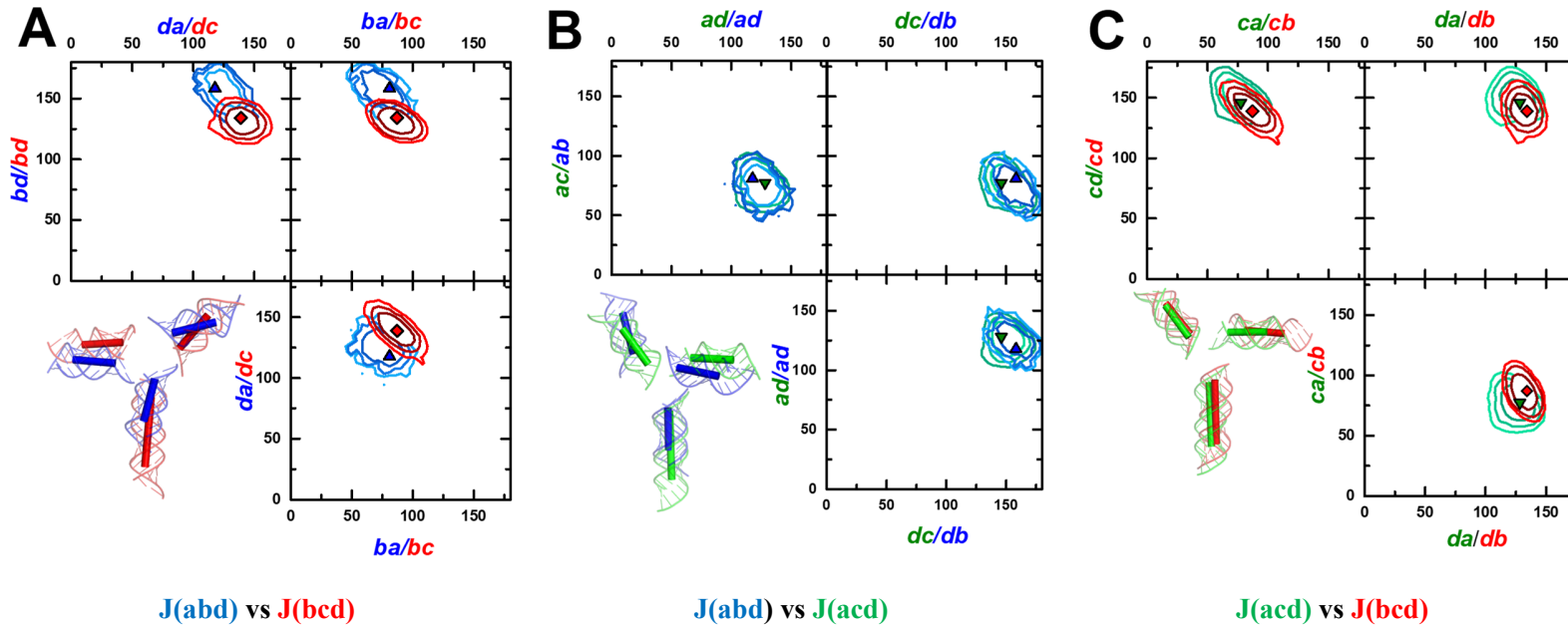


Figure 3.37 Topological confinement of structures, that contain helix D: $J(abd)$ in blue, $J(acd)$ in green and $J(bcd)$ in red in terms of mutual angles. Structures with the lowest χ_r^2 are indicated with triangles or diamonds in corresponding color. Alignment is carried out via helix D: (A) comparison of $J(abd)$ and $J(bcd)$; (B) comparison of $J(abd)$ and $J(acd)$; (C) comparison of $J(acd)$ and $J(bcd)$. 3D structures with the lowest χ_r^2 are aligned and presented in the insets of every figure. Alignment is carried via helix D: (A) comparison of $J(abd)$ and $J(bcd)$; (B) comparison of $J(abd)$ and $J(acd)$; (C) comparison of $J(acd)$ and $J(bcd)$.

3.3.8.5 Comparison of two alignment methods

To summarize, the structures can be aligned either via shape or via a particular helix (by sequence). In the latter case, the structures can be compared only in pairs. In Figure 3.38 I summarize the results for the best structures based on different specific alignment (Figure 3.30B, Figure 3.34-Figure 3.37) and compare these two approaches. The horizontal axis indicates how similar two structures are if aligned via shape and the vertical axis indicates how similar two structures are if aligned via sequence. In both cases, angular RMSD values of the mutual angles between the best structures are compared. For example, the angular RMSD between J(abc) and J(bcd) in case of alignment via shape is calculated as

$$\begin{aligned} RMSD^\circ = & \hspace{20em} (110) \\ = & \sqrt{\left(\text{angle I}(J(abc)) - \text{angle I}(J(bcd))\right)^2 + \left(\text{angle II}(J(abc)) - \text{angle II}(J(bcd))\right)^2 +} \\ & \hspace{10em} + \left(\text{angle III}(J(abc)) - \text{angle III}(J(bcd))\right)^2 \end{aligned}$$

Figure 3.38 demonstrates that structures that are overlaid via shape appear much more similar than when overlaid by sequence: the largest RMSD is $\sim 85^\circ$ for the sequence-based comparison compared to $\sim 26^\circ$ for the shape-based. Most of the pairs follow the diagonal 1:1 line, indicating that both alignment methods reveal their similarity. However the discrepancies between J(bcd)/J(abc) and J(acd)/J(abd) in overlay by sequence are significant, indicating that J(abc) sequence is more sensitive for structural alignment.

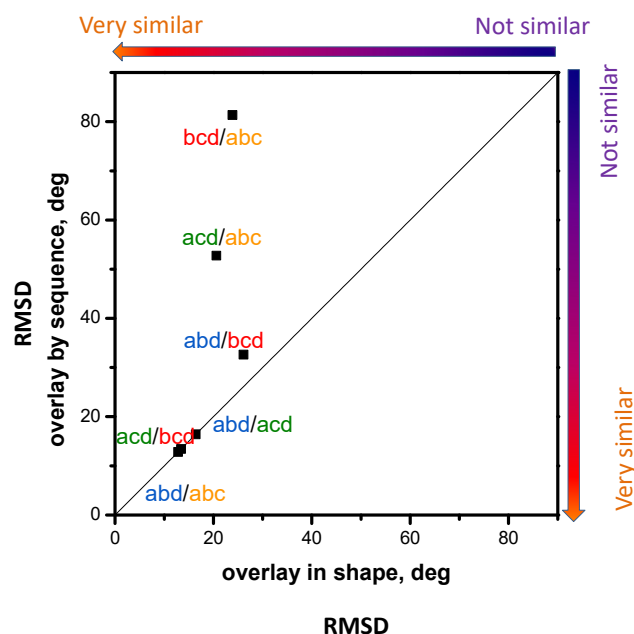


Figure 3.38 Schematic pairwise structural comparison based on alignment via shape (x-axis) (Figure 3.30B) and alignment via sequence (y-axis) (Figure 3.34-Figure 3.37). Black line is 1:1 line. RMSD of all mutual angles of the best structures are used as a criterion for comparison.

Since it seems that the shape of structures for different 3WJ sequences is similar within the errors (Figure 3.30B), it is natural to ask, if a single model fits to the combined FRET data collected for all molecules. In order to investigate this, I select the best common cross-sequence representative structure. To do that, I assume that two conformers, which have an angular RMSD of less than 10° from each other, correspond to the same model. Subsequently, I look for a set of 4 conformers, each corresponding to one 3WJ sequence, that have an angular RMSD from the common representative of less than 10° and the sum of their respective χ^2 is minimized:

$$\begin{cases} RMSD(J(i) \text{ vs } J(\text{comm. rep.})) < 10^\circ; \quad i \in \{abc, abd, bcd, acd\} \\ \text{argmin}\{\chi^2(J(abc)) + \chi^2(J(abd)) + \chi^2(J(bcd)) + \chi^2(J(acd))\} \end{cases} \quad (111)$$

The selected common representative for each RNA 3WJ is shown in Table 3.23. χ_r^2 is calculated in the same manner as it was done for the docked structures (Chapter 3.2.10), e.g. $\chi_r^2(J(abd)) =$

$$\frac{\chi^2}{N_{\text{measurements}} - N_{\text{fit.param.}}} = \frac{62}{42-6} = 1.7 \quad \text{and for the common representative: } \chi_r^2(\text{comm.rep.}) = \frac{\chi_{J(abc)}^2 + \chi_{J(abd)}^2 + \chi_{J(bcd)}^2 + \chi_{J(acd)}^2}{N_{\text{measurements}} - N_{\text{fit.param.}}} = \frac{319}{44+42+42+44-6} = 1.9.$$

Table 3.23 (A) Euler angles values and χ_r^2 for the most representative RNA 3WJs and common representative structure. χ_r^2 of the best structures after docking (Table 3.19) are added for comparison; (B) Euler angles for the best structures after docking (Figure 3.31) with respective χ_r^2 .

A							
Structure	φ_{II}	θ_{II}	ψ_{II}	φ_{III}	θ_{III}	ψ_{III}	χ_r^2
Common representative	60.7	144.8	-85.1	-118.5	88.6	156.5	1.9
J(abd)	54.4	155.4	-84.0	-117.7	89.6	157.4	1.7
J(bcd)	61.3	139.4	-74.5	-116.4	93.9	159.2	1.7
J(acd)	66.8	151.9	-85.7	-99.6	79.7	164.9	1.7
J(abc)	54.3	141.9	-86.6	-133.9	80.8	142.0	3.4
B							
Structure	φ_{II}	θ_{II}	ψ_{II}	φ_{III}	θ_{III}	ψ_{III}	χ_r^2
J(abd)	6.4	158.3	-90.7	-145.0	80.9	156.7	1.2
J(bcd)	96.5	138.8	-75.2	-78.8	87.0	-169.3	1.1
J(acd)	66.1	146.1	-101.5	-77.1	77.4	160.4	1.3
J(abc)	31.8	153.0	-108.4	-143.4	87.8	134.6	2.0

These conformers can be found within the 68% confidence intervals for the mutual and Euler angles for helix *II* for all sequences (gray star in Figure 3.39B). For the Euler angles of helix *III* the common representative structures are within the 95% confidence intervals (gray star in Figure 3.40B).

Pairwise comparison and RMSD between P atoms of RNA 3WJ with respect to the common representative are presented in Figure 3.39A.

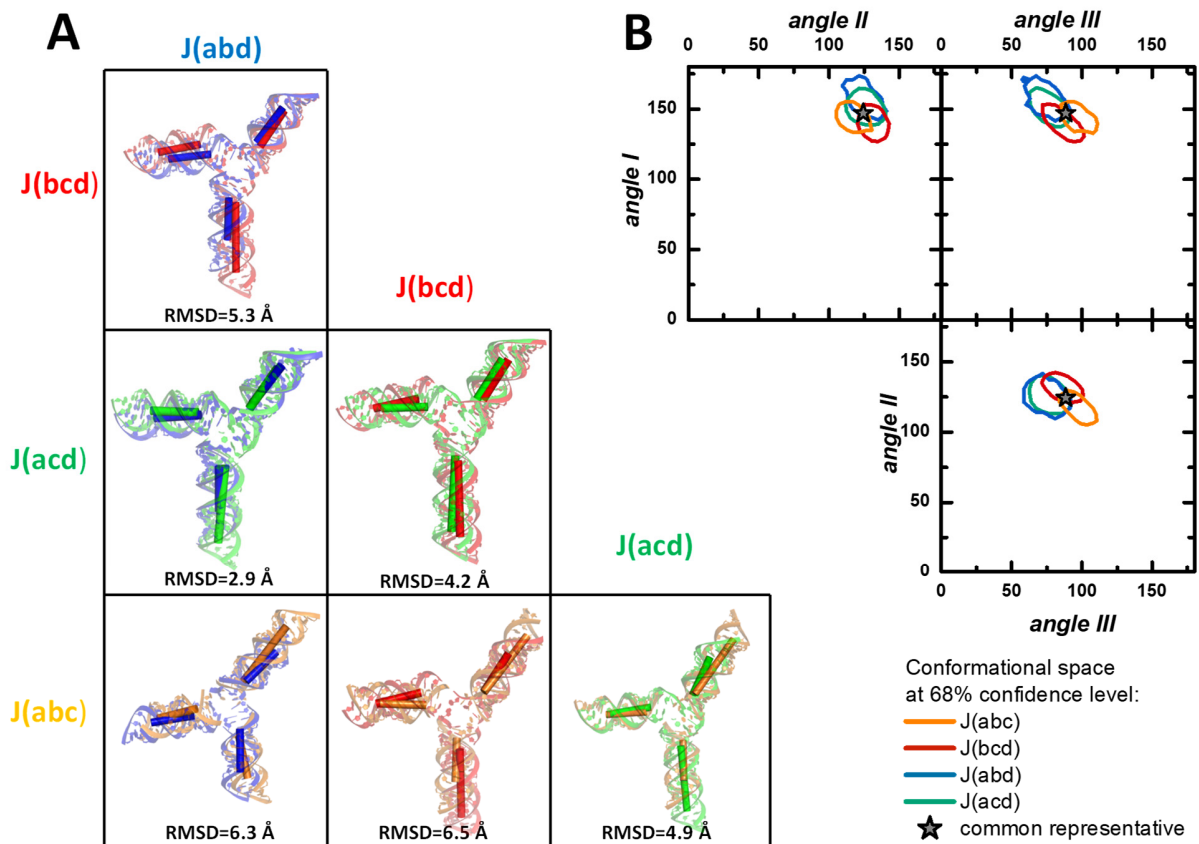


Figure 3.39 (A) Visualization of the common representative model for each RNA 3WJ aligned by two in all possible combinations via mutual angles. Alignment is carried out only via helices without junction. This plot should be read as a matrix, e.g. the first column represents overlay of J(abd) with all other possible structures, whereas second row represents alignment with J(acd). The matrix element in the first column and second row shows the overlay between J(abd) and J(acd). The RMSD values between phosphorous atoms are shown below each overlay; (B) Mutual angles with 68% confidence interval. Gray star indicates the common representative structure.

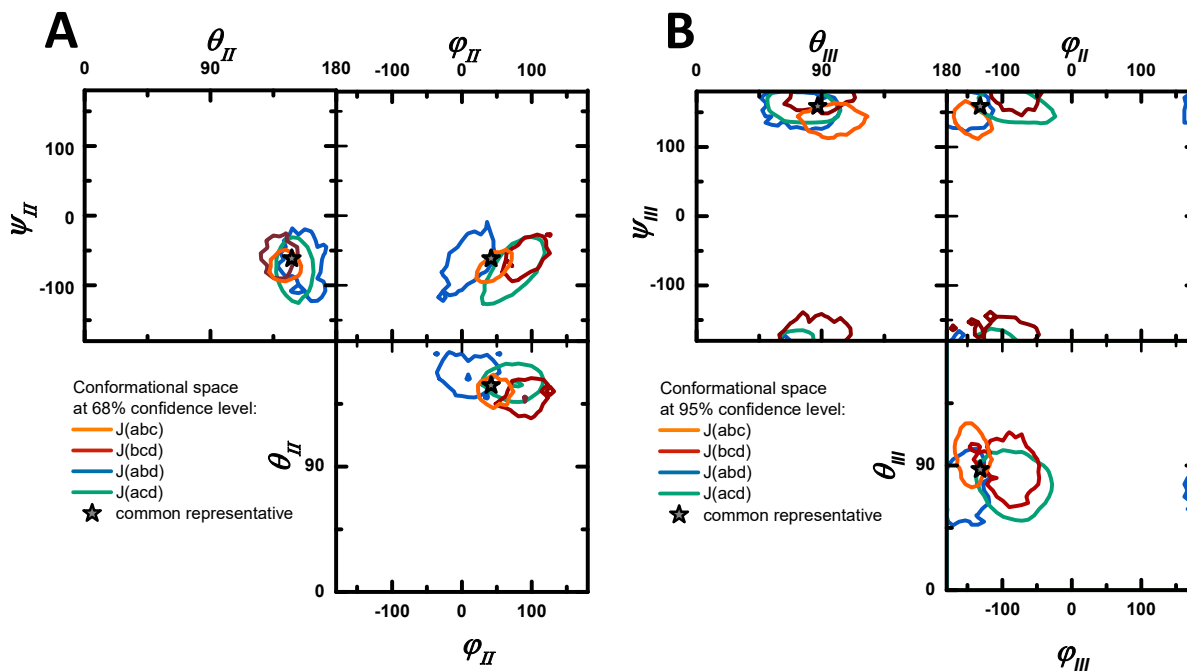


Figure 3.40 Error range for orientations of helices forming the angle II (A): contour represents 68% confidence interval for bootstrapped structures $J(bcd)$ in the red, $J(acd)$ in green, $J(abd)$ in blue and $J(abc)$ in orange. Common representative is marked with gray star. (B): helices forming angle III . Contour represents 95% confidence interval for bootstrapped structures $J(bcd)$ in the red, $J(acd)$ in green, $J(abd)$ in blue and $J(abc)$ in orange. The common representative is marked with gray star.

As indicated in Table 3.23, χ_r^2 values are much higher than for the best docked structures (Table 3.19). One of possible reasons is that the selected structures could reveal the approximation of a dynamic average ensemble and thus the static model is not exact. Another possible reason is that $J(abc)$ has higher χ_r^2 than other RNA 3WJ and thus accordingly to Eq.(111) this value affects χ_r^2 (common representative).

χ_r^2 for $J(abc)$ is much larger than for any other RNA 3WJ ($\chi_r^2(J(abc)) = 3.4$ vs $\chi_r^2(J(abd)) = 1.7$). This can be attributed to the fact that $J(abc)$ is more symmetric than other junctions and could be represented by a separate model. For this reason I found the common representative model for only three sequences (Table 3.24). The results of this procedure shows a slight decrease of χ_r^2 . The χ_r^2 of the common representative structure is lower than the χ_r^2 of individual molecules because the same 6 degrees of freedom in the individual molecules are subtracted from each molecule, despite the fact that these are the same degrees of freedom of a single model. These results in a slight overestimation of the individual χ_r^2 . The argument about dynamic averaging of structures remains plausible.

Table 3.24 Mutual angles values and χ_r^2 for the most representative RNA 3WJs and common representative structure excluding J(abc) from the generation procedure.

structure	φ_{II}	θ_{II}	ψ_{II}	φ_{III}	θ_{III}	ψ_{III}	χ_r^2
Common representative	62.6	140.4	-76.0	-108.0	84.0	164.2	1.4
J(abd)	54.4	155.4	-84.0	-117.7	89.6	157.4	1.7
J(bcd)	74.9	132.7	-78.5	-103.7	100.0	174.7	1.5
J(acd)	70.4	147.4	-72.0	-88.2	84.0	158.6	1.6

To conclude, it is possible to find a common structure that can represent all of the RNA 3WJ if alignment via shape is carried out. For example, the common representative structures of J(bcd) and J(acd) are very similar with RMSD=3.4 Å between P atoms (Figure 3.39). However, the common representative structure is not symmetric, helical positions are not equivalent and this manifests in different mutual angles when alignment via sequence is applied.

3.4 Conclusions and future directions

In my study I employed single-molecule and ensemble fluorescence methods to resolve the structure of RNA 3WJs with various sequences. The main technique during my investigation is quantitative FRET measurements, which are based on the simultaneous acquisition of multiple fluorescence parameters and thus have indisputable advantage to deliver precise and accurate spatial and temporal information. During the work, I was able to improve the sample preparation protocol that increased hybridization yield approximately 2-times and allowed to have better contrast between FRET active bursts and donor only bursts that is especially critical for low FRET species.

Associated analysis included construction and inspection of 2D frequency histograms that resolved structural heterogeneities and excluded dynamics on the ms-time scale. Complementary PDA analysis showed that RNA 3WJs have one dominant conformer and one minor conformer due to incomplete hybridization of the molecule. I also characterized individual states e.g. extracted FRET-averaged distances $\langle R_{DA} \rangle_E$ with their population fractions and estimated donor only population. In order to report the measured distances with high accuracy and precision, I also implemented a detailed error analysis that includes all experimental contributions e.g. the calibration parameters and correction factors, and modeling error.

To extract structural information, I combined fluorescence methods with computational structural modeling. FRET-averaged distances $\langle R_{DA} \rangle_E$ and their corresponding errors were used to construct 3D models of RNA 3WJ. Chosen model explicitly accounted for base pair and was compared with other competitive models that account for different hydrogen bond flexibility (Table 3.3-Table 3.4). To demonstrate that the designed 3D structure satisfies the experimental data, I conducted statistical analysis, employing the goodness of fit parameter χ_r^2 and the RMSD to differentiate between the clusters of solutions. With this analysis toolkit, I was able to define a structural model with a precision of $\sim 2 \text{ \AA}$.

Moreover, all obtained RNA 3WJs were compared in terms of their overall shape, planarity and whether structures exhibit particular coaxial stacking, as these factors are crucial for determining binding sites of the partner molecules. I showed that, even though all studied RNAs have similar shape within the 95% confidence interval (Figure 3.30B), the sequence determines possible coaxial stacking or no stacking at all. The results demonstrate that helices *B* and *D* prefer to have coaxial stacking if one of them is present in the construct (Figure 3.30). I also found a set of Euler angles that can describe each RNA 3WJ within 68% (and 95% for Helix *III*) confidence interval (common representative structure in Table 3.23). On the other hand, if structures are aligned via sequence, in some cases strong topological diversity is observed and the structures are not similar within given confidence intervals (Figure 3.34B, Figure 3.35A-B).

During the data analysis, I revealed that the utilized fluorophores exhibit different fluorescence properties at different labeling sites. The RNA microenvironment determines the fluorescence properties of the dye and, as RNA 3WJs have multiple labeling positions (up to 14) this manifests in diverse fluorescence characteristics. In Chapter 3.3.1, I presented a systematic study of the site specific behavior of the donor Alexa488 and acceptor Cy5. Schematically, I differentiate three local environments: internal helical part, end of the helix and the junction. For each microenvironment I present fluorescence lifetime, quantum yield and anisotropy for the studied dyes and compare them with properties of the untethered dye. The data demonstrates that when Cy5 is exposed to the helical termini, the fluorescence quantum yield and anisotropy increase due to the hindering of cis-trans isomerization and possible sticking to the helical end. On the other hand, when donor Alexa488 reaches the helically GC-rich termini or is exposed to Guanine in the helical middle, weakly fluorescent RNA-dye complex is registered, indicating possible quenching by Guanine via PET. Experiments indicate shorter $\Phi_{F,D}$ for end-labeled positions in comparison to the internal or free dye.

Outlook:

I demonstrated that single-molecule FRET analysis was successfully resolves RNA 3WJ structures. Well defined systems like these open the possibility for solving more complex nucleic acid systems with more

junctions or loops. Undoubtedly, the implemented toolkit is also applicable for structural determination of proteins and nucleic acid-protein complexes. Obtained data for site specific fluorescence properties can be applicable for many other RNA and even DNA complexes or can be used as a guide for optimal planning of the future labeling networks. This information is also relevant for studies with other type of dyes, as it sends a strong message that the labeled dyes do not exhibit the same fluorescence properties as free dyes and usage of the wrong values of the fluorescence parameters will strongly affect the precision of the calculated distance.

Finally, resolving the 3D structure is a key to understand the interaction between RNA and their binding partners due to their sequence-specific recognition and mutual helical orientation. Still there is little known about subsequent binding events of the formed complex and its rearrangements or kinetics. Advancing this knowledge may be a key to amplify the research on binding therapeutic targets to specific RNAs.

3.5 Supporting information

3.5.1 eTCSPC fluorescence decay measurements of single labeled RNA 3WJ

3.5.1.1 Donor only lifetime measurements

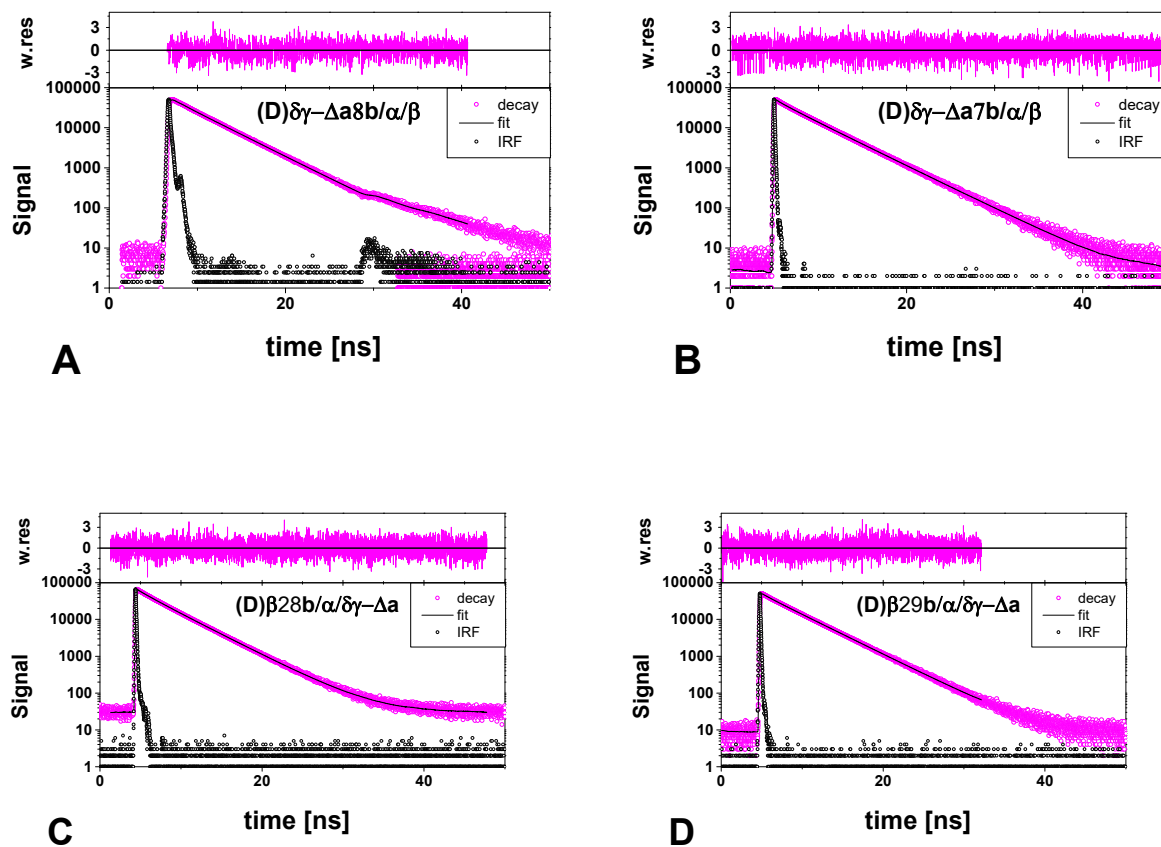
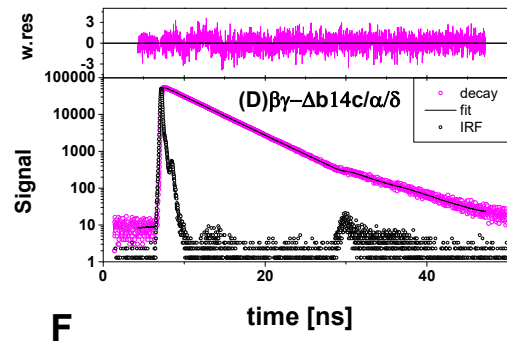
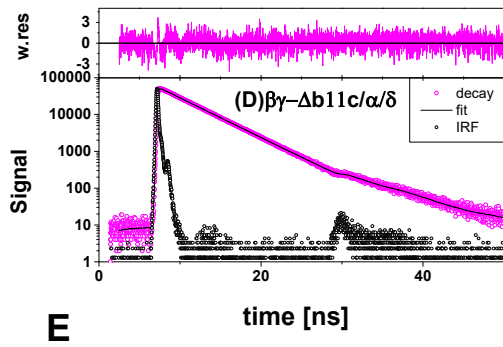
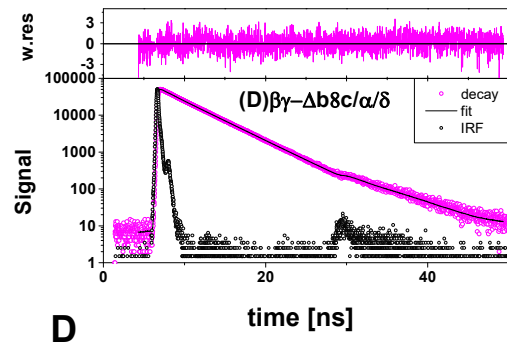
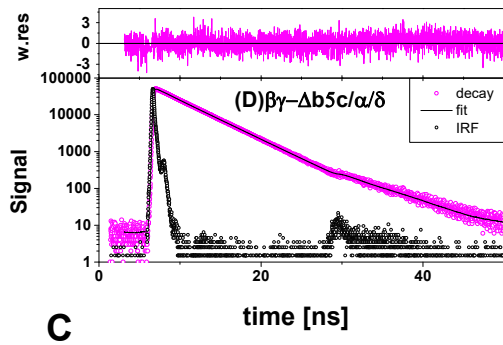
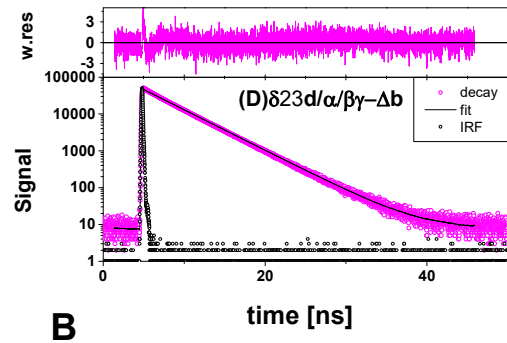
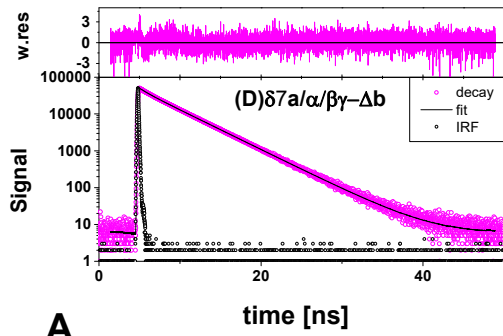


Figure 3.41 eTCSPC measurements of fluorescence donor only decays for J(bcd) construct labeled with Alexa488. Experimental data (purple circles), fits (black curve) and IRF (black open circles) are shown. Weighted residuals are presented above each plot (magenta solid lines). See Table 3.6-3.7 for fitting parameters.



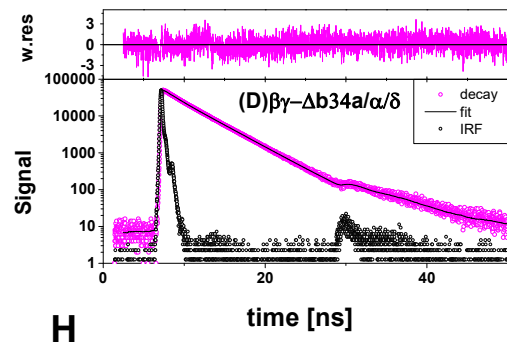
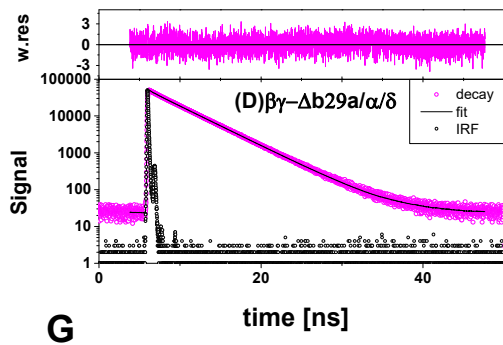
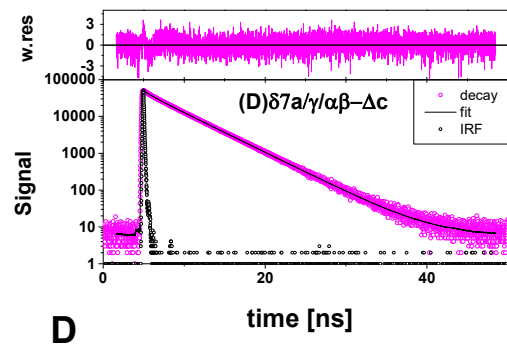
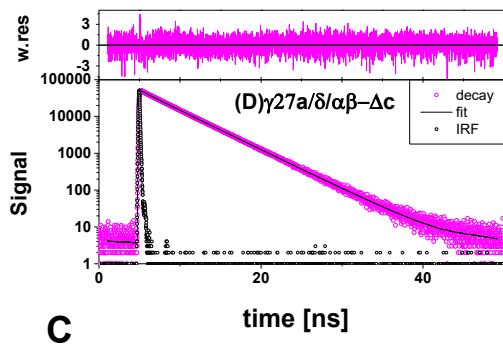
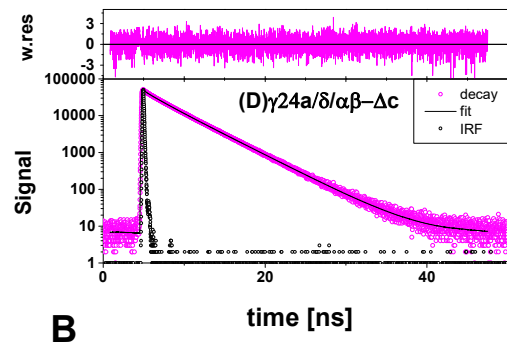
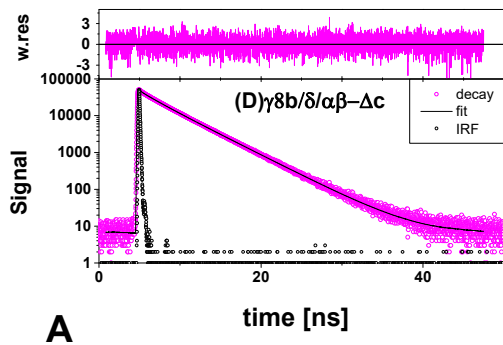


Figure 3.42 eTCSPC measurements of fluorescence donor only decays for J(acd) construct labeled with Alexa488. Experimental data (purple circles), fits (black curve) and IRF (black open circles) are shown. Weighted residuals are presented above each plot (magenta solid lines). See Table 3.6-3.7 for fitting parameters.



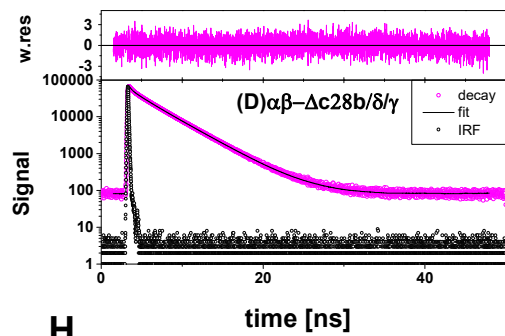
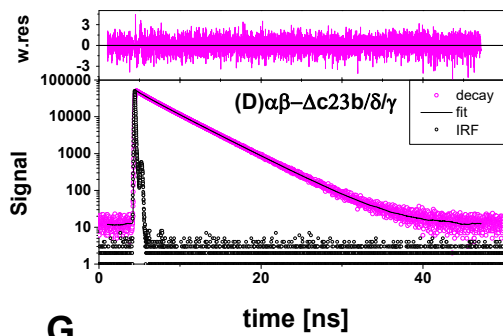
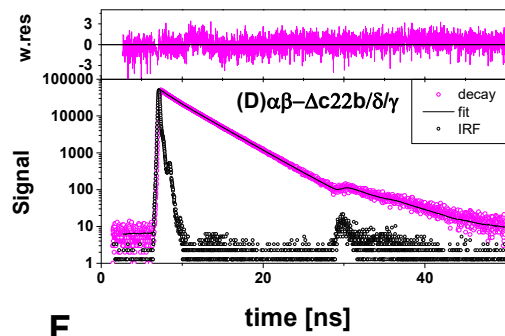
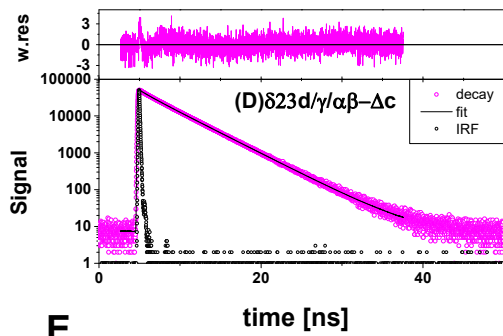
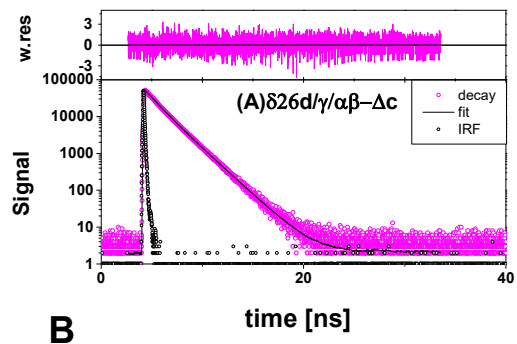
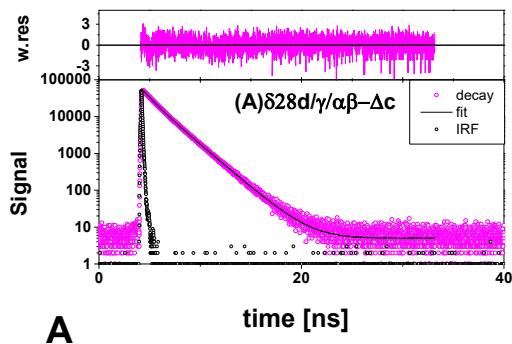


Figure 3.43 eTCSPC measurements of fluorescence donor only decays for J(abd) construct labeled with Alexa488. Experimental data (purple circles), fits (black curve) and IRF (black open circles) are shown. Weighted residuals are presented above each plot (magenta solid lines). See Table 3.6-3.7 for fitting parameters.

3.5.1.2 Acceptor only lifetime measurements



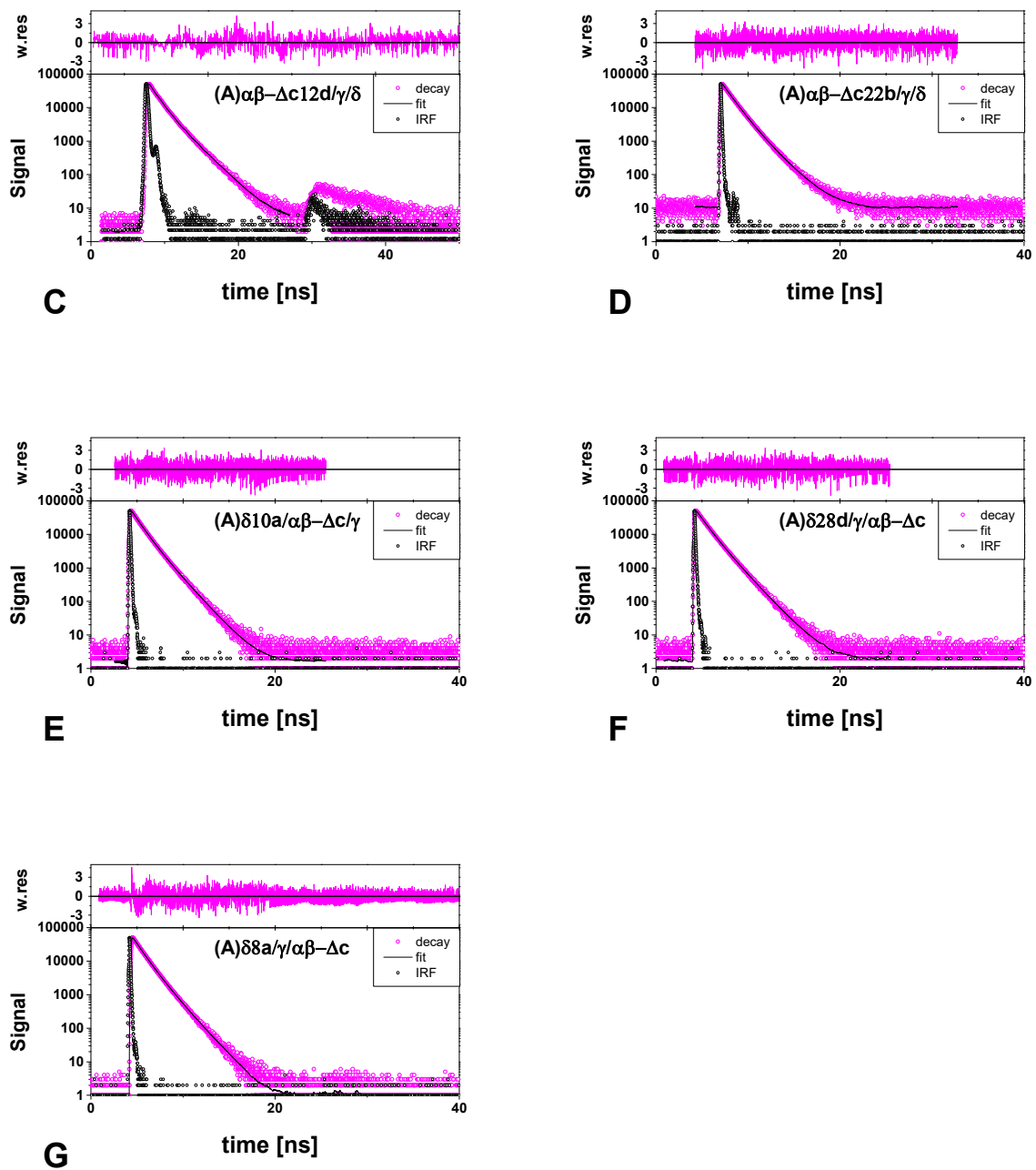
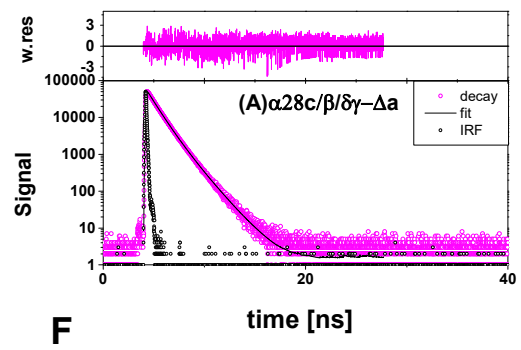
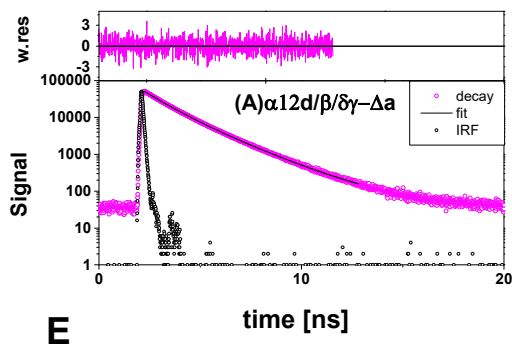
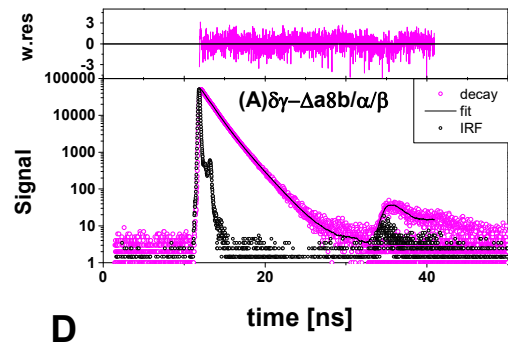
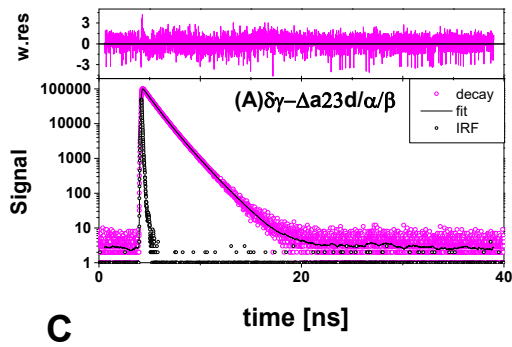
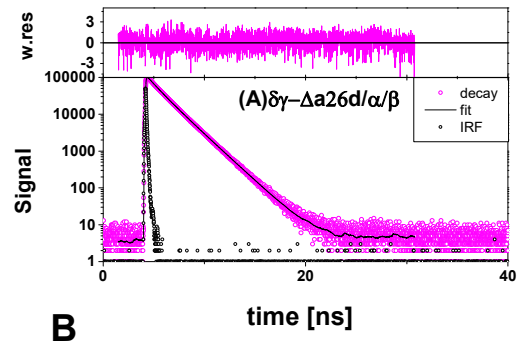
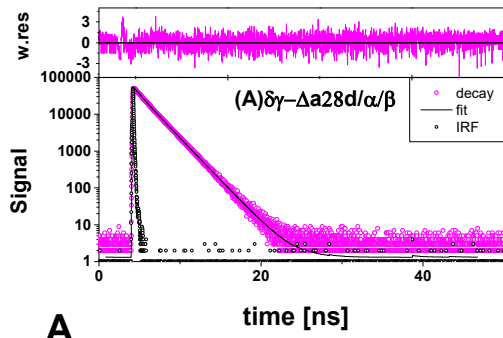


Figure 3.44 eTCSPC measurements of fluorescence acceptor only decays for J(abd) construct labeled with Cy5. Experimental data (purple circles), fits (black curve) and IRF (black open circles) are shown. Weighted residuals are presented above each plot (magenta solid lines). See Table 3.5 for fitting parameters.



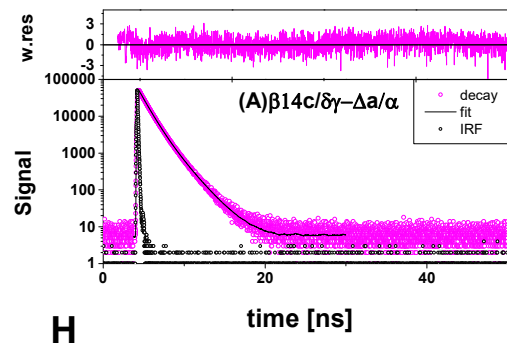
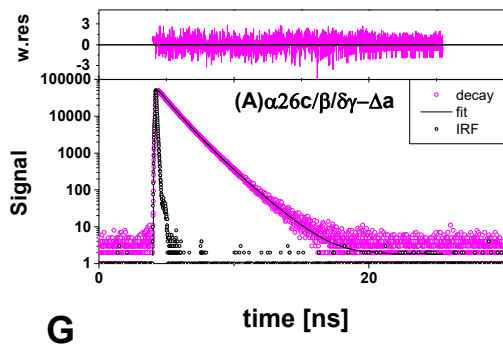
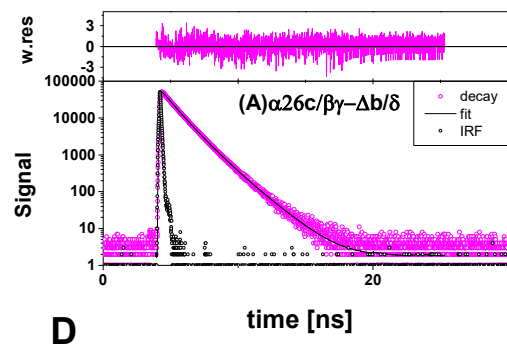
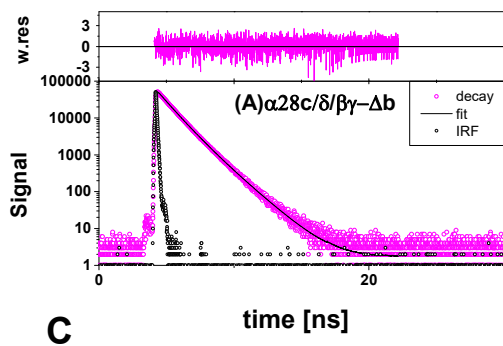
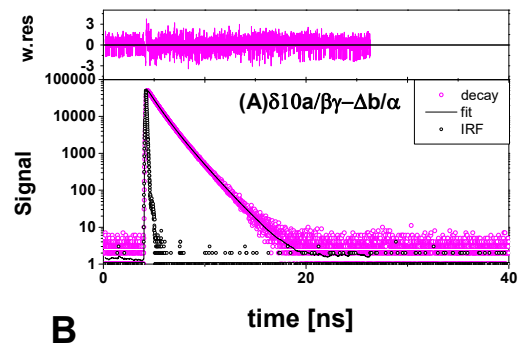
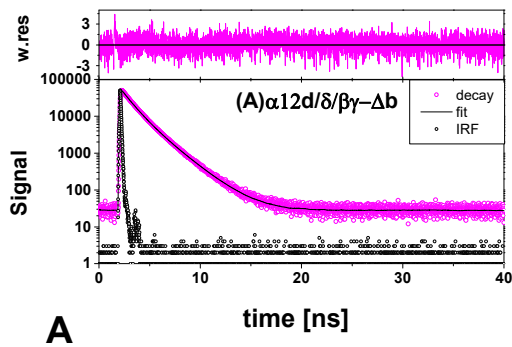


Figure 3.45 eTCSPC measurements of fluorescence acceptor only decays for J(bcd) construct labeled with Cy5. Experimental data (purple circles), fits (black curve) and IRF (black open circles) are shown. Weighted residuals are presented above each plot (magenta solid lines). See Table 3.5 for fitting parameters.



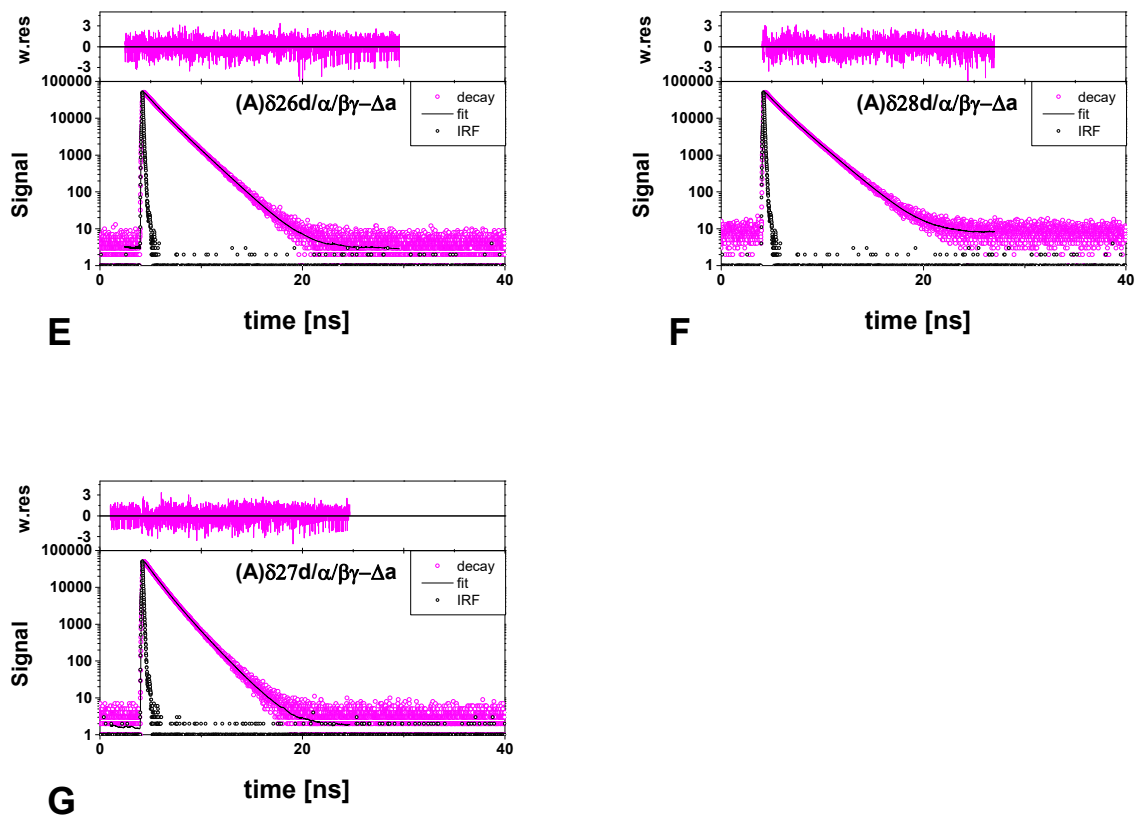
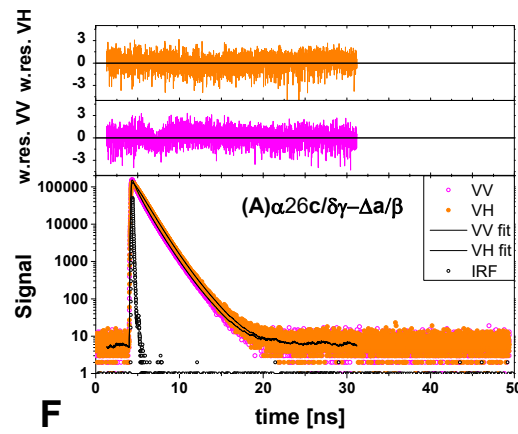
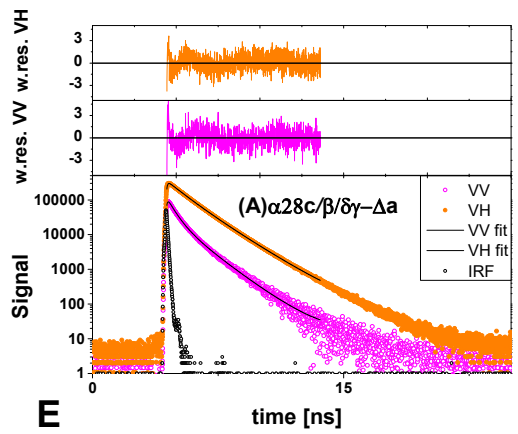
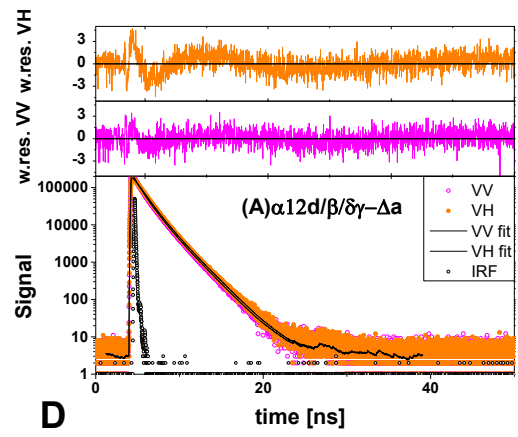
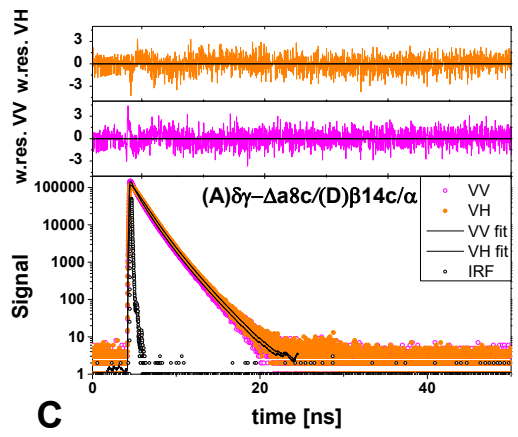
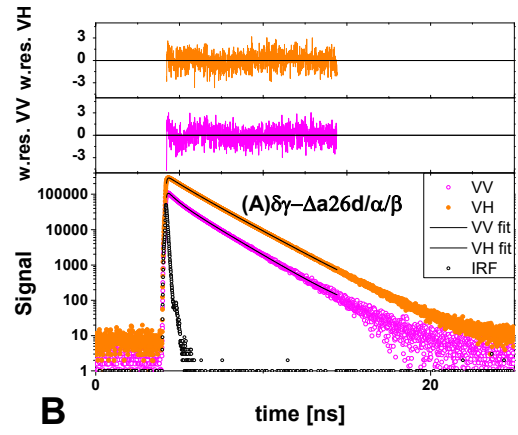
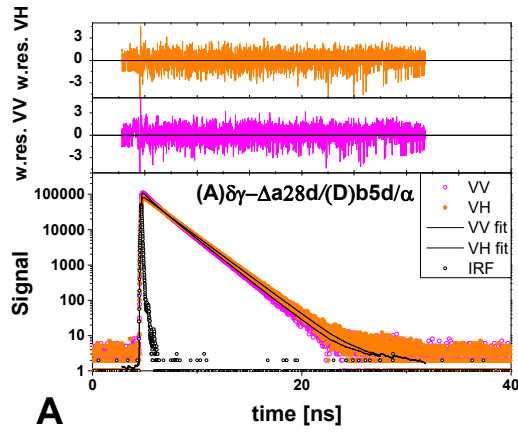


Figure 3.46 eTCSPC measurements of fluorescence acceptor only decays for J(acd) construct labeled with Cy5. Experimental data (purple circles), fits (black curve) and IRF (black open circles) are shown. Weighted residuals are presented above each plot (magenta solid lines). See Table 3.5 for fitting parameters.

3.5.2 eTCSPC polarized fluorescence decay measurements of acceptor labeled RNA3WJ



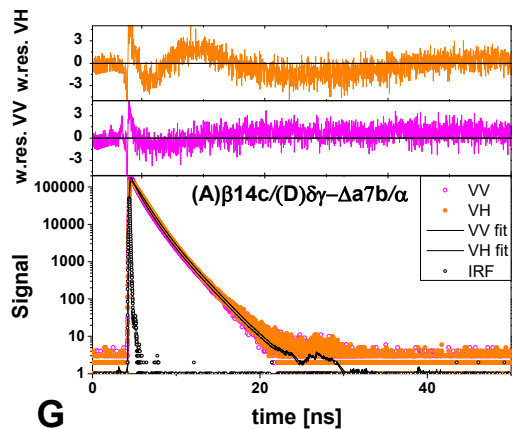
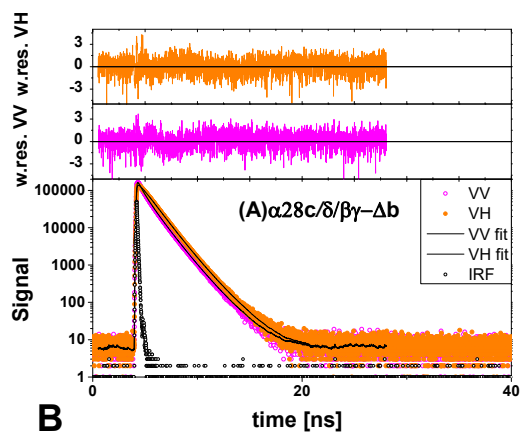
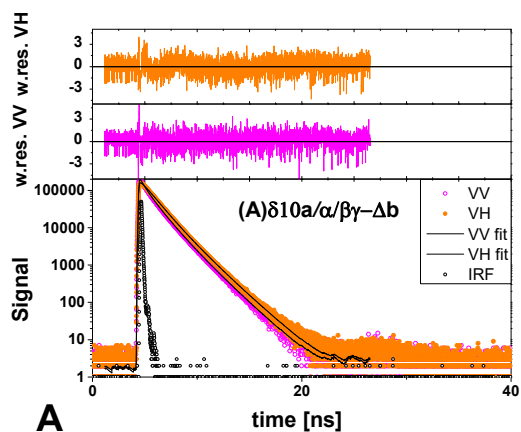


Figure 3.47 Typical fluorescence signal in parallel and perpendicular polarization channels (magenta and orange) with the corresponding fits (black) for J(bcd) structures labeled with acceptor Cy5 with weighted residuals on the top. The fit results are presented in the Table 3.8. The fit quality was judged by χ_r^2 .



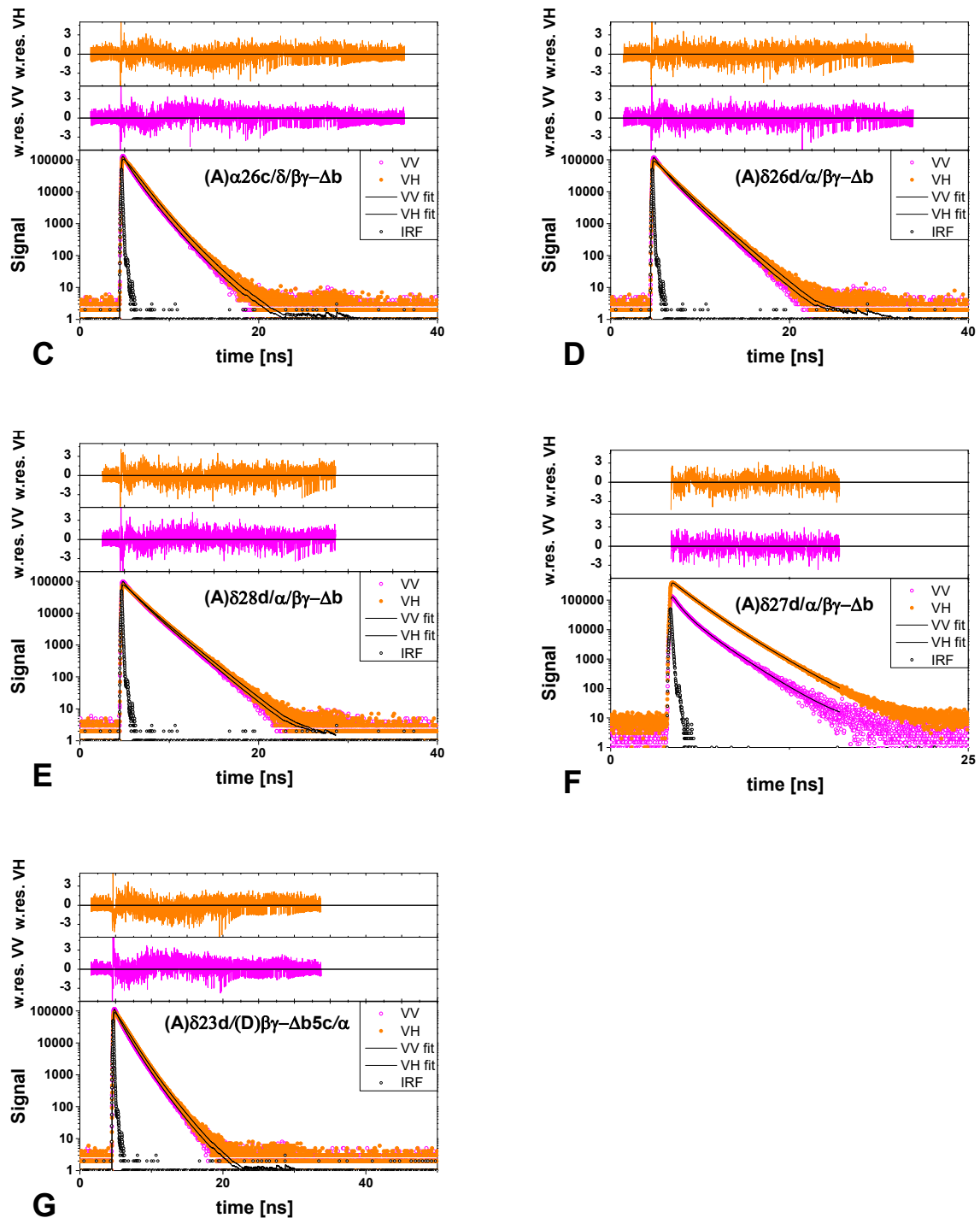
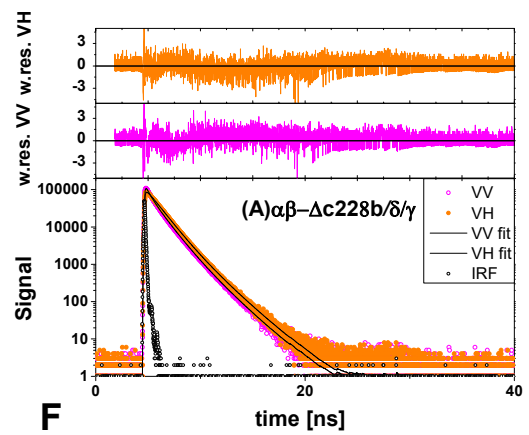
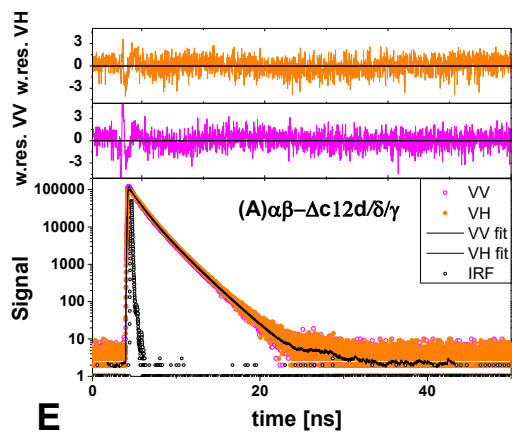
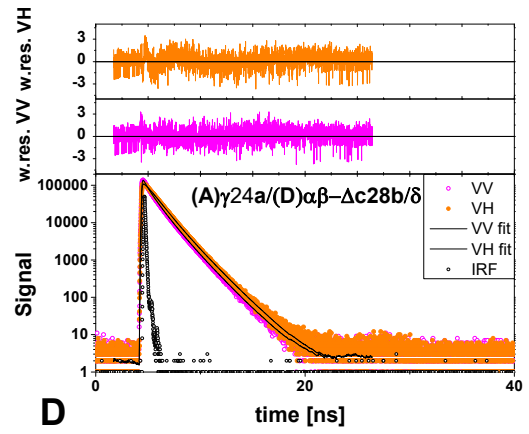
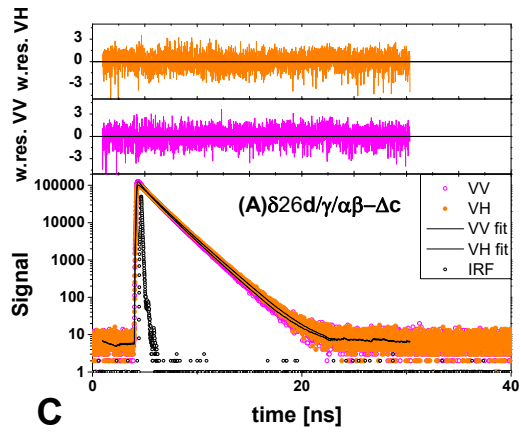
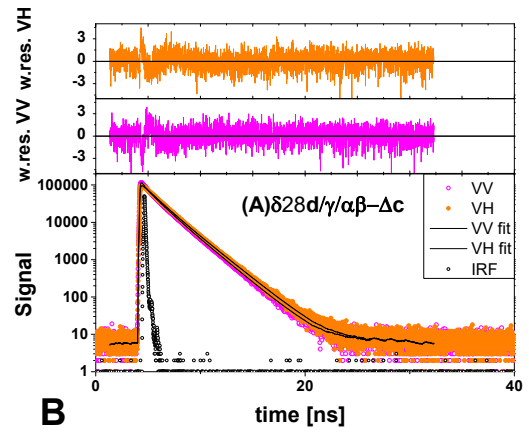
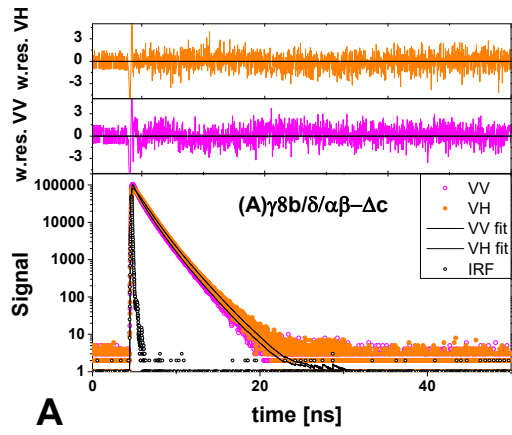


Figure 3.48 Typical fluorescence signal in parallel and perpendicular polarization channels (magenta and orange) with the corresponding fits (black) for J(acd) structures labeled with acceptor Cy5 with weighted residuals on the top. The fit results are presented in the Table 3.8. The fit quality was judged by χ_r^2 .



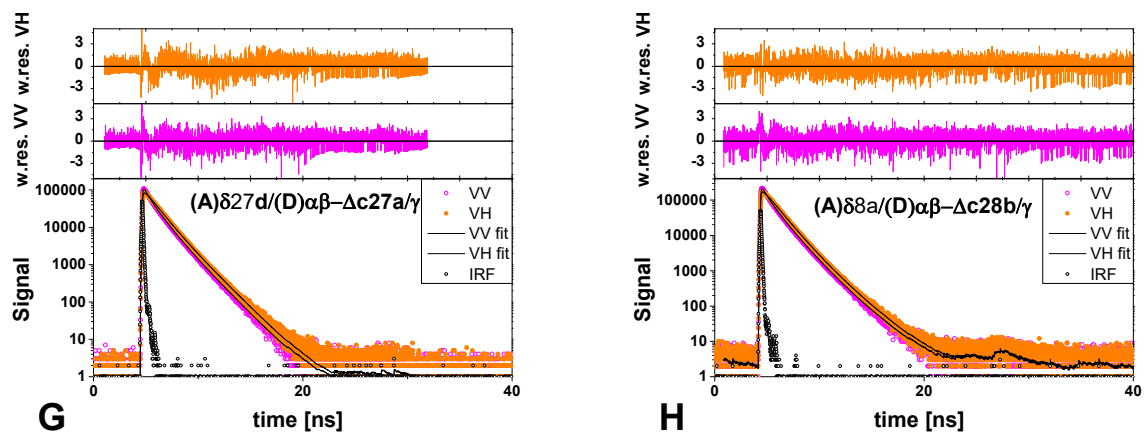
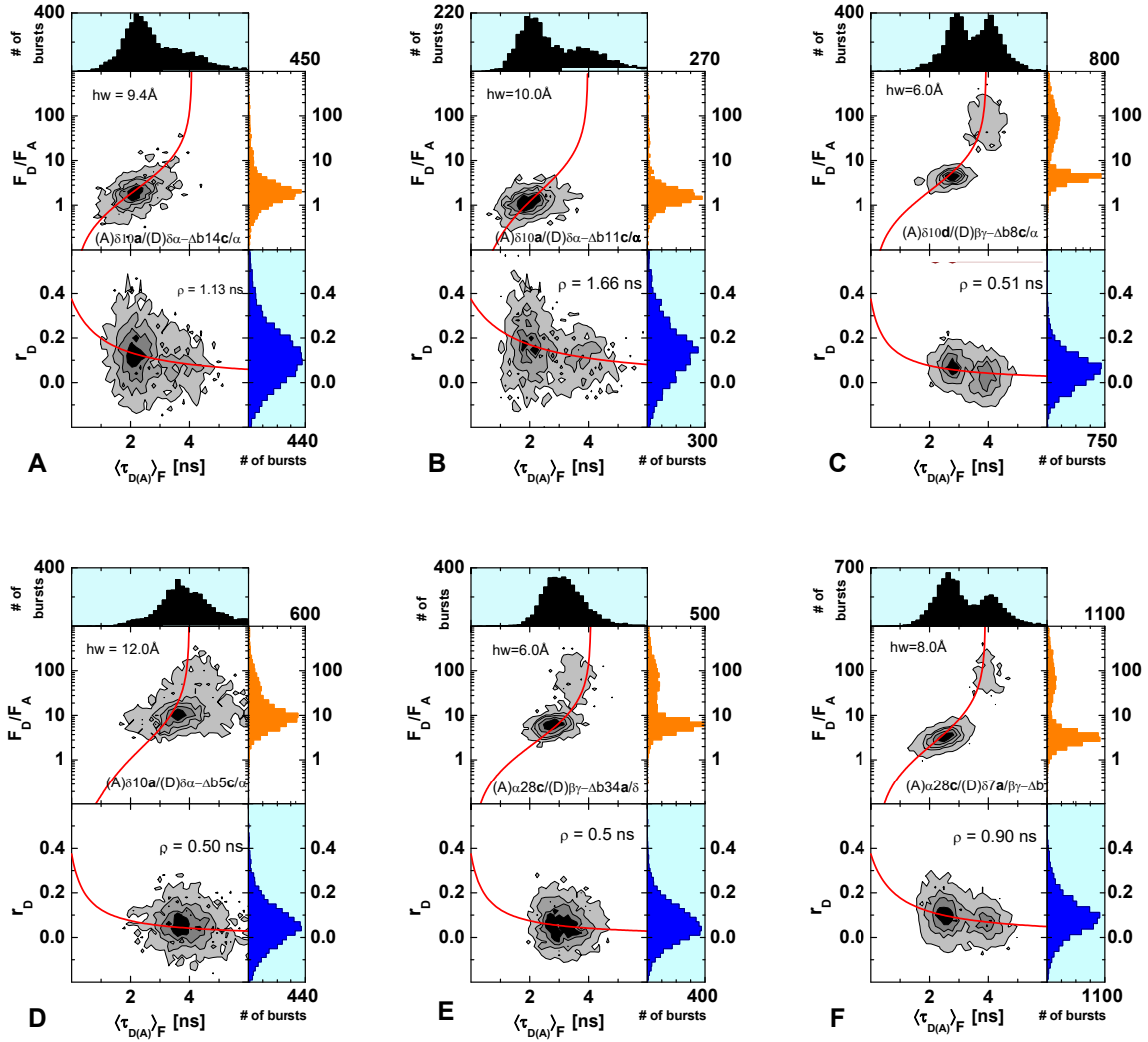


Figure 3.49 Typical fluorescence signal in parallel and perpendicular polarization channels (magenta and orange) with the corresponding fits (black) for J(abd) structures labeled with acceptor Cy5 with weighted residuals on the top. The fit results are presented in the Table 3.8. The fit quality was judged by χ_r^2 .

3.5.3 Additional 2D MFD histograms and static FRET lines

3.5.3.1 2D MFD histograms



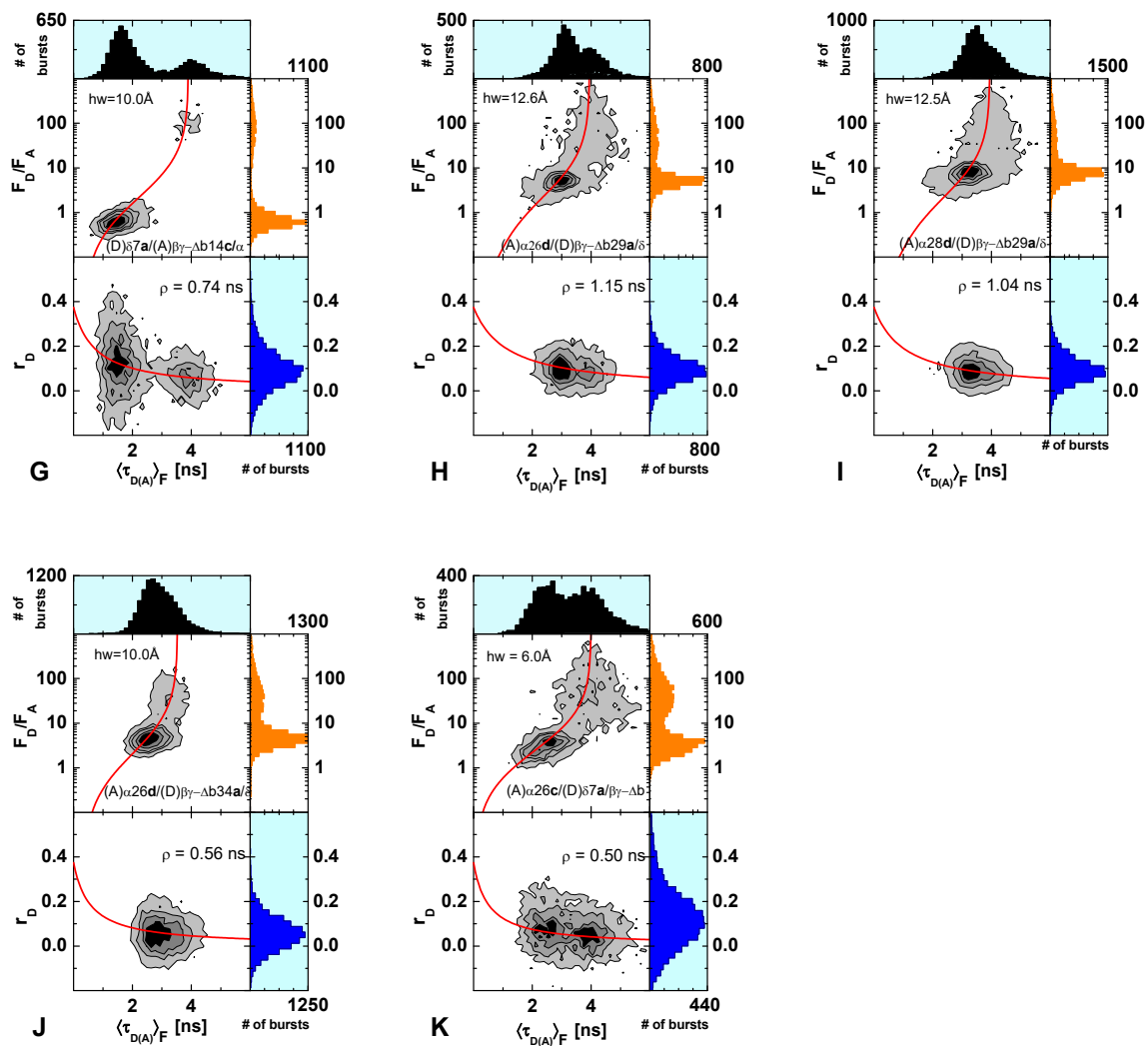
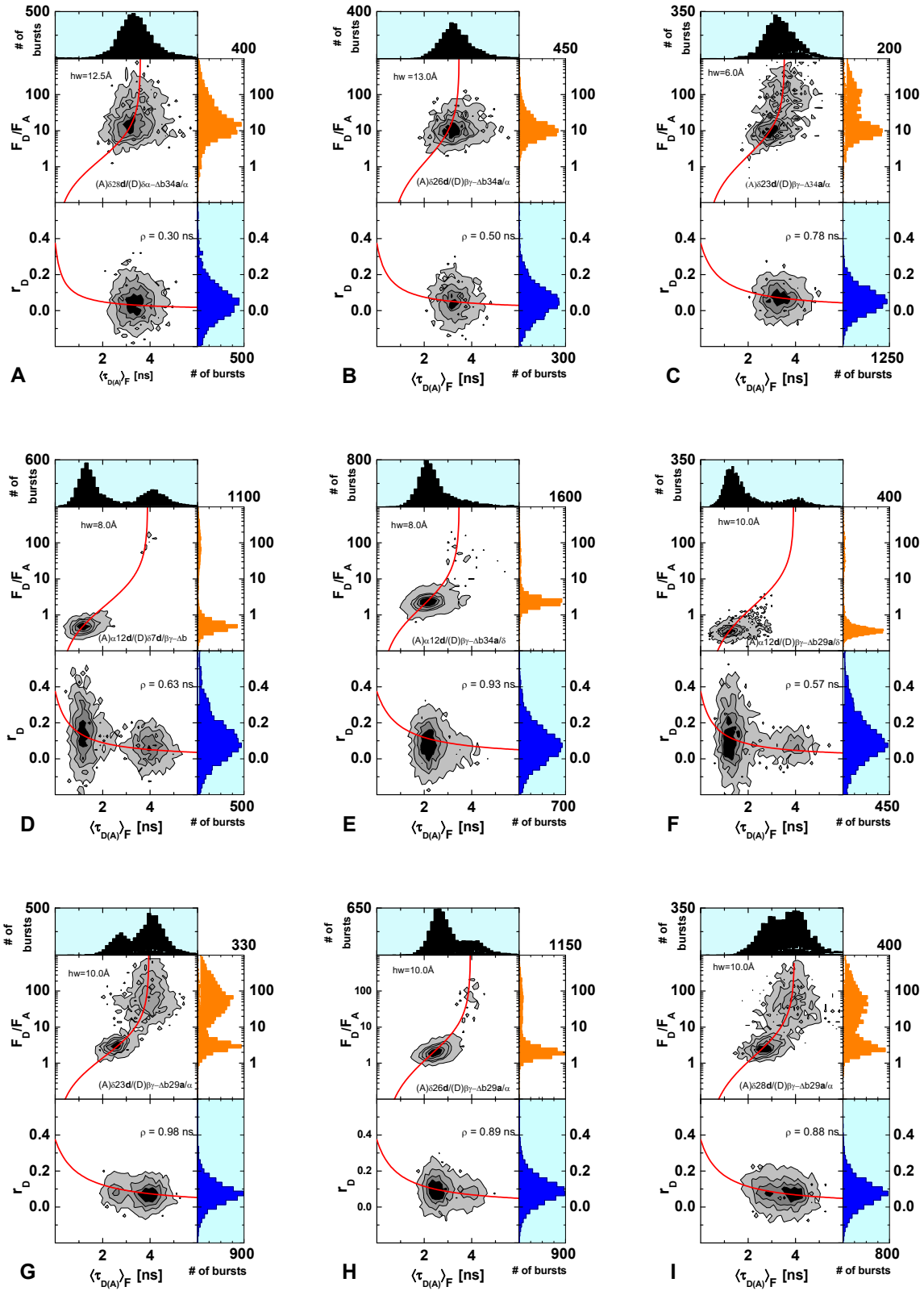


Figure 3.50 2D burst frequency histograms of J(acd) with fluorescence labels on helices *a* and *c*: Upper panel: F_D/F_A vs fluorescence donor lifetime in presence of acceptor $\langle \tau_{D(A)F} \rangle$. Static FRET line is shown as red curve; Lower panel: the donor fluorescence anisotropy r_D vs $\langle \tau_{D(A)F} \rangle$. Perrin line is shown as red line.



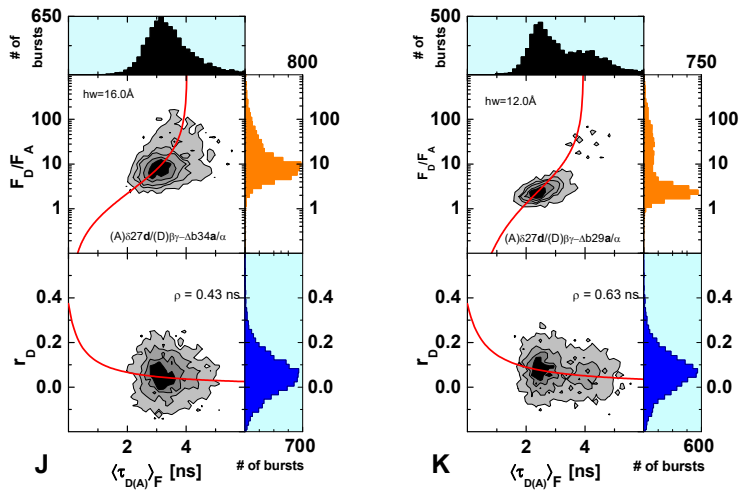
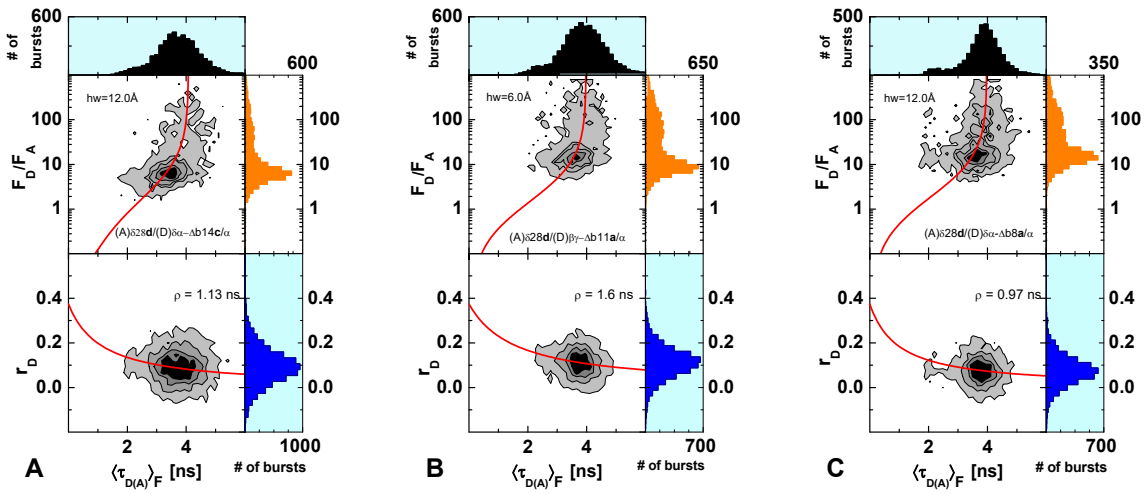
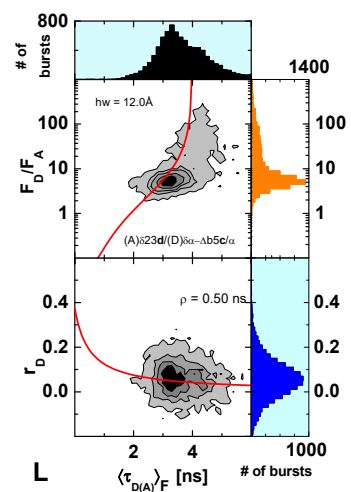
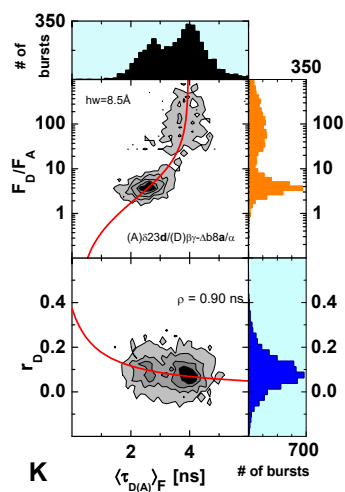
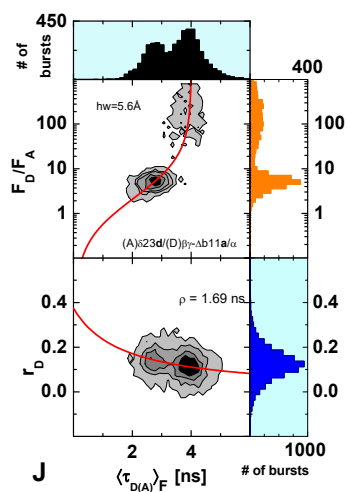
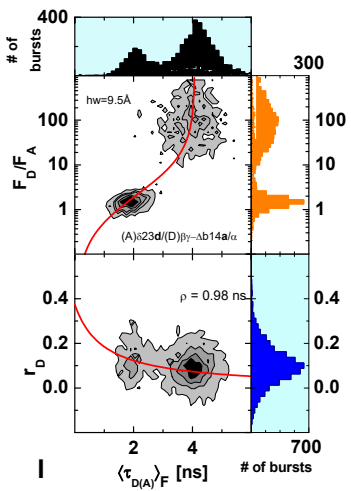
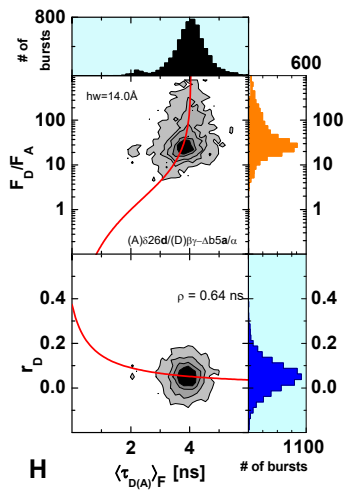
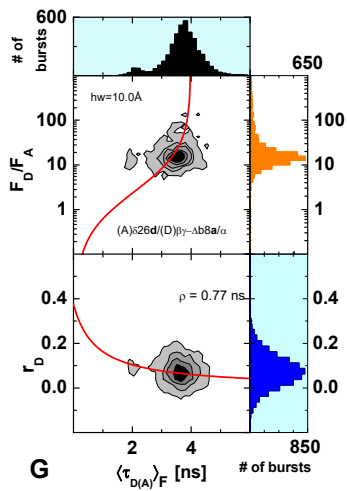
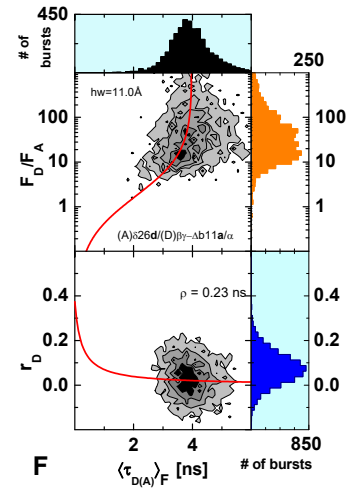
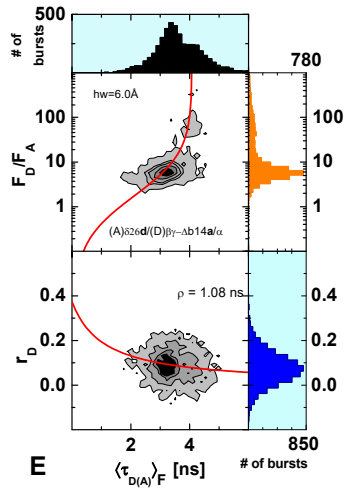
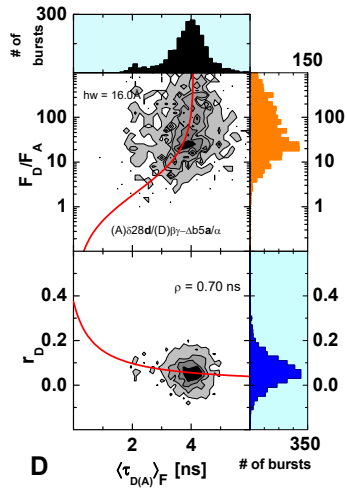
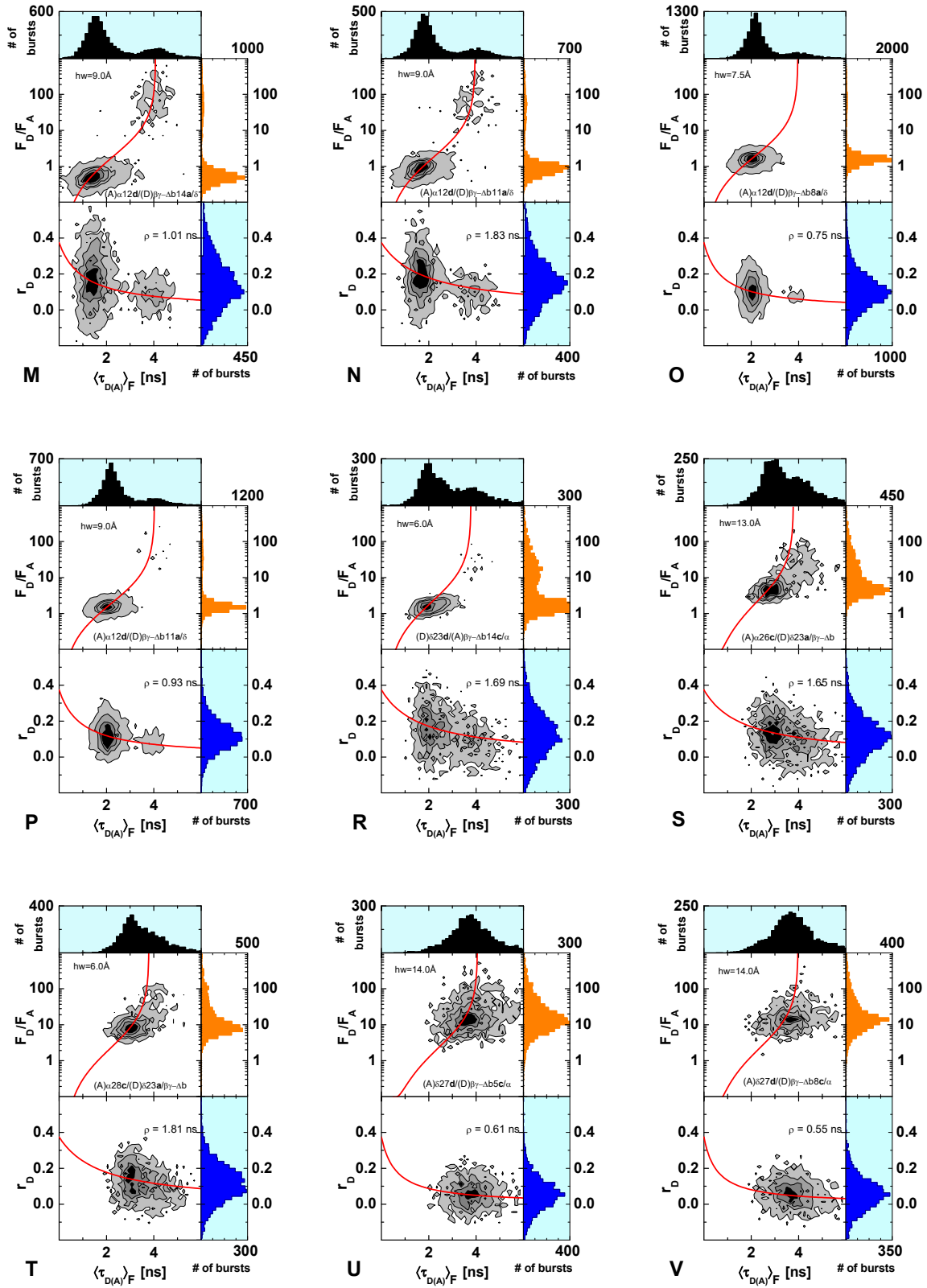


Figure 3.51 2D burst frequency histograms of J(acd) with fluorescence labels on helices *a* and *d*: Upper panel: F_D/F_A vs fluorescence donor lifetime in presence of acceptor $\langle \tau_{D(A)F} \rangle$. Static FRET line is shown as red curve; Lower panel: the donor fluorescence anisotropy r_D vs $\langle \tau_{D(A)F} \rangle$. Perrin line is shown as red line.







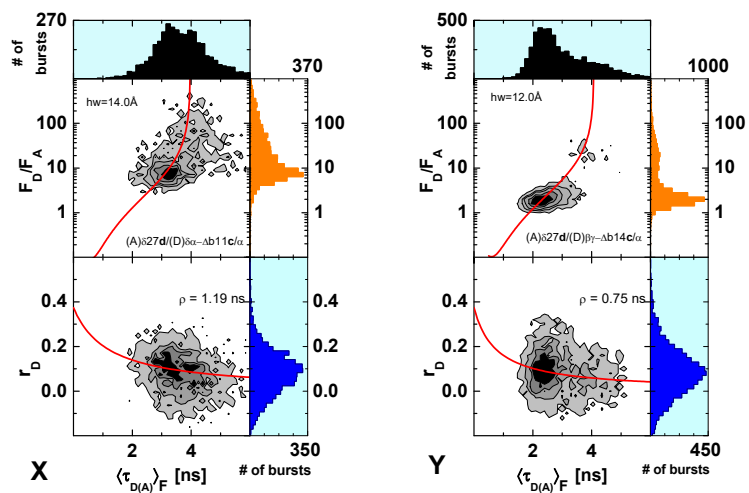
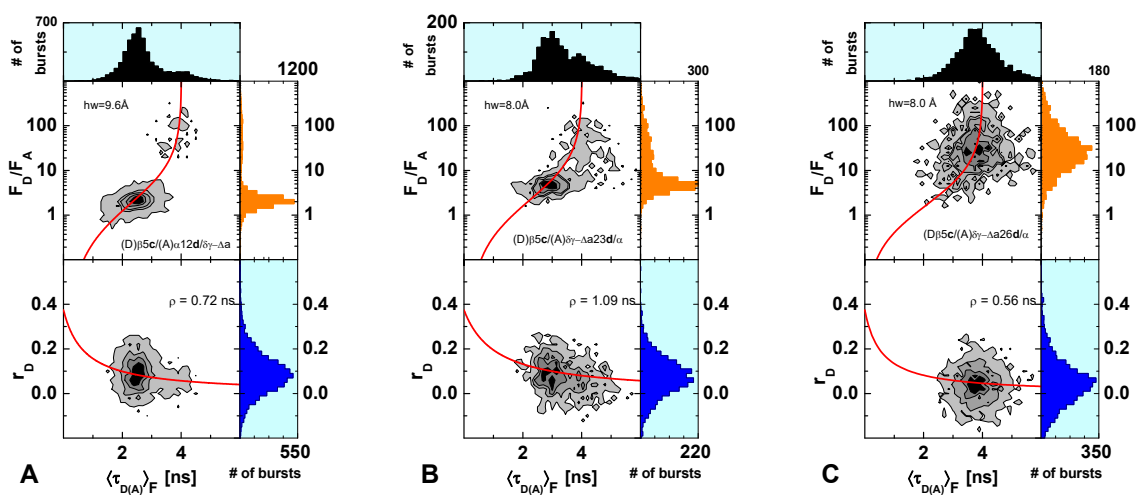
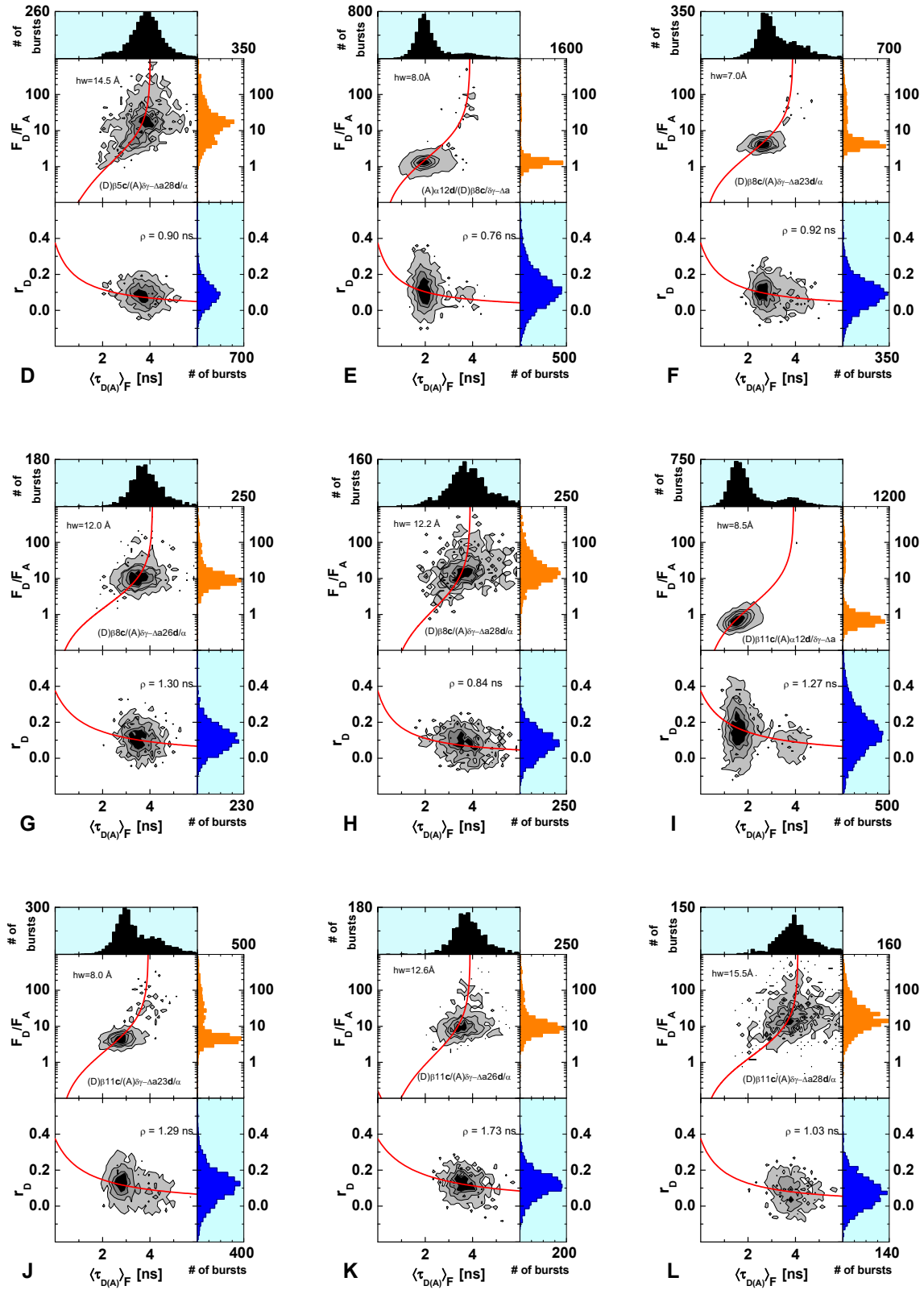


Figure 3.52 2D burst frequency histograms of J(acd) with fluorescence labels on helices *c* and *d*: Upper panel: F_D/F_A vs fluorescence donor lifetime in presence of acceptor $\langle \tau_{D(A)} \rangle_F$. Static FRET line is shown as red curve; Lower panel: the donor fluorescence anisotropy r_D vs $\langle \tau_{D(A)} \rangle_F$. Perrin line is shown as red line.





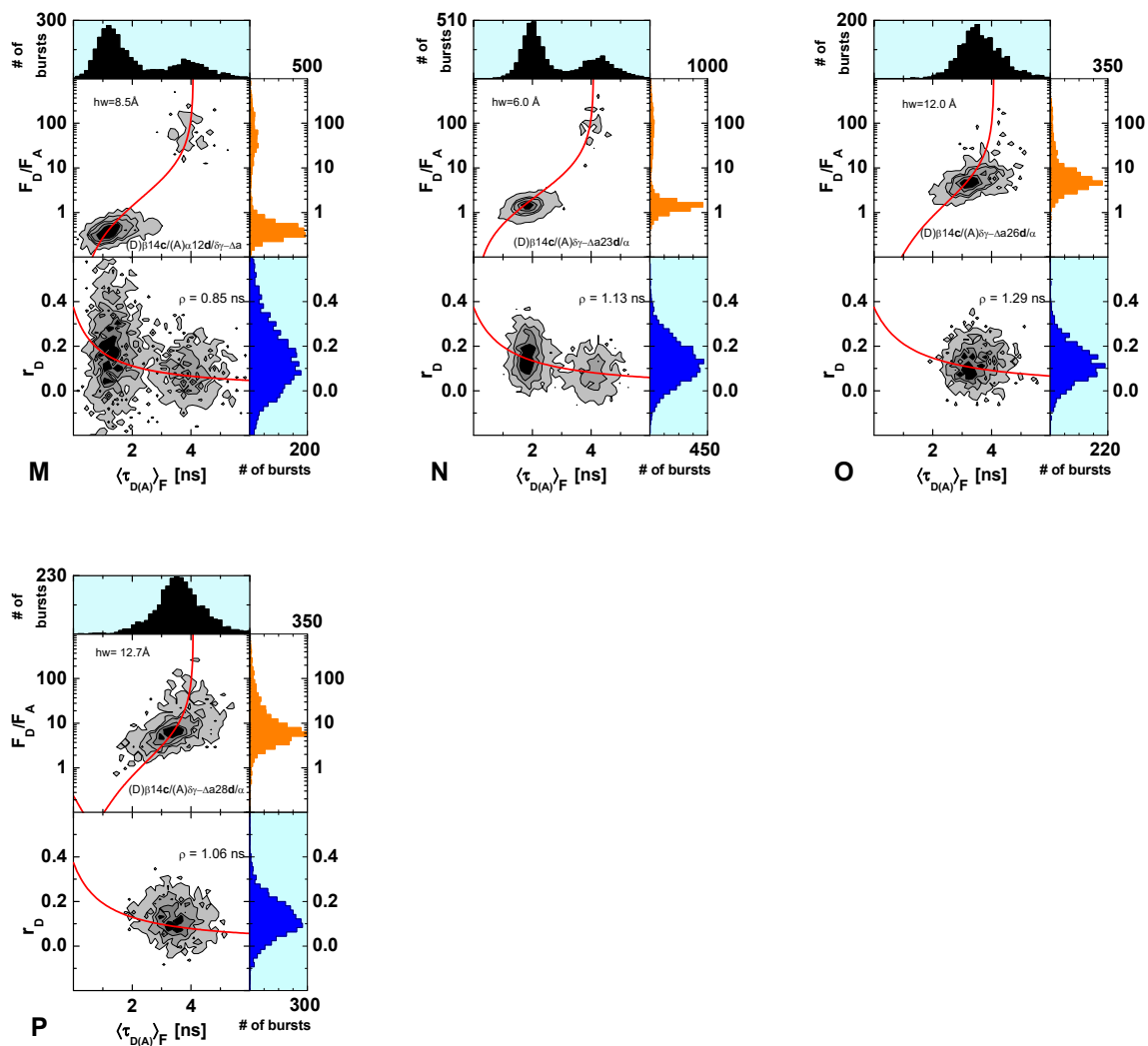
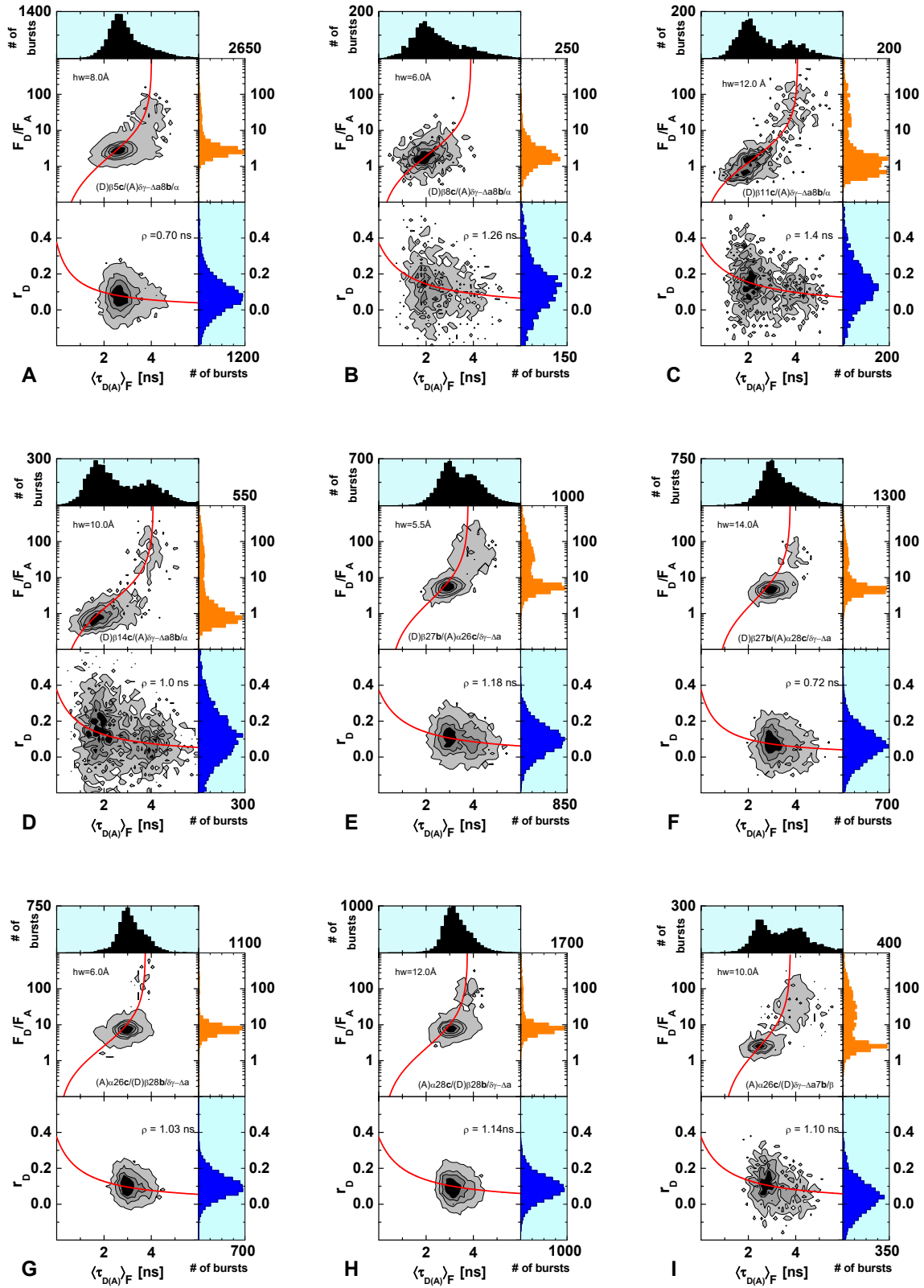


Figure 3.53 2D burst frequency histograms of J(bcd) with fluorescence labels on helices *c* and *d*: Upper panel: F_D/F_A vs fluorescence donor lifetime in presence of acceptor $\langle \tau_{D(A)F} \rangle$. Static FRET line is shown as red curve; Lower panel: the donor fluorescence anisotropy r_D vs $\langle \tau_{D(A)F} \rangle$. Perrin line is shown as red line.



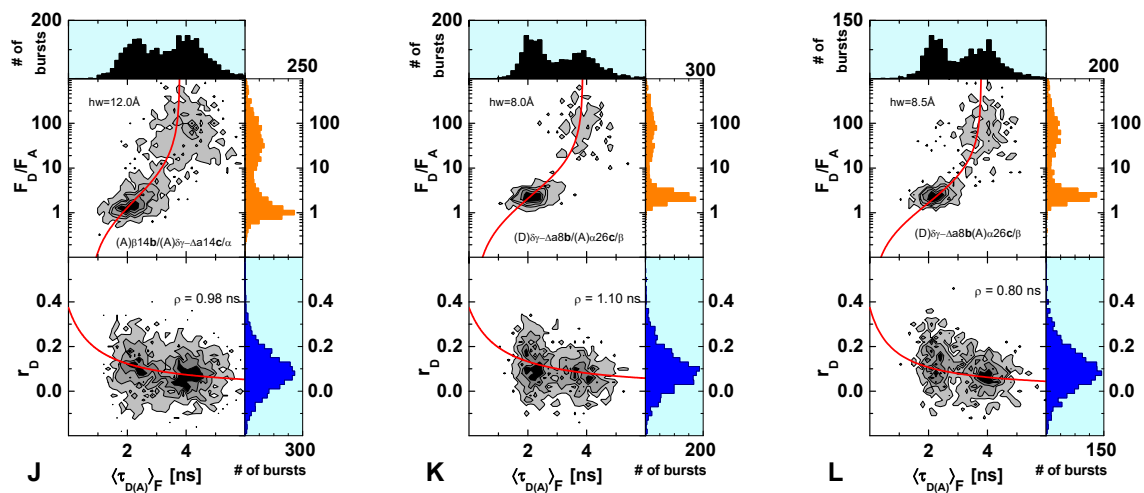
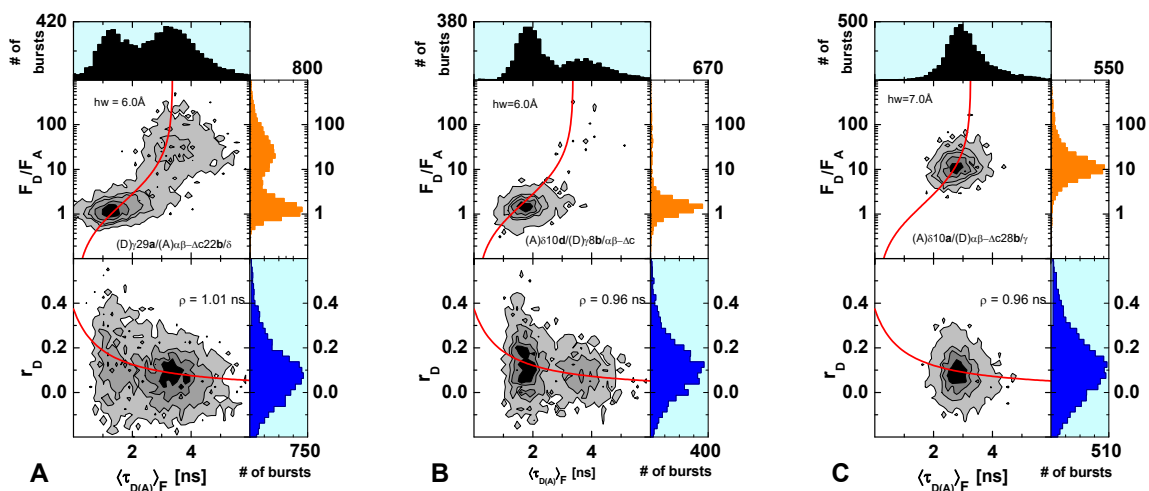


Figure 3.54 2D burst frequency histograms of J(bcd) with fluorescence labels on helices *b* and *c*: Upper panel: F_D/F_A vs fluorescence donor lifetime in presence of acceptor $\langle \tau_{D(A)F} \rangle$. Static FRET line is shown as red curve; Lower panel: the donor fluorescence anisotropy r_D vs $\langle \tau_{D(A)F} \rangle$. Perrin line is shown as red line.



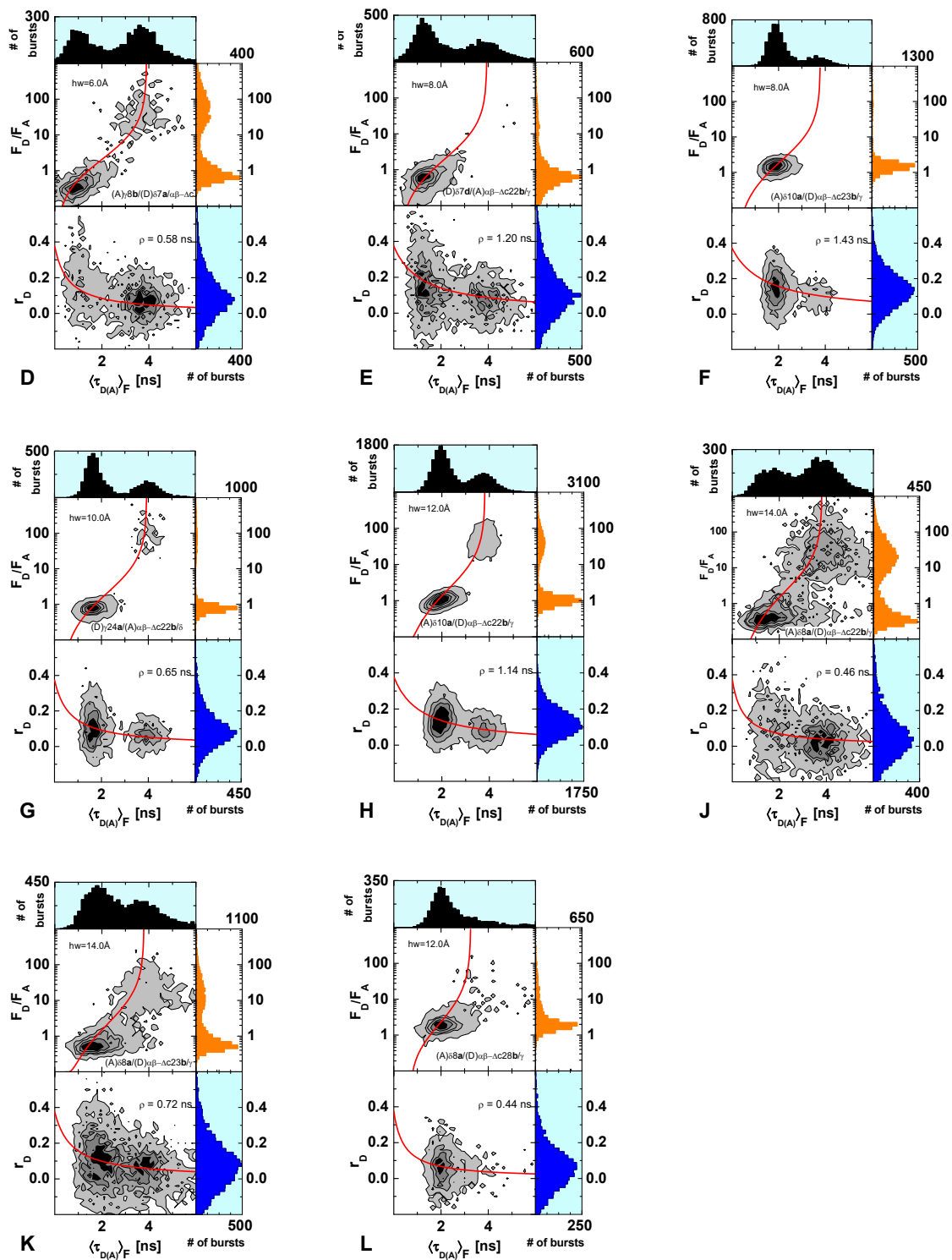
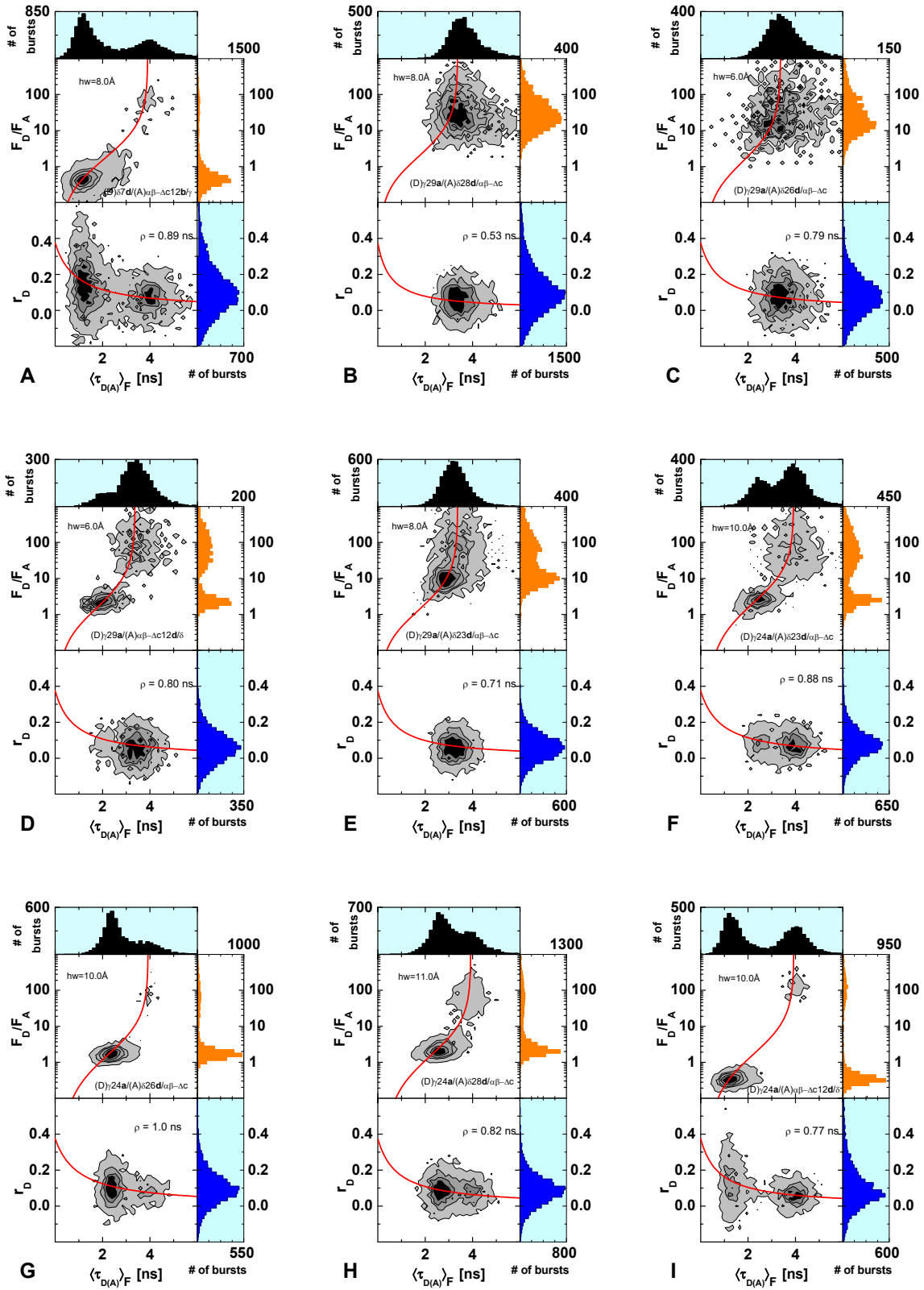


Figure 3.55 2D burst frequency histograms of J(abd) with fluorescence labels on helices *a* and *b*: Upper panel: F_D/F_A vs fluorescence donor lifetime in presence of acceptor $\langle \tau_{D(A)F} \rangle$. Static FRET line is shown as red curve; Lower panel: the donor fluorescence anisotropy r_D vs $\langle \tau_{D(A)F} \rangle$. Perrin line is shown as red line.



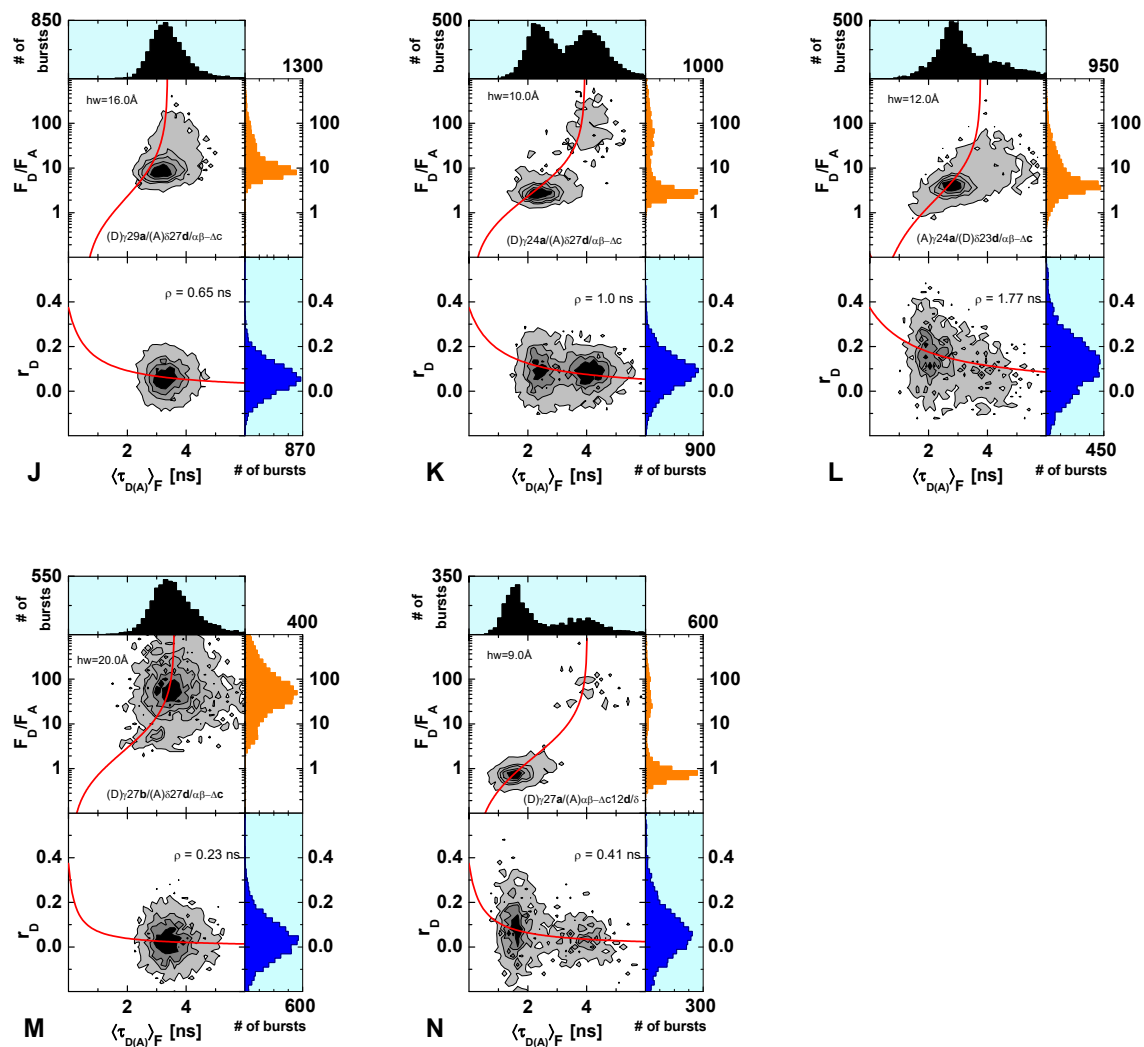
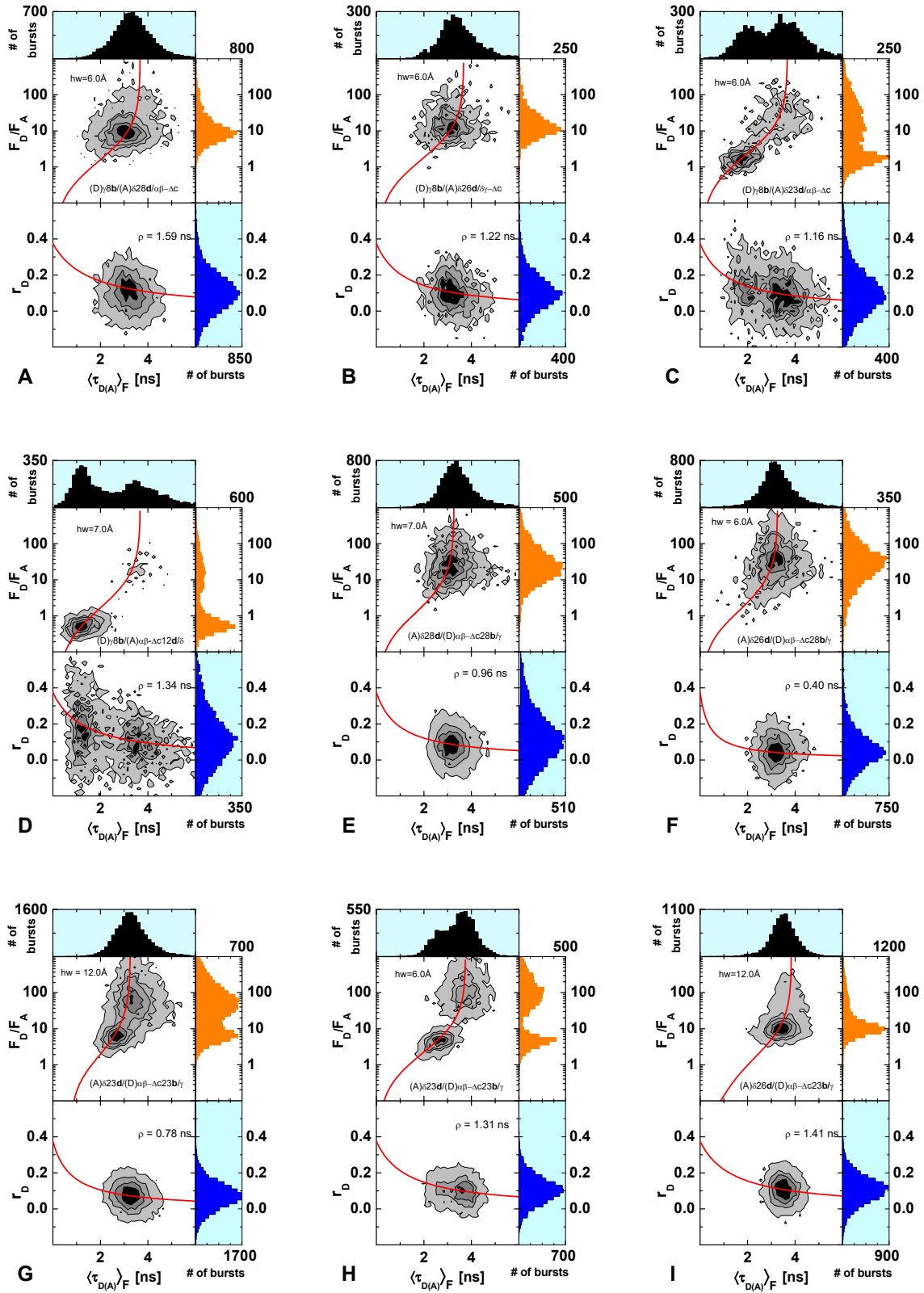


Figure 3.56 2D burst frequency histograms of J(abd) with fluorescence labels on helices *a* and *d*: Upper panel: F_D/F_A vs fluorescence donor lifetime in presence of acceptor $\langle \tau_{D(A)F} \rangle$. Static FRET line is shown as red curve; Lower panel: the donor fluorescence anisotropy r_D vs $\langle \tau_{D(A)F} \rangle$. Perrin line is shown as red line.



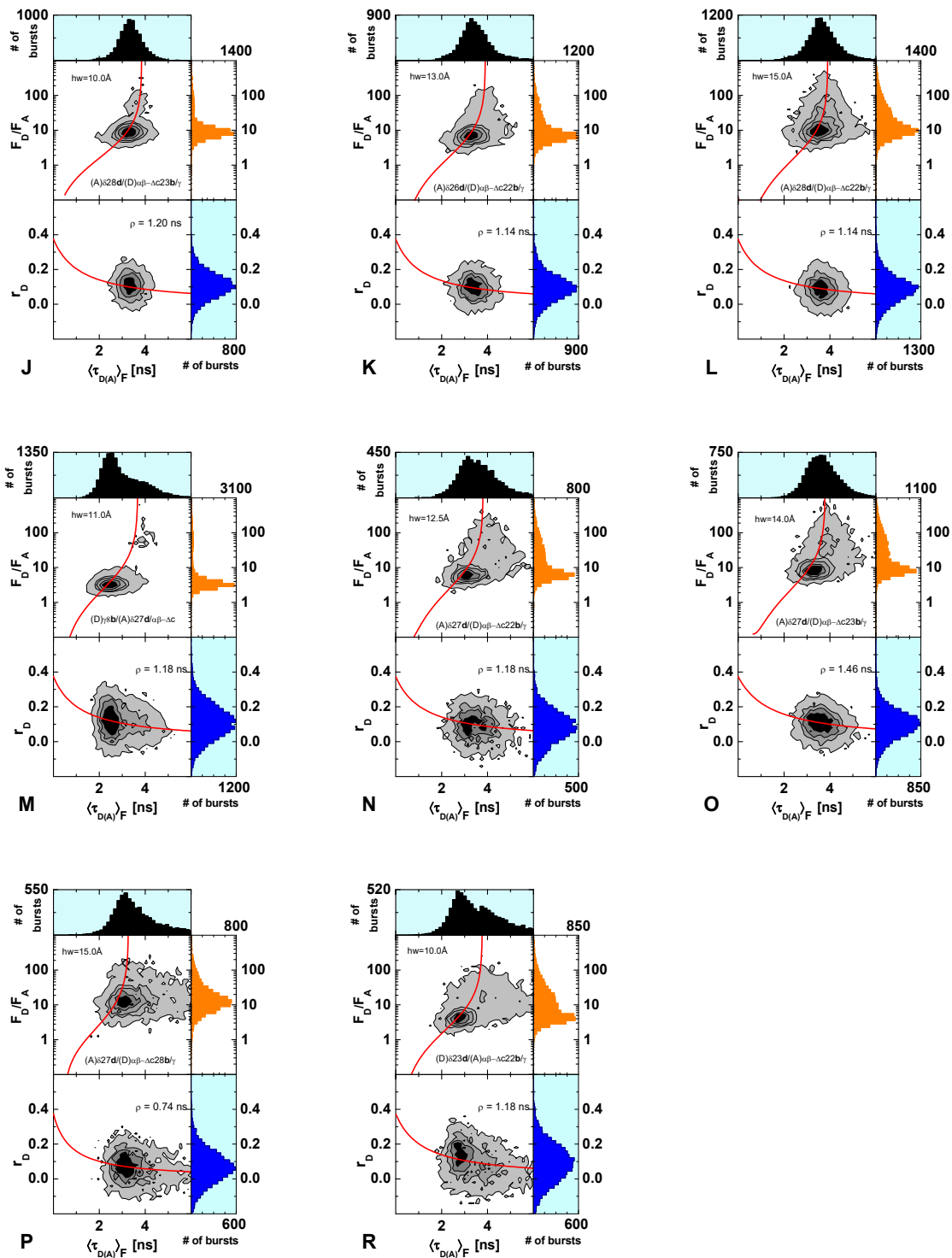


Figure 3.57 2D burst frequency histograms of J(abd) with fluorescence labels on helices *b* and *d*: Upper panel: F_D/F_A vs fluorescence donor lifetime in presence of acceptor $\langle \tau_{D(A)F} \rangle$. Static FRET line is shown as red curve; Lower panel: the donor fluorescence anisotropy r_D vs $\langle \tau_{D(A)F} \rangle$. Perrin line is shown as red line.

3.5.3.2 Static FRET lines

A compilation of all static FRET lines used to fit FRET and donor only populations on 2D MFD plots (3.5.3.1)

Table 3.25 Static FRET line for 2D MFD plots for J(acd) structure.

FRET pair	Static FRET line	Half width
((A)δ10a/(D)βγ-Δb14c/α	(0.7930/0.3450)/((4.0782/((-0.0367*x^3)+(0.2678*x^2)+0.5295*x+-0.0478))-1)	9.4
(A)δ10a/(D)βγ-Δb11c/α	(0.7930/0.3450)/((4.0782/((-0.0367*x^3)+(0.2678*x^2)+0.5295*x+-0.0478))-1)	10.8
(A)δ28d/(D)βγ-Δb14c/α	(0.7923/0.4730)/((4.0776/((-0.0367*x^3)+(0.2677*x^2)+0.5304*x+-0.0479))-1)	12
(A)δ28d/(D)βγ-Δb34a/α	(0.6235/0.4290)/((3.5908/((-0.05*x^3)+(0.2762*x^2)+0.669*x+-0.0609))-1)	12.5
(A)δ26d/(D)βγ-Δb34a/α	(0.5981/0.4030)/((3.4723/((-0.1418*x^3)+(0.9018*x^2)+-0.4058*x+-0.0552))-1)	13
(A)δ23d/(D)βγ-Δb34a/α	(0.6418/0.3120)/((3.5315/((-0.0895*x^3)+(0.5670*x^2)+0.1334*x+-0.0716))-1)	6.0
(A)δ23d/(D)βγ-Δb14a/α	(0.7923/0.3300)/((4.0776/((-0.0367*x^3)+(0.2677*x^2)+0.5304*x+-0.0479))-1)	6.0
(A)δ23d/(D)βγ-Δb11a/α	(0.7649/0.3300)/((3.9756/((-0.0392*x^3)+(0.2742*x^2)+0.5405*x+-0.0488))-1)	5.6
(A)δ23d/(D)βγ-Δb8a/α	(0.7458/0.3120)/((3.9777/((-0.0399*x^3)+(0.2682*x^2)+0.5767*x+-0.0535))-1)	8.5
(A)δ28d/(D)βγ-Δb11a/α	(0.7649/0.4730)/((3.9756/((-0.0392*x^3)+(0.2742*x^2)+0.5405*x+-0.0488))-1)	12.0
(A)δ28d/(D)βγ-Δb8a/α	(0.7458/0.3800)/((3.9777/((-0.0399*x^3)+(0.2682*x^2)+0.5767*x+-0.0535))-1)	12.0
(A)δ28d/(D)βγ-Δb5a/α	(0.7930/0.3450)/((4.0782/((-0.0367*x^3)+(0.2678*x^2)+0.5295*x+-0.0478))-1)	16.0
(A)α28c/(D)βγ-Δb34a/δ	(0.7923/0.3100)/((4.0776/((-0.0367*x^3)+(0.2677*x^2)+0.5304*x+-0.0479))-1)	14.0
(A)δ10d/(D)βγ-Δb8c/α	(0.7368/0.3210)/((3.9279/((-0.0410*x^3)+(0.2726*x^2)+0.5747*x+-0.0530))-1)	7.0
(A)α28c/(D)δ7a/βγ-Δb	(0.6739/0.2910)/((3.8960/((-0.0603*x^3)+(0.3921*x^2)+0.4146*x+-0.1089))-1)	9.0
(A)δ26d/(D)βγ-Δb14a/α	(0.7923/0.4071)/((4.0776/((-0.0367*x^3)+(0.2677*x^2)+0.5304*x+-0.0479))-1)	10.0
(A)δ26d/(D)βγ-Δb11a/α	(0.7649/0.4070)/((3.9756/((-0.0392*x^3)+(0.2742*x^2)+0.5405*x+-0.0488))-1)	11.0
(A)δ26d/(D)βγ-Δb8a/α	(0.7458/0.2810)/((3.9777/((-0.0399*x^3)+(0.2682*x^2)+0.5767*x+-0.0535))-1)	10.0
(A)δ26d/(D)βγ-Δb5a/α	(0.7759/0.4030)/((4.0460/((-0.0933*x^3)+(0.7352*x^2)+-0.4838*x+0.1485))-1)	14.0
(D)δ7a/(A)βγ-Δb14c/α	(0.6739/0.3050)/((3.8960/((-0.0824*x^3)+(0.5683*x^2)+0.0640*x+-0.1102))-1)	10.0
(A)δ10a/(D)βγ-Δb5c/α	(0.7662/0.3450)/((3.9885/((-0.1152*x^3)+(0.9140*x^2)+-0.9039*x+0.3621))-1)	12.0
(A)α12d/(D)δ7d/βγ-Δb	(0.6739/0.3700)/((3.8960/((-0.0603*x^3)+(0.3921*x^2)+0.4146*x+-0.1089))-1)	8.0
(A)α12d/(D)βγ-Δb14a/δ	(0.7923/0.3700)/((4.0776/((-0.0642*x^3)+(0.4967*x^2)+0.0489*x+-0.0306))-1)	9.0
(A)α12d/(D)βγ-Δb29a/δ	(0.7380/0.3700)/((3.9244/((-0.0835*x^3)+(0.6156*x^2)+-0.1287*x+-0.0045))-1)	10.0
(A)α26d/(D)βγ-Δb29a/δ	(0.7308/0.2860)/((3.9489/((-0.1247*x^3)+(0.9699*x^2)+-0.9740*x+0.3513))-1)	12.3

FRET pair	Static FRET line	Half width
(A) α 28d/(D) $\beta\gamma$ - Δ b29a/ δ	$(0.7308/0.4730)/((3.9489/((-0.0402*x^3)+(0.2665*x^2)+0.5874*x+0.0538))-1)$	12.5
(A) δ 23d/(D) $\beta\gamma$ - Δ b29a/ α	$(0.7308/0.4730)/((3.9489/((-0.0402*x^3)+(0.2665*x^2)+0.5874*x+0.0538))-1)$	10.0
(A) δ 26d/(D) $\beta\gamma$ - Δ b29a/ α	$(0.7308/0.4030)/((3.9489/((-0.0821*x^3)+(0.6052*x^2)+-0.1058*x+0.0168))-1)$	10.0
(A) δ 28d/(D) $\beta\gamma$ - Δ b29a/ α	$(0.7308/0.4280)/((3.9489/((-0.0821*x^3)+(0.6052*x^2)+-0.1058*x+0.0168))-1)$	10.0
(A) α 26d/(D) $\beta\gamma$ - Δ b34a/ δ	$(0.6291/0.2860)/((3.5309/((-0.1047*x^3)+(0.6657*x^2)+-0.0257*x+0.0705))-1)$	12.0
(A) α 26c/(D) δ 7a/ $\beta\gamma$ - Δ b	$(0.800/0.286)/((4.0/((-0.0376*x^3)+(0.2794*x^2)+0.4934*x+0.0432))-1)$	11.0
(A) α 12d/(D) $\beta\gamma$ - Δ b11a/ δ	$(0.7605/0.3700)/((3.9631/((-0.0686*x^3)+(0.5105*x^2)+0.0644*x+0.0388))-1)$	9.0
(A) α 12d/(D) $\beta\gamma$ - Δ b8a/ δ	$(0.7470/0.3700)/((3.9741/((-0.0530*x^3)+(0.3727*x^2)+0.3744*x+0.0752))-1)$	7.5
(A) α 12d/(D) $\beta\gamma$ - Δ b11a/ δ	$(0.7716/0.3700)/((4.0277/((-0.0557*x^3)+(0.4100*x^2)+0.2679*x+0.0676))-1)$	8.0
(A) α 12d/(D) $\beta\gamma$ - Δ b34a/ δ	$(0.5981/0.3700)/((3.4723/((-0.0791*x^3)+(0.4507*x^2)+0.4199*x+0.1094))-1)$	8.0
(D) δ 23d/(A) $\beta\gamma$ - Δ b14c/ α	$(0.7183/0.3050)/((3.7858/((-0.0838*x^3)+(0.5906*x^2)+-0.0278*x+0.0290))-1)$	9.5
(A) α 26c/(D) δ 23a/ $\beta\gamma$ - Δ b	$(0.7183/0.2860)/((3.7858/((-0.1285*x^3)+(0.9563*x^2)+-0.8573*x+0.2972))-1)$	13.0
(A) α 28c/(D) δ 23a/ $\beta\gamma$ - Δ b	$(0.7220/0.2910)/((3.7928/((-0.0911*x^3)+(0.6516*x^2)+-0.1645*x+0.0097))-1)$	6.0
(A) δ 27d/(D) $\beta\gamma$ - Δ b34a/ α	$(0.7716/0.2900)/((4.0277/((-0.0384*x^3)+(0.2694*x^2)+0.5492*x+0.0504))-1)$	16.0
(A) δ 27d/(D) $\beta\gamma$ - Δ b29a/ α	$(0.7308/0.2860)/((3.9489/((-0.1148*x^3)+(0.8834*x^2)+-0.7596*x+0.2406))-1)$	12.0
(A) δ 27d/(D) $\beta\gamma$ - Δ b14c/ α	$(0.7923/0.2860)/((4.0776/((-0.1106*x^3)+(0.9062*x^2)+-0.9594*x+0.4193))-1)$	12.0
(A) δ 27d/(D) $\beta\gamma$ - Δ b11c/ α	$(0.7649/0.2860)/((3.9756/((-0.1164*x^3)+(0.9245*x^2)+-0.9308*x+0.3809))-1)$	14.0
(A) δ 27d/(D) $\beta\gamma$ - Δ b8c/ α	$(0.7458/0.2860)/((3.9777/((-0.1136*x^3)+(0.8841*x^2)+-0.7873*x+0.2687))-1)$	14.0
(A) δ 27d/(D) $\beta\gamma$ - Δ b5c/ α	$(0.7841/0.2860)/((4.0584/((-0.1112*x^3)+(0.9015*x^2)+-0.9236*x+0.3880))-1)$	14.0
(A) δ 23d/(D) $\beta\gamma$ - Δ b5c/ α	$(0.7619/0.3150)/((3.9755/((-0.1159*x^3)+(0.9158*x^2)+-0.8987*x+0.3561))-1)$	12.0

Table 3.26 Static FRET line for 2D MFD plots for J(bcd) structure.

FRET pair	Static FRET line	Half width
(D) β 14c/(A) $\delta\gamma$ - Δ a28d/ α	$(0.7723/0.4920)/((4.0791/((-0.0372*x^3)+(0.2617*x^2)+0.5629*x+0.0518))-1)$	12.7
(D) β 11c/(A) $\delta\gamma$ - Δ a28d/ α	$(0.820/0.4920)/((4.1/((-0.0356*x^3)+(0.2711*x^2)+0.4964*x+0.044))-1)$	15.5
(D) β 8c/(A) $\delta\gamma$ - Δ a28d/ α	$(0.6936/0.4920)/((3.8831/((-0.0424*x^3)+(0.2626*x^2)+0.6418*x+0.0605))-1)$	12.2
(D) β 5c/(A) $\delta\gamma$ - Δ a28d/ α	$0.7807/0.4920)/((4.0159/((-0.1144*x^3)+(0.9200*x^2)+0.9495*x+0.4021))-1)$	14.5
(D) β 27b/(A) $\delta\gamma$ - Δ a28d/a	$(0.6294/0.4920)/((3.7781/((-0.1145*x^3)+(0.7832*x^2)+0.2907*x+0.1279))-1)$	12.0
(D) β 14c/(A) $\delta\gamma$ - Δ a26d/a	$(0.7723/0.4260)/((4.0791/((-0.1084*x^3)+(0.8732*x^2)+0.8371*x+0.3194))-1)$	11.8
(D) β 11c/(A) $\delta\gamma$ - Δ a26d/a	$(0.82/0.426)/((4.1/((-0.0356*x^3)+(0.2711*x^2)+0.496*x+0.044))-1)$	12.4
(D) β 8c/(A) $\delta\gamma$ - Δ a26d/a	$(0.82/0.426)/((4.1/((-0.0356*x^3)+(0.2711*x^2)+0.496*x+0.044))-1)$	12.0
(D) β 5c/(A) $\delta\gamma$ - Δ a26d/a	$(0.7788/0.426)/((4.0121/((-0.0389*x^3)+(0.2756*x^2)+0.5320*x+0.0484))-1)$	8.0
(D) β 14c/(A) $\delta\gamma$ - Δ a23d/ α	$(0.7723/0.313)/((4.0791/((-0.0372*x^3)+(0.2617*x^2)+0.5629*x+0.0518))-1)$	6.0
(D) β 27b/(A) $\delta\gamma$ - Δ a26d/a	$(0.6294/0.4260)/((3.7781/((-0.0441*x^3)+(0.2443*x^2)+0.7221*x+0.0663))-1)$	14.0
(D) β 11c/(A) $\delta\gamma$ - Δ a23d/ α	$(0.7276/0.313)/((3.927/((-0.0407*x^3)+(0.2686*x^2)+0.5860*x+0.0536))-1)$	8.0
(D) β 8c/(A) $\delta\gamma$ - Δ a23d/ α	$(0.6936/0.313)/((3.8831/((-0.0424*x^3)+(0.2606*x^2)+0.6418*x+0.0605))-1)$	7.0
(D) β 5c/(A) $\delta\gamma$ - Δ a23d/ α	$(0.7807/0.3130)/((4.0159/((-0.0669*x^3)+(0.5069*x^2)+0.0512*x+0.0333))-1)$	8.0
(D) $\delta\gamma$ - Δ a8b/(A) α 26c/ β	$(0.7306/0.2810)/((3.8703/((-0.0426*x^3)+(0.2802*x^2)+0.5653*x+0.0518))-1)$	8.0
(D) $\delta\gamma$ - Δ a8b/(A) α 28c/ β	$(0.6294/0.4260)/((3.7781/((-0.0441*x^3)+(0.2443*x^2)+0.7221*x+0.0663))-1)$	8.5
(D) β 5c/(A) $\delta\gamma$ - Δ a8b/ α	$(0.7807/0.3590)/((4.0159/((-0.0669*x^3)+(0.5069*x^2)+0.0512*x+0.0333))-1)$	8.0
(D) β 11c/(A) $\delta\gamma$ - Δ a8b/ α	$(0.7723/0.4920)/((4.0791/((-0.0372*x^3)+(0.2617*x^2)+0.5629*x+0.0518))-1)$	12.0
(D) β 27b/(A) α 26c/ $\delta\gamma$ - Δ a	$(0.6294/0.2840)/((3.7781/((-0.0932*x^3)+(0.6162*x^2)+0.0415*x+0.1510))-1)$	5.5
(D) β 27b/(A) α 28c/ $\delta\gamma$ - Δ a	$(0.6294/0.2790)/((3.7781/((-0.1145*x^3)+(0.7832*x^2)+0.2907*x+0.1279))-1)$	14.0
(D) β 14c/(A) $\delta\gamma$ - Δ a8b/ α	$(0.7723/0.3590)/((4.0791/((-0.0644*x^3)+(0.4873*x^2)+0.0952*x+0.0513))-1)$	10.0
(D) β 5c/(A) α 12b/ $\delta\gamma$ - Δ a	$(0.7807/0.3810)/((4.0159/((-0.0669*x^3)+(0.5069*x^2)+0.0512*x+0.0333))-1)$	9.6
(D) β 14c/(A) α 12b/ $\delta\gamma$ - Δ a	$(0.7723/0.3810)/((4.0791/((-0.0541*x^3)+(0.4007*x^2)+0.2828*x+0.0716))-1)$	8.5
(D) β 11c/(A) α 12b/ $\delta\gamma$ - Δ a	$(0.7276/0.3810)/((3.9274/((-0.0592*x^3)+(0.4138*x^2)+0.3066*x+0.0783))-1)$	8.5
(A) α 12d/(D) $\delta\gamma$ - Δ a8b/ β	$(0.7306/0.3810)/((3.8703/((-0.0941*x^3)+(0.6930*x^2)+0.2855*x+0.0480))-1)$	10.5
(A) α 12d/(D) β 27b/ $\delta\gamma$ - Δ a	$(0.6294/0.3810)/((3.7781/((-0.0868*x^3)+(0.5667*x^2)+0.1371*x+0.1505))-1)$	12.0
(D) β 28c/(A) $\delta\gamma$ - Δ a23d/ α	$(0.6936/0.3810)/((3.8831/((-0.0610*x^3)+(0.4042*x^2)+0.3745*x+0.0987))-1)$	8.0
(D) β 28b/(A) $\delta\gamma$ - Δ a26d/ α	$(0.6715/0.4260)/((3.7522/((-0.1075*x^3)+(0.7476*x^2)+0.2886*x+0.0106))-1)$	11.0

FRET pair	Static FRET line	Half width
(D) β 28b/(A) $\delta\gamma$ - Δ a28d/ α	$(0.6976/0.4920)/((3.6025/((-0.1477*x^3)+(1.0617*x^2)+-1.0152*x+0.3853))-1)$	12.6
(A) α 26c/(D) β 28b/ $\delta\gamma$ - Δ a	$(0.6715/0.2790)/((3.7522/((-0.0473*x^3)+(0.2834*x^2)+0.6161*x+0.0561))-1)$	6.0
(A) α 12d/(D) β 28b/ $\delta\gamma$ - Δ a	$(0.6778/0.3810)/((3.7545/((-0.0673*x^3)+(0.4365*x^2)+0.3321*x+0.0875))-1)$	9.5
(A) α 28c/(D) β 28b/ $\delta\gamma$ - Δ a	$(0.6715/0.2790)/((3.7522/((-0.0674*x^3)+(0.4339*x^2)+0.3443*x+0.0911))-1)$	12.0
(D) β 27c/(A) $\delta\gamma$ - Δ a23d/ α	$(0.6294/0.3130)/((3.7781/((-0.1506*x^3)+(1.0715*x^2)+-0.9049*x+0.0238))-1)$	12.0
(D) β 29b/(A) $\delta\gamma$ - Δ a28d/ α	$(0.7680/0.4920)/((3.9926/((-0.0807*x^3)+(0.6161*x^2)+-0.1801*x+0.0269))-1)$	6.0
(D) β 29b/(A) $\delta\gamma$ - Δ a26d/ α	$(0.7624/0.4260)/((3.9627/((-0.0578*x^3)+(0.4200*x^2)+0.2590*x+0.0649))-1)$	6.0
(D) β 29b/(A) $\delta\gamma$ - Δ a23d/ α	$(0.7587/0.3130)/((3.9428/((-0.0584*x^3)+(0.4227*x^2)+0.2577*x+0.0645))-1)$	8.2
(A) α 12d/(D) β 29b/ $\delta\gamma$ - Δ a	$(0.7587/0.3810)/((3.9428/((-0.0831*x^3)+(0.6267*x^2)+-0.1867*x+0.0289))-1)$	10.0
(A) β 14c/(D) $\delta\gamma$ - Δ a14b/ α	$(0.6241/0.3310)/((3.7816/((-0.1126*x^3)+(0.7537*x^2)+-0.1842*x+0.2118))-1)$	12.0
(A) α 26c/(D) $\delta\gamma$ - Δ a7b/ β	$(0.6294/0.3130)/((3.7781/((-0.1506*x^3)+(1.0715*x^2)+-0.9049*x+0.0238))-1)$	10.0
(A) α 12d/(D) $\delta\gamma$ - Δ a7b/ β	$(0.7031/0.3810)/((3.9120/((-0.0978*x^3)+(0.7112*x^2)+-0.2844*x+0.0030))-1)$	11.0
(D) β 8c/(A) $\delta\gamma$ - Δ a8b/ α	$(0.6947/0.3590)/((3.8924/((-0.0422*x^3)+(0.2595*x^2)+0.6432*x+0.0607))-1)$	6.0

Table 3.27 Static FRET line for 2D MFD plots for J(abd) structure.

FRET pair	Static FRET line	Half width
(D)Y8b/(A)δ10a/αβ-Δc	$(0.5328/0.3210)/((3.3649/((-0.0559*x^3)+(0.2470*x^2)+0.8234*x+0.0763))-1)$	6.0
(D)Y8b/(A)δ26d/αβ-Δc	$(0.6731/0.4090)/((3.6737/((-0.0495*x^3)+(0.2935*x^2)+0.6043*x+0.0563))-1)$	6.0
(D)Y8b/(A)δ28d/αβ-Δc	$(0.6731/0.4730)/((3.6737/((-0.0495*x^3)+(0.2935*x^2)+0.6043*x+0.0563))-1)$	6.0
(D)Y8b/(A)δ23d/αβ-Δc	$(0.6731/0.3120)/((3.6737/((-0.0495*x^3)+(0.2935*x^2)+0.6043*x+0.0563))-1)$	2.0
(D)Y8b/(A)αβ-Δc12d/δ	$(0.6731/0.3890)/((3.6737/((-0.0701*x^3)+(0.4451*x^2)+0.3342*x+0.0884))-1)$	7.0
(A)δ10a/(D)αβ-Δc28b/γ	$(0.4463/0.3450)/((3.2571/((-0.0544*x^3)+(0.1822*x^2)+1.0093*x+0.0880))-1)$	7.0
(A)δ28d/(D)αβ-Δc28b/γ	$(0.4463/0.4730)/((3.2571/((-0.0544*x^3)+(0.1822*x^2)+1.0093*x+0.0880))-1)$	7.0
(A)δ26d/(D)αβ-Δc28b/γ	$(0.4437/0.4090)/((3.2535/((-0.0542*x^3)+(0.1788*x^2)+1.0177*x+0.0887))-1)$	9.0
(A)δ23d/(D)αβ-Δc28b/γ	$(0.4463/0.3120)/((3.2571/((-0.1134*x^3)+(0.5188*x^2)+0.7560*x+0.7919))-1)$	13.0
(D)δ7d/(A)αβ-Δc22b/γ	$(0.7160/0.3210)/((3.9413/((-0.0695*x^3)+(0.4928*x^2)+0.1572*x+0.0788))-1)$	8.0
(D)δ7d/(A)αβ-Δc12b/γ	$(0.6744/0.3890)/((3.9050/((-0.0600*x^3)+(0.3903*x^2)+0.4176*x+0.1098))-1)$	8.0
(A)Y8b/(D)δ7a/αβ-Δc	$(0.6739/0.3330)/((3.8960/((-0.0416*x^3)+(0.2481*x^2)+0.6796*x+0.0636))-1)$	6.0
(D)Y29a/(A)αβ-Δc12d/δ	$(0.5328/0.3890)/((3.3649/((-0.0683*x^3)+(0.3267*x^2)+0.7055*x+0.1105))-1)$	6.0
(D)Y29a/(A)δ28d/αβ-Δc	$(0.5328/0.3180)/((3.3649/((-0.0559*x^3)+(0.2470*x^2)+0.8234*x+0.0763))-1)$	8.0
(D)Y29a/(A)δ26d/αβ-Δc	$(0.5328/0.4050)/((3.3649/((-0.0803*x^3)+(0.4055*x^2)+0.5873*x+0.1492))-1)$	6.0
(D)Y29a/(A)δ23d/αβ-Δc	$(0.5328/0.4600)/((3.3649/((-0.0559*x^3)+(0.2470*x^2)+0.8234*x+0.0763))-1)$	8.0
(D)Y29a/(A)αβ-Δc22b/δ	$(0.5328/0.3210)/((3.3649/((-0.0559*x^3)+(0.2470*x^2)+0.8234*x+0.0763))-1)$	6.0
(A)δ10a/(D)αβ-Δc23b/γ	$(0.7389/0.3030)/((3.7911/((-0.0772*x^3)+(0.5514*x^2)+0.0256*x+0.0259))-1)$	8.0
(D)Y24a/(A)δ23d/αβ-Δc	$(0.7191/0.3120)/((3.9291/((-0.0826*x^3)+(0.5996*x^2)+-0.0712*x+0.0363))-1)$	10.0
(D)Y24a/(A)δ26d/αβ-Δc	$(0.7191/0.4050)/((3.9291/((-0.0826*x^3)+(0.5996*x^2)+-0.0712*x+0.0363))-1)$	10.0
(D)Y24a/(A)δ28d/αβ-Δc	$(0.7191/0.4280)/((3.9291/((-0.0826*x^3)+(0.5996*x^2)+-0.0712*x+0.0363))-1)$	11.0
(D)Y24a/(A)αβ-Δc22b/δ	$(0.7184/0.3210)/((3.9318/((-0.0825*x^3)+(0.5986*x^2)+-0.0692*x+0.0374))-1)$	10.0
(D)Y24a/(A)αβ-Δc12d/δ	$(0.7184/0.3890)/((3.9318/((-0.0825*x^3)+(0.5986*x^2)+-0.0692*x+0.0374))-1)$	10.0
(A)δ10a/(D)αβ-Δc22b/γ	$(0.7155/0.3030)/((3.8126/((-0.1253*x^3)+(0.9345*x^2)+-0.8126*x+0.2678))-1)$	12.0
(A)δ26d/(D)αβ-Δc22b/γ	$(0.7340/0.4090)/((3.9101/((-0.0998*x^3)+(0.7466*x^2)+-0.4178*x+0.0933))-1)$	13.0
(A)δ28d/(D)αβ-Δc22b/γ	$(0.7340/0.4730)/((3.9101/((-0.1181*x^3)+(0.9028*x^2)+-0.7922*x+0.2645))-1)$	15.0
(D)Y29a/(A)δ27d/αβ-Δc	$(0.5328/0.2680)/((3.3649/((-0.1193*x^3)+(0.6668*x^2)+0.1902*x+0.2827))-1)$	16.0
(A)δ27d/(D)αβ-Δc22b/γ	$(0.7162/0.2680)/((3.8109/((-0.1366*x^3)+(1.0301*x^2)+-1.0446*x+0.3907))-1)$	13.0
(A)δ27d/(D)αβ-Δc23b/γ	$(0.7380/0.2680)/((3.7903/((-0.1440*x^3)+(1.1030*x^2)+-1.2579*x+0.5540))-1)$	14.0

FRET pair	Static FRET line	Half width
(D)Y24a/(A)δ27d/αβ-Δc	$(0.7209/0.2860)/((3.9391/((-0.0407*x^3)+(0.2639*x^2)+0.6053*x+-0.0561))-1)$	10.0
(D)Y8b/(A)δ27d/αβ-Δc	$(0.6731/0.2680)/((3.6737/((-0.1131*x^3)+(0.7762*x^2)+-0.3314*x+0.0219))-1)$	11.0
(D)δ23d/(A)αβ-Δc22b/γ	$(0.7153/0.3410)/((3.7724/((-0.0921*x^3)+(0.6532*x^2)+-0.1541*x+0.0031))-1)$	10.0
(A)Y24a/(D)δ23d/αβ-Δc	$(0.7153/0.3210)/((3.7724/((-0.1189*x^3)+(0.8713*x^2)+-0.6452*x+0.1910))-1)$	12.0
(A)δ26d/(D)αβ-Δc23b/γ	$(0.7480/0.4050)/((3.8471/((-0.1271*x^3)+(0.9761*x^2)+-0.9772*x+0.3953))-1)$	12.0
(D)Y27b/(A)δ27d/αβ-Δc	$(0.6251/0.2680)/((3.5887/((-0.0528*x^3)+(0.2879*x^2)+0.6622*x+-0.0611))-1)$	20.0
(A)δ27d/(D)αβ-Δc28b/γ	$(0.4544/0.2680)/((3.2601/((-0.1008*x^3)+(0.4686*x^2)+0.6610*x+-0.3880))-1)$	15.0
(A)δ28d/(D)αβ-Δc23b/γ	$(0.7480/0.4280)/((3.8471/((-0.0437*x^3)+(0.2953*x^2)+0.5219*x+-0.0466))-1)$	10.0
(A)δ23d/(D)αβ-Δc23b/γ	$(0.7309/0.3120)/((3.7522/((-0.0461*x^3)+(0.3047*x^2)+0.5163*x+-0.0455))-1)$	6.0
(A)δ8a/(D)αβ-Δc22b/γ	$(0.7155/0.2760)/((3.8126/((-0.1253*x^3)+(0.9345*x^2)+-0.8126*x+0.2678))-1)$	14.0
(A)δ8a/(D)αβ-Δc23b/γ	$(0.7377/0.2760)/((3.7901/((-0.1318*x^3)+(0.9986*x^2)+-0.9984*x+0.4027))-1)$	14.0
(A)δ8a/(D)αβ-Δc28b/γ	$(0.4463/0.2760)/((3.2571/((-0.1099*x^3)+(0.5040*x^2)+0.7316*x+-0.6778))-1)$	12.0
(D)Y27a/(A)αβ-Δc12d/δ	$(0.7784/0.3890)/((4.0196/((-0.0558*x^3)+(0.4143*x^2)+0.2519*x+-0.0628))-1)$	9.0

3.5.4 PDA analysis

3.5.4.1 Additional S_g/S_r histograms

Measurements of $J(acd)$

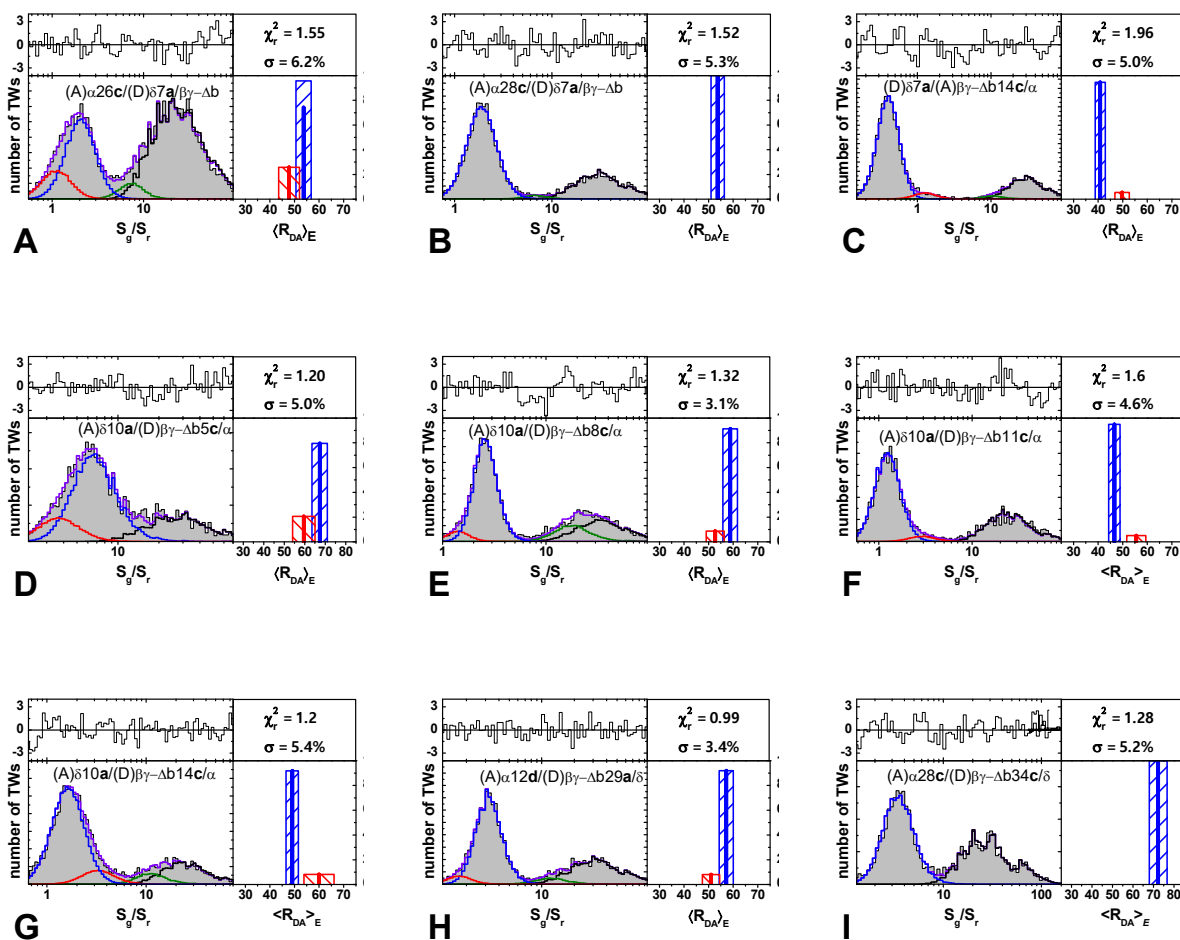
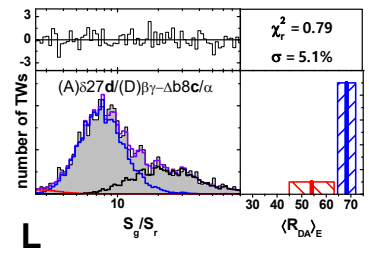
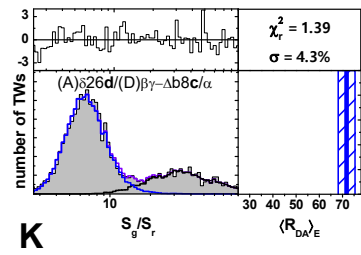
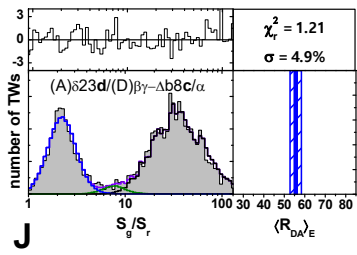
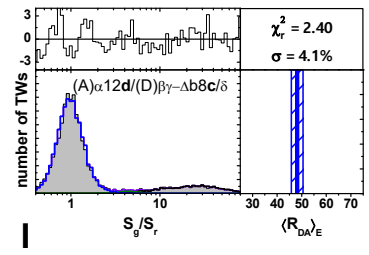
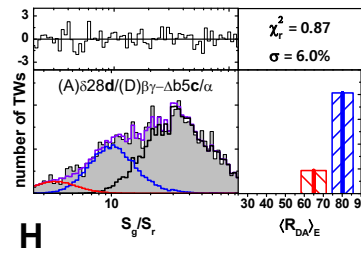
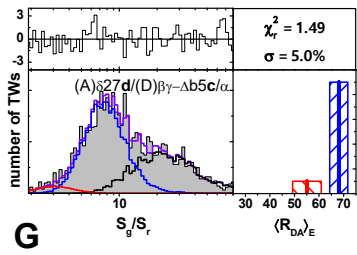
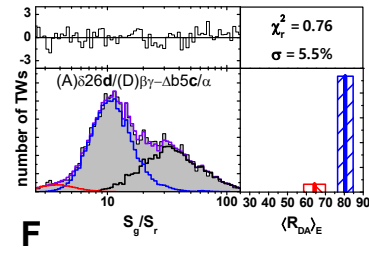
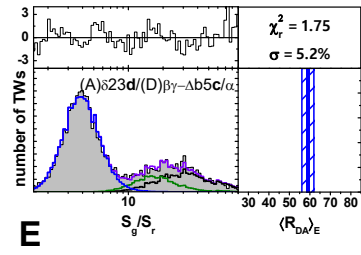
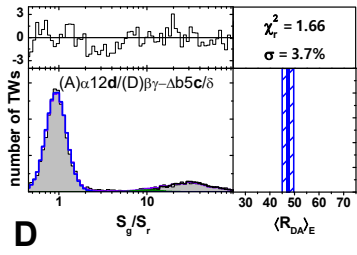
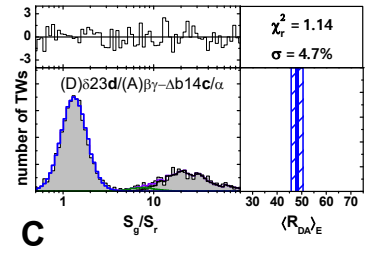
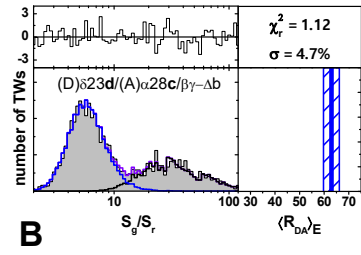
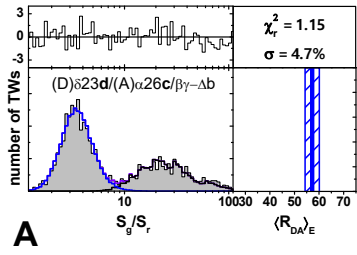


Figure 3.58 Results of PDA analysis for the samples with fluorescence labels on the helices a and c . Left panel: S_g/S_r histogram of experimental data (gray area) is fitted (purple solid line) with major population $\langle R_{DA} \rangle_{E1}$ (blue) and minor $\langle R_{DA} \rangle_{E1}$ population (red), donor only fraction (black) and impurity (green) with global apparent width σ . Goodness of the fit is judged with weighted residuals (upper left panel). Right panel: fitted distances for the major (blue solid line) and minor (red solid line) states with their relative amplitudes and confidence intervals (stipped boxes).



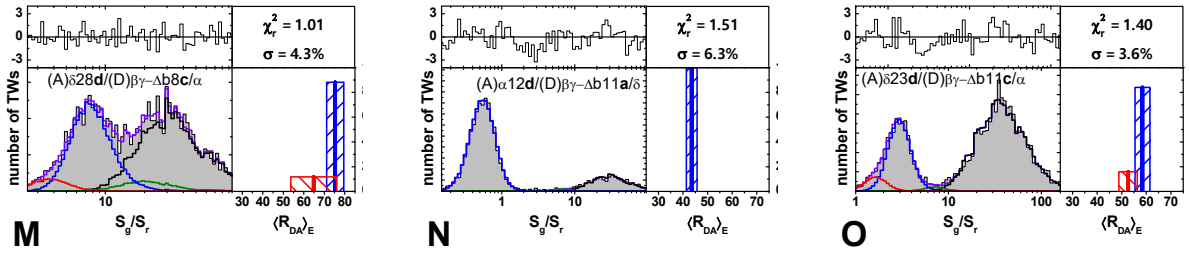
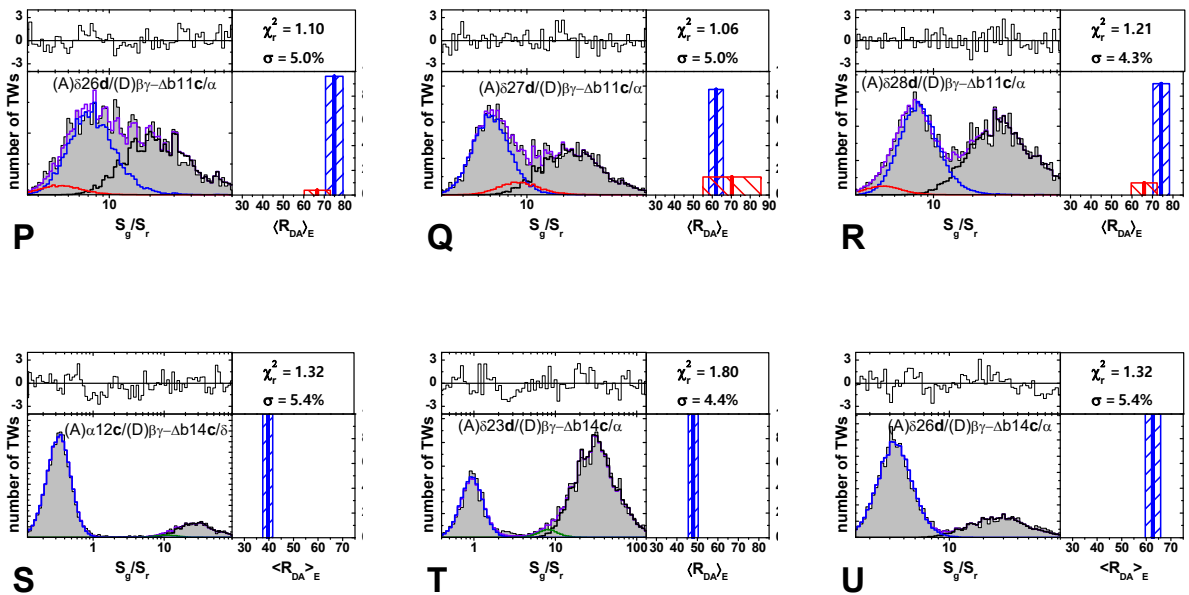


Figure 3.59 Results of PDA analysis for the samples with fluorescence labels on the helices *c* and *d*. Left panel: S_g/S_r histogram of experimental data (gray area) is fitted (purple solid line) with major population $\langle R_{DA} \rangle_{E1}$ (blue) and minor $\langle R_{DA} \rangle_{E2}$ population (red), donor only fraction (black) and impurity (green) with global apparent width σ . Goodness of the fit is judged with weighted residuals (upper left panel). Right panel: fitted distances for the major (blue solid line) and minor (red solid line) states with their relative amplitudes and confidence intervals (stripped boxes).



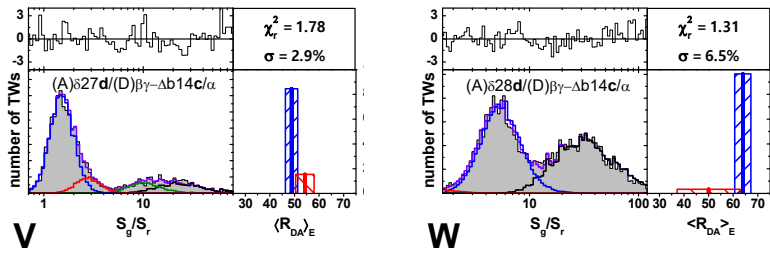
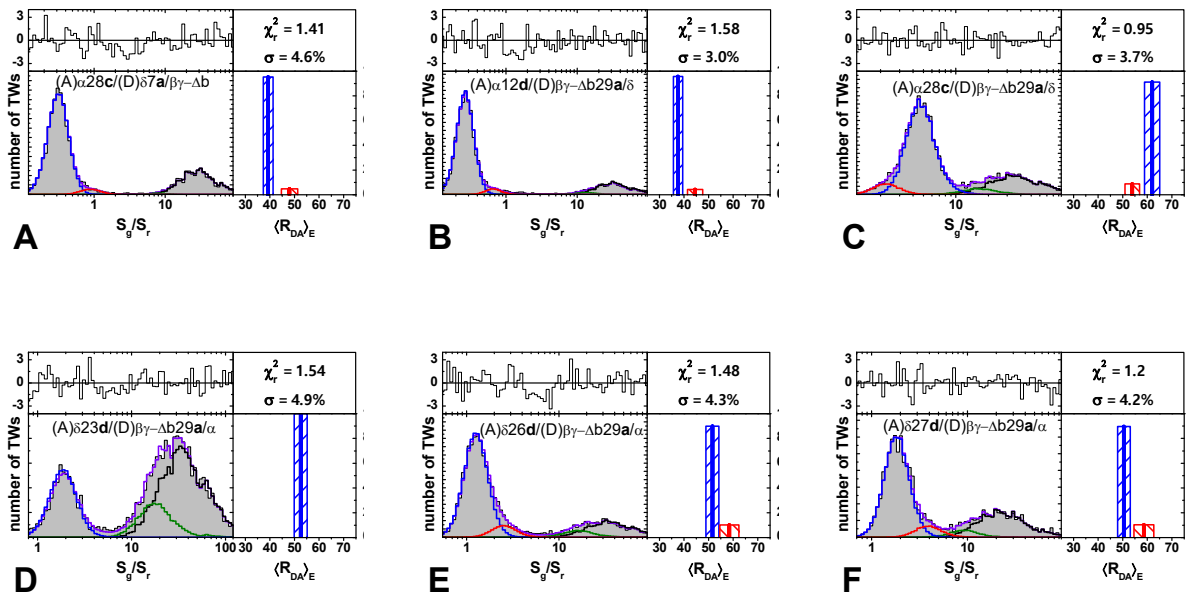


Figure 3.60 Results of PDA analysis for the samples with fluorescence labels on the helices *c* and *d*. Left panel: S_g/S_r histogram of experimental data (gray area) is fitted (purple solid line) with major population $\langle R_{DA} \rangle_{E1}$ (blue) and minor $\langle R_{DA} \rangle_{E1}$ population (red), donor only fraction (black) and impurity (green) with global apparent width σ . Goodness of the fit is judged with weighted residuals (upper left panel). Right panel: fitted distances for the major (blue solid line) and minor (red solid line) states with their relative amplitudes and confidence intervals (stripped boxes).



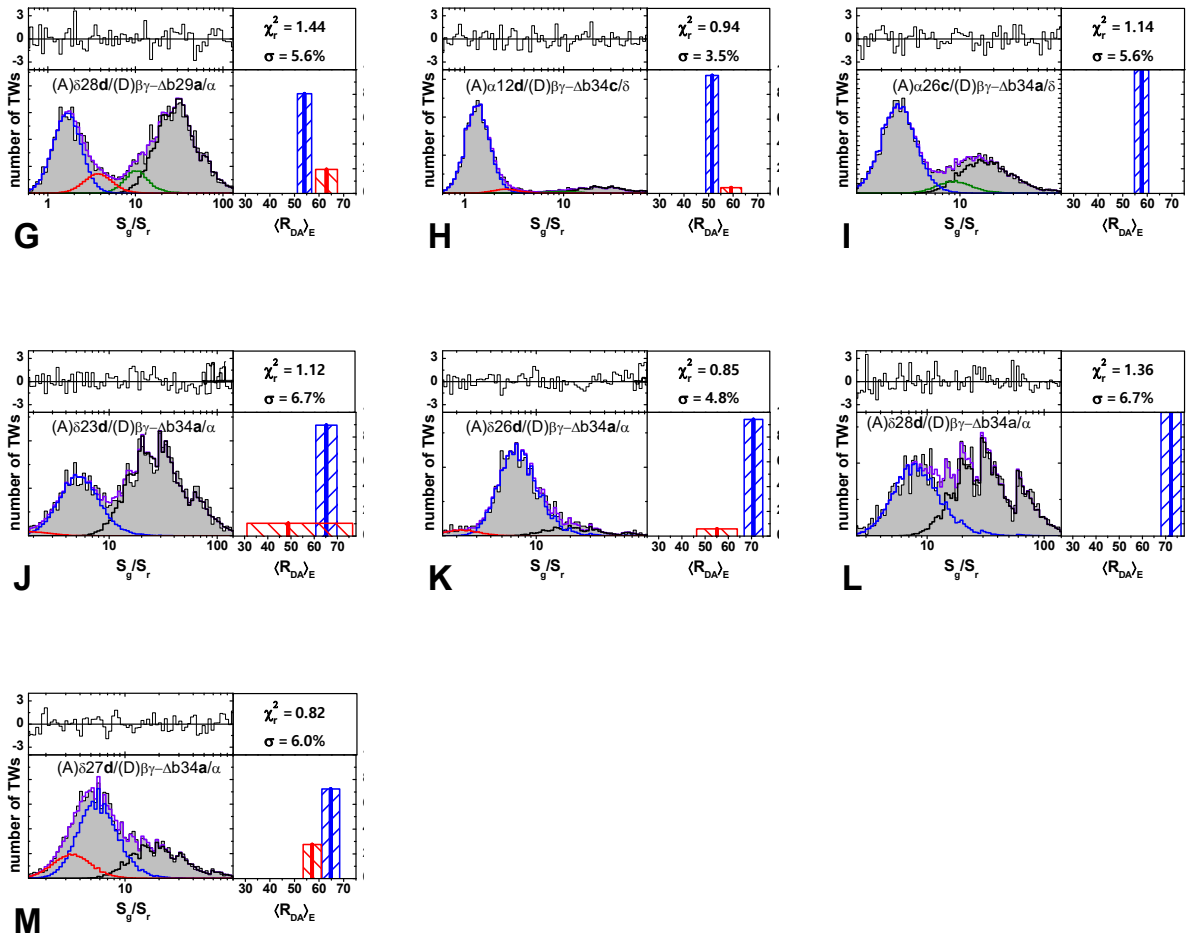


Figure 3.61 Results of PDA analysis for the samples with fluorescence labels on the helices *a* and *d*. Left panel: S_g/S_r histogram of experimental data (gray area) is fitted (purple solid line) with major population $\langle R_{DA} \rangle_{E1}$ (blue) and minor $\langle R_{DA} \rangle_{E1}$ population (red), donor only fraction (black) and impurity (green) with global apparent width σ . Goodness of the fit is judged with weighted residuals (upper left panel). Right panel: fitted distances for the major (blue solid line) and minor (red solid line) states with their relative amplitudes and confidence intervals (stripped boxes).

Measurements of $J(abd)$

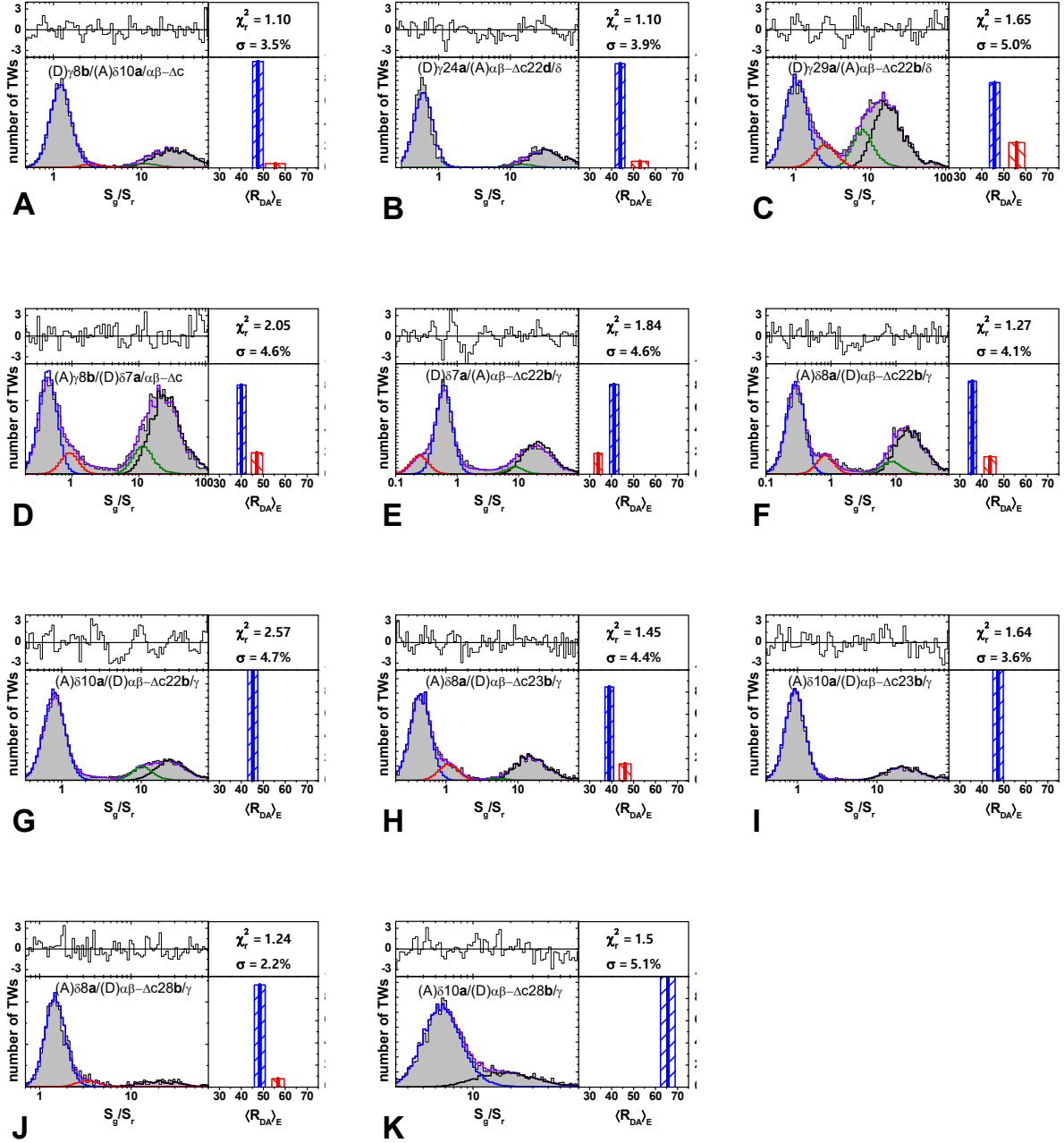
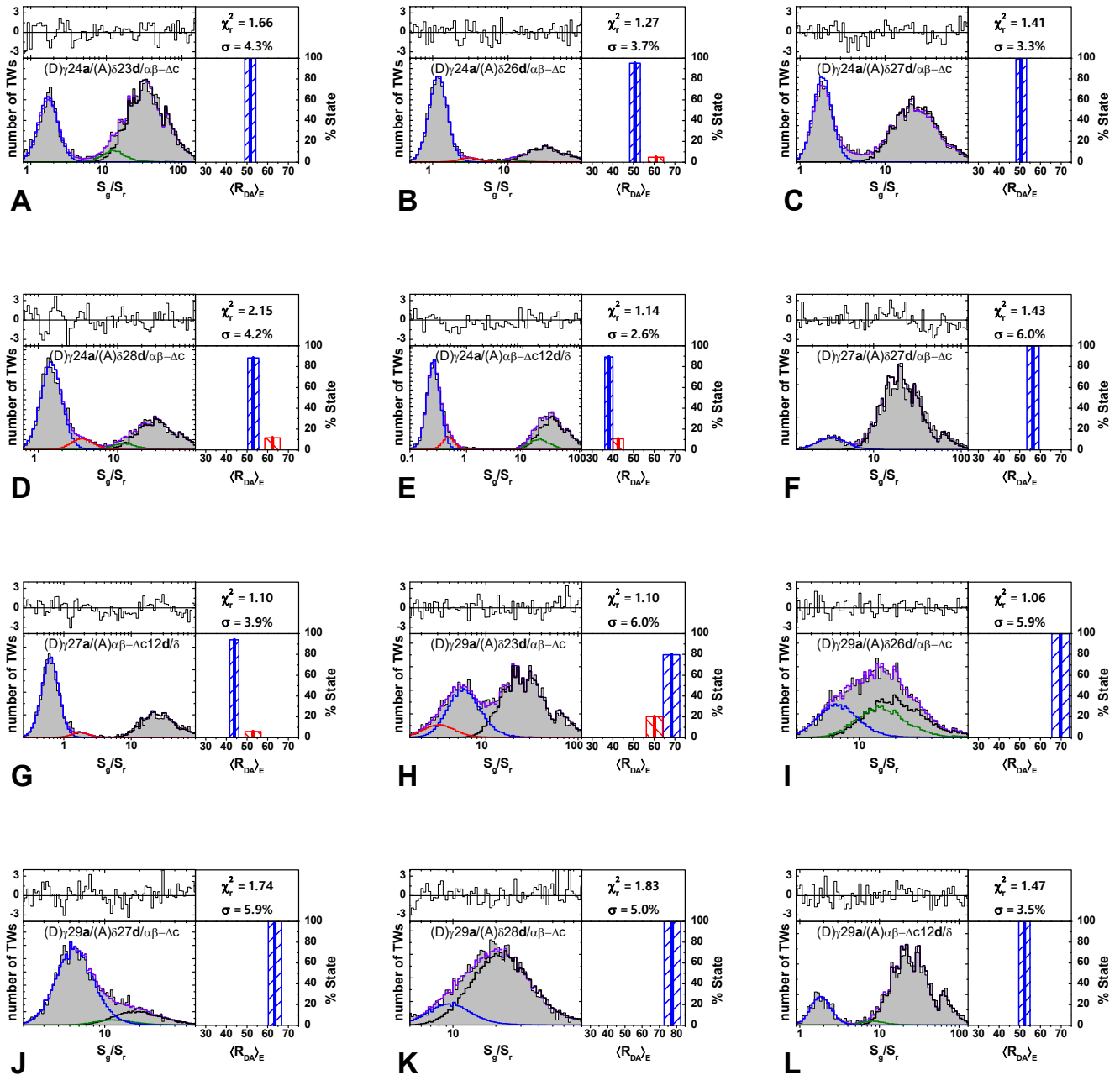


Figure 3.62 Results of PDA analysis for the samples with fluorescence labels on the helices a and b . Left panel: S_g/S_r histogram of experimental data (gray area) is fitted (purple solid line) with major population $\langle R_{DA} \rangle_{E1}$ (blue) and minor $\langle R_{DA} \rangle_{E1}$ population (red), donor only fraction (black) and impurity (green) with global apparent width σ . Goodness of the fit is judged with weighted residuals (upper left panel). Right panel: fitted distances for the major

(blue solid line) and minor (red solid line) states with their relative amplitudes and confidence intervals (stripped boxes).



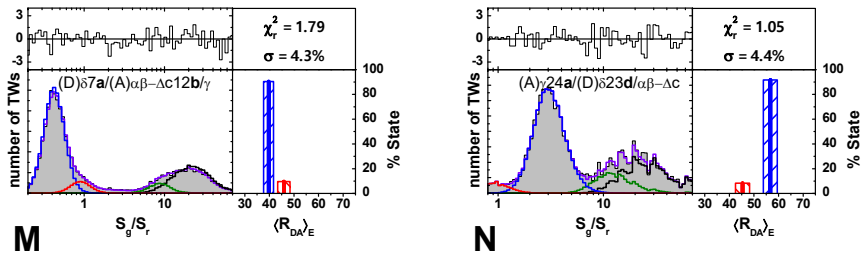
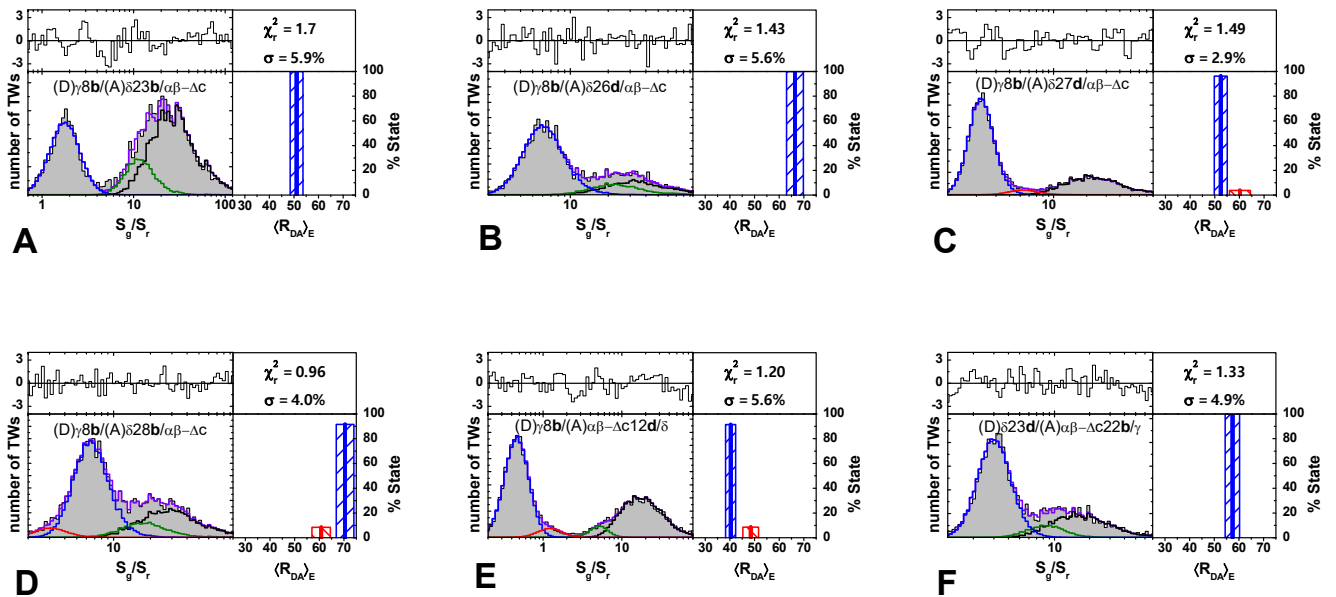


Figure 3.63 Results of PDA analysis for the samples with fluorescence labels on the helices *a* and *d*. Left panel: S_g/S_r histogram of experimental data (gray area) is fitted (purple solid line) with major population $\langle R_{DA} \rangle_{E1}$ (blue) and minor $\langle R_{DA} \rangle_{E1}$ population (red), donor only fraction (black) and impurity (green) with global apparent width σ . Goodness of the fit is judged with weighted residuals (upper left panel). Right panel: fitted distances for the major (blue solid line) and minor (red solid line) states with their relative amplitudes and confidence intervals (stripped boxes).



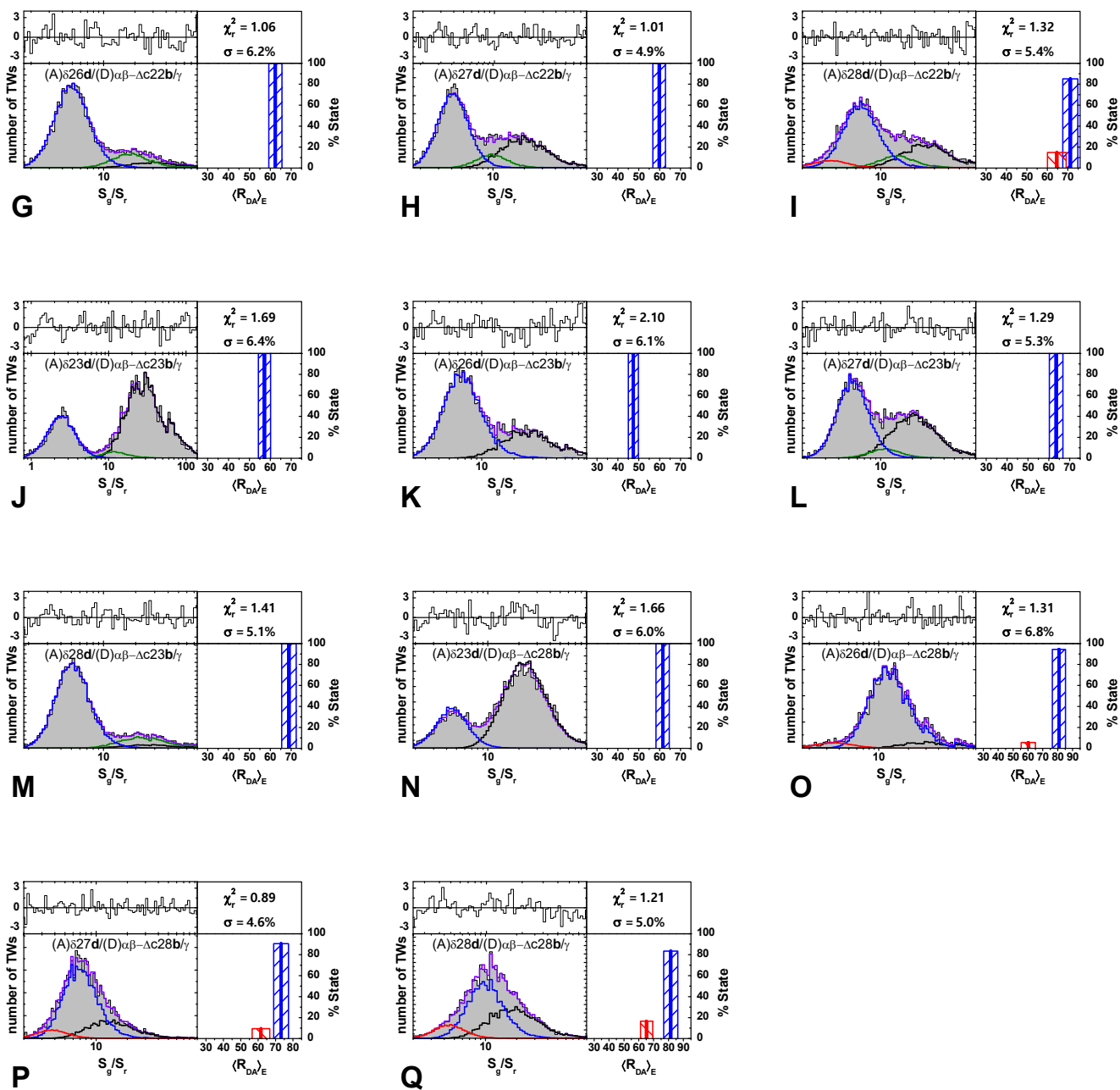


Figure 3.64 Results of PDA analysis for the samples with fluorescence labels on the helices *b* and *d*. Left panel: S_g/S_r histogram of experimental data (gray area) is fitted (purple solid line) with major population $\langle R_{DA} \rangle_{E1}$ (blue) and minor $\langle R_{DA} \rangle_{E1}$ population (red), donor only fraction (black) and impurity (green) with global apparent width σ . Goodness of the fit is judged with weighted residuals (upper left panel). Right panel: fitted distances for the major (blue solid line) and minor (red solid line) states with their relative amplitudes and confidence intervals (stripped boxes).

Measurements of $J(bcd)$

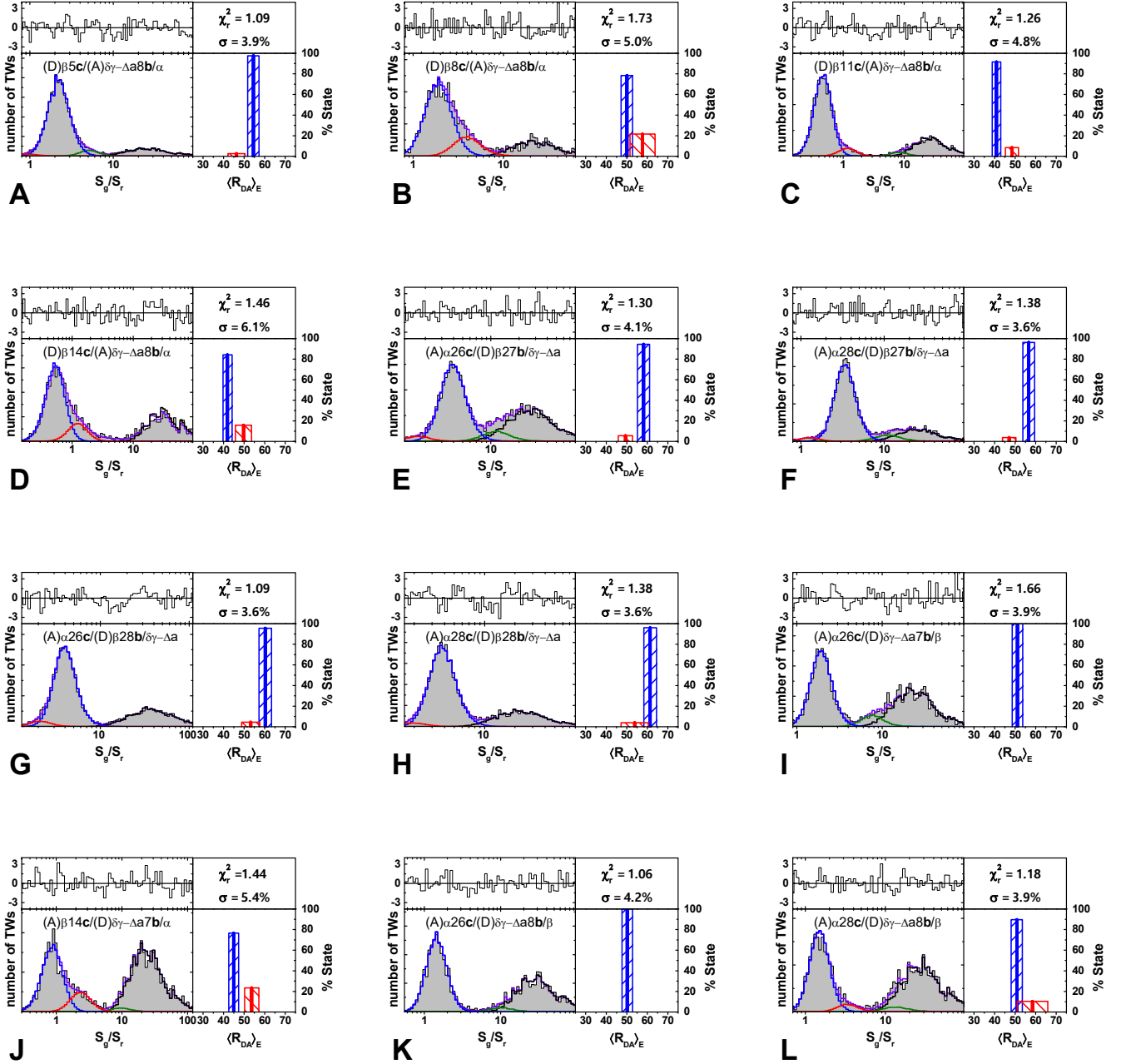
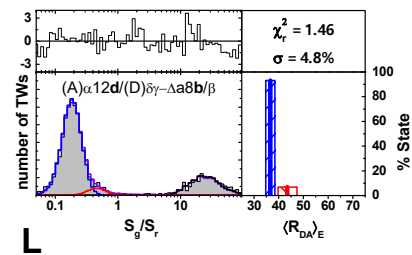
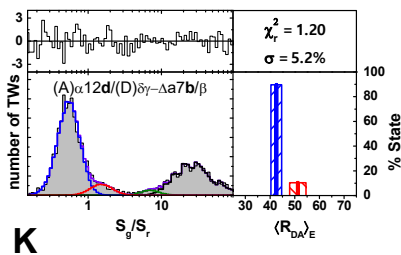
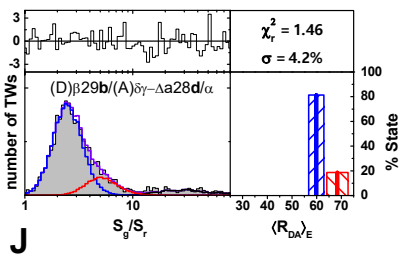
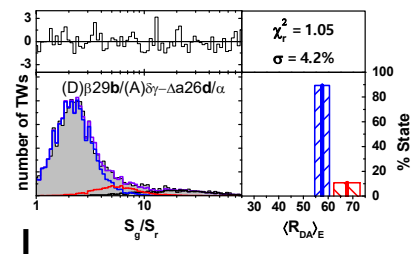
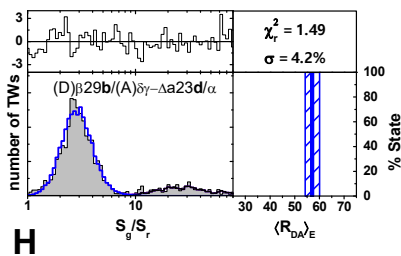
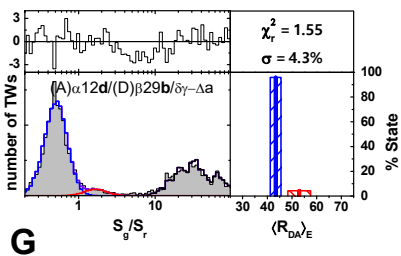
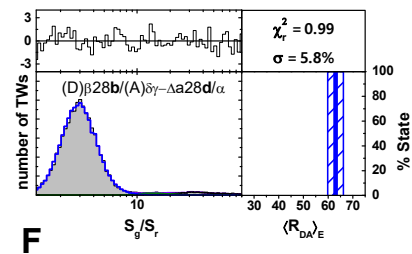
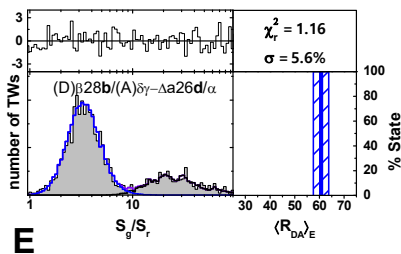
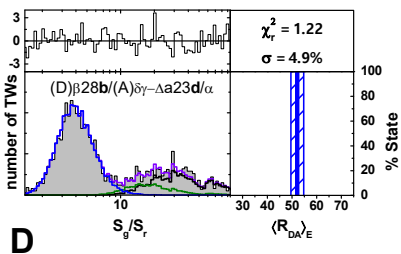
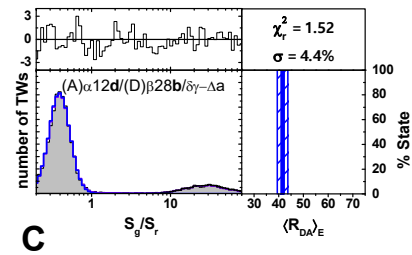
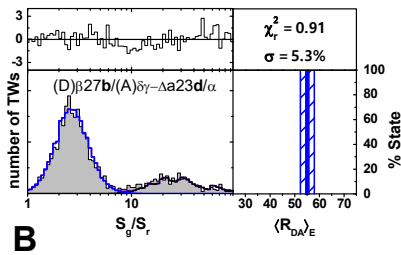
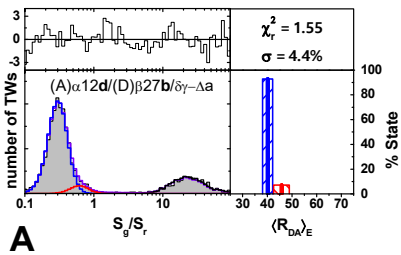


Figure 3.65 Results of PDA analysis for the samples with fluorescence labels on the helices b and c . Left panel: S_g/S_r histogram of experimental data (gray area) is fitted (purple solid line) with major population $\langle R_{DA} \rangle_{E1}$ (blue) and minor $\langle R_{DA} \rangle_{E1}$ population (red), donor only fraction (black) and impurity (green) with global apparent width σ . Goodness of the fit is judged with weighted residuals (upper left panel). Right panel: fitted distances for the major

(blue solid line) and minor (red solid line) states with their relative amplitudes and confidence intervals (stripped boxes).



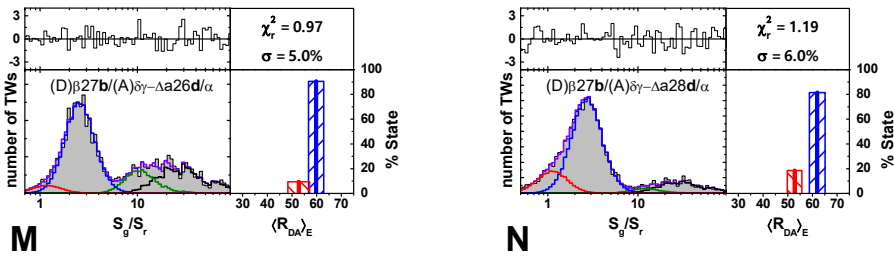
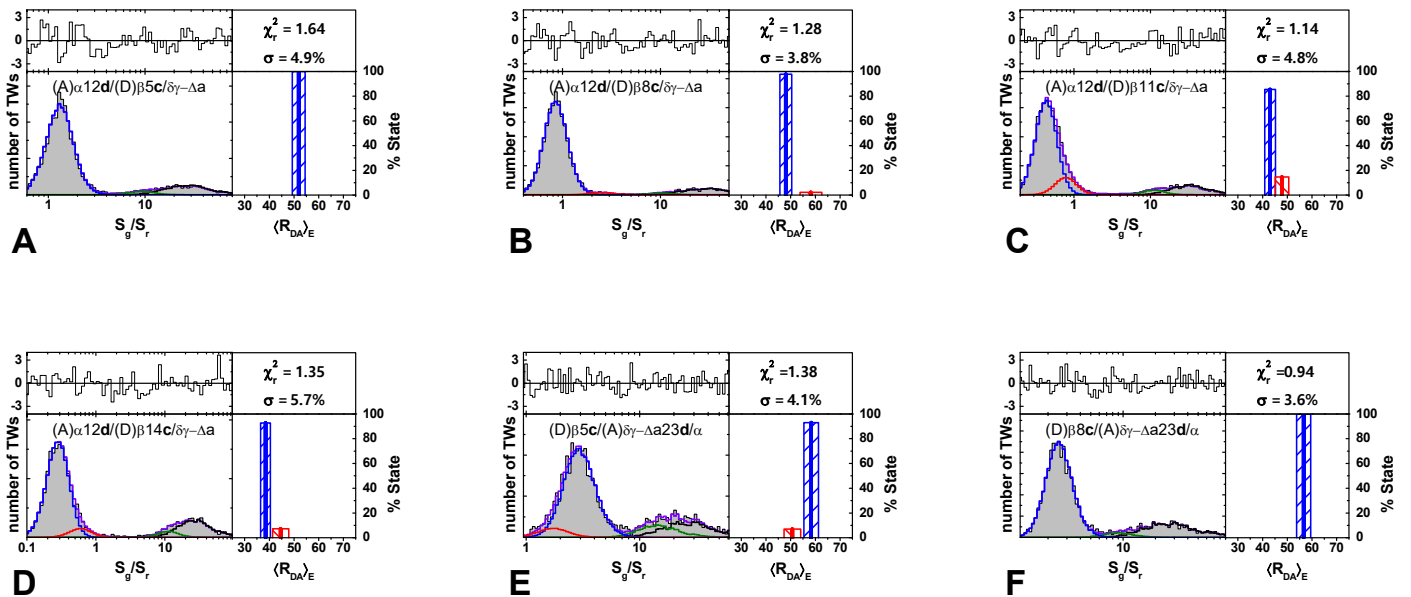


Figure 3.66 Results of PDA analysis for the samples with fluorescence labels on the helices *b* and *d*. Left panel: S_g/S_r histogram of experimental data (gray area) is fitted (purple solid line) with major population $\langle R_{DA} \rangle_{E1}$ (blue) and minor $\langle R_{DA} \rangle_{E1}$ population (red), donor only fraction (black) and impurity (green) with global apparent width σ . Goodness of the fit is judged with weighted residuals (upper left panel). Right panel: fitted distances for the major (blue solid line) and minor (red solid line) states with their relative amplitudes and confidence intervals (stripped boxes).



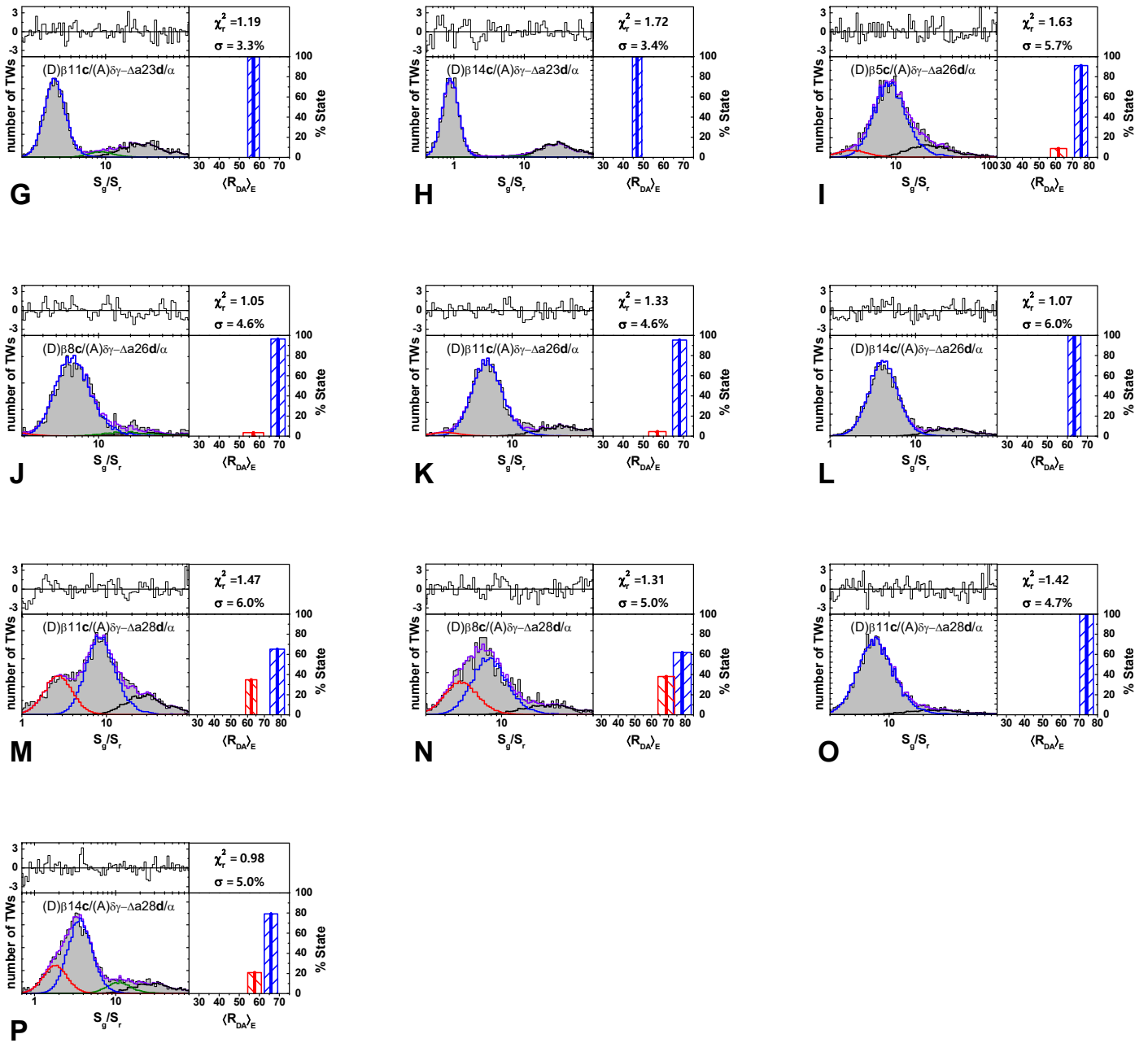


Figure 3.67 Results of PDA analysis for the samples with fluorescence labels on the helices *c* and *d*. Left panel: S_g/S_r histogram of experimental data (gray area) is fitted (purple solid line) with major population $\langle R_{DA} \rangle_{E1}$ (blue) and minor $\langle R_{DA} \rangle_{E1}$ population (red), donor only fraction (black) and impurity (green) with global apparent width σ . Goodness of the fit is judged with weighted residuals (upper left panel). Right panel: fitted distances for the major (blue solid line) and minor (red solid line) states with their relative amplitudes and confidence intervals (stripped boxes).

3.5.4.2 Tables with fitting parameters

Table 3.28 PDA fitting parameters for J(acd). See Chapter 3.5.4.1 for data and corresponding fits.

FRET pair	$\langle R_{DA} \rangle_{E1}$, Å	A_1 , %	$\langle R_{DA} \rangle_{E2}$, Å	A_2 , %	σ , %	Impurities R_{DA} , Å	Impurities, %	Donly, %	χ_r^2
(A) $\delta 10a$ /(D) $\beta\gamma$ - $\Delta b14c/\alpha$	49.4	70.1	59.9	5.2	6.0	74.8	3.2	21.5	1.48
(A) $\delta 10a$ /(D) $\beta\gamma$ - $\Delta b11c/\alpha$	46.6	62.4	55.2	3.5	4.6			34.1	1.33
(A) $\delta 28d$ /(D) $\beta\gamma$ - $\Delta b14c/\alpha$	63.9	51.6			6.5			48.4	1.13
(A) $\delta 28d$ /(D) $\beta\gamma$ - $\Delta b34a/\alpha$	72.3	40.2			6.7			59.8	1.35
(A) $\delta 26d$ /(D) $\beta\gamma$ - $\Delta b34a/\alpha$	70.9	85.0	55.1	5.2	4.8			9.8	0.85
(A) $\delta 23d$ /(D) $\beta\gamma$ - $\Delta b34a/\alpha$	65.6	31.7	53.7	2.0	6.7			66.3	1.12
(A) $\delta 23d$ /(D) $\beta\gamma$ - $\Delta b14a/\alpha$	47.9	24.4			4.4	73.7	2.7	72.9	1.80
(A) $\delta 23d$ /(D) $\beta\gamma$ - $\Delta b11a/\alpha$	58.5	25.7	52.6	4.9	3.6	69.2	1.3	68.1	1.40
(A) $\delta 23d$ /(D) $\beta\gamma$ - $\Delta b8a/\alpha$	55.6	34.3			5.2	70.4	2.2	63.5	1.21
(A) $\delta 28d$ /(D) $\beta\gamma$ - $\Delta b11a/\alpha$	74.2	41.0	65.5	3.7	4.3			55.2	1.21
(A) $\delta 28d$ /(D) $\beta\gamma$ - $\Delta b8a/\alpha$	75.3	37.0	65.0	4.7	4.3	101	5.4	52.9	1.01
(A) $\delta 28d$ /(D) $\beta\gamma$ - $\Delta b5a/\alpha$	80.3	27.7	64.7	6.6	6.0			65.7	0.87
(A) $\alpha 28c$ /(D) $\beta\gamma$ - $\Delta b34a/\delta$	60.1	55.3			5.2			44.7	1.29
(A) $\delta 10d$ /(D) $\beta\gamma$ - $\Delta b8c/\alpha$	56.8	56.2	50.9	5.4	3.1	85.7	12.3	26.1	1.62
(A) $\alpha 28c$ /(D) $\delta 7a/\beta\gamma$ - Δb	53.7	67.9			5.3	69.5	2.1	30.0	1.57
(A) $\delta 26d$ /(D) $\beta\gamma$ - $\Delta b14a/\alpha$	62.7	73.8			5.4			26.2	1.32
(A) $\delta 26d$ /(D) $\beta\gamma$ - $\Delta b11a/\alpha$	74.9	46.7	66.6	4.8	5.0			48.5	1.10
(A) $\delta 26d$ /(D) $\beta\gamma$ - $\Delta b8a/\alpha$	72.1	72.5			4.4			27.5	1.39
(A) $\delta 26d$ /(D) $\beta\gamma$ - $\Delta b5a/\alpha$	80.5	57.1	64.5	4.0	5.5			38.9	0.76
(D) $\delta 7a$ /(A) $\beta\gamma$ - $\Delta b14c/\alpha$	40.8	70.8	50.1	4.0	5.1	76.2	1.9	23.3	1.96

FRET pair	$\langle R_{DA} \rangle_{E1}$, Å	A_1 , %	$\langle R_{DA} \rangle_{E2}$, Å	A_2 , %	σ , %	Impurities R_{DA} , Å	Impurities, %	Donly, %	χ^2_r
(A) $\delta 10a$ /(D) $\beta\gamma$ - $\Delta b 5c/\alpha$	67.3	58.9	59.6	15.2	5.0			25.9	1.20
(A) $\alpha 12d$ /(D) $\delta 7d/\beta\gamma$ - Δb	39.3	69.1	46.7	3.7	4.6	69.5	0.3	26.8	1.41
(A) $\alpha 12d$ /(D) $\beta\gamma$ - $\Delta b 14a/\delta$	39.6	81.1			6.1	78.2	1.7	17.2	1.33
(A) $\alpha 12d$ /(D) $\beta\gamma$ - $\Delta b 29a/\delta$	37.6	77.2	44.2	3.8	3.1	79.6	1.7	17.3	1.58
(A) $\alpha 26d$ /(D) $\beta\gamma$ - $\Delta b 29a/\delta$	57.2	58.3	51.0	5.0	3.4	76.2	4.8	31.9	0.98
(A) $\alpha 28d$ /(D) $\beta\gamma$ - $\Delta b 29a/\delta$	62.0	64.1	54.1	6.9	3.7	82.8	5.0	24.0	0.95
(A) $\delta 23d$ /(D) $\beta\gamma$ - $\Delta b 29a/\alpha$	52.5	25.9			4.9	85.3	15.9	58.2	1.56
(A) $\delta 26d$ /(D) $\beta\gamma$ - $\Delta b 29a/\alpha$	51.5	66.8	57.7	9.2	4.1	89.7	4.4	19.6	1.48
(A) $\delta 28d$ /(D) $\beta\gamma$ - $\Delta b 29a/\alpha$	54.1	32.1	63.0	7.8	5.7	78.1	7.7	52.4	1.44
(A) $\alpha 26d$ /(D) $\beta\gamma$ - $\Delta b 34a/\delta$	56.2	60.0			5.6	75.2	8.3	31.7	1.15
(A) $\alpha 26c$ /(D) $\delta 7a/\beta\gamma$ - Δb	53.7	27.9	47.8	9.7	6.2	70.0	4.5	58.0	1.54
(A) $\alpha 12d$ /(D) $\beta\gamma$ - $\Delta b 11a/\delta$	43.5	80.7			6.2	74.1	0.6	18.6	1.39
(A) $\alpha 12d$ /(D) $\beta\gamma$ - $\Delta b 8a/\delta$	48.2	83.9			4.0	65.2	0.7	15.5	2.50
(A) $\alpha 12d$ /(D) $\beta\gamma$ - $\Delta b 11a/\delta$	47.4	81.9			3.7	75.6	1.6	16.5	1.66
(A) $\alpha 12d$ /(D) $\beta\gamma$ - $\Delta b 34a/\delta$	51.5	82.6	59.2	4.0	3.5	75.9	2.3	11.0	0.92
(D) $\delta 23d$ /(A) $\beta\gamma$ - $\Delta b 14c/\alpha$	48.1	72.1			4.7	68.5	2.6	25.3	1.14
(A) $\alpha 26c$ /(D) $\delta 23a/\beta\gamma$ - Δb	57.2	62.6			4.7			37.4	1.15
(A) $\alpha 28c$ /(D) $\delta 23a/\beta\gamma$ - Δb	63.0	65.3			4.7			34.7	1.12
(A) $\delta 27d$ /(D) $\beta\gamma$ - $\Delta b 34a/\alpha$	64.4	53.5	57.3	16.3	6.0			30.2	0.82
(A) $\delta 27d$ /(D) $\beta\gamma$ - $\Delta b 29a/\alpha$	50.5	60.4	59.0	6.8	4.1	74.2	7.3	25.4	1.17
(A) $\delta 27d$ /(D) $\beta\gamma$ - $\Delta b 14c/\alpha$	48.9	65.4	54.2	12.0	2.9	74.9	10.4	12.2	1.78
(A) $\delta 27d$ /(D) $\beta\gamma$ - $\Delta b 11c/\alpha$	62.0	47.4	70.4	8.1	5.0			44.4	1.06

FRET pair	$\langle R_{DA} \rangle_{E1}$, Å	A_1 , %	$\langle R_{DA} \rangle_{E2}$, Å	A_2 , %	σ , %	Impurities R_{DA} , Å	Impurities, %	Donly, %	χ_r^2
(A) $\delta 27d$ /(D) $\beta\gamma$ - $\Delta b8c/\alpha$	68.3	66.9	54.0	3.0	5.1			30.1	0.79
(A) $\delta 27d$ /(D) $\beta\gamma$ - $\Delta b5c/\alpha$	68.2	57.2	55.9	3.9	5.0			38.9	1.49
(A) $\delta 23d$ /(D) $\beta\gamma$ - $\Delta b5c/\alpha$	59.1	66.9			5.2	83.9	12.4	20.7	1.76

Table 3.29 PDA fitting parameters for J(bcd). See Chapter 3.5.4.1 for data and corresponding fits.

FRET pair	$\langle R_{DA} \rangle_{E1}$, Å	A_1 , %	$\langle R_{DA} \rangle_{E2}$, Å	A_2 , %	σ , %	Impurities R_{DA} , Å	Impurities, %	Donly, %	χ_r^2
(D) $\beta 14c$ /(A) $\delta\gamma$ - $\Delta a28d/\alpha$	66.4	57.3	58.2	21.3	5.0	84.5	8.6	12.8	0.98
(D) $\beta 11c$ /(A) $\delta\gamma$ - $\Delta a28d/\alpha$	74.0	91.6			4.7			8.4	1.42
(D) $\beta 8c$ /(A) $\delta\gamma$ - $\Delta a28d/\alpha$	78.0	55.4	68.5	30.2	5.0			14.4	1.31
(D) $\beta 5c$ /(A) $\delta\gamma$ - $\Delta a28d/\alpha$	78.7	55.1	61.9	26.3	6.0			18.6	1.47
(D) $\beta 27b$ /(A) $\delta\gamma$ - $\Delta a28d/\alpha$	62.0	69.4	52.8	15.8	6.0	89.9	5.2	9.5	1.32
(D) $\beta 14c$ /(A) $\delta\gamma$ - $\Delta a26d/\alpha$	63.5	87.5			6.0			12.5	1.07
(D) $\beta 11c$ /(A) $\delta\gamma$ - $\Delta a26d/\alpha$	68.0	80.0	57.0	3.7	4.6			16.3	1.33
(D) $\beta 8c$ /(A) $\delta\gamma$ - $\Delta a26d/\alpha$	68.7	86.3	57.3	3.3	4.6	93.7	5.1	5.3	1.05
(D) $\beta 5c$ /(A) $\delta\gamma$ - $\Delta a26d/\alpha$	75.7	76.9	61.3	6.6	5.7			16.6	1.63
(D) $\beta 14c$ /(A) $\delta\gamma$ - $\Delta a23d/\alpha$	46.9	71.0			3.4	72.4	1.3	27.8	1.72
(D) $\beta 27b$ /(A) $\delta\gamma$ - $\Delta a26d/\alpha$	59.7	55.6	51.7	4.6	5.0	80.8	14.4	25.5	0.96
(D) $\beta 11c$ /(A) $\delta\gamma$ - $\Delta a23d/\alpha$	57.0	69.8			3.3	73.6	5.6	24.6	1.19
(D) $\beta 8c$ /(A) $\delta\gamma$ - $\Delta a23d/\alpha$	56.6	74.2			3.6	73.8	4.0	21.8	0.94
(D) $\beta 5c$ /(A) $\delta\gamma$ - $\Delta a23d/\alpha$	58.3	65.1	50.7	5.0	4.1	80.8	12.5	17.5	1.38
(D) $\delta\gamma$ - $\Delta a8b$ /(A) $\alpha 26c/\beta$	50.1	52.0			4.2	74.5	3.1	44.9	1.06

FRET pair	$\langle R_{DA} \rangle_{E1}$, Å	A_1 , %	$\langle R_{DA} \rangle_{E2}$, Å	A_2 , %	σ , %	Impurities R_{DA} , Å	Impurities, %	Donly, %	χ^2_r
(D) $\delta\gamma$ - $\Delta a8b$ /(A) $\alpha 26c$ / β	50.6	43.9	59.9	5.0	3.4	80.0	7.8	43.3	1.18
(D) $\beta 5c$ /(A) $\delta\gamma$ - $\Delta a8b$ / α	54.5	78.3	46.3	2.0	3.9	64.2	5.2	14.6	1.09
(D) $\beta 11c$ /(A) $\delta\gamma$ - $\Delta a8b$ / α	40.9	65.7	48.5	6.0	4.8	71.2	2.9	25.4	1.26
(D) $\beta 27b$ /(A) $\alpha 26c$ / $\delta\gamma$ - Δa	58.2	51.5	49.4	3.0	4.1	74.3	7.3	38.2	1.30
(D) $\beta 27b$ /(A) $\alpha 28c$ / $\delta\gamma$ - Δa	56.6	70.3	47.1	2.8	3.6	74.2	6.7	20.2	1.38
(D) $\beta 14c$ /(A) $\delta\gamma$ - $\Delta a8b$ / α	41.9	57.5	49.7	10.8	6.1			31.7	1.46
(D) $\beta 5c$ /(A) $\alpha 12d$ / $\delta\gamma$ - Δa	51.9	82.5			4.9	76.8	2.9	14.6	1.64
(D) $\beta 14c$ /(A) $\alpha 12d$ / $\delta\gamma$ - Δa	38.4	70.5	44.4	6.3	5.7	79.9	4.1	19.0	1.35
(D) $\beta 11c$ /(A) $\alpha 12d$ / $\delta\gamma$ - Δa	42.6	71.1	47.4	12.8	4.8	79.3	3.5	12.6	1.14
(A) $\alpha 12d$ /(D) $\delta\gamma$ - $\Delta a8b$ / β	36.6	72.0	43.4	4.9	4.8			23.1	1.46
(A) $\alpha 12d$ /(D) $\beta 27b$ / $\delta\gamma$ - Δa	40.1	72.1	45.8	5.7	4.4			22.2	1.55
(A) $\alpha 12d$ /(D) $\beta 8c$ / $\delta\gamma$ - Δa	48.0	85.1	58.4	2.0	3.8	78.1	1.6	11.3	1.28
(D) $\beta 28b$ /(A) $\delta\gamma$ - $\Delta a 23d$ / α	59.0	64.8			4.8	83.9	10.5	24.7	1.2
(D) $\beta 28b$ /(A) $\delta\gamma$ - $\Delta a 26d$ / α	60.8	73.9			5.8			26.1	1.15
(D) $\beta 28b$ /(A) $\delta\gamma$ - $\Delta a 28d$ / α	63.0	94.0			5.8	80.5	0.9	5.1	0.99
(A) $\alpha 26c$ /(D) $\beta 28b$ / $\delta\gamma$ - Δa	60.3	66.6	53.6	4.1	3.6			29.3	1.09
(A) $\alpha 12d$ /(D) $\beta 28b$ / $\delta\gamma$ - Δa	41.6	85.7			4.5			14.3	1.52
(A) $\alpha 28c$ /(D) $\beta 28b$ / $\delta\gamma$ - Δa	61.4	71.1	53.9	2.9	3.6			26.0	1.38
(D) $\beta 27b$ /(A) $\delta\gamma$ - $\Delta a 23d$ / α	55.2	78.4			5.3			21.6	0.91
(D) $\beta 29b$ /(A) $\delta\gamma$ - $\Delta a 28d$ / α	60.0	76.0	69.0	15.9	4.2			8.1	1.46
(D) $\beta 29b$ /(A) $\delta\gamma$ - $\Delta a 26d$ / α	57.6	82.1	67.6	9.8	4.2			8.1	1.05
(D) $\beta 29b$ /(A) $\delta\gamma$ - $\Delta a 23d$ / α	56.8	84.5			4.1			15.5	1.27

FRET pair	$\langle R_{DA} \rangle_{E1}$, Å	A_1 , %	$\langle R_{DA} \rangle_{E2}$, Å	A_2 , %	σ , %	Impurities R_{DA} , Å	Impurities, %	Donly, %	χ^2_r
(A) $\alpha 12d$ /(D) $\beta 29b/\delta\gamma$ - Δa	43.4	84.5	52.9	3.7	4.3			11.7	1.55
(A) $\beta 14c$ /(D) $\delta\gamma$ - $\Delta a 14b/\alpha$	45.0	35.1	54.0	10.5	5.5	73.5	1.9	52.4	1.45
(A) $\alpha 26c$ /(D) $\delta\gamma$ - $\Delta a 7b/\beta$	51.2	48.9			3.9	68.0	7.5	43.7	1.66
(A) $\alpha 12d$ /(D) $\delta\gamma$ - $\Delta a 7b/\beta$	42.5	58.0	51.3	6.7	5.2	69.2	2.6	32.6	1.2

Table 3.30 PDA fitting parameters for J(abd). See Chapter 3.5.4.1 for data and corresponding fits.

FRET pair	$\langle R_{DA} \rangle_{E1}$, Å	A_2 , %	$\langle R_{DA} \rangle_{E2}$, Å	A_2 , %	σ , %	Impurities R_{DA} , Å	Impurities, %	Donly, %	χ^2_r
(D)Y8b/(A)δ10a/αβ-Δc	47.5	65.6	55.5	2.7	3.5	76.4	4.1	27.6	1.1
(D)Y8b/(A)δ26d/αβ-Δc	66.4	68.			5.6	96.8	12.4	19.6	1.43
(D)Y8b/(A)δ28d/αβ-Δc	70.5	56.5	60.5	5.0	4.1	93.4	11.0	27.4	0.96
(D)Y8b/(A)δ23d/αβ-Δc	50.9	31.5			5.9	76.1	14.8	53.8	1.71
(D)Y8b/(A)αβ-Δc12d/δ	40.3	53.8	48.7	4.8	5.6	65.3	4.6	36.8	1.2
(A)δ10a/(D)αβ-Δc28b/γ	65.6	78.6			5.1			21.4	1.5
(A)δ28d/(D)αβ-Δc28b/γ	81.7	51.9	65.5	10.6	5.0			37.4	1.21
(A)δ26d/(D)αβ-Δc28b/γ	80.4	85.9	62.0	6.7	6.8			7.5	1.31
(A)δ23d/(D)αβ-Δc28b/γ	60.7	25.1			6.0			74.9	1.66
(D)δ7d/(A)αβ-Δc22b/γ	41.1	50.8	33.8	11.7	4.6	71.0	4.3	33.2	1.84
(D)δ7d/(A)αβ-Δc12b/γ	39.7	60.2	45.9	6.4	4.25	71.7	3.2	30.1	1.79
(A)Y8b/(D)δ7a/αβ-Δc	76.6	17.2			5.0			82.8	1.81
(D)Y29a/(A)αβ-Δc12d/δ	52.3	15.9			3.5	71.4	2.6	81.5	1.47
(D)Y29a/(A)δ28d/αβ-Δc	76.6	17.2			5.0			82.8	1.81
(D)Y29a/(A)δ26d/αβ-Δc	69.6	26.9			5.9	95.1	29.4	43.7	1.06
(D)Y29a/(A)δ23d/αβ-Δc	68.4	32.0	60.1	8.1	6.0			59.9	1.1
(D)Y29a/(A)αβ-Δc22b/δ	48.3	38.1	57.3	9.8	5.0	75.1	15.3	36.8	1.65
(A)δ10a/(D)αβ-Δc23b/γ	47.4	77.8			3.6			22.2	1.64
(D)Y24a/(A)δ23d/αβ-Δc	51.6	28.4			4.3	77.2	5.6	66.0	1.67
(D)Y24a/(A)δ26d/αβ-Δc	50.7	70.2	60.3	3.5	3.7	78.2	2.0	24.3	1.27
(D)Y24a/(A)δ28d/αβ-Δc	53.0	54.4	62.5	7.1	4.2	81.4	4.4	34.2	2.15

β - Δ c									
FRET pair	$\langle R_{DA} \rangle_{E1}$, Å	A_2 , %	$\langle R_{DA} \rangle_{E2}$, Å	A_2 , %	σ , %	Impurities R_{DA} , Å	Impurities, %	Donly, %	χ_r^2
(D)Y24a/(A) $\alpha\beta$ - Δ c22b/ δ	42.6	65.7			3.1	82.3	5.8	28.6	1.57
(D)Y24a/(A) $\alpha\beta$ - Δ c12d/ δ	38.0	48.9	42.6	6.1	2.6	92.1	9.0	36.1	1.14
(A) δ 10a/(D) $\alpha\beta$ - Δ c22b/ γ	46.2	66.9			4.6	77.6	10.1	23.0	3.1
(A) δ 26d/(D) $\alpha\beta$ - Δ c22b/ γ	66.2	78.8			5.9	92.8	14.2	7.0	1.9
(A) δ 28d/(D) $\alpha\beta$ - Δ c22b/ γ	72.9	46.9	66.3	10.5	4.4	92.4	17.8	24.7	1.55
(D)Y29a/(A) δ 27d/ $\alpha\beta$ - Δ c	64.0	77.0			5.9	81.0	5.3	17.7	1.7
(A) δ 27d/(D) $\alpha\beta$ - Δ c22b/ γ	59.4	56.5			4.7	79.5	16.9	26.6	1.21
(A) δ 27d/(D) $\alpha\beta$ - Δ c23b/ γ	63.5	52.5			5.3	76.9	6.0	41.5	1.29
(D)Y24a/(A) δ 27d/ $\alpha\beta$ - Δ c	50.8	37.7			3.3			62.3	1.41
(D)Y8b/(A) δ 27d/ $\alpha\beta$ - Δ c	52.4	66.1	60.2	2.6	2.9			31.3	1.49
(D) δ 23d/(A) $\alpha\beta$ - Δ c22b/ γ	57.4	65.5			4.9	74.1	8.7	25.7	1.33
(A)Y24a/(D) δ 23d/ $\alpha\beta$ - Δ c	56.7	55.3	45.4	5.0	4.4	77.7	12.4	27.3	1.07
(A) δ 26d/(D) $\alpha\beta$ - Δ c23b/ γ	70.8	69.4			6.1			30.6	2.1
(D)Y27b/(A) δ 27d/ $\alpha\beta$ - Δ c	57.9	10.5			6.0			89.5	1.5
(A) δ 27d/(D) $\alpha\beta$ - Δ c28b/ γ	73.2	70.5	61.7	7.3	4.7			22.2	0.89
(A) δ 28d/(D) $\alpha\beta$ - Δ c23b/ γ	68.9	81.1			5.2			18.9	1.03
(A) δ 23d/(D) $\alpha\beta$ - Δ c23b/ γ	57.2	27.4			6.4	80.5	3.6	69.0	1.69
(A) δ 8a/(D) $\alpha\beta$ - Δ c22b/ γ	35.7	47.3	43.7	9.0	4.1	72.9	7.2	36.6	1.27
(A) δ 8a/(D) $\alpha\beta$ - Δ c23b/ γ	39.1	60.1	46.7	10.0	4.3	63.7	4.3	25.6	1.45
(A) δ 8a/(D) $\alpha\beta$ - Δ c28b/ γ	48.4	83.5	56.7	6.3	2.2			10.1	1.24
(D)Y27a/(A) $\alpha\beta$ - Δ c12d/ δ	43.8	60.0	52.9	3.8	3.9			36.6	1.1

Chapter 4 Single-molecule FRET reveals multiscale chromatin dynamics modulated by HP1 α

Sinan Kilic^{1,4}, Suren Felekyan², **Olga Doroshenko**², Iuliia Boichenko¹, Mykola Dimura², Hayk Vardanyan², Louise C. Bryan¹, Gaurav Arya³, Claus A.M. Seidel² & Beat Fierz¹

¹Laboratory of Biophysical Chemistry of Macromolecules, Institute of Chemical Sciences and Engineering, Ecole Polytechnique Fédérale de Lausanne (EPFL), 1015 Lausanne, Switzerland

²Institut für Physikalische Chemie, Lehrstuhl für Molekulare Physikalische Chemie, Heinrich-Heine-Universität, Universitätsstraße 1, Düsseldorf, Germany

³Pratt School of Engineering, Duke University, 144 Hudson Hall, Box 90300, Durham, NC 27708, USA

⁴Present address: Department of Molecular Mechanisms of Disease, University of Zurich, 8057 Zurich, Switzerland

4.1 Introduction

Nucleosome compaction into chromatin fiber is a prerequisite in regulatory functions such as DNA transcription, replication and repair. Determination of the chromatin structure and dynamic is essential to understand genome function¹⁶⁶. This intriguing albeit challenging task as chromatin dynamic covers wide temporal scale from sub-microseconds to hours. Previous studies with x-ray crystallography and cryo-EM report zigzag chromatin model, with straight linker DNA between two stacks of nucleosome cores (Figure 4.1)^{14,167}. Others¹⁶⁸ support alternative solenoid structural model. Also dynamic rearrangements of the nucleosome arrays¹⁶⁹ and partial unwrapping of nucleosome-wound DNA^{49,170-172} have been reported but detailed information on the dynamic timescale is however poorly understood. It is also interesting to investigate binding dynamic of chromatin with various partners, e.g. chromatin effectors. Here we investigate interaction between highly dynamic heterochromatin protein 1 α (HP1 α) with chromatin and the induction mechanism of chromatin arrangement. There is still limited knowledge of the timescale of such interaction, mainly due to experimental constraints arising from the megadalton-scale and structural heterogeneity of chromatin.

To provide insights into structural and dynamic rearrangement we combine confocal microscopy of freely diffusing molecules in solution with total internal reflection fluorescence (TIRF) microscopy of surface attached molecules. We employ two fluorescent dye pairs with different distance sensitivities that enable to register interdyer distances up to 150 Å. Further combining experimental data with structural modeling methods we can identify structural heterogeneities and exchange kinetics and present dynamic-register model of chromatin fiber, modulated by HP1 α protein.

4.2 Results

Reconstitution of site-specifically labeled chromatin fibers

One of the key challenges in this work was to label precisely 12-mer nucleosome array. We thus developed a method to assemble chromatin DNA constructs containing 12 copies of the “601” nucleosome positioning sequence⁷³ separated by 30 bp linker-DNA. We used preparative ligations of two recombinant and three synthetic fragments, the latter of which carried the fluorescent labels (Figure 4.1b). A convergent DNA assembly procedure with intermediate purification steps ensured the efficient and accurate incorporation of exactly one donor and one acceptor dye into chromatin DNA at defined positions.

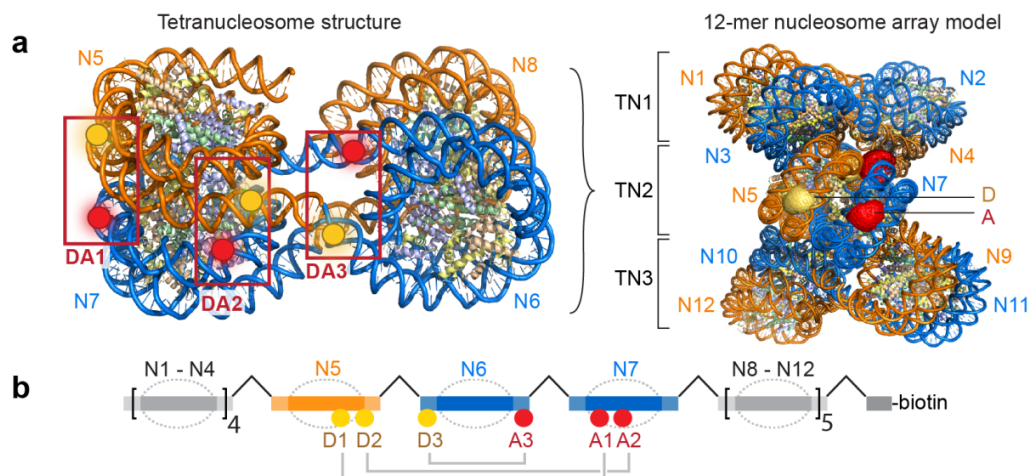


Figure 4.1 (a) Left: Tetranucleosome structure based on ref.¹⁶⁷ showing the 3 dye pairs DA1, DA2 and DA3. Right: 12-mer chromatin fiber as a stack of three tetranucleosome (TN) units, modeled using the cryoEM structure of a chromatin fiber¹⁶⁸. The middle tetranucleosome carries the fluorescent labels, whose accessible volume is displayed. D: donor, A: acceptor labels, N: nucleosomes. (b) Schematic view of the preparative DNA ligation used to introduce fluorescent labels.

In order to probe different inter- and intra-domain contacts we employ three dye pairs DA1, DA2 and DA3 in the center of the 12-mer nucleosome array (N1-N12) (Figure 4.1a, b). DA1 senses stacking between nucleosomes N5 and N7 at a position close to the H2A-H2B four-helix bundle contacts¹⁶⁹. DA2 measures inter-nucleosome interactions closer to the dyad (N5 to N7). DA3 reports on dynamic modes within the linker DNA flanking the central nucleosome (N6). In order to cover possible long inter-dye distances (up to 150 Å) we employed Alexa568 as donor and Alexa 647 as acceptor as this pair has large Förster Radius $R_0 = 82$ Å.

smFRET reveals structural heterogeneity in chromatin fibers

To investigate chromatin structure and dynamics on the millisecond to second timescale we employ single-molecule total internal reflection fluorescence (smTIRF) microscopy. Briefly, generated time traces of FRET efficiency (E_{FRET}) revealed conformational changes in real-time in presence of Mg^{2+} ions and systematic increase of E_{FRET} with salt concentration for DA1-3. Moreover study of anti-correlated fluctuations in the time traces of donor and acceptor fluorescence emission indicated structural dynamics. We report structural motions for DA2 positions (relaxation time $t_R = 0.2-0.3$ s), fast dynamics at the detection limit for DA1 ($t_R \sim 0.1$ s) and quasistatic behavior for DA3 (Figure 2, Publication II).

Chromatin fibers exist in two structural registers

smTIRF exposed multiscale dynamics featuring multiple FRET species in rapid exchange that is beyond the method but could be resolved with smFRET with confocal multi-parameter fluorescence detection (MFD)¹⁷³. This method extends the accessible dynamic timescale to the sub-microsecond range and resolves structural states with sub-nm accuracy¹⁷⁴. In this experiment I use one color excitation (OCE) technique to perform the measurements for chromatin in configurations DA1-3 and analyzed obtained MFD data as described⁷³. Data revealed a complex population distribution involved in dynamic exchange (Figure 4.2a) not observed in free DNA or donor-only labeled chromatin fibers (S. Figure 8c, d, Publication II). Based on this analysis, the data could only consistently be described by two dynamic FRET-lines (dark and bright blue lines, Figure 4.2a), indicating two coexisting subpopulations of dynamic chromatin fibers which are distinct within the observation time of ~ 10 ms. Intersections of the dynamic with the static FRET-lines identify four limiting FRET species involved in the exchange: *A*, *B*, *C* and *D*, indicated by the horizontal lines in Figure 4.2a. Braces (e.g. ¹⁷⁵) indicate conformational states sharing indistinguishable FRET efficiencies.

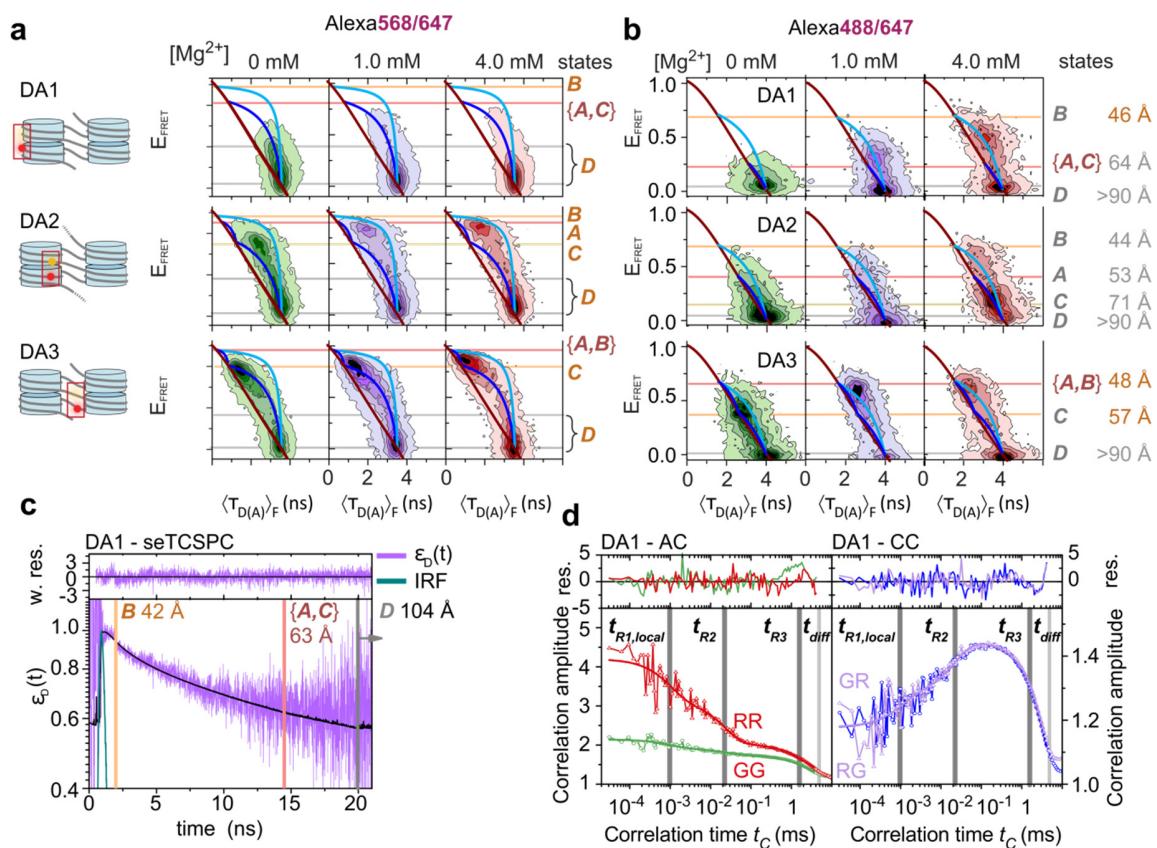


Figure 4.2 (a) 2D MFD histograms for chromatin fibers DA1-3 (Alexa568/647) at indicated Mg²⁺ concentrations. Red line: static FRET-line. Dark and bright blue lines (for parameters of all FRET-lines see Supplementary Note, step 2, Publication II). Red, orange, yellow and grey lines: FRET species *A-D* (see also Figure 4.3). (b) 2D MFD histograms

for chromatin fibers DA1-3 labeled with Alexa488/647 at indicated Mg^{2+} concentrations. Red line: static FRET-line, Dark and bright blue lines: dynamic FRET-lines. (c) Sub-ensemble fluorescence lifetime analysis for DA1-labeled fibers (Alexa488/647) at 1 mM $MgCl_2$ and $E_{FRET} > 0.065$. IRF: Instrument response function. (d) Auto- (left panel) and cross- (right panel) correlation functions of the donor (G) and acceptor (R) emission channels for the same sub-ensemble as in panel c.

Also a complementary analysis procedure of sub-ensemble fluorescence lifetime analysis corroborated the FRET species for each labeling pair DA1-3. Similarly, model-free fluorescence correlation analysis from DA1-3 revealed at least four kinetic species (*A-D*) (S. Figure 11, Publication II). To conclude, I demonstrate compact chromatin fibers ($E_{FRET} > 0.8$) in rapid exchange with extended structures (Figure 4.2a) for FRET pairs. Two dynamic FRET-lines point to at least two independent dynamic transitions, revealing distinct limiting FRET species with high E_{FRET} (compact species, *A-C*) and with very low E_{FRET} (open species, *D*), respectively. These transitions immediately reveal two populations of chromatin fibers with unique internal exchange dynamics but without interchange between the populations at ms timescale.

Revealing structural states in dynamic chromatin fibers

To improve spatial resolution at shorter distances (S. Figure 8b, Publication II) I performed MFD experiments by replacing donor with Alexa Fluor 488 ($R_0 = 52 \text{ \AA}$) and employing pulsed interleaved excitation (PIE)⁸⁹ technique that allows to select FRET-active bursts only. Intensity-derived E_{FRET} and the average (fluorescence-weighted) donor lifetime $\langle \tau_{D(A)} \rangle_F$ plots showed FRET distributions were also located on two dynamic FRET-lines (Figure 4.2b). As a profit, compact states (*A*, *B* and *C*) were now better resolved, however confirming two distinct fiber populations with fast internal dynamics. To characterize further the underlying structural states and interchanging dynamics, we integrated information from TIRF data (Figure 2, Publication II), fluorescence correlation analysis (S. Figure 11, Publication II) sub-ensemble lifetime analysis (S. Figure 10, Publication II) and from MFD histograms (Figure 4.2). Sub-ensemble fluorescence lifetime analysis provides a complementary method to directly resolve the individual FRET efficiencies (and thus R_{DA} -values) within a dynamic ensemble¹⁷⁶. As an example I demonstrate analysis for DA1 for FRET-selected species and compute a FRET-induced fluorescence decay of the donor $\varepsilon_D(t)$ (Figure 4.2c and S. Note, step 3, Publication II). Global analysis of the decay shows three corresponding FRET-species $\{A, C\}$, *B* and *D*, closely matching the limiting FRET states observed in 2D – MFD histograms (Figure 4.2a,b). On the other hand we analyzed autocorrelation functions for the donor- and acceptor channels, as well as the cross-correlation between donor- and acceptor fluorescence channels (Figure 4.2d and S. Figure 11, S. Note, step 4, Publication II) to directly access model-free molecular dynamics. This analysis supports the existence of structural dynamics

between the FRET species $\{A, C\}$, B and D for DA1 and revealed two slow kinetic exchange processes with relaxation time constants t_R of 21 μ s and 3 ms.

Resolving conformational dynamics in chromatin fibers

In order to characterize the two dynamic populations in chromatin fibers, and to resolve their underlying structural states we combined previously analyzed data from TIRF measurements, MFD histograms, sub-ensemble lifetime analysis and fluorescence correlation analysis for DA1-3. We further used this information for dynamic photon distribution analysis (dynPDA) (S. Note, steps 6-8, Publication II)¹⁷⁷ that enables to resolve recovered inter-dye distance and exchange dynamics between the states. Using the recovered inter-dye distance sets as constraints, we assigned molecular structures to species (A - D), based on available high-resolution structural data¹⁴ and coarse-grained simulations¹⁷⁸ (Figure 4.3b,c, S. Figure 12-13 and S. Note, steps 9-10, Publication II). Distance constraints from DA1 and DA2 demonstrated that FRET-species A and B correspond to conformational states with defined tetranucleosome units in two different interaction registers relative to the FRET labels. Register 1 (A) positions the label pairs in the same tetranucleosome unit (Figure 4.3a, b). This chromatin fiber conformation is consistent with the reported cryo-EM structure of a 12-mer chromatin fiber¹⁶⁸. In the contrary for Register 2 (B), FRET pairs are located across two neighboring tetranucleosome units. Species (C) corresponds to a distorted (twisted) tetranucleosome state within register 1. Finally, species (D) corresponds to an ensemble of open chromatin fiber conformations.

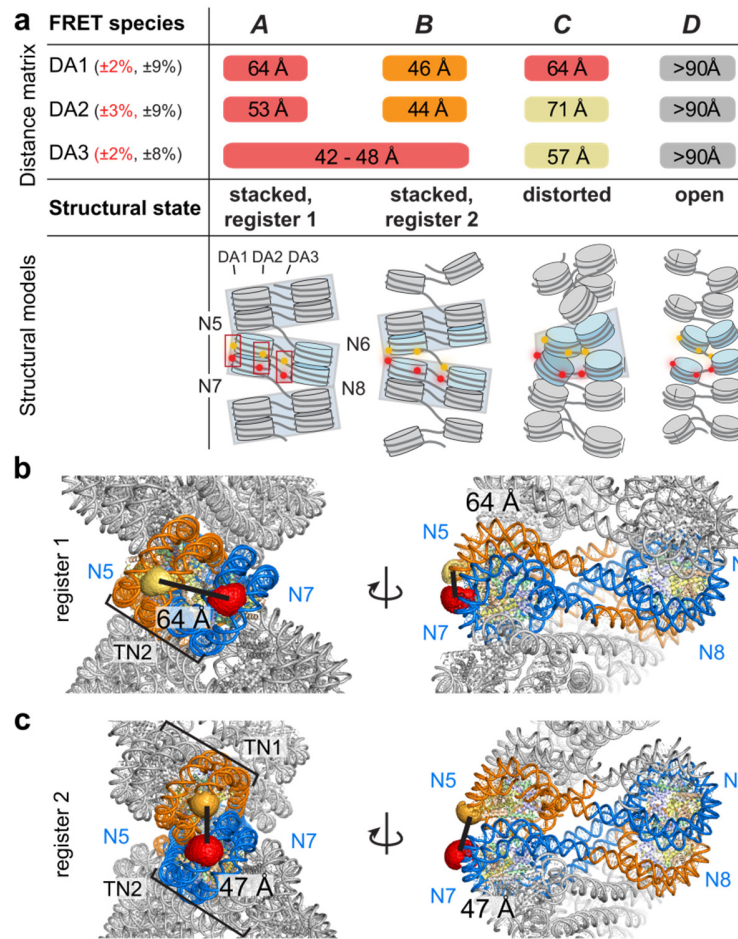


Figure 4.3 (a) Matrix of the inter-dye distances R_{DA} for DA1, DA2 and DA3 obtained from dynPDA. Species that cannot be discriminated with a given FRET pair are labeled with the same color and/or a continuous box. Percentages given in brackets: uncertainties in the observed distances. Red: Precision ($\Delta R_{DA}(R_{DA})$), relevant for relative R_{DA} . Black: Absolute uncertainty, mainly determined by the uncertainty in R_0 . The registers of tetranucleosome units are indicated by light grey boxes. (b) Molecular structure model of a chromatin array, consisting of a stack of 3 tetranucleosomes (register 1) with DA1-positioned dyes in the central tetranucleosome, based on ref.¹⁶⁸. The inter-dye distance was evaluated using simulated dye accessible contact volumes (ACV)¹⁷⁴. (c) Molecular structure of a chromatin array, consisting of a stack of 2 tetranucleosomes, flanked by two unstacked nucleosomes at each side (register 2) with DA1-positioned dyes on the two central tetranucleosomes and inter-dye distance from ACV-calculations. Molecular models for DA2 and DA3 are reported in Supplementary Figures. 12-13, Publication II.

A dynamic-register model for chromatin dynamics

To formulate an appropriate kinetic model for chromatin fibers, we applied certain criteria that should satisfy observed data and be physical meaningful for DA1-3. We list the requirements in (S. Figure 15,

Publication II) and test suggested trial models. We performed global fits over the Mg^{2+} dependence for each dataset DA1-3. Model that fulfils all criteria contains two branches: one branch connecting species (A,C) to (D), the second branch connecting species (B) to (D) (Figure 4.4d-f, S. Figures. 16-18, Publication II). An analysis of DA1 (Figure 4.4d) indicated that stacked nucleosome (A , register 1) exchange with open conformations (D) with a relaxation time $\tau_R = 3.7 \pm 0.3$ ms, B to D , register 2 with $\tau_R = 60 \pm 10 \mu s$. DA2 reveals partial nucleosome disengagement (species C) on a 0.5 ± 0.06 ms timescale, followed by a transition to (D) within 2.6 ± 0.5 ms. DA3, finally, reported on linker-DNA fluctuation.

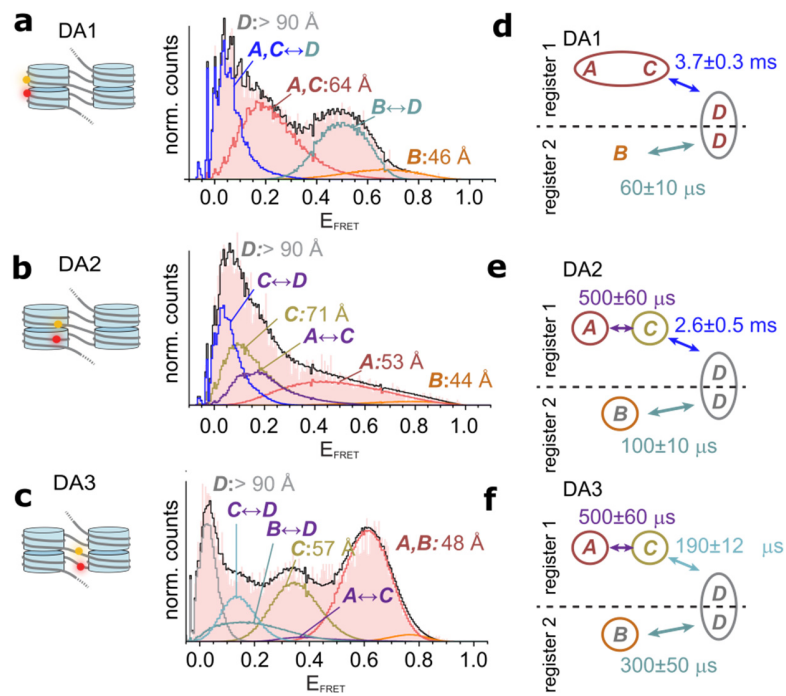


Figure 4.4 (a-c) dynPDA analysis of MFD data. Red histogram: Experimental data, black line: PDA fit to the kinetic models corresponding to the indicated state connectivities (Figures 5d-f). Gaussian distributions in orange hues or grey: Distributions corresponding to FRET-states indicated in Figure 4.3a: A (red), B (orange), C (yellow) D (grey). Blue hues: Distributions originating from dynamic exchange between FRET species: $A \leftrightarrow C$ (violet), $C \leftrightarrow D$ (dark blue), $B \leftrightarrow D$ (grey blue). (a) dynPDA analysis of MFD data for DA1 (at 4 mM Mg^{2+}) using the kinetic connectivity outlined in (d). (b) dynPDA analysis of MFD data for DA2 (at 3 mM Mg^{2+}) using the kinetic connectivity outlined in (e). (c) dynPDA analysis of MFD data for DA2 (at 3 mM Mg^{2+}) using the kinetic connectivity outlined in (f). (d-f) Kinetic connectivity maps for DA1-3 used for dynPDA, which describe the experimental data. The indicated time constants are given for 2 mM Mg^{2+} .

HP1 α induces a dynamically compacted chromatin structure

Finally we investigate how heterochromatin protein 1 α (HP1 α) affects the internal structure and dynamics of chromatin fibers. We thus reconstituted DA1 and DA2 chromatin fibers containing either unmethylated

(H3K9me0) or chemically produced H3K9me3 (S. Figure 19a,b, Publication II) and measured smFRET in the presence of 1 μ M HP1 α using TIRF microscopy (Figure 4.5a,b). The results demonstrate that binding of HP1 α results in dynamically compacted chromatin. It also stabilizes nucleosome stacking primarily towards the center of the chromatin fiber, where the FRET efficiency reaches the value ($E_{FRET} > 0.8$) of the limiting species A, B resolved by MFD measurements (Figure 4.2a). Phosphorylated HP1 α increased the compacting effect by stabilization of nucleosome binding and by strengthening HP1 α interactions beyond the dimer (Figure 4.5c, d).

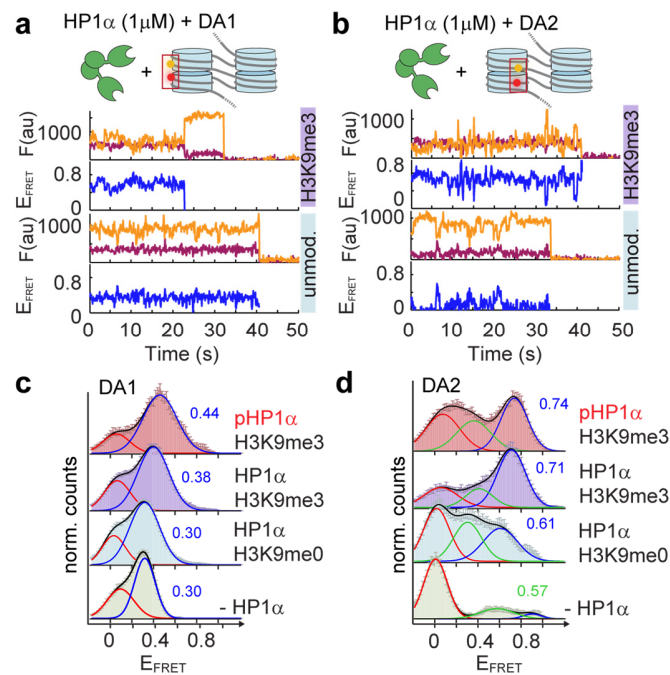


Figure 4.5 (a) FRET traces for DA1, containing no modification or H3K9me3 in the presence of 1 μ M HP1 α and the absence of Mg^{2+} . (b) FRET trace for DA2, containing no modification or H3K9me3 in the presence of 1 μ M HP1 α . (c) FRET populations for DA1, showing H3K9me3 dependent compaction by HP1 α and phosphorylated HP1 α (pHP1 α). (d) FRET populations for DA2, demonstrating close contacts induced by HP1 α / pHP1 α . (c-d) Error bars: s.e.m. For the number of traces, parameters of the Gaussian fits, see Supplementary Note and Supplementary Table 5, Publication II..

4.3 Conclusions

Combining confocal microscopy of freely diffusing molecules in solution with TIRF revealed structural and dynamic information about chromatin fibers. In this work we propose a dynamic-register model to describe higher-order chromatin structure and demonstrate multiscale chromatin dynamics across five orders of magnitude in time. We show that in a chromatin fiber a nucleosome can, at any time, engage in tetranucleosome contacts with only one of its two neighbors within the two-start helix that result in at

least two interchanging interaction registers. Neighboring tetranucleosomes can exchange their interaction register, by concerted unfolding, followed by refolding in the alternative register.

We also report that tetranucleosome contacts alternate between different registers on the 100-ms timescale. And finally, the effect of HP1 α on the chromatin fibers depending on the presence of H3K9me3 is studied. Study reveals that such chromatin effectors stabilize specific conformations from the rapidly exchanging ensemble, thereby enacting a biological output.

Chapter 5 Conclusions

FRET method has been identified as significant in structural biology to study structural conformations and dynamical exchange. The establishment of methodological guidance facilitates research recognition within the community and promotes quality control and data exchange among the researches. **Chapter 2** demonstrates the consistency of FRET method implementation among worldwide community. Here I report that by following proposed step-by-step procedure FRET efficiency value between the labs can be reported with standard deviation $\Delta E = \pm 0.5$. All correction parameters that distort recorded signal are discussed in great detail and their contribution to the error propagation of experimental uncertainty are discussed. In addition to the methodology utilized fluorescent dyes on different linkers were characterized by conducting time-resolved experiments, reporting fluorescence anisotropy, lifetime and quantum yield.

Single-molecule FRET experiments together with computational structural modeling were successfully implemented to resolve spatial models of various RNA three-way junctions. Experimental data was analyzed with MFD and experimental distances were recovered with PDA approach. They were later used as modeling restraints in the structural analysis. Also like in **Chapter 2**, thorough error analysis of all experimental parameters was done and finally propagated to the distance uncertainty. Finally resolved structures with different sequence were compared by diverse geometric means and it has been shown that studied RNAs are similar in shape but manifest different coaxial stacking or no stacking at all. Additional advantage of the fluorescence experiments are probing dyes at various microenvironment. With 14 different labeling positions I demonstrated that fluorophores exhibit site-specific fluorescence properties.

In **Chapter 4** two sm-FRET methods were united to resolve structural and dynamical process of chromatin fiber. It was possible to disentangle two distinct registers and formulate an underlying kinetic scheme. Based on these results, individual tetranucleosomes can open on millisecond timescale, whereas interaction between neighbors is detected in the microsecond time regime. Finally, interaction of the chromatin fiber with HP1 α reveals increase of the compactization, as HP1 α stabilizes inter-nucleosome contacts during interaction.

To conclude, in this work I did not only study the nucleic acids at different structural level (**Chapter 2**, **Chapter 3** and **Chapter 4**) but also refined the method (**Chapter 3**) and contributed to the methodological development in the community (**Chapter 2**).

Abbreviations and nomenclature

3WJ	Three way junction
APD	Avalanche photodiode
α	Emission crosstalk
AV	Accessible volume
$\langle B_{R G} \rangle$	Background signal in red detector given donor excitation
B_R	Background signal in red detector given donor excitation
$\langle B_{G G} \rangle$	Background signal in green detector given donor excitation
B_G	Background signal in green detector given donor excitation
DNA	Deoxyribonucleic acid
$\langle E \rangle$	Time-averaged FRET efficiency
E	FRET efficiency
$\varepsilon_{R D}(\lambda_{em})$	emission spectral coefficient
$\varepsilon_{G D}(\lambda_{em})$	emission spectral coefficient
FPS	FRET position and screening
$F_{G G}$	Fluorescence signal in green detector given donor excitation
$F_{R G}$	Fluorescence signal in red detector given donor excitation
F_D	Donor fluorescence signals
$F_{D D}$	Donor fluorescence signals
F_A	Acceptor fluorescence signals
$F_{A D}$	Acceptor fluorescence signals
$F_{ }$	fluorescence signals of the donor with parallel polarization
F_{\perp}	fluorescence signals of the donor with perpendicular polarization

FRET	Förster resonance energy transfer
$\Phi_{F,D}$	Fluorescence quantum yield of the donor
$\Phi_{F,A}$	Fluorescence quantum yield of the acceptor
g	g-factor
g_G	Detection efficiency of the green detector
g_R	Detection efficiency of the red detector
γ	Correction factor that includes detection efficiency ratio and fluorescence quantum yield ratio
HF	High FRET
IRF	Instrument response function
J	Spectral overlap integral
κ^2	orientation factor
λ	Wavelength [nm]
l_1 and l_2	compensating factors for the signal depolarization by the objective due to the high numerical aperture
LF	Low FRET
MFD	Multiparameter fluorescence detection
MLE	maximum likelihood estimator
n	Refractive index
N_{dof}	degree of freedom
PDB	Protein data base
PDA	Photon distribution analysis
$\langle R_{DA} \rangle_E$	FRET-efficiency weighted average distance from PDA
R_{mp}	distance between mean donor and acceptor positions
$r(t)$	Time resolved anisotropy

r_∞	Residual anisotropy
r_D	Steady state fluorescence anisotropy
r_0	Fundamental anisotropy
ρ	Rotation correlation time
Rh101	Rhodamine 101
Rh110	Rhodamine 110
R_0	Förster radius
RMSD	Root-mean-square distance
RNA	Ribonucleic acid
σ	Half width of Gaussian distribution
$S_{G G}$	Total uncorrected signal in green detector given donor excitation
S_G	Total uncorrected signal in green detector given donor excitation
$S_{R G}$	Total uncorrected signal in red detector given donor excitation
S_R	Total uncorrected signal in red detector given donor excitation
s_D and s_A	Trapped fraction of the donor/acceptor
TCSPC	Time correlated single photon counting
$\langle \tau \rangle_x$	Species weighted averaged fluorescence lifetime
$\langle \tau_{D(A)} \rangle_f$	Fluorescence weighted donor lifetime in presence of acceptor
$\tau_{D(0)}$	Fluorescence donor lifetime
τ -SPAD	Single Photon Avalanche Diode detector
$x^{(i)}$	Fraction of the i^{th} component
χ^2	Goodness of the fit
\otimes	circular convolution

Acknowledgement

I would like to thank many people who supported and encouraged me during dissertation, without them this thesis would not have been possible.

I would like to express my deep gratitude to Prof. Dr. Claus Seidel for the opportunity to learn the cutting edge technique in his group and conduct interesting projects that I can present in this thesis. Without his enthusiastic encouragement and useful critique this work would not be possible.

I also gratefully acknowledge:

My second supervisor Prof. Dr. Ing. Gerhard Steger.

Dr. Thomas Peulen and Dr. Oleg Opanasyuk for their invaluable help with data analysis, scientific discussions and just great colleagues I shared office with. Especially, I would like to thank Oleg for his endless support with “FRET challenge” project.

Dr. Hayk Vardanyan and Dr. Simon Sindbert who gave me a great start with RNA project and smooth introduction to the working environment.

Dr. Suren Felekyan for always being available to any scientific questions, his tremendous help with data analysis, and continuous maintenance of the setup and software. I learned a lot from him during our “Chromatin fiber” project.

Dr. Ralf Kühnemuth for useful discussion, setups maintenance during “FRET challenge” project and being endless inspiration for “Old New Year” gathering.

Prof. Dr. Beat Fierz for the fruitful collaboration and for giving an excellent example of work efficiency. Whole team, who worked on “chromatin array” project, in particular Dr. Sinan Kilic for being a great project partner.

Prof. Dr. Thorsten Hugel, with whom I had a pleasure to work during “FRET challenge” project and for his tremendous enthusiasm that led to the paper publication.

My dear Dr. Deborah Sandrin for being an amazing friend for me and the best colleague ever. Her endless supervision with chemicals was vital, also I had so much fun to work with her during praktikums, but more important, she introduced proper coffee into my life.

Dr. Qijun Ma for her never-ending optimism in any situation, for “no jokes” in my office, for all the fun during our joint trips and conferences and for creating always a friendly atmosphere in the lab.

Aiswaria for being an excellent partner during RNA project and for proofreading my thesis.

Dr.Christian Hanke for his contribution to discussions, MD simulations for RNA project and proofreading results in “RNA 3WJ project”.

Dr. Anders Barth for final discussions and for proofreading results in “RNA 3WJ project”.

Frau Veronika Mendorf for taking over the bureaucracy burden.

Whole Seidel’s lab for creating pleasant working atmosphere and friendly environment.

My parents and my sister, who always believed in me and their unconditional presence in my life.

And finally, I would like to thank Mykola Dimura who was with me from the beginning of this journey, for his endless help and insightful suggestions in all my projects, for being an excellent partner during “Chromatin fiber” and “RNA 3WJ” projects, and for everyday support and encouragement.

Chapter 6 References

1. Schuler, B. & Eaton, W. A. Protein folding studied by single-molecule FRET. *Curr. Opin. Struct. Biol.* **18**, 16-26 (2008).
2. Gambin, Y. & Deniz, A. A. Multicolor single-molecule FRET to explore protein folding and binding. *Mol Biosyst* **6**, 1540-1547 (2010).
3. Deniz, A. A. *et al.* Single-molecule protein folding: diffusion fluorescence resonance energy transfer studies of the denaturation of chymotrypsin inhibitor 2. *Proc Natl Acad Sci U S A* **97**, 5179-5184 (2000).
4. Schuler, B., Lipman, E. A., Steinbach, P. J., Kumke, M. & Eaton, W. A. Polyproline and the "Spectroscopic Ruler" Revisited with Single-Molecule Fluorescence. *Proc. Natl. Acad. Sci. USA* **102**, 2754-2759 (2005).
5. Majumdar, Z. K., Hickerson, R., Noller, H. F. & Clegg, R. M. Measurements of internal distance changes of the 30S ribosome using FRET with multiple donor-acceptor pairs: quantitative spectroscopic methods. *J. Mol. Biol.* **351**, 1123-1145 (2005).
6. Andrec, M., Levy, R. M. & Talaga, D. S. Direct Determination of Kinetic Rates from Single-Molecule Photon Arrival Trajectories Using Hidden Markov Models. *J. Phys. Chem. A* **107**, 7454-7464 (2003).
7. Nesmelov, Y. E. *et al.* Structural kinetics of myosin by transient time-resolved FRET. *Proc Natl Acad Sci U S A* **108**, 1891-1896 (2011).
8. Gansen, A. *et al.* High precision FRET studies reveal reversible transitions in nucleosomes between microseconds and minutes. *Nat. Commun.* **9**, 4628 (2018).
9. Lilley, D. M. J. Folding of branched RNA species. *Biopolymers* **48**, 101-112 (1998).
10. Schroeder, R., Barta, A. & Semrad, K. Strategies for RNA folding and assembly. *Nat. Rev. Mol. Cell Biol.* **5**, 908-919 (2004).
11. Scott, W. G., Horan, L. H. & Martick, M. The hammerhead ribozyme: structure, catalysis, and gene regulation. *Prog Mol Biol Transl Sci* **120**, 1-23 (2013).
12. Tamura, M. & Holbrook, S. R. Sequence and structural conservation in RNA ribose zippers. *J. Mol. Biol.* **320**, 455-474 (2002).
13. Holbrook, S. R. Structural principles from large RNAs. *Annu. Rev. Biophys.* **37**, 445-464 (2008).
14. Schalch, T., Duda, S., Sargent, D. F. & Richmond, T. J. X-ray structure of a tetranucleosome and its implications for the chromatin fibre. *Nature* **436**, 138-141 (2005).
15. Kilic, S. *et al.* Single-molecule FRET reveals multiscale chromatin dynamics modulated by HP1alpha. *Nat. Commun.* **9**, 235 (2018).
16. Tucker, B. J. & Breaker, R. R. Riboswitches as versatile gene control elements. *Curr. Opin. Struct. Biol.* **15**, 342-348 (2005).

17. Matsuoka, S. *et al.* Water-mediated recognition of simple alkyl chains by heart-type fatty-acid-binding protein. *Angew Chem Int Ed Engl* **54**, 1508-1511 (2015).
18. Eriksson, U. K. *et al.* Subangstrom resolution X-ray structure details aquaporin-water interactions. *Science* **340**, 1346-1349 (2013).
19. Henzler-Wildman, K. A. *et al.* A hierarchy of timescales in protein dynamics is linked to enzyme catalysis. *Nature* **450**, 913-916 (2007).
20. Cavalli, A., Salvatella, X., Dobson, C. M. & Vendruscolo, M. Protein structure determination from NMR chemical shifts. *Proc. Natl. Acad. Sci. USA* **104**, 9615-9620 (2007).
21. Kalinin, S. *et al.* A Toolkit and Benchmark Study for FRET-restrained High-Precision Structural Modeling. *Nat. Meth.* **9**, 1218-1227 (2012).
22. Wing, R. *et al.* Crystal structure analysis of a complete turn of B-DNA. *Nature* **287**, 755-758 (1980).
23. Benevides, J. M. & Thomas, G. J., Jr. Characterization of DNA structures by Raman spectroscopy: high-salt and low-salt forms of double helical poly(dG-dC) in H₂O and D₂O solutions and application to B, Z and A-DNA. *Nucleic Acids Res.* **11**, 5747-5761 (1983).
24. Yakovchuk, P., Protozanova, E. & Frank-Kamenetskii, M. D. Base-stacking and base-pairing contributions into thermal stability of the DNA double helix. *Nucleic Acids Res.* **34**, 564-574 (2006).
25. Clausen-Schaumann, H., Rief, M., Tolksdorf, C. & Gaub, H. E. Mechanical stability of single DNA molecules. *Biophys. J.* **78**, 1997-2007 (2000).
26. Calladine, C. H., D.; Luisi, B.; Travers A. *Understanding DNA*. 352 (2004).
27. Wozniak, A. K., Schröder, G. F., Grubmüller, H., Seidel, C. A. M. & Oesterhelt, F. Single-Molecule FRET Measures Bends and Kinks in DNA. *Proc. Natl. Acad. Sci. USA* **105**, 18337-18342 (2008).
28. Seeman, N. C. An overview of structural DNA nanotechnology. *Mol. Biotechnol.* **37**, 246-257 (2007).
29. Ghosh, I., Stains, C. I., Ooi, A. T. & Segal, D. J. Direct detection of double-stranded DNA: Molecular methods and applications for DNA diagnostics. *Mol Biosyst* **2**, 551-560 (2006).
30. Hofig, H., Gabba, M., Pobleto, S., Kempe, D. & Fitter, J. Inter-dye distance distributions studied by a combination of single-molecule FRET-filtered lifetime measurements and a weighted accessible volume (wAV) algorithm. *Molecules* **19**, 19269-19291 (2014).
31. Klostermeier, D. & Millar, D. P. Time-resolved fluorescence resonance energy transfer: a versatile tool for the analysis of nucleic acids. *Biopolymers* **61**, 159-179 (2001).
32. Digman, M. A., Caiolfa, V. R., Zamai, M. & Gratton, E. The phasor approach to fluorescence lifetime imaging analysis. *Biophys. J.* **94**, L14-16 (2008).

33. Peulen, T. O., Opanasyuk, O. & Seidel, C. A. M. Combining Graphical and Analytical Methods with Molecular Simulations to Analyze Time-Resolved FRET-Measurements of Labeled Macromolecules Accurately. *J. Phys. Chem. B* **121**, in press, DOI: 10.1021/acs.jpccb.1027b03441 (2017).
34. Denny, S. K. & Greenleaf, W. J. Linking RNA Sequence, Structure, and Function on Massively Parallel High-Throughput Sequencers. *Cold Spring Harb Perspect Biol* (2018).
35. Zampetaki, A., Albrecht, A. & Steinhofel, K. Long Non-coding RNA Structure and Function: Is There a Link? *Front Physiol* **9**, 1201 (2018).
36. Lafontaine, D. A., Norman, D. G. & Lilley, D. M. J. The global structure of the VS ribozyme. *EMBO J.* **21**, 2461-2471 (2002).
37. Doudna, J. A. & Cech, T. R. The chemical repertoire of natural ribozymes. *Nature* **418**, 222-228 (2002).
38. Leontis, N. B., Lescoute, A. & Westhof, E. The building blocks and motifs of RNA architecture. *Curr. Opin. Struct. Biol.* **16**, 279-287 (2006).
39. Laing, C. & Schlick, T. Analysis of four-way junctions in RNA structures. *J. Mol. Biol.* **390**, 547-559 (2009).
40. Lamiable, A. *et al.* Automated prediction of three-way junction topological families in RNA secondary structures. *Comput. Biol. Chem.* **37**, 1-5 (2012).
41. Sutton, J. L. & Pollack, L. Tuning RNA Flexibility with Helix Length and Junction Sequence. *Biophys. J.* **109**, 2644-2653 (2015).
42. Lilley, D. M. Structures of helical junctions in nucleic acids. *Q. Rev. Biophys.* **33**, 109-159 (2000).
43. Kalinin, S., Sisamakias, E., Magennis, S. W., Felekyan, S. & Seidel, C. A. M. On the origin of broadening of single-molecule FRET efficiency distributions beyond shot noise limits. *J. Phys. Chem. B* **114**, 6197-6206 (2010).
44. Sindbert, S. *et al.* Accurate Distance Determination of Nucleic Acids via Förster Resonance Energy Transfer: Implications of Dye Linker Length and Rigidity. *J. Am. Chem. Soc.* **133**, 2463-2480 (2011).
45. Woodcock, C. L., Frado, L. L. & Rattner, J. B. The higher-order structure of chromatin: evidence for a helical ribbon arrangement. *J. Cell Biol.* **99**, 42-52 (1984).
46. Finch, J. T. & Klug, A. Solenoidal model for superstructure in chromatin. *Proc Natl Acad Sci U S A* **73**, 1897-1901 (1976).
47. Graziano, V., Gerchman, S. E., Schneider, D. K. & Ramakrishnan, V. Histone H1 is located in the interior of the chromatin 30-nm filament. *Nature* **368**, 351-354 (1994).
48. Luger, K., Mader, A. W., Richmond, R. K., Sargent, D. F. & Richmond, T. J. Crystal structure of the nucleosome core particle at 2.8 Å resolution. *Nature* **389**, 251-260 (1997).
49. Li, G. & Widom, J. Nucleosomes facilitate their own invasion. *Nat. Struct. Mol. Biol.* **11**, 763-769 (2004).

50. Poirier, M. G., Oh, E., Tims, H. S. & Widom, J. Dynamics and function of compact nucleosome arrays. *Nat. Struct. Mol. Biol.* **16**, 938-944 (2009).
51. Kruithof, M. *et al.* Single-molecule force spectroscopy reveals a highly compliant helical folding for the 30-nm chromatin fiber. *Nat. Struct. Mol. Biol.* **16**, 534-540 (2009).
52. Fierz, B. & Poirier, M. G. Biophysics of Chromatin Dynamics. *Annu. Rev. Biophys.* (2019).
53. Kilic, S., Bachmann, A. L., Bryan, L. C. & Fierz, B. Multivalency governs HP1alpha association dynamics with the silent chromatin state. *Nat. Commun.* **6**, 7313 (2015).
54. Cheutin, T. *et al.* Maintenance of stable heterochromatin domains by dynamic HP1 binding. *Science* **299**, 721-725 (2003).
55. Bannister, A. J. *et al.* Selective recognition of methylated lysine 9 on histone H3 by the HP1 chromo domain. *Nature* **410**, 120-124 (2001).
56. Förster, T. Zwischenmolekulare Energiewanderung und Fluoreszenz. *Ann.Phys.* **437**, 55-75 (1948).
57. Stryer, L. & Haugland, R. P. Energy Transfer: a Spectroscopic Ruler. *Proc Natl Acad Sci U S A* **58**, 719-726 (1967).
58. Murchie, A. I. *et al.* Fluorescence Energy Transfer Shows that the Four-Way DNA Junction is a Right-Handed Cross of Antiparallel Molecules. *Nature* **341**, 763-766 (1989).
59. Mekler, V. *et al.* Structural Organization of Bacterial RNA Polymerase Holoenzyme and the RNA Polymerase-promoter Open Complex. *Cell* **108**, 599-614 (2002).
60. Ha, T. *et al.* Probing the Interaction Between Two Single Molecules: Fluorescence Resonance Energy Transfer Between a Single Donor and a Single Acceptor. *Proc. Natl. Acad. Sci. USA* **93**, 6264-6268 (1996).
61. Choi, U. B. *et al.* Single-Molecule FRET-derived Model of the Synaptotagmin 1-SNARE Fusion Complex. *Nat. Struct. Mol. Biol.* **17**, 318-U384 (2010).
62. Hellenkamp, B., Wortmann, P., Kandzia, F., Zacharias, M. & Hugel, T. Multidomain Structure and Correlated Dynamics Determined by Self-Consistent FRET Networks. *Nat. Meth.* **14**, 174-180 (2017).
63. Eilert, T., Beckers, M., Drechsler, F. & Michaelis, J. Fast-NPS—A Markov Chain Monte Carlo-based Analysis Tool to Obtain Structural Information from Single-Molecule FRET Measurements. *Comput. Phys. Commun.* **218**, in press: <http://dx.doi.org/10.1016/j.cpc.2017.1005.1027> (2017).
64. Hofmann, D., Korzdorfer, T. & Kummel, S. Energy Transfer and Forster's Dipole Coupling Approximation Investigated in a Real-Time Kohn-Sham Scheme. *Phys.Rev.A* **82** (2010).
65. Spiegel, J. D., Fulle, S., Kleinschmidt, M., Gohlke, H. & Marian, C. M. Failure of the IDA in FRET Systems at Close Inter-Dye Distances is Moderated by Frequent Low $k(2)$ Values. *J. Phys. Chem. B* **120**, 8845-8862 (2016).

66. Sakon, J. J. & Weninger, K. R. Detecting the conformation of individual proteins in live cells. *Nat. Meth.* **7**, 203-205 (2010).
67. Muschielok, A. *et al.* A Nano-Positioning System for Macromolecular Structural Analysis. *Nat. Meth.* **5**, 965-971 (2008).
68. Beckers, M., Drechsler, F., Eilert, T., Nagy, J. & Michaelis, J. Quantitative Structural Information from Single-Molecule FRET. *Farad. Discuss.* **184**, 117-129 (2015).
69. Dimura, M. *et al.* Quantitative FRET Studies and Integrative Modeling Unravel the Structure and Dynamics of Biomolecular Systems. *Curr. Opin. Struct. Biol.* **40**, 163-185 (2016).
70. Brunger, A. T., Strop, P., Vrljic, M., Chu, S. & Weninger, K. R. Three-Dimensional Molecular Modeling with Single Molecule FRET. *J. Struct. Biol.* **173**, 497-505 (2011).
71. Sabanayagam, C. R., Eid, J. S. & Meller, A. Using Fluorescence Resonance Energy Transfer to Measure Distances Along Individual DNA Molecules: Corrections due to Nonideal Transfer. *J. Chem. Phys.* **122**, 61103-61107 (2005).
72. McCann, J. J., Choi, U. B., Zheng, L., Weninger, K. & Bowen, M. E. Optimizing Methods to Recover Absolute FRET Efficiency from Immobilized Single Molecules. *Biophys. J.* **99**, 961-970 (2010).
73. Sisamakris, E., Valeri, A., Kalinin, S., Rothwell, P. J. & Seidel, C. A. M. Accurate Single-Molecule FRET Studies Using Multiparameter Fluorescence Detection. *Methods Enzymol.* **475**, 455-514 (2010).
74. Lee, N. K. *et al.* Accurate FRET Measurements Within Single Diffusing Biomolecules Using Alternating-Laser Excitation. *Biophys. J.* **88**, 2939-2953 (2005).
75. Hohlbein, J., Craggs, T. D. & Cordes, T. Alternating-Laser Excitation: Single-Molecule FRET and Beyond. *Chem. Soc. Rev.* **43**, 1156-1171 (2014).
76. Margeat, E. *et al.* Direct Observation of Abortive Initiation and Promoter Escape Within Single Immobilized Transcription Complexes. *Biophys. J.* **90**, 1419-1431 (2006).
77. Ivani, I. *et al.* Parmbsc1: a refined force field for DNA simulations. *Nat Methods* **13**, 55-58 (2016).
78. Kapanidis, A. N. *et al.* Fluorescence-aided molecule sorting: analysis of structure and interactions by alternating-laser excitation of single molecules. *Proc Natl Acad Sci U S A* **101**, 8936-8941 (2004).
79. Müller, B. K., Zaychikov, E., Bräuchle, C. & Lamb, D. C. Pulsed Interleaved Excitation. *Biophys. J.* **89**, 3508-3522 (2005).
80. Stelzl, L. S., Erlenbach, N., Heinz, M., Prisner, T. F. & Hummer, G. Resolving the Conformational Dynamics of DNA with Angstrom Resolution by Pulsed Electron-Electron Double Resonance and Molecular Dynamics. *J. Am. Chem. Soc.* **139**, 11674-11677 (2017).

81. Levitus, M. & Ranjit, S. Cyanine dyes in biophysical research: the photophysics of polymethine fluorescent dyes in biomolecular environments. *Q. Rev. Biophys.*, 1-29 (2010).
82. Hendrix, J. & Lamb, D. C. Pulsed Interleaved Excitation: Principles and Applications. *Fluorescence Fluctuation Spectroscopy (Ffs), Pt A* **518**, 205-243 (2013).
83. Nir, E. *et al.* Shot-Noise Limited Single-Molecule FRET Histograms: Comparison Between Theory and Experiments. *J. Phys. Chem. B* **110**, 22103-22124 (2006).
84. Barth, A., Voith von Voithenberg, L. & DC., L. MFD-PIE and PIE-FI: Ways to Extract More Information with TCSPC. in *Advanced Photon Counting: Applicatios, Methods, Instrumentation* Vol. 15 129-157 (Springer, 2015).
85. Preus, S., Hildebrandt, L. L. & Birkedal, V. Optimal Background Estimators in Single-Molecule FRET Microscopy. *Biophys. J.* **111**, 1278-1286 (2016).
86. Hildebrandt, L. L., Preus, S. & Birkedal, V. Quantitative Single Molecule FRET Efficiencies Using TIRF Microscopy. *Farad. Discuss.* **184**, 131-142 (2015).
87. Deniz, A. A. *et al.* Single-Pair Fluorescence Resonance Energy Transfer on Freely Diffusing Molecules: Observation of Forster Distance Dependence and Subpopulations. *Proc. Natl. Acad. Sci. USA* **96**, 3670-3675 (1999).
88. Antonik, M., Felekyan, S., Gaiduk, A. & Seidel, C. A. M. Separating Structural Heterogeneities from Stochastic Variations in Fluorescence Resonance Energy Transfer Distributions via Photon Distribution Analysis. *J. Phys. Chem. B* **110**, 6970-6978 (2006).
89. Kalinin, S., Valeri, A., Antonik, M., Felekyan, S. & Seidel, C. A. M. Detection of Structural Dynamics by FRET: A Photon Distribution and Fluorescence Lifetime Analysis of Systems with Multiple States. *J. Phys. Chem. B* **114**, 7983-7995 (2010).
90. Clegg, R. M. Förster Resonance Energy Transfer - FRET What Is It, Why Do It, And How It's Done. in *Laboratory Techniques in Biochemistry and Molecular Biology* Vol. 33 (ed TWJ. Gadella) 1-57 (Elsevier Science, 2009).
91. Braslavsky, S. E. *et al.* Pitfalls and Limitations in the Practical Use of Förster's Theory of Resonance Energy Transfer. *Photochem. Photobiol. Sci.* **7**, 1444-1448 (2008).
92. Knox, R. S. & van Amerongen, H. Refractive Index Dependence of the Forster Resonance Excitation Transfer Rate. *J. Phys. Chem. B* **106**, 5289-5293 (2002).
93. Voros, J. The Density and Refractive Index of Adsorbing Protein Layers. *Biophys. J.* **87**, 553-561 (2004).
94. Clegg, R. M. Fluorescence Resonance Energy Transfer and Nucleic Acids. *Methods Enzymol.* **211**, 353-388 (1992).
95. Case, D. A. *et al.* The Amber biomolecular simulation programs. *J. Comput. Chem.* **26**, 1668-1688 (2005).

96. Jorgensen, W. L., Chandrasekhar, J., Madura, J. D., Impey, R. W. & Klein, M. L. Comparison of Simple Potential Functions for Simulating Liquid Water. *J. Chem. Phys.* **79**, 926-935 (1983).
97. Joung, I. S. & Cheatham, T. E., 3rd. Determination of alkali and halide monovalent ion parameters for use in explicitly solvated biomolecular simulations. *J. Phys. Chem. B* **112**, 9020-9041 (2008).
98. Li, P., Roberts, B. P., Chakravorty, D. K. & Merz, K. M., Jr. Rational Design of Particle Mesh Ewald Compatible Lennard-Jones Parameters for +2 Metal Cations in Explicit Solvent. *J. Chem. Theory Comput.* **9**, 2733-2748 (2013).
99. Gohlke, H., Kiel, C. & Case, D. A. Insights into protein-protein binding by binding free energy calculation and free energy decomposition for the Ras-Raf and Ras-RalGDS complexes. *J. Mol. Biol.* **330**, 891-913 (2003).
100. Widengren, J., Schweinberger, E., Berger, S. & Seidel, C. A. M. Two new concepts to measure fluorescence resonance energy transfer via fluorescence correlation spectroscopy: Theory and experimental realizations. *J. Phys. Chem. A* **105**, 6851-6866 (2001).
101. Vöpel, T. *et al.* Triphosphate induced dimerization of human guanylate binding protein 1 involves association of the C-terminal helices: A joint double electron-electron resonance and FRET study. *Biochemistry* **53**, 4590-4600 (2014).
102. Ponting, C. P., Oliver, P. L. & Reik, W. Evolution and functions of long noncoding RNAs. *Cell* **136**, 629-641 (2009).
103. Alberts B., J. A., Lewis J. *Molecular Biology of the Cell. 4th edition.* (Garland Science, 2002).
104. Lilley, D. M. Mechanisms of RNA catalysis. *Philos. Trans. R. Soc. Lond. B Biol. Sci.* **366**, 2910-2917 (2011).
105. Ge X. Q., L. H. Noncoding RNAs in the regulation of DNA replication. *Trends Biochem. Sci.* **39**, 341-343 (2014).
106. Hammann, C., Norman, D. G. & Lilley, D. M. Dissection of the ion-induced folding of the hammerhead ribozyme using 19F NMR. *Proc Natl Acad Sci U S A* **98**, 5503-5508 (2001).
107. Cooper, T. A., Wan, L. & Dreyfuss, G. RNA and disease. *Cell* **136**, 777-793 (2009).
108. Moore, M. J. From birth to death: the complex lives of eukaryotic mRNAs. *Science* **309**, 1514-1518 (2005).
109. Kim, S. H. *et al.* The general structure of transfer RNA molecules. *Proc Natl Acad Sci U S A* **71**, 4970-4974 (1974).
110. Batey, R. T., Gilbert, S. D. & Montange, R. K. Structure of a natural guanine-responsive riboswitch complexed with the metabolite hypoxanthine. *Nature* **432**, 411-415 (2004).
111. Guthrie, C. & Patterson, B. Spliceosomal snRNAs. *Annu. Rev. Genet.* **22**, 387-419 (1988).

112. Myslinski, E., Branlant, C., Wieben, E. D. & Pederson, T. The small nuclear RNAs of *Drosophila*. *J. Mol. Biol.* **180**, 927-945 (1984).
113. Noller, H. F. RNA structure: reading the ribosome. *Science* **309**, 1508-1514 (2005).
114. Chu, V. B. *et al.* Do conformational biases of simple helical junctions influence RNA folding stability and specificity? *RNA* **15**, 2195-2205 (2009).
115. Glisovic, T., Bachorik, J. L., Yong, J. & Dreyfuss, G. RNA-binding proteins and post-transcriptional gene regulation. *FEBS Lett.* **582**, 1977-1986 (2008).
116. Rupert, P. B., Massey, A. P., Sigurdsson, S. T. & Ferre-D'Amare, A. R. Transition state stabilization by a catalytic RNA. *Science* **298**, 1421-1424 (2002).
117. Zheng, Q. *et al.* On the Mechanisms of Cyanine Fluorophore Photostabilization. *J Phys Chem Lett* **3**, 2200-2203 (2012).
118. Zheng, Q. *et al.* Ultra-stable organic fluorophores for single-molecule research. *Chem. Soc. Rev.* **43**, 1044-1056 (2014).
119. Panchuk-Voloshina, N. *et al.* Alexa dyes, a series of new fluorescent dyes that yield exceptionally bright, photostable conjugates. *J. Histochem. Cytochem.* **47**, 1179-1188 (1999).
120. Vandenberk, N., Barth, A., Borrenberghs, D., Hofkens, J. & Hendrix, J. Evaluation of Blue and Far-Red Dye Pairs in Single-Molecule Förster Resonance Energy Transfer Experiments. *J. Phys. Chem. B* **122**, 4249-4266 (2018).
121. Aitken, C. E., Marshall, R. A. & Puglisi, J. D. An oxygen scavenging system for improvement of dye stability in single-molecule fluorescence experiments. *Biophys. J.* **94**, 1826-1835 (2008).
122. Moerner, W. E. & Kador, L. Optical detection and spectroscopy of single molecules in a solid. *Phys. Rev. Lett.* **62**, 2535-2538 (1989).
123. Fessl, T. *et al.* Towards characterization of DNA structure under physiological conditions in vivo at the single-molecule level using single-pair FRET. *Nucleic Acids Res.* **40**, e121 (2012).
124. Lerner, E. *et al.* Toward dynamic structural biology: Two decades of single-molecule Förster resonance energy transfer. *Science* **359** (2018).
125. Sindbert, S. *FRET restrained high-precision structural modeling of biomolecules* PhD thesis, Heinrich Heine University Düsseldorf, (2012).
126. Vardanyan, H. *FRET restrained high-precision structural modeling of RNA junction* PhD thesis, Heinrich Heine University Düsseldorf, (2014).
127. Sobczak, J. P., Martin, T. G., Gerling, T. & Dietz, H. Rapid folding of DNA into nanoscale shapes at constant temperature. *Science* **338**, 1458-1461 (2012).
128. Kudryavtsev, V. *et al.* Combining MFD and PIE for Accurate Single-Pair Förster Resonance Energy Transfer Measurements. *ChemPhysChem* **13**, 1060-1078 (2012).
129. Rasnik, I., McKinney, S. A. & Ha, T. Nonblinking and long-lasting single-molecule fluorescence imaging. *Nat Methods* **3**, 891-893 (2006).

130. Zander, C. *et al.* Detection and characterization of single molecules in aqueous solution. *Applied Physics B-Lasers and Optics* **63**, 517-523 (1996).
131. Maus, M. *et al.* An experimental comparison of the maximum likelihood estimation and nonlinear least-squares fluorescence lifetime analysis of single molecules. *Anal. Chem.* **73**, 2078-2086 (2001).
132. Koshioka, M., Sasaki, K. & Masuhara, H. Time-Dependent Fluorescence Depolarization Analysis in 3-Dimensional Microspectroscopy. *Appl. Spectrosc.* **49**, 224-228 (1995).
133. Vamosi, G., Gohlke, C. & Clegg, R. M. Fluorescence characteristics of 5-carboxytetramethylrhodamine linked covalently to the 5' end of oligonucleotides: multiple conformers of single-stranded and double-stranded dye-DNA complexes. *Biophys. J.* **71**, 972-994 (1996).
134. Neubauer, H. *et al.* Orientational and dynamical heterogeneity of rhodamine 6G terminally attached to a DNA helix revealed by NMR and single-molecule fluorescence spectroscopy. *J. Am. Chem. Soc.* **129**, 12746-12755 (2007).
135. Kretschy, N., Sack, M. & Somoza, M. M. Sequence-Dependent Fluorescence of Cy3- and Cy5-Labeled Double-Stranded DNA. *Bioconjug. Chem.* **27**, 840-848 (2016).
136. Kalinin, S., Felekyan, S., Valeri, A. & Seidel, C. A. Characterizing multiple molecular States in single-molecule multiparameter fluorescence detection by probability distribution analysis. *J. Phys. Chem. B* **112**, 8361-8374 (2008).
137. Kalinin, S., Felekyan, S., Antonik, M. & Seidel, C. A. M. Probability distribution analysis of single-molecule fluorescence anisotropy and resonance energy transfer. *J. Phys. Chem. B* **111**, 10253-10262 (2007).
138. Hellenkamp, B. *et al.* Precision and accuracy of single-molecule FRET measurements-a multi-laboratory benchmark study. *Nat Methods* **15**, 669-676 (2018).
139. Straume, M., Fraiser-Cadoret, S.G., Johnson, M.L. *Least-squares analysis of fluorescence data. In topics in Fluorescence Spectroscopy.* Vol. 2 177-239 (New York: Plenum Press, 1991).
140. Phil, G. *Bayesian Logical Data Analysis for the Physical Sciences: A Comparative Approach with Mathematica.* (Cambridge University Press, 2005).
141. Van der Meer, B. W. Kappa-squared: from nuisance to new sense. *J. Biotechnol.* **82**, 96-181 (2002).
142. Dale, R. E., Eisinger, J. & Blumberg, W. E. The orientational freedom of molecular probes. The orientation factor in intramolecular energy transfer. *Biophys. J.* **26**, 161-193 (1979).
143. Cai, Q. *et al.* Nanometer distance measurements in RNA using site-directed spin labeling. *Biophys. J.* **93**, 2110-2117 (2007).
144. Toulmin, A. *et al.* Conformational Heterogeneity in a Fully Complementary DNA Three-Way Junction with a GC-Rich Branchpoint. *Biochemistry* **56**, 4985-4991 (2017).

145. Bernardo, J. M., Smith, A.F.M. *Bayesian Theory*. (1993).
146. Liebeschuetz, J. W., Cole, J. C. & Korb, O. Pose prediction and virtual screening performance of GOLD scoring functions in a standardized test. *J. Comput-Aided. Mol. Des.* **26**, 737-748 (2012).
147. Efron, B. Jackknife, Bootstrap and Other Resampling Methods in Regression-Analysis - Discussion. *Annals of Statistics* **14**, 1301-1304 (1986).
148. Agbavwe, C. & Somoza, M. M. Sequence-Dependent Fluorescence of Cyanine Dyes on Microarrays. *Plos One* **6** (2011).
149. Iqbal, A., Wang, L., Thompson, K. C., Lilley, D. M. & Norman, D. G. The structure of cyanine 5 terminally attached to double-stranded DNA: implications for FRET studies. *Biochemistry* **47**, 7857-7862 (2008).
150. Norman, D. G., Grainger, R. J., Uhrin, D. & Lilley, D. M. Location of cyanine-3 on double-stranded DNA: importance for fluorescence resonance energy transfer studies. *Biochemistry* **39**, 6317-6324 (2000).
151. Stennett, E. M. S., Ciuba, M. A. & Levitus, M. Photophysical processes in single molecule organic fluorescent probes. *Chem. Soc. Rev.* **43**, 1057-1075 (2014).
152. Iqbal, A. *et al.* Orientation dependence in fluorescent energy transfer between Cy3 and Cy5 terminally attached to double-stranded nucleic acids. *Proc. Natl. Acad. Sci. USA* **105**, 11176-11181 (2008).
153. Andreatta, D. *et al.* Ultrafast dynamics in DNA: "fraying" at the end of the helix. *J. Am. Chem. Soc.* **128**, 6885-6892 (2006).
154. Leroy, J. L., Kochoyan, M., Huynh-Dinh, T. & Gueron, M. Characterization of base-pair opening in deoxynucleotide duplexes using catalyzed exchange of the imino proton. *J. Mol. Biol.* **200**, 223-238 (1988).
155. Nonin, S., Leroy, J. L. & Gueron, M. Terminal base pairs of oligodeoxynucleotides: imino proton exchange and fraying. *Biochemistry* **34**, 10652-10659 (1995).
156. Dornberger, U., Leijon, M. & Fritzsche, H. High base pair opening rates in tracts of GC base pairs. *J. Biol. Chem.* **274**, 6957-6962 (1999).
157. Chen, H., Ahsan, S. S., Santiago-Berrios, M. B., Abruna, H. D. & Webb, W. W. Mechanisms of quenching of Alexa fluorophores by natural amino acids. *J. Am. Chem. Soc.* **132**, 7244-7245 (2010).
158. Nazarenko, I., Pires, R., Lowe, B., Obaidy, M. & Rashtchian, A. Effect of primary and secondary structure of oligodeoxyribonucleotides on the fluorescent properties of conjugated dyes. *Nucleic Acids Res.* **30**, 2089-2195 (2002).
159. DeLano, W. L. The PyMOL Molecular Graphics System. (2002).
160. Bailor, M. H., Sun, X. & Al-Hashimi, H. M. Topology links RNA secondary structure with global conformation, dynamics, and adaptation. *Science* **327**, 202-206 (2010).
161. Bailor, M. H., Mustoe, A. M., Brooks, C. L., 3rd & Al-Hashimi, H. M. Topological constraints: using RNA secondary structure to model 3D conformation,

- folding pathways, and dynamic adaptation. *Curr. Opin. Struct. Biol.* **21**, 296-305 (2011).
162. Wong, C. W. *Introduction to mathematical physics: methods & concepts*. (OUP Oxford, 2013).
 163. Mustoe, A. M., Bailor, M. H., Teixeira, R. M., Brooks, C. L., 3rd & Al-Hashimi, H. M. New insights into the fundamental role of topological constraints as a determinant of two-way junction conformation. *Nucleic Acids Res.* **40**, 892-904 (2012).
 164. Ha, T. *et al.* Ligand-induced conformational changes observed in single RNA molecules. *Proc Natl Acad Sci U S A* **96**, 9077-9082 (1999).
 165. Chandra Sanyal, S. & Liljas, A. The end of the beginning: structural studies of ribosomal proteins. *Curr. Opin. Struct. Biol.* **10**, 633-636 (2000).
 166. Luger, K., Dechassa, M. L. & Tremethick, D. J. New insights into nucleosome and chromatin structure: an ordered state or a disordered affair? *Nat. Rev. Mol. Cell Biol.* **13**, 436-447 (2012).
 167. Song, F. *et al.* Cryo-EM study of the chromatin fiber reveals a double helix twisted by tetranucleosomal units. *Science* **344**, 376-380 (2014).
 168. Robinson, P. J., Fairall, L., Huynh, V. A. & Rhodes, D. EM measurements define the dimensions of the "30-nm" chromatin fiber: evidence for a compact, interdigitated structure. *Proc Natl Acad Sci U S A* **103**, 6506-6511 (2006).
 169. Cui, Y. & Bustamante, C. Pulling a single chromatin fiber reveals the forces that maintain its higher-order structure. *Proc Natl Acad Sci U S A* **97**, 127-132 (2000).
 170. Koopmans, W. J., Brehm, A., Logie, C., Schmidt, T. & van Noort, J. Single-pair FRET microscopy reveals mononucleosome dynamics. *J. Fluoresc.* **17**, 785-795 (2007).
 171. Wei, S., Falk, S. J., Black, B. E. & Lee, T. H. A novel hybrid single molecule approach reveals spontaneous DNA motion in the nucleosome. *Nucleic Acids Res.* **43**, e111 (2015).
 172. Gansen, A. *et al.* Nucleosome disassembly intermediates characterized by single-molecule FRET. *Proc Natl Acad Sci U S A* **106**, 15308-15313 (2009).
 173. Laurence, T. A., Kong, X., Jager, M. & Weiss, S. Probing structural heterogeneities and fluctuations of nucleic acids and denatured proteins. *Proc Natl Acad Sci U S A* **102**, 17348-17353 (2005).
 174. Lowary, P. T. & Widom, J. New DNA sequence rules for high affinity binding to histone octamer and sequence-directed nucleosome positioning. *J. Mol. Biol.* **276**, 19-42 (1998).
 175. *NIST/SEMATECH e-Handbook of Statistical Methods*, <<http://www.itl.nist.gov/div898/handbook/>> (2016).
 176. Ngo, T. T., Zhang, Q., Zhou, R., Yodh, J. G. & Ha, T. Asymmetric unwrapping of nucleosomes under tension directed by DNA local flexibility. *Cell* **160**, 1135-1144 (2015).

177. Arya, G., Zhang, Q. & Schlick, T. Flexible histone tails in a new mesoscopic oligonucleosome model. *Biophys. J.* **91**, 133-150 (2006).
178. Fan, J. Y., Rangasamy, D., Luger, K. & Tremethick, D. J. H2A.Z alters the nucleosome surface to promote HP1alpha-mediated chromatin fiber folding. *Mol. Cell* **16**, 655-661 (2004).

Precision and accuracy of single-molecule FRET measurements—a multi-laboratory benchmark study

Björn Hellenkamp^{1,2,33}, Sonja Schmid^{1,3,33}, Olga Doroshenko⁴, Oleg Opanasyuk⁴, Ralf Kühnemuth⁴, Soheila Rezaei Adariani⁵, Benjamin Ambrose⁶, Mikayel Aznauryan⁷, Anders Barth⁸, Victoria Birkedal⁷, Mark E. Bowen⁹, Hongtao Chen¹⁰, Thorben Cordes^{11,12}, Tobias Eilert¹³, Carel Fijen¹⁴, Christian Gebhardt¹², Markus Götz¹⁵, Giorgos Gouridis^{11,12}, Enrico Gratton¹⁰, Taekjip Ha¹⁵, Pengyu Hao¹⁶, Christian A. Hanke⁴, Andreas Hartmann¹⁷, Jelle Hendrix^{18,19}, Lasse L. Hildebrandt⁷, Verena Hirschfeld²⁰, Johannes Hohlbein^{14,21}, Boyang Hua¹⁵, Christian G. Hübner²⁰, Eleni Kallis¹³, Achillefs N. Kapanidis²², Jae-Yeol Kim²³, Georg Krainer^{17,24}, Don C. Lamb⁸, Nam Ki Lee²³, Edward A. Lemke^{25,26,27}, Brié Levesque⁹, Marcia Levitus²⁸, James J. McCann⁹, Nikolaus Naredi-Rainer⁸, Daniel Nettels²⁹, Thuy Ngo¹⁵, Ruoyi Qiu¹⁶, Nicole C. Robb²², Carlheinz Röcker¹³, Hugo Sanabria⁵, Michael Schlierf¹⁷, Tim Schröder³⁰, Benjamin Schuler²⁹, Henning Seidel²⁰, Lisa Streit¹³, Johann Thurn¹, Philip Tinnefeld^{30,31}, Swati Tyagi²⁷, Niels Vandenberg¹⁸, Andrés Manuel Vera³⁰, Keith R. Weninger¹⁶, Bettina Wünsch³¹, Inna S. Yanez-Orozco⁵, Jens Michaelis^{13*}, Claus A. M. Seidel^{4*}, Timothy D. Craggs^{6,22*} and Thorsten Hugel^{1,32*}

Single-molecule Förster resonance energy transfer (smFRET) is increasingly being used to determine distances, structures, and dynamics of biomolecules *in vitro* and *in vivo*. However, generalized protocols and FRET standards to ensure the reproducibility and accuracy of measurements of FRET efficiencies are currently lacking. Here we report the results of a comparative blind study in which 20 labs determined the FRET efficiencies (E) of several dye-labeled DNA duplexes. Using a unified, straightforward method, we obtained FRET efficiencies with s.d. between ± 0.02 and ± 0.05 . We suggest experimental and computational procedures for converting FRET efficiencies into accurate distances, and discuss potential uncertainties in the experiment and the modeling. Our quantitative assessment of the reproducibility of intensity-based smFRET measurements and a unified correction procedure represents an important step toward the validation of distance networks, with the ultimate aim of achieving reliable structural models of biomolecular systems by smFRET-based hybrid methods.

FRET¹, also known as fluorescence resonance energy transfer, is a well-established method for studying biomolecular conformations and dynamics at both the ensemble^{2–4} and the single-molecule level^{5–10}. In such experiments, the energy transfer between donor and acceptor fluorophores is quantified with respect to their proximity¹. The fluorophores are usually attached via flexible linkers to defined positions of the system under investigation. The transfer efficiency depends on the interdyer distance, which is well described by Förster's theory for distances $> 30 \text{ \AA}$ ^{11,12}. Accordingly, FRET has been termed a 'spectroscopic ruler' for measurements on the molecular scale³, capable of determining distances *in vitro*, and even in cells¹³, with potentially ångström-level accuracy and precision. In its single-molecule implementation, FRET largely overcomes ensemble-averaging and time-averaging and can uncover individual species in heterogeneous and dynamic biomolecular complexes, as well as transient intermediates⁵.

The two most popular smFRET approaches for use in determining distances are confocal microscopy of freely diffusing molecules

in solution and total internal reflection fluorescence (TIRF) microscopy of surface-attached molecules. Various fluorescence-intensity- and lifetime-based procedures have been proposed with the aim of determining FRET efficiencies^{10,14–20}. Here we focus on intensity-based measurements in which the FRET efficiency E is determined from donor and acceptor photon counts and subsequently used to calculate the interfluorophore distance according to Förster's theory.

So far most intensity-based smFRET studies have characterized relative changes in FRET efficiency. This ratiometric approach is often sufficient to distinguish different conformations of a biomolecule (e.g., an open conformation with low FRET efficiency versus a closed conformation with high FRET efficiency) and to determine their interconversion kinetics. However, knowledge about distances provides additional information that can be used, for example, to compare an experimental structure with known structures, or to assign conformations to different structural states. In combination with other structural measurements and computer simulations,

A full list of affiliations appears at the end of the paper.

ANALYSIS

FRET-derived distances are increasingly being used to generate novel biomolecular structural models via hybrid methods^{9,21–26}.

However, it is difficult to compare and validate distance measurements from different labs, especially when detailed methodological descriptions are lacking. In addition, different methods for data acquisition and analysis, which often involve custom-built microscopes and in-house software, can have very different uncertainties and specific pitfalls. To overcome these issues, here we describe general methodological recommendations and well-characterized standard samples for FRET that can enable researchers to validate results and estimate the accuracy and precision of distance measurements. This approach should allow the scientific community to confirm the consistency of smFRET-derived distances and structural models. To facilitate data validation across the field, we recommend the use of a unified nomenclature to report specific FRET-related parameters.

The presented step-by-step procedure for obtaining FRET efficiencies and relevant correction parameters was tested in a worldwide, comparative, blind study by 20 participating labs. We show that, for standardized double-stranded DNA FRET samples, FRET efficiencies can be determined with an s.d. value of less than ± 0.05 .

To convert the measured smFRET efficiencies to distances, we used the Förster equation (equation (3)); all numbered equations cited in this paper can be found in the Methods section), which critically depends on the dye-pair-specific Förster radius, R_0 . We discuss the measurements required to determine R_0 and the associated uncertainties. Additional uncertainty arises from the fact that many positions are sampled by the dye relative to the biomolecule to which it is attached. Therefore, specific models are used to describe the dynamic movement of the dye molecule during the recording of each FRET-efficiency measurement^{22,23}. The investigation of the uncertainties in FRET-efficiency determination and the conversion into distance measurements enabled us to specify uncertainties for individual FRET-derived distances.

Results

Benchmark samples and approaches. We chose double-stranded DNA as a FRET standard for several reasons: DNA sequences can be synthesized, FRET dyes can be specifically tethered at desired positions, the structure of B-form DNA is well characterized, and the samples are stable at room temperature long enough that they can be shipped to labs around the world. The donor and acceptor dyes were attached via C2 or C6 amino linkers to thymidines of opposite strands (Supplementary Fig. 1). These thymidines were separated by 23 bp, 15 bp (Fig. 1), or 11 bp (Supplementary Fig. 1, Supplementary Table 1, and Supplementary Note 1). The attachment positions were known only to the reference lab that designed the samples. The samples were designed in such a way that we were able to determine all correction parameters and carry out a self-consistency test (described below).

In this study we used Alexa Fluor and Atto dyes because of their high quantum yields and well-studied characteristics (Supplementary Note 2). Eight hybridized double-stranded FRET samples were shipped to all participating labs. In the main text, we focus on four FRET samples that were measured by most labs in our study:

- 1-lo: Atto 550/Atto 647N; 23-bp separation
- 1-mid: Atto 550/Atto 647N; 15-bp separation
- 2-lo: Atto 550/Alexa Fluor 647; 23-bp separation
- 2-mid: Atto 550/Alexa Fluor 647; 15-bp separation

In revision, 13 labs evaluated two additional samples:

- 1-hi: Atto 550/Atto 647N; 11-bp separation
- 2-hi: Atto 550/Alexa Fluor 647; 11-bp separation

NATURE METHODS

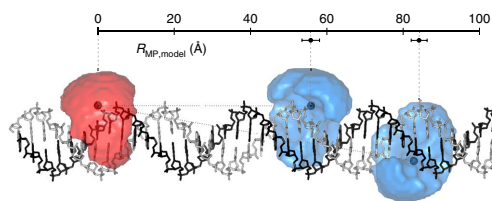


Fig. 1 | Schematic of the FRET standard molecules. Double-stranded DNA was labeled with a FRET pair at 15-bp or 23-bp separation for the “lo” and “mid” samples, respectively (sequences are provided in the Methods). The accessible volumes (AVs) of the dyes (donor, blue; acceptor, red) are illustrated as semi-transparent surfaces and were calculated with freely available software⁵. The mean dye positions are indicated by darker spheres (assuming homogeneously distributed dye positions; Supplementary Note 3). The distance between the mean dye positions is defined as $R_{MP,model}$. Calculated values for $R_{MP,model}$ and the errors obtained by varying parameters of the AV model are shown (Supplementary Note 3). The B-DNA model was generated with Nucleic Acid Builder version 04/17/2017 for Amber²⁷.

In this nomenclature, the number refers to the dye pair, and lo, mid, and hi indicate low-efficiency, medium-efficiency, and high-efficiency configurations, respectively. The results with other FRET pairs (Alexa Fluor 488/Alexa Fluor 594 and Alexa Fluor 488/Atto 647N) at these positions, per lab, for all samples and for different methods, are reported in Supplementary Fig. 2 and Supplementary Note 2.

To avoid dye stacking^{28,29}, we designed the DNA molecules such that the dyes were attached to internal positions sufficiently far from the duplex ends. As a first test for the suitability of the labels, we checked the fluorescence lifetimes and time-resolved anisotropies (Supplementary Table 2) of all donor-only and acceptor-only samples. The results indicated that there was no significant quenching or stacking and that all dyes were sufficiently mobile at these positions (Supplementary Note 2).

Most measurements were carried out on custom-built setups that featured at least two separate spectral detection channels for donor and acceptor emission (Supplementary Figs. 3 and 4). Results obtained with different fluorophores (samples 3 and 4) and different FRET methods (ensemble lifetime³⁰, single-molecule lifetime¹⁶, and a phasor approach³¹) are presented in Supplementary Fig. 2 and Supplementary Notes 1 and 2.

A robust correction procedure to determine absolute fluorescence intensities is needed. The ideal solution is a ratiometric approach that, for intensity-based confocal FRET measurements, was pioneered by Weiss and coworkers and uses alternating two-color laser excitation (ALEX) with microsecond pulses^{7,32}. In this approach the fluorescence signal after donor excitation is divided by the total fluorescence signal after donor and acceptor excitation (referred to as apparent stoichiometry; see equation (16)), to correct for dye and instrument properties¹⁷. The ALEX approach was also adapted for TIRF measurements³⁰. To increase time resolution and to enable time-resolved spectroscopy, Lamb and coworkers introduced pulsed interleaved excitation with picosecond pulses³³.

Procedure to determine the experimental FRET efficiency (E). In both confocal and TIRF microscopy, the expectation value of the FRET efficiency $\langle E \rangle$ is computed from the corrected FRET efficiency histogram. In this section, first we outline a concise and robust procedure to obtain $\langle E \rangle$. Then we describe distance and uncertainty calculations, assuming a suitable model for the interdy distance distribution and dynamics^{6,11,34}. Finally, we derive self-consistency

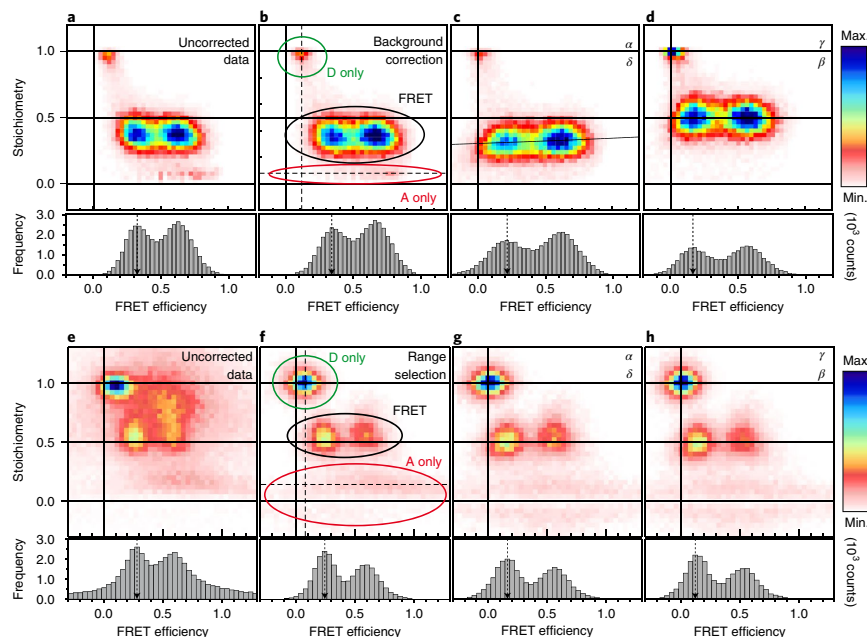


Fig. 2 | Stepwise data correction for 1-lo and 1-mid samples. a–d, Workflow for correction of the confocal data for background (a → b); leakage (factor α); and direct excitation (δ) (b → c), excitation, and detection factors (β, γ) (c → d). **e–h**, Workflow for correction of TIRF data for background and photobleaching by selection of the prebleached range (e → f); leakage; and direct excitation (f → g), detection, and excitation factors (g → h). The efficiency histograms show a projection of the data with a stoichiometry between 0.3 and 0.7. The general terms “stoichiometry” and “FRET efficiency” are used in place of the corresponding specific terms for each correction step. Donor (D)-only, FRET, and acceptor (A)-only populations are specified.

arguments and comparisons to structural models to confirm the accuracy of this approach.

Our general procedure is largely based on a previous approach¹⁷, with modifications to establish a robust workflow and standardize the nomenclature. Intensity-based determination of FRET efficiencies requires consideration of the following correction factors (details in the Methods section): background signal correction (BG) from donor and acceptor channels; α , a factor for spectral cross-talk arising from donor fluorescence leakage in the acceptor channel; δ , a factor for direct excitation of the acceptor with the donor laser; and a detection correction factor (γ). The optimal way to determine these factors is to alternate the excitation between two colors, which allows for determination of the FRET efficiency (E) and the relative stoichiometry (S) of donor and acceptor dyes, for each single-molecule event. This requires the additional excitation correction factor β to normalize the excitation rates.

The following step-by-step guide presents separate instructions for confocal and TIRF experiments; notably, the order of the steps is crucial (Methods).

Diffusing molecules: confocal microscopy. Photon arrival times from individual molecules freely diffusing through the laser focus of a confocal microscope are registered. Signal threshold criteria are applied, and bursts are collected and analyzed. From the data, first a 2D histogram of the uncorrected FRET efficiency (E_{app}) versus the uncorrected stoichiometry (S_{app}) is generated (Fig. 2a). Then the average number of background photons is subtracted for each channel separately (Fig. 2b). Next, to obtain the FRET sensitized acceptor

signal ($F_{A|D}$), one must subtract the donor leakage ($\alpha^{II}I_{D|Dex}$) and direct excitation ($\delta^{II}I_{Aem|Aex}$) from the acceptor signal after donor excitation. As samples never comprise 100% photoactive donor and acceptor dyes, the donor-only and acceptor-only populations are selected from the measurement and used to determine the leakage and direct excitation (Fig. 2c). After this correction step, the donor-only population should have an average FRET efficiency of 0, and the acceptor-only population should have an average stoichiometry of 0.

The last step deals with the detection correction factor γ and the excitation correction factor β . If at least two species (two different samples or two populations within a sample) with different interdy distances are present, they can be used to obtain the ‘global γ -correction’. If one species with substantial distance fluctuations (e.g., from intrinsic conformational changes) is present, a ‘single-species γ -correction’ may be possible. Both correction schemes assume that the fluorescence quantum yields and extinction coefficients of the dyes are independent of the attachment point. The correction factors obtained by the reference lab are compiled in Supplementary Table 3. The final corrected FRET efficiency histograms are shown in Fig. 2d. The expected efficiencies (E) are obtained as the mean of a Gaussian fit to the respective efficiency distributions. After correction, we noted a substantial shift of the FRET-efficiency peak positions, especially for the low-FRET-efficiency peak ($E \sim 0.25$ uncorrected to $E \sim 0.15$ when fully corrected).

Surface-attached molecules: TIRF microscopy. The correction procedure for TIRF-based smFRET experiments is similar to the

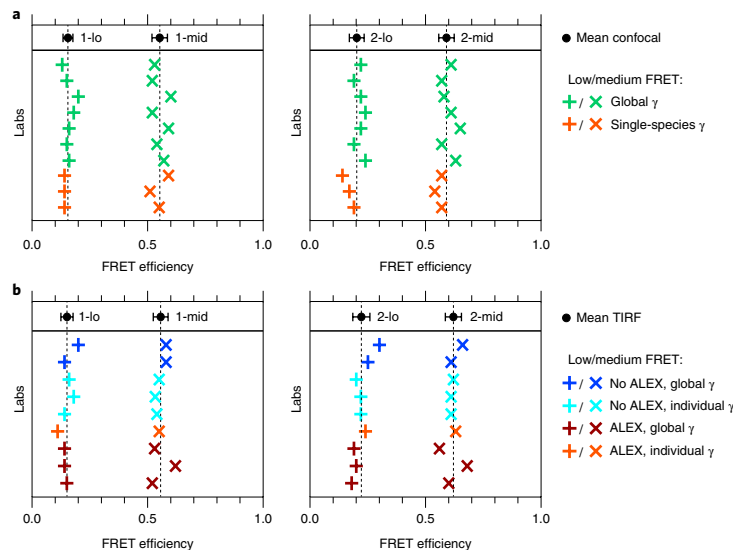


Fig. 3 | Summary of the results of the intensity-based methods. a, Confocal measurements. **b**, TIRF measurements. Note that some laboratories performed measurements with both methods. The mean \pm s.d. is depicted in the upper portion of each plot. Dashed lines indicate mean values (summarized in Supplementary Table 4). Example correction factors are given in Supplementary Table 3.

procedure for confocal-based experiments. In the procedure used for ALEX data²⁰, a 2D histogram of the uncorrected FRET efficiency versus the uncorrected stoichiometry is generated (Fig. 2c). The background subtraction is critical in TIRF microscopy, as it can contribute substantially to the measured signal. Different approaches can be used to accurately determine the background signal, such as measuring the background in the vicinity of the selected particle or measuring the intensity after photobleaching (Fig. 2f). After background correction, the leakage and direct excitation can be calculated from the ALEX data as for confocal microscopy (Fig. 2g).

Again, determination of the correction factors β and γ is critical¹⁵. As with confocal microscopy, one can use the stoichiometry information available from ALEX when multiple populations are present to determine an average detection correction factor (global γ -correction). In TIRF microscopy, the detection correction factor can also be determined on a molecule-by-molecule basis, provided the acceptor photobleaches before the donor (individual γ -correction). In this case, the increase in the fluorescence of the donor can be directly compared to the intensity of the acceptor before photobleaching. A 2D histogram of corrected FRET efficiency versus corrected stoichiometry is shown in Fig. 2h.

In the absence of alternating laser excitation, the following problems occasionally arose during this study: (i) the low-FRET-efficiency values were shifted systematically to higher efficiencies, because FRET-efficiency values at the lower edge were overlooked owing to noise; (ii) the direct excitation was difficult to detect and correct because of its small signal-to-noise ratio; and (iii) acceptor bleaching was difficult to detect for low FRET efficiencies. Therefore, we strongly recommend implementing ALEX in order to obtain accurate FRET data.

Nine of the twenty participating labs determined FRET efficiencies by confocal methods for samples 1 and 2 (Fig. 3a). Seven of the twenty participating labs determined FRET efficiencies by TIRF-based methods (Fig. 3b). The combined data from all labs for

measurements of samples 1 and 2 agree very well, with s.d. for the complete dataset of $\Delta E < \pm 0.05$. This is a remarkable result, considering that different setup types were used (confocal- and TIRF-based setups) and different correction procedures were applied (e.g., individual, global, or single-species γ -correction).

Distance determination. The ultimate goal of this approach is to derive distances from FRET efficiencies. The efficiency-to-distance conversion requires knowledge of the Förster radius, R_0 , for the specific FRET pair used and of a specific dye model describing the behavior of the dye attached to the macromolecule^{22,23}. In the following, we describe (i) how R_0 can be determined and (ii) how to use a specific dye model to calculate two additional values, $R_{(E)}$ and R_{MP} . $R_{(E)}$ is the apparent distance between the donor and the acceptor, which is directly related to the experimental FRET efficiency (E) that is averaged over all sampled donor-acceptor distances R_{DA} (equation (5)), but it is not a physical distance. R_{MP} is the real distance between the center points (mean positions) of the accessible volumes and deviates from $R_{(E)}$ because of the different averaging in distance and efficiency space. R_{MP} cannot be measured directly but is important, for example, for mapping the physical distances required for structural modeling³⁴.

R_0 is a function of equation (7) and depends on the index of refraction of the medium between the two fluorophores (n_m), the spectral overlap integral (J), the fluorescence quantum yield of the donor (Φ_{FD}), and the relative dipole orientation factor (κ^2) (an estimate of their uncertainties is provided in the Methods section). Our model assumes that the FRET rate (k_{FRET}) is much slower than the rotational relaxation rate (k_{rot}) of the dye and that the translational diffusion rate (k_{diff}) allows the dye to sample the entire accessible volume within the experimental integration time ($1/k_{int}$), that is, $k_{rot} \gg k_{FRET} \gg k_{diff} \gg k_{int}$. The validity of these assumptions is justified by experimental observables discussed in the Methods.

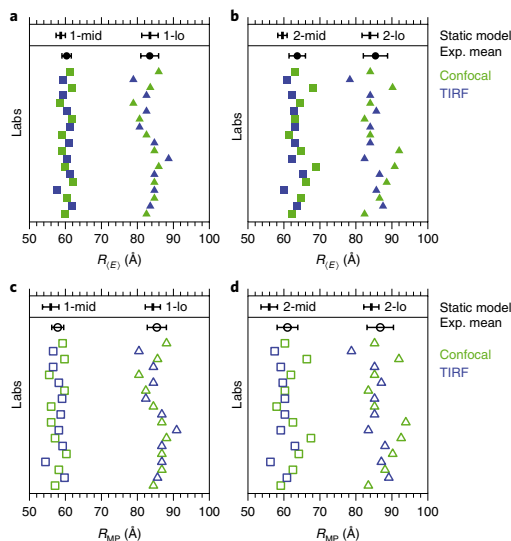


Fig. 4 | Mean interdye distances determined from 19 E values measured in 16 different labs. a, b, $R_{(E)}$ for samples 1 (a) and 2 (b). **c, d**, R_{MP} for samples 1 (c) and 2 (d). Data are shown as individual values (colored symbols) and as the mean (black dots) and s.d., assuming $R_0 = 62.6$ Å and $R_0 = 68.0$ Å for samples 1 and 2, respectively. The black bars at the top of each plot indicate the static model values and their error (determined by variation of model parameters); see Supplementary Table 4 for values. The depicted errors include only the statistical variations of the FRET efficiencies, and do not include the error in the Förster radii; thus these errors represent the precision of the measurement, but not the accuracy. Exp., experimental.

The determined Förster radii for samples 1 and 2 are given in Supplementary Table 4. Note that literature values differ mainly because donor fluorescence quantum yields are not specified and the refractive index of water is often assumed, whereas we used $n_{im} = 1.40$ here. Our careful error analysis led to an error estimate of 7% for the determined R_0 , which is relatively large (mainly owing to the uncertainty in κ^2).

We used the measured smFRET efficiencies and the calculated Förster radii to compute the apparent distance $R_{(E)}$ from each lab's data (equation (5)). Figure 4a,b shows the calculated values for these apparent distances for samples 1 and 2 for each data point in Fig. 3. The average values for all labs are given in Supplementary Table 4, together with model values based on knowledge of the dye attachment positions, the static DNA structure, and the mobile dye model (Supplementary Note 3). Considering the error ranges, the experimental and model values agree very well with each other (the deviations range between 0 and 8%).

Although this study focused on measurements on DNA, the described FRET analysis and error estimation are fully generalizable to other systems (e.g., proteins), assuming mobile dyes are used. What becomes more difficult with proteins is specific dye labeling, and the determination of an appropriate dye model, if the dyes are not sufficiently mobile (Supplementary Note 3). $R_{(E)}$ corresponds to the real distance R_{MP} only in the hypothetical case in which both dyes are unpolarized point sources, with zero accessible volume (AV). In all other cases, R_{MP} is the only physical distance. It can be calculated in two ways: (i) if the dye model and the local environment of the dye are known, simulation tools such as the FRET

Positioning and Screening tool⁸ can be used to compute R_{MP} from $R_{(E)}$ for a given pair of AVs; or (ii) if the structure of the investigated molecule is unknown a priori, a sphere is a useful assumption for the AV. In both cases, a lookup table is used to convert $R_{(E)}$ to R_{MP} for defined AVs and R_0 values (Supplementary Note 5). Our results for these calculations, given as distances determined via the former approach, are shown in Fig. 4c,d and Supplementary Table 4. The respective model values are based on the center points of the AVs depicted in Fig. 1 and given in Supplementary Table 4 (details in Supplementary Note 3).

Distance uncertainties. We estimated all uncertainty sources arising from both the measurement of the corrected FRET efficiencies and the determination of the Förster radius, and propagated them into distance uncertainties. We discuss the error in determining the distance between two freely rotating but spatially fixed dipoles, R_{DA} , with the Förster equation (equation (26)). Figure 5a shows how uncertainty in each of the correction factors (α , γ , and δ) and the background signals (BG_D , BG_A) is translated into the uncertainty of R_{DA} (Supplementary Note 6). The uncertainty of R_{MP} is similar but depends on the dye model and the AVs. The solid gray line in Fig. 5a shows the sum of these efficiency-dependent uncertainties, which are mainly setup-specific quantities. For the extremes of the distances, the largest contribution to the uncertainty in R_{DA} arises from background photons in the donor and acceptor channels. In the presented example with $R_0 = 62.6$ Å, the total uncertainty ΔR_{DA} based on the setup-specific uncertainties is less than 4 Å for 35 Å $< R_{DA} < 90$ Å. Notably, in confocal measurements, larger intensity thresholds can decrease this uncertainty further. The uncertainty in R_{DA} arising from errors in R_0 (blue line in Fig. 5b) is added to the efficiency-related uncertainty in R_{DA} (bold gray line in Fig. 5b) to estimate the total experimental uncertainty in R_{DA} (black line in Fig. 5b). The uncertainties for determining R_0 are dominated by the dipole orientation factor κ^2 and the refractive index n_{im} (Methods). Including the uncertainty in R_0 , the error $\Delta R_{DA, total}$ for a single smFRET-based distance between two freely rotating point dipoles is less than 6 Å for 35 Å $< R_{DA} < 80$ Å. The uncertainty is considerably reduced when multiple distances are calculated and self-consistency in distance networks is exploited⁹. Besides background contributions, an R_{DA} shorter than 30 Å may lead to larger errors due to (i) potential dye–dye interactions and (ii) the dynamic averaging of the dipole orientations being reduced owing to an increased FRET rate.

Comparing distinct dye pairs. To validate the model assumption of a freely rotating and diffusing dye, we developed a self-consistency argument based on the relationship between different dye pairs that bypasses several experimental uncertainties. We define the ratio R_{rel} for two dye pairs as the ratio of their respective $R_{(E)}$ values (Methods, equation (30)). This ratio is quasi-independent of R_0 , because all dye parameters that are contained in R_0 are approximately eliminated by our DNA design. Therefore, these ratios should be similar for all investigated dye pairs, which we indeed found was the case (Supplementary Table 4). When comparing, for example, the low- to mid-distances for three dye pairs with $E > 0.1$, we obtained a mean R_{rel} of 1.34 and a maximum deviation of 2.7%. This is a relative error of 2.3%, which is less than the estimated error of our measured distances of 2.8% (Fig. 5a). This further demonstrates the validity of the assumptions for the dye model and averaging regime used here. This concept is discussed further in the Methods.

Although calculated model distances are based on a static model for the DNA structure, DNA is known not to be completely rigid¹⁵. We tested our DNA model by carrying out molecular dynamics simulations using the DNA molecule (without attached dye molecules; Supplementary Note 7) and found that the averaged expected FRET efficiency obtained with the computed dynamically varying slightly bent DNA structure led to comparable but slightly longer distances

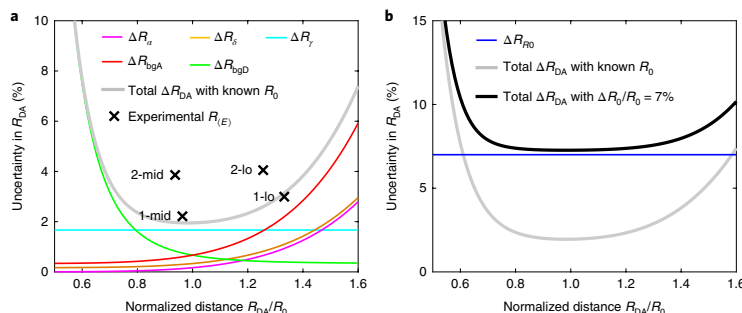


Fig. 5 | Error propagation of experimental uncertainty. **a**, R_{DA} uncertainty contributions from the experimental correction factors: ΔR_γ (gamma factor), ΔR_{bgD} and ΔR_{bgA} (background), ΔR_{leak} (leakage), ΔR_{direct} (direct excitation), and total uncertainty with known R_0 ; crosses indicate the uncertainty of experimental values of $R_{(E)}$ across the labs. **b**, Uncertainty in R_{DA} (black line) based on the efficiency-related uncertainty (gray line) and the uncertainty for determining R_0 (blue line). Here we used the following uncertainties, which were determined for the confocal-based measurements on sample 1: $\Delta R_\gamma/R_0 = 7\%$, $\Delta\gamma/\gamma = 10\%$, $\Delta f^{(BG)}/f = 2\%$, $\Delta\alpha/\alpha = 10\%$, and $\Delta\delta/\delta = 10\%$. Absolute values are presented in Supplementary Table 3.

than for the static model. The deviations between the models and data were reduced (Supplementary Table 4) for those cases where we observed larger deviations with static models.

Discussion

Despite differences in the setups used, the reported intensity-based FRET efficiencies were consistent between labs in this study. We attribute this remarkable consistency ($\Delta E < \pm 0.05$) to the use of a general step-by-step procedure for the experiments and data analysis.

We also showed that the factors required for the correction of FRET efficiency can be determined with high precision, regardless of the setup type and acquisition software used. Together the measurement errors caused an uncertainty in R_{DA} of less than 5%, which agrees well with the variations between the different labs. Ultimately, we were interested in the absolute distances derived from these FRET efficiencies. Figure 5 shows that any distance between $0.6 R_0$ and $1.6 R_0$ could be determined with an uncertainty of less than $\pm 6 \text{ \AA}$. This fits well with the distance uncertainty measured across the labs and corresponds to a distance range from 35 to 80 \AA for the dye pairs used in sample 1. This estimation is valid if the dyes are sufficiently mobile, as has been supported by time-resolved anisotropy measurements and further confirmed by a self-consistency argument. The s.d. for sample 2 was slightly larger than that for sample 1 (Fig. 5a), which could be explained by specific photophysical properties. The values for samples 3 and 4 (Supplementary Table 4) showed similar precision, considering the smaller number of measurements.

For the samples 1-hi and 2-hi, which were measured after each lab verified its setup and procedure, the precision was further increased by almost a factor of two (Supplementary Table 4), possibly owing to the thorough characterization during this study.

We also tested the accuracy of the experimentally derived distances by comparing them with distances in the static model. For every single FRET pair we found excellent agreement between 0.1% and 4.1% (0.4–2.4 \AA) for sample 1 and agreement mostly within the range of experimental error between 3.1% and 9.0% (2.7–5.5 \AA) for sample 2. The deviations could be even smaller for dynamic DNA models. For sample 2, which had the cyanine-based dye Alexa Fluor 647 instead of the carbopyronine-based dye Atto 647N as an acceptor, the lower accuracy could be explained by imperfect sampling of the full AV or dye-specific photophysical properties (details are presented in Supplementary Table 2). It was shown previously that cyanine dyes are sensitive to their local environment¹⁶ and therefore

require especially careful characterization for each newly labeled biomolecule.

For future work, it will be powerful to complement intensity-based smFRET studies with single-molecule lifetime studies, as the picosecond time resolution could provide additional information on calibration and fast dynamic biomolecular exchange. In addition, it will be important to establish appropriate dye models for more complex (protein) systems in which the local chemistry may affect dye mobility (Supplementary Note 4). However, when used with mobile dyes (which can be checked via anisotropy and lifetime experiments; Supplementary Note 2), the dye model here is fully generalizable to any biomolecular system^{8,9}.

The results from different labs and the successful self-consistency test clearly show the great potential of absolute smFRET-based distances for investigations of biomolecular conformations and dynamics, as well as for integrative structural modeling. The ability to accurately determine distances on the molecular scale with smFRET experiments and to estimate the uncertainty of the measurements provides the groundwork for smFRET-based structural and hybrid approaches. Together with the automated selection of the most informative pairwise labeling positions²³ and fast analysis procedures^{8–10}, we anticipate that smFRET-based structural methods will become an important tool for de novo structural determination and structure validation, especially for large and flexible structures with which the application of other structural biology methods is difficult.

Methods

Methods, including statements of data availability and any associated accession codes and references, are available at <https://doi.org/10.1038/s41592-018-0085-0>.

Received: 5 October 2017; Accepted: 25 May 2018;

Published online: 31 August 2018

References

1. Förster, T. Zwischenmolekulare Energiewanderung und Fluoreszenz. *Ann. Phys.* **437**, 55–75 (1948).
2. Stryer, L. & Haugland, R. P. Energy transfer: a spectroscopic ruler. *Proc. Natl. Acad. Sci. USA* **58**, 719–726 (1967).
3. Murchie, A. I. et al. Fluorescence energy transfer shows that the four-way DNA junction is a right-handed cross of antiparallel molecules. *Nature* **341**, 763–766 (1989).
4. Mekler, V. et al. Structural organization of bacterial RNA polymerase holoenzyme and the RNA polymerase-promoter open complex. *Cell* **108**, 599–614 (2002).

5. Ha, T. et al. Probing the interaction between two single molecules: fluorescence resonance energy transfer between a single donor and a single acceptor. *Proc. Natl Acad. Sci. USA* **93**, 6264–6268 (1996).
6. Schuler, B., Lipman, E. A., Steinbach, P. J., Kumke, M. & Eaton, W. A. Polyproline and the “spectroscopic ruler” revisited with single-molecule fluorescence. *Proc. Natl Acad. Sci. USA* **102**, 2754–2759 (2005).
7. Choi, U. B. et al. Single-molecule FRET-derived model of the synaptotagmin 1-SNARE fusion complex. *Nat. Struct. Mol. Biol.* **17**, 318–384 (2010).
8. Kalinin, S. et al. A toolkit and benchmark study for FRET-restrained high-precision structural modeling. *Nat. Methods* **9**, 1218–1227 (2012).
9. Hellenkamp, B., Wörtmann, P., Kandzia, F., Zacharias, M. & Hugel, T. Multidomain structure and correlated dynamics determined by self-consistent FRET Networks. *Nat. Methods* **14**, 174–180 (2017).
10. Eilert, T., Beckers, M., Drechsler, F. & Michaelis, J. Fast-NPS—a Markov chain Monte Carlo-based analysis tool to obtain structural information from single-molecule FRET measurements. *Comput. Phys. Commun.* **219**, 377–389 (2017).
11. Hofmann, D., Korzdorfer, T. & Kummel, S. Energy transfer and Förster’s dipole coupling approximation investigated in a real-time Kohn-Sham scheme. *Phys. Rev. A* **82**, 012509 (2010).
12. Spiegel, J. D., Fulle, S., Kleinschmidt, M., Gohlke, H. & Marian, C. M. Failure of the IDA in FRET systems at close inter-dye distances is moderated by frequent low k^2 values. *J. Phys. Chem. B* **120**, 8845–8862 (2016).
13. Sakon, J. J. & Weninger, K. R. Detecting the conformation of individual proteins in live cells. *Nat. Methods* **7**, 203–205 (2010).
14. Sabanayagam, C. R., Eid, J. S. & Meller, A. Using fluorescence resonance energy transfer to measure distances along individual DNA molecules: corrections due to nonideal transfer. *J. Chem. Phys.* **122**, 61103–61107 (2005).
15. McCann, J. J., Choi, U. B., Zheng, L., Weninger, K. & Bowen, M. E. Optimizing methods to recover absolute FRET efficiency from immobilized single molecules. *Biophys. J.* **99**, 961–970 (2010).
16. Sisamakos, E., Valeri, A., Kalinin, S., Rothwell, P. J. & Seidel, C. A. M. Accurate single-molecule FRET studies using multiparameter fluorescence detection. *Methods Enzymol.* **475**, 455–514 (2010).
17. Lee, N. K. et al. Accurate FRET measurements within single diffusing biomolecules using alternating-laser excitation. *Biophys. J.* **88**, 2939–2953 (2005).
18. Kudryavtsev, V. et al. Combining MFD and PIE for accurate single-pair Förster resonance energy transfer measurements. *ChemPhysChem* **13**, 1060–1078 (2012).
19. Hohlbein, J., Craggs, T. D. & Cordes, T. Alternating-laser excitation: single-molecule FRET and beyond. *Chem. Soc. Rev.* **43**, 1156–1171 (2014).
20. Margeat, E. et al. Direct observation of abortive initiation and promoter escape within single immobilized transcription complexes. *Biophys. J.* **90**, 1419–1431 (2006).
21. Muschielok, A. et al. A nano-positioning system for macromolecular structural analysis. *Nat. Methods* **5**, 965–971 (2008).
22. Beckers, M., Drechsler, F., Eilert, T., Nagy, J. & Michaelis, J. Quantitative structural information from single-molecule FRET. *Faraday Discuss.* **184**, 117–129 (2015).
23. Dimura, M. et al. Quantitative FRET studies and integrative modeling unravel the structure and dynamics of biomolecular systems. *Curr. Opin. Struct. Biol.* **40**, 163–185 (2016).
24. Brunger, A. T., Strop, P., Vrljic, M., Chu, S. & Weninger, K. R. Three-dimensional molecular modeling with single molecule FRET. *J. Struct. Biol.* **173**, 497–505 (2011).
25. Craggs, T. D. et al. Substrate conformational dynamics drive structure-specific recognition of gapped DNA by DNA polymerase. *bioRxiv* Preprint at <https://www.biorxiv.org/content/early/2018/02/10/263038> (2018).
26. Nagy, J., Eilert, T. & Michaelis, J. Precision and accuracy in smFRET based structural studies—a benchmark study of the FAST-Nano-Positioning System. *J. Chem. Phys.* **148**, 123308 (2018).
27. Ivani, I. et al. Parmbsc1: a refined force field for DNA simulations. *Nat. Methods* **13**, 55–58 (2016).
28. Neubauer, H. et al. Orientational and dynamical heterogeneity of rhodamine 6G terminally attached to a DNA helix revealed by NMR and single-molecule fluorescence spectroscopy. *J. Am. Chem. Soc.* **129**, 12746–12755 (2007).
29. Iqbal, A. et al. Orientation dependence in fluorescent energy transfer between Cy3 and Cy5 terminally attached to double-stranded nucleic acids. *Proc. Natl Acad. Sci. USA* **105**, 11176–11181 (2008).
30. Peulen, T. O., Opanasyuk, O. & Seidel, C. A. M. Combining graphical and analytical methods with molecular simulations to analyze time-resolved FRET-measurements of labeled macromolecules accurately. *J. Phys. Chem. B* **121**, 8211–8241 (2017).
31. Digman, M. A., Caiola, V. R., Zamai, M. & Gratton, E. The Phasor approach to fluorescence lifetime imaging analysis. *Biophys. J.* **84**, L14–L16 (2008).
32. Kapanidis, A. N. et al. Fluorescence-aided molecule sorting: analysis of structure and interactions by alternating-laser excitation of single molecules. *Proc. Natl Acad. Sci. USA* **101**, 8936–8941 (2004).
33. Müller, B. K., Zaychikov, E., Bräuchle, C. & Lamb, D. C. Pulsed interleaved excitation. *Biophys. J.* **89**, 3508–3522 (2005).
34. Wozniak, A. K., Schröder, G. F., Grubmüller, H., Seidel, C. A. M. & Osterheld, F. Single-molecule FRET measures bends and kinks in DNA. *Proc. Natl Acad. Sci. USA* **105**, 18337–18342 (2008).
35. Stelzl, L. S., Erlenbach, N., Heinz, M., Prisner, T. F. & Hummer, G. Resolving the conformational dynamics of DNA with ångström resolution by pulsed electron-electron double resonance and molecular dynamics. *J. Am. Chem. Soc.* **139**, 11674–11677 (2017).
36. Levitus, M. & Ranjit, S. Cyanine dyes in biophysical research: the photophysics of polymethine fluorescent dyes in biomolecular environments. *Q. Rev. Biophys.* **44**, 123–151 (2011).

Acknowledgements

We thank the Eaton lab for early measurements that helped us design this study. We thank T. Peulen, M. Dimura, and R. McDonald for stimulating discussions on FRET measurements, data analysis, and modeling, and B. Bulat for measuring fluorescence quantum yields of Atto 550 and 1-mid (Atto 550). We also thank the company Atto-Tec for providing a reference sample of the dye Atto 550 for fluorescence characterization. The authors acknowledge networking support by the Dr. Wilhelm Heinrich und Else Heraeus Foundation and COST Action CM1306 “Understanding Movement and Mechanism in Molecular Machines.” The idea of a worldwide benchmark study of standard FRET rulers emerged at the 512th WE Heraeus Seminar “Single molecule kinetics” (Bad Honnef, Germany, 2012) and evolved further during the international COST symposium “Integrating spectroscopic and theoretical methods to analyse molecular machines” (Castle of Ringberg, Germany, 2014).

This work was supported by the European Research Council (ERC; grant agreement nos. 261227 (to A.N.K.), 646451 (to E.L.), 638536 (to T.C.), 671208 (to C.A.M.S.), and 681891 (to T. Hugel)), the Deutsche Forschungsgemeinschaft (DFG) (grant MI 749/4-1 to J.M., grant TI 329/10-1 to P.T., and grant SCHL 1896/3-1 to M.S.), the Swiss National Science Foundation (to B.S.), the German Federal Ministry of Education and Research (BMBWF; 03Z2EN11 to M.S.), Research Foundation Flanders (FWO; grant G0B4915N to J. Hendrix), the Agency for Innovation by Science and Technology (IWT Flanders; doctoral scholarship to N.V.), the Danish Council for Independent Research (Sapere Aude grant 0602-01670B to V.B.), the Novo Nordisk Foundation (NNF15OC0017956 to V.B.), the UK BBSRC (grant BB/H01795X/1 to A.N.K.), the National Institute of Mental Health (grant MH081923 to M.E.B.), Clemson University (start-up funds to H. Sanabria, S.R.A., and I.S.Y.-O.), the NIH (grants GM109832 and GM118508 to K.R.W.; grant GM112659 to T. Ha), the NSF (Career Award MCS1749778 to H. Sanabria), the Carl-Zeiss-Stiftung (doctoral fellowship to E.K.), the Stipendienstiftung Rheinland-Pfalz (doctoral scholarship to G.K.), the Braunschweig International Graduate School of Metrology (B-IGSM; to B.W.), the DFG Research Training Group (GrK1952/1 “Metrology for Complex Nanosystems” to B.W.), the University of Sheffield (start-up funds to T.D.C.), and the National Research Foundation of Korea funded by the Ministry of Science and ICT (NRF-2017R1A2B3010309 to N.K.L.).

Author contributions

B. Hellenkamp, T. Hugel, J.M., and C.A.M.S. designed the research; B. Hellenkamp, S.S., O.D., O.O., R.K., S.R.A., B.A., M.A., A.B., H.C., T.E., C.F., C.G., G.G., P.H., C.A.H., A.H., J. Hendrix, L.L.H., V.H., J. Hohlbein, B. Hua, E.K., J.-Y.K., G.K., B.L., J.J.M., N.N.-R., D.N., T.N., R.Q., N.C.R., C.R., T.S., H.S., L.S., J.T., S.T., N.V., A.M.V., B.W., I.S.Y.-O., and T.D.C. performed measurements; B. Hellenkamp, S.S., and T. Hugel compared the measurements; all of the aforementioned authors and V.B., M.E.B., T.C., M.G., E.G., T. Ha, C.G.H., A.N.K., D.C.L., N.K.L., E.A.L., M.L., H. Sanabria, H. Seidel, M.S., B.S., P.T., K.R.W., J.M., and C.S. contributed to the analysis of the data and commented on the manuscript; B. Hellenkamp, S.S., T.D.C., J.M., C.A.M.S., and T. Hugel wrote the manuscript in consultation with O.D. and O.O.; and O.D. performed the calculations of the model distances.

Competing interests

The authors declare no competing interests.

Additional information

Supplementary information is available for this paper at <https://doi.org/10.1038/s41592-018-0085-0>.

Reprints and permissions information is available at www.nature.com/reprints.

Correspondence and requests for materials should be addressed to J.M. or C.A.M.S. or T.D.C. or T.H.

Publisher’s note: Springer Nature remains neutral with regard to jurisdictional claims in published maps and institutional affiliations.



Open Access This article is licensed under a Creative Commons Attribution 4.0 International License, which permits use, sharing, adaptation, distribution and reproduction in any medium or format, as long as you give appropriate credit to the original author(s) and the source, provide a link to the Creative Commons license, and indicate if changes were made. The images or other third party material in this article are included in the article’s Creative Commons license, unless indicated otherwise in a credit line to the material. If material is not included in the article’s Creative Commons license and your intended use is not permitted by statutory regulation or exceeds the permitted use, you will need to obtain permission directly from the copyright holder. To view a copy of this license, visit <http://creativecommons.org/licenses/by/4.0/>.

¹Institute of Physical Chemistry, University of Freiburg, Freiburg im Breisgau, Germany. ²Engineering and Applied Sciences, Columbia University, New York, NY, USA. ³Department of Bionanoscience, Kavli Institute of Nanoscience Delft, Delft University of Technology, Delft, the Netherlands. ⁴Molecular Physical Chemistry, Heinrich-Heine-Universität Düsseldorf, Düsseldorf, Germany. ⁵Department of Physics and Astronomy, Clemson University, Clemson, SC, USA. ⁶Department of Chemistry, University of Sheffield, Sheffield, UK. ⁷Interdisciplinary Nanoscience Center (iNANO) and Department of Chemistry, Aarhus University, Aarhus, Denmark. ⁸Physical Chemistry, Department of Chemistry, Nanosystems Initiative Munich (NIM), Center for Integrated Protein Science Munich (CIPSM) and Center for Nanoscience (CeNS), Ludwig-Maximilians-Universität München, Munich, Germany. ⁹Department of Physiology & Biophysics, Stony Brook University, Stony Brook, NY, USA. ¹⁰Department of Biomedical Engineering, University of California, Irvine, Irvine, CA, USA. ¹¹Molecular Microscopy Research Group, Zernike Institute for Advanced Materials, University of Groningen, Groningen, the Netherlands. ¹²Physical and Synthetic Biology, Faculty of Biology, Ludwig-Maximilians-Universität München, Planegg-Martinsried, Germany. ¹³Institute for Biophysics, Ulm University, Ulm, Germany. ¹⁴Laboratory of Biophysics, Wageningen University & Research, Wageningen, the Netherlands. ¹⁵Department of Biomedical Engineering, John Hopkins University, Baltimore, MD, USA. ¹⁶Department of Physics, North Carolina State University, Raleigh, NC, USA. ¹⁷B CUBE—Center for Molecular Bioengineering, TU Dresden, Dresden, Germany. ¹⁸Laboratory for Photochemistry and Spectroscopy, Department of Chemistry, University of Leuven, Leuven, Belgium. ¹⁹Dynamic Bioimaging Lab, Advanced Optical Microscopy Center and Biomedical Research Institute, Hasselt University, Hasselt, Belgium. ²⁰Institute of Physics, University of Lübeck, Lübeck, Germany. ²¹Microspectroscopy Research Facility Wageningen, Wageningen University & Research, Wageningen, the Netherlands. ²²Gene Machines Group, Clarendon Laboratory, Department of Physics, University of Oxford, Oxford, UK. ²³School of Chemistry, Seoul National University, Seoul, South Korea. ²⁴Molecular Biophysics, Technische Universität Kaiserslautern (TUK), Kaiserslautern, Germany. ²⁵Departments of Biology and Chemistry, Pharmacy and Geosciences, Johannes Gutenberg-University Mainz, Mainz, Germany. ²⁶Institute of Molecular Biology (IMB), Mainz, Germany. ²⁷Structural and Computational Biology Unit, European Molecular Biology Laboratory (EMBL), Heidelberg, Germany. ²⁸School of Molecular Sciences and The Biodesign Institute, Arizona State University, Tempe, AZ, USA. ²⁹Department of Biochemistry, University of Zurich, Zurich, Switzerland. ³⁰Department of Chemistry, Ludwig-Maximilians-Universität München, München, Germany. ³¹Institute of Physical & Theoretical Chemistry, Braunschweig Integrated Centre of Systems Biology (BRICS), and Laboratory for Emerging Nanometrology (LENA), Braunschweig University of Technology, Braunschweig, Germany. ³²BIOSS Centre for Biological Signalling Studies, University of Freiburg, Freiburg im Breisgau, Germany. ³³These authors contributed equally: Björn Hellenkamp, Sonja Schmid. *e-mail: jens.michaelis@uni-ulm.de; cseidel@hhu.de; t.craggs@sheffield.ac.uk; thorsten.hugel@pc.uni-freiburg.de

Methods

Nomenclature and definitions. See Supplementary Table 5 for a summary of the following section.

The FRET efficiency E is defined as

$$E = \frac{F_{A|D}}{F_{D|D} + F_{A|D}} \quad (1)$$

where F is the signal. The stoichiometry S is defined as

$$S = \frac{F_{D|D} + F_{A|D}}{F_{D|D} + F_{A|D} + F_{A|A}} \quad (2)$$

The FRET efficiency for a single donor-acceptor distance R_{DA} is defined as

$$E = \frac{1}{1 + R_{DA}^6/R_0^6} \quad (3)$$

The mean FRET efficiency for a discrete distribution of donor-acceptor distances with the position vectors $\mathbf{R}_{D(i)}$ and $\mathbf{R}_{A(j)}$ is calculated as

$$\langle E \rangle = \frac{1}{nm} \sum_{i=1}^n \sum_{j=1}^m \frac{1}{1 + |\mathbf{R}_{A(j)} - \mathbf{R}_{D(i)}|^6/R_0^6} \quad (4)$$

The apparent donor-acceptor distance $R_{(E)}$ is computed from the average FRET efficiency for a distance distribution. It is a FRET-averaged quantity that is also referred to as the FRET-averaged distance $\langle R_{DA} \rangle_E$ (ref. 3):

$$R_{(E)} \equiv \langle R_{(E)} \rangle = R_0(E^{-1} - 1)^{1/6} \quad (5)$$

The distance between the mean dye positions with the position vectors $\mathbf{R}_{D(i)}$ and $\mathbf{R}_{A(j)}$ is obtained by normalization of sums over all positions within the respective AVs:

$$R_{MP} = |\langle \mathbf{R}_{D(i)} \rangle - \langle \mathbf{R}_{A(j)} \rangle| = \left| \frac{1}{n} \sum_{i=1}^n \mathbf{R}_{D(i)} - \frac{1}{m} \sum_{j=1}^m \mathbf{R}_{A(j)} \right| \quad (6)$$

Definitions of abbreviations in subscripts and superscripts are as follows:

- D or A: donor or acceptor
- A|D: acceptor fluorescence upon donor excitation (similarly for D|D, A|A, etc.)
- Aem|Dex: intensity in the acceptor channel upon donor excitation (similarly for Dem|Dex, Aem|Aex, etc.)
- app: apparent, that is, including systematic, experimental offsets
- BG: background
- DO/AO: donor-only/acceptor-only species
- DA: FRET species
- i-iii: (i) the uncorrected intensity; (ii) intensity after BG correction; (iii) intensity after BG, α , and δ corrections

The four correction factors are defined as follows.

Leakage of donor fluorescence into the acceptor channel:

$$\alpha = \frac{g_{R|D}}{g_{G|D}} = \frac{\langle {}^i E_{app}^{(DO)} \rangle}{1 - \langle {}^i E_{app}^{(DO)} \rangle}$$

Normalization of excitation intensities I and cross-sections σ of the acceptor and donor:

$$\beta = \frac{\sigma_{A|R} I_{Aex}}{\sigma_{D|G} I_{Dex}}$$

Normalization of effective fluorescence quantum yields, ${}^{eff}\Phi_F = a_s \Phi_F$, and detection efficiencies g of the acceptor and donor, where a_s is the fraction of molecules in the bright state and Φ_F is the fluorescence quantum yield without photophysical (saturation) effects:

$$\gamma = \frac{g_{R|A} {}^{eff}\Phi_{F,A}}{g_{G|D} {}^{eff}\Phi_{F,D}}$$

Direct acceptor excitation by the donor excitation laser (lower wavelength):

$$\delta = \frac{\sigma_{A|G} I_{Dex}}{\sigma_{A|R} I_{Aex}} = \frac{\langle {}^{ii}\Phi_{app}^{(AO)} \rangle}{1 - \langle {}^{ii}\Phi_{app}^{(AO)} \rangle}$$

where I is the experimentally observed intensity; F indicates the corrected fluorescence intensity; $\Phi_{F,A}$ and $\Phi_{F,D}$ are the fluorescence quantum yield of the acceptor and the donor, respectively; $g_{R|A}$ and $g_{G|D}$ represent the detection efficiency of the red detector (R) if only the acceptor was excited or green detector (G) if the donor was excited (analogously for other combinations); and $\sigma_{A|G}$ is the excitation

cross-section for the acceptor when excited with green laser (analogously for the other combinations).

The Förster radius (in angstroms) for a given J in the units shown below is given by

$$\frac{R_0}{\text{\AA}} = 0.2108 \sqrt[6]{\frac{\Phi_{F,D} \kappa^2}{n_{im}^4} \frac{J}{\text{M}^{-1} \text{cm}^{-1} \text{nm}^4}} \quad (7)$$

with the dipole orientation factor $\kappa^2 = (\cos \theta_{AD} - 3 \cos \theta_D \cos \theta_A)^2$ and the spectral overlap integral (in $\text{cm}^{-1} \text{M}^{-1} \text{nm}^4$)

$$J = \int_0^\infty \overline{F}_D(\lambda) \epsilon_A(\lambda) \lambda^4 d\lambda$$

with the normalized spectral radiant intensity of the excited donor (in nm^{-1}), defined as the emission intensity F per unit wavelength,

$$\overline{F}_D(\lambda) \text{ with } \int_0^\infty \overline{F}_D(\lambda) d\lambda = 1$$

and the extinction coefficient of the acceptor (in $\text{M}^{-1} \text{cm}^{-1}$), $\epsilon_A(\lambda)$, and the refractive index of the medium between the dyes, n_{im} .

Samples. Altogether, eight different FRET samples were designed with the acceptor dyes positioned 15 or 23 bp away from the donor dyes. The exact sequences and dye positions are given in Supplementary Table 1 and Supplementary Note 1. We ordered them from IBA GmbH (Göttingen), which synthesized and labeled the single DNA strands and then carried out HPLC purification. Here the dyes were attached to a thymidine (dT), which is known to cause the least fluorescence quenching of all nucleotides³⁶.

Most labs measured the four DNA samples listed in Supplementary Table 1. Therefore, we focus on these four samples in the main text of this paper. The additional samples and the corresponding measurements are described in Supplementary Note 1, Supplementary Fig. 2, and Supplementary Table 4. A buffer consisting of 20 mM MgCl₂, 5 mM NaCl, 5 mM Tris, pH 7.5, was requested for all measurements, with de-gassing just before the measurement at room temperature.

The linker lengths were chosen in such a way that all dyes had about the same number of flexible bonds between the dipole axis and the DNA. Atto 550, Alexa Fluor 647, and Atto 647N already have an intrinsic flexible part between the C-linker starts (Supplementary Fig. 1). In addition, the DNAs were designed such that the distance ratio between the high-FRET-efficiency and low-FRET-efficiency samples should be the same for all samples, largely independent of R_0 .

Details on all used setups and analysis software are presented in Supplementary Note 8.

General correction procedure. The FRET efficiency E and stoichiometry S are defined in equations (1) and (3). Determination of the corrected FRET E and S is based largely on the approach of Lee et al.¹⁷ and consists of the following steps: (1) data acquisition, (2) generation of uncorrected 2D histograms for E versus S , (3) background subtraction, (4) correction for position-specific excitation in TIRF experiments, (5) correction for leakage and direct acceptor excitation, and (6) correction for excitation intensities and absorption cross-sections, quantum yields, and detection efficiencies.

Data acquisition. The sample with both dyes is measured, and three intensity time traces are extracted: acceptor emission upon donor excitation ($I_{Aem|Dex}$), donor emission upon donor excitation ($I_{Dem|Dex}$), and acceptor emission upon acceptor excitation ($I_{Aem|Aex}$).

For the confocal setups, a straightforward burst identification is carried out in which the trace is separated into 1-ms bins. Usually a minimum threshold (e.g., 50 photons) is applied to the sum of the donor and acceptor signals after donor excitation for each bin. This threshold is used again in every step, such that the number of bursts used may change from step to step (if the γ correction factor is not equal to 1). Some labs use sophisticated burst-search algorithms. For example, the dual-channel burst search^{38,39} recognizes the potential bleaching of each dye within bursts. Note that the choice of burst-search algorithm can influence the γ correction factor. For standard applications, the simple binning method is often sufficient, especially for well-characterized dyes and low laser powers. This study shows that the results do not depend heavily on these conditions (if they are applied properly), as every lab used its own setup and procedure at this stage. The number of photon bursts per measurement was typically between 1,000 and 10,000.

For the TIRF setups, traces with one acceptor and one donor are selected, defined by a bleaching step. In addition, only the relevant range of each trajectory (i.e., prior to photobleaching of either dye) is included in all subsequent steps. The mean length of the time traces analyzed by the reference lab was 47 frames (18.8 s) for the 185 traces of sample 1-lo and 15 frames (6 s) for the 124 traces of sample 2-lo measured at an ALEX sampling rate of 2.5 Hz. For sample 1, bleaching was

ANALYSIS

NATURE METHODS

donor limited, whereas bleaching for sample 2 was acceptor limited, which explains the significant difference in frame lengths. For details on the analysis from the reference lab, see ref.⁴⁰.

2D histogram. A 2D histogram (Fig. 2a,c) of the apparent (uncorrected) stoichiometry, ${}^{\text{iii}}S_{\text{app}}$, versus the apparent FRET efficiency, ${}^{\text{iii}}E_{\text{app}}$, defined by equations (8) and (9), is generated, where

$${}^{\text{iii}}S_{\text{app}} = \frac{I_{\text{Aem|Dex}} + I_{\text{Dem|Dex}}}{I_{\text{Aem|Dex}} + I_{\text{Dem|Dex}} + I_{\text{Aem|Aex}}} \quad (8)$$

$${}^{\text{iii}}E_{\text{app}} = \frac{I_{\text{Aem|Dex}}}{I_{\text{Aem|Dex}} + I_{\text{Dem|Dex}}} \quad (9)$$

Background correction. Background I^{BG} is removed from each uncorrected intensity I separately, thus leading to the background-corrected intensities ${}^{\text{ii}}I$, ${}^{\text{iii}}S_{\text{app}}$, and ${}^{\text{iii}}E_{\text{app}}$:

$$\begin{aligned} {}^{\text{ii}}I_{\text{Dem|Dex}} &= I_{\text{Dem|Dex}} - I_{\text{Dem|Dex}}^{\text{(BG)}} \\ {}^{\text{ii}}I_{\text{Aem|Aex}} &= I_{\text{Aem|Aex}} - I_{\text{Aem|Aex}}^{\text{(BG)}} \\ {}^{\text{ii}}I_{\text{Aem|Dex}} &= I_{\text{Aem|Dex}} - I_{\text{Aem|Dex}}^{\text{(BG)}} \end{aligned} \quad (10)$$

For confocal measurements, one can determine the background by averaging the photon count rate for all time bins that are below a certain threshold, which is defined, for example, by the maximum in the frequency-versus-intensity plot (the density of bursts should not be too high). Note that a previous measurement of only the buffer can uncover potential fluorescent contaminants, but may differ substantially from the background of the actual measurement. The background intensity is then subtracted from the intensity of each burst in each channel (equation (10)). Typical background values are 0.5–1 photon/ms (Fig. 2b).

For TIRF measurements, various trace-wise or global background corrections can be applied. The most common method defines background as the individual offset (time average) after photobleaching of both dyes in each trace. Other possibilities include selecting the darkest spots in the illuminated area and subtracting an average background time trace from the data, or using a local background, for example, with a mask around the particle. The latter two options have the advantage that possible (exponential) background bleaching is also corrected. We did not investigate the influence of the kind of background correction during this study, but a recent study showed that not all background estimators are suitable for samples with a high molecule surface coverage⁴¹.

To summarize, a correction of the background is very important but can be done very well in different ways.

Position-specific excitation correction (optional for TIRF). The concurrent excitation profiles of both lasers are key for accurate measurements (Supplementary Fig. 5). Experimental variations across the field of view are accounted for by a position-specific normalization:

$${}^{\text{ii}}I_{\text{Aem|Aex}}^{\text{(profile)}} = {}^{\text{ii}}I_{\text{Aem|Aex}} \frac{I_{\text{D}}(x', y')}{I_{\text{A}}(x, y)} \quad (11)$$

where $I_{\text{D}}(x', y')$ and $I_{\text{A}}(x, y)$ denote the excitation intensities at corresponding positions in the donor or acceptor image, respectively. Individual excitation profiles are determined as the mean image of a stack of images recorded across a sample chamber with dense dye coverage.

Leakage (α) and direct excitation (δ). After the background correction, the leakage fraction of the donor emission into the acceptor detection channel and the fraction of the direct excitation of the acceptor by the donor-excitation laser are determined. The correction factor for leakage (α) is determined by equation (12), using the FRET efficiency of the donor-only population (“D only” in Fig. 2b,f). The correction factor for direct excitation (β) is determined by equation (13) from the stoichiometry of the acceptor-only population (“A only” in Fig. 2b,f).

$$\alpha = \frac{\langle {}^{\text{ii}}E_{\text{app}}^{\text{(DO)}} \rangle}{1 - \langle {}^{\text{ii}}E_{\text{app}} \rangle} \quad (12)$$

$$\delta = \frac{\langle {}^{\text{iii}}S_{\text{app}}^{\text{(AO)}} \rangle}{1 - \langle {}^{\text{iii}}S_{\text{app}}^{\text{(AO)}} \rangle} \quad (13)$$

where ${}^{\text{ii}}E_{\text{app}}^{\text{(DO)}}$ and ${}^{\text{iii}}S_{\text{app}}^{\text{(AO)}}$ are calculated from the background-corrected intensities ${}^{\text{ii}}I$ of the corresponding population, donor-only or acceptor-only, respectively. This correction, together with the previous background correction, results in the

donor-only population being located at $E = 0$, $S = 1$ and the acceptor-only population at $S = 0$, $E = 0, \dots, 1$. The corrected acceptor fluorescence after donor excitation, $F_{\text{A|D}}$, is given by equation (14), which yields the updated expressions for the FRET efficiency and stoichiometry, equations (15) and (16), respectively.

$$F_{\text{A|D}} = {}^{\text{ii}}I_{\text{Aem|Dex}} - \alpha {}^{\text{ii}}I_{\text{Dem|Dex}} - \delta {}^{\text{ii}}I_{\text{Aem|Aex}} \quad (14)$$

$${}^{\text{iii}}E_{\text{app}} = \frac{F_{\text{A|D}}}{F_{\text{A|D}} + {}^{\text{ii}}I_{\text{Dem|Dex}}} \quad (15)$$

$${}^{\text{iii}}S_{\text{app}} = \frac{F_{\text{A|D}} + {}^{\text{ii}}I_{\text{Dem|Dex}}}{F_{\text{A|D}} + {}^{\text{ii}}I_{\text{Dem|Dex}} + {}^{\text{ii}}I_{\text{Aem|Aex}}} \quad (16)$$

In principle, the leaked donor signal could be added back to the donor emission channel⁴². However, this would require precise knowledge about spectral detection efficiencies, which is not otherwise required, and has no effect on the final accuracy of the measurement. As the determination of α and δ influences the γ and β correction in the next step, both correction steps can be repeated in an iterative manner if required (e.g., if the γ and β factors deviate largely from 1).

γ and β correction factors. Differences in the excitation intensities and cross-section, as well as quantum yields and detection efficiencies, are accounted for by use of the correction factors γ and β , respectively. If the fluorescence quantum yields do not depend on efficiencies or if such dependence is negligible (homogeneous approximation), mean values of efficiencies $\langle {}^{\text{iii}}E_{\text{app}}^{\text{(DA)}} \rangle$ and of stoichiometries $\langle {}^{\text{iii}}S_{\text{app}}^{\text{(DA)}} \rangle$ are related by equation (17):

$${}^{\text{iii}}S_{\text{app}}^{\text{(DA)}} = (1 + \gamma\beta + (1 - \gamma)\beta) {}^{\text{iii}}E_{\text{app}}^{\text{(DA)}}^{-1} \quad (17)$$

So, in the homogeneous approximation, γ and β correction factors can be determined by fitting of FRET populations to the histogram of ${}^{\text{iii}}S_{\text{app}}^{\text{(DA)}}$ versus ${}^{\text{iii}}E_{\text{app}}^{\text{(DA)}}$ with the line defined by equation (17). As this method relies on the analysis of ${}^{\text{iii}}S_{\text{app}}^{\text{(DA)}}$ and ${}^{\text{iii}}E_{\text{app}}^{\text{(DA)}}$ values obtained from multiple species, we term this method global γ -correction. Such a fit can be performed for all FRET populations together, for any of their subsets, and, in principle, for each single-species population separately (see below). Alternatively, a linear fit of inverse $\langle {}^{\text{iii}}S_{\text{app}}^{\text{(DA)}} \rangle$ versus $\langle {}^{\text{iii}}E_{\text{app}}^{\text{(DA)}} \rangle$ with γ -intercept a and slope b can be performed.

In this case, $\beta = a + b - 1$ and $\gamma = (a - 1) / (a + b - 1)$.

Error propagation, however, is more straightforward if equation (17) is used. If there is a complex dependence between properties of dyes and efficiencies, the homogeneous approximation is no longer applicable. In this case, the relationship between ${}^{\text{iii}}S_{\text{app}}^{\text{(DA)}}$ and ${}^{\text{iii}}E_{\text{app}}^{\text{(DA)}}$ for different populations (or even subpopulations for the same single species) cannot be described by equation (17) with a single γ correction factor. Here, γ can be determined for a single species. We call this ‘single-species γ -correction’. This works only if the efficiency broadening is dominated by distance fluctuations. The reason for this assumption is the dependency of these correction factors on both the stoichiometry and the distance-dependent efficiency. In our study, global and local γ -correction yielded similar results. Therefore, the homogeneous approximation, with distance fluctuations as the main cause for efficiency broadening, can be assumed for samples 1 and 2. Systematic variation of the γ correction factor yields an error of about 10%.

Alternatively, determination of γ and β factors can be done trace-wise, as in, for example, msALEX experiments⁴³, where the γ factor is determined as the ratio of the decrease in acceptor signal and the increase in donor signal after acceptor bleaching. We call such an alternative correction individual γ -correction⁴³. The analysis of local distributions can provide valuable insights about properties of the studied system.

After γ and β correction, the corrected donor (acceptor) fluorescence after donor (acceptor) excitation $F_{\text{D|D}}$ ($F_{\text{A|A}}$) amounts to

$$F_{\text{D|D}} = \gamma {}^{\text{ii}}I_{\text{Dem|Dex}} \quad (18)$$

$$F_{\text{A|A}} = \frac{1}{\beta} {}^{\text{ii}}I_{\text{Aem|Aex}} \quad (19)$$

Fully corrected values. Application of all corrections leads to the estimates of real FRET efficiencies E and stoichiometries S from the background-corrected intensities ${}^{\text{ii}}I$. The explicit expressions of fully corrected FRET efficiency and stoichiometry are

$$E = \frac{[{}^{\text{ii}}I_{\text{Aem|Dex}} - \alpha {}^{\text{ii}}I_{\text{Dem|Dex}} - \delta {}^{\text{ii}}I_{\text{Aem|Aex}}]}{\gamma [{}^{\text{ii}}I_{\text{Dem|Dex}}] + [{}^{\text{ii}}I_{\text{Aem|Dex}} - \alpha {}^{\text{ii}}I_{\text{Dem|Dex}} - \delta {}^{\text{ii}}I_{\text{Aem|Aex}}]} \quad (20)$$

$$S = \frac{\gamma [{}^{\text{ii}}I_{\text{Dem|Dex}}] + [{}^{\text{ii}}I_{\text{Aem|Dex}} - \alpha {}^{\text{ii}}I_{\text{Dem|Dex}} - \delta {}^{\text{ii}}I_{\text{Aem|Aex}}]}{\gamma [{}^{\text{ii}}I_{\text{Dem|Dex}}] + [{}^{\text{ii}}I_{\text{Aem|Dex}} - \alpha {}^{\text{ii}}I_{\text{Dem|Dex}} - \delta {}^{\text{ii}}I_{\text{Aem|Aex}}] + 1/\beta [{}^{\text{ii}}I_{\text{Aem|Aex}}]} \quad (21)$$

Plots of the E -versus- S histogram are shown in Fig. 2d,h. Now, the FRET population should be symmetric to the line for $S=0.5$. The donor-only population should still be located at $E=0$, and the acceptor-only population should be at $S=0$. Finally, the corrected FRET efficiency histogram is generated from events with a stoichiometry of $0.3 < S < 0.7$ (histograms in Fig. 2). The expected value of the corrected FRET efficiencies E is deduced as the center of a Gaussian fit to the efficiency histogram. This is a good approximation for FRET efficiencies in the range from about 0.1 to 0.9. In theory, the shot-noise limited efficiencies follow a binomial distribution if the photon number per burst is constant. For extreme efficiencies or data with a small average number of photons per burst, the efficiency distribution can no longer be approximated with a Gaussian. In this case and also in the case of efficiency broadening due to distance fluctuations, a detailed analysis of the photon statistics can be useful^{38,44–46}.

Uncertainty in distance due to R_0 . According to Förster theory⁷, the FRET efficiency E and the distance R are related by equation (3). In this study, we focused on the comparison of E values across different labs in a blind study. Many excellent reviews have been published on how to determine the Förster radius $R_0^{46,47,48}$, and a complete discussion would be beyond the scope of the current study. In the following, we estimate and discuss the different sources of uncertainty in R_0 by utilizing standard error propagation (see also Supplementary Note 6 and ref. 49). R_0 is given by equation (7).

The 6th power of the Förster radius is proportional to the relative dipole orientation factor κ^2 , the donor quantum yield $\Phi_{F,D}$, the overlap integral J , and n^{-4} , where n is the refractive index of the medium:

$$R_0^6 \sim \kappa^2 \cdot \Phi_{F,D} \cdot J \cdot n^{-4} \quad (22)$$

For Fig. 5b, we used a total Förster radius related distance uncertainty of 7%, which is justified by the following estimate. Please note that the error in the dipole orientation factor is always specific for the investigated system, whereas the errors in the donor quantum yield, overlap integral and refractive index are more general, although their mean values do also depend on the environment.

The refractive index. Different values for the refractive index in FRET systems have been used historically, but ideally the refractive index of the donor–acceptor intervening medium n_m should be used. Some experimental studies suggest that the use of the refractive index of the solvent may be appropriate, but this is still open for discussion (see, e.g., the discussion in ref. 49).

$$R_0^6(n) \sim n_m^{-4} \quad (23)$$

In the worst case, this value n_m might be anywhere between the refractive index of the solvent ($n_{\text{water}} = 1.33$) and a refractive index of the dissolved molecule ($n < n_m = 1.52$) (ref. 50), that is, $n_{\text{water}} < n_m < n_{\text{dye}}$. This would result in a maximum uncertainty of $\Delta n_m < 0.085$. As recommended by Clegg⁵¹, we used $n_m = 1.40$ to minimize this uncertainty (Supplementary Table 6). The distance uncertainty propagated from the uncertainty of the refractive indices can then be assumed to be

$$\Delta R_0(n) \approx \frac{4}{6} R_0 \frac{\Delta n_m}{n} < 0.04 \cdot R_0 \quad (24)$$

The donor quantum yield $\Phi_{F,D}$ is position dependent; therefore we measured the fluorescence lifetimes and quantum yields of the free dye Atto 550 and the 1-hi, 1-mid, and 1-lo donor-only labeled samples (Supplementary Table 2).

In agreement with the work of Sindbert et al.⁷, the uncertainty of the quantum yield is estimated at $\Delta \Phi_{F,D} = 5\%$, arising from the uncertainties of the Φ_F values of reference dyes and the precision of the absorption and fluorescence measurements. Thus, the distance uncertainty due to the quantum yield is estimated as

$$\Delta R_0(\Phi_{F,D}) \approx \frac{R_0}{6} \frac{\Delta \Phi_{F,D}}{\Phi_{F,D}} = 0.01 \cdot R_0 \quad (25)$$

The overlap integral J was measured for the unbound dyes in solution (Atto 550 and Atto 647N), as well as for samples 1-lo and 1-mid. This resulted in a deviation of about 10% for J when we used the literature values for the extinction coefficients. All single-stranded labeled DNA samples used in this study were purified with HPLC columns providing a labeling efficiency of at least 95%. The labeling efficiencies of the single-stranded singly labeled DNA and of the double-stranded singly labeled DNA samples were determined by the ratio of the absorption maxima of the dye and the DNA and were all above 97%. This indicates an error of the assumed extinction coefficient of less than 3%. Thus, the distance uncertainty due to the overlap spectra and a correct absolute acceptor extinction coefficient can be estimated by equation (26). However,

the uncertainty in the acceptor extinction coefficient might be larger for other environments, such as when bound to a protein.

$$\Delta R_0(J) \approx \frac{R_0}{6} \frac{\Delta J}{J} = 0.025 \cdot R_0 \quad (26)$$

In addition to the above uncertainty estimation, the J -related uncertainty can also be obtained through verification of the self-consistency of a β -factor network⁷. Finally, we found little uncertainty when we used the well-tested dye Atto 647N. Fluorescence spectra were measured on a Fluoromax4 spectrofluorimeter (Horiba, Germany). Absorbance spectra were recorded on a Cary5000 UV-VIS spectrometer (Agilent, USA) (Supplementary Fig. 6).

The κ^2 factor and model assumptions. The uncertainty in the distance depends on the dye model used²¹. Several factors need to be considered, given the model assumptions of unrestricted dye rotation, equal sampling of the entire accessible volume, and the rate inequality $k_{\text{rot}} \gg k_{\text{FRET}} \gg k_{\text{diff}} \gg k_{\text{int}}$.

First, the use of $\kappa^2 = 2/3$ is justified if $k_{\text{rot}} \gg k_{\text{FRET}}$, because then there is rotational averaging of the dipole orientation during energy transfer. k_{rot} is determined from the rotational correlation time $\rho_1 < 1$ ns, and k_{FRET} is determined from the fluorescence lifetimes $1 \text{ ns} < \tau_n < 5$ ns. Hence the condition $k_{\text{rot}} \gg k_{\text{FRET}}$ is not strictly fulfilled. We estimate the error this introduces into κ^2 from the time-resolved anisotropies of donor and acceptor dyes. If the transfer rate is smaller than the fast component of the anisotropy decay (rotational correlation time) of donor and acceptor, then the combined anisotropy, r_c , is given by the residual donor and acceptor anisotropies ($r_{D,\infty}$ and $r_{A,\infty}$, respectively):

$$r_c = \sqrt{r_{A,\infty}^2 + r_{D,\infty}^2} \quad (27)$$

In theory, the donor and the acceptor anisotropy should be determined at the time of energy transfer. If the transfer rate is much slower than the fast component of the anisotropy decay of donor and acceptor, the residual anisotropy can be used (Supplementary Fig. 7)⁵. Also, the steady-state anisotropy values can give an indication of the rotational freedom of the dyes on the relevant time scales, if the inherent effect by the fluorescence lifetimes is taken into account (refer to the Perrin equation, $r(\tau) = r_0 / (1 + (\tau/\phi))$, where r is the observed anisotropy, r_0 is the intrinsic anisotropy of the molecule, τ is the fluorescence lifetime, and ϕ is the rotational time constant; Supplementary Table 2 and Supplementary Fig. 8).

If the steady-state anisotropy and r_c are low (< 0.2), one can assume (but not prove) sufficient isotropic coupling (rotational averaging), that is, $\kappa^2 = 2/3$, with an uncertainty of about 5% (ref. 7):

$$\Delta R_0(\kappa^2, r_c < 0.2) \approx 0.05 \cdot R_0 \quad (28)$$

Spatial sampling. In addition, it is assumed that both dyes remain in a fixed location for the duration of the donor lifetime, that is, $k_{\text{FRET}} \gg k_{\text{diff}}$, where k_{diff} is defined as the inverse of the diffusion time through the complete AV. Recently the diffusion coefficient for a tethered Alexa Fluor 488 dye was determined to be $D = 10 \text{ Å}^2/\text{ns}$ (ref. 52). Therefore, k_{diff} is smaller than k_{FRET} . For short distances ($< 5 \text{ Å}$) the rates become similar, but the effect on the interdy distance distribution within the donor's lifetime is small, as has been observed in time-resolved experiments. We also assumed that, in the experiment, the efficiencies are averaged over all possible interdy positions. This is the case when $k_{\text{diff}} \gg k_{\text{rot}}$, which is a very good assumption for TIRF experiments with $k_{\text{rot}} > 100$ ms, and also for confocal experiments with k_{rot} values around 1 ms.

Overall uncertainty in R_0 . Time-resolved anisotropy measurements of samples 1 and 2 resulted in combined anisotropies less than 0.1. Therefore, we assumed isotropic coupling to obtain R_{MF} . The R_{MF} values matched the model distances very well, further supporting these assumptions. Finally, an experimental study of κ^2 distributions also yielded typical errors of 5% (ref. 7).

The overall uncertainty for the Förster radius would then result in

$$\Delta R_0(n^{-4}, \Phi_{F,D}, J, \kappa^2) = \sqrt{\Delta R_0(n)^2 + \Delta R_0(\Phi_{F,D})^2 + \Delta R_0(J)^2 + \Delta R_0(\kappa^2)^2} \lesssim 0.07 \cdot R_0 \quad (29)$$

The absolute values determined for this study are summarized in Supplementary Table 6. Please note that the photophysical properties of dyes vary in different buffers and when the dyes are attached to different biomolecules. Therefore, all four quantities that contribute to the uncertainty in R_0 should be measured for the system under investigation. When supplier values or values from other studies are applied, the uncertainty can be much larger. The values specified here could be further evaluated and tested in another blind study.

Comparing distinct dye pairs. Even though time-resolved fluorescence anisotropy can show whether dye rotation is fast, the possibility of dyes interacting with the DNA cannot be fully excluded. Thus, it is not clear whether the dye molecule is completely free to sample the computed AV (free diffusion), or whether there are sites of attraction (preferred regions) or sites of repulsion (disallowed regions). To validate the model assumption of a freely rotating and diffusing dye, we define the

ANALYSIS

NATURE METHODS

ratio R_{rel} for two apparent distances measured with the same dye pair (e.g., when comparing the low- to the mid-distance):

$$\begin{aligned}
 R_{rel} &= \frac{R_{(E),lo}}{R_{(E),mid}} \\
 &= \frac{R_{0,lo} \sqrt{1/E_{lo}-1}}{R_{0,mid} \sqrt{1/E_{mid}-1}} \\
 &= \sqrt{\frac{\kappa_{lo}^2 \Phi_{D,lo} J_{lo}^4}{\kappa_{mid}^2 \Phi_{D,mid} J_{mid}^4}} \sqrt{\frac{1/E_{lo}-1}{1/E_{mid}-1}} \\
 &= f \sqrt{\frac{1/E_{lo}-1}{1/E_{mid}-1}}
 \end{aligned} \tag{30}$$

For comparison of the other apparent distances, the ratio is adapted accordingly. Computed values relative to the mid-distance are shown in Supplementary Table 4. Note that R_{rel} values are (quasi) independent of R_0 for the following reasons: first, the donor positions in the lo, mid, and hi constructs are kept constant between samples 1, 2, 3 and 4, respectively. Therefore, the following assumptions can be made: (i) the ratios of the donor quantum yields are identical; (ii) the ratios of the spectral overlaps J for the lo, mid, and hi samples of one and the same dye pair should be the same; (iii) for a given geometry (Fig. 1) the refractive indices n_m of the medium between the dyes should also be very similar; and (iv) the ratios of the orientation factors κ^2 should be nearly equal, as the measured donor anisotropies are low for the lo, mid, and hi positions. Second, the acceptor extinction coefficients cancel each other out, as the acceptor is at the same position for the lo, mid, and hi constructs within a sample. Thus, the different dye pairs and the model used in this study should all give similar values for R_{rel} . Therefore, we compared the R_{rel} values for different dye pairs to determine whether for a particular dye pair the model assumptions are in agreement with the experimental data. Given our relative error in the determined distance of at most 2.8% (Fig. 5a), this is actually the case for all dye pairs investigated.

Reporting Summary. Further information on research design is available in the Nature Research Reporting Summary linked to this article.

Code availability. All custom code used herein is available from the authors upon reasonable request.

Data availability. All data are available from the corresponding authors upon reasonable request. The raw data for Fig. 2 are available at Zenodo (<https://doi.org/10.5281/zenodo.1249497>).

References

- Sindbert, S. et al. Accurate distance determination of nucleic acids via Förster resonance energy transfer: implications of dye linker length and rigidity. *J. Am. Chem. Soc.* **133**, 2463–2480 (2011).
- Nir, E. et al. Shot-noise limited single-molecule FRET histograms: comparison between theory and experiments. *J. Phys. Chem. B* **110**, 22103–22124 (2006).
- Barth, A., Voith von Voithenberg, L. & Lamb, D. C. MFD-PIE and PIE-FI: ways to extract more information with TCSPC. in *Advanced Photon Counting* Vol. 15 (eds Kapusta, P., Wahl, M. & Erdmann, R.) 129–157 (Springer, Cham, 2015).
- Schmid, S. & Hugel, T. Efficient use of single molecule time traces to resolve kinetic rates, models and uncertainties. *J. Chem. Phys.* **148**, 123312 (2018).
- Preus, S., Hildebrandt, L. L. & Birkedal, V. Optimal background estimators in single-molecule FRET microscopy. *Biophys. J.* **111**, 1278–1286 (2016).
- Neher, R. & Neher, E. Optimizing imaging parameters for the separation of multiple labels in a fluorescence image. *J. Microsc.* **213**, 46–62 (2004).
- Hildebrandt, L. L., Preus, S. & Birkedal, V. Quantitative single molecule FRET efficiencies using TIRF microscopy. *Faraday Discuss.* **184**, 131–142 (2015).
- Deniz, A. A. et al. Single-pair fluorescence resonance energy transfer on freely diffusing molecules: observation of Förster distance dependence and subpopulations. *Proc. Natl Acad. Sci. USA* **96**, 3670–3675 (1999).
- Antonik, M., Felekyan, S., Gaiduk, A. & Seidel, C. A. M. Separating structural heterogeneities from stochastic variations in fluorescence resonance energy transfer distributions via photon distribution analysis. *J. Phys. Chem. B* **110**, 6970–6978 (2006).
- Kalinin, S., Valeri, A., Antonik, M., Felekyan, S. & Seidel, C. A. M. Detection of structural dynamics by FRET: a photon distribution and fluorescence lifetime analysis of systems with multiple states. *J. Phys. Chem. B* **114**, 7983–7995 (2010).
- Clegg, R. M. Förster resonance energy transfer—FRET what is it, why do it, and how it's done. in *Laboratory Techniques in Biochemistry and Molecular Biology* Vol. 33 (ed Gadella, T. W. J.) 1–57 (Elsevier, Amsterdam, 2009).
- Braslavsky, S. E. et al. Pitfalls and limitations in the practical use of Förster's theory of resonance energy transfer. *Photochem. Photobiol. Sci.* **7**, 1444–1448 (2008).
- Knox, R. S. & van Amerongen, H. Refractive index dependence of the Förster resonance excitation transfer rate. *J. Phys. Chem. B* **106**, 5289–5293 (2002).
- Voros, J. The density and refractive index of adsorbing protein layers. *Biophys. J.* **87**, 553–561 (2004).
- Clegg, R. M. Fluorescence resonance energy transfer and nucleic acids. *Methods Enzymol.* **211**, 353–388 (1992).

Reporting Summary

Nature Research wishes to improve the reproducibility of the work that we publish. This form provides structure for consistency and transparency in reporting. For further information on Nature Research policies, see [Authors & Referees](#) and the [Editorial Policy Checklist](#).

Statistical parameters

When statistical analyses are reported, confirm that the following items are present in the relevant location (e.g. figure legend, table legend, main text, or Methods section).

- | | |
|-------------------------------------|---|
| n/a | Confirmed |
| <input type="checkbox"/> | <input checked="" type="checkbox"/> The <u>exact sample size</u> (n) for each experimental group/condition, given as a discrete number and unit of measurement |
| <input type="checkbox"/> | <input checked="" type="checkbox"/> An indication of whether measurements were taken from distinct samples or whether the same sample was measured repeatedly |
| <input checked="" type="checkbox"/> | <input type="checkbox"/> The statistical test(s) used AND whether they are one- or two-sided
<i>Only common tests should be described solely by name; describe more complex techniques in the Methods section.</i> |
| <input checked="" type="checkbox"/> | <input type="checkbox"/> A description of all covariates tested |
| <input checked="" type="checkbox"/> | <input type="checkbox"/> A description of any assumptions or corrections, such as tests of normality and adjustment for multiple comparisons |
| <input type="checkbox"/> | <input checked="" type="checkbox"/> A full description of the statistics including <u>central tendency</u> (e.g. means) or other basic estimates (e.g. regression coefficient) AND <u>variation</u> (e.g. standard deviation) or associated <u>estimates of uncertainty</u> (e.g. confidence intervals) |
| <input checked="" type="checkbox"/> | <input type="checkbox"/> For null hypothesis testing, the test statistic (e.g. F , t , r) with confidence intervals, effect sizes, degrees of freedom and P value noted
<i>Give P values as exact values whenever suitable.</i> |
| <input checked="" type="checkbox"/> | <input type="checkbox"/> For Bayesian analysis, information on the choice of priors and Markov chain Monte Carlo settings |
| <input checked="" type="checkbox"/> | <input type="checkbox"/> For hierarchical and complex designs, identification of the appropriate level for tests and full reporting of outcomes |
| <input checked="" type="checkbox"/> | <input type="checkbox"/> Estimates of effect sizes (e.g. Cohen's d , Pearson's r), indicating how they were calculated |
| <input type="checkbox"/> | <input checked="" type="checkbox"/> Clearly defined error bars
<i>State explicitly what error bars represent (e.g. SD, SE, CI)</i> |

Our web collection on [statistics for biologists](#) may be useful.

Software and code

Policy information about [availability of computer code](#)

Data collection

There was no common software used and no special code developed, but each group used their own custom softwares. The protocol gave enough detail that the results did not depend on the particular software used, one of the strengths of this study.

Data analysis

A major part of this manuscript is to describe the data analysis in great detail. This is independent of the software used, one of the main outcomes of this study.

For manuscripts utilizing custom algorithms or software that are central to the research but not yet described in published literature, software must be made available to editors/reviewers upon request. We strongly encourage code deposition in a community repository (e.g. GitHub). See the Nature Research [guidelines for submitting code & software](#) for further information.

Data

Publication I

Policy information about [availability of data](#)

All manuscripts must include a [data availability statement](#). This statement should provide the following information, where applicable:

- Accession codes, unique identifiers, or web links for publicly available datasets
- A list of figures that have associated raw data
- A description of any restrictions on data availability

All data is available upon request from the authors. The data of figure 2 is available on Zenodo at: <http://doi.org/10.5281/zenodo.1249497>.

Field-specific reporting

Please select the best fit for your research. If you are not sure, read the appropriate sections before making your selection.

Life sciences Behavioural & social sciences

For a reference copy of the document with all sections, see nature.com/authors/policies/ReportingSummary-flat.pdf

Life sciences

Study design

All studies must disclose on these points even when the disclosure is negative.

Sample size	We invited 22 labs and 20 labs finally responded. All resulting uncertainties are given, they take the sample size into account. Finally, similar results were obtained for different samples measured by a different number of labs (not all labs could measure all samples).
Data exclusions	No data was excluded from the analysis.
Replication	Each lab was asked to perform experiments according to standards used in the lab. Reproducibility in this respect is already given by the multi-laboratory approach used in this study.
Randomization	The samples were randomly allocated to the various labs
Blinding	Data collection and analysis was blind

Materials & experimental systems

Policy information about [availability of materials](#)

- n/a Involved in the study
- Unique materials
- Antibodies
- Eukaryotic cell lines
- Research animals
- Human research participants

Method-specific reporting

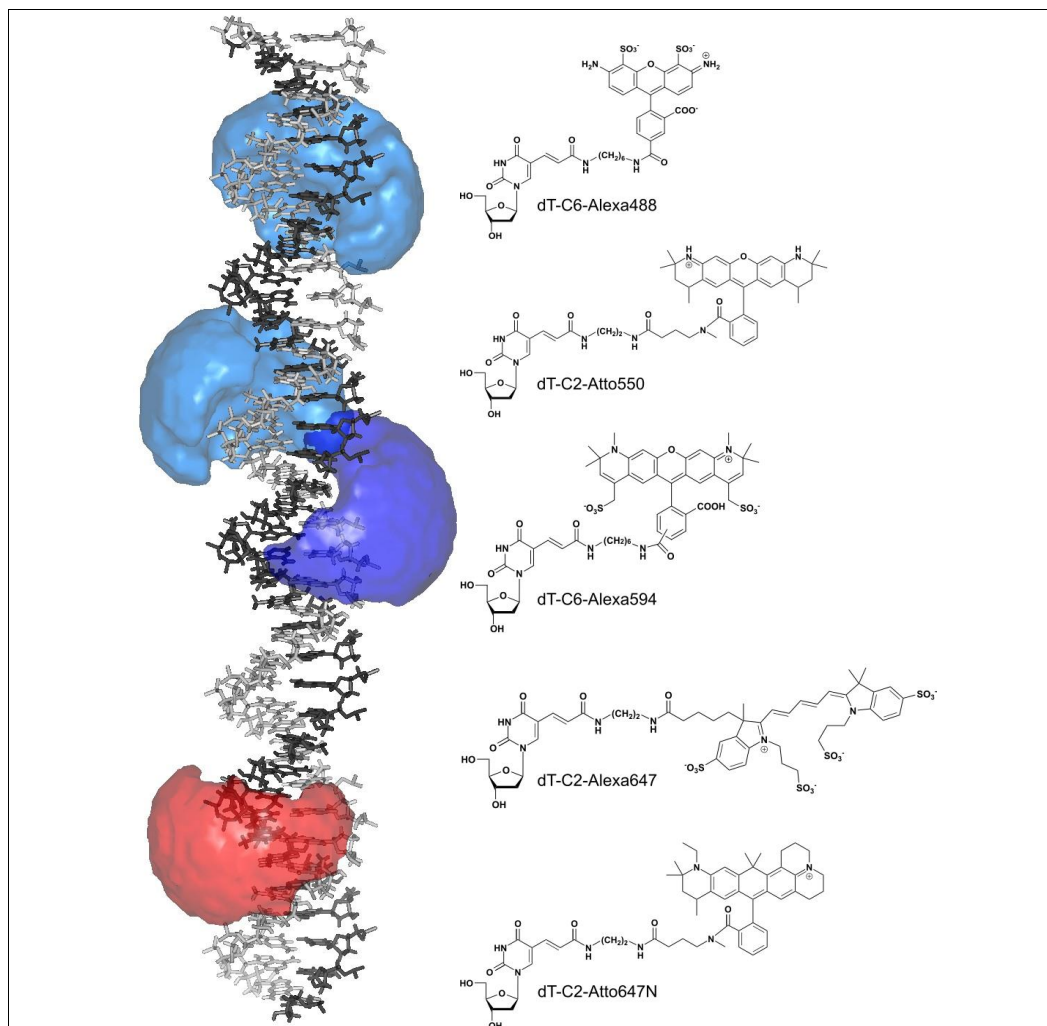
- n/a Involved in the study
- ChIP-seq
- Flow cytometry
- Magnetic resonance imaging

In the format provided by the authors and unedited.

Precision and accuracy of single-molecule FRET measurements—a multi-laboratory benchmark study

Björn Hellenkamp^{1,2,33}, Sonja Schmid^{1,3,33}, Olga Doroshenko⁴, Oleg Opanasyuk⁴, Ralf Kühnemuth⁴, Soheila Rezaei Adariani⁵, Benjamin Ambrose⁶, Mikayel Aznauryan⁷, Anders Barth⁸, Victoria Birkedal⁷, Mark E. Bowen⁹, Hongtao Chen¹⁰, Thorben Cordes^{11,12}, Tobias Eilert¹³, Carel Fijen¹⁴, Christian Gebhardt¹², Markus Götz¹⁵, Giorgos Gouridis^{11,12}, Enrico Gratton¹⁰, Taekjip Ha¹⁵, Pengyu Hao¹⁶, Christian A. Hanke⁴, Andreas Hartmann¹⁷, Jelle Hendrix^{18,19}, Lasse L. Hildebrandt⁷, Verena Hirschfeld²⁰, Johannes Hohlbein^{14,21}, Boyang Hua¹⁵, Christian G. Hübner²⁰, Eleni Kallis¹³, Achillefs N. Kapanidis²², Jae-Yeol Kim²³, Georg Krainer^{17,24}, Don C. Lamb⁸, Nam Ki Lee²³, Edward A. Lemke^{15,25,26,27}, Brié Levesque⁹, Marcia Levitus²⁸, James J. McCann⁹, Nikolaus Naredi-Rainer⁸, Daniel Nettels²⁹, Thuy Ngo¹⁵, Ruoyi Qiu¹⁶, Nicole C. Robb²², Carlheinz Röcker¹³, Hugo Sanabria¹⁵, Michael Schlierf¹⁷, Tim Schröder³⁰, Benjamin Schuler²⁹, Henning Seidel²⁰, Lisa Streit¹³, Johann Thurn¹, Philip Tinnefeld^{30,31}, Swati Tyagi²⁷, Niels Vandenberg¹⁸, Andrés Manuel Vera³⁰, Keith R. Weninger¹⁶, Bettina Wünsch³¹, Inna S. Yanez-Orozco⁵, Jens Michaelis^{13*}, Claus A. M. Seidel^{4*}, Timothy D. Craggs^{6,22*} and Thorsten Hugel^{1,32*}

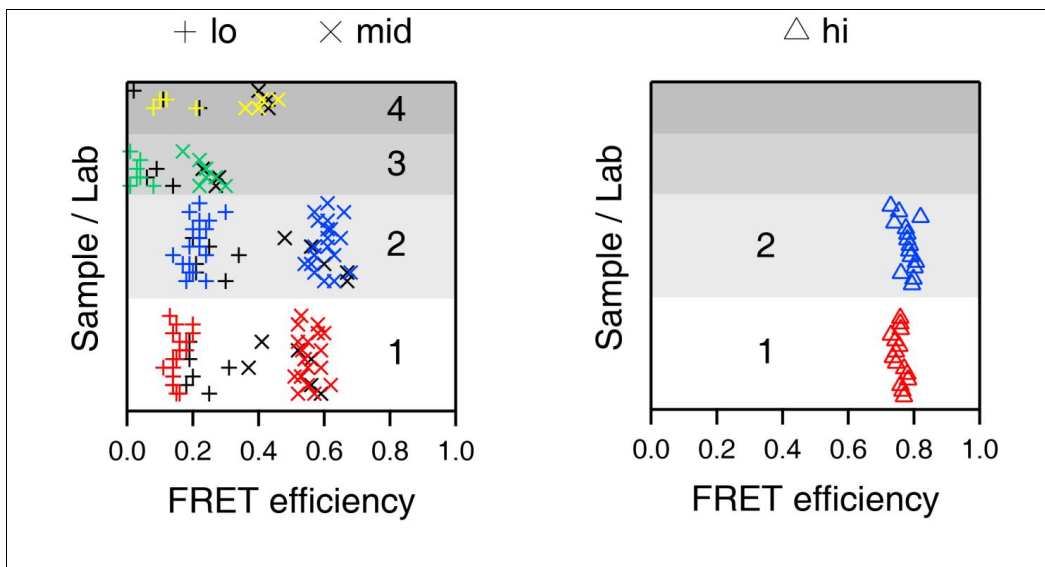
¹Institute of Physical Chemistry, University of Freiburg, Freiburg im Breisgau, Germany. ²Engineering and Applied Sciences, Columbia University, New York, NY, USA. ³Department of Bionanoscience, Kavli Institute of Nanoscience Delft, Delft University of Technology, Delft, the Netherlands. ⁴Molecular Physical Chemistry, Heinrich-Heine-Universität Düsseldorf, Düsseldorf, Germany. ⁵Department of Physics and Astronomy, Clemson University, Clemson, SC, USA. ⁶Department of Chemistry, University of Sheffield, Sheffield, UK. ⁷Interdisciplinary Nanoscience Center (iNANO) and Department of Chemistry, Aarhus University, Aarhus, Denmark. ⁸Physical Chemistry, Department of Chemistry, Nanosystems Initiative Munich (NIM), Center for Integrated Protein Science Munich (CIPSM) and Center for Nanoscience (CeNS), Ludwig-Maximilians-Universität München, Munich, Germany. ⁹Department of Physiology & Biophysics, Stony Brook University, Stony Brook, NY, USA. ¹⁰Department of Biomedical Engineering, University of California, Irvine, Irvine, CA, USA. ¹¹Molecular Microscopy Research Group, Zernike Institute for Advanced Materials, University of Groningen, Groningen, the Netherlands. ¹²Physical and Synthetic Biology, Faculty of Biology, Ludwig-Maximilians-Universität München, Planegg-Martinsried, Germany. ¹³Institute for Biophysics, Ulm University, Ulm, Germany. ¹⁴Laboratory of Biophysics, Wageningen University & Research, Wageningen, the Netherlands. ¹⁵Department of Biomedical Engineering, Johns Hopkins University, Baltimore, MD, USA. ¹⁶Department of Physics, North Carolina State University, Raleigh, NC, USA. ¹⁷B CUBE—Center for Molecular Bioengineering, TU Dresden, Dresden, Germany. ¹⁸Laboratory for Photochemistry and Spectroscopy, Department of Chemistry, University of Leuven, Leuven, Belgium. ¹⁹Dynamic Bioimaging Lab, Advanced Optical Microscopy Center and Biomedical Research Institute, Hasselt University, Hasselt, Belgium. ²⁰Institute of Physics, University of Lübeck, Lübeck, Germany. ²¹Microspectroscopy Research Facility Wageningen, Wageningen University & Research, Wageningen, the Netherlands. ²²Gene Machines Group, Clarendon Laboratory, Department of Physics, University of Oxford, Oxford, UK. ²³School of Chemistry, Seoul National University, Seoul, South Korea. ²⁴Molecular Biophysics, Technische Universität Kaiserslautern (TUK), Kaiserslautern, Germany. ²⁵Departments of Biology and Chemistry, Pharmacy and Geosciences, Johannes Gutenberg-University Mainz, Mainz, Germany. ²⁶Institute of Molecular Biology (IMB), Mainz, Germany. ²⁷Structural and Computational Biology Unit, European Molecular Biology Laboratory (EMBL), Heidelberg, Germany. ²⁸School of Molecular Sciences and The Biodesign Institute, Arizona State University, Tempe, AZ, USA. ²⁹Department of Biochemistry, University of Zurich, Zurich, Switzerland. ³⁰Department of Chemistry, Ludwig-Maximilians-Universität München, München, Germany. ³¹Institute of Physical & Theoretical Chemistry, Braunschweig Integrated Centre of Systems Biology (BRICS), and Laboratory for Emerging Nanometrology (LENA), Braunschweig University of Technology, Braunschweig, Germany. ³²BIOSS Centre for Biological Signalling Studies, University of Freiburg, Freiburg im Breisgau, Germany. ³³These authors contributed equally: Björn Hellenkamp, Sonja Schmid. *e-mail: jens.michaelis@uni-ulm.de; cseidel@hhu.de; t.craggs@sheffield.ac.uk; thorsten.hugel@pc.uni-freiburg.de



Supplementary Figure 1

DNA sample and utilized dyes.

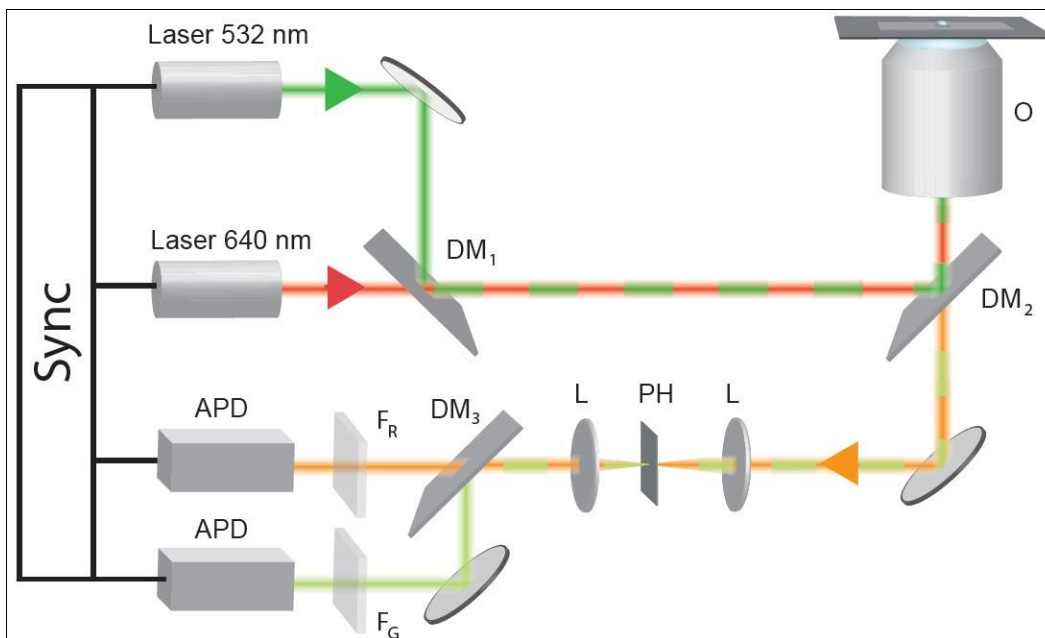
Left: DNA model with dye accessible volumes of the donor (blue) and acceptor (red) that were used in this study, indicating lo-, mid- and hi-FRET samples. Right: Structural formula of the dyes used in this study. Based on dyes from Molecular Probes / Thermo Fisher Scientific (Waltham, USA) and Atto-tec (Siegen, D).



Supplementary Figure 2

FRET efficiencies of all labs for all measured samples as indicated.

FRET efficiencies of all labs for all measured samples as indicated. Sample 1 to 4 (see Supplementary Table 1 and Supplementary Note 1) are color coded (red, blue, green, yellow) for all data points from intensity-based techniques. For a table of $R_{(E)}$ and R_{MP} and sample size for these measurements see Supplementary Table 4. Ensemble lifetime, single molecule lifetime and phasor approach derived data is shown in black. The FRET efficiencies (means and s.d.) for these measurements (depicted in black, sample size n) are: $E_{1a} = 0.21 \pm 0.05$ (n = 6); $E_{1b} = 0.51 \pm 0.08$ (n = 6); $E_{2a} = 0.25 \pm 0.06$ (n = 4); $E_{2b} = 0.59 \pm 0.07$ (n = 4); $E_{3a} = 0.10 \pm 0.04$ (n = 3); $E_{3b} = 0.26 \pm 0.03$ (n = 3); $E_{4a} = 0.12 \pm 0.10$ (n = 3); $E_{1a} = 0.42 \pm 0.02$ (n = 3). The left figure depicts all measurements from the main study, the right figure depicts all measurements from the later measurements of two additional samples (1-hi, 2-hi).

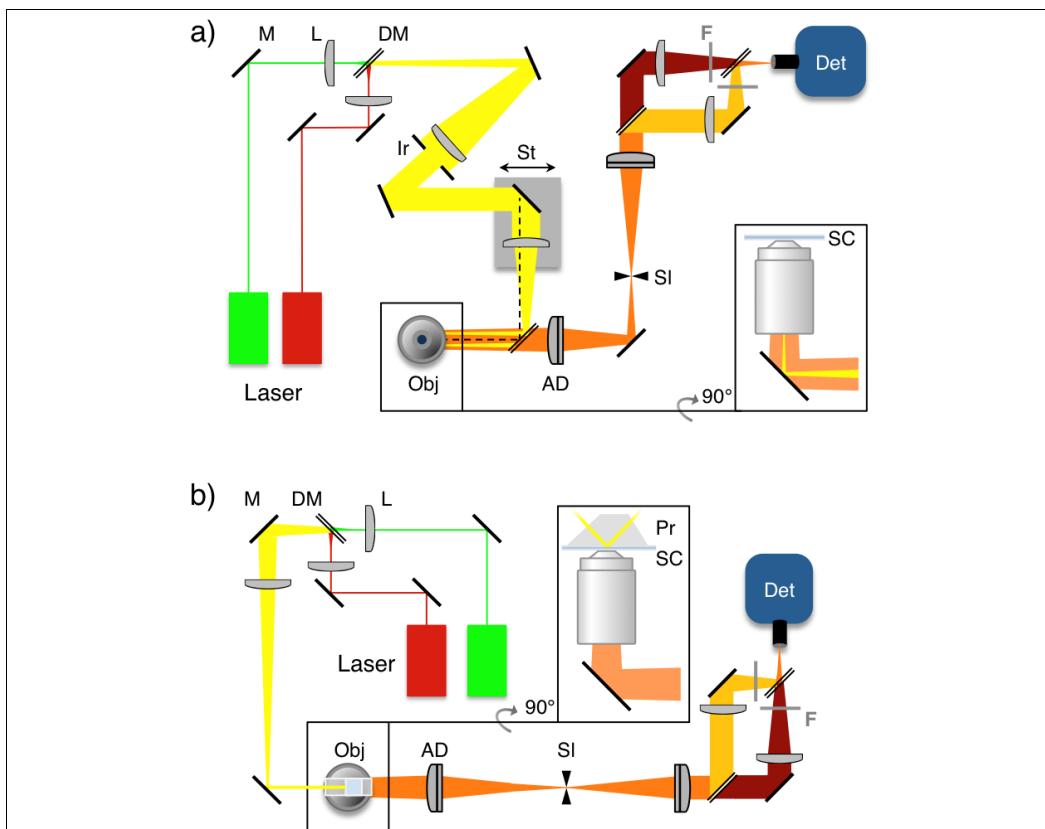


Supplementary Figure 3

Schematics of a typical confocal setup with alternating laser excitation / pulsed interleaved.

Schematics of a typical confocal setup with alternating laser excitation / pulsed interleaved excitation and color-sensitive detection. The most important elements are specified: Objective (O), dichroic mirror (DM), pinhole (P), spectral filter (F), avalanche photo diode (APD) and electronic micro- or picosecond synchronization of laser pulses and single photon counting (Sync).

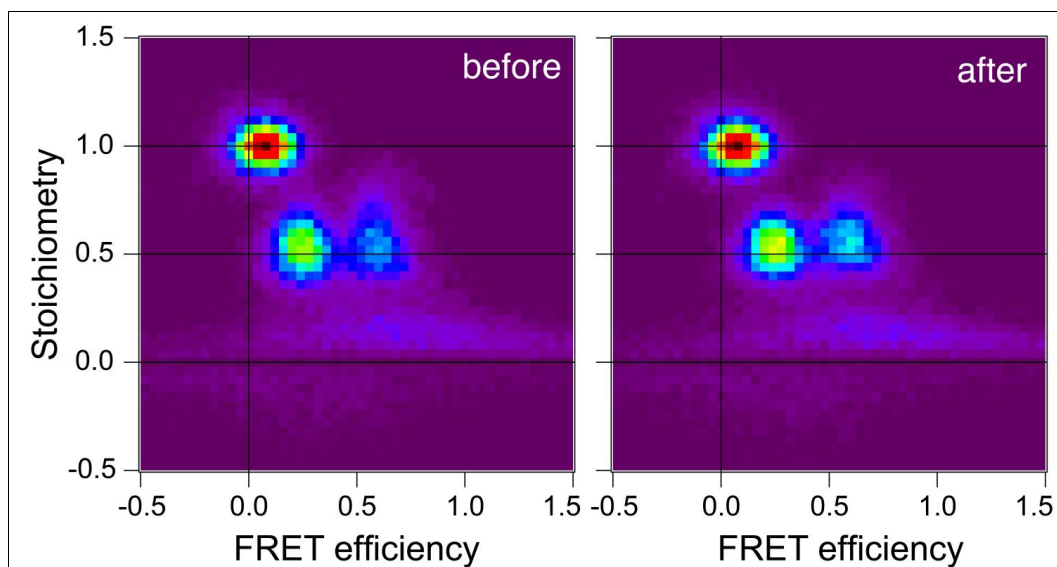
Elements used for the correction factors in Table 2 (main text) were: F34-641 Laser clean-up filter z 640/10 (right after Laser 640 nm); DM₁: F43-537 laser beam splitter z 532 RDC ; DM₂: F53-534 Dual Line beam splitter z 532/633; DM₃: F33-647 laser- laser beam splitter 640 DCXR; F_G: F37-582 Brightline HC 582/75; F_R: F47-700 ET Bandpass 700/75; Objective: Cfi plan apo VC 60xWI, NA1.2; Detectors: MPD Picoquant (green), tau-SPAD, Picoquant (red); Pinholes: 100 μm; ; Laser power at sample: ≈ 100 μW; Beam diameter ≈ 2 mm; Diffusion time of Atto550 and Atto647N around 0.42 ms and 0.50 ms, respectively. For details on all used setups and analysis software, see Supplementary Note 8.



Supplementary Figure 4

Schematic designs of an objective-type (a) and a prism-type TIRF setup (b).

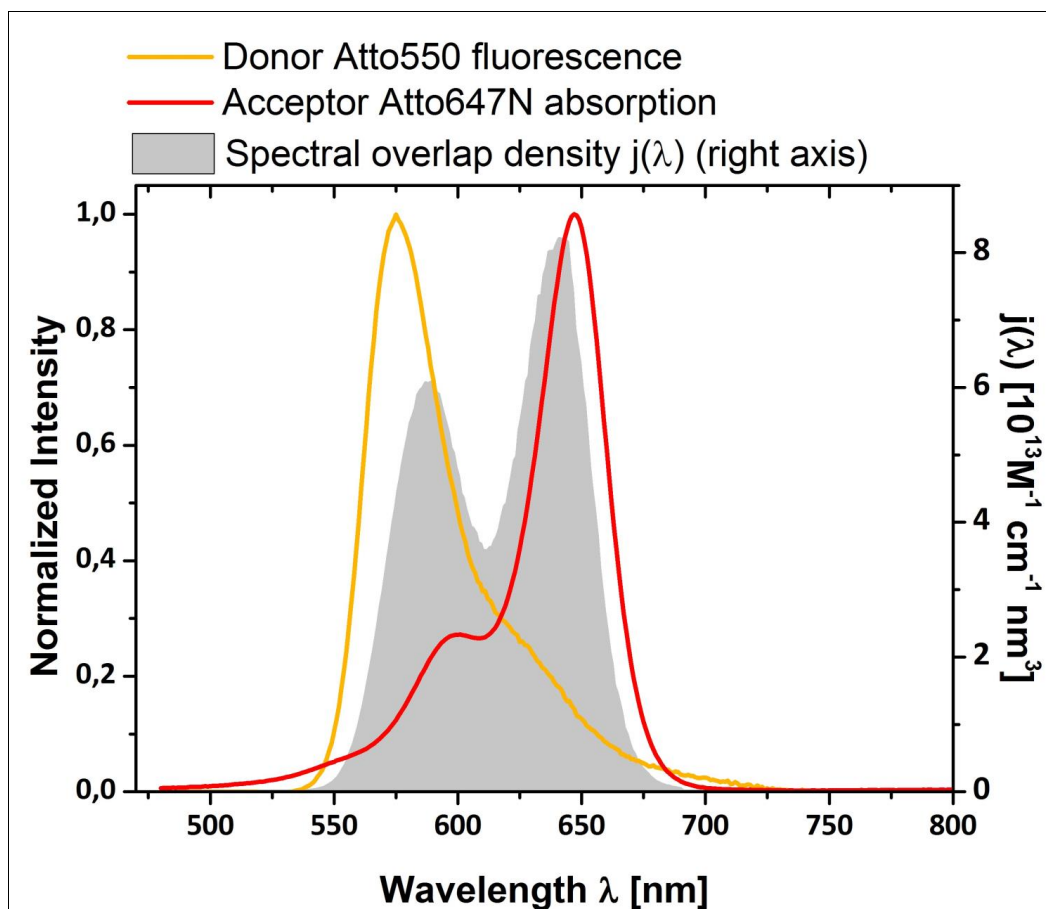
Green and red lasers are used to excite donor and acceptor dyes, respectively. M, mirror. L, lens. DM, dichroic mirror. Obj, objective. AD, achromatic doublet lens. SI, tunable slit. F, filters. Det, detector (e.g. electron multiplying charge-coupled device camera, EMCCD). The inset shows a side view of the objective with the out-of-plane (45°) mirror below. SC, sample chamber. Ir, iris. St, translation stage, Pr, prism. The dashed black line in (a) indicates the *on-axis* path to the objective, in contrast to the displayed *off-axis* path for TIR illumination. Elements used for the correction factors in Table 2 (main text) were: Dichroic before objective: F53-534 (AHF), Dichroics in detection: F33-726 and F33-644 (AHF). Band pass filters in detection: BP F39-572 and BP F37-677 (AHF). SI: SP40 (Owis), Objective: CFI Apo TIRF 100x, NA 1.49 (Nikon). Camera: EMCCD, iXonUltra, Andor. Lasers: 532nm, Compass 215M (Coherent) and 635nm, Lasiris (Stoker Yale). Note that we have used a Dichroic in the fluorescence excitation and emission path that reflects the higher wavelength, but this does not have any effect on the FRET efficiency measurement and related determination of correction factors. For details on all used setups and analysis software, see Supplementary Note 8.



Supplementary Figure 5

Correcting for differences in the excitation intensity in TIRF microscopy.

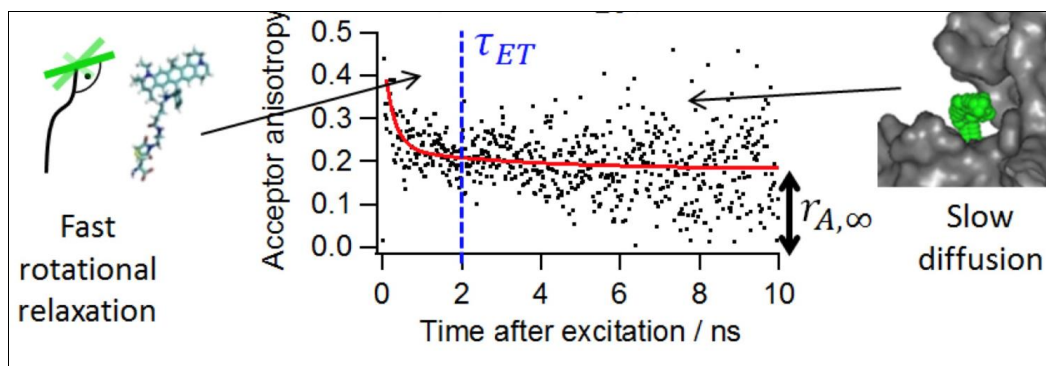
Accounting for the differences in the excitation intensity profiles of the green and red laser across the field of view. The individual excitation profiles are determined as the mean image of a stack of images recorded while moving across a dense layer of dyes. In contrast to the uncorrected case (“before”), a position specific normalization creates narrower and more symmetric SE-populations (“after”). The standard corrections described in the main text are performed subsequently.



Supplementary Figure 6

Computation of the spectral overlap integral J

Computation of the spectral overlap integral J for the FRET pair Atto550-Atto647N in sample 1. Normalized donor fluorescence and acceptor absorption spectra normalized to the maximum (left scale). Spectral overlap density $j(\lambda)$ (right scale) to compute the spectral overlap integral J [$\text{cm}^{-1}\text{M}^{-1}\text{nm}^4$] with $J = \int_0^\infty j(\lambda) d\lambda$ and $j(\lambda) = \bar{F}_D(\lambda)\epsilon_A(\lambda)\lambda^4$. The extinction coefficient ϵ_A of Atto647N was assumed to be $150000 \text{ M}^{-1}\text{cm}^{-1}$ at the maximum as provided by the manufacturer. The donor fluorescence and the acceptor absorption spectra were recorded in two laboratories in at least three independent experiments. Spectra with a flat baseline were selected. The computation was performed once.

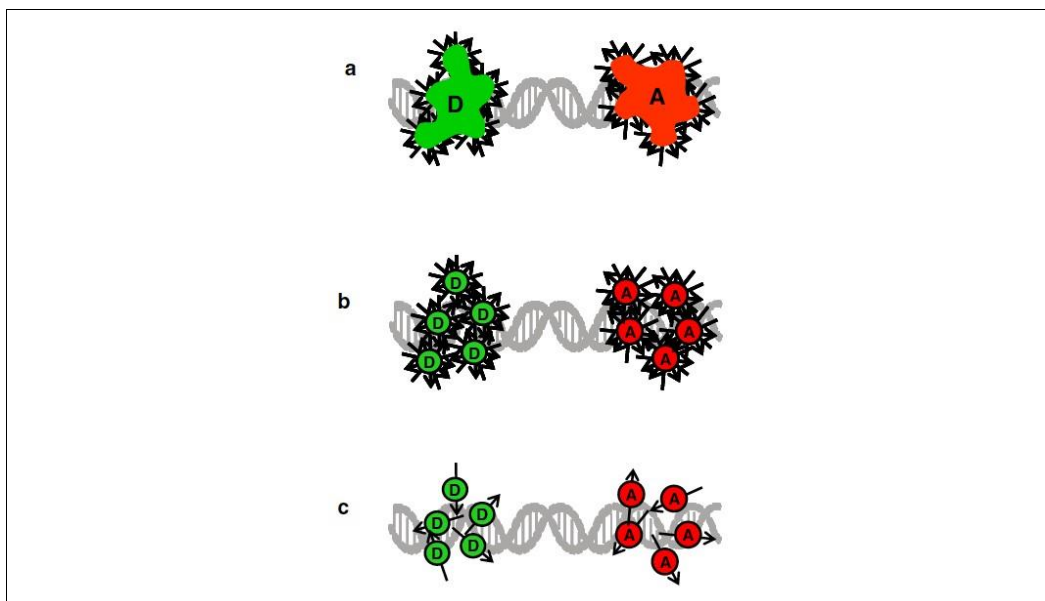


Supplementary Figure 7

Time-resolved anisotropies and FRET

The time-resolved anisotropies of dyes bound to a larger object (e.g. DNA or protein) normally consist of a fast decay from rotational relaxation of the dipole (left) and of a slow decay from translational relaxation (right). $\tau_{ET} = 1/k_{FRET}$: time of energy transfer; $r_{A,\infty}$: residual anisotropy of dye A. (Figure from ref. ¹). The data exemplarily shown is from a single measurement.

¹ Hellenkamp, B., Wortmann, P., Kandzia, F., Zacharias, M. & Hugel, T. Multidomain Structure and Correlated Dynamics Determined by Self-Consistent FRET Networks. *Nat. Meth.* 14, 174-180 (2017).



Supplementary Figure 8

Visualizations of different averages for efficiencies according to different fluorophore dynamics.

(a) Dynamic average, which applies in the case of the fluorophore movements being faster than the rate of energy transfer. There the rate of energy transfer has to be calculated taking into account the average over all possible distances and orientations. (b) Intermediate case, called the isotropic average, where the orientational variation of the fluorophores is faster than the rate of energy transfer while the positional variation is slower (c) Static case, where the fluorophore movements are much slower than the rate of energy transfer. In this case each distance and respective fluorophore orientation has to be taken into account with its individual transfer efficiency. These efficiencies then are averaged by the measurement process. (Figure from ref. ²).

² Wozniak, A. K., Schröder, G. F., Grubmüller, H., Seidel, C. A. M. & Oesterhelt, F. *Single-Molecule FRET Measures Bends and Kinks in DNA*. *Proc. Natl. Acad. Sci. USA* 105, 18337-18342 (2008).

Supplementary Material:

Precision and accuracy of single-molecule FRET measurements – a worldwide benchmark study

Björn Hellenkamp^{1a,°}, Sonja Schmid^{1a,°}, Olga Doroshenko²⁰, Oleg Opanasyuk²⁰, Ralf Kühnemuth²⁰, Soheila Rezaei Adariani¹⁵, Benjamin Ambrose², Mikayel Aznauryan⁹, Anders Barth²¹, Victoria Birkedal⁹, Mark E. Bowen¹¹, Hongtao Chen²⁶, Thorben Cordes^{14,25}, Tobias Eilert¹⁹, Carel Fijen⁷, Christian Gebhardt²⁵, Markus Götz^{1a}, Giorgos Gouridis^{14,25}, Enrico Gratton²⁶, Taekjip Ha²², Pengyu Hao¹², Christian A. Hanke²⁰, Andreas Hartmann¹⁷, Jelle Hendrix^{5,6}, Lasse L. Hildebrandt⁹, Verena Hirschfeld¹⁶, Johannes Hohlbein^{7,8}, Boyang Hua²², Christian G. Hübner¹⁶, Eleni Kallis¹⁹, Achillefs N. Kapanidis¹⁰, Jae-Yeol Kim²³, Georg Krainer^{17,18}, Don C. Lamb²¹, Nam Ki Lee²³, Edward A. Lemke^{3a,b,c}, Brié Levesque¹¹, Marcia Levitus²⁴, James J. McCann¹¹, Nikolaus Naredi-Rainer²¹, Daniel Nettels⁴, Thuy Ngo²², Ruoyi Qiu¹², Nicole C. Robb¹⁰, Carlheinz Röcker¹⁹, Hugo Sanabria¹⁵, Michael Schlierf¹⁷, Tim Schröder²⁷, Benjamin Schuler⁴, Henning Seidel¹⁶, Lisa Streit¹⁹, Johann Thurn^{1a}, Philip Tinnefeld^{13,27}, Swati Tyagi^{3c}, Niels Vandenberk⁵, Andrés Manuel Vera²⁷, Keith R. Weninger¹², Bettina Wünsch¹³, Inna S. Yanez-Orozco¹⁵, Jens Michaelis^{19,*}, Claus A.M. Seidel^{20,*}, Timothy D. Craggs^{2,10,*}, Thorsten Hugel^{1a,b,*}

Supplementary Information	Page
Supplementary Table 1 Samples	3
Supplementary Table 2 Spectroscopic parameters of the dyes in samples 1 and 2.	4
Supplementary Table 3 Typical correction factors	6
Supplementary Table 4 Resulting efficiencies and (relative) distances	6
Supplementary Table 5 Nomenclature and definitions	7
Supplementary Table 6 Typical dye parameters	8
Supplementary Note 1: Further samples	9
Supplementary Note 2 Time-resolved experiments	10
Supplementary Note 3 AV simulations to compute donor acceptor distances	15
Supplementary Note 4 FRET efficiency measurements and distance determinations in more complex systems, e.g. proteins	16
Supplementary Note 5 R _(E) to R _{MP} conversion	17

Supplementary Note 6 Error propagation	20
Supplementary Note 7 MD simulations	21
Supplementary Note 8 Setup and data analysis details	25
Bibliography	35

Supplementary Table 1. The main focus in the manuscript are the 1 and 2 samples. The so-called donor strand (D-strand) is labeled with donor dye and acceptor strand (A-strand) with acceptor dye. The labeling sites of the donor and acceptor are shown in green and in red on the sequence respectively. See Supplementary Note 1 for further samples.

Name	Base position (Linker), strand	Dyes (Donor/Acceptor)	Sequence
1-lo	T 31(C2), D-strand T 31(C2), A-strand	Atto550 NHS Ester/ Atto647N NHS	5' - GAG CTG AAA GTG TCG AGT TTG TTT GAG TGT TTG TCT GG - 3' 3' - CTC GAC TTT CAC AGC TCA AAC AAA CTC ACA AAC AGA CC - 5' - biotin
1-mid	T 23(C2), D-strand T 31(C2), A-strand	Atto550 NHS Ester/ Atto647N NHS	5' - GAG CTG AAA GTG TCG AGT TTG TTT GAG TGT TTG TCT GG - 3' 3' - CTC GAC TTT CAC AGC TCA AAC AAA CTC ACA AAC AGA CC - 5' - biotin
1-hi	T 19(C2), D-strand T 31(C2), A-strand	Atto550 NHS Ester/ Atto647N NHS	5' - GAG CTG AAA GTG TCG AGT TTG TTT GAG TGT TTG TCT GG - 3' 3' - CTC GAC TTT CAC AGC TCA AAC AAA CTC ACA AAC AGA CC - 5' - biotin
2-lo:	T 31(C2), D-strand T 31(C2), A-strand	Atto550 NHS Ester/ Alexa647 NHS Ester	5' - GAG CTG AAA GTG TCG AGT TTG TTT GAG TGT TTG TCT GG - 3' 3' - CTC GAC TTT CAC AGC TCA AAC AAA CTC ACA AAC AGA CC - 5' - biotin
2-mid:	T 23(C2), D-strand T 31(C2), A-strand	Atto550 NHS Ester/ Alexa647 NHS Ester	5' - GAG CTG AAA GTG TCG AGT TTG TTT GAG TGT TTG TCT GG - 3' 3' - CTC GAC TTT CAC AGC TCA AAC AAA CTC ACA AAC AGA CC - 5' - biotin
2-hi:	T 19(C2), D-strand T 31(C2), A-strand	Atto550 NHS Ester/ Alexa647 NHS Ester	5' - GAG CTG AAA GTG TCG AGT TTG TTT GAG TGT TTG TCT GG - 3' 3' - CTC GAC TTT CAC AGC TCA AAC AAA CTC ACA AAC AGA CC - 5' - biotin

Supplementary Table 2: Spectroscopic parameters of the dyes in samples 1 and 2. Residual anisotropy r_{∞} , combined anisotropy r_c , fluorescence quantum yields of donor and acceptor $\Phi_{F,D}$ and $\Phi_{F,A}$, respectively (determined according to the procedure detailed in the online methods), and species average fluorescence lifetimes $\langle \tau \rangle_x$ for the samples 1 (Atto550 /Atto647N) and the samples 2 (Atto550 /Alexa647). All measurements were done in 20mM MgCl₂,5mM NaCl,5mM TRIS at pH 7.5 measurement buffer.

Sample 1	1-lo (Atto550)	1-lo (Atto647N)	1-mid (Atto550)	1-mid (Atto647N)	1-hi (Atto550)	1-hi (Atto647N)
Base position (Linker), strand	T 31,(C2), D-strand	T 31(C2), A-strand	T 23(C2), D-strand	T 31(C2), A-strand	T 19 (C2), D-strand	T 31(C2), A-strand
Residual anisotropy $r_{A,\infty}$ or $r_{D,\infty}$ [a]	0.08	0.07	0.11	0.07	0.13	0.07
Combined anisotropy r_c	0.07		0.09		0.10	
Steady state anisotropy r_S	0.11	0.09	0.13	0.09	0.15	0.09
Lifetime $\langle \tau \rangle_x /$ ns (SD: 2%) [b]	3.76	3.62	3.81	3.62	3.74	3.62
Fluorescence quantum yield $\Phi_{F,D}$ or $\Phi_{F,A}$	0.76±0.015 [c]	0.65 [d]	0.77±0.015 [c]	0.65 [d]	0.76±0.015 [c]	0.65 [d]
fraction bright a_b [g]	≈ 1 [e]	≈ 1 [e]	≈ 1 [e]	≈ 1 [e]	≈ 1 [e]	≈ 1 [e]
R_0 [Å]	62.6					
$\langle \Phi_{F,D} \rangle$	0.765±0.015					
ϵ_A [M ⁻¹ cm ⁻¹]	150000					
J [cm ⁻¹ nm ⁴ M ⁻¹]	5.180·10 ¹⁵					
n_{im}	1.40					
κ^2	2/3					
Sample 2	2-lo (Atto550)	2-lo (Alexa647)	2-mid (Atto550)	2-mid (Alexa647)	2-hi (Atto550)	2-hi (Alexa647)
Base position (Linker), strand	T 31, (C2), D-strand	T 31(C2), A-strand	T 23(C2), D-strand	T 31(C2), A-strand	T 19 (C2), D-strand	T 31(C2), A-strand
Residual anisotropy $r_{A,\infty}$ or $r_{D,\infty}$ [a]	0.08	0.05	0.11	0.05	0.13	0.05
Combined anisotropy r_c	0.06		0.07		0.10	
Steady state anisotropy r_S	0.11	0.15	0.14	0.14	0.15	0.14
Lifetime $\langle \tau \rangle_x /$ ns (SD: 2%) [b]	3.76	1.19	3.81	1.19	3.74	1.19
Fluorescence quantum yield $\Phi_{F,D}$ or $\Phi_{F,A}$ [g]	0.77±0.015 [c]	0.39±0.015 [d]	0.77±0.015 [c]	0.39±0.015 [d]	0.77±0.015 [c]	0.39±0.015 [d]

fraction bright	≈ 1	0.75 ± 0.02	≈ 1	0.85 ± 0.02	≈ 1	0.86 ± 0.02
a_b [g]	[e]	[f]	[e]	[f]	[e]	[f]
R_n [Å]	68.0					
$\langle \Phi_{FD} \rangle$	0.765					
ϵ_A [M ⁻¹ cm ⁻¹]	270000					
J [cm ⁻¹ nm ⁴ M ⁻¹]	$8.502 \cdot 10^{15}$					
n_{im}	1.40					
κ^2	2/3					

[a] The depolarization time of all species are given together with their amplitudes in *Supplementary Table N2.2*.

[b] The fluorescence lifetimes of all species are given together with their species fractions in *Supplementary Table N2.1*.

[c] Measured relative to Rhodamine 6G in a steady state spectrometer in air-saturated Ethanol with $\Phi_{F,Rh6G} = 0.95$. In the same measurement we obtained for the free dye $\Phi_{F,Atto550} = 0.8 \pm 0.014$ and $\tau_{Atto550} = 3.60$ ns $\pm 2\%$, which corresponds to the values given by the manufacturer.

[d] The following reference values for the free dyes in solution were used from the manufacturers to scale the fluorescence quantum via the fluorescence lifetime of the free dye:

$\Phi_{F,Atto647N} = 0.65$; $\tau_{Atto647N} = 3.5$ ns; $\Phi_{F,Alexa647} = 0.33 \pm 0.015$; $\tau_{Alexa647} = 1.0$ ns. The parameters of Alexa647 agree nicely with the values for free Cy5 $\Phi_{F,Cy5} = 0.32 \pm 0.015$ and $\Phi_{F,Cy5} = 0.38 \pm 0.015$ Cy5-labelled dsDNA¹

A fluorescence lifetime analysis to relate the quantum yield Φ'_F and lifetime τ' specified by the manufacturer to the measured lifetime τ and quantum yield Φ_F :

$$\Phi_F = \Phi'_F \cdot \tau / \tau'$$

Here, we assume that the manufacturer Φ'_F is correct, that the radiative constant is unchanged and that the lifetime decay is monoexponential. For many dyes in distinct environments, this might not be the case.

[e] The excitation irradiance is usually low enough (especially in TIRF experiments) to avoid the population of dark states (triplet and radical states). The fraction of bright species a_b can be determined by fluorescence correlation spectroscopy.

[f] Cyanine dyes exhibit saturation effects due to cis-trans isomerization². Moreover, Widengren et al³ have shown that that the fraction of bright trans state a_b depends slightly on the FRET efficiency. In this study, we determined a_b by fluorescence correlation analysis of the FRET-sensitized acceptor signal in a confocal setup.

[g] Note that the correction factor γ was experimentally determined in this work. For completeness, we want to point out that the definition of γ in Online Methods section 1 can be used to compute the ratio of the detection efficiencies $g_{R|A}/g_{G|D}$ to check the detection performance of the setup provided the effective fluorescence quantum yields Φ_F are known. Therefore we list the steady fluorescence quantum yields Φ_F and the fraction of bright species a_b .

Supplementary Table 3: Typical correction factors for sample 1 (Atto550-Atto647N) at given setups (reference lab). For the instrumental details of the setups see Supplementary Figures 3 and 4.

Factor	Experiment type	
	confocal	TIRF
α	0.11	0.07
β	1.80	0.85
γ	1.20	1.14
δ	0.11	0.065

Supplementary Table 4: Summary of resulting mean efficiencies $\langle E \rangle$, apparent distance $R_{(E)}$, mean position distance R_{MP} and corresponding model distances $R_{(E)}^{(model)}$ (Supplementary Note 3) and dynamic model distances $R_{(E)}^{(dynamic\ model)}$ (Supplementary Note 7) and the experimental ratio $R_{rel} = R_{(E)}^{(i)} / R_{(E)}^{(mid)}$ and the model $R_{rel}^{(model)} = R_{(E)}^{(model/i)} / R_{(E)}^{(model,mid)}$ for all intensity based measurements. The errors (standard deviations) report on the precision of the measurements and not their accuracy. Literature values differ mainly because the refractive index of water is often assumed, while we used $n_{im} = 1.40$ here (see Online Methods, Section 4.1). Note that these errors only include the statistical variations of the FRET efficiencies, but do not include the error in the Förster radii, thus these errors represent the precision of the measurement, but not the accuracy. Including the knowledge of the dye attachment positions, a static structure of the DNA and this particular dye model, we computed also model values as described in Supplementary Note 3, which are also given here.

Sample	N	$\langle E \rangle$	R_0 [Å]	$R_{(E)}$ [Å]	$R_{(E)}^{(model)}$ [Å]	$R_{(E)}^{(dynamic\ model)}$ [Å]	R_{rel}	$R_{rel}^{(model)}$	R_{MP} [Å]	$R_{MP}^{(model)}$ [Å]
1-lo	19	0.15±0.02	62.6±4.0	83.4±2.5	83.5±2.4	83.9	1.38	1.42	85.4±2.7	84.2±2.1
1-mid	19	0.56±0.03		60.3±1.3	58.7±1.6	60.3	1	1	58.2±1.7	55.8±2.3
1-hi	13	0.76±0.015		51.8±0.7	51.6±2.9	51.9	0.86	0.88	47.0±1.0	46.6±3.2
2-lo	19	0.21±0.04	68.0±5.0	85.4±3.4	83.9±2.2	84.2	1.34	1.41	86.9±3.7	84.2±2.4
2-mid	19	0.60±0.05		63.7±2.3	59.6±1.3	61.0	1	1	61.3±2.9	55.8±2.6
2-hi	13	0.78±0.025		55.0±1.3	52.3±1.9	52.6	0.86	0.88	50.1±1.8	46.6±1.8
3-lo	7	0.04±0.02	49.3[a]	89.5±12.3	82.4±2.4	83.1	1.49	1.46	85.7±5.3	84.0±2.1
3-mid	7	0.24±0.04	57.0[a]	60.1±2.3	56.4±1.6	58.4	1	1	61.1±2.9	55.7±2.3
4-lo	4	0.13±0.06		79.6±6.2	82.6±2.4	83.5	1.31	1.43	82.9±6.8	83.8±2.1
4-mid	4	0.41±0.04		60.7±1.7	57.6±1.6	59.5	1	1	60.4±2.3	55.5±2.3

[a] The R_0 for these samples have been taken from the literature and converted from a refractive index of $n_{im} = 1.33$ to $n_{im} = 1.40$:

Sample 3: $R_0 = 49.3$ Å from ref. ⁴

Sample 4: $R_0 = 57.0$ Å from ref. ⁵

Supplementary Table 5: Nomenclature and definitions. Since the nomenclature for FRET-based experiments is not consistent, we propose and use the following terms in this manuscript.

Central Definitions:		
$E = \frac{F_{A D}}{F_{D D} + F_{A D}}$	FRET efficiency	(1)
$S = \frac{F_{D D} + F_{A D}}{F_{D D} + F_{A D} + F_{A A}}$	Stoichiometry	(2)
$E = \frac{1}{1 + R_{DA}^6/R_0^6}$	FRET efficiency for a single donor acceptor distance R_{DA}	(3)
$\langle E \rangle = \frac{1}{nm} \sum_{i=1}^n \sum_{j=1}^m \frac{1}{1 + \mathbf{R}_{A(j)} - \mathbf{R}_{D(i)} ^6/R_0^6}$	Mean FRET efficiency for a discrete distribution of donor acceptor distances with the position vectors $\mathbf{R}_{D(i)}$ and $\mathbf{R}_{A(j)}$	(4)
$R_{(E)} \equiv R(\langle E \rangle) = R_0(\langle E \rangle^{-1} - 1)^{1/6}$	The apparent donor acceptor distance is computed from the average FRET efficiency for a distance distribution. It is a FRET averaged quantity which was also referred to as FRET-averaged distance $\langle R_{DA} \rangle_E$ (ref ¹).	(5)
$R_{MP} = \left \langle \mathbf{R}_{D(i)} \rangle - \langle \mathbf{R}_{A(j)} \rangle \right $ $= \left \frac{1}{n} \sum_{i=1}^n \mathbf{R}_{D(i)} - \frac{1}{m} \sum_{j=1}^m \mathbf{R}_{A(j)} \right $	Distance between the mean dye positions with the position vectors $\langle \mathbf{R}_{D(i)} \rangle$ and $\langle \mathbf{R}_{A(j)} \rangle$	(6)
Subscripts:		
D or A	Concerning donor or acceptor	
$A D$	Acceptor fluorescence given donor excitation, $D D, A A$ accordingly	
$Aem Dex$	Intensity in the acceptor channel given donor excitation, $Dem Dex, Aem Aex$, accordingly	
app	apparent, i.e. including systematic, experimental offsets	
Superscripts:		
BG	Background	
DO/AO	Donor-only species/ Acceptor-only species	
DA	FRET species	
i - iii	Indicates (i) the uncorrected intensity; (ii) intensity after BG correction; (iii) intensity after BG, alpha and delta corrections	
Correction Factors:		
$\alpha = \frac{g_{R D}}{g_{G D}} = \frac{\langle {}^{ii}E_{app}^{(DO)} \rangle}{1 - \langle {}^{ii}E_{app}^{(DO)} \rangle}$	Leakage of D fluorescence into A channel	
$\beta = \frac{\sigma_{A R} I_{Aex}}{\sigma_{D G} I_{Dex}}$	Normalization of excitation intensities, I , and cross-sections, σ , of A and D	
$\gamma = \frac{g_{R A} {}^{eff} \Phi_{F,A}}{g_{G D} {}^{eff} \Phi_{F,D}}$	Normalization of effective fluorescence quantum yields, ${}^{eff} \Phi_{F=a_b} \cdot \Phi_F$, and detection efficiencies, g , of A and D. a_b is the fraction of molecules in the bright state and Φ_F is the fluorescence quantum yield without photophysical (saturation) effects.	

$\delta = \frac{\sigma_{A G} I_{Dex}}{\sigma_{A R} I_{Aex}} = \frac{\langle ii S_{app}^{(AO)} \rangle}{1 - \langle ii S_{app}^{(AO)} \rangle}$	Direct acceptor excitation by the donor excitation laser (lower wavelength)
Primary Quantities:	
I	Experimentally observed intensity
F	Corrected fluorescence intensity
τ	Fluorescence lifetime [ns]
$\Phi_{F,A}$ or $\Phi_{F,D}$	Fluorescence quantum yield of A and D, respectively
r	Fluorescence anisotropy
R	Inter-dye distance [Å]
$\frac{R_0}{\text{Å}} = 0.2108 \sqrt[6]{\left(\frac{\Phi_{F,D} \kappa^2}{n_{im}^4}\right) \frac{J}{M^{-1} cm^{-1} nm^4}}$	Förster radius [Å], for a given J in units below (7)
$\kappa^2 = (\cos \theta_{AD} - 3 \cos \theta_D \cos \theta_A)^2$	Dipole orientation factor
$J = \int_0^\infty \bar{F}_D(\lambda) \varepsilon_A(\lambda) \lambda^4 d\lambda$	Spectral overlap integral [$cm^{-1} M^{-1} nm^4$] (see Supplementary Figure 6)
$\bar{F}_D(\lambda) \text{ with } \int_0^\infty \bar{F}_D(\lambda) d\lambda = 1$	Normalized spectral radiant intensity of the excited donor [nm^{-1}], defined as the derivative of the emission intensity F with respect to the wavelength.
$\varepsilon_A(\lambda)$	Extinction coefficient of A [$M^{-1} cm^{-1}$]
n_{im}	Refractive index of the medium in-between the dyes
$g_{R A}$ or $g_{G D}$	Detection efficiency of the red detector (R) if only acceptor was excited or green detector (G) if donor was excited. Analogous for others.
$\sigma_{A G}$	Excitation cross-section for acceptor when excited with green laser. Analogous for the others.

Supplementary Table 6: Typical parameters for sample 1 and sample 2 that define R_0 (Seidel lab). For their determination see Online Methods section 4.

dye pairs	κ^2	n_{im}	$\Phi_{F,D}$	$\varepsilon_A [M^{-1} cm^{-1}]$	$J [cm^{-1} M^{-1} nm^4]$	$R_0 [\text{Å}]$
Atto550-Atto647N	2/3	1.40	0.765	150000	$5.180 \cdot 10^{15}$	62.6
Atto550-Alexa647	2/3	1.40	0.765	270000	$8.502 \cdot 10^{15}$	68.0

Supplementary Note 1: Further samples

Name	Base position (Linker), strand	Dyes (Donor/ Acceptor)	Sequence
3-lo	T 31(C6), D-strand	Alexa488 Tetrafluorophenyl ester/	5'- GAG CTG AAA GTG TCG AGT TTG TTT GAG TGT TTG TCT GG-3'
	T 31(C2), A-strand	Atto647N NHS	3'- CTC GAC T TT CAC AGC TCA AAC AAA CTC ACA AAC AGA CC-5' - biotin
3-mid:	T 23(C6), D-strand	Alexa488 Tetrafluorophenyl ester/	5'- GAG CTG AAA GTG TCG AGT TTG T TT GAG TGT TTG TCT GG-3'
	T 31(C2), A-strand	Atto647N NHS	3'- CTC GAC T TT CAC AGC TCA AAC AAA CTC ACA AAC AGA CC-5' -biotin
4-lo:	T 31(C6), D-strand	Alexa488 Tetrafluorophenyl ester/	5'- GAG CTG AAA GTG TCG AGT TTG TTT GAG TGT TTG TCT GG-3'
	T 31(C6), A-strand	Alexa594 NHS	3'- CTC GAC T TT CAC AGC TCA AAC AAA CTC ACA AAC AGA CC-5' - biotin
4-mid:	T 23(C6), D-strand	Alexa488 Tetrafluorophenyl Ester/	5'- GAG CTG AAA GTG TCG AGT TTG T TT GAG TGT TTG TCT GG-3'
	T 31(C6), A-strand	Alexa594 NHS	3'- CTC GAC T TT CAC AGC TCA AAC AAA CTC ACA AAC AGA CC-5' - biotin

Even for samples 3 and 4 the precision of the hi-samples, where all individual FRET efficiencies were in a sensitive range of the specific dye pairs, is very good (2 - 4 %). Moreover, the experimental and model values of the low- and hi-samples agree very well with each other (the deviations range between 2 and 10 %). This suggests that we do not have dye artifacts for all four FRET pairs. The results obtained for the different FRET pairs will be important in the future to judge key aspects of different fluorophore properties.

NHS: N-hydroxysuccinidylester (mixed isomers according to the manufacturer)
TFP: (tetrafluorophenyl) ester (pure isomer according to the manufacturer)

Supplementary Note 2: Time-resolved experiments

Global fit of the time-resolved polarized and magic angle fluorescence ensemble data

All polarization resolved fluorescence decay curves ($F_{VV}(t), F_{VH}(t)$) with the Polarizer / Analyzer settings (Vertical, V /Horizontal, H) of singly labeled molecules were studied in ensemble experiments in the Seidel lab by high-precision time correlated single-photon counting and were fitted jointly with corresponding magic angle (M) fluorescence decay $f_{VM}(t) = f(t)$. To reduce the number of parameters in the fits we used the so called homogenous approximation⁶. We assumed that de-excitation and depolarization of dyes are independent, i.e. in each donor de-excitation state dyes are characterized by the same set of depolarization times. For this case we can write model functions for the decay of the excited state population $f(t)$ and the fluorescence anisotropy $r(t)$:

$$f_{VV}(t) = f(t)[1 + 2r(t)] \quad (2.1)$$

$$f_{VH}(t) = f(t)[1 - r(t)] \quad (2.2)$$

$$\text{with } f(t) = \sum_i x_i e^{-t/\tau_i} \quad \text{and } r(t) = \sum_j b^{(j)} e^{-t/\rho_j}$$

Here, τ is the fluorescence lifetime and ρ is the depolarization times. x_i is (with $\sum_i x^{(i)} = 1$) the species fraction of molecules having the lifetime τ_i and the factor b_j is fraction of molecules having the depolarization time ρ_j where the fundamental anisotropy r_0 is given by $\sum_j b^{(j)} = r_0$ and the residual anisotropy is given by $b^{(3)} = r_\infty$. A maximum of three species for i and j were necessary to obtain satisfactory fits judged by χ^2_r .

To fit real experimental decays IRF, background and amplitudes of the VV , VH signals are accounted as:

$$F_{VV}(t) = F_0 \cdot IRF_{VV}(t) \otimes f_{VV}(t) + B_{VV} \quad (2.3)$$

$$F_{VH}(t) = g_{VV/VH} F_0 \cdot IRF_{VH}(t) \otimes f_{VH}(t) + B_{VH} \quad (2.4)$$

Where $g_{VV/VH}$ is a correction factor for a polarization dependent detection efficiency, F_0 - amplitude scaling factor, $IRF_{VV}(t)$, $IRF_{VH}(t)$ - instrument response functions and B_{VV} , B_{VH} - background values. The “ \otimes ” sign designates circular convolution.

The fit results for fluorescent signal in parallel and perpendicular polarization planes with respect to the vertically polarized excitation light with their rotation correlation times and amplitudes for D-only and A-only labeled DNA are presented in Supplementary Tables N2.1 and N2.2. The measured data and fitted curves with their weighted residuals are presented in the first column of the Supplementary Figure N2.1. Typical magic angle fluorescence decays are shown in the right column of the Supplementary Figure N2.1.

As expected¹, the amplitude b_l for the fast depolarization motion with ρ_l is approximately a factor 2 larger for dyes where the transition dipole moment is more perpendicular to the linker (disc case: Alexa 488 and Alexa594) than for dyes with a more parallel the transition dipole moment (cone case: Atto550, Atto647N and Alexa647) (compare Supplementary Figure 1 and Supplementary Table N2.2). Note that some dyes (e.g. Alexa488 and Alexa594) depolarize especially fast, because they have a large fraction of the fastest depolarization time such that $k_{rot} \gg k_{FRET}$ might be satisfied

for even higher FRET efficiencies. The depolarization of these dyes is best described by a disc model ².

Supplementary Table N2.1: Fluorescence lifetimes τ_i and their amplitudes x_i for all studied Donor-only (DO) and Acceptor-only samples (AO). The quality of the fit was judged by χ^2_r . [a,b]

Base position (Linker), strand	Dye [c]	Sample (DO or AO)	τ_1 [ns] (x_1)	τ_2 [ns] (x_2)	τ_3 [ns] (x_3)	$\langle \tau \rangle_x$ [ns]	χ^2_r [d]
T 31(C2), D-strand	Atto550	1-lo (DO), 2-lo (DO)	0.74 (0.03)	3.47 (0.59)	4.44 (0.38)	3.76	1.03
T 23(C2), D-strand	Atto550	1-mid (DO), 2-mid (DO)	0.86 (0.03)	3.54 (0.63)	4.59 (0.34)	3.81	1.02
T 19(C2), D-strand	Atto550	1-hi (DO), 2-hi (DO)	0.50 (0.04)	3.02 (0.30)	4.31 (0.66)	3.74	1.05
T 31(C2), A-strand	Atto647N	1-(AO), 3-(AO)	0.24 (0.04)	3.40 (0.52)	4.19 (0.44)	3.62	1.03
T 31 (C2), A-strand	Alexa647	2-(AO)	0.66 (0.05)	1.18 (0.90)	1.90 (0.05)	1.19	1.00
T 31(C6), D-strand	Alexa488	3-lo (DO)	0.36 (0.03)	2.37 (0.05)	4.11 (0.92)	3.91	1.03
T 23(C6), D-strand	Alexa488	3-mid (DO)	0.37 (0.04)	2.70 (0.04)	4.13 (0.92)	3.92	1.08
T 31 (C6), A-strand	Alexa594	4-(AO)	0.31 (0.03)	3.76 (0.64)	4.55 (0.33)	3.91	0.99

[a] in 20mM MgCl₂, 5mM NaCl, 5mM TRIS at pH 7.5 measurement buffer.

[b] typical errors: average lifetime: $\tau \pm 0.02$ ns. Three lifetime: shortest lifetime $\tau_1 \pm 20\%$ (with $x_1 \sim 15\%$), $\tau_2 \pm 10\%$ (with $x_2 \sim 25\%$), $\tau_3 \pm 3\%$ (with $x_3 \sim 15\%$).

[c] Spectral settings:

Atto550 (fluor. max 574 nm): excitation wavelength 552 nm, emission wavelength 580 nm (bandpass 5.4 nm).

Atto647N (fluor. max 664 nm): excitation wavelength 635 nm, emission wavelength 665 nm (bandpass 9.2 nm).

Alexa647 (fluor. max 665 nm): excitation wavelength 635 nm, emission wavelength 665 nm (bandpass 8.1 nm).

Alexa488 (fluor. max 525 nm): excitation wavelength 485 nm, emission wavelength 520 nm (bandpass 9.2 nm).

Alexa594 (fluor. max 617 nm): excitation wavelength 590 nm, emission wavelength 617 nm (bandpass 8.1 nm).

Note that the fluorescence lifetime analysis exhibited signatures of solvent relaxation. Therefore, we use wide bandpasses.

[d] χ^2_r was computed from a non-linear least squares fit of the corresponding model function to TCSPC data. Thus, χ^2_r refers to a single data set.

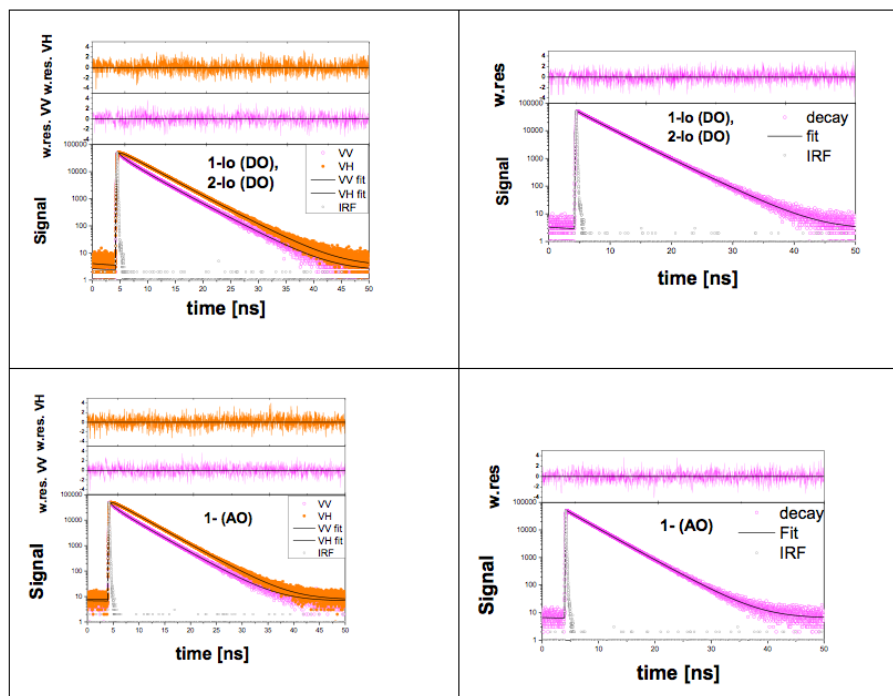
Supplementary Table N2.2: Rotation correlation times ρ_i with correspondent amplitudes b_i for Donor-only (DO) ($r_0=0.38$) and Acceptor-only (AO) ($r_0=0.38$) samples. The 1σ confidence range for the longest correlation time is indicated in square brackets. The fit model is described by eqs 2.1-2.2 with the model functions eqs. 2.3-2.4. The quality of the fit was judged by χ^2_r .

Base position (Linker),strand	dye	Sample (DO or AO)	ρ_1 [ns] (b_1)	ρ_2 [ns] (b_2)	ρ_3 [ns] (1σ conf.) ($b_3 = r_\infty$) [b]	χ^2_r [c]
T 31(C2), D-strand	Atto550	1-lo (DO), 2-lo (DO)	0.63 (0.14)	3.08 (0.16)	174 [97-540] (0.08)	1.04
T 23(C2), D-strand	Atto550	1-mid (DO), 2-mid (DO)	0.58 (0.12)	2.76 (0.15)	63 [50-86] (0.11)	1.01
T 19(C2), D-strand	Atto550	1-hi (DO), 2-hi (DO)	0.47 (0.10)	2.49 (0.16)	29.99 (0.13)	1.03
T 31(C2), A-strand	Atto647N	1-(AO), 3-(AO)	0.41 (0.14)	2.05 (0.17)	46 [37-62] (0.07)	1.01
T 31 (C2), A-strand	Alexa647 [a]	2 -(AO)	0.32 (0.09)	1.14 (0.23)	1e5 [125- ∞] (0.06)	0.99
T 31(C6), D-strand	Alexa488	3-lo (DO)	0.25 (0.22)	1.31 (0.12)	31 [24-42] (0.04)	1.03
T 23(C6), D-strand	Alexa488	3-mid (DO)	0.26 (0.22)	1.43 (0.12)	37 [31-46] (0.04)	1.04
T 31 (C6), D-strand	Alexa594	4-(AO)	0.46 (0.22)	1.88 (0.09)	77 [58-121] (0.07)	1.02

[a] Only VV, VH depolarization curves used for fitting in this case.

[b] Due to fluctuations in the G-factor determinations we have small systematic errors; i.e. $\rho_3 > 20$ ns and not the fitted value

[c] χ^2_r was computed from a non-linear least squares fit of the corresponding model function to. Thus, χ^2_r refers to a single data set.



Supplementary Figure N2.1: Left panels: Typical fluorescent signal in parallel and perpendicular polarization channels (magenta and orange) with the corresponding fits (black) for 1-lo (DO), 2-lo (DO), 1-(AO) samples with weighted residuals on the top. Right panels: the corresponding magic angle fluorescence decay curves with weighted residuals on the top. The fit results are displayed in Supplementary Tables N2.1 and N2.2 using fit procedure described by eqs 2.1-2.2 with the model functions eqs 2.3-2.4. The quality of the non-linear fit of the corresponding model function to TCSPC data was judged by χ^2_r . Thus, χ^2_r is a measure for the goodness of fit to a single data set.

Species average lifetime determination

Magic angle fluorescence decays were described with three fluorescence lifetimes τ_i and the species fractions x_i and thus species averaged lifetime $\langle \tau \rangle_x$ was calculated as:

$$\langle \tau \rangle_x = x_1 \tau_1 + x_2 \tau_2 + x_3 \tau_3 \tag{2.5}$$

Experimental deviations obtained during lifetime-based experiments

The lifetime-based measurements had a significantly lower precision and accuracy than intensity-based measurements. The following factors might be responsible for the observed deviations in the fluorescence lifetime-based FRET experiments:

1. The precision propagates differently for intensity based and time-resolved techniques. In intensity-based FRET measurements the relative error of a normalized donor-acceptor

distance changes less with increasing distance. The precision of time-resolved FRET measurements is highest for small DA distances (the minimum is $R_{DA}/R_0 \approx 0.7$) which were not the focus of this study⁷.

2. Time-resolved techniques strongly depend on a representative (chemically equivalent) Donor-only reference sample that is crucial for resolving large distances accurately.
3. If in the ensemble measurements the FRET sample contains also molecules, which are labeled with a donor, it becomes very difficult to resolve species with low FRET efficiencies.
4. The accuracy of time-resolved FRET measurements depends on an appropriate fit model. It is crucial to consider the heterogeneity of the donor lifetimes and dye-linker distributions (eq. 27 in ref. ⁶). Moreover, the analysis model should allow fitting a variable fraction of donor-only species, which was needed for all provided samples. Altogether, this results in complex fit models which are not widely used in the FRET community because they are difficult to implement in commercial software. In contrast, some groups analyzed the donor decays by a simple series of exponentials, which results in a systematic shift of the obtained FRET parameters.

Thus, all four effects in time-resolved FRET measurements contributed to the fact that the precision and accuracy of the distances recovered especially for all lo-samples was markedly lower than that of intensity-based methods.

In contrast, the FRET efficiencies and inter-dye distances of the 1-hi and 2-hi samples were recovered very accurately by the Seidel lab as predicted by Ref⁶ (Fig. 11), because the effects 1-3 do not apply anymore.

Supplementary Note 3: AV simulations to compute donor acceptor distances

The model for the double-stranded B-DNA is generated using the Nucleic Acid Builder version 04/17/2017 for Amber⁸ (see Figure 1, main text). For modelling the dye molecule, we use a geometrical approach that considers sterically allowed dye positions within the linker length from the attachment point with equal probability. This defines the accessible volume (AV)⁹. The dye molecules are modeled as ellipsoids (approximated by three radii; AV3-Model) and AVs are generated using the FPS software¹⁰. For the distance computation a dye pair specific Förster Radius is used; i.e., it is assumed that within the AV the dye molecule samples all positions isotropically, however, for a single excitation it is at a fixed position. Moreover, it is assumed that dye rotation is so fast, that all possible orientations are sampled during the fluorescence lifetime and thus the factor $\langle \kappa^2 \rangle = 2/3$ (isotropic coupling).

The boundary tolerance (called ‘allowed sphere’ in the FPS software) is used to ignore small residues that are fixed in the PDB-model, but flexible in solution. The larger this value, the larger the structural parts that are ignored for the AV generation. The labelling position is the C7 of the thymine (the C-atom of the thymine’s methyl group). All mean geometric dyes parameters are estimated with ChemDraw software (see Supplementary Table N3.1). Further used parameters are: Boundary tolerance 0.5, accessible volume grid (rel.) 0.2; Min. grid [Å] 0.4, Search nodes: 3 and E samples: 200.

Supplementary Table N3.1: Recommended dye parameters for the AV simulations with AV3-model.

	linker length [Å]	linker width [Å]	R1 [Å]	R2 [Å]	R3 [Å]
dT-C6-Alexa488	20.5	4.5	5.0	4.5	1.5
dT-C2-Atto550	20.4	4.5	7.1	5.0	1.5
dT-C6-Alexa594	20.0	4.5	8.1	3.2	2.6
dT-C2-Alexa647	21.0	4.5	11.0	4.7	1.5
dt-C2-Atto647N	20.4	4.5	7.2	4.5	1.5

Error estimation. For each sample the distances between mean dye positions (R_{MP}^{model}) and expected experimentally observed apparent distance $R_{(E)}^{model}$ are calculated (see Supplementary Table 4). The error for the model distances is estimated by varying the linker lengths (from 10 to 21 Å), linker width (from 4.0 to 5.0 Å), the dye model (single sphere with the radius 6 Å (AV1 model) and ellipsoid with three radii R1=7.1 Å, R2=4.5 Å and R3=1.8 Å (AV3 model) and the boundary tolerance between dye and DNA (0.5 and 1.5 Å). The standard deviation of all DA distances computed by FPS was used as error.

Supplementary Note 4: FRET efficiency measurements and distance determinations in more complex systems, e.g. proteins.

The described determination of FRET efficiencies and their transformation into distances is fully generalizable to more complex systems like protein samples. However, uncertainties can arise from insufficient dynamic averaging of dye position and orientation, which might be caused by static or dynamic site specific dye quenching as well as transient interactions between the dye molecule and its local environment. This can (and should) be tested for each dye pair by measuring the time-resolved anisotropies of donor-acceptor labelled samples. As a result of such tests, dye pairs with insufficient dynamic averaging (a combined anisotropy of donor and acceptor > 0.2) can either be removed from the analysis¹¹ or described using different dye models¹²⁻¹⁴ (see also Online Methods). If this is done, the described error analysis is also fully transferable to protein systems. Note that the determined distance uncertainties (Fig. 5 and Online Methods) already include an estimated error for insufficient dynamic averaging.

Significant challenges arise from the need to label proteins with both donor and acceptor dyes. In systems where *intermolecular* distances are required, e.g. between different polypeptides (exchangeable homo dimers or hetero dimers), or between a protein and its bound DNA substrate, a single unique site on the protein for dye attachment is sufficient. In the case of homo dimers, the samples with two donors or two acceptors (about 25 % each) that will remain after the exchange, can be selected out following the ALEX procedure described in the main text. A single unique reaction site is often achieved using a unique reactive cysteine residue coupling to a maleimide-derivative of the chosen dye. However, this requires that other native, reactive cysteines are mutated (often to serine) and that the resulting ‘cys-lite’ protein remains active. For proteins with native reactive cysteines that cannot be removed by mutagenesis, incorporation of an unnatural amino acid carrying a completely orthogonal chemistry for dye attachment, or incorporation of specific peptide tags that can be site specifically labelled using enzymatic dye transfer reactions¹⁵ are possible strategies.

Intramolecular FRET measurements can be more challenging, given the need to put both the donor and acceptor on the same molecule. The stochastic labelling of double cysteine mutants, leads to at least four labelled populations (AD, DA, DD, AA). A key strength of the presented ALEX method is the ability to separate the FRET species (DA, AD) from donor-only (DD) or acceptor-only (AA) labelled species. The difference between mixed populations of donors attached at two different positions (i.e. DA vs AD) can be an issue for the width of the measured FRET distribution but becomes smaller with increasing linker lengths and presumably depends on the spatial separation of the dyes. For linkers comparable to the ones used in this study the standard deviation was previously determined to be ~ 0.8 Å (Ref⁶, Fig. 13). For some systems the differential reactivity of the two cysteines can be exploited to enable a biased labelling of the system¹⁶. Even a moderate (threefold) difference in local reactivity can yield highly specific double-labeling with sequential addition of the maleimide-dye derivatives. Alternatively, a combination with unnatural amino acids with mutually orthogonal reactivities can be incorporated¹⁷ (for a review see ref¹⁸).

Future work will involve a comparative blind study using protein samples. This will be an even larger study and the next step towards having FRET-based structures in the PDB. Yet it is important to note that the current study is essential as the pre-requisite to a future protein study, as it e.g. presents all the procedures unified across the field for the first time.

Supplementary Note 5: $R_{(E)}$ to R_{MP} conversion

For the conversion between $R_{(E)}$ and R_{MP} we distinguish two cases, a known and unknown environment of the dye molecule:

Case 1, the local environment of the dye molecule is known. Here, we use average (apparent) distances from different data-sources, i.e., $R_{(E)}$ from experiment, and R_{MP} from coarse-grained-structural modeling to generate conversion functions. Typically, we use coarse-grained simulations to approximate accessible volumes (AVs) for biomolecules¹⁰. These AVs are translated / rotated and the average apparent DA distance ($R_{(E)}$) and the distance R_{MP} are calculated, which introduces noise. The resulting conversion tables are approximated by third order polynomials. Here we used the AVs for the samples 1,2,3,4 low and high FRET correspondingly. For the polynomial $R_{MP} = (a_0 + a_1 R_{(E)} + a_2 R_{(E)}^2 + a_3 R_{(E)}^3)$ the coefficients are given in the Supplementary Table N5.1 for all FRET pairs.

Note that the conversion functions are specific for the chosen dye pair because they depend on the Förster Radius of the FRET pair and the used dye parameters for the AV simulation. The differences between AVs in different molecular environments (DNA or protein) become smaller the less restricted the dye is. The offset of the conversion function depends on the size of the dye spheres and the linker lengths.

Supplementary Table N5.1. Conversion polynomial for $R_{MP} = (a_0 + a_1 R_{(E)} + a_2 R_{(E)}^2 + a_3 R_{(E)}^3)$ using the dye pair specific R_0 and specific AVs of the samples 1, 2, 3 and 4, respectively. Note that these polynomials are only valid for this specific geometry and dyes.

FRET pair	R_0 [Å]	a_0 [Å]	a_1	a_2 [Å] ⁻¹	a_3 [Å] ⁻²
Atto550-Atto647N	62.6	-41.8	2.13	$-0.92 \cdot 10^{-2}$	$2.40 \cdot 10^{-5}$
Atto550-Alexa647	68.0	-40.3	1.99	$-0.74 \cdot 10^{-2}$	$1.67 \cdot 10^{-5}$
Alexa488-Atto647N	49.3	-53.8	2.83	$-1.89 \cdot 10^{-2}$	$6.17 \cdot 10^{-5}$
Alexa488-Alexa594	57.0	-43.9	2.24	$-1.02 \cdot 10^{-2}$	$2.48 \cdot 10^{-5}$

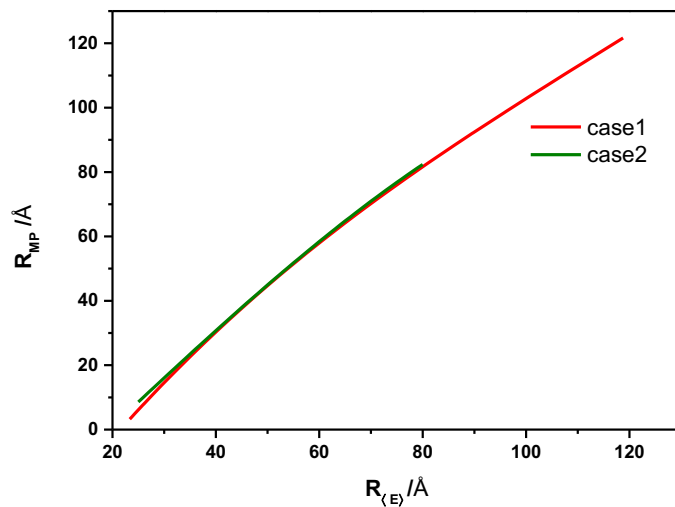
Case 2, the local environment of the dye molecule is not known. Here, we make the most general assumption that the AV can be approximated by a sphere with its radius estimated from the size of the dye and linker length (slightly smaller than the dye and linker length). This allows us to estimate the conversion of $R_{(E)}$ to R_{MP} by performing Monte Carlo simulations¹⁹. In the Monte Carlo simulation, we place 10,000 positions uniformly distributed within a sphere of 18 Å radius for both dyes. For a given distance of the mean position of these spheres (R_{MP}) we calculate the respective FRET efficiencies via the Förster formula with an orientation factor of $\kappa^2 = 2/3$. The mean of these values is an unbiased estimate for the expected value of the FRET efficiency. We vary the mean position distance from 0.5 R_0 to 1.5 R_0 and fit the resulting means with a third order polynomial (coefficients a_0 , a_1 , a_2 and a_3). For convenience the conversion coefficients for a large range of used Förster radii were determined and given here in Supplementary Table N5.2.

The equivalence of both approaches is demonstrated in Supplementary Figure N5.1 for the dye pair Atto550-Atto647N.

Supplementary Table N5.2.: Coefficients for the conversion polynomials $R_{(E)}$ to R_{MP} for case 2. These are valid for the specified Förster radius R_0 .

R_0 [Å]	a_0 [Å]	a_1	a_2 [Å] ⁻¹	a_3 [Å] ⁻²
50	-33.6	1.65	$3.25 \cdot 10^{-3}$	$-7.26 \cdot 10^{-5}$
51	-34.0	1.70	$1.55 \cdot 10^{-3}$	$-5.68 \cdot 10^{-5}$
52	-33.0	1.64	$2.25 \cdot 10^{-3}$	$-5.85 \cdot 10^{-5}$
53	-31.7	1.57	$2.93 \cdot 10^{-3}$	$-5.91 \cdot 10^{-5}$
54	-32.8	1.64	$1.27 \cdot 10^{-3}$	$-4.65 \cdot 10^{-5}$
55	-32.0	1.61	$1.43 \cdot 10^{-3}$	$-4.46 \cdot 10^{-5}$
56	-30.0	1.51	$2.78 \cdot 10^{-3}$	$-4.98 \cdot 10^{-5}$
57	-30.0	1.51	$2.19 \cdot 10^{-3}$	$-4.39 \cdot 10^{-5}$
58	-30.0	1.52	$1.73 \cdot 10^{-3}$	$-3.91 \cdot 10^{-5}$
59	-27.7	1.42	$3.03 \cdot 10^{-3}$	$-4.37 \cdot 10^{-5}$
60	-29.1	1.49	$1.55 \cdot 10^{-3}$	$-3.42 \cdot 10^{-5}$
61	-27.5	1.42	$2.36 \cdot 10^{-3}$	$-3.67 \cdot 10^{-5}$
62	-26.5	1.37	$2.77 \cdot 10^{-3}$	$-3.74 \cdot 10^{-5}$
63	-27.3	1.42	$1.67 \cdot 10^{-3}$	$-2.99 \cdot 10^{-5}$
64	-25.6	1.35	$2.56 \cdot 10^{-3}$	$-3.28 \cdot 10^{-5}$
65	-26.1	1.38	$1.88 \cdot 10^{-3}$	$-2.83 \cdot 10^{-5}$
66	-26.4	1.39	$1.42 \cdot 10^{-3}$	$-2.50 \cdot 10^{-5}$
67	-24.9	1.33	$2.07 \cdot 10^{-3}$	$-2.69 \cdot 10^{-5}$
68	-24.1	1.30	$2.27 \cdot 10^{-3}$	$-2.68 \cdot 10^{-5}$
69	-24.2	1.31	$1.90 \cdot 10^{-3}$	$-2.39 \cdot 10^{-5}$
70	-23.3	1.28	$2.29 \cdot 10^{-3}$	$-2.49 \cdot 10^{-5}$
71	-24.4	1.33	$1.30 \cdot 10^{-3}$	$-1.95 \cdot 10^{-5}$
72	-23.4	1.29	$1.80 \cdot 10^{-3}$	$-2.11 \cdot 10^{-5}$
73	-22.6	1.27	$1.86 \cdot 10^{-3}$	$-2.04 \cdot 10^{-5}$
74	-23.0	1.28	$1.53 \cdot 10^{-3}$	$-1.84 \cdot 10^{-5}$
75	-22.4	1.26	$1.62 \cdot 10^{-3}$	$-1.80 \cdot 10^{-5}$
76	-21.8	1.24	$1.70 \cdot 10^{-3}$	$-1.77 \cdot 10^{-5}$
77	-21.6	1.24	$1.58 \cdot 10^{-3}$	$-1.66 \cdot 10^{-5}$
78	-21.8	1.25	$1.28 \cdot 10^{-3}$	$-1.47 \cdot 10^{-5}$
79	-21.2	1.23	$1.44 \cdot 10^{-3}$	$-1.49 \cdot 10^{-5}$
80	-21.2	1.24	$1.32 \cdot 10^{-3}$	$-1.41 \cdot 10^{-5}$
81	-20.5	1.22	$1.43 \cdot 10^{-3}$	$-1.39 \cdot 10^{-5}$
82	-20.3	1.21	$1.40 \cdot 10^{-3}$	$-1.34 \cdot 10^{-5}$
83	-20.5	1.22	$1.17 \cdot 10^{-3}$	$-1.20 \cdot 10^{-5}$
84	-19.8	1.20	$1.36 \cdot 10^{-3}$	$-1.24 \cdot 10^{-5}$
85	-20.3	1.22	$0.96 \cdot 10^{-3}$	$-1.05 \cdot 10^{-5}$
86	-19.5	1.19	$1.20 \cdot 10^{-3}$	$-1.10 \cdot 10^{-5}$
87	-19.1	1.18	$1.22 \cdot 10^{-3}$	$-1.08 \cdot 10^{-5}$
88	-19.0	1.18	$1.15 \cdot 10^{-3}$	$-1.02 \cdot 10^{-5}$
89	-19.0	1.18	$1.04 \cdot 10^{-3}$	$-0.95 \cdot 10^{-5}$
90	-18.8	1.18	$0.99 \cdot 10^{-3}$	$-0.91 \cdot 10^{-5}$

We tested that the polynomials derived using case 1 or case 2 yield almost identical conversion functions (Supplementary Figure N5.1).



Supplementary Figure N5.1. Polynomial $R_{MP} = a_0 + a_1 R_{(E)} + a_2 R_{(E)}^2 + a_3 R_{(E)}^3$ for the dye pair Atto550-Atto647N with AVs for DNA (case 1: $R_0 = 62.6 \text{ Å}$) and with the approximation by a sphere (case 2: $R_0 = 62.0 \text{ Å}$). Interpolated points in steps of 1 Å .

Supplementary Note 6: Error propagation

Based on the measurements of sample 1-lo and 1-hi, we performed an error propagation using $\Delta E = 0.033$ (which was the precision for these two best investigated samples). *Figure 5* follows from the following distance uncertainty:

$$\Delta R(R_0, \Delta R_0, \Delta E | R) = \sqrt{\left(\frac{\partial R(R_0, E)}{\partial R_0} \cdot \Delta R_0\right)^2 + \left(\frac{\partial R(R_0, E)}{\partial E} \cdot \Delta E\right)^2} = \sqrt{\left(\frac{R}{R_0} \cdot \Delta R_0\right)^2 + \left(\frac{1}{6} \left(1 + \left(\frac{R}{R_0}\right)^6\right)^2 \left(\frac{R}{R_0}\right)^{-5} R_0 \cdot \Delta E\right)^2} \quad (6.1)$$

In the following, we performed more detailed error propagation with disentangled error sources. We estimate the uncertainties of all quantities separately and propagate them towards an uncertainty in the distance. The overall uncertainty in the distance is given by:

$$\Delta R(R_0, \Delta R_0, \gamma, \Delta \gamma, \langle F \rangle, \Delta I_{Dem|Dex}^{(BG)}, \Delta I_{Aem|Dex}^{(BG)}, \Delta \beta, \Delta \alpha | R) = \sqrt{\Delta R_{R_0}^2 + \Delta R_{\gamma}^2 + \Delta R_{bgD}^2 + \Delta R_{bgA}^2 + \Delta R_{\alpha}^2 + \Delta R_{\delta}^2} \quad (6.2)$$

with the following error contribution for the Förster radius:

$$\Delta R_{R_0}(R) = R \frac{\Delta R_0}{R_0} \quad (6.3)$$

And the following error contribution for the gamma factor:

$$\Delta R_{\gamma}(R) = \frac{R}{6} \cdot \frac{\Delta \gamma}{\gamma} \quad (6.4)$$

And the following error contribution for the background in the donor channel after donor excitation:

$$\Delta R_{bgD}(R) = \frac{R}{6} \left[\gamma \left(1 + \left(\frac{R_0}{R}\right)^6\right) + \alpha \left(1 + \left(\frac{R}{R_0}\right)^6\right) \right] \cdot \frac{\Delta I_{Dem|Dex}^{(BG)}}{\langle F \rangle} \quad (6.5)$$

And the following error contribution for the background in the acceptor channel after donor:

$$\Delta R_{bgA}(R) = -\frac{R}{6} \left(1 + \left(\frac{R}{R_0}\right)^6\right) \cdot \frac{\Delta I_{Aem|Dex}^{(BG)}}{\langle F \rangle} \quad (6.6)$$

And the following error contribution for the direct excitation factor of the acceptor with the green laser:

$$\Delta R_{\delta}(R) = -\frac{R}{6} \beta \left(1 + \left(\frac{R}{R_0}\right)^6\right) \cdot \Delta \delta \quad (6.7)$$

And the following error contribution for the leakage factor of donor fluorescence in the acceptor channel:

$$\Delta R_{\alpha}(R) = -\frac{R}{6} \frac{1}{\gamma} \left(\frac{R}{R_0}\right)^6 \cdot \Delta \alpha \quad (6.8)$$

Please note that for determination of background we set $\gamma = \beta = 1$ and $\alpha = \delta = 0$. This represents the ideal values. Further parameters and uncertainties are taken from the reference lab: $\Delta \gamma / \gamma = 0.1$, $\langle F \rangle = 50$, $\Delta I_{Dem|Dex}^{(BG)} = 1$, $\Delta I_{Aem|Dex}^{(BG)} = 1$, $\Delta \delta / \delta = 0.1$, $\Delta \alpha / \alpha = 0.1$, $\Delta R_0 = 0.07$. See Online Methods, Section 1 and 3 for the nomenclature and details on the Förster radius. $\langle F \rangle$ is the average sum of the corrected donor and acceptor fluorescence.

The above error analysis is based on R_{DA} and may be further propagated to the apparent donor-acceptor distance $R_{(E)}$ and the distance between the mean positions of the dyes, R_{MP} , when the above model assumption of a freely rotating and diffusing dye is applied. This becomes very involved and does not show significant deviations from *Figure 5* in the main text.

Supplementary Note 7: MD simulations

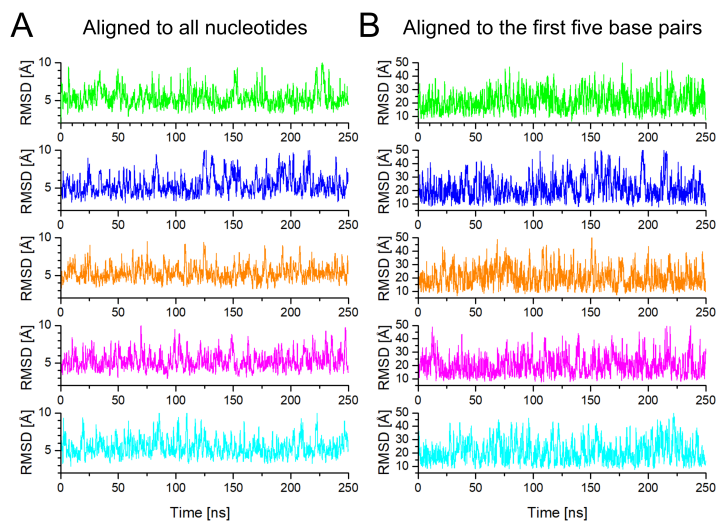
While the analysis in this paper used a static model for the double-stranded DNA structure, there is plenty of experimental and theoretical evidence that DNA is not completely rigid²⁰⁻²³. Therefore, we performed Molecular dynamics (MD) simulations of the DNA molecule to explore its rigidity using the latest force fields which were reported to be consistent with experimental observables of the conformational flexibility of dsDNA.

The all-atom MD simulations were performed with the Amber16 suite of programs²⁴ using the bsc1 force field⁸. The initial structure of the B-DNA molecule, which was generated by 3D-DART (see main text), was placed in an octahedral box of TIP3P water molecules²⁵, such that the distance between the edge of the water box and the closest DNA atom was at least 11 Å. MgCl₂ and NaCl were added to achieve concentrations of 20 mM and 10 mM, respectively. For Na⁺ and Cl⁻, the parameters by Joung and Cheatham²⁶ were used, while for Mg²⁺ the parameters by Li et al.²⁷ were used.

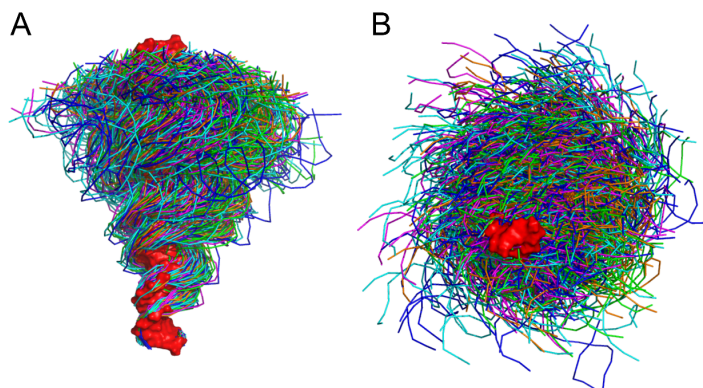
Each system was then prepared based on a protocol used earlier²⁸. The simulation system was minimized by 200 steps of steepest descent and subsequently 50 steps of conjugate gradient minimization. The minimized system was heated from 100 to 300 K over 50 ps, and subsequently the solvent density was adjusted for 150 ps by NPT-MD simulation. During the previous two steps, harmonic force restraints were applied on all solute atoms with force constants of 5 kcal mol⁻¹ Å⁻². These harmonic force restraints were gradually reduced to 1 kcal mol⁻¹ Å⁻² during 250 ps of NVT-MD simulation. This step was followed by 50 ps of NVT-MD simulation without positional restraints. Subsequently, we performed five independent MD simulations of 250 ns length each. The time step for all MD simulations was 2 fs. Coordinates were extracted from the simulations every 20 ps. The traces of the RMSD as a function of calculation time show that the calculations have converged (Supplementary Figure N.7.1).

We used the FPS program¹⁰ to calculate FRET efficiencies for the structural ensemble of the MD simulation, i.e. for each structure the AVs with the spatial dye (D and A) distributions is calculated and the average FRET efficiency is computed.

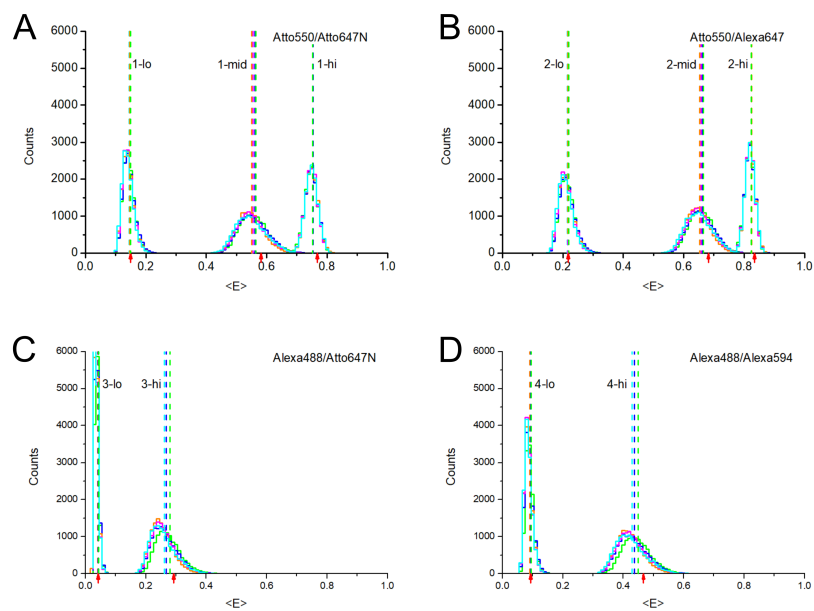
The ensembles from the MD simulations suggest that the DNA is not completely rigid, but exhibits some bending motion (Supplementary Figure N.7.2). The obtained distributions of FRET efficiencies show that the ensembles from the MD simulations yield comparable, but slightly lower mean FRET efficiencies and thus longer distances than for the static model (Supplementary Figure N.7.3, Supplementary Table N.7.1).



Supplementary Figure N.7.1: RMSD calculated over the simulation time for the five simulations performed. The RMSD was calculated with respect to the straight DNA molecules, which served as starting structure, considering all atoms for the calculation after aligning the structures to the straight DNA using all atoms (A) and only the first five base pairs (B). For better visibility, the lines were smoothed with a sliding average window of length 200 ps.



Supplementary Figure N.7.2: Structural ensembles from the MD simulations. The starting structure (red surface representation) was overlaid with conformations extracted from the MD simulations using the first 5 base pairs of the DNA. The five independent MD simulations are shown as differently colored ribbons (green, blue, orange, magenta, and cyan). For visibility, snapshots extracted every 2 ns were used for this representation. A: Side view; B: Top view.



Supplementary Figure N.7.3: Distribution of FRET efficiencies calculated for the conformation extracted from the MD simulations for the four samples (A: Atto550/Atto647N, B: Atto550/Alexa647, C: Alexa488/Atto647N, D: Alexa488/Alexa594). The five colors (green, blue, orange, magenta, and cyan) correspond to the five independent MD simulations performed. Vertical dashed lines indicate the mean of the distribution, while the red arrows below the X-axis indicate the values calculated for the starting structure.

Supplementary Table N.7.1: Comparison of FRET efficiencies $\langle E \rangle_{dyn}$ and corresponding DA distances $R_{(E)}^{(dyn)}$ calculated from the five MD simulations to the values from experiments ($\langle E \rangle_{exp}$, $R_{(E)}^{(exp)}$) and the static model with $\langle E \rangle_{static}$.

Sample	$\langle E \rangle_{dyn}$ ^[a]	$\langle E \rangle_{static}$ ^[b]	$\langle E \rangle_{exp}$ ^[c]	$R_{(E)}^{(dyn)}$ [Å] ^[d]	$R_{(E)}^{(exp)}$ [Å] ^[e]
Atto550/Atto647N					
1-lo	0.15	0.15	0.15 ± 0.02	83.9	83.4 ± 2.5
1-mid	0.56	0.58	0.56 ± 0.03	60.3	60.3 ± 1.3
1-hi	0.75	0.77	0.76 ± 0.02	51.9	51.7 ± 0.9
Atto550/Alexa647					
2-lo	0.22	0.22	0.21 ± 0.04	84.2	85.4 ± 3.4
2-mid	0.66	0.68	0.60 ± 0.05	61.0	63.7 ± 2.3
2-hi	0.82	0.83	0.78 ± 0.03	52.6	55.1 ± 1.6
Alexa488/Atto647N					
3-lo	0.04	0.04	0.04 ± 0.02	83.1	89.5 ± 12.3
3-mid	0.27	0.29	0.24 ± 0.04	58.4	60.1 ± 2.3
Alexa488/Alexa594					
4-lo	0.09	0.09	0.13 ± 0.06	83.5	79.6 ± 6.2
4-mid	0.44	0.47	0.41 ± 0.04	59.5	60.7 ± 1.7

[a] Calculated as average over the five simulations (the standard deviation is in all cases below 0.008).

[b] Calculated for the static starting structure.

[c] From measurements (cf. Supplementary Table 4).

[d] Calculated from $\langle E \rangle_{dyn}$ using Formula (5) in the main text. The SD is not significant (determined by an error propagation from [a]).

[e] Calculated from experiments (cf. Supplementary Table 4).

Supplementary Note 8: Description of setups and analysis software
(in alphabetic order)

Birkedal lab (TIRF)

Single-molecule FRET experiments were performed on surface-immobilized molecules using a prism-based total internal reflection microscope with a set up similar to Supplementary Figure 4b. About 5 pM labeled molecules were immobilized inside a coverslide chamber and imaged using alternating laser excitation with 532 and 648 nm diode lasers (Cobolt) or with 514 and 630 nm lasers (Coherent). Fluorescence from the donor and acceptor fluorophores was spatially separated using a wedge mirror (Chroma Technology Corp.) and detected with two color channels onto an EMCCD camera (iXON 3 897, Andor). Details of the experimental setup and immobilization procedures are published elsewhere²⁹.

Movies were recorded with a 200 ms integration time per frame and analyzed using the iSMS software³⁰. The newest version of the software is available at www.isms.au.dk.

Bowen lab (TIRF)

Samples were imaged using a prism-based Total Internal Reflection Fluorescence microscope constructed on an IX71 base with a 60x, 1.2 NA water-immersion objective (Olympus, Center Valley, PA)³¹. Alternating laser excitation, with mechanical shutters (Uniblitz, Rochester, NY), was used to confirm the presence of both a donor and acceptor dye in all molecules used for analysis. Samples were excited with: a laser diode at 635 nm (Newport Corporation, Irvine, CA) for Alexa 647 and Atto 647N; a diode pumped solid-state laser at 532 nm (Newport Corporation, Irvine, CA) for Atto 550; or a laser diode at 473 nm (Photop Technologies Inc. Chasworth, Ca) for Alexa 488. Emission from donor and acceptor was separated using an Optosplit ratiometric image splitter (Cairn Research Ltd, Faversham UK). For experiments with Atto 550 and Alexa 647 (or Atto 647N), we used a 645 nm dichroic mirror with a 585/70 band pass filter for the donor channel and a 670/30 band pass filter for the acceptor channel. For experiments with Alexa 488 and Atto 647N, we used a 593 nm dichroic mirror with a 550/100 band pass filter for the donor channel and a 700/75 band pass filter for the acceptor channel (all filters from Chroma, Bellows Falls, VT). The replicate images were relayed to a single iXon DU-897 EMCCD camera (Andor Technologies, Belfast, UK) at a frame rate of 10 Hz.

Data was processed in home written MATLAB scripts to cross-correlate the replicate images and extract time traces for diffraction limited spots with intensity above baseline³². Single molecules were verified by selecting only events showing single step photobleaching to baseline. The γ correction was individually calculated for each selected molecule based upon the relative changes in intensities before and after the photobleaching event.

Cordes Lab (confocal)

Measurements were performed on a confocal setup, as shown in Supplementary Figure 3, but with the addition of a fiber coupling between the laser combining dichroic mirror DM1 and the second dichroic mirror DM2 to improve and clean the beam profile³³.

Elements used were: ZET532/10x (Chroma/AHF) and ZET640/10x (Chroma/AHF) laser clean-up filter (right after Laser 532 and 640 nm); polarization maintaining single-mode fiber P3-488PM-FC-2 (Thorlabs); DM2: Dual line beam splitter ZT532/640rpc (Chroma/AHF); DM3: laser-laser beam splitter H643 LPXR (AHF); FG: BrightLine HC 582/75 (Semrock/AHF); FR: Longpass 647 LP Edge Basic (Semrock/AHF); Objective: Super achromat objective UPLSAPO60XW (Olympus); Detectors: SPAD SPCM-AQRH-64 (Excelitas); Pinholes: 50 μ m; Laser power at sample: \approx 60 μ W for 532 nm and \approx 25 μ W for 640 nm; Beam diameter \approx 12 mm.

Laser-APD synchronization and readout is performed with NI-Card PCI-6602 (National Instruments) and a LabView (LabVIEW 2009) based home written software³³.

Analysis was also done with a LabView based home written software.

Craggs lab (confocal)

Setup is similar to Supplementary Figure 3, with the following specifications: Lasers used are 515 nm and 635 nm – LuxX plus, precoupled (No DM₁). DM₂ is a Chroma ZT532/640rpc excitation dichroic. The objective O is a Olympus x60 objective UPLSAPO 60XO (WD = 0.17 mm). The lens L is a Edmond Optics 49793 (50 mm focal length). The pinhole PH is a 20 μ m (Newport PNH-20). The dichroic DM₃ is a 640 nm longpass (Chroma NC395323 – T640lpxr). The F_G is a Semrock: FF01-582/75-25. The F_R a Semrock: FF01-679/41-25. The APD an Excelitas SPCM-AQRH-14.

The following description is from Bennet et al.³⁴:

smFRET data were acquired using a custom built confocal microscope and alternating laser excitation. Two diode lasers (515 nm and 635 nm – LuxX plus) were directly modulated (100 us, duty cycle 45%) and combined into an optical fibre. The output beam was collimated and then cropped to 2.5 mm diameter by an iris. The beam was directed into the back of the objective (Olympus UPLSAPO 60 \times NA = 1.35 oil immersion) using a dichroic mirror (Chroma ZT532/640 rpc 3 mm) with the fluorescence emission collected by the same objective, focussed onto a 20 μ m pinhole and then split (dichroic mirror: Chroma NC395323 – T640lpxr) for detection by two avalanche photodiodes (SPCM-AQRH-14 and SPCM-NIR-14, Excilias). Photon arrival times were recorded by a national instruments card (PCIe-6353), with the acquisition controlled using custom software (LabView 7.1).

Gratton lab (confocal)

The measurements were done on a modified Olympus FV1000 laser scanning confocal microscope. It is similar to Supplementary Figure 3. Our excitation source was a 20 MHz supercontinuum laser (SC390, Fianium Inc). A filter-wheel with eight interference bandpass filters was used to select desired excitation wavelengths. In our measurements, one set data was collected with the excitation from 530-550nm and the emission from 560-620nm. The other set data was collected with the excitation from 483-493nm and the emission from 505-525nm. An Olympus60 \times water objective (Olympus UPlanSApo, NA=1.2) was used to focus the laser beam and collect the emission signal.

The internal PMT was modified to send the signal out to a FastFLIM system (ISS Inc), which was synchronized with the 20MHz frequency output from the laser.

Data was then collected and analyzed by SimFCS (available from <http://www.lfd.uci.edu/>).

Ha lab (TIRF)

Measurements were done on a setup similar to Supplement Figure 4. Instead of using lenses and dichroic mirrors in the excitation pathway to combine the lasers, half-wave plates and a polarizing beam splitter cube were used. The collected fluorescence then passes a slit as shown, and is split with a dichroic and redirected through a lens using only mirrors, so that the two images are put beside each other on the camera chip.

Dichroics in detection: FF640-FDi01-25×36 (Semrock). Filters in detection: BLP02-561R-25 (F1, Semrock) and ZET633TopNotch (F2, Chroma). Objective: water immersion, 60 ×/1.2 NA (Olympus). Camera: EMCCD (iXon 897, Andor). Lasers: 532 nm (Compass 315M, Coherent) and 633 nm (06-MLD, Cobolt).³⁵

Data were analyzed by custom-made MatLab codes.

Hendrix lab (confocal)

Our multi-parameter fluorescence detection setup equipped with pulsed interleaved excitation is conceptually identical to the confocal microscope presented in Supplementary Figure 3. Emission from a pulsed 483-nm laser diode (LDH-P-C-470, Picoquant, Berlin, Germany) was cleaned up (Chroma ET485/20x, F49-482, AHF Analysentechnik, Tübingen, Germany), emission from a 635-nm laser diode (LDH-P-C-635B, Picoquant) was cleaned up (Chroma z635/10x, Picoquant) and both lasers were alternated at 26.67 MHz (PDL 828 Sepia2, Picoquant), delayed ~18-ns with respect to each other and combined via a 483-nm-reflecting dichroic mirror in a single-mode optical fiber (coupler: 60FC-4-RGBV11-47, fiber: PMC-400Si-2.6-NA012-3-APC-150-P, Schäfter und Kirchhoff GmbH, Hamburg, Germany). After collimation (60FC-L-4-RGBV11-47, SuK GmbH), the linear polarization was cleaned up (Codixx VIS-600-BC-W01, F22-601, AHF) and the light was reflected on a 3-mm thick excitation polychroic mirror (Chroma zt470-488/640rpc, F58-PQ08, AHF) upward and into the back port of the microscope (IX70, Olympus Belgium NV, Berchem, Belgium) via two mirrors and upward to the sample (3-mm thick Full Reflective Ag Mirror, F21-005, AHF, mounted in a TIRF Filter Cube for BX2/IX2, F91-960, AHF) to the objective (UPLSAPO-60XW, Olympus). Sample emission was transmitted focused through a 75- μ m pinhole (P75S, Thorlabs, Munich, Germany) via an achromatic lens (AC254-200-A-ML, Thorlabs), collimated again (AC254-50-A-ML, Thorlabs) and spectrally split (Chroma T560lpxr, F48-559, AHF). The blue range was filtered (Chroma ET525/50m, F47-525, AHF) and polarization was split (PBS251, Thorlabs). The red range was also filtered (Chroma ET705/100m, AHF) and polarization was split (PBS252, Thorlabs). Photons were detected on four avalanche photodiodes (Perkin Elmer or EG&G SPCM-AQR12/14), which were connected to a time-correlated single photon counting (TCSPC) device (SPC-630, Becker & Hickl GmbH, Berlin, Germany) over a router (HRT-82,

Becker & Hickl) and power supply (DSN 102, Picoquant). Signals were stored in 12-bit first-in-first-out (FIFO) files.

All analyses of experimental data were performed in the software package PAM³⁶. The software is available as source code, requiring MATLAB to run, or as pre-compiled standalone distributions for Windows or MacOS at <http://www.cup.uni-muenchen.de/pc/lamb/software/pam.html> or hosted in Git repositories under <http://www.gitlab.com/PAM-PIE/PAM> and <http://www.gitlab.com/PAM-PIE/PAMcompiled>. Sample data is provided under <http://www.gitlab.com/PAM-PIE/PAM-sampled>. A detailed manual is found under <http://pam.readthedocs.io>.

Hohlbein lab (TIRF)

Our setup is conceptually identical to the TIRF microscope presented in Supplementary Figure 4 (for TIRF)³⁷. For excitation, we used a fibre-coupled laser engine (Omicron, Germany) equipped with four lasers of different wavelengths (405 nm, 473 nm, 561 nm, and 642 nm). A home-written LabVIEW program independently controlled the laser intensities and triggered the camera. The single mode fibre generated a Gaussian shaped beam profile and a point source output at the other end of the fibre. The divergent light is collimated ($f = 100$ mm, Thorlabs, Germany) and a second lens focuses ($f = 200$ mm, Thorlabs, Germany) the light back into the back focal plane of a 100x NA 1.49 TIRF objective (Nikon, Japan). A polychroic mirror (zt405/473/561/640rpc, Chroma, USA) and a multibandpass filter (zet405/473/561/640m, Chroma, USA) are used to block any laser light in the emission path. After spatial filtering of the fluorescence with a two-lens system consisting of two tube lenses ($f = 200$ mm, Thorlabs, Germany) and an adjustable slit (Thorlabs, Germany), the light was spectrally split using two dichroic mirrors (zt561rdc and zt640rdc, Chroma) and a mirror into three beams corresponding to a blue, green, and red fluorescence detection channel. The three beams were then focused ($f = 300$ mm) on an Ixon Ultra 897 emCCD camera with 512 x 512 pixel (Andor, Northern-Ireland) that was operated in a photon-counting mode.

For image analysis we used a modified version of TwoTone, a freely available, MATLAB-based software package, which identifies molecules and measures the photon counts by fitting the molecular point spread functions to two dimensional Gaussians³⁸.

Hübner lab (confocal)

The setup was similar to Supplementary Figure 3 with the following components. Donor and acceptor excitation was done with a cw laser at 532 nm (GCL-005-L-LK, Crystalaser, Reno, NV) for the donor and a 635 nm pulsed laser diode (LDH-P-635+Sepia -PDL-808, Picoquant GmbH, Germany) using 100 ps pulses at 10 MHz for the acceptor. Lasers were put through a glass fiber (SMC-460, Schäfter und Kirchhoff) and collimated with UPLSAPO 4X collimation lens. Combining the lasers was accomplished with dichroic mirror Q555LP (Chroma, DM1). Dichroic DM2 was a Z532/633 (Chroma). Fluorescence collection and focusing was done with a CFI Plan Apo VC 60XWI (Nikon) objective. Lenses L1 and L2 focussing the fluorescence on a 50 μ m pinhole (P50H, Thorlabs) were two tube lenses ($f=200$ mm, MXA20696, Nikon). Fluorescence

separation was done with dichroic 640DCXR (Chroma, DM3). For fluorescence clean-up the filters FF01-582/75 (Semrock) were used for donor and HQ650/100 (Chroma) for acceptor fluorescence. The signal was then collected with SPCM-AQRH-14 (Excelitas) APDs. TCSPC electronics were a TimeHarp 200 (Picoquant).

For the measurements a home written software based on LabView (National Instruments) and for the data reduction an Igor Pro (Wavemetrics) based home written software was used.

Kapanidis lab (confocal)

smFRET experiments were carried out on a custom-built confocal microscope^{39,40}, as shown schematically in Supplementary Figure 3. The setup was modified to allow ALEX of donor and acceptor fluorophores. Custom-written LabVIEW software was used to register and evaluate the detected signal.

Data analysis was carried out using custom-written Matlab software⁴¹.

Lamb lab (confocal)

Single-molecule FRET experiments with pulsed-interleaved excitation (PIE) and multiparameter fluorescence detection (MFD) were performed on a homebuilt confocal microscope as described previously⁴². In addition to the schematic shown in Supplementary Figure 3, a polarizing beam splitter is installed after the confocal pinhole to split the signal by polarization before the dichroic mirror (640DCXR, AHF Analysentechnik). Pulsed-interleaved excitation was performed at 532 nm (PicoTA 530, PicoQuant) and 640 nm (LDH-D-C640, PicoQuant) at a repetition rate of 26.67 MHz with a delay of ~18 ns and a laser power of 100 μ W. Fluorescence emission was filtered (donor: Brightline HQ582/75, acceptor: Brightline HQ700/75, AHF Analysentechnik), focused on avalanche photodiodes (SPCM-AQR, Perkin-Elmer) and recorded on single-photon-counting cards (SPC-154, Becker&Hickl). Data analysis was performed using the *PAM* software package written in MATLAB (The MathWorks)³⁶. Single-molecule events were identified using a sliding-time-window burst search algorithm with a countrate threshold of 10 kHz, a time window of 500 μ s and a minimum photon number of 100. To remove photoblinking and -bleaching events, the ALEX-2CDE filter was applied using an upper threshold of 10 (ref. ⁴³).

Lee lab (confocal)

We performed smFRET measurement using a home-built confocal microscope, similar with the setup described in Supplementary Figure 3, which has been well described in our previous works^{44,45}. The alternation of two lasers (ALEX) was achieved using acoustic-optic modulators. The data acquisition and analysis were performed using a home-built software based on LabVIEW program as described before⁴⁶.

Lemke lab (confocal)

The setup was as described in Supplementary Figure 3 and previously in detail in refs. ^{47,48}, with the following elements changed. Lasers were a LDH 485 (Picoquant) and a SuperK Extreme (NKT Photonics) filtered with a 572/15 bandpass alternating at 26,6 Mhz and combined onto the laser path with DM1= R488-Di01. Dichroic Mirror DM2 was a ZT 488/561/660 (AHF) and for DM3 a zt

561 RDC-UF (Chroma) and a FF650-D01 (Semrock) were used in sequence for three detection channels. For the three detection channels the filters 525/50 ET (Semrock), 620/60 ET (Chroma) and 700/75 ET (Chroma) were used. The analysis was done using self-written code in IgorPro (Wavemetrics) following procedures described in detail in refs.^{49,50}.

Levitus Lab (confocal)

Fluorescence intensity decays were acquired at room temperature using the timecorrelated single photon counting technique. A fiber supercontinuum laser (Fianium SC450) was used as the excitation source. The laser provides 6 ps pulses at a variable repetition rate, set at 20 MHz. The laser output was sent through an acousto-optical tunable filter (Fianium AOTF) to obtain 552 nm excitation. Fluorescence emission was collected at a 90° angle and detected using a double-grating monochromator (Jobin-Yvon, Gemini-180) and a microchannel plate photomultiplier tube (Hamamatsu R3809U-50). The emission monochromator was set to 580 nm. The polarization of the emission was collected at the magic angle relative to the excitation. A single photon counting card (Becker-Hickl, SPC830) was used for data acquisition. The IRF was measured with a 3% Ludox scattering solution (Sigma-Aldrich, MO) and had a fwhm of approximately 80 ps when measured at 552 nm. The data were deconvoluted and fitted with a sum of exponential terms using software written in-house (ASUFIT). The quality of the fit was evaluated based on the residuals.

Michaelis lab (Confocal)

The confocal setup used for this study has been described in detail recently⁵¹. It resembles the one depicted in supplementary figure 3, but with the major addition of polarization sensitivity. A polarizing beam splitting cube positioned after the collimating lens behind the pinhole splits the light into its components parallel and perpendicular with respect to the excitation light. Each of the two resulting beams is then split by a dichroic mirror and focused onto an APD after passing an emission filter, similar to what is shown in supplementary figure 3. Differing from Schwarz et al. 2018, a different polychroic mirror was used during the initial measurements of samples 1-lo, 1-mid, 2-lo and 2-mid (Triple Line zt488/532/658, AHF Analysentechnik AG, Tübingen, Germany). The setup also provides an additional 488nm laser line and the filters and dichroic mirrors can be exchanged in order to perform smFRET experiments with a 488nm-excitabile donor and a 647nm-excitabile acceptor (e.g. samples 3-lo and 3-mid described in supplementary note 6).

For data analysis, an earlier version of the software package PAM (PIE analysis with MATLAB) was used³⁶. The newest version of the software is available via <https://gitlab.com/PAM-PIE/PAM>.

Michaelis lab (TIRF)

All TIRF-measurements were conducted using a custom-build prism-type TIRF setup which has been described in detail recently⁵². The setup is similar to the setup described in Supplementary Figure 4, only with some minor additions namely an acousto-optic tunable filter (AOTFnC-VIS, AA *Opto-Electronic*) and an IR-laser based auto-focus system. The AOTF allows for the selection of the excitation wavelength and the control of laser intensity and duration.

The acquired data was analyzed using a custom-written software called *SM-FRET* which was described in detail⁵².

Sanabria Lab (confocal)

The home built confocal system and data analysis at the Sanabrias' lab was recently described in detail^{53,54}. It is similar to the one described in Supplementary Figure 3, but with four detectors and different spectral windows. Differences are briefly described below. The microscope body is an Olympus IX-73 with a 60X, 1.2 NA collar (0.17) corrected Olympus objective. It uses Pulsed Interleaved Excitation (PIE)⁴² with diode lasers at 485 nm and 640 nm (PicoQuant, Germany) operated at 40 MHz with 25 ns interleaved time. The power at the objective was 120 μ W at 485 nm and 39 μ W at 640 nm. Emitted photons were collected through the same objective and spatially filtered through a 70 μ m pinhole to limit the effective confocal detection volume. Fluorescence emission is separated into parallel and perpendicular polarization components at two different spectral windows using band pass filters ET525/50 and ET720/150 (Chroma Technology Co.) for donor and acceptor, respectively. In total, four photon-detectors are used—two for donor (PMA Hybrid model 40 PicoQuant, Germany) and two for acceptor (PMA Hybrid model 50, PicoQuant, Germany). To insure temporal data registration of the 4 synchronized input channels, we used a HydraHarp 400 TCSPC module (PicoQuant, Germany) in Time-Tagged Time-Resolved mode.

Data analysis uses Multiparameter Fluorescence Detection software suit developed at the Seidel's lab (<http://www.mpc.hhu.de/software/software-package.html>).

Schlierf Lab (confocal)

Observations of single-molecule fluorescence were made on a custom-built dual-color and dual-polarization confocal setup based on an inverted microscope (Eclipse Ti-E, Nikon, Tokyo, Japan) as previously described in^{55,56}. Briefly, donor and acceptor fluorophores were excited with linearly polarized 530-nm and 640-nm picosecond pulsed laser sources (LDH-P-FA-530L and LDH-D-C-640, both from PicoQuant, Berlin, Germany) driven in pulsed interleaved excitation mode at a total repetition rate of 50 MHz. The laser beams were coupled to a polarization-maintaining single-mode optical fiber (P3-488PM-FC-2, Thorlabs, NJ, USA), collimated (60FC-T-4-RGBV42-47, Schäfer und Kirchhoff, Hamburg, Germany), and focused by a water immersion objective (CFI Plan Apo WI 60x, NA 1.2, Nikon). Emitted fluorescent light was collected by the same objective, separated from the excitation light by a dual-edge dichroic mirror (zt532/642rpc, Chroma, Bellows Falls, VT, USA), and focused on a 50- μ m pinhole (Thorlabs). Donor and acceptor photons were spectrally separated by single-edge dichroic mirrors (FF650-Di01, Semrock, USA) after a polarizing beam splitter (CM1-PBS251, Thorlabs), band-pass-filtered (FF01-582/75, Semrock, Rochester, NY, USA; ET700/75M, Chroma), and focused onto four single-photon-counting avalanche diodes (τ -SPADs, PicoQuant). Photons were registered by four individual time-correlated single-photon counting modules (Hydra Harp, PicoQuant) with a time resolution of 16 ps. Synchronization with the lasers for alternating excitation was accomplished with the aid of a diode laser driver (PDL828, PicoQuant).

Data analysis was performed with custom-written Matlab scripts (Mathworks, USA) and single-molecule events were identified from the acquired photon stream by a burst search algorithm as described in^{57,58}. The analysis software is available upon request.

Schuler Lab (confocal)

A commercial confocal instrument (MT200, PicoQuant, Berlin) or a custom-built instrument⁵⁹ were used for the measurements. Both instruments were equipped with an UplanApo 60×/1.20-W objective (Olympus), a 100- μ m confocal pinhole, and HydraHarp 400 counting electronics (PicoQuant, Berlin). They were operated with pulsed interleaved excitation (20 MHz) in a configuration similar to that shown in Supplementary Figure 3 with the following components.

In the MT200 setup a 485-nm pulsed diode laser (LDH-D-C-485, Picoquant) was used for donor excitation, and a SC-450-4 supercontinuum fiber laser (Fianium) filtered with a z582/15 bandpass filter (Chroma) for acceptor excitation. Dichroic mirror DM2 was a BS R405/488/594 (Semrock) and DM3 a 585DCXR (Chroma). Donor fluorescence was filtered with a ET 525/50 (Chroma) and recorded with a SPCM-AQRH-14 (PerkinElmer Optoelectronics) APD. Acceptor fluorescence was filtered with an HQ 650/100 (Chroma) and recorded with a SPCM-AQR-14 APD (PerkinElmer Optoelectronics) APD.

In the custom built setup, the donor was excited with a SC-450-4 supercontinuum fiber laser (Fianium) filtered with a BrightLine HC 520/5 band-pass filter (Semrock) and acceptor excitation was done with a 635nm pulsed diode laser (LDH-D-C-635M, PicoQuant). In this instrument, the dichroic mirrors here were a zt405/530/630rpc (Chroma) for DM2 and a 635DCXR (Chroma) for DM3. Donor fluorescence was filtered with an ET585/65m (Chroma) and recorded with a τ -SPAD (PicoQuant). Acceptor fluorescence was cleaned up with LP647RU and HC750/SP (Chroma) filters and recorded with an SPCM-AQR-14 APD (PerkinElmer Optoelectronics). Data were analyzed using custom-developed software written in C++ and Mathematica.

Seidel Lab

Ensemble Time Correlated Single Photon Counting (eTCSPC)

Fluorescence lifetime decays were recorded by FT300 setup (PicoQuant, Germany) using a white light laser from NKT Photonics (Germany) with repetition rate 20 MHz for excitation. All samples were measured in Quartz Ultra-Micro-cuvettes (Helma #105.252.85.40), with a total sample volume of 20 μ l. A Ludox scattering solution was used to record the instrument response function (IRF). The detailed measurement conditions for the experiments are provided in the Table N8.1.

Table N8.1: Settings for Picoquant FT300 setup

Settings/dye	Atto 550	Alexa 488	Atto 647N	Alexa647	Alexa 594
Excitation, nm	552	485	635	635	590
Emission, nm	580	520	665	665	617
Bandpass, nm	5.4	9.2	9.2	8.1	8.1
Excitation filter	none	ZET 488/10x	ZET 635/20x	ZET 635/20x	none
Emission filter	FGL 570	FGL 515	FGL 645	FGL 645	FGL 610

Confocal setup 1 (for samples labelled with Alexa488-Atto647N)

The general scheme of the setup is described by Sisamakris et al.⁵⁰ (see Fig. 18.5 therein). All sample solutions were measured in NUNC chambers (Lab-Tek, Thermo Scientific, Germany) with 300 μ L sample volume. The fluorescent donor molecules (Alexa 488) are excited by a pulsed diode laser (LDH-D-C 485, PicoQuant), at 485 nm operated at 64 MHz, 110 μ W at the sample in one color excitation experiment or at 32 MHz in PIE experiment, 110 μ W at the sample. The laser light is guided into the epi-illuminated confocal microscope (Olympus IX71, Hamburg, Germany) by dichroic beamsplitter FF500/646-Di01 (Semrock, USA) focussed by a water immersion objective (UPlanSApo 60x/1.2w, Olympus Hamburg, Germany). In PIE experiments the fluorescent acceptor molecules (Atto647N) are additionally excited by 635 nm pulsed diode laser (LDH-D-C 640, PicoQuant). The emitted fluorescence is collected through the objective and spatially filtered using a pinhole with typical diameter with 100 μ m. Then, the signal is split into parallel and perpendicular components via a polarizing beam splitter and then at two different spectral windows (e.g. “green” and “red”) and then split again using 50/50 beam splitters resulting in a total of eight detection channels. Additionally green (HQ 520/35 nm for Alexa488) from AHF, Tübingen, Germany and red (HQ 720/150 nm for Atto647N) bandpass filters (AHF, Tübingen, Germany) are placed in front of the detectors to provide the registration only of the fluorescence photons coming from the acceptor and donor molecules. Detection is performed using eight avalanche photodiodes (4 green channels: τ -SPAD (PicoQuant, Germany) and 4 red channels: AQR 14 (Perkin Elmer). The detector outputs were recorded by a TCSPC module (HydraHarp 400, PicoQuant).

Confocal setup 2 (for samples labelled with Atto550-Atto647N)

The confocal setup 2 is similar to the confocal setup 1 described above. It has the following components (only the differences are mentioned):

Confocal microscope: Olympus IX71 (Hamburg, Germany).

Objective: Olympus UPlanSApo 60x/1.2w (Hamburg, Germany).

Dichroic Beamsplitter: F68-532_zt532/640NIRpo (AHF, Tübingen, Germany).

Fluorescence dichroic beamsplitter: T640lpxr (AHF, Tübingen, Germany).

Diode lasers: 530 nm (LDH-P-FA 530B, PicoQuant) and 640 nm (LDH-D-C 640, PicoQuant), both with a repetition rate 32 MHz and with a power 75.5 μ W and 16.7 μ W at the sample, respectively.

Bandpass filters: green ET595/50 and red HQ730/140.

2 green and 2 red detectors: both SPCM-AQRH 14 (Excelitas, USA).

Confocal setup 3 (for samples labelled with Alexa488-Alexa594)

The confocal setup 3 is similar to the confocal setup 1 described above. It has the following components (only the differences are mentioned):

Confocal microscope (Olympus IX70, Hamburg, Germany).

Dichroic beam splitter: Q505LP (AHF, Tübingen, Germany).

Fluorescence dichroic beamsplitter: 595 LP DCXR (AHF, Tübingen, Germany).

Diode lasers: 495 nm (PicoQuant, Germany) with a repetition rate of 32 MHz and a power at the sample of 110 μ W.

Bandpass filters: green HQ520/66, red HQ630/60.

2 green and 2 red detectors: SPCM-AQRH 14 (Perkin Elmer).
TCSPC module SPC 132 (Becker&Hickl, Germany).

The recorded data were analyzed with a home-written LabView software that was developed in the Seidel lab and is described in ref. ⁵⁰. The software is available on the homepage of the Seidel group (<http://www.mpc.hhu.de/software/software-package.html>).

To analyze the recorded fluorescence bursts, a burst search algorithm according to reference ⁶⁰ was applied. The confocal setups were calibrated by the PIE measurements as described in this work or by FRET-lines relating the donor fluorescence lifetime to the intensity-based FRET efficiency as described in ref. ⁶¹.

Tinnefeld lab (confocal)

The measurements were carried out on a custom-built confocal microscope ⁶² based on an IX 71 (Olympus) similar to the setup shown in Supplementary Figure 3 with alternating laser excitation. Pulsed Lasers (637 nm, 80 MHz, LDH-D-C-640; 532 nm 80 MHz, LDH-P-FA-530B; both PicoQuant) were powered by a Sepia 2 (PicoQuant) unit. Both lasers were combined by a dichroic mirror (640 LPXR, AHF). In addition to the setup shown in Supplementary Figure 3, the lasers were alternated by an acousto optical tunable filter (AOTFnc-VIS, AA optoelectronic) and coupled into a single mode fiber (P3-488PM-FC-2, Thorlabs) to obtain a Gaussian beam profile. After a linear polarizer (LPVISE100 A, Thorlabs) and lambda quarter plate (AQWP05M 600, Thorlabs), circular polarized light was obtained. After a dual band dichroic beam splitter (z532/633, AHF), the light was focused by an oil-immersion objective (UPLSAPO 100XO, NA 1.40, Olympus). The emitted light was collected by the same objective and focused on a 50 μ m pinhole (Linos). Subsequently, the fluorescence was split by a dichroic mirror (640DCXR, AHF) into a green (Brightline HC582/75, AHF; RazorEdge LP 532, Semrock) and red (Bandpass ET 700/75m, AHF; RazorEdge LP 647, Semrock) detection channel. Two SPADs (τ -SPAD 100, PicoQuant) accounted for the detection. The SPAD signals were registered by a TCSPC card (SPC-830, Becker&Hickl). The setup was controlled with custom-made LabView (National Instruments) software. Recorded data were analyzed with a LabView software ⁶³. To analyze the recorded fluorescence bursts, a burst search algorithm according to reference ⁶⁴ was applied.

Weninger lab (TIRF)

The microscope is similar to that in Supplementary Figure 4 ³¹. Briefly, we illuminate immobilized samples at the surface of a quartz microscope slide with prism-type total internal reflection of laser beams at the quartz/buffer interface. Alternating illumination of 532 nm or 640 nm allows sequential excitation of donor and acceptor dyes when using Atto 550, Alexa 647 and Atto 647N. Fluorescence emission is collected by a 1.20 N.A. water-immersion microscope objective (Olympus UIS2 UPlanSApo 60x/1.20 W). The fluorescence image is spectrally divided with a Dualview splitter (DV2, Photometrics) incorporating a 645dxc dichroic mirror with a 585/70 bandpass filter (donor) and a 700/75 bandpass filter (acceptor) (all from Chroma Technology Corp.). The spectrally divided image is detected with an emCCD (Cascade 521B, Photometrics) operating at 10 Hz.

We use home-written analysis software implemented in MATLAB (MathWorks)³². Immobilized single molecules are detected in a ten-frame averaged image as pixels of maximum intensity above an empirically determined threshold (typically based on the statistics of all pixels in the field of view as 7 standard deviations above the average), separated by five or more pixels from any neighboring maxima. Fluorescence intensity for a single molecule is extracted from each frame of a movie as the sum of the 4 brightest pixels in a 3x3 pixel region centered on the local maximum. Before a FRET experiment, we acquire a spectrally split image of a field of immobilized, fluorescent 100 nm diameter polystyrene spheres that emit broadly into both channels to build a mapping between donor and acceptor channels using the MATLAB image processing toolbox command `cp2tfom`. This mapping is applied to movies containing FRET data to obtain donor and acceptors intensities from immobilized single molecules. Background for each detected molecule is calculated locally as the median value of the 16x16 pixel region around the identified peak pixel. The background value is subtracted from the single molecule intensity values. The background value is verified by requiring the background-subtracted intensity time-trace for a single molecule emission return to zero upon a single step photobleaching event. Leakage between donor and acceptor channels is measured separately using singly labeled samples. FRET efficiency is then calculated as described in the main text.

Bibliography:

1. Sindbert, S. *et al.* Accurate Distance Determination of Nucleic Acids via Förster Resonance Energy Transfer: Implications of Dye Linker Length and Rigidity. *J. Am. Chem. Soc.* **133**, 2463-2480 (2011).
2. Widengren, J. & Schwille, P. Characterization of photoinduced isomerization and back-isomerization of the cyanine dye Cy5 by fluorescence correlation spectroscopy. *J. Phys. Chem. A* **104**, 6416-6428 (2000).
3. Widengren, J., Schweinberger, E., Berger, S. & Seidel, C. A. M. Two new concepts to measure fluorescence resonance energy transfer via fluorescence correlation spectroscopy: Theory and experimental realizations. *J. Phys. Chem. A* **105**, 6851-6866 (2001).
4. Hendrix, J. & Lamb, D. C. Pulsed Interleaved Excitation: Principles and Applications. *Fluorescence Fluctuation Spectroscopy (Ffs), Pt A* **518**, 205-243 (2013).
5. Margeat, E. *et al.* Direct Observation of Abortive Initiation and Promoter Escape Within Single Immobilized Transcription Complexes. *Biophys. J.* **90**, 1419-1431 (2006).
6. Peulen, T. O., Opanasyuk, O. & Seidel, C. A. M. Combining graphical and analytical methods with molecular simulations to analyze time-resolved FRET-measurements of labeled macromolecules accurately. *J. Phys. Chem. B* **121**, 8211-8241 (2017).
7. Wozniak, A. K., Schröder, G. F., Grubmüller, H., Seidel, C. A. M. & Oesterhelt, F. Single-Molecule FRET Measures Bends and Kinks in DNA. *Proc. Natl. Acad. Sci. USA* **105**, 18337-18342 (2008).
8. Ivani, I. *et al.* Parmbsc1: a refined force field for DNA simulations. *Nat. Meth.* **13**, 55-58 (2016).
9. Muschielok, A. *et al.* A Nano-Positioning System for Macromolecular Structural Analysis. *Nat. Meth.* **5**, 965-971 (2008).
10. Kalinin, S. *et al.* A toolkit and benchmark study for FRET-restrained high-precision structural modeling. *Nat. Meth.* **9**, 1218-1227 (2012).

11. Hellenkamp, B., Wortmann, P., Kandzia, F., Zacharias, M. & Hugel, T. Multidomain Structure and Correlated Dynamics Determined by Self-Consistent FRET Networks. *Nat. Meth.* **14**, 174-180 (2017).
12. Beckers, M., Drechsler, F., Eilert, T., Nagy, J. & Michaelis, J. Quantitative Structural Information from Single-Molecule FRET. *Farad. Discuss.* **184**, 117-129 (2015).
13. Dimura, M. *et al.* Quantitative FRET Studies and Integrative Modeling Unravel the Structure and Dynamics of Biomolecular Systems. *Curr. Opin. Struct. Biol.* **40**, 163-185 (2016).
14. Nagy, J., Eilert, T. & Michaelis, J. Precision and Accuracy in smFRET based structural studies - a benchmark study of the FAST-Nano-Positioning System. *J. Chem. Phys.* **148** (2018).
15. Treutlein, B. *et al.* Dynamic architecture of a minimal RNA polymerase II open promoter complex. *Mol. Cell* **46**, 136-146 (2012).
16. Hohlbein, J. *et al.* Conformational landscapes of DNA polymerase I and mutator derivatives establish fidelity checkpoints for nucleotide insertion. *Nat. Commun.* **4**, 2131 (2013).
17. Tyagi, S. & Lemke, E. A. Genetically encoded click chemistry for single-molecule FRET of proteins. *Methods Cell Biol.* **113**, 169-187 (2013).
18. Tyagi, S. & Lemke, E. A. Single-molecule FRET and crosslinking studies in structural biology enabled by noncanonical amino acids. *Curr. Opin. Struct. Biol.* **32**, 66-73 (2015).
19. Eilert, T., Beckers, M., Drechsler, F. & Michaelis, J. Fast-NPS - A Markov chain Monte Carlo-based analysis tool to obtain structural information from single-molecule FRET measurements. *Comput. Phys. Commun.* **219**, 377-389 (2017).
20. Lipfert, J. *et al.* Double-stranded RNA under force and torque: Similarities to and striking differences from double-stranded DNA. *Proc. Natl. Acad. Sci. USA* **111**, 15408-15413 (2014).
21. Liebl, K., Drsata, T., Lankas, F., Lipfert, J. & Zacharias, M. Explaining the striking difference in twist-stretch coupling between DNA and RNA: A comparative molecular dynamics analysis. *Nucleic Acids Res.* **43**, 10143-10156 (2015).
22. Stelzl, L. S., Erlenbach, N., Heinz, M., Prisner, T. F. & Hummer, G. Resolving the conformational dynamics of DNA with Ångström resolution by pulsed electron-electron double resonance and molecular dynamics. *J. Am. Chem. Soc.* **139**, 11674-11677 (2017).
23. Vafabakhsh, R. & Ha, T. Extreme Bendability of DNA Less than 100 Base Pairs Long Revealed by Single-Molecule Cyclization. *Science* **337**, 1097-1101 (2012).
24. Case, D. A. *et al.* AMBER 2016. (University of California, San Francisco, 2016).
25. Jorgensen, W. L., Chandrasekhar, J., Madura, J. D., Impey, R. W. & Klein, M. L. Comparison of Simple Potential Functions for Simulating Liquid Water. *J. Chem. Phys.* **79**, 926-935 (1983).
26. Joung, I. S. & Cheatham, T. E. Determination of alkali and halide monovalent ion parameters for use in explicitly solvated biomolecular simulations. *J. Phys. Chem. B* **112**, 9020-9041 (2008).
27. Li, P. F., Roberts, B. P., Chakravorty, D. K. & Merz, K. M. Rational design of particle mesh ewald compatible Lennard-Jones parameters for +2 metal cations in explicit solvent. *J. Chem. Theory Comput.* **9**, 2733-2748 (2013).
28. Gohlke, H., Kiel, C. & Case, D. A. Insights into protein-protein binding by binding free energy calculation and free energy decomposition for the Ras-Raf and Ras-RalGDS complexes. *J. Mol. Biol.* **330**, 891-913 (2003).
29. Kruger, A. C., Hildebrandt, L. L., Kragh, S. L. & Birkedal, V. Structural dynamics of nucleic acids by single-molecule FRET. *Methods Cell Biol.* **113**, 1-37 (2013).
30. Preus, S., Noer, S. L., Hildebrandt, L. L., Gudnason, D. & Birkedal, V. iSMS: single-molecule FRET microscopy software. *Nat Methods* **12**, 593-594 (2015).
31. McCann, J. J., Choi, U. B., Zheng, L., Weninger, K. & Bowen, M. E. Optimizing Methods to Recover Absolute FRET Efficiency from Immobilized Single Molecules. *Biophys. J.* **99**, 961-970 (2010).

32. Choi, U. B., Weninger, K. R. & Bowen, M. E. Immobilization of proteins for single-molecule fluorescence resonance energy transfer measurements of conformation and dynamics. *Methods Mol. Biol.* **896**, 3-20 (2012).
33. Gouridis, G. *et al.* Conformational dynamics in substrate-binding domains influences transport in the ABC importer GlnPQ. *Nat. Struct. Mol. Biol.* **22**, 57-64 (2015).
34. Bennet, I. A. *et al.* Regional conformational flexibility couples substrate specificity and scissile phosphate diester selectivity in human flap endonuclease 1. *Nucleic Acids Res.* **46**, 5618-5633 (2018).
35. Hua, B. *et al.* An improved surface passivation method for single-molecule studies. *Nat Methods* **11**, 1233-1236 (2014).
36. Schrimpf, W., Barth, A., Hendrix, J. & Lamb, D. C. PAM: A Framework for Integrated Analysis of Imaging, Single-Molecule, and Ensemble Fluorescence Data. *Biophys. J.* **114**, 1518-1528 (2018).
37. Farooq, S. & Hohlbein, J. Camera-based single-molecule FRET detection with improved time resolution. *Phys. Chem. Chem. Phys.* **17**, 27862-27872 (2015).
38. Holden, S. J. *et al.* Defining the limits of single-molecule FRET resolution in TIRF microscopy. *Biophys. J.* **99**, 3102-3111 (2010).
39. Santoso, Y. *et al.* Conformational transitions in DNA polymerase I revealed by single-molecule FRET. *Proc Natl Acad Sci U S A* **107**, 715-720 (2010).
40. Robb, N. C. *et al.* The transcription bubble of the RNA polymerase-promoter open complex exhibits conformational heterogeneity and millisecond-scale dynamics: implications for transcription start-site selection. *J. Mol. Biol.* **425**, 875-885 (2013).
41. Tomescu, A. I., Robb, N. C., Hengrung, N., Fodor, E. & Kapanidis, A. N. Single-molecule FRET reveals a corkscrew RNA structure for the polymerase-bound influenza virus promoter. *Proc Natl Acad Sci U S A* **111**, E3335-3342 (2014).
42. Kudryavtsev, V. *et al.* Combining MFD and PIE for Accurate Single-Pair Förster Resonance Energy Transfer Measurements. *ChemPhysChem* **13**, 1060-1078 (2012).
43. Tomov, T. E. *et al.* Disentangling Subpopulations in Single-Molecule FRET and ALEX Experiments with Photon Distribution Analysis. *Biophys. J.* **102**, 1163-1173 (2012).
44. Kim, C., Kim, J. Y., Kim, S. H., Lee, B. I. & Lee, N. K. Direct characterization of protein oligomers and their quaternary structures by single-molecule FRET. *Chem Commun (Camb)* **48**, 1138-1140 (2012).
45. Kim, J. Y. *et al.* Solution single-vesicle assay reveals PIP2-mediated sequential actions of synaptotagmin-1 on SNAREs. *EMBO J.* **31**, 2144-2155 (2012).
46. Lee, N. K. *et al.* Accurate FRET Measurements Within Single Diffusing Biomolecules Using Alternating-Laser Excitation. *Biophys. J.* **88**, 2939-2953 (2005).
47. Milles, S., Koehler, C., Gambin, Y., Deniz, A. A. & Lemke, E. A. Intramolecular three-colour single pair FRET of intrinsically disordered proteins with increased dynamic range. *Mol Biosyst* **8**, 2531-2534 (2012).
48. Milles, S. & Lemke, E. A. Single Molecule Study of the Intrinsically Disordered FG-Repeat Nucleoporin 153. *Biophys. J.* **101**, 1710-1719 (2011).
49. Eggeling, C. *et al.* Data registration and selective single-molecule analysis using multi-parameter fluorescence detection. *J. Biotechnol.* **86**, 163-180 (2001).
50. Sisamakris, E., Valeri, A., Kalinin, S., Rothwell, P. J. & Seidel, C. A. M. Accurate Single-Molecule FRET Studies Using Multiparameter Fluorescence Detection. *Methods Enzymol.* **475**, 455-514 (2010).
51. Schwarz, M. *et al.* Single-molecule nucleosome remodeling by INO80 and effects of histone tails. *FEBS Lett.* **592**, 318-331 (2018).

52. Dörfler, T., Eilert, T., Rocker, C., Nagy, J. & Michaelis, J. Structural Information from Single-molecule FRET Experiments Using the Fast Nano-positioning System. *Jove-Journal of Visualized Experiments* (2017).
53. Dolino, D. M., Rezaei Adariani, S., Shaikh, S. A., Jayaraman, V. & Sanabria, H. Conformational selection and submillisecond dynamics of the ligand-binding domain of the N-methyl-D-Aspartate receptor. *J Biol Chem* **291**, 16175-16185 (2016).
54. Ma, J. *et al.* High Precision FRET at Single-molecule Level for Biomolecule Structure Determination. *J Vis Exp*, e55623 (2017).
55. Hartmann, A., Krainer, G. & Schlierf, M. Different fluorophore labeling strategies and designs affect millisecond kinetics of DNA hairpins. *Molecules* **19**, 13735-13754 (2014).
56. Krainer, G., Hartmann, A. & Schlierf, M. farFRET: Extending the Range in Single-Molecule FRET Experiments beyond 10 nm. *Nano Lett* **15**, 5826-5829 (2015).
57. Hartmann, A., Krainer, G., Keller, S. & Schlierf, M. Quantification of Millisecond Protein-Folding Dynamics in Membrane-Mimetic Environments by Single-Molecule Forster Resonance Energy Transfer Spectroscopy. *Anal. Chem.* **87**, 11224-11232 (2015).
58. Krainer, G., Hartmann, A., Anandamurugan, A., Gracia, P. & Schlierf, M. Ultrafast protein folding through polar interactions in membrane-mimetic environments. *J. Mol. Biol.* **430** (2018).
59. König, I. *et al.* Single-molecule spectroscopy of protein conformational dynamics in live eukaryotic cells. *Nat. Meth.* **12**, 773-779 (2015).
60. Fries, J. R., Brand, L., Eggeling, C., Kollner, M. & Seidel, C. A. M. Quantitative identification of different single molecules by selective time-resolved confocal fluorescence spectroscopy. *J. Phys. Chem. A* **102**, 6601-6613 (1998).
61. Kalinin, S., Valeri, A., Antonik, M., Felekyan, S. & Seidel, C. A. M. Detection of Structural Dynamics by FRET: A Photon Distribution and Fluorescence Lifetime Analysis of Systems with Multiple States. *J. Phys. Chem. B* **114**, 7983-7995 (2010).
62. Nickels, P. C. *et al.* Molecular force spectroscopy with a DNA origami-based nanoscopic force clamp. *Science* **354**, 305-307 (2016).
63. Kapanidis, A. N. *et al.* Fluorescence-aided molecule sorting: Analysis of structure and interactions by alternating-laser excitation of single molecules. *Proc. Natl. Acad. Sci. USA* **101**, 8936-8941 (2004).
64. Nir, E. *et al.* Shot-Noise Limited Single-Molecule FRET Histograms: Comparison Between Theory and Experiments. *J. Phys. Chem. B* **110**, 22103-22124 (2006).



ARTICLE

DOI: 10.1038/s41467-017-02619-5

OPEN

Single-molecule FRET reveals multiscale chromatin dynamics modulated by HP1 α

Sinan Kilic^{1,4}, Suren Felekyan², Olga Doroshenko², Luliia Boichenko¹, Mykola Dimura², Hayk Vardanyan², Louise C. Bryan¹, Gaurav Arya³, Claus A.M. Seidel² & Beat Fierz¹

The dynamic architecture of chromatin fibers, a key determinant of genome regulation, is poorly understood. Here, we employ multimodal single-molecule Förster resonance energy transfer studies to reveal structural states and their interconversion kinetics in chromatin fibers. We show that nucleosomes engage in short-lived (micro- to milliseconds) stacking interactions with one of their neighbors. This results in discrete tetranucleosome units with distinct interaction registers that interconvert within hundreds of milliseconds. Additionally, we find that dynamic chromatin architecture is modulated by the multivalent architectural protein heterochromatin protein 1 α (HP1 α), which engages methylated histone tails and thereby transiently stabilizes stacked nucleosomes. This compacted state nevertheless remains dynamic, exhibiting fluctuations on the timescale of HP1 α residence times. Overall, this study reveals that exposure of internal DNA sites and nucleosome surfaces in chromatin fibers is governed by an intrinsic dynamic hierarchy from micro- to milliseconds, allowing the gene regulation machinery to access compact chromatin.

¹Laboratory of Biophysical Chemistry of Macromolecules, Institute of Chemical Sciences and Engineering (ISIC), Ecole Polytechnique Fédérale de Lausanne (EPFL), 1015 Lausanne, Switzerland. ²Institut für Physikalische Chemie, Lehrstuhl für Molekulare Physikalische Chemie, Heinrich-Heine-Universität, Universitätsstraße 1, 40225 Düsseldorf, Germany. ³Pratt School of Engineering, Duke University, 144 Hudson Hall, Box 90300, Durham, NC 27708, USA. ⁴Present address: Department of Molecular Mechanisms of Disease, University of Zurich, 8057 Zurich, Switzerland. Correspondence and requests for materials should be addressed to C.A.M.S. (email: cseidel@hhu.de) or to B.F. (email: beat.fierz@epfl.ch)

Chromatin is critical to gene regulatory processes, as it dictates the accessibility of DNA to proteins such as transcription factors (TFs) and gene expression machinery¹. The elucidation of the structure and dynamics of chromatin is a challenge spanning orders of magnitude in spatial (Å to micrometers) and temporal (sub-microseconds to hours) scales². Genomic approaches have enabled researchers to probe the structure of chromatin *in vivo*^{3–5}, albeit as static snapshots and averaged over cellular populations. High-resolution structural studies on reconstituted chromatin provided models of chromatin as a two-start helix with two intertwined stacks of nucleosomes and compact tetranucleosomes as basic units (Fig. 1a)^{6,7}. Within such a two-start fiber context, inter-nucleosome interactions are mediated by the H4 tail contacting the H2A acidic patch¹, and by a contact between the C-terminal helices of H2A and H2B^{6,7}. Other experiments have supported solenoid chromatin structural models⁸ or mixed, heterogeneous populations⁹, depending on

linker DNA length and the presence of linker histones. As observed in the cryo-EM structure of a chromatin fiber (Fig. 1a), tetranucleosomes arrange in a defined interaction register (i.e., defining which nucleosomes interact with each other).

Irrespective of the local architecture, chromatin structure is highly dynamic: Mononucleosomes exhibit partial unwrapping of nucleosome-wound DNA^{10–13}, which modulates binding site accessibility for TFs^{14,15} and controls the rate of transcription by RNA polymerase¹⁶. Dynamic rearrangements beyond the nucleosome were observed using fluorescence approaches in trinucleosomes¹⁷ and using force spectroscopy on chromatin fibers under tension^{18–21}. However, structural rearrangements in unperturbed chromatin fibers, and the timescales thereof, remain unresolved.

Heterochromatin protein 1α (HP1α, CBX5), a defining component of transcriptionally silent heterochromatin, has been shown to interact with H3 tri-methylated at lysine 9 (H3K9me3)

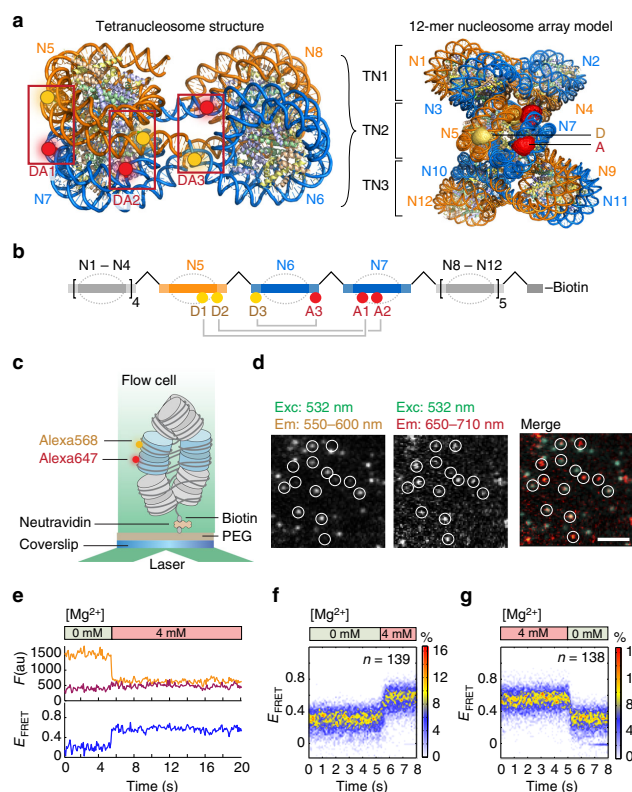


Fig. 1 smFRET system to detect real-time chromatin conformational dynamics. **a** Left: Tetranucleosome structure based on ref. ⁶ showing the three dye pairs DA1, DA2, and DA3. Right: 12-mer chromatin fiber as a stack of three tetranucleosome (TN) units, modeled using the cryo-EM structure of a chromatin fiber⁷. For exact dye positions, see Supplementary Fig. 1. The middle tetranucleosome carries the fluorescent labels, whose accessible volume is displayed. D donor, A acceptor labels, N nucleosomes. **b** Schematic view of the preparative DNA ligation used to introduce fluorescent labels. **c** Scheme of the TIRF experiment to measure intra-array smFRET. **d** Microscopic images showing FRET data of single chromatin arrays at 4 mM Mg²⁺, scale bar: 5 μm. **e** Trace from dynamic compaction of chromatin fibers by influx of 4 mM Mg²⁺. **f** DA1 chromatin fibers compact dynamically by influx of 4 mM Mg²⁺ at 5 s as reported by a rapid increase in FRET. Displayed: Overlay of indicated number of traces from single fibers. Only traces exhibiting a FRET change were included in the analysis (65%). **g** DA1 chromatin decompacts rapidly upon removal of Mg²⁺ by injection of low-salt buffer/EDTA. Only traces exhibiting a FRET change were included in the analysis (74%)

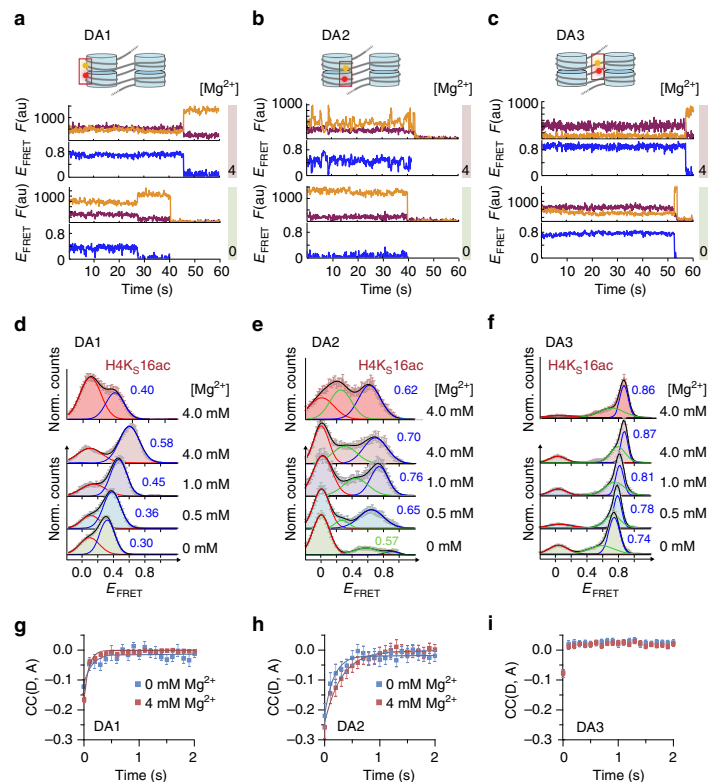


Fig. 2 Multi-perspective smTIRF-FRET reveals dynamic chromatin compaction. **a** Single-molecule traces (donor: orange, acceptor: red, FRET: blue) for DA1 at 0 mM Mg^{2+} (bottom), 4 mM Mg^{2+} (top) until either donor or acceptor dye photobleaching. For analysis methods, see Supplementary Note, step 1 **b** FRET traces for DA2, same conditions as in **a**. **c** FRET traces for DA3, same conditions as in **a**. **d** FRET populations observed for DA1 at the indicated Mg^{2+} concentrations, as well as in the presence of H4K₅16ac. **e** FRET populations for DA2, same conditions as in **d**. **f** FRET populations for DA3, same conditions as in **d**. **d-f** Error bars: s.e.m. For the number of traces, parameters of the Gaussian fits, see Supplementary Table 5. **g** Donor-acceptor channel cross-correlation analysis of DA1. Fits, 0 mM Mg^{2+} : cross-correlation relaxation time $t_R = 140 \pm 101$ ms ($n = 76$); 4 mM Mg^{2+} : $t_R = 73 \pm 13$ ms ($n = 229$). **h** Donor-acceptor channel cross-correlation analysis of DA2. Fits, 0 mM Mg^{2+} : $t_R = 169 \pm 79$ ms ($n = 61$); 4 mM Mg^{2+} : $t_R = 312 \pm 108$ ms ($n = 52$). **i** Donor-acceptor channel cross-correlation analysis of DA3. **g-i** Error bars: s.e.m. For the number of traces, see Supplementary Table 5. Fit uncertainties correspond to 95% confidence intervals of a global fit of the indicated number of traces. For the percentage of dynamic traces, see Supplementary Table 6

in a multivalent fashion. HP1 α is a key architectural protein and is involved in establishing a compact chromatin state, thereby contributing to gene silencing^{22–28}. Importantly, it has been revealed that HP1 α is highly dynamic, with residence times on chromatin from milliseconds to seconds^{23,27,29,30}. Thus, it is not clear how HP1 proteins induce chromatin compaction. Moreover, no detailed information is available about the internal structure of such compact states. The lack of precise information on chromatin dynamics in general, and of chromatin-effector complexes in particular, is mainly due to experimental constraints arising from the megadalton scale, molecular complexity, and structural heterogeneity of chromatin. Knowledge of the timescale of chromatin structural rearrangements, modulated by histone PTMs or by chromatin effectors^{21,25,31,32}, is however central for understanding the role of chromatin in gene regulation.

In this study, we combine two single-molecule Förster resonance energy transfer (smFRET)³³ methods, covering detection timescales from microseconds up to seconds, to directly map local

chromatin structural states and measure their interconversion dynamics. We fluorescently label chromatin fibers at three distinct sets of internal positions yielding structural information from several vantage points. Using two fluorescent dye pairs with different distance sensitivities (i.e., Förster Radii, R_0) allows us to measure a wide range of inter-dye distances ($R_{D,A}$) with sub-nm precision. Employing this multipronged approach combined with dynamic structural biology methods (building on our FRET positioning and screening toolkit, FPS)³⁴, we identify distinct structural states in chromatin fibers and determine their exchange kinetics. We reveal that nucleosomes engage in stacking interactions, which rapidly interchange on the micro- to millisecond timescale. HP1 α binding to modified chromatin fibers results in a compact but dynamic chromatin state, as HP1 α transiently stabilizes stacked nucleosomes. Together, our study establishes a dynamic-register model of local chromatin fiber motions regulated by effector proteins.

Results

Reconstitution of site-specifically labeled chromatin fibers. A key prerequisite for our smFRET studies is the introduction of a single dye pair with base-pair precision into chromatin fibers. We thus developed a method to assemble chromatin DNA constructs containing 12 copies of the “601” nucleosome positioning sequence³⁵ separated by 30 bp linker DNA. We used preparative ligations of two recombinant and three synthetic fragments, the latter of which carried the fluorescent labels (Fig. 1b, Supplementary Figs. 1–3, and Supplementary Tables 1–4). A convergent DNA assembly procedure with intermediate purification steps ensured the efficient and accurate incorporation of exactly one donor and one acceptor dye into chromatin DNA at defined positions. Guided by structural modeling^{6,7,17}, we decided on three dye configurations (Donor–Acceptor position 1, DA1), DA2 and DA3 (Fig. 1b), employing Alexa Fluor 568 (Alexa568) as FRET donor and Alexa Fluor 647 (Alexa647) as FRET acceptor. This pair has the advantage of a large Förster radius $R_0 = 82 \text{ \AA}$, enabling measurement of large inter-dye distances (up to 150 \AA). Each dye pair was positioned in the center of the 12-mer nucleosome array (N1–N12) to probe distinct contacts and motions (Fig. 1a, b). DA1 senses stacking between nucleosomes N5 and N7 at a position close to the H2A–H2B four-helix bundle contacts¹⁷. DA2 measures inter-nucleosome interactions closer to the dyad (N5–N7). DA3 reports on dynamic modes within the linker DNA flanking the central nucleosome (N6). Chromatin fibers were reconstituted on double-labeled DNA templates (either DA1, DA2, or DA3) using recombinant human histone octamers (Supplementary Fig. 4). Ensemble measurements confirmed that all three dye configurations in chromatin resulted in increasing FRET as a function of magnesium-induced compaction, compatible with a two-start fiber model^{6,7} (Supplementary Fig. 5a–l). Chromatin fibers labeled on nucleosome positions N5 and N6 (nearest-neighbor in sequence), which only make contact in a one-start fiber configuration, did not demonstrate measurable FRET. This finding, together with structural modeling, ruled out that solenoid or one-start fiber structures contribute to the measured FRET signal (Supplementary Fig. 5m–o).

smFRET reveals structural heterogeneity in chromatin fibers.

We proceeded to investigate the conformational and dynamic properties of the assembled chromatin fibers using single-molecule imaging. In a first set of experiments, we applied single-molecule total internal reflection fluorescence (smTIRF) microscopy with a time resolution of 100 ms, to investigate chromatin structure and dynamics on the millisecond to seconds timescale (Fig. 1c). We immobilized DA1-labeled chromatin fibers in flow channels and measured their donor and acceptor fluorescence emission (Fig. 1d). Traces were selected according to a predefined set of selection criteria, e.g., the presence of a donor and an acceptor dye, and a minimal trace length in time (Supplementary Fig. 6g). We then generated time traces of FRET efficiency (E_{FRET}) (Supplementary Note, step 1). Chromatin compaction induced by rapid injection of bivalent cations (4 mM Mg^{2+}) resulted in a fast (<0.5 s) increase in E_{FRET} (Fig. 1e, f). Conversely, rapid removal of Mg^{2+} ions induced chromatin decompaction on a similarly rapid timescale (Fig. 1g). We can thus directly observe real-time conformational changes in single chromatin fibers. Moreover, these experiments reveal that the formation of chromatin higher-order structure occurs on the millisecond timescale.

Next, we systematically explored chromatin conformational changes as a function of bivalent cation concentration (0, 0.5, 1.0, and 4.0 mM Mg^{2+}) from our three structural vantage points (Fig. 2). We recorded time traces of FRET efficiency for DA1

(Fig. 2a), DA2 (Fig. 2b), and DA3 (Fig. 2c), which demonstrated an increase in E_{FRET} with Mg^{2+} for all positions, albeit to different extents. For DA1, E_{FRET} histograms revealed a broad FRET distribution, which could be described with two Gaussians centered at low (<0.1) and intermediate (0.3–0.6) FRET efficiency values (Fig. 2d). In contrast, DA3 and DA2 showed a more complex pattern with one population at low E_{FRET} and at least two populations associated with intermediate-to-high FRET efficiency (Fig. 2e, f). With increasing Mg^{2+} concentration, for all arrays (DA1–3) the populations with $E_{\text{FRET}} > 0.1$ gradually shifted to higher FRET efficiency values, indicating an induction of nucleosome stacking.

As a confirmation that we indeed measured nucleosome stacking, we investigated the effect of acetylation of H4 at K16, which has been shown to abolish a key contact between the H4 tail and the H2A acidic patch of the neighboring nucleosome³¹. We thus synthesized a close chemical analog of this modification, H4K_S16ac (Supplementary Fig. 7). Inclusion of H4K_S16ac resulted in a significant reduction in internucleosomal stacking contacts observed by DA1 (Fig. 2d). A reduction in nucleosomal contacts was also registered by DA2 (Fig. 2e), whereas DA3 did not demonstrate a measurable change compared to the unmodified fiber (Fig. 2f). Thus, H4K16 acetylation results in a loss of defined and stable nucleosome stacking by disrupting a key internucleosomal interaction, while keeping the overall fiber geometry intact.

Considering unmodified chromatin fibers, we further resolved anti-correlated fluctuations in the time traces of donor and acceptor fluorescence emission (Fig. 2a–c), in particular for DA2, indicating structural dynamics. Cross-correlation analysis of donor and acceptor fluorescence fluctuations [CC(D,A)] revealed structural motions for DA2 positions (relaxation time $t_R = 0.2\text{--}0.3 \text{ s}$, Fig. 2h), fast dynamics at the detection limit for DA1 ($t_R \sim 0.1 \text{ s}$, Fig. 2g) and quasistatic behavior for DA3 (Fig. 2i). Together, the data from DA1–3 point toward complex multiscale dynamics featuring multiple FRET species in rapid exchange, which are not clearly resolvable with smTIRF.

Chromatin fibers exist in two structural registers.

We thus employed a second approach, smFRET with confocal multiparameter fluorescence detection (MFD)³⁶, to study freely diffusing single chromatin fibers (Fig. 3a). This method extends the accessible dynamic timescale to the sub-microsecond range and resolves structural states with sub-nm accuracy³⁴. For a set of excitation lasers (485 and 635 nm), our experimental setup allowed the application of pulsed interleaved excitation (PIE)³⁷ to filter out detections arising from donor-only molecules. To analyze MFD data, each photon burst (i.e., a single-molecule detection) is plotted in a 2D histogram as a function of two FRET indicators: the intensity-derived E_{FRET} and the average (fluorescence-weighted) donor lifetime $\langle \tau_{\text{D(A)}} \rangle_F$ (Fig. 3b, c). As an example, molecules with two conformational states A and D, which remain static during their passage through the confocal volume are located as two populations on a static FRET line (dark red line, Fig. 3b). In contrast, molecules undergoing structural exchange dynamics with a characteristic relaxation time t_R between the limiting structural states A and D are detected by a broadened intermediate peak, reminiscent of NMR signals in the intermediate exchange regime (Fig. 3c). Moreover, these dynamically broadened populations are located on a dynamic FRET line (blue line, Fig. 3c), which connects the limiting FRET species involved in the fast exchange (intersection of blue and red line in Fig. 3c)³⁸.

We performed MFD measurements for chromatin fibers carrying FRET dye pairs in configurations DA1–3 (exciting at

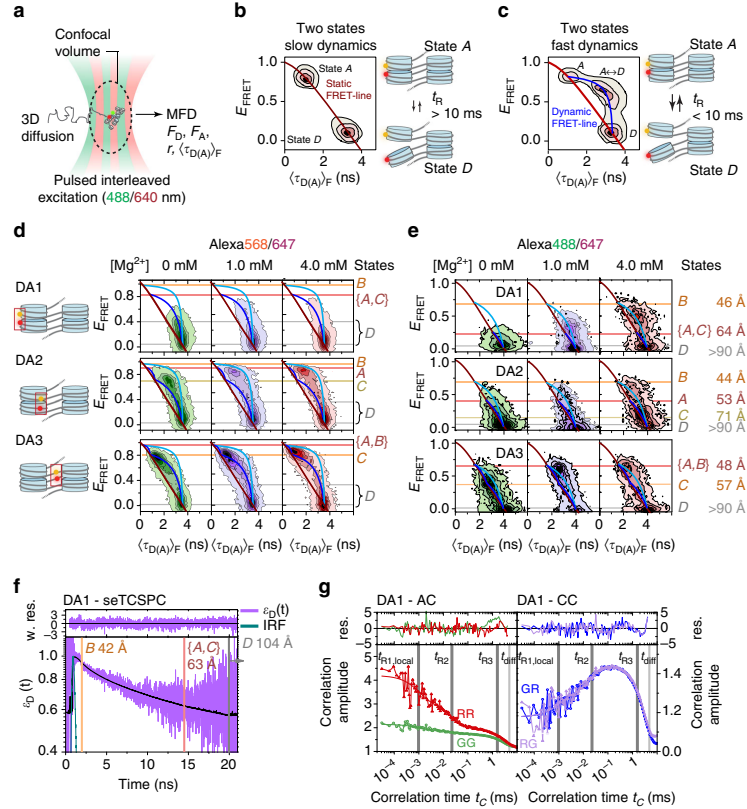


Fig. 3 Multiscale chromatin dynamics in two registers revealed by MFD. **a** Scheme of PIE-MFD: Species-averaged donor and acceptor emission intensities (F_D , F_A), intensity-averaged donor lifetime ($\tau_{D(A)F}$) and anisotropy (r) are simultaneously measured for each molecule diffusing through the confocal volume. **b** Principle of MFD analysis: If dynamics between two states A and D are slow (relaxation time $t_R \gg 10$ ms), distinct structural states are resolved by E_{FRET} and $\langle \tau_{D(A)F} \rangle$, falling on the static FRET line (red). **c** Fast dynamics ($t_R < 10$ ms) result in an intermediate peak (labeled A \leftrightarrow D) on a dynamic FRET line (blue). Peak shape analysis reveals t_R (Fig. 5). **d** 2D-MFD histograms for chromatin fibers DA1-3 (Alexa568/647) at indicated Mg^{2+} concentrations. These histograms contain contributions from donor-only labeled chromatin fibers. Red line: static FRET line. Dark and bright blue lines: Two dynamic FRET lines for the two tetranucleosome registers 1 and 2, indicating dynamic exchange with $t_R < 10$ ms (for parameters of all FRET lines, see Supplementary Note, step 2). Red, orange, yellow, and gray lines: FRET species A-D (see also Fig. 4a). **e** 2D-MFD histograms for chromatin fibers DA1-3 labeled with Alexa488/647 at indicated Mg^{2+} concentrations. Red line: static FRET line; dark and bright blue lines: dynamic FRET lines. **f** Subensemble fluorescence lifetime analysis for DA1-labeled fibers (Alexa488/647) at 1 mM $MgCl_2$ and $E_{FRET} > 0.065$. The FRET-induced donor decay $\varepsilon_D(t)$ was fitted with contributions from FRET species {A, C}, B and D (for details and fit parameters of eqs. 3.1–6, see Supplementary Note, step 3), corresponding to the indicated inter-dye distances. IRF: instrument response function. **g** Auto- (left panel) and cross (right panel)-correlation functions of the donor (G) and acceptor (R) emission channels for the same subensemble as in **f**. Global analysis of FCS curves reveals FRET dynamics with two global structural relaxation times ($\tau_{R2} = 27$ μ s (27%); $\tau_{R3} = 3.1$ ms (56%)), a term describing local fluctuations ($t_{R1,local} = 2.6$ μ s (17%)) and an apparent diffusion time for all curves ($t_{diff} = 4.96$ ms) (for details and fit parameters of Eq. 4.1, see Supplementary Note, step 4)

530 nm, which precluded PIE), which revealed a complex population distribution involved in dynamic exchange (Fig. 3d) not observed in free DNA or donor-only labeled chromatin fibers (Supplementary Fig. 8c, d). Due to the absence of PIE in those measurements, donor-only labeled chromatin fibers ($E_{FRET} = 0$) contributed also to the total observed signal. An iterative 11-step workflow (Supplementary Fig. 9) allowed us to resolve distinct structural states by their characteristic FRET efficiencies and dynamics. Based on this analysis, the data could only consistently be described by two dynamic FRET lines (dark and bright blue

lines, Fig. 3d), indicating two coexisting subpopulations of dynamic chromatin fibers, which are distinct within the observation time of ~ 10 ms.

From the intersections of the dynamic with the static FRET lines, we identified four limiting FRET species involved in the exchange: A, B, C, and D, indicated by the horizontal lines in Fig. 3d. Braces (e.g., {A, C}) indicate conformational states sharing indistinguishable FRET efficiencies. Importantly, a complementary analysis procedure within our workflow (Supplementary Fig. 9), subensemble fluorescence lifetime analysis,

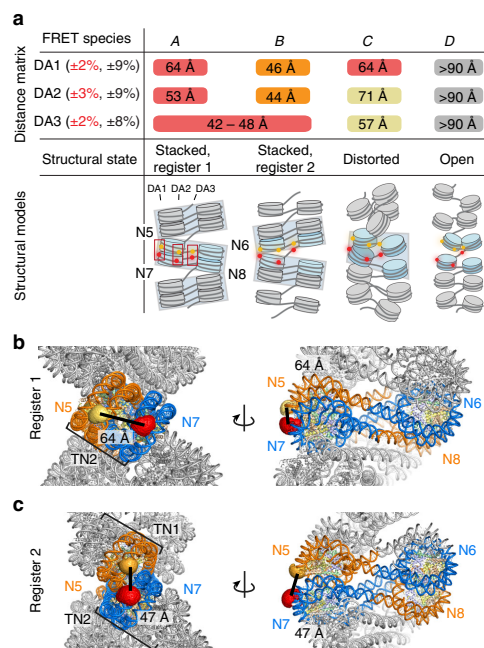


Fig. 4 Chromatin fibers exist in two rapidly interchanging tetranucleosome stacking registers. **a** Matrix of the inter-dye distances R_{DA} for DA1, DA2, and DA3 obtained from dynPDA. Species that cannot be discriminated with a given FRET pair are labeled with the same color and/or a continuous box. Percentages given in brackets: uncertainties in the observed distances. Red: precision ($\Delta R_{DA}/R_{DA}$), relevant for relative R_{DA} , calculated as s.d. between three PDA analyses of data sets comprising a fraction (70%) of all measured data (subsampling). Black: Absolute uncertainty, mainly determined by the uncertainty in R_0 (Supplementary Note, step 9 and Supplementary Table 7). The combined average inter-dye distances R_{DA} over DA1–3 allow us to map each FRET species to a class of corresponding structural states of chromatin (Supplementary Figs. 12 and 13, Supplementary Table 8, and Supplementary Note, steps 9 and 10). The registers of tetranucleosome units are indicated by light gray boxes. **b** Structural model of a chromatin array, consisting of a stack of three tetranucleosomes (register 1) with DA1-positioned dyes in the central tetranucleosome, based on ref. 7. The inter-dye distance was evaluated using simulated dye accessible contact volumes (ACV)³⁴. **c** Molecular structure of a chromatin array, consisting of a stack of two tetranucleosomes, flanked by two unstacked nucleosomes at each side (register 2) with DA1-positioned dyes on the two central tetranucleosomes and inter-dye distance from ACV calculations. Molecular models for DA2 and DA3 are reported in Supplementary Figs. 12 and 13

corroborated the FRET species for each labeling pair DA1–3. Similarly, model-free fluorescence correlation analysis from DA1–3 revealed conformational dynamics with at least three relaxation times, thus involving at least four kinetic species (A–D). Finally, the FRET line parameters were determined in independent experiments³⁸ (see Supplementary Note, step 2).

In summary, for all vantage points DA1–3 our analysis revealed compact chromatin fibers ($E_{FRET} > 0.8$) in rapid exchange with extended structures (Fig. 3d). At least two independent dynamic transitions were consistently resolved, as indicated by

the two dynamic FRET lines, revealing distinct limiting FRET species with high E_{FRET} (compact species, A–C) and with very low E_{FRET} (open species, D), respectively. The existence of two dynamic transitions, as indicated by the two FRET lines, directly revealed two populations of chromatin fibers. Each population shows unique internal exchange dynamics but no interchange between the populations is observed during the ~10 ms observation time. Chromatin fibers are thus structurally and dynamically heterogeneous at the local level.

Revealing structural states in dynamic chromatin fibers. To delineate the fiber architectures corresponding to these populations, we performed MFD experiments using Alexa Fluor 488 as a FRET donor ($R_0 = 52 \text{ \AA}$). This FRET donor substantially improved the spatial resolution at shorter distances (Supplementary Fig. 8b). Importantly, excitation at 485 nm enabled us to employ PIE. We thus could exclude donor-only labeled chromatin fibers. In agreement with the previous MFD measurements (Fig. 3d), FRET distributions were also located on two dynamic FRET lines (Fig. 3e). Due to the altered distance sensitivity of the Alexa488/647 FRET pair, compact states (A, B, and C) were now better resolved. As a result, in these experiments the dynamic FRET lines fell closer to the static FRET lines (while remaining well defined), as compared to measurements with Alexa568/647. Together, these measurements with two different labeling schemes confirm the existence of four structural states in two distinct fiber populations interchanging with fast internal dynamics.

Subensemble fluorescence lifetime analysis provides an alternative method to directly resolve the individual FRET efficiencies (and thus R_{DA} values) within a dynamic ensemble. In effect, it provides a nanosecond snapshot of the coexisting FRET species, independent of their exchange dynamics. We thus averaged photon bursts from DA1 (selecting only bursts with $E_{FRET} > 0.065$) and computed a FRET-induced fluorescence decay of the donor $\epsilon_D(t)$ (Fig. 3f and Supplementary Note, step 3)³⁹. The nonlinear decay of $\epsilon_D(t)$ on a log scale directly demonstrated the existence of at least three FRET species. We employed a global analysis to resolve the inter-dye distances characteristic for the three corresponding FRET species {A, C}, B and D (Fig. 3f and Supplementary Fig. 10), closely matching the limiting FRET states observed in 2D-MFD histograms (Fig. 3d, e).

Fluorescence correlation analysis enables a direct and model-free assessment of molecular dynamics. We thus analyzed the autocorrelation functions for the donor and acceptor channels, as well as the cross-correlation between donor and acceptor fluorescence channels (Fig. 3g, and Supplementary Fig. 11, and Supplementary Note, step 4). For DA1, this analysis directly confirmed the existence of structural dynamics between the FRET species {A, C}, B and D, revealing two slow kinetic exchange processes with relaxation time constants t_R of 27 μs and 3.1 ms. However, solely based on this analysis, the relaxation times could not be attributed to individual conformational dynamics.

Resolving conformational dynamics in chromatin fibers. An integrated approach is required to characterize the two dynamic populations in chromatin fibers, and to resolve their underlying structural states. We thus proceeded along our workflow for dynamic structural biology (Supplementary Fig. 9 and Supplementary Note): Using the combined information from TIRF measurements, MFD histograms, subensemble lifetime analysis, and fluorescence correlation analysis for DA1–3, we were able to analyze the experimental data with dynamic photon distribution analysis (dynPDA)³⁸ (Supplementary Note, steps 6–8). This is an approach comparable to the analysis of NMR relaxation

dispersion experiments, resolving subpopulations and their exchange dynamics. While dynPDA is an inherently iterative method, for clarity we first address structural considerations followed by a discussion of the observed dynamics.

Our dynamic–structural biology approach revealed high-precision inter-dye distances (displayed as a distance matrix in Fig. 4a) for species (A–D) with respect to the three vantage points of the samples DA1–3 (Fig. 4a). Using the recovered inter-dye distance sets as constraints, we assigned molecular structures to species (A–D), based on available high-resolution structural data^{6,7} and coarse-grained simulations⁴⁰ (Fig. 4b, c, Supplementary Figs. 12 and 13, and Supplementary Note, steps 9 and 10). Distance constraints from DA1 and DA2 showed that FRET species A and B correspond to conformational states with defined tetranucleosome units in two different interaction registers relative to the FRET labels. Register 1 (A) positions the label pairs in the same tetranucleosome unit (Fig. 4a, b). This chromatin fiber conformation is consistent with the reported cryo-EM structure of a 12-mer chromatin fiber⁷. Register 2 (B) positions the FRET labels across two neighboring tetranucleosome units, indicating a fiber structure that exhibits altered nucleosome interactions (Fig. 4a, c). Species (C) corresponds to a distorted (twisted) tetranucleosome state within register 1. Finally, species (D) corresponds to an ensemble of open chromatin fiber conformations.

From the DA1 vantage point, the two compact species (A) and (C) shared a single inter-dye distance, resulting in the apparent FRET species {A, C}. This can be rationalized as the DA1 dye pair is close to a key internucleosomal interaction, mediated via the H2A–H2B four-helix bundle^{6,7}. This interaction restricts local internucleosomal motions. DA2, in contrast, detected the distorted tetranucleosome state (C), which for this vantage point exhibits an increased inter-dye distance. Hence, stacked nucleosomes exhibit more structural flexibility close to the dyad. Finally, all three dye pairs DA1–3 reported on the species (D), accounting for open chromatin devoid of local internucleosomal interactions.

A dynamic register model for chromatin dynamics. To uncover fundamental motions within chromatin fibers, the kinetic connectivity of the chromatin structural states must be elucidated. We thus employed all the previously discussed information to formulate kinetic models, which were employed to fit the experimental FRET efficiency histograms by dynPDA (Fig. 5a–c, Supplementary Fig. 14, and Supplementary Note, steps 5–8). To find an appropriate kinetic model, we performed global fits over the Mg^{2+} dependence for each data set DA1–3. We tested a set of 3- and 4-state kinetic models describing distinct kinetic connectivities between species (A–D) (Fig. 5d–f and Supplementary Fig. 15). In agreement with two dynamic populations detected in MFD plots, a successful and consistent fit for all label pairs was achieved with a kinetic model containing two branches: one branch connecting species (A, C) to (D), the second branch connecting species (B) to (D) (Fig. 5d–f and Supplementary Figs. 16–18). The revealed kinetic information provided insights into the dynamics of chromatin fibers: an analysis of DA1 (Fig. 5d) indicated that stacked nucleosome (A, register 1) exchange with open conformations (D) with a relaxation time $\tau_R = 3.7 \pm 0.3$ ms (uncertainties of relaxation times: s.d. between three PDA analyses of data sets comprising a fraction (70%) of all measured data (subsampling)). These motions are two orders of magnitude slower compared to fluctuations between tetranucleosomes (B–D, register 2, $\tau_R = 60 \pm 10$ μ s). This is consistent with the significant free energy (around 13 kT) associated with nucleosome stacking²⁰. DA2 provided further insight into intra-tetranucleosome dynamics (Fig. 5e), where structural distortions

(i.e., torsional fluctuations and partial nucleosome disengagement, species C) occur on a 0.5 ± 0.06 ms timescale, followed by a transition to D within 2.6 ± 0.5 ms. DA3, finally, reported on linker DNA fluctuations (Fig. 5f). Here, we detected increased (C–D) transition rates, indicating a contribution from transient DNA unwrapping dynamics^{12,13,41}. Analyzing the populations of species A–D for DA1–3 over the range of Mg^{2+} concentrations revealed a coherent picture of the dynamic chromatin structure (Fig. 5g–i): Compact conformers in register 1 (A, C) were about twice as highly populated as register 2 contacts (B). Thus, register 1 with maximally three formed tetranucleosomes is energetically more favorable than register 2 that can only encompass two stacked tetranucleosome units. Compact conformers were increasingly more populated at higher bivalent ion concentrations, but remained in rapid exchange with open and compact chromatin. Finally, between 20 and 40% of all observed chromatin fibers did not show any measurable dynamics on the MFD timescale (observed for all species (A–D), see Supplementary Figs. 16–18). This indicates the presence of chromatin structures separated by significant barriers from the rapidly exchanging structural ensemble (locked states), consistent with the observation of slow dynamics in TIRF-FRET measurements.

Together, our smFRET measurements revealed intriguing multiscale chromatin dynamics across five orders of magnitude in time. We propose a unified model (the dynamic-register model) to describe higher-order chromatin structure and its local dynamics (Fig. 6 and Supplementary Note, step 11). In a chromatin fiber a nucleosome can, at any time, engage in tetranucleosome contacts with only one of its two neighbors within the two-start helix. On a short range, this results in at least two interchanging interaction registers. The exchange pathway between registers 1 and 2 always leads through local fiber unfolding and subsequent reformation of the (altered) tetranucleosome contacts.

A chromatin fiber has more conformational degrees of freedom than those directly probed by FRET in this study. Thus, we use structural and dynamic features to subdivide the observable FRET species A–D further into an ensemble of conformational states (indicated by the numerical index in Fig. 6). Fluctuations observable in smTIRF-FRET (and quasistatic molecules in MFD) indicate the existence of nucleosome interactions stable for a few hundreds of milliseconds (locked states A_1, B_1) as well as dynamic species (unlocked states A_2, B_2). In register 1, we observed rearrangements of the nucleosome interface allowing tetranucleosomes to open on a millisecond timescale (to A_3, C , and the ensemble of open states D_n). In contrast, neighboring tetranucleosomes in register 2 are only loosely associated, resulting in sub-millisecond interaction dynamics governed by shallow energy barriers (B_2 to D_1 and D_n). Importantly, this dynamic ensemble of higher-order structures (or supertertiary structure⁴²) with multiple conformational states and dynamic transitions is a fundamental property of chromatin fibers. Elementary states are observed both in extended and compact fibers, but are populated to different extents. Our analysis thus suggests that these elementary states and their transitions govern the biochemical accessibility, regulation, and biological function of chromatin.

HP1 α induces a dynamically compacted chromatin structure. Having established this dynamic model of chromatin, we asked how HP1 α affects the internal structure and dynamics of chromatin fibers. Previous studies indicated that HP1 α can compact chromatin^{25,43} and that it can cross-bridge H3K9me3-modified nucleosomes²⁸. However, no information was available about the internal structure of HP1 α -complexed chromatin. Single-

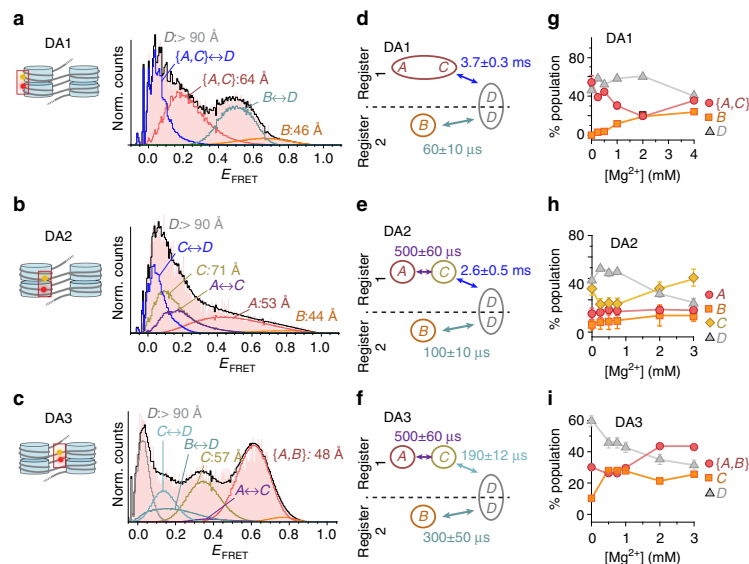


Fig. 5 Chromatin exhibits multiscale dynamics. **a–c** dynPDA analysis of MFD data (for a detailed description, see Supplementary Note, steps 6–8). Red histogram: Experimental data, black line: PDA fit to the kinetic models corresponding to the indicated state connectivities (Fig. 5d–f). Gaussian distributions in orange hues or gray: Distributions corresponding to the indicated FRET states indicated in Fig. 4a: A (red), B (orange), C (yellow), and D (gray). Blue hues: Distributions originating from dynamic exchange between FRET species: A \leftrightarrow C (violet), C \leftrightarrow D (dark blue), B \leftrightarrow D (gray blue). **a** dynPDA analysis of MFD data for DA1 (at 4 mM Mg^{2+}) using the kinetic connectivity outlined in Fig. 5d. **b** dynPDA analysis of MFD data for DA2 (at 3 mM Mg^{2+}) using the kinetic connectivity outlined in Fig. 5e. **c** dynPDA analysis of MFD data for DA3 (at 3 mM Mg^{2+}) using the kinetic connectivity outlined in Fig. 5f. **d–f** Kinetic connectivity maps for DA1–3 used for dynPDA, which describe the experimental data. Two dynamic equilibria (registers) are observed: Register 1 comprises species A, C, and D (as characterized by their inter-dye distance, R_{DA}), exchanging with the indicated relaxation times. Register 2 comprises species B and D in equilibrium. Register exchange within D is not permitted in the model on the investigated timescales, as indicated by the dashed line. The indicated time constants are given for 2 mM Mg^{2+} . For the individual rate constants, see Supplementary Figs. 16–18). Uncertainties: s.d. between three PDA analyses of data sets comprising a fraction (70%) of all measured data (subsampling). **g** Relative combined populations of observed species A–D for DA1 as a function of $[\text{Mg}^{2+}]$ (for the individual contributions of static and dynamic molecules, see Supplementary Figs. 16–18). **h** Relative combined populations for species A–D for DA2. **i** Relative combined populations for species A–D for DA3. For the full PDA fits, see Supplementary Figs. 16–18. Error bars: s.d. between three dynPDA analyses of data sets comprising a fraction (70%) of all measured data (subsampling). In some cases, the error bars are smaller than the symbol size

molecule-binding studies revealed that HP1 α interacts with chromatin on the 250 ms timescale²⁷, matching the time resolution of our FRET-TIRF approach. We thus reconstituted DA1 and DA2 chromatin fibers containing either unmethylated (H3K9me0) or chemically produced H3K9me3 (Supplementary Fig. 19a, b) and measured smFRET in the presence of 1 μM HP1 α using TIRF microscopy (Fig. 7a, b). The presence of HP1 α resulted in H3K9me3-dependent chromatin compaction as observed by an increase in E_{FRET} from the vantage points DA1 and, in particular, from DA2 (Fig. 7c, d). The larger effect on DA2 indicates that HP1 α stabilizes nucleosome stacking primarily toward the center of the chromatin fiber, where the FRET efficiency reaches the value ($E_{\text{FRET}} > 0.8$) of the limiting species A, B resolved by MFD measurements (Fig. 3d). This comparison directly shows that the HP1 α -compacted state involves the same inter-nucleosome contacts as observed in the absence of HP1 α .

HP1 α is post-translationally modified in particular by phosphorylation of its N-terminal extension (NTE)⁴⁴. Intriguingly, this modification not only stabilizes H3K9me3 binding^{45–47} leads to HP1 α oligomerization and phase separation behavior important for heterochromatin establishment^{48,49}. We thus produced phosphorylated HP1 α (pHP1 α , Supplementary Fig. 19f–i). Phosphorylation indeed increased the compacting

effect by stabilization of nucleosome binding and by strengthening HP1 α interactions beyond the dimer (Fig. 7c, d). Intriguingly, the analysis of FRET traces by cross-correlation analysis of donor and acceptor fluorescence revealed high-amplitude dynamic fluctuations with a sub-second relaxation time in the presence of HP1 α (Fig. 7e, f). Thus, chromatin fibers compacted by HP1 α do not adopt a stably closed conformation, but in contrary remain highly dynamic and exhibit structural fluctuations on the sub-second timescale.

Finally, we wondered how fast HP1 α could compact chromatin fibers. We thus injected 1 μM HP1 α into flow cells containing H3K9me3-modified chromatin fibers and monitoring FRET via the DA2 FRET pairs. The accumulated traces revealed an increase of compaction with a time constant of 1.1 ± 0.4 s (Fig. 7g, h, fit uncertainties correspond to 95% confidence intervals, global fit of $n = 86$ traces). Thus, HP1 α needs to accumulate on chromatin to reach a critical density before compaction can take effect.

In summary, we find that HP1 α transiently stabilizes interacting nucleosomes in chromatin fibers. This is most likely achieved by cross-bridging nucleosomes through H3K9me3 interactions^{24,25,28} (Fig. 7i), a process which occurs on the hundreds of milliseconds timescale consistent with measured residence times for HP1 α ²⁷.

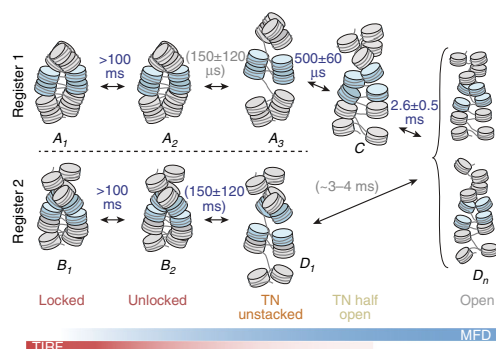


Fig. 6 The dynamic register model of chromatin fiber dynamics (for details see text). The colored bars indicate the sensitivities of the two applied smFRET methods. The letters A, B, C, and D correspond to observed FRET species (Fig. 4a). Nucleosomes highlighted in blue are labeled and thus observed in the experiment. Numbered states correspond to different chromatin conformations, which exhibit the same FRET efficiency for DA1-3 but which can be kinetically differentiated. FRET species A includes conformational states $\{A_1, A_2, A_3\}$ for which stacked nucleosomes are observed. FRET species B includes all states $\{B_1, B_2\}$ corresponding to observation across two neighboring tetranucleosome units. FRET species D (low-FRET states) includes locally unstacked nucleosomes (D_1) and the ensemble of open fibers (D_n). Gray relaxation time constants are indirectly inferred; blue relaxation times are directly observed. The error ranges represent s.d. between observations of the same dynamic process with different FRET label pairs (for $B_2 \leftrightarrow D_1$), or directly from PDA subsampling (Fig. 5)

Discussion

The structural dynamics of chromatin dictate biochemical access to the DNA and thus directly impinge on dynamic regulatory processes, such as TF binding, transcription, or DNA repair. A detailed knowledge of the structural states and exchange timescales within chromatin is therefore of critical importance. Previous experiments indicated that chromatin is highly dynamic^{17–21}, but stopped short of a detailed structural and kinetic exploration of unconstrained chromatin fibers.

Here, we employed two distinct smFRET approaches with access to complementary experimental timescales to reveal the structural and dynamic landscape of chromatin fibers. Based on our results, we formulated a dynamic-register model (Fig. 6) describing the fundamental dynamic modes governing biochemical access to compact chromatin. Our data are in agreement with the tetranucleosome as a fundamental unit of chromatin fibers²¹. We however discover a distinct set of motions within and between tetranucleosome units that introduce dynamic heterogeneity into chromatin structure. Individual tetranucleosomes can spontaneously open on the millisecond timescale. In contrast, interactions between neighboring tetranucleosomes fluctuate in the microsecond time regime. Neighboring tetranucleosomes can exchange their interaction register on the hundred millisecond timescale, by concerted unfolding, followed by refolding in the alternative register.

The existence of such a fundamental dynamic landscape of chromatin is analogous to the situation in proteins, where intrinsic motions govern function^{50,51}. In chromatin, fiber dynamics are coupled to processes such as the target search of TFs, e.g., through sliding and hopping⁵². As these interaction modes require direct access to the DNA, local chromatin dynamics control the fundamental timescale of DNA sampling

and thereby set a speed limit for TF-binding kinetics. Intriguingly, direct observations of TF chromatin sampling in vivo reveal that these interactions occur on similar timescales as the local chromatin dynamics revealed in this work^{33,34}. Finally, dynamic coupling mechanisms are not limited to TFs, but extend to other processes such as chromatin remodeling⁵⁵ or gene transcription itself⁵⁶.

Our measurements revealed that individual nucleosomes engage in short-lived (milliseconds to hundreds of milliseconds) stacking interactions with their neighbors, forming tetranucleosome units. Tetranucleosome contacts hinder access to linker DNA⁶ and occlude the nucleosome acidic patch, the major interaction site for many chromatin effectors^{57–59}. In agreement, structural^{6,7} and force spectroscopy studies reported tetranucleosomes as basic organizational units of chromatin²¹. The observation of both a population of short-lived (milliseconds) as well as long-lived tetranucleosome states (locked states with lifetimes of hundreds of milliseconds) demonstrates that several inter-nucleosome interactions have to be released to allow rapid local fiber dynamics. One intriguing possibility is that long-lived (locked) states arise due to stabilizing long-range inter-nucleosomal interactions outside the tetranucleosome unit, which provide additional stability to chromatin fiber structure.

Importantly, we found that tetranucleosome contacts alternate between different registers on the 100-ms timescale. The interchange between registers requires cooperative motions between neighboring tetranucleosome units, at least over the range of four to eight nucleosomes. It is thus conceivable that structural disturbances in the fiber, e.g., by a bound TF, have long range effects on neighboring genomic loci by a modulation of DNA site exposure dynamics. Indeed, cooperative and collaborative effects between TF-binding sites have been observed over distances significantly exceeding a single nucleosome⁶⁰, pointing toward a role of long-range chromatin organization.

Several genome-wide studies have determined the existence and prevalence of tetranucleosome contacts in vivo, employing analysis of nucleosome contacts by electron microscopy⁶¹, Micro-C⁴ or in situ radical fragmentation of chromatin⁵. Long stretches of ordered chromatin structure are however not readily observed in interphase nuclei⁶². Our findings regarding the rapid dynamics and heterogeneity provide a rationale for this absence of order over large spatial and temporal scales. Rather, internucleosomal contacts are in constant exchange, forming local transient structures that are permissive for chromatin effectors.

The inherent flexibility and structural adaptability gives chromatin an inhomogeneous dynamic secondary structure with conformational fluctuations ranging over several orders of magnitude in time and space. This makes chromatin an ideal hub for interactions with diverse partners, including architectural such as H1, as well as a large range of chromatin effectors. Our developed methods for dynamic structural biology of chromatin enabled us to systematically determine local effects on such dynamic interactions.

Here we explored how HP1 α , a key heterochromatin component, affects chromatin fibers depending on the presence of H3K9me3. We found that HP1 α transiently stabilizes internucleosome contacts, most probably through multivalent engagement of two PTMs on different nucleosomes²⁷. This results in an increased population of compact states, reducing local chromatin accessibility. In agreement, the presence of HP1 α in vivo is correlated with increased tetranucleosome contacts⁵.

Strikingly, HP1 α -compacted chromatin fibers remained highly dynamic (Fig. 7i). First, HP1 α interacts with DNA in addition to H3K9me3^{28,36}, which might directly modulate local chromatin motions. Second, HP1 α has a stronger compacting effect around the nucleosome dyad. This suggests that the protein has a

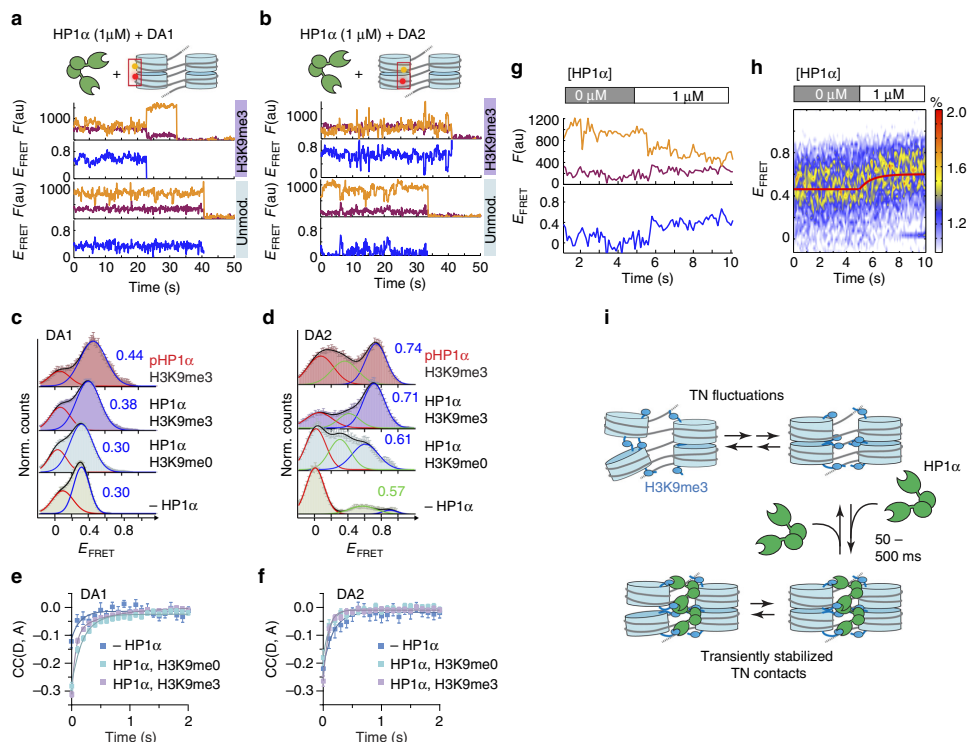


Fig. 7 HP1 α binding results in dynamically compacted chromatin. **a** FRET traces for DA1, containing no modification or H3K9me3 in the presence of 1 μ M HP1 α and the absence of Mg $^{2+}$. **b** FRET trace for DA2, containing no modification or H3K9me3 in the presence of 1 μ M HP1 α . **c** FRET populations for DA1, showing H3K9me3-dependent compaction by HP1 α and phosphorylated HP1 α (pHP1 α). **d** FRET populations for DA2, demonstrating close contacts induced by HP1 α /pHP1 α . **e, f** Error bars: s.e.m. For the number of traces, parameters of the Gaussian fits, see Supplementary Table 5. **e** Donor-acceptor channel cross-correlation analysis of DA1 in the presence of 1 μ M HP1 α . Fits, H3K9me0: $t_{R,1}$ = 200 \pm 25 ms (n = 530), H3K9me3: $t_{R,1}$ = 64 \pm 13 ms (72%), $t_{R,2}$ = 640 \pm 126 ms (28%) (n = 430). **f** Donor-acceptor channel cross-correlation analysis of DA2 in the presence of 1 μ M HP1 α . Fits, H3K9me0: $t_{R,1}$ = 123 \pm 38 ms (n = 99); H3K9me3: $t_{R,1}$ = 66 \pm 16 ms (88%), $t_{R,2}$ = 930 \pm 543 ms (12%) (n = 106). Fit uncertainties correspond to 95% confidence intervals of a global fit of the indicated number of traces. For the percentage of dynamic traces, see Supplementary Table 6. **e, f** Error bars: s.e.m. For the number of traces, see Supplementary Table 5. **g** Stochastic compaction of chromatin induced by injection of HP1 α at 5 s. **h** 2D histogram of multiple injections. Only traces exhibiting a FRET change were included in the analysis (42%). The fit yields a time constant of 1.1 \pm 0.4 s (fit uncertainties correspond to 95% confidence intervals, global fit of n = 86 traces). **i** Model of transient stabilization of tetranucleosomes, which still retain some internal flexibility, by HP1 α

tendency to bind at central as opposed to peripheral sites within a chromatin fiber. Third, individual HP1 α molecules do not remain stably bound to fibers, but exhibit rapid exchange dynamics *in vitro*²⁷ and *in vivo*^{23,29,30} on the hundreds of millisecond to seconds timescale. Rapid HP1 α turnover will thus stochastically release the stabilization of local nucleosome stacking interactions allowing local exposure of internal sites.

Functionally, the dynamic HP1 α -compacted state remains permissive for biochemical access to the fiber, albeit to a reduced degree. Moreover, we expect bound HP1 α to impair tetranucleosome register exchange, as this requires transient opening of two neighboring tetranucleosomes. Together, these effects therefore contribute to repression of transcription in heterochromatin. Nevertheless, as all DNA sites and nucleosome surfaces are eventually exposed, effectors such as pioneer TFs⁶³ or even the transcription machinery can still invade the heterochromatin state. In agreement, heterochromatin regions generally are transcribed at low levels⁶⁴. Moreover, local accessibility makes

rapid chromatin regulation possible as a function of cellular stimuli⁶⁵.

In summary, our single-molecule studies reveal dynamic heterogeneity within chromatin fibers, where the intrinsic dynamics are determined by a complex energy landscape. Dynamic higher order or supertertiary structure is governed by interactions of tetranucleosomes that form the fundamental structural units and provide local cooperativity through register exchange dynamics. Chromatin effectors, such as HP1 α , selectively modulate this energy landscape by stabilizing specific conformations from the rapidly exchanging ensemble, thereby enacting a biological output. Thus, the mutual interplay between chromatin dynamics and effector proteins controls downstream biological processes.

Methods

Plasmid generation, purification, and DNA fragment isolation. Plasmids for chromatin DNA production (recP1, recP5) were generated in DH5 α cells grown in 6 L 2xTY medium and isolated by alkaline lysis followed by preparative gel

filtration as follows: After 18–20 h culture, cells were harvested by centrifugation, resuspended and homogenized in 80 mL alkaline lysis solution I (50 mM glucose, 25 mM Tris, 10 mM EDTA, pH 8.0). Homogenate was diluted to 120 mL with the same solution. An aliquot of 240 mL alkaline lysis solution II (0.2 M NaOH, 1% SDS) was added and mixed. An aliquot of 240 mL alkaline lysis solution III (4 M KAc, 2 M Acetic acid) was added to neutralize the solution followed by mixing and subsequent incubation for 15 min at 4 °C. The supernatant was recovered by centrifugation and filtered through miracloth. In total, 0.52 volumes of isopropanol were added and the mixture was allowed to stand for 20 min at room temperature, followed by centrifugation at 11,000 \times g for 20 min at room temperature. The pellet was redissolved in 30 mL TE 10/50, 100 units of RNase A were added and allowed to digest 2 h at 37 °C. Solid KCl was added to a final concentration of 2.0 M and the volume was adjusted to 35–40 mL. The sample was centrifuged and the supernatant loaded onto a 50 mL sepharose. This was injected into a 550 mL sepharose 6 XK 50/300 column and the pure plasmid was collected in the dead volume. The plasmid was precipitated with 0.5 volumes of isopropanol and redissolved in TE 10/0.1.

An aliquot of 75–85 pmol of plasmid DNA was buffer exchanged to H₂O and mixed with CutSmart buffer (NEB) and water to a final volume of 200 μ L. Fifty units of Bsal-HF and 50 units of DraIII-HF were added to digest for 8–10 h, then another 20 units of each enzyme was added to get the digestion to completion (additional 20 units were added if not complete). Sixty units of EcoRV-HF were added and digestion was continued for 6–10 h (Supplementary Fig. 1f–i). Two rounds of stepwise PEG precipitation were performed to separate the excised fragment of interest from the plasmid backbone fragments using concentrations of PEG from 7.0 to 8.5% (Supplementary Fig. 1j, k). After two rounds, a final cleanup step was done using a Zymo Clean and Concentrator 100 column.

Preparation of fluorescently labeled DNA fragments. An aliquot of 5–10 nmol of oligonucleotide at a concentration of ~1 mM, washed by ethanol precipitation, was diluted with 25 μ L oligo labeling buffer (0.1 M sodium tetraborate, pH 8.5 (9.25 for TTP ester labeling). A 0.6 μ L sample was taken and diluted with 50 μ L oligonucleotide RP-HPLC solvent A (95% 0.1 M TEAA, 5% ACN). An aliquot of 40 μ L of this was injected for analysis by RP-HPLC on an InertSustain 3 μ m, 4.6 \times 150 mm GL sciences C18 analytical column using a gradient of 0–100% oligonucleotide RP-HPLC solvent B (70% 0.1 M TEAA, 30% ACN) in 20 min. An aliquot of 5 μ L of 5 mM NHS-ester dye in DMSO was added and the reaction allowed to proceed 4–8 h at room temperature. The progression of the reaction was monitored by RP-HPLC. Further, dye was added if required, until >50% oligonucleotide was labeled. The oligonucleotide was precipitated twice with ethanol to remove residual dye. It was redissolved in 30 μ L MQ H₂O and diluted with 70 μ L oligo RP-HPLC solvent A. Labeled oligonucleotides were purified by RP-HPLC using the same gradient and column as above and collected manually followed by ethanol precipitation. The purified labeled oligonucleotide was redissolved in MQ H₂O to give a concentration of 2.5 μ M (Supplementary Fig. 2a–i).

Labeled PCR segments were generated by mixing Thermopol (1x), template (0.02 ng μ L⁻¹), forward primer (0.250 μ M), reverse primer (0.250 μ M), and dNTPs (0.2 mM each) with water in $N \times 50 \mu$ L to the final concentrations given in the parentheses. $N \times 1.25$ units Taq DNA polymerase was added, the solution was gently mixed followed by aliquoting 50 μ L into each of N PCR tubes. Thermocycling was done with 12 s initial denaturation at 94 °C followed by 30 cycles of 12 s denaturation at 94 °C, 12 s annealing at 60–65 °C, and 12 s extension at 72 °C. Final extension was done for 12 s at 72 °C. PCR product from the N tubes were pooled and stored in the freezer.

An aliquot of 450–500 μ L of PCR product was purified with 3x QIAquick PCR purification columns according to the manufacturer's protocol. Following elution, the DNA was ethanol precipitated and redissolved in ~100 μ L MQ H₂O. PCR-generated pieces were digested by mixing 75–85 pmol of each piece in 200 μ L with 10x CutSmart to a final concentration of 1x and a sample taken. The pieces were digested as done for the recombinant pieces. Samples were taken and analyzed on a 2% agarose gel alongside the undigested samples (Supplementary Fig. 2j). The digestion reactions were purified with QIAquick PCR purification columns and the concentration was determined by UV spectroscopy.

Convergent DNA ligations for 12 \times 601 arrays. An aliquot of 30–60 pmol of each DNA piece was used for large-scale ligation to generate the intermediates in combined volumes of 200–400 μ L (Supplementary Fig. 3a). P2 was ligated to P1 in 20% excess for 2 h, then P3 was added in 20% excess relative to P2 and ligation allowed to proceed overnight. P4 was ligated to P5 in 20% excess for 2 h, then the biotinylated anchor was added in twofold excess relative to P5 and the ligation allowed to proceed 12–16 h (Supplementary Fig. 3b–d). The pieces were purified by PEG precipitation using a stepwise (0.5% steps) increase in PEG from 7.0 to 8.0% (Supplementary Fig. 3e, f). Pellets were redissolved in 60 μ L TE buffer (10 mM Tris, 0.1 mM EDTA, pH 8.0) and redissolved pellets and the final supernatant were analyzed by agarose gel to verify that the pellets at 7.0 and 7.5% typically contained the intermediates separated from the starting pieces. These were pooled and stored for later ligations. An aliquot of 15–35 pmol of the 6 \times 601 intermediates were mixed using 5–10% excess P4–P5-anchor in 1x T4 DNA ligase buffer with 600 U of ligase and left to ligate for 10–16 h. The formation of the product was confirmed by agarose gel electrophoresis and purified by stepwise PEG precipitation in the range

5.0–6.0% (Supplementary Fig. 3g, h). The pellets were redissolved in TE(10/0.1) and analyzed by gel electrophoresis to pool the purified double-labeled array DNA.

Chemically modified histones. Preparation of H4K₅I6ac was performed by radical-mediated thiol-ene addition⁶⁶. H4 carrying a K16 to cysteine point mutation (K16C) was expressed and purified from inclusion bodies²⁷. For the installation of the acetyl-lysine analog, H4K16C was dissolved in 0.2 M acetate buffer, pH 4 to a final concentration of 1 mM. Subsequently, 50 mM *N*-vinylacetamide, 5 mM VA-044 and 15 mM glutathione were added, and the reaction was incubated at 45 °C for 2 h. The reaction was monitored by HPLC and MS until complete, followed by semi-preparative RP-HPLC purification of the product (Supplementary Fig. 7a, b).

For the synthesis of H3K9me3²⁷, a peptide corresponding to H3(1–14)K9me3-NH₂ (carrying a C-terminal hydrazide) was produced by solid phase peptide synthesis. Truncated H3 [H3(Δ 1–14)A15C] was expressed as an N-terminal fusion to small ubiquitin like modifier (SUMO) carrying a His6-tag. After a denaturing Ni:NTA affinity purification, the protein was refolded and SUMO was cleaved by SUMO protease, followed by purification of H3(Δ 1–14)A15C by RP-HPLC. In a typical ligation reaction, 3 μ mol H3(1–14)K9me3-NH₂ was dissolved in ligation buffer (200 mM phosphate pH 3, 6 M GdmCl) at –10 °C. NaNO₂ was added dropwise to a final concentration of 15 mM. The reaction was subsequently incubated at –20 °C for 20 min. H3(Δ 1–14)A15C was dissolved in ligation buffer (200 mM phosphate pH 8, 6 M GdmCl, 300 mM mercaptophenyl acetic acid (MPAA)) and added to the peptide. The pH was adjusted to 7.5 and after completion of the reaction (as observed by RP-HPLC), the product (H3K9me3A15C) was purified by semi-preparative RP-HPLC. H3K9me3A15C was finally dissolved in desulfurization buffer (200 M phosphate pH 6.5, 6 M GdmCl, 250 mM tris(2-carboxyethyl)phosphine (TCEP)). Glutathione (40 mM) and a radical initiator, VA-044 (20 mM), were added, and the pH was readjusted to 6.5. The reaction mixture was incubated at 42 °C until the protein was completely desulfurized, followed by semi-preparative HPLC purification (Supplementary Fig. 19a, b).

Chromatin assembly. Chromatin arrays were reconstituted on a scale of 6.5–30 pmol (based on 601 DNA), 12 \times 601 array DNA was mixed with 1.5 molar excess of MMTV buffer DNA, NaCl to a final concentration of 2 M and water, followed by mixing and addition of 2–2.4 molar equivalents of histone octamers, containing either recombinant or chemically prepared modified histones (Supplementary Figs. 7 and 19). The mixture was transferred to a micro-dialysis tube and dialyzed with a linear gradient from TEK2000 (10 mM Tris, 0.1 mM EDTA, 200 mM KCl) to TEK10 over 16–18 h. The dialysis tube was transferred to 200–600 mL TEK10 for another 1 h of dialysis. The chromatin assembly mixture was taken out of the dialysis tube and centrifuged at 21,000 \times g for 10 min followed by transfer of the supernatant to a fresh tube. The concentration and volume of the mixture was determined. Gel analysis was done with 0.25–0.50 pmol of chromatin assembly sample (calculated based on the total 260 nm absorption and the extinction coefficient for each nucleosome repeat) mixed to 10 μ L with TEK10 and 5–7% sucrose added from a 25% stock. Samples were run in 0.7% agarose gels made with 0.25x TB, using the same as running buffer at 90 V for 90–100 min.

For ensemble FRET analysis, which requires removal of MMTV DNA and nucleosomes, 5–10% of the volume was taken aside for analysis and the remainder was mixed with an equal volume of 6 mM Mg²⁺ for precipitation on ice for 10 min followed by 10 min centrifugation at 21,000 \times g. The supernatant was transferred to another tube and the chromatin pellet redissolved in a similar volume of TEK10 as present prior to precipitation. Similar volumes as taken for chromatin assembly analysis were used for subsequent analysis of the recovered chromatin. For Scal digestion, a similar volume of sample in 1x CutSmart buffer was mixed with 10 units of Scal-HF followed by digestion for 5–7 h. Samples of chromatin before and after precipitation and after Scal digestion were analyzed as described above. Gels were visualized in fluorescence channels and then stained with GelRed for visualization of DNA and nucleosome/chromatin bands (Supplementary Fig. 4a–o).

Ensemble FRET measurements on chromatin. Chromatin samples isolated after magnesium precipitation were diluted to a final volume of typically 220–250 μ L, resulting in a concentration that yields a spectral count of around 90,000–130,000 cps for maximum donor fluorescence emission, prior to chromatin compaction. The sample was then split in 4 \times 50 μ L volumes. TEK10 and Mg²⁺ from stocks of 10 or 50 mM was added along with TEK10 to a final volume of 55 μ L, 5 min prior to measuring. After standing 5 min, the sample was transferred to the fluorescence micro-cuvette for measurement of the spectra (two repeats), followed by measurement of the donor anisotropy (two repeats). This was done for all the samples in the range 0–4 mM Mg²⁺ (Supplementary Fig. 5a–l, o). For all measurements, the following settings were used on the fluorescence spectrometer: excitation at 575 nm with 4 nm slit width, and detection over the range of 585–700 nm with 5 nm slit width. For anisotropy measurements, the emission slit width was opened to 10 nm and measurements were performed at 592 nm.

Preparing of flow chambers. Borosilicate glass slides with two rows of four holes and borosilicate coverslips were sonicated standing upright in glass containers for 20 min in MQ H₂O, then in acetone and then in ethanol. They were cleaned in piranha solution (25% v/v H₂O₂ and 75% v/v H₂SO₄) in the same glass containers for 1 h, followed by washing with MQ H₂O until reaching neutral pH. A 500 mL Erlenmeyer flask was cleaned in the same way. The Erlenmeyer flask, coverslips and slides were all sonicated in acetone for 10 min. A solution of 3% v/v aminopropyltriethylsilane in acetone was prepared in the Erlenmeyer flask and used to immerse the microscopy glass and incubated for 20 min. The aminosilane was disposed, the slides were washed in water and dried with N₂. Flow chambers were assembled from one glass slide and one coverslip separated by double sided 0.12 mm tape positioned between each hole in the glass slide. The ends were sealed with epoxy glue and the silanized slides stored under vacuum in the freezer until use.

Silanized glass flow chambers stored in the freezer were allowed to warm for 20–30 min. Then a pipette tip as inlet reservoir and outlet sources were neatly fitted in each of the 2 × 4 holes on each side of the flow chamber and glued in place with epoxy glue. The glue was allowed to solidify for 30–40 min. Subsequently, 350 µL of 0.1 M tetraborate buffer at pH 8.5 was used to dissolve ~1 mg of biotin-mPEG (5000 kDa)-SVA, and 175 µL from this was transferred to 20 mg mPEG(5000 kDa)-SVA to generate a transparent clouding-point solution after 10 s of centrifugation. This was mixed to homogeneity with a pipette and centrifuged again for 10 s before 40–45 µL aliquots were loaded into each of the four channels in the flow chamber. The PEGylation reaction was allowed to continue for the next 2½–4 h, after which the solution was washed out with degassed ultra-pure water.

smTIRF measurements. Measurements were carried out with a micro-mirror TIRF system⁶⁷ (MadCityLabs) using Coherent Obis Laser lines at 405, 488, 532 and 640 nm, a 100x NA 1.49 Nikon CFI Apochromat TIRF objective (Nikon) as well as an iXon Ultra EMCCD camera (Andor), operated by custom-made Labview (National Instruments) software. For imaging, buffers with/without biomolecules were deposited in the inlet reservoir of microfluidic flow cells and drawn into the chamber with tubing connected from the outlet to a 1 mL syringe operated manually or with a motor-driven syringe pump. For each experiment, the imaging chambers were washed with 200–300 µL T50 (10 mM TrisHCl, pH 8.5, 50 mM NaCl), followed by incubation with 50 µL 0.2 mg mL⁻¹ neutravidin for 5 min. This was washed out with another 400–500 µL T50. Then, 0.5–2 µL of chromatin assembly reaction at a concentration of 5–40 ng µL⁻¹ was loaded into the chamber while monitoring acceptor emission, to assess chromatin coverage. Chromatin was loaded until reaching 150–400 chromatin arrays in a 25 × 50 µm field of view. Excess chromatin was washed out with T50 followed by exchange to imaging buffer (40 mM KCl, 50 mM Tris, 2 mM Trolox, 2 mM nitrobenzyl alcohol (NBA), 2 mM cyclooctatetraene (COT), 10% glycerol and 3.2% glucose) supplemented with GODCAT (100x stock solution: 165 U mL⁻¹ glucose oxidase, 2170 U mL⁻¹ catalase). For imaging, a programmed sequence was employed to switch the field of view to a new area followed by adjusting the focus. Then the camera was triggered to acquire 1300–2000 frames with 532 nm excitation and 100 ms time resolution followed by a final change to 640 nm excitation. For sequences requiring timed programmed injection, after 5000 ms the pump was triggered (Fig. 1). For experiments with magnesium and HP1α, the mixture with the desired concentration was prepared and loaded into the inlet reservoir followed by injection into the channel and imaging as described above.

From acquired movies, the background was extracted in ImageJ using a rolling ball algorithm. Trace extraction and analysis was performed in custom-written MATLAB software. The donor and the acceptor images were non-isotropically aligned using a transformation matrix generated from 8 to 10 sets of peaks appearing in both the donor and the acceptor channels. Peaks were automatically detected in the initial acceptor image prior to donor excitation and the same peaks were selected in the donor channel. Peaks that were tightly clustered, close to the edges or above a set intensity threshold in either the donor or the acceptor channels indicating aggregation were removed from analysis. The analysis was then limited to the peaks appearing in both the donor and the acceptor channel and these traces were extracted for further analysis.

Traces were selected based on the following criteria: (1) Initial total fluorescence of the donor and the β-corrected acceptor of >600 counts over baseline (at 900 EM gain). (2) At least 5 s prior to bleaching of acceptor or donor. Note that for injection experiments (Fig. 1f, g or Fig. 7h), the required trace length was raised to 10 s. (3) Single bleaching event for donor or acceptor. (3.a) If acceptor bleaches first; leads to anti-correlated increase in donor to same total fluorescence level as prior to bleaching. (3.b) If donor bleaches first, the acceptor dye must still be fluorescent when directly probed at the end of the experiment. (4) Bleaching of the donor dye during the 120 s of acquisition to allow an unambiguous determination of background levels. See Supplementary Fig. 6 for a graphical representation.

MFD sample cell preparation. 24 × 40 × 1.5 mm coverslips were silanized as described above for the cleaning and passivation to generate the microfluidic channels. Two silicon gaskets were cut out with a scalpel and placed on top of a coverslip. An aliquot of 20 mg mPEG(5000 kDa)-SVA was suspended in 175 µL 0.1 M tetraborate buffer at pH 8.5. The mPEG-SVA suspension was centrifuged at 13,300 × g for 10 s and pipetted up and down before distributing approximately 40 µL in each silicon gasket on a coverslip to PEGylate. The PEGylation reaction

was allowed to proceed for the next 1–2 h before the solution was washed away by first removing the mPEG(5000 kDa)-SVA solution and then washing three times with MQ H₂O. For one of the washes, the water was allowed to stay in the gasket for 5 min before removing it. The gaskets were then filled with measurement buffer, and stayed like this until usage.

MFD measurement procedures. Chromatin fibers with the FRET pair Alexa488/647: MFD measurements with pulsed interleaved excitation (PIE) were essentially performed as shown in ref.⁶⁸ employing a confocal epi-illuminated setup based on an Olympus IX70 inverted microscope. In PIE measurements, donor and acceptor are sequentially excited by rapidly alternating laser pulses. MFD can be performed on both dyes, allowing computation of the donor–acceptor ratio (stoichiometry, S) for each particle. Excitation is achieved using 485 nm and 635 nm pulsed diode lasers (LDH-D-C 485 and LDH-P-C-635B, respectively; both PicoQuant (Berlin, Germany)) operated at 32 MHz and shifted by 15.625 ns (total frequency of both Lasers 64 MHz) focused into the sample solution by a 60×/1.2 NA water immersion objective (UPLAPO 60x, Olympus, Germany). Laser power in the sample was $L_G = 36 \mu\text{W}$ and $L_R = 7.5 \mu\text{W}$, respectively. We used the excitation beamsplitter FF550/646 (AHF, Germany) to split laser light and fluorescence. For confocal detection, a 100 µm pinhole was applied for spatial filtering. The fluorescence photon train was divided into its parallel and perpendicular components by a polarizing beamsplitter cube (VISHT11, Gsänger) and then into spectral ranges below and above 595 nm by dichroic detection beamsplitters (595 LPXR, AHF). After separating the fluorescence signal according to color and polarization, each of the four channels was split again using 50/50 beamsplitters in order to get dead time free filtered FCS curves, resulting in a total of eight detection channels. Photons were detected by eight avalanche photodiodes (green channels: τ-SPAD-100, PicoQuant; red channels: SPCM-AQR-14, Perkin Elmer). Additionally, green (HQ 520/35 nm for Alexa488) and red (HQ 720/150 nm for Alexa647) bandpass filters (AHF, Germany) in front of the detectors ensured that only fluorescence from the acceptor and donor molecules were registered, while residual laser light and Raman scattering from the solvent were blocked. The detector outputs were recorded by a TCSPC module (HydraHarp 400, PicoQuant) and stored on a PC. Data were taken for at least 90 min per sample. Bursts of fluorescence photons are distinguished from the background of 0.5–1 kHz by applying certain threshold intensity criteria⁶⁸. For analysis, several parameters, including fluorescence lifetime, anisotropy, and FRET efficiency, were computed per burst to classify the molecules according to multidimensional relations between these parameters. For MFD measurements at SMD conditions, assembled chromatin was diluted to a concentration of approximately 50 pM (1–100 µL from assembly stock solution) in measurement buffer (40 mM KCl, 50 mM Tris and 10% v/v glycerol, pH ~7.2) containing the desired amount of magnesium. This was then deposited into the silicon gasket on a passivated coverslip that had been washed with the same measurement buffer prior to deposition of the sample.

Chromatin fibers with the FRET pair Alexa568/647: MFD measurements were performed with one color excitation using a 530 nm amplified pulsed diode laser (LDH-FA 530B, PicoQuant (Berlin, Germany)) with a repetition rate of 64 MHz. The rest of the setup was identical except the customized dichroic beamsplitters (excitation beamsplitter F68-532m zt532/640/NIR rpc (AHF, Germany), dichroic detection beamsplitters F48-642, T640LPXR (AHF) and bandpass filters (HQ 595/50 (AHF) for the new donor Alexa568 and adapted bandpass filters (HQ 730/140, (AHF) for the acceptor Alexa647.

Dynamic structural biology analysis. All procedures (11 steps) are outlined in Supplementary Fig. 9 and described in detail in the Supplementary Note. Long timescale dynamics were analyzed by smTIRF (Figs. 1–2 and step 1). Short timescale dynamics were detected in MFD plots (Fig. 3 and step 2). The FRET efficiency levels corresponding to the chromatin structural states were determined by sub-ensemble fluorescence lifetime measurements (step 3 and Supplementary Fig. 10) and dynamic PDA of signal intensities (step 7 and Supplementary Figs. 16–18). Dynamics were analyzed by burst-ID FCS analysis (step 4 and Supplementary Fig. 11). Contributions from photobleaching and blinking were analyzed (step 5 and Supplementary Fig. 14). Kinetic models consistent with the analysis from steps 1–5 were formulated (step 6, Fig. 5 and Supplementary Fig. 15), and used for fitting using dynamic PDA (step 7 and Supplementary Figs. 16–18). Obtained kinetic and structural models were validated (step 8). Uncertainties in the measured distances were evaluated (step 9) and structural models of compact (step 9, Supplementary Fig. 12) and open chromatin fibers (step 10, Supplementary Fig. 13) were produced. Finally, models were validated to produce a global structural and kinetic model (step 11).

Code availability. All custom-made computer code is available upon request from the corresponding authors.

Data availability. The smTIRF data sets have been deposited at www.zenodo.org under the accession codes 1040772, 1069675, and 1069677. All other data supporting these findings are available from the corresponding authors on reasonable request.

Received: 10 July 2017 Accepted: 11 December 2017

Published online: 16 January 2018

References

- Luger, K., Dechassa, M. L. & Tremethick, D. J. New insights into nucleosome and chromatin structure: an ordered state or a disordered affair? *Nat. Rev. Mol. Cell Biol.* **13**, 436–447 (2012).
- Cuvier, O. & Fierz, B. Dynamic chromatin technologies: from individual molecules to epigenomic regulation in cells. *Nat. Rev. Genet.* **18**, 457–472 (2017).
- Bonev, B. & Cavalli, G. Organization and function of the 3D genome. *Nat. Rev. Genet.* **17**, 661–678 (2016).
- Hsieh, T. H. et al. Mapping nucleosome resolution chromosome folding in yeast by micro-C. *Cell* **162**, 108–119 (2015).
- Risca, V. L., Denny, S. K., Straight, A. F. & Greenleaf, W. J. Variable chromatin structure revealed by in situ spatially correlated DNA cleavage mapping. *Nature* **541**, 237–241 (2017).
- Schalch, T., Duda, S., Sargent, D. F. & Richmond, T. J. X-ray structure of a tetranucleosome and its implications for the chromatin fibre. *Nature* **436**, 138–141 (2005).
- Song, F. et al. Cryo-EM study of the chromatin fiber reveals a double helix twisted by tetranucleosomal units. *Science* **344**, 376–380 (2014).
- Robinson, P. J., Fairall, L., Huynh, V. A. & Rhodes, D. EM measurements define the dimensions of the “30-nm” chromatin fiber: evidence for a compact, interdigitated structure. *Proc. Natl Acad. Sci. USA* **103**, 6506–6511 (2006).
- Grigoryev, S. A., Arya, G., Correll, S., Woodcock, C. L. & Schlick, T. Evidence for heteromorphic chromatin fibers from analysis of nucleosome interactions. *Proc. Natl Acad. Sci. USA* **106**, 13317–13322 (2009).
- Li, G. & Widom, J. Nucleosomes facilitate their own invasion. *Nat. Struct. Mol. Biol.* **11**, 763–769 (2004).
- Koopmans, W. J., Brehm, A., Logie, C., Schmidt, T. & van Noort, J. Single-pair FRET microscopy reveals mononucleosome dynamics. *J. Fluoresc.* **17**, 785–795 (2007).
- Wei, S., Falk, S. J., Black, B. E. & Lee, T. H. A novel hybrid single molecule approach reveals spontaneous DNA motion in the nucleosome. *Nucleic Acids Res.* **43**, e111 (2015).
- Gansen, A. et al. Nucleosome disassembly intermediates characterized by single-molecule FRET. *Proc. Natl Acad. Sci. USA* **106**, 15308–15313 (2009).
- Luo, Y., North, J. A., Rose, S. D. & Poirier, M. G. Nucleosomes accelerate transcription factor dissociation. *Nucleic Acids Res.* **42**, 3017–3027 (2014).
- Poirier, M. G., Bussiek, M., Langowski, J. & Widom, J. Spontaneous access to DNA target sites in folded chromatin fibers. *J. Mol. Biol.* **379**, 772–786 (2008).
- Hodges, C., Bintu, L., Lubkowska, L., Kashlev, M. & Bustamante, C. Nucleosomal fluctuations govern the transcription dynamics of RNA polymerase II. *Science* **325**, 626–628 (2009).
- Poirier, M. G., Oh, E., Tims, H. S. & Widom, J. Dynamics and function of compact nucleosome arrays. *Nat. Struct. Mol. Biol.* **16**, 938–944 (2009).
- Cui, Y. & Bustamante, C. Pulling a single chromatin fiber reveals the forces that maintain its higher-order structure. *Proc. Natl Acad. Sci. USA* **97**, 127–132 (2000).
- Pope, L. H. et al. Single chromatin fiber stretching reveals physically distinct populations of disassembly events. *Biophys. J.* **88**, 3572–3583 (2005).
- Kruthoff, M. et al. Single-molecule force spectroscopy reveals a highly compliant helical folding for the 30-nm chromatin fiber. *Nat. Struct. Mol. Biol.* **16**, 534–540 (2009).
- Li, W. et al. FACT remodels the tetranucleosomal unit of chromatin fibers for gene transcription. *Mol. Cell* **64**, 120–133 (2016).
- Bannister, A. J. et al. Selective recognition of methylated lysine 9 on histone H3 by the HP1 chromo domain. *Nature* **410**, 120–124 (2001).
- Cheutin, T. et al. Maintenance of stable heterochromatin domains by dynamic HP1 binding. *Science* **299**, 721–725 (2003).
- Canzio, D. et al. Chromodomain-mediated oligomerization of HP1 suggests a nucleosome-bridging mechanism for heterochromatin assembly. *Mol. Cell* **41**, 67–81 (2011).
- Azzaz, A. M. et al. Human heterochromatin protein 1alpha promotes nucleosome associations that drive chromatin condensation. *J. Biol. Chem.* **289**, 6850–6861 (2014).
- Muller-Ott, K. et al. Specificity, propagation, and memory of pericentric heterochromatin. *Mol. Syst. Biol.* **10**, 746 (2014).
- Kilic, S., Bachmann, A. L., Bryan, L. C. & Fierz, B. Multivalency governs HP1alpha association dynamics with the silent chromatin state. *Nat. Commun.* **6**, 7313 (2015).
- Hiragami-Hamada, K. et al. Dynamic and flexible H3K9me3 bridging via HP1beta dimerization establishes a plastic state of condensed chromatin. *Nat. Commun.* **7**, 11310 (2016).
- Festenstein, R. et al. Modulation of heterochromatin protein 1 dynamics in primary Mammalian cells. *Science* **299**, 719–721 (2003).
- Muller, K. P. et al. Multiscale analysis of dynamics and interactions of heterochromatin protein 1 by fluorescence fluctuation microscopy. *Biophys. J.* **97**, 2876–2885 (2009).
- Shogren-Knaak, M. et al. Histone H4-K16 acetylation controls chromatin structure and protein interactions. *Science* **311**, 844–847 (2006).
- Fierz, B. et al. Histone H2B ubiquitylation disrupts local and higher-order chromatin compaction. *Nat. Chem. Biol.* **7**, 113–119 (2011).
- Ha, T. et al. Probing the interaction between two single molecules: fluorescence resonance energy transfer between a single donor and a single acceptor. *Proc. Natl Acad. Sci. USA* **93**, 6264–6268 (1996).
- Kalinin, S. et al. A toolkit and benchmark study for FRET-restrained high-precision structural modeling. *Nat. Methods* **9**, 1218–1225 (2012).
- Lowary, P. T. & Widom, J. New DNA sequence rules for high affinity binding to histone octamer and sequence-directed nucleosome positioning. *J. Mol. Biol.* **276**, 19–42 (1998).
- Sisamakits, E., Valeri, A., Kalinin, S., Rothwell, P. J. & Seidel, C. A. M. Accurate single-molecule FRET studies using multiparameter fluorescence detection. *Methods Enzymol.* **475**, 455–514 (2010).
- Laurence, T. A., Kong, X., Jager, M. & Weiss, S. Probing structural heterogeneities and fluctuations of nucleic acids and denatured proteins. *Proc. Natl Acad. Sci. USA* **102**, 17348–17353 (2005).
- Kalinin, S., Valeri, A., Antonik, M., Felckyan, S. & Seidel, C. A. M. Detection of structural dynamics by FRET: a photon distribution and fluorescence lifetime analysis of systems with multiple states. *J. Phys. Chem. B* **114**, 7983–7995 (2010).
- Peulen, T. O., Opanasyuk, O. & Seidel, C. A. M. Combining graphical and analytical methods with molecular simulations to analyze time-resolved FRET measurements of labeled macromolecules accurately. *J. Phys. Chem. B* **121**, 8211–8241 (2017).
- Arya, G., Zhang, Q. & Schlick, T. Flexible histone tails in a new mesoscopic oligonucleosome model. *Biophys. J.* **91**, 133–150 (2006).
- Ngo, T. T., Zhang, Q., Zhou, R., Yodh, J. G. & Ha, T. Asymmetric unwrapping of nucleosomes under tension directed by DNA local flexibility. *Cell* **160**, 1135–1144 (2015).
- Tomba, P. On the supertertiary structure of proteins. *Nat. Chem. Biol.* **8**, 597–600 (2012).
- Fan, J. Y., Rangasamy, D., Luger, K. & Tremethick, D. J. H2A.Z alters the nucleosome surface to promote HP1alpha-mediated chromatin fiber folding. *Mol. Cell* **16**, 655–661 (2004).
- LeRoy, G. et al. Heterochromatin protein 1 is extensively decorated with histone code-like post-translational modifications. *Mol. Cell. Proteomics* **8**, 2432–2442 (2009).
- Nishibuchi, G. et al. N-terminal phosphorylation of HP1alpha increases its nucleosome-binding specificity. *Nucleic Acids Res.* **42**, 12498–12511 (2014).
- Hiragami-Hamada, K. et al. N-terminal phosphorylation of HP1alpha promotes its chromatin binding. *Mol. Cell. Biol.* **31**, 1186–1200 (2011).
- Bryan, L. C. et al. Single-molecule kinetic analysis of HP1-chromatin binding reveals a dynamic network of histone modification and DNA interactions. *Nucleic Acids Res.* **45**, 10504–10517 (2017).
- Larson, A. G. et al. Liquid droplet formation by HP1alpha suggests a role for phase separation in heterochromatin. *Nature* **547**, 236–240 (2017).
- Strom, A. R. et al. Phase separation drives heterochromatin domain formation. *Nature* **547**, 241–245 (2017).
- Henzler-Wildman, K. & Kern, D. Dynamic personalities of proteins. *Nature* **450**, 964–972 (2007).
- Eisenmesser, E. Z. et al. Intrinsic dynamics of an enzyme underlies catalysis. *Nature* **438**, 117–121 (2005).
- Halford, S. E. & Marko, J. F. How do site-specific DNA-binding proteins find their targets? *Nucleic Acids Res.* **32**, 3040–3052 (2004).
- Morisaki, T., Muller, W. G., Golob, N., Mazza, D. & McNally, J. G. Single-molecule analysis of transcription factor binding at transcription sites in live cells. *Nat. Commun.* **5**, 4456 (2014).
- Chen, J. et al. Single-molecule dynamics of enhancosome assembly in embryonic stem cells. *Cell* **156**, 1274–1285 (2014).
- Blosser, T. R., Yang, J. G., Stone, M. D., Narlikar, G. J. & Zhuang, X. Dynamics of nucleosome remodelling by individual ACF complexes. *Nature* **462**, 1022–1027 (2009).
- Fitz, V. et al. Nucleosomal arrangement affects single-molecule transcription dynamics. *Proc. Natl Acad. Sci. USA* **113**, 12733–12738 (2016).
- Mattiroli, F., Uckelmann, M., Sahtoe, D. D., van Dijk, W. J. & Sixma, T. K. The nucleosome acidic patch plays a critical role in RNF168-dependent ubiquitination of histone H2A. *Nat. Commun.* **5**, 3291 (2014).
- Leung, J. W. et al. Nucleosome acidic patch promotes RNF168- and RING1B/BMI1-dependent H2AX and H2A ubiquitination and DNA damage signaling. *PLoS Genet.* **10**, e1004178 (2014).

59. McGinty, R. K., Henrici, R. C. & Tan, S. Crystal structure of the PRC1 ubiquitylation module bound to the nucleosome. *Nature* **514**, 591–596 (2014).
60. Karczewski, K. J. et al. Cooperative transcription factor associations discovered using regulatory variation. *Proc. Natl Acad. Sci. USA* **108**, 13353–13358 (2011).
61. Grigoryev, S. A. et al. Hierarchical looping of zigzag nucleosome chains in metaphase chromosomes. *Proc. Natl Acad. Sci. USA* **113**, 1238–1243 (2016).
62. Ricci, M. A., Manzo, C., Garcia-Parajo, M. F., Lakadamyali, M. & Cosma, M. P. Chromatin fibers are formed by heterogeneous groups of nucleosomes in vivo. *Cell* **160**, 1145–1158 (2015).
63. Zaret, K. S. & Carroll, J. S. Pioneer transcription factors: establishing competence for gene expression. *Genes Dev.* **25**, 2227–2241 (2011).
64. Keller, C. et al. HPI(Swi6) mediates the recognition and destruction of heterochromatic RNA transcripts. *Mol. Cell* **47**, 215–227 (2012).
65. Ayoub, N., Jayasekharan, A. D., Bernal, J. A. & Venkitaraman, A. R. HPI-beta mobilization promotes chromatin changes that initiate the DNA damage response. *Nature* **453**, 682–686 (2008).
66. Li, F. et al. A direct method for site-specific protein acetylation. *Angew. Chem. Int. Ed. Engl.* **50**, 9611–9614 (2011).
67. Larson, J. et al. Design and construction of a multiwavelength, micromirror total internal reflectance fluorescence microscope. *Nat. Protoc.* **9**, 2317–2328 (2014).
68. Kudryavtsev, V. et al. Combining MFD and PIE for accurate single-pair Förster resonance energy transfer measurements. *Chemphyschem* **13**, 1060–1078 (2012).

Acknowledgements

We thank Jun-ichi Nakayama for the CK2 expression plasmid, Nicolas Sambiagio for assistance with sample preparations. We thank Manuel M. Müller, Jeffrey C. Hansen, Wilma K. Olson, and Nicolas Clauvelin for stimulating discussions during the initial phase of this research. This work was supported by the Sandoz Family Foundation, the Swiss National Science Foundation (Grant 31003A_173169), the European Research Council through the Consolidator Grant 2017 chromo-SUMMIT (724022) and EPFL (B. F.), the Boehringer Ingelheim Foundation (S.K.), and the European Research Council through the Advanced Grant 2014 hybridFRET (671208) to C.A.M.S.

Author contributions

B.F. coordinated the project. B.F., S.K. and C.A.M.S. conceived and designed the studies. B.F. supervised chromatin synthesis and reconstitution, and smTIRF studies. C.A.M.S.

supervised the confocal smFRET studies and quantitative FRET analysis. S.K. synthesized labeled chromatin fibers, modified histones, and performed smTIRF experiments. I.B. produced phosphorylated HP1 α and performed TIRF experiments. L.C.B. produced synthetic histones. S.F., O.D., S.K. and H.V. performed and analyzed confocal FRET experiments. Kinetic modeling was performed by S.F., C.A.M.S. and B.F. PDA was performed by S.F. G.A. performed coarse-grained simulations. G.A. and B.F. generated chromatin models. O.D. and M.D. performed FPS analysis with chromatin models. All authors were involved in data analysis and interpretation. All coauthors wrote the manuscript.

Additional information

Supplementary Information accompanies this paper at <https://doi.org/10.1038/s41467-017-02619-5>.

Competing interests: The authors declare no competing financial interests.

Reprints and permission information is available online at <http://npg.nature.com/reprintsandpermissions/>

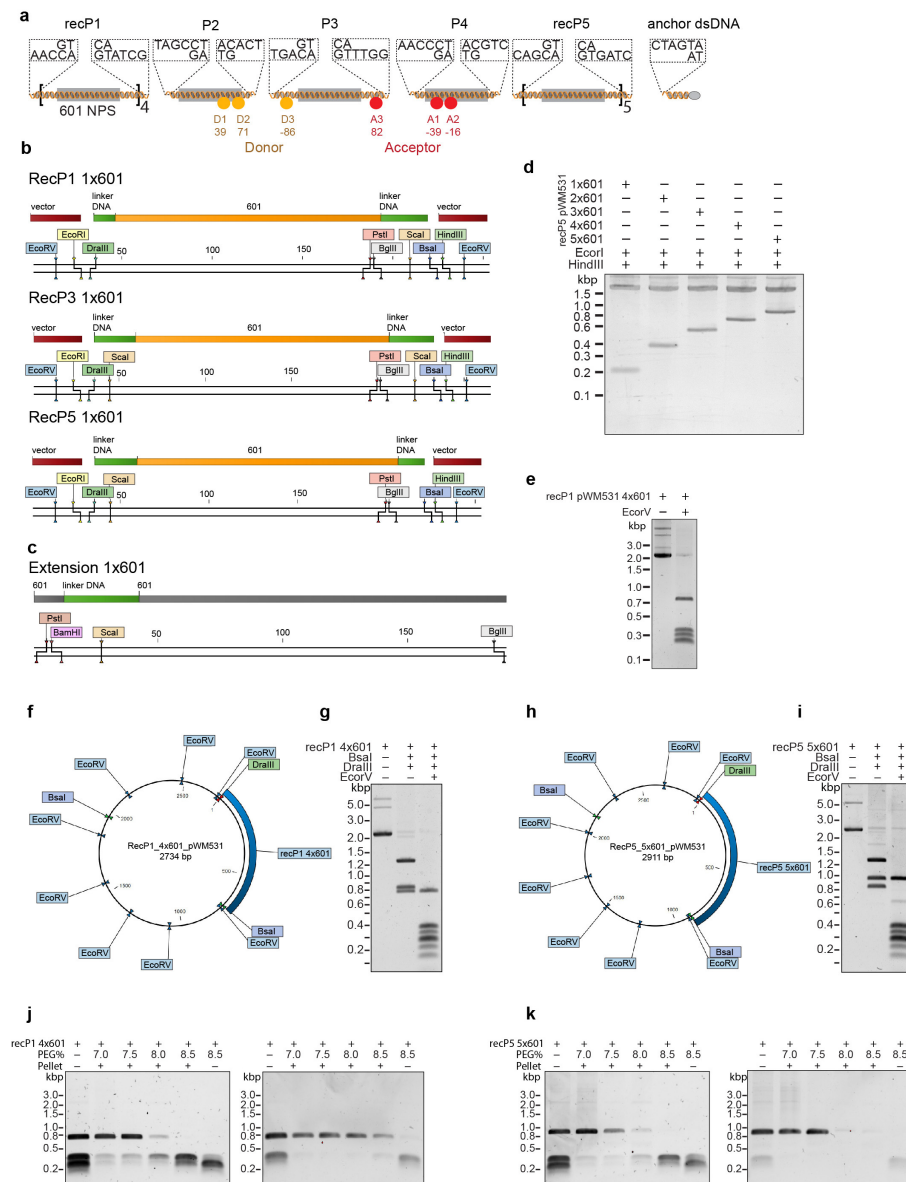
Publisher's note: Springer Nature remains neutral with regard to jurisdictional claims in published maps and institutional affiliations.



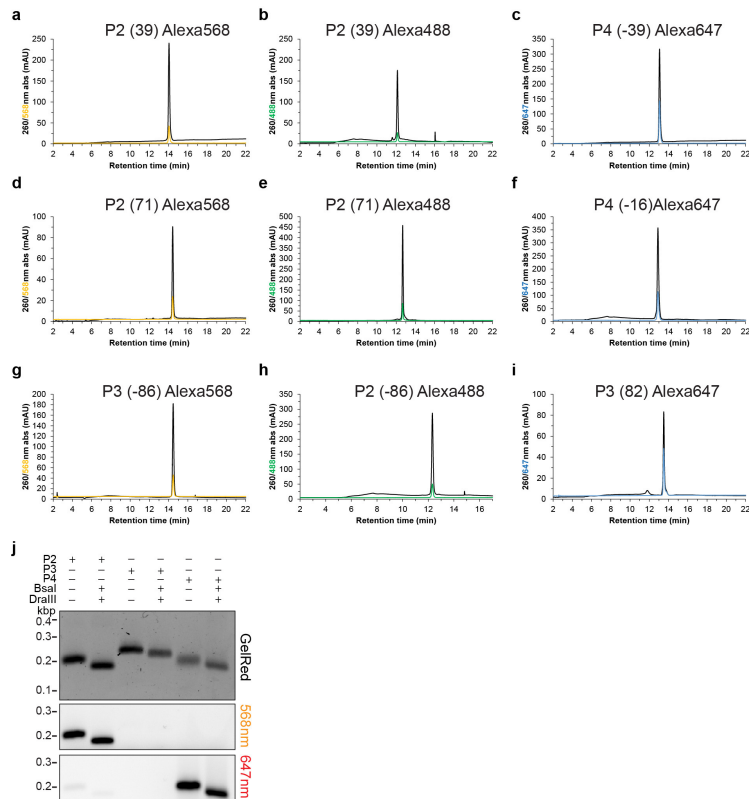
Open Access This article is licensed under a Creative Commons Attribution 4.0 International License, which permits use, sharing, adaptation, distribution and reproduction in any medium or format, as long as you give appropriate credit to the original author(s) and the source, provide a link to the Creative Commons license, and indicate if changes were made. The images or other third party material in this article are included in the article's Creative Commons license, unless indicated otherwise in a credit line to the material. If material is not included in the article's Creative Commons license and your intended use is not permitted by statutory regulation or exceeds the permitted use, you will need to obtain permission directly from the copyright holder. To view a copy of this license, visit <http://creativecommons.org/licenses/by/4.0/>.

© The Author(s) 2018

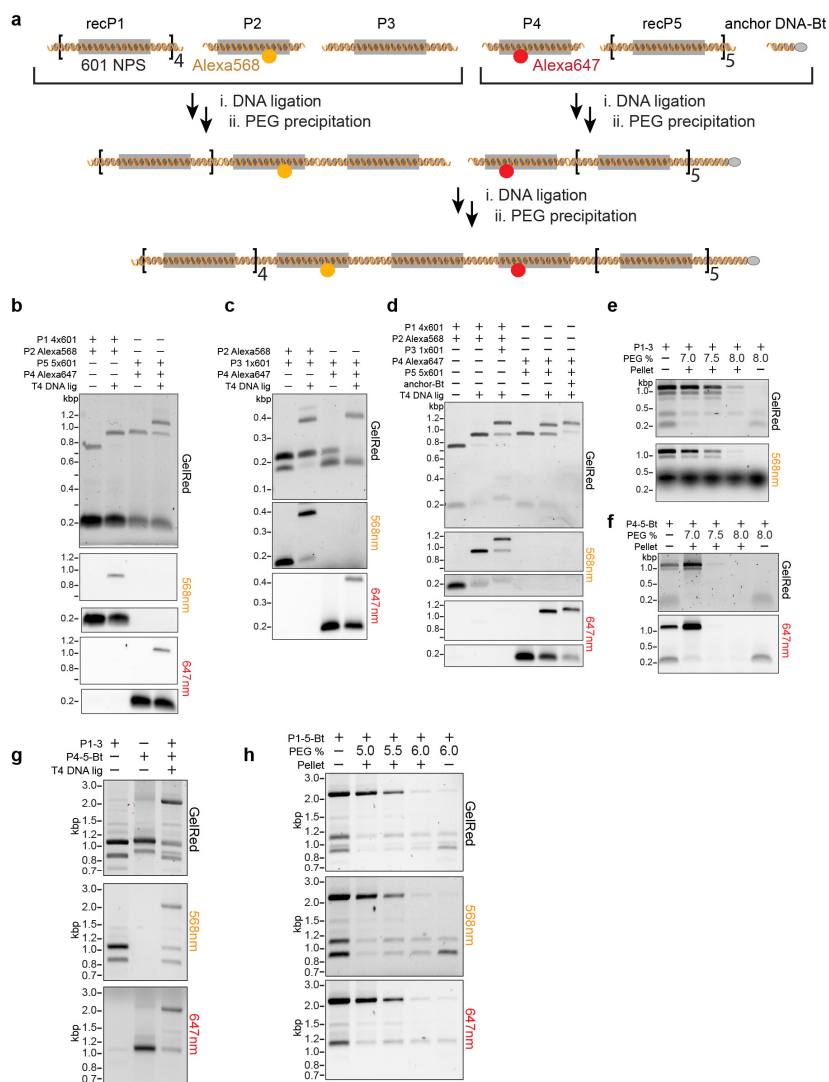
Supplementary Figures



Supplementary Figure 1 | Design, cloning and isolation of recombinant chromatin DNA fragments P1 and P5. (a) General design of the library allowing the introduction of FRET pairs into 12-mer chromatin array DNA by a preparative 6-piece ligation of two recombinant (recP1, recP5) and 4 synthetic (P2, P3, P4, anchor) DNA fragments. The anchor contains a biotin for immobilization (grey sphere). Donor (Alexa Fluor 568 (Alexa568) or Alexa Fluor 488, (Alexa488)), Acceptor (Alexa Fluor 647, (Alexa647)). The exact label positions (D1, D2, D3 and A1, A2, and A3; to form DA1, DA2 and DA3) are indicated relative to the 601 sequence, and are compiled in **Supplementary Table 3 & 4**. (b) Design of the three recombinant constructs for cloning of chromatin DNA fragments. EcoRV, BsaI and DraIII sites are for DNA fragment excision and plasmid fragmentation. Scal sites are for quality control of chromatin assemblies to result in individual nucleosomes. PstI and BglII sites are for extension of the array. (c) Design of 1x601 nucleosome positioning sequence extension piece. PstI, BamHI and BglII sites are for extension of the array. (d) Cloned array DNA pieces of increasing lengths from 1-5x601 excised from the plasmid backbone in recP5. (e) Excision of 4x601 DNA from recP1 by EcoRV after modular transfer from other piece. (f) Scheme of recP1 4x601 in pWM531 outlining restriction sites for EcoRV, BsaI and DraIII. (g) Excision of piece of recP1 4x601 with non-palindromic overhangs by complete digestion first with BsaI and DraIII followed by plasmid backbone fragmentation by EcoRV. (h) Scheme of recP5 4x601 in pWM531 outlining restriction sites for EcoRV, BsaI and DraIII. (i) Excision of piece of recP1 4x601 with non-palindromic overhangs by complete digestion first with BsaI and DraIII followed by plasmid backbone degradation with EcoRV. (j-k) Purification of excised recP1 4x601 (i) and recP5 5x601 (j) from plasmid backbone fragments by iterative PEG precipitation. For uncropped gels, see **Supplementary Figure 20**.

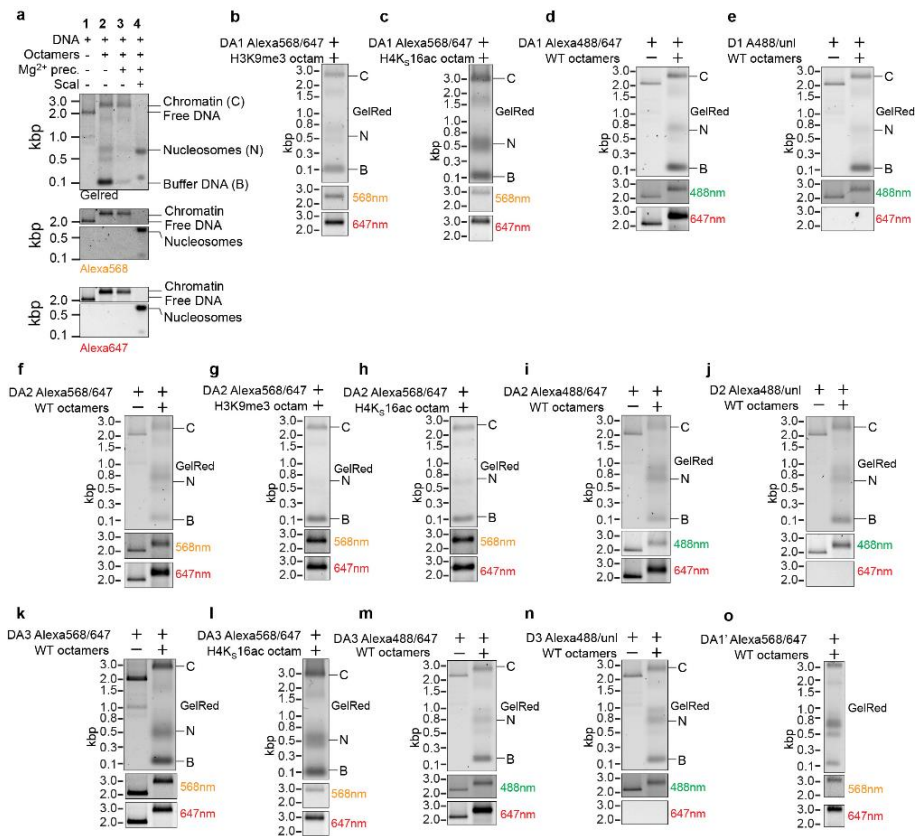


Supplementary Figure 2 | Synthetic oligonucleotide labeling and production of synthetic/PCR-amplified fragments P2-P4. (a-i) RP-HPLC analysis of final labeled oligonucleotides for introduction of site-specific labels into PCR pieces. The number in brackets is the final labeling position relative to the nucleosome dyad (see also **Supplementary Tables 1-4**). (j) Agarose gel analysis of example PCR-generated pieces P2 (Alexa568 labeled), P3 (unlabeled) and P4 (Alexa647 labeled) before and after digestion with BsaI and DraIII to produce unique non-palindromic cohesive ends. For uncropped gels, see **Supplementary Figure 20**.



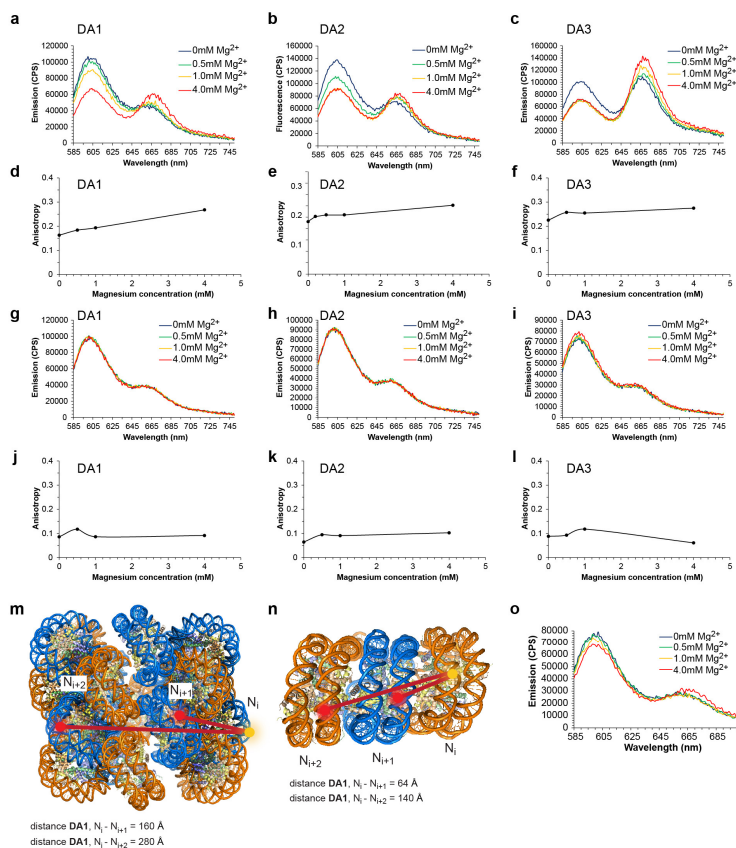
Supplementary Figure 3 | Production of 12x 601 array DNA containing FRET labels. (a) Scheme for convergent assembly and purification of 12x array DNA shown for DA1. Pieces recP1 4x601, P2 1x601 and P3 1x601 are ligated and the intermediate 6x601 purified by PEG precipitation from the individual pieces. A similar procedure was used to generate P4 1x601, recP5 5x601 and the dsDNA anchor to produce another 6x601 intermediate and biotinylated (Bt) anchor for TIRF immobilization. The two intermediate 6x601 pieces are

ligated to produce the 12x601 array DNA with internal fluorophores and the Bt-anchor followed by PEG precipitation to separate from the intermediates. **(b-c)** Test ligations to ensure complete digestion of recP1 4x601 and recP5 5x601, P2 1x601, P3 1x601 at key junctions. Complete displacement of the starting pieces upon ligation with excess cognate pieces shows full digestion. **(d)** Samples from large-scale ligations to produce intermediates analyzed to show near-completion of every ligation step. **(e-f)** PEG purification of the 6x601 intermediates to separate from 1x601 pieces that might interfere with final ligation between intermediates. **(g)** Ligation to produce final 12x601 piece displaying the intermediates before and after ligation. **(h)** PEG purification of final 12x601 arrays with <5% remaining of singly labeled and/or DNA lacking the Bt-anchor. For uncropped gels, see **Supplementary Figure 20**.

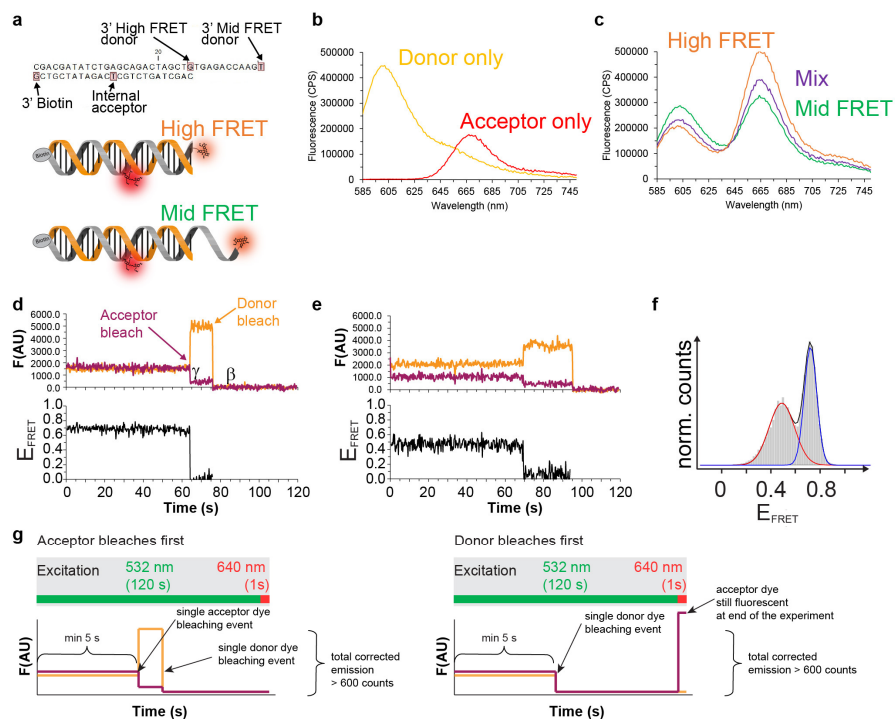


Supplementary Figure 4 | Chromatin formation on DA1-3 fluorescently labeled DNA. (a) Analysis of chromatin formation on fluorescently labeled array DNA by agarose gel electrophoresis. Lane 1: Free DA1-labeled array DNA. Lane 2: Assembled chromatin arrays. To avoid overloading array DNA with histone octamers, low-affinity buffer DNA (B) is added, resulting in the formation of a small amount of buffer nucleosomes (N). Lane 3: Chromatin arrays are purified by Mg²⁺ precipitation. Lane 4: Digestion with the restriction enzyme Scal liberates mononucleosomes. The absence of higher-order aggregates or significant amounts of free DNA demonstrates the saturation of chromatin arrays. **(b)**, Formation of DA1 chromatin arrays with Alexa568/647 labels and H3K9me3 containing histone octamers, **(c)**, DA1 chromatin arrays with Alexa568/647 labels and H4K₅16ac octamers. **(d)** DA1 chromatin arrays with Alexa Fluor 488 (Alexa488) and Alexa647 labels. **e**, D1 chromatin arrays with an Alexa488 label (Donor-only). **(f)** DA2 chromatin arrays with Alexa568/647 labels

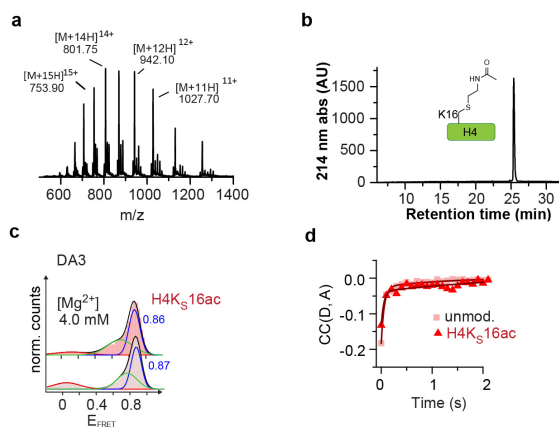
and unmodified histone octamers. **(g)** DA2 chromatin arrays with Alexa568/647 labels and H3K9me3 containing octamers. **(h)** DA2 chromatin arrays with Alexa568/647 labels and H4K_s16ac containing histone octamers. **(i)** DA2 chromatin arrays with Alexa488/647 labels and unmodified histone octamers. **(j)** D2 chromatin arrays with an Alexa488 label (Donor only). **(k)** DA3 chromatin arrays with Alexa568/647 labels and unmodified histone octamers. **(l)** DA3 chromatin arrays with Alexa568/647 labels and H4K_s16ac histone octamers. **(m)** DA3 chromatin arrays with Alexa488/647 labels and unmodified histone octamers. **(n)** D3 chromatin arrays with an Alexa488 label (Donor only). **(o)** DA1' chromatin arrays with Alexa568/647 with an n, n+1 dye spacing to test FRET in solenoid structures. For uncropped gels, see **Supplementary Figure 20**.



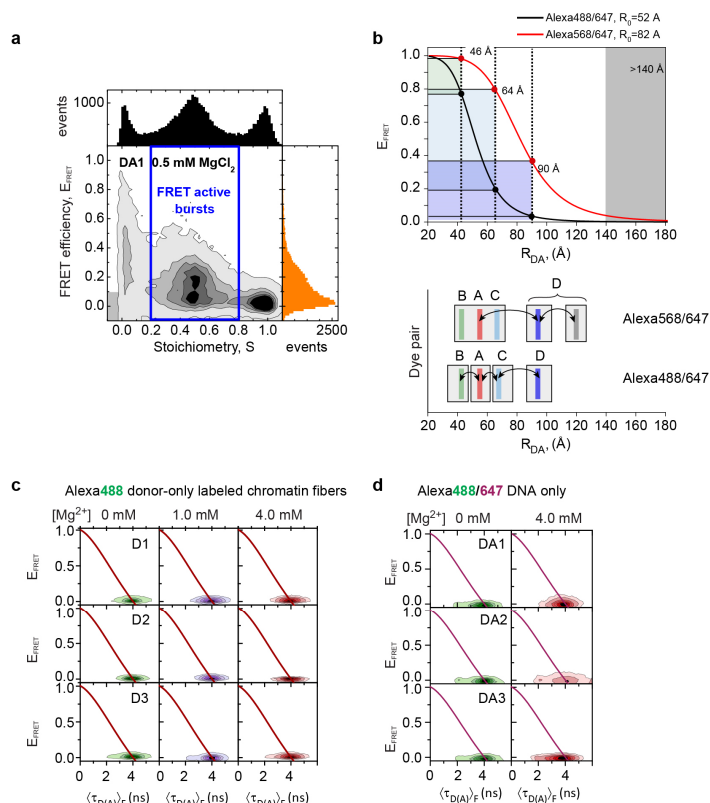
Supplementary Figure 5 | Fluorescence spectra and donor anisotropies in chromatinized and non-chromatinized double-labeled array DNA (Alexa568/647). (a-c) Ensemble spectra of chromatin samples upon compaction with magnesium, showing distinct responses dependent on the positions of the FRET pairs. (d-f) Anisotropy of the donor in the chromatin arrays at increasing magnesium concentrations. (g-i) Spectra of the double-labeled DNA samples in absence of nucleosomes. (j-l) Anisotropy of the donor in absence of nucleosomes. (m) Alternative chromatin structure (interdigitated solenoid) based on a model from ref. ¹, exhibiting inter-dye distances (DA1) outside the FRET detection radius (see also **Supplementary Fig. 8b**). (n) Alternative chromatin structure (solenoid) with continuous stacking of nucleosomes, exhibiting inter-dye distances within FRET detection radius only for N_i, N_{i+1} labeling distance. (o) Fluorescence data on **DA1'** chromatin array with a N_i, N_{i+1} label configuration, exhibiting minor FRET increase and thus indicating that solenoid structures do not contribute to the measured FRET signal.



Supplementary Figure 6 | Characterization of FRET pair at the single-molecule level. (See **Supplementary Note, step 1: smTIRF**). **(a)** Sequences and locations of fluorophores and biotin on constructs used to calibrate ensemble and smFRET with Alexa Fluor 568 and Alexa Fluor 647. **(b)** Spectra acquired from ensemble FRET by excitation at 575nm from single-stranded oligonucleotides labeled with each of the two respective dyes. **(c)** Spectra from the individual dsDNA constructs showing distance-dependent FRET. **(d)** Schematic of the two annealed dsDNA constructs. **(e)** Trace from high FRET DNA piece at the single-molecule level with TIRF with indications of bleaching events, the relative detection efficiencies γ , between donor and acceptor and the donor bleedthrough to the acceptor β , for calculations of the corresponding FRET efficiencies. **(e)** Trace from mid FRET DNA piece with sm FRET. **(f)** Histograms from mixture between two DNA pieces showing the ability to distinguish between different populations using the FRET pair. **(g)** Trace selection criteria: Shown are the two types of acceptable traces that were used for all smTIRF analyses, as judged by trace length, emission and dye bleaching behavior. For details see **Materials and Methods** or **Supplementary Note**, paragraph **smTIRF measurements**.

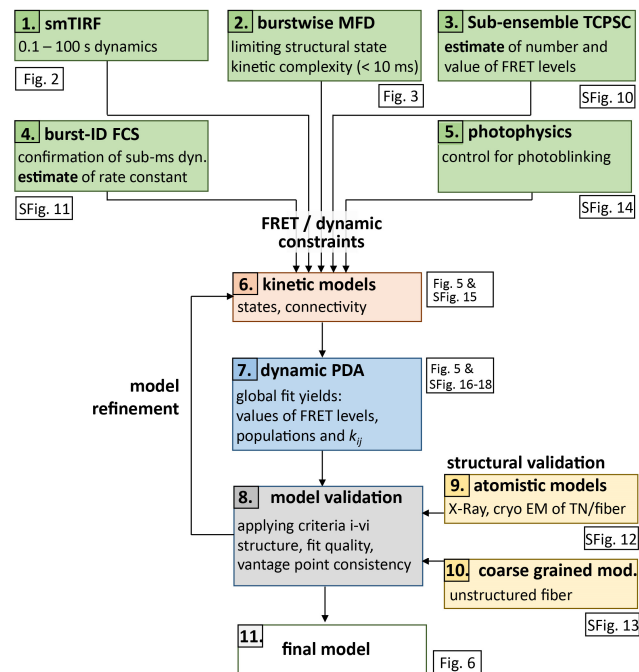


Supplementary Figure 7 | H4K₅16ac analytical data and impact in DA3. H4K₅16ac is produced by reacting the mutant H4, H4K16C, with N-vinylacetamide in the presence of radical promoter (VA-044) and glutathione². (a) MS spectrum of semisynthetic H4K₅16ac. (Expected mass: 11211Da, observed mass 11211Da) (b) RP-HPLC analysis of H4K₅16ac. (c) FRET histogram for DA3 at 4mM Mg²⁺ with or without acetylation on H4 K16. (d) Donor-acceptor channel cross-correlation analysis of DA1, overlay of data for 4 mM Mg²⁺ for unmodified chromatin, as well as H4K₅16ac at 4 mM Mg²⁺. The fit for H4K₅16ac results in a relaxation time $t_R = 50$ ms. For the percentage of dynamic traces, see **Supplementary Table 6**.

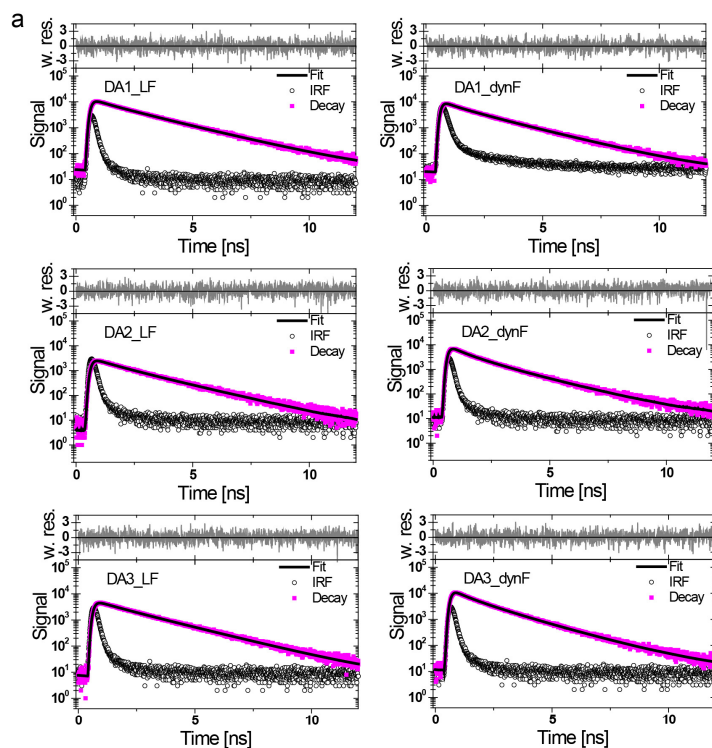


Supplementary Figure 8 | MFD measurements of chromatin arrays DA1-3 with Alexa568/647 and Alexa488/647 labeling schemes. (See **Supplementary Note, step 2: 2D MFD plots with FRET lines**.) (a) MFD histogram of E_{FRET} vs Stoichiometry for DA1 (Alexa488/647) in 0.5 mM Mg²⁺. Blue box: Selection of bursts of double-labeled chromatin arrays capable of FRET (FRET active population). (b) E_{FRET} as a function of inter-dye distance for the two employed dye-pairs, Alexa568/647 and Alexa488/647. For illustration, representative inter-dye distances and their associated E_{FRET} values observed in DA1 are indicated. Alexa568/647 and Alexa488/647 have different sensitivities: Alexa568/647 allows the detection of long-range dynamics beyond 120 Å, whereas Alexa488/647 enables the investigation of sub-states and their exchange dynamics below 70 Å. (c) MFD plots of donor-only, Alexa488-labeled chromatin fibers (D1, D2 and D3). Dark red line: static FRET line. See **Supplementary Methods, step 2, Static and dynamic FRET-lines**. (d) MFD plots of Alexa488/647 labeled DNA (DA1, DA2 and DA3), demonstrating the absence of FRET or dynamics without the presence of chromatin.

Dynamic single - molecule structural biology workflow:



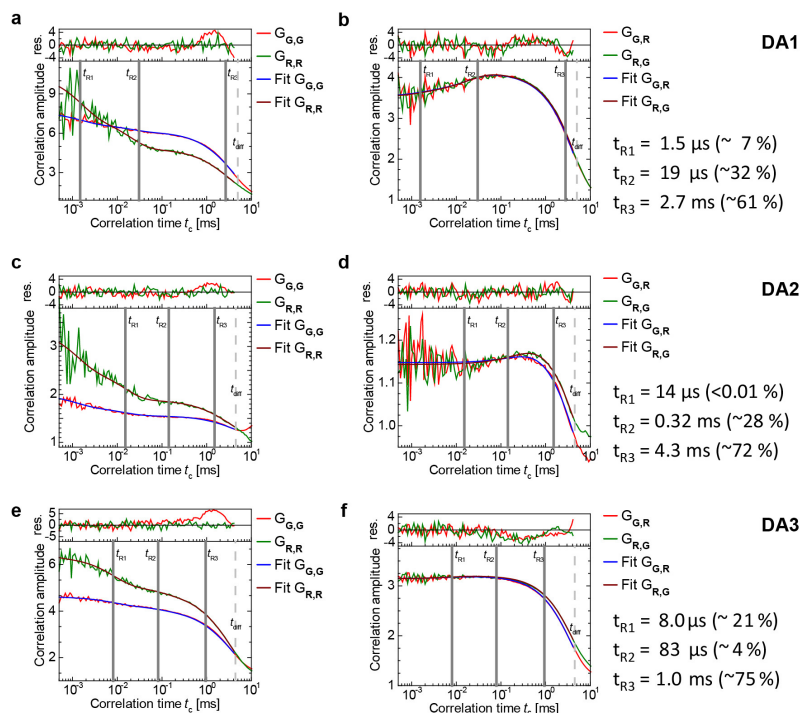
Supplementary Figure 9 | Dynamic single-molecule structural biology workflow. (See **Supplementary Note**, Dynamic structural biology analysis). The workflow is comprised of 11 steps: 5 experimental methods (shaded in green), design of the kinetic model (in orange), data analysis with dynamic PDA methods (in blue), validation of the model (gray), structural validation (in yellow) and confirmation of the final model (white). Small boxes: Indicating Figures containing the relevant data, “SFig” refers to Supplementary Figures.



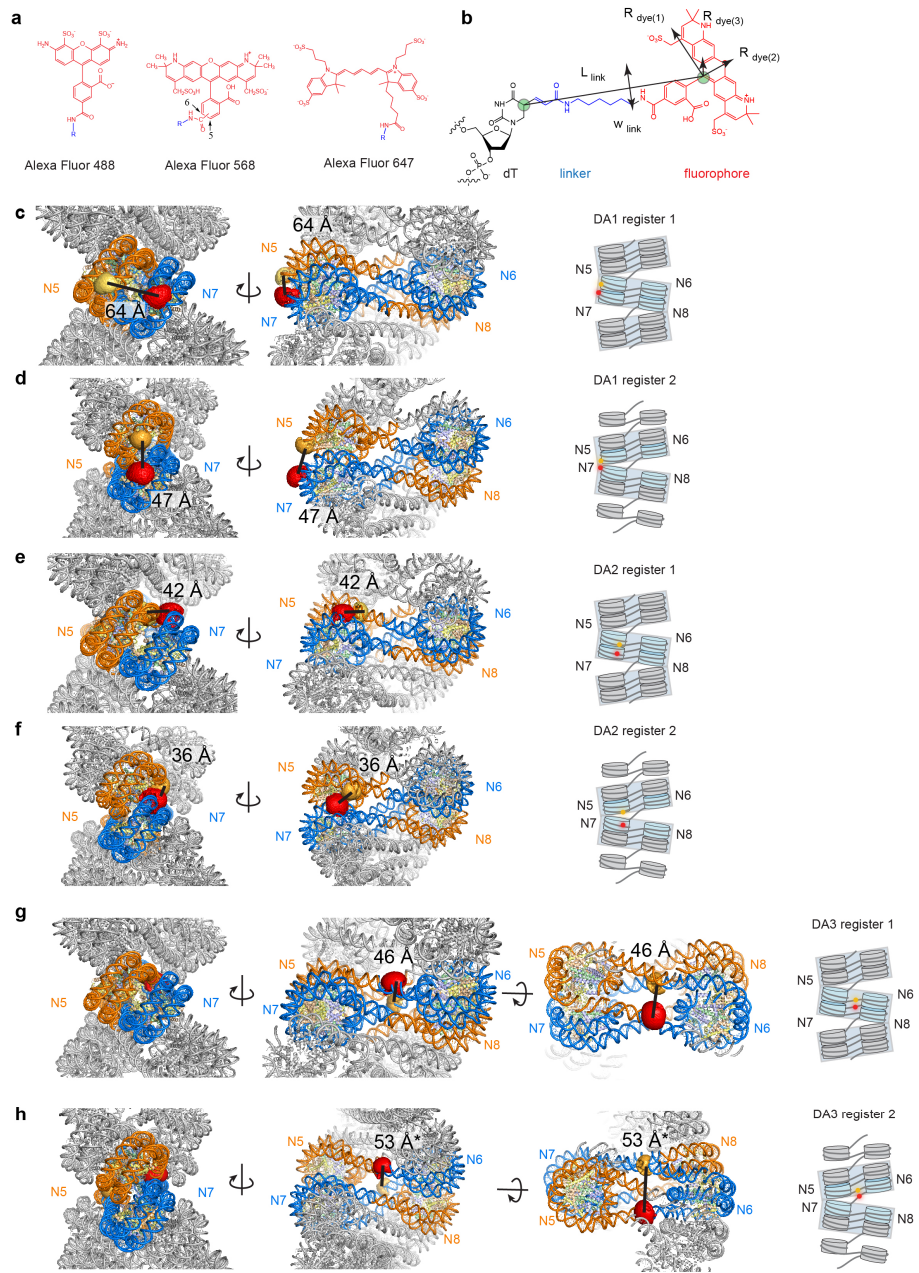
b

subpopulations	$R_{DA,1}$ (Å)	x_1	$R_{DA,2}$ (Å)	x_2	$R_{DA,3}$ (Å)	x_3	χ^2_R
DA1 LF	46	0.40			90	0.60	0.98
DA1 dynFRET	41	0.42	65	0.18	120	0.40	0.98
DA2 LF			52	0.39	128	0.61	1.06
DA2 dynFRET	42	0.41	55	0.35	120	0.24	1.15
DA3 LF			54	0.24	120	0.76	1.06
DA3 dynFRET	40	0.36	57	0.45	120	0.19	1.02

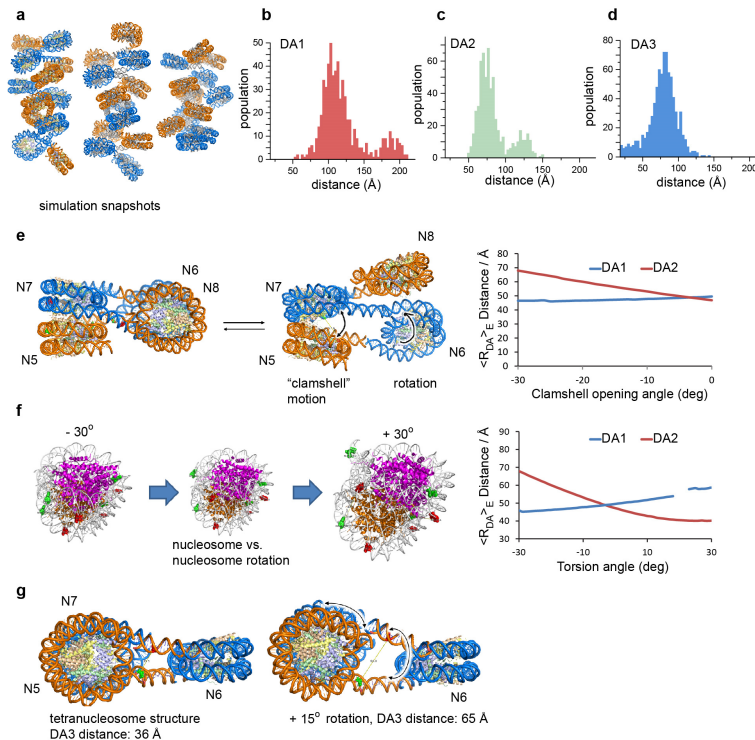
Supplementary Figure 10 | seTCSPC of DA1-3 (Alexa488/647) in 0.5 mM Mg^{2+} . (See **Supplementary Note, step 3**: Sub-ensemble TCSPC). **(a)** Fluorescence decays (magenta) with corresponding fit (black line). Left panel: fits for accumulated LF bursts; right panel: fits for accumulated dynF bursts. In the global fit (see **Supplementary Note, step 3**) the DOnly decay $f_{D(0)}$ was approximated by a single donor fluorescence lifetime ($\tau_{D(0)} = 4.1$ ns) and the decay of the FRET-population $f_{D(A)}$ with 3 Gaussian distributed distances and the same fixed half-width $\sigma_{DA} = 6$ Å. The fit quality is illustrated by weighted residuals (in the upper panel) by χ^2_R . **(b)** Fit results for the LF and dynF populations by eq.(3.3) - (3.4). IRF: Instrument response function.



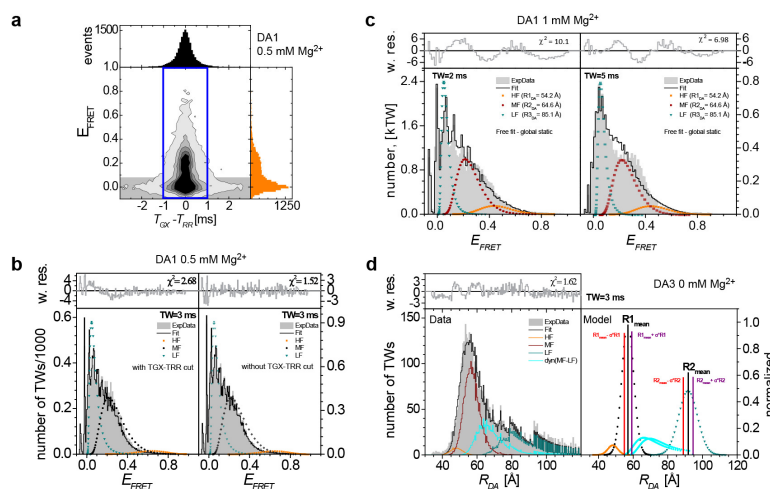
Supplementary Figure 11 | Model-free dynamic analysis by fluorescence correlation functions of arrays DA1-3 (Alex488/647) at 0.75 mM Mg^{2+} . (See **Supplementary Note, step 4: Burst-ID FCS**). The analysis by auto- and cross-correlation functions³ shows FRET related anti-correlated dynamics with three relaxation time t_{R1} , t_{R2} , and t_{R3} in the ms- and sub-ms time range. **(a)** Burst-ID donor-donor ($G_{G,G}$) and acceptor-acceptor ($G_{R,R}$) auto-correlation functions for DA1 chromatin fibers with an additional bunching term in the auto-correlation functions to consider also dye blinking with the corresponding amplitudes $B^{(G)} = 0.09$ and $B^{(R)} = 0.27$, respectively, and the relaxation time $t_B = 44 \text{ns}$. **(b)** Burst-ID cross-correlation functions $G_{G,R}$ and $G_{R,G}$ of donor-acceptor (G-R) and acceptor-donor (R-G) signal, respectively. The timescales of observed processes are obtained by a global fit of all correlation functions for one FRET pair and are shown on the right. **(c-d)** Auto- and cross-correlation functions for DA2 with the additional bunching amplitudes $B^{(G)} = 0.25$ and $B^{(R)} = 0.33$, respectively, and the relaxation time $t_B = 1.2 \mu\text{s}$. **(e-f)** Auto- and cross-correlation functions for DA3 with the additional bunching amplitudes $B^{(G)} = 0.12$ and $B^{(R)} = 0.25$, respectively, and the relaxation time $t_B = 0.13 \mu\text{s}$.










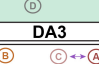
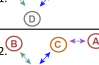




Supplementary Figure 12 | Structural models for the compact chromatin state. (See **Supplementary Note, step 9:** Structural models of compact chromatin states). For a comparison between measured and calculated distances, see **Supplementary Table 8.** **(a)** Chemical structures of the fluorescent labels Alexa488, Alexa568 and Alexa647. **(b)** Chemical structure of the dye linked to a dT nucleotide. To calculate the dye accessible contact volumes for these dyes, the structure was approximated by an ellipsoid ($R_{dye(1)}$, $R_{dye(2)}$ and $R_{dye(3)}$) connected by a linker of length (L_{link}) and width (w_{link}). Accessible contact volume dye model was used where part of AV which is closer than 3 Å from the macromolecular surface is defined to have higher dye density ρ_{dye}^4 . For the parameters used for the different dyes, see **step 9: FRET positioning and screening calculations.** **(c)** Molecular structure of a compact chromatin array, consisting of a stack of 3 tetranucleosomes (4-4-4, register 1) with DA1-positioned dyes in the central tetranucleosome. The model was produced by fitting nucleosomes into the electron density of the cryoEM structure of a 177-bp nucleosome array, ref. ⁵. The inter-dye distance was evaluated using simulated dye accessible contact volumes (ACV)⁶. **(d)** Molecular structure of a chromatin array, consisting of a stack of 2 tetranucleosomes, flanked by two unstacked nucleosomes at each side (2-4-4-2, register 2) with DA1-positioned dyes on the two central tetranucleosomes and inter-dye distance from ACV-calculations. **(e)** Inter-dye distance for DA2 dyes in register 1 compacted arrays. **(f)** Inter-dye distance for DA2 dyes in register 2 compacted arrays. **(g)** Inter-dye distance for DA3 dyes in register 1 compacted arrays. Linker DNA was introduced extending the nucleosomal DNA connecting neighboring nucleosomes. The distance is calculated between the phosphate groups of the modified bases (P-P distance). **(h)** Inter-dye distance for DA3 dyes in register 2 compacted arrays. Linker DNA was introduced extending the nucleosomal DNA connecting neighboring nucleosomes. Shown are calculated P-P distances.



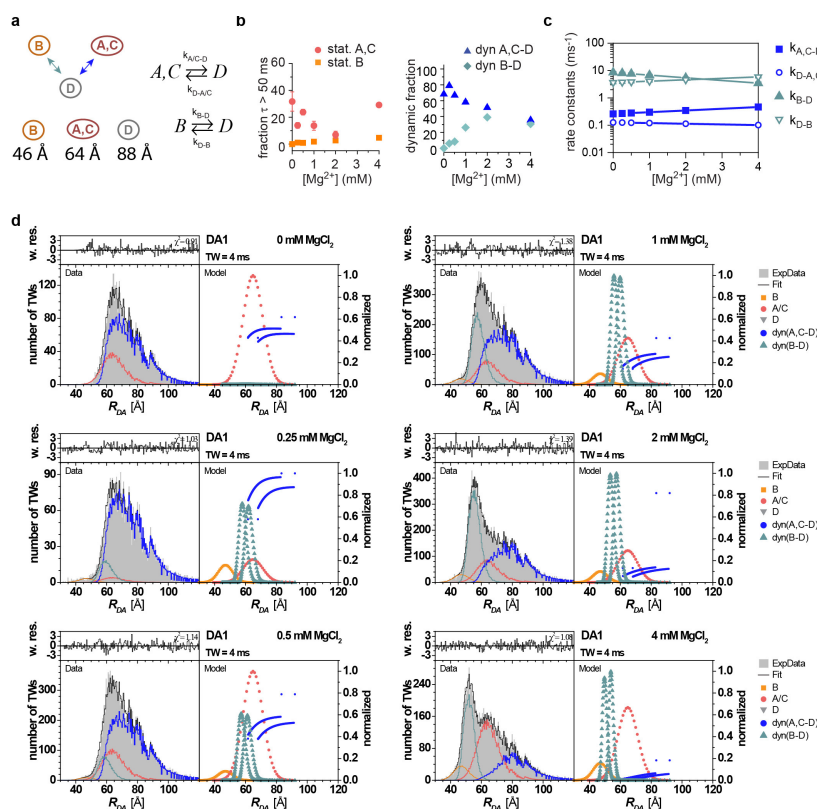
Supplementary Figure 13 | Structural models open and dynamic chromatin states. (See **Supplementary Note, step 10**: Structural models of open and dynamic states). **(a)** Representative snapshots from coarse grained simulations of chromatin fibers following ref. ⁷. **(b)** Calculated distance distributions between DA1 dye pairs (between phosphate groups of the modified bases, P-P distances) in the open chromatin ensembles for 100 structures with 12 nucleosomes each. **(c)** Calculated P-P distance distributions between DA2 dye pairs in open chromatin ensembles from the same structure set as in **b**. **(d)** Calculated P-P distance distributions between DA3 dye pairs in open chromatin ensembles for the same structure set as in **b**. **(b-d)** Distances are calculated between P atoms of the labeled nucleotide. **(e)** Dependence of DA1 and DA2 FRET averaged inter-dye distance on “clamshell”-type opening of the tetranucleosome interface. DA1 is not sensitive to this mode of motion, in contrast to DA2. **(f)** Dependence of DA1 and DA2 inter-dye distance on rotational motions between two nucleosomes. DA2 shows stronger angular dependency compared to DA1. **(g)** Effect of rotational motion on DA3 FRET averaged inter-dye distance showing that this dye pair is sensitive to the distorted tetranucleosome state (State C in **Fig. 4a**).



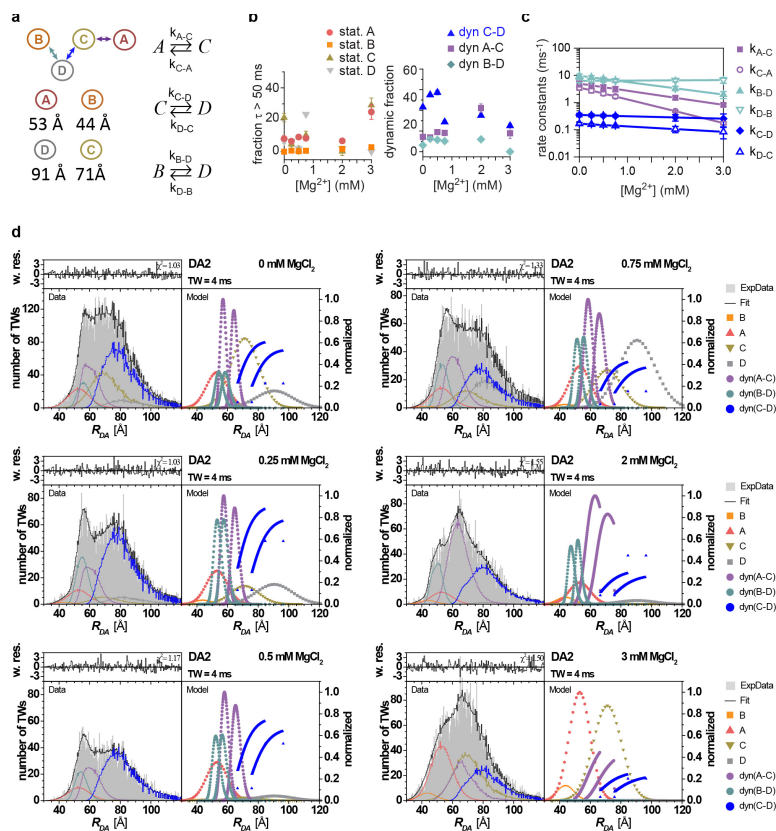
Supplementary Figure 14 | Photobleaching and photoblinking analysis & principles of PDA analysis. (See **Supplementary Note, step 5:** Photobleaching and photoblinking analysis, and **step 7:** General description of PDA analysis). **(a)** Example of the photobleaching and photoblinking analysis for DA1 (Alexa488/647) in 0.5 mM Mg^{2+} . FRET efficiency vs $T_{GX}-T_{RR}$ is arranged in a 2D histogram, demonstrating the procedure of the macrotime filter ($|T_{GX}-T_{RR}| < 1$ ms). Bursts selected for the macrotime cut are in the blue box. For a definition of the parameter see **Dynamic Analysis, step 5**. **(b)** PDA analysis of the FRET efficiency histograms of the selected bursts (right panel) and un-filtered bursts (left panel). The difference between the two analyses is very small. **Principles of PDA analysis:** **(c)** DA1 (Alexa488/647) in 1 mM Mg^{2+} . A global fit for two TWs (2 ms (left panel) and 5 ms (right panel) using a joint fit model (3 static Gaussian distributed distances) demonstrates that a static model inappropriate. Experimental data histogram is shown in gray, fit in black line and resulting static FRET states in orange, dark cyan and wine. **(d)** Dynamic PDA analysis overview using DA3 (Alexa488/647) at 0 mM Mg^{2+} as an example. Left panel: experimental data histogram is shown in gray and resulting shot-noise limited model distribution as a black line. It is described by the contribution of a High FRET species (HF, orange), medium FRET species (MF, wine), low FRET species (LF, dark cyan) and a dynamic species in a two-state dynamic distribution between MF and LF (cyan line). Right panel: The model distance distribution is given by a sum of static Gaussian-distributed distances (R1, MF: (wine symbols), R2, LF: (dark cyan symbols)) and dynamic mixing between $(R1_{mean} - \sigma_1$ and $R2_{mean} - \sigma_2)$ and $(R1_{mean} + \sigma_1$ and $R2_{mean} + \sigma_2)$ distributions (cyan symbols), where $\sigma_i = \sigma * R_i$ and $\sigma = 0.06$.

Connectivity plot	Equations	Selection criteria:					
		i. connectivity	ii. state #	iii. parameter boundaries	iv. fit stability	v. goodness of fit	vi. consistency
DA1							
1. 	$A, C \rightleftharpoons D$ $A, C \rightleftharpoons B$ $B \rightleftharpoons D$	+	+	-	-	+	-
2. 	$A, C \rightleftharpoons D$ $B \rightleftharpoons D$	+	+	+	+	+	+
DA2							
1. 	$A, C \rightleftharpoons D$ $A, C \rightleftharpoons B$	-	+	-	-	+	-
2. 	$B \rightleftharpoons D$ $A, C \rightleftharpoons D$	+	+	-	-	-	+
3. 		-	+	+	+	+	-
4. 	$A \rightleftharpoons C$ $C \rightleftharpoons D$ $A \rightleftharpoons D$ $B \rightleftharpoons D$	+	+	-	-	-	+
5. 	$A \rightleftharpoons C$ $A \rightleftharpoons D$ $B \rightleftharpoons D$	-	+	+	+	+	+
6. 	$A \rightleftharpoons C$ $C \rightleftharpoons D$ $B \rightleftharpoons D$	+	+	+	+	+	+
DA3							
1. 	$A \rightleftharpoons C$ $C \rightleftharpoons D$ $B \rightleftharpoons D$	-	-	-	+	+	+
2. 	$A, B \rightleftharpoons C$ $C \rightleftharpoons D$ $A, B \rightleftharpoons D$	+	+	+	-	+	-
3. 	$A, B \rightleftharpoons D$ $C \rightleftharpoons D$	-	+	+	+	+	-
4. 	$A, B \rightleftharpoons C$ $C \rightleftharpoons D$	+	+	+	+	-	-
5. 	$A \rightleftharpoons C$ $C \rightleftharpoons D$ $B \rightleftharpoons D$	+	+	+	+	+	+

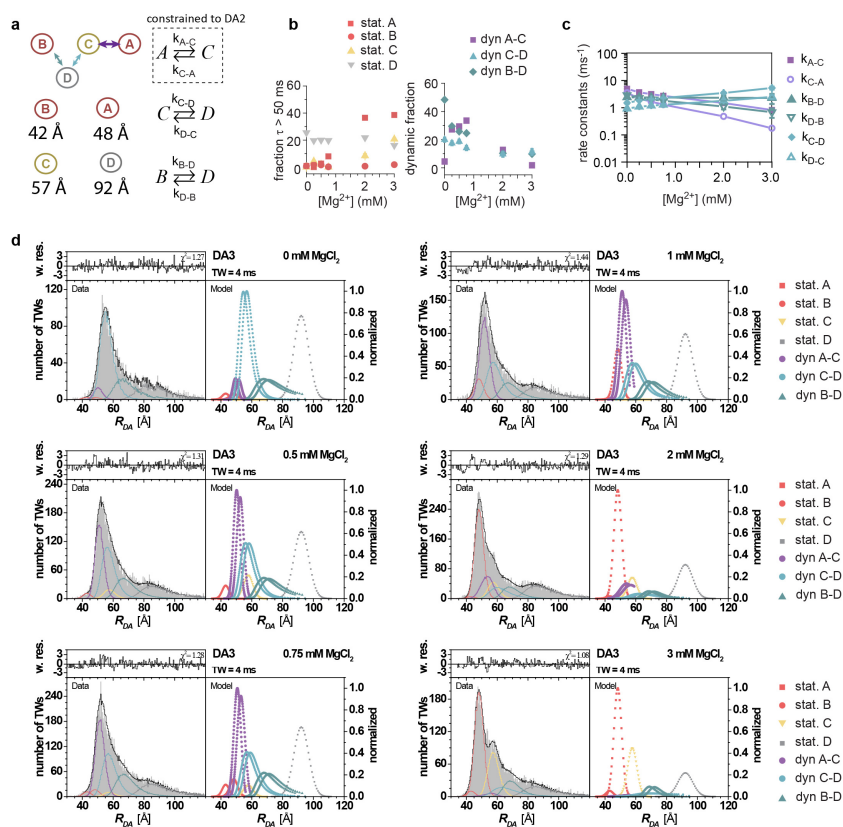
Supplementary Figure 15 | List of the trial models in PDA analysis for DA1-3. (See **Supplementary Note, step 8: Validation of kinetic models**). The first column represents sketches of applied models for particular FRET dye configuration. The model was evaluated with several selection criteria, see **step 8, Validation of kinetic models**. Cases when criteria meets the model are marked in green, the discrepancy are in red. The model was chosen if all criteria are satisfied.



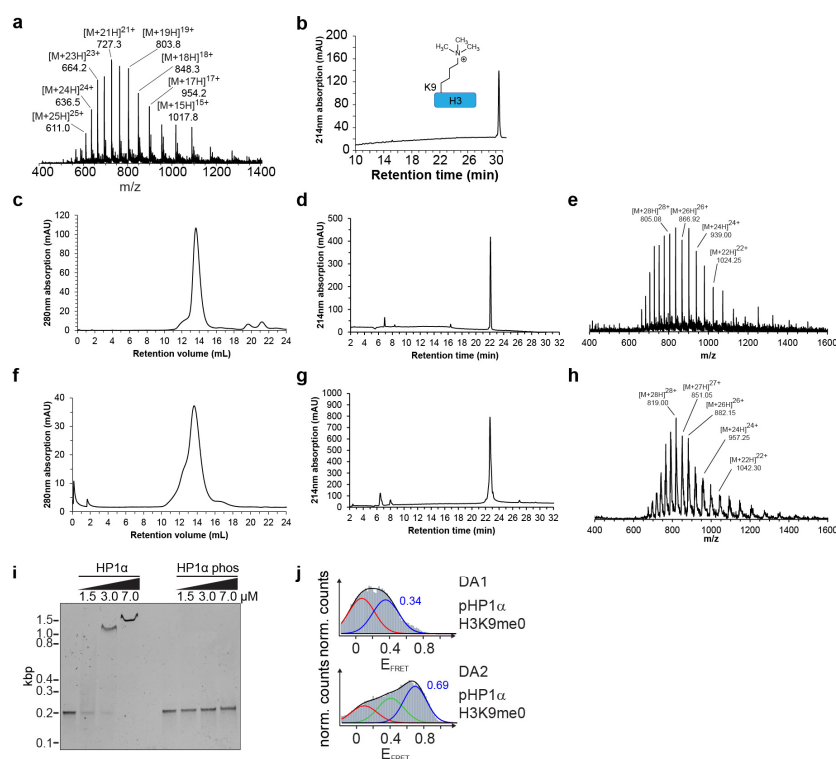
Supplementary Figure 16 | PDA fit of MFD data for DA1 (Alexa488/647). (See **Supplementary Note, step 7:** General description of PDA analysis & **step 8:** Validation of kinetic models). **(a)** Minimal dynamic model used to globally fit the experimental data. Distances in Å are given for the states {A,C} (are not differentiated by DA1), B, and D. **(b)** Left panel: Fractions of molecules which appear static on the MFD timescale (10 ms). Right panel: Dynamic fractions – molecule exchanging between the indicated states with rate constants given in **c**. **(c)** Rate constants obtained from the global PDA fit. **(b-c)** Error bars: s.d. between three PDA analyses of datasets comprising a fraction (70%) of all measured data (subsampling). Note that in some cases the error bars are smaller than the symbol size. **(d)** Individual PDA fits of the model given in **c** to the experimental data at the indicated conditions, showing the fit, residuals as well as the underlying static (symbols in red hues and grey) and dynamic (symbols in blue hues) molecular distributions.



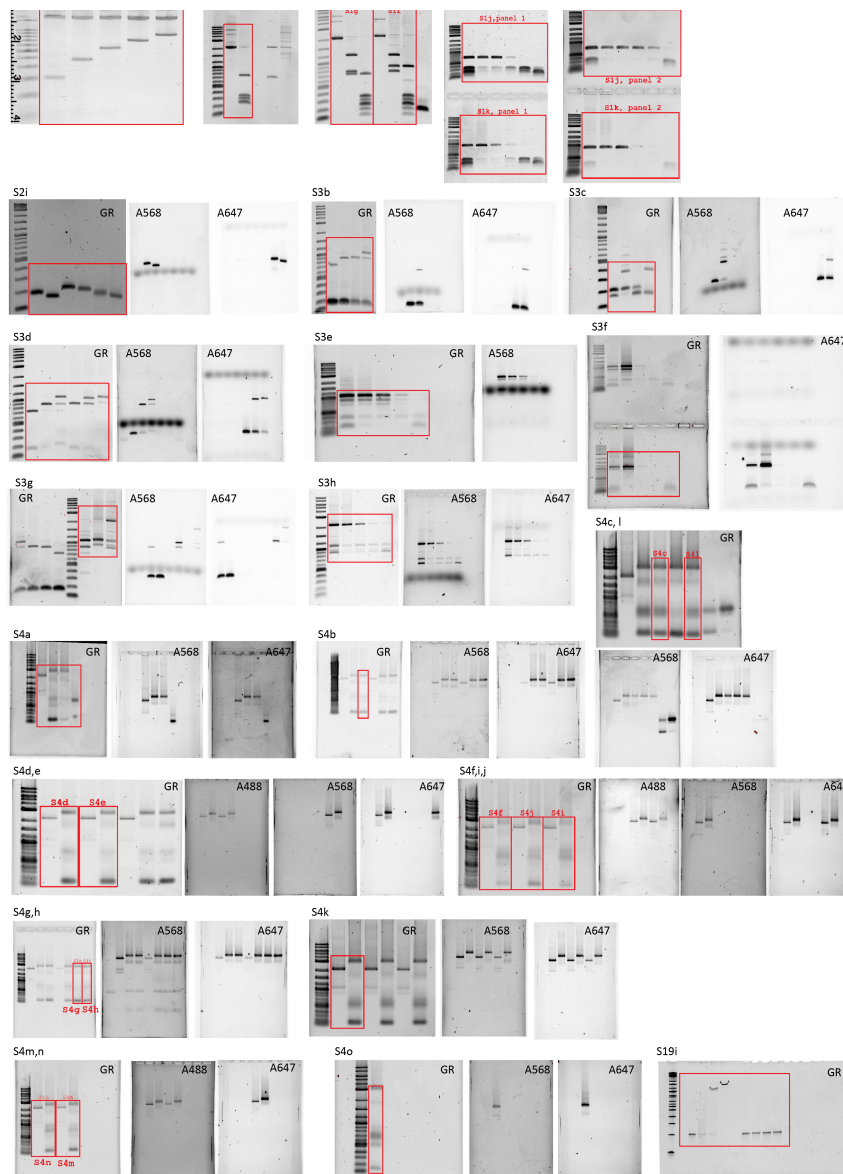
Supplementary Figure 17 | PDA fit of MFD data for DA2 (Alexa488/647). (See **Supplementary Note, step 7:** General description of PDA analysis & **step 8:** Validation of kinetic models). **(a)** Minimal dynamic model used to globally fit the experimental data. Distances in Å are given for the states A, B, C and D. **(b)** Left panel: Fractions of molecules which appear static on the MFD timescale (10 ms). Right panel: Dynamic fractions – molecule exchanging between the indicated states with rate constants given in **c**. **(c)** Rate constants obtained from the global PDA fit. **(b-c)** Error bars: s.d. between three PDA analyses of datasets comprising a fraction (70%) of all measured data (subsampling). Note that in some cases the error bars are smaller than the symbol size. **(d)** Individual PDA fits of the model given in **a** to the experimental data at the indicated conditions, showing the fit, residuals as well as the underlying static (symbols in red hues and grey) and dynamic (symbols in blue hues) molecular distributions.



Supplementary Figure 18 | PDA fit of MFD data for DA3 (Alexa488/647). (See **Supplementary Note, step 7:** General description of PDA analysis & **step 8:** Validation of kinetic models). **(a)** Minimal dynamic model used to globally fit the experimental data. Distances are given in Å. **(b)** Left panel: Fractions of molecules which appear static on the MFD timescale (10 ms). Right panel: Dynamic fractions – molecule exchanging between the indicated states with rate constants given in **c**. **(c)** Rate constants obtained from the global PDA fit. **(b-c)** Error bars: s.d. between three PDA analyses of datasets comprising a fraction (70%) of all measured data (subsampling). Note that in some cases the error bars are smaller than the symbol size. **(d)** Individual PDA fits of the model given in **a** to the experimental data at the indicated conditions, showing the fit, residuals as well as the underlying static (symbols in red hues and grey) and dynamic (symbols in blue hues) molecular distributions.



Supplementary Figure 19 | Expression and purification of wt and phosphorylated HP1 α . H3K9me3 is produced by expressed protein ligation. The modified histone peptide H3(1-14)K9me3-NH₂ is converted to a C-terminal thioester and ligated to the N-terminally truncated histone protein H3(Δ 1-14)A15C, followed by desulfurization⁸. (a) MS spectrum of semisynthetic H3K9me3. (Expected mass: 15251.8Da, observed mass 15252.0 Da) (b) RP-HPLC analysis of H3K9me3. (c) Gel-filtration analysis of HP1 α , which elutes at the expected volume for the dimeric protein. (d) HPLC analysis of HP1 α with a 0-70%B gradient. (e) ESI-MS analysis of HP1 α (Expected mass 22506.2Da, observed mass 22513.0Da) (f) Gel-filtration analysis of phosphorylated HP1 α (phosHP1 α), which elutes at the expected volume for the dimeric protein with a shoulder potentially accounting for a tetrameric population. (g) HPLC analysis of phosHP1 α with a 0-70%B gradient. (h) ESI-MS phosHP1 α (Expected mass 22906.2Da, observed mass 22905.0), demonstrating the presence of 5 P_i groups. (i) Gel-shift with HP1 α and phosHP1 α demonstrating a loss in nonspecific DNA binding affinity for the phosphorylated protein in accordance with ref.⁹. (j) Histograms of pHP1a incubated with DA1 or DA2 containing unmethylated H3.



Supplementary Figure 20 | Images of all uncropped gels. All uncropped gels from Supplementary Figures S1, S2, S3, S4 and S19, stained with GelRed (GR) or imaged using fluorescence from the indicated dyes.

Supplementary Tables

Fragment	Sequence
P1	<p>-100 -95 -90 -85 -80 -75 -70 -65 -60 -55 -50 -45 -40 -35 -30 -25 CACTTGGTGGCGGCCGCCCTGGAGAATCCCGGTGCCGAGGCCGCTCAATTGGTCGTAGACAGCTCTA -20 -15 -10 -5 0 5 10 15 20 25 30 35 40 45 50 55 GCACCGCTTAAACGCACGTACGCGCTGTCCCCCGCGTTTAAACGCCAAGGGGATTACCCCTAGTCTCCAGGCACGTGT 60 65 70 75 80 85 90 95 100 105 CAGATACTGCAGAGATCTCTAGATCCATGGAGTACTTGGTCTCATAGC</p>
P2	<p>-100 -95 -90 -85 -80 -75 -70 -65 -60 -55 -50 -45 -40 -35 -30 -25 GATCGGTCTCATAGCCTGGAGAATCCCGGTGCCGAGGCCGCTCAATTGGTCGTAGACAGCTCTA -20 -15 -10 -5 0 5 10 15 20 25 30 35 40 45 50 55 GCACCGCTTAAACGCACGTACGCGCTGTCCCCCGCGTTTAAACGCCAAGGGGATTACCCCTAGTCTCCAGGCACGTGT 60 65 70 75 80 85 90 95 100 105 CAGATATATACATCTGTCCACTGTGGATC</p>
P3	<p>-100 -95 -90 -85 -80 -75 -70 -65 -60 -55 -50 -45 -40 -35 -30 -25 CACACTGTGCCAAGTACTTACGCGGCCGCCCTGGAGAATCCCGGTGCCGAGGCCGCTCAATTGGTCGTAGACAGCTCTA -20 -15 -10 -5 0 5 10 15 20 25 30 35 40 45 50 55 GCACCGCTTAAACGCACGTACGCGCTGTCCCCCGCGTTTAAACGCCAAGGGGATTACCCCTAGTCTCCAGGCACGTGT 60 65 70 75 80 85 90 95 100 105 CAGATACTGCAGAGATCTCTAGATCCATGGAGTACTTGGTCTCAACC</p>
P4	<p>-100 -95 -90 -85 -80 -75 -70 -65 -60 -55 -50 -45 -40 -35 -30 -25 GATCGGTCTCAAACCCTGGAGAATCCCGGTGCCGAGGCCGCTCAATTGGTCGTAGACAGCTCTA -20 -15 -10 -5 0 5 10 15 20 25 30 35 40 45 50 55 GCACCGCTTAAACGCACGTACGCGCTGTCCCCCGCGTTTAAACGCCAAGGGGATTACCCCTAGTCTCCAGGCACGTGT 60 65 70 75 80 85 90 95 100 105 CAGATATATACATCTGTCCAGTCTGGATC</p>
P5	<p>-100 -95 -90 -85 -80 -75 -70 -65 -60 -55 -50 -45 -40 -35 -30 -25 CACGTCGTGCCAAGTACTTACGCGGCCGCCCTGGAGAATCCCGGTGCCGAGGCCGCTCAATTGGTCGTAGACAGCTCTA -20 -15 -10 -5 0 5 10 15 20 25 30 35 40 45 50 55 GCACCGCTTAAACGCACGTACGCGCTGTCCCCCGCGTTTAAACGCCAAGGGGATTACCCCTAGTCTCCAGGCACGTGT 60 65 70 75 80 85 90 95 100 105 TCAGATACTGCAGAGATCTCTAGATCCCGTCTCACTAA</p>

Supplementary Table 1 | Sequences of 1x601 pieces for recombinant and PCR-generated pieces. 601 sequences (for recombinant pieces with slight end modifications) indicated in bold. The labeled base pairs are indicated in red. The numbering is given as number of base-pairs relative to the dyad in the 601 sequence.

Name	Sequence
P2_pos39_rev	5'-GATCCACAGTGTGACAGGATGTATATATCTGACACGTGCCTGGAGACTAGGGAG-3'
P2_pos71_rev	5'-GATCCACAGTGTGACTGGATGTATATATCTGACACGTGC-3'
P3_pos-86_fwd	5'-GATCGCACACTGTGCCAAGTACTTACGCGGCCGCCCTGGAGAATCC-3'
P3_pos82_rev	5'-GATCGCGGTTTGAGACCAAGTACTCCATGGATCTAGAGATCTCTGC-3'
P4_pos-39_fwd	5'-GATCGGTCTCAAACCCTGGAGAATCCCGGTGCCGAGGCCGCTCAATTGGTCGTAGACAGC3'
P4_pos-16_fwd	5'-GATCGGTCTCAAACCCTGGAGAATCCCGGTGCCGAGGCCGCTCAATTGGTCGTAGACAGCTCTAGCAGCTTAAACGCACGTACGC-3'
recP5_Anchor_fwd	5'-ph-CTAATAGTCTGCTCAGTACTCGTCGTAGATCCATGGTCCGATTACGCGG-3'
recP5_Anchor_rev	5'-biotin-CCGCGTAATCGGACCATGGATCTAGCGACGAGTACTGACGAGACTA-3'

Supplementary Table 2 | Oligonucleotides sequences used for labeling and anchoring. The numbering for the label positions is given relative to the nucleosome dyad.

Piece	Donor fluorophore	Labeling position(s)	Acceptor fluorophore	Labeling position(s)
P2	Alexa Fluor 488	39	-	-
P2	Alexa Fluor 568	39	-	-
P2	Alexa Fluor 488	71	-	-
P2	Alexa Fluor 568	71	-	-
P2	-	-	-	-
P3	Alexa Fluor 488	-86	Alexa Fluor 647	82
P3	Alexa Fluor 568	-86	Alexa Fluor 647	82
P3	-	-	-	-
P4	-	-	Alexa Fluor 647	-39
P4	-	-	Alexa Fluor 647	-16
P4	-	-	-	-

Supplementary Table 3 | Overview of 1x601 PCR pieces generated from labeled and unlabeled primers. Position of label and the donor/acceptor fluorophore used are indicated. The positions are indicated as base-pairs relative to the dyad in the 601 sequence (see also **Supplementary Tables 1 and 2**).

Construct	Donor	Donor Position	Acceptor	Acceptor position
DA1	Alexa488	N5 (39)	Alexa647	N7 (-39)
DA1	Alexa568	N5 (39)	Alexa647	N7 (-39)
D1	Alexa488	N5 (39)	unlabeled	N/A
DA1'	Alexa488	N5 (39)	Alexa647	N6 (-39)
DA2	Alexa488	N5 (71)	Alexa647	N7 (-16)
DA2	Alexa568	N5 (71)	Alexa647	N7 (-16)
D2	Alexa488	N5 (71)	unlabeled	N/A
DA3	Alexa488	N6 (-86)	Alexa647	N6 (82)
DA3	Alexa568	N6 (-86)	Alexa647	N6 (82)
D3	Alexa488	N6 (-86)	unlabeled	N/A

Supplementary Table 4 | Overview of constructed 12x601 DNA pieces with different combinations of labels. The nucleosome position is indicated as N_i , with $i = 1-12$. The number in brackets is the label position relative to the dyad in the 601 sequence (see also **Supplementary Tables 1-3**).

Data	n	Peak 1			Peak 2			Peak 3			
		A_1	C_1	σ_1	A_2	C_2	σ_2	A_3	C_3	σ_3	
D A 1	0mM Mg ²⁺	448	2.45	0.07	0.17	5.02	0.30	0.14	-	-	-
	0.5mM Mg ²⁺	205	1.81	0.09	0.17	5.18	0.36	0.14	-	-	-
	1.0mM Mg ²⁺	156	1.68	0.12	0.22	5.13	0.45	0.14	-	-	-
	4.0mM Mg ²⁺	789	1.65	0.07	0.22	4.17	0.58	0.17	-	-	-
	4.0mM Mg ²⁺ Ac	146	3.76	0.08	0.20	2.38	0.40	0.17	-	-	-
	HP1a K9me0	964	1.88	0.01	0.14	4.02	0.30	0.20	-	-	-
	HP1a K9me3	797	1.79	0.04	0.17	3.82	0.38	0.20	-	-	-
	HP1a_p K9me0	179	3.32	0.04	0.14	3.19	0.33	0.17	-	-	-
	HP1a_p K9me3	262	1.28	0.03	0.17	3.88	0.44	0.22	-	-	-
	D A 2	0mM Mg ²⁺	174	5.37	0.00	0.14	0.44	0.90	0.10	0.92	0.57
0.5mM Mg ²⁺		132	3.98	0.01	0.14	1.88	0.65	0.22	0.81	0.27	0.10
1.0mM Mg ²⁺		103	2.83	0.02	0.17	2.07	0.75	0.17	1.23	0.45	0.22
4.0mM Mg ²⁺		138	2.86	0.00	0.14	1.96	0.70	0.22	1.31	0.30	0.22
4.0mM Mg ²⁺ Ac		113	1.35	0.01	0.22	2.13	0.62	0.20	1.84	0.25	0.20
HP1a K9me0		260	2.45	0.01	0.17	1.52	0.61	0.22	1.81	0.30	0.17
HP1a K9me3		252	1.20	0.05	0.22	3.49	0.71	0.17	1.12	0.41	0.17
HP1a_p K9me0		901	0.63	0.04	0.17	3.01	0.66	0.17	2.21	0.33	0.22
HP1a_p K9me3		275	1.67	0.07	0.22	2.40	0.74	0.17	1.37	0.36	0.22
D A 3		0mM Mg ²⁺	216	1.40	0.03	0.17	5.90	0.74	0.10	1.34	0.58
	0.5mM Mg ²⁺	165	0.85	0.05	0.20	7.57	0.78	0.00	2.94	0.72	0.14
	1.0mM Mg ²⁺	155	1.29	0.03	0.14	6.08	0.81	0.10	2.66	0.75	0.17
	4.0mM Mg ²⁺	145	1.34	0.02	0.14	6.75	0.87	0.00	3.39	0.79	0.14
	4.0mM Mg ²⁺ Ac	130	0.45	0.04	0.22	7.13	0.86	0.10	2.14	0.70	0.22

Supplementary Table 5 | Gaussian fits of FRET distributions from Fig. 2 and 4. Histograms of the E_{FRET} values of combined traces (number of traces: n) were fitted using the indicated number of Gaussians with amplitude A_i , center C_i and width σ_i . Ac: Chromatin fiber contains H4K₅16Ac

	0mM Mg ²⁺	4.0mM Mg ²⁺	4.0mM Mg ²⁺ Ac	HP1	
				H3K9me0	H3K9me3
DA1	17 %	29 %	22 %	55 %	54 %
DA2	35 %	38 %	26 %	38 %	42 %
DA3	20 %	20 %	19 %	X	X

Supplementary Table 6 | Percentage of dynamic traces observed in smTIRF. Traces are identified as dynamic by cross-correlation (CC) analysis of donor versus acceptor fluorescence emission. Dynamic traces exhibit a CC amplitude of < -0.1 and a CC relaxation time > 100 ms.

Contributions to ΔR_{DA}	DA1	DA2	DA3
Calibration contributions to the uncertainty, $\Delta R_{DA,cal}$ in step 2 [a]			
Uncertainty of the correction factor, γ , $\Delta R_{DA}(\Delta\gamma)$, mainly due to $\Delta\Phi_{FA}$ (Summary 9.3: $\langle\Phi_{FA}\rangle = 0.368$ with $\Delta\Phi_{FA} = 0.017$)	0.008	0.008	0.008
Uncertainty of correction factors, α , β and δ , $\Delta R_{DA}(\Delta\alpha, \Delta\beta, \Delta\delta)$	< 0.005	< 0.005	< 0.005
Uncertainty of signal correction by background, $B_{Xem Xex}$, $\Delta B_{Xem Xex}$	< 0.005	< 0.005	< 0.005
Contributions to the uncertainty ΔR_0 [b]			
Uncertainty of refractive index, $\Delta R_0(n)$ [c]	0.040	0.040	0.040
Uncertainty of donor fluorescence quantum yield Φ_{FD} , $\Delta R_0(\Phi_{FD})$ [c]	0.020	0.020	0.020
Uncertainty of spectral overlap integral J , $\Delta R_0(J)$ [c]	0.025	0.025	0.025
Uncertainty of FRET orientations factor, κ^2 , $\Delta R_0(\kappa^2)$ [d]	0.071	0.070	0.060
Total accuracy ΔR_0	0.088	0.087	0.079
Noise contributions to the uncertainty $\Delta R_{DA,noise}(R_{DA})$			
Precision to fit R_{DA} by dynPDA, $\Delta R_{DA}(R_{DA})$ [e]	0.020	0.030	0.020
Uncertainty by A heterogeneity, $\Delta R_{DA}(A_{het})$ [f]	0.0001	0.0038	0.0051
Total uncertainty to compute R_{DA}, $\Delta R_{DA}(\Delta R_{DA,cal}, \Delta R_0, \Delta R_{DA,noise}(R_{DA}, \Delta A_{het}))$ [g]	0.090	0.092	0.081

[a] Adapted from ref. ¹⁰.

[b] Adapted from ref. ¹¹.

[c] Values from ref. ¹¹.

[d] We computed the densities of κ^2 (see section 3.5 of ref. ¹²) using the residual anisotropies of the donor, $r_{inf,D}$ (Summary 9.2), and of the acceptor, $r_{inf,A}$ (Summary 9.4), to determine the uncertainty $\Delta\kappa^2$ and the corresponding $\Delta R_0(\kappa^2)$.

[e] See Step 9, section **Determination of uncertainties in measured R_{DA} distances** and **Supplementary Figures 16-18**.

[f] See Step 9, Summary 9.3.

[g] Calculated according to eq. (9.7).

Supplementary Table 7 | Accuracy and precision of the inter-dye distance calculation R_{DA} . Relative uncertainties are reported for individual contributions (see **Supplementary Note, Step 9**) followed by the calculated total accuracy ΔR_0 , and the total uncertainty ΔR_{DA} . For values in % multiply by 100. Error propagation was performed according to refs. ^{10,11} using eq. (9.7).

	Model	Experiment	Model	Experiment
	$\langle R_{DA,m} \rangle_E$, register 1, (Å)	$\langle R_{DA,exp} \rangle_E$, register 1, (Å)	$\langle R_{DA,m} \rangle_E$, register 2, (Å)	$\langle R_{DA,exp} \rangle_E$, register 2, (Å)
DA1	64	64	47	46
DA2	41	53	36	44
DA3	48 [a]	42-48	53 [a]	42-48

[a] linear linker DNA to connect the two nucleosomes in a register was assumed.

Supplementary Table 8 | Correlation between FRET-averaged inter-dye distances of the structural models, $\langle R_{DA,m} \rangle_E$, and of the experiments, $\langle R_{DA,exp} \rangle_E$, for the Alexa488/647 FRET pair. Experimental distances $\langle R_{DA,exp} \rangle_E$ of DA 1-3 were obtained from PDA analysis (**Supplementary Figures 16 - 18**). The model distances were calculated for the tetranucleosome model (register 1 and 2) considering the total experimental uncertainty $\Delta R_{DA}(\Delta E_{FRET}, \Delta R_0, \Delta R_{DA,noise}(R_{DA}, \Delta A_{het}))$ (**Supplementary Table 7**) using ACV analysis (**Supplementary Note, step 9**, sections Determination of the uncertainties for structural modeling (ACV parameters), and FRET positioning and screening calculations (**Supplementary Figures 12 and 13**). Considering DA2, there are two possible explanations for the deviations between $\langle R_{DA,m} \rangle_E$ and $\langle R_{DA,exp} \rangle_E$: (1) Local dynamics could be present (clamshell and torsion by 10 degrees, see **Supplementary Fig. 13**). (2) In addition, in view of the low Mg^{2+} concentrations and the absence of H1, the stacking of the nucleosome arrays could differ in solution from that in the X-ray¹³ or cryoEM⁵ structure.

Supplementary Note

Dynamic structural biology analysis:	30
Step 1: smTIRF	32
Step 2: 2D MFD plots with FRET lines and calibration of the FRET measurements	33
Calculation of FRET efficiencies EFRET from fluorescence signals	34
Expanding the dynamic range of smFRET studies.	35
Static and dynamic FRET lines.	35
Step 3: Sub-ensemble TCSPC	36
Step 4: Burst-ID FCS	38
Step 5: Photobleaching and photoblinking analysis	39
Step 6: Evaluation of kinetic networks between FRET species compatible with experimental data	40
Step 7: General description of PDA analysis	40
Calculation of donor acceptor distances from fluorescence signals	41
Dynamic PDA.	41
Step 8: Validation of kinetic models	43
Step 9: Relating measured R_{DA} distances to structural models of compact chromatin states	43
Determination of the uncertainties for structural modeling.	44
Summary of dye properties of the donor Alexa488.	44
Summary of acceptor dye properties.	45
Determination of uncertainties in measured R_{DA} distances	47
Model building	48
FRET positioning and screening calculations	48
Step 10: Structural models of open and dynamic states	49
Coarse grained simulations	50
Step 11: Final model and its validation - A unified model of chromatin dynamics	51

Dynamic structural biology analysis:

We used a combination of experimental observables (described in detail below) for structural and kinetic analyses to establish a model for chromatin dynamics, as shown in **Fig. 6**. We established an 11-step workflow for dynamic structural biology (**Supplementary Fig. 9**), involving a sequence of steps:

Step 1: Measuring FRET efficiencies over time in **smTIRF** we explored chromatin dynamics in the 100 ms – seconds regime. Employing cross-correlation analysis we observed that between 20-55% of fibers showed dynamics on the 50-500 ms timescale (**Fig. 2** and **Supplementary Table 6**).

Step 2: 2D MFD plots. We measured smFRET with confocal multi-parameter fluorescence detection (MFD). E_{FRET} vs fluorescence-weighted average fluorescence lifetime of the donor dye in presence of the acceptor $\langle \tau_{D(A)} \rangle_F$ enabled us to identify rapid dynamics and allowed us to detect the coexisting dynamic chromatin populations in two different tetranucleosome interaction registers (register 1 and 2). In the presence of dynamic exchange between conformations with different E_{FRET} and exchange kinetics faster than the molecular dwell time in the confocal detection volume (< 10 ms), deviations from the ideal relationship between $\langle \tau_{D(A)} \rangle_F$ and E_{FRET} (the static FRET line) can be detected in burst-wise analysis¹⁴. This is because E_{FRET} values derived from fluorescence intensities are averaged per molecular species fractions, whereas average fluorescence lifetimes are computed per brightness by the applied maximum-likelihood analysis¹⁵. This disagreement is captured by a dynamic FRET line. For the chromatin arrays DA1-3 MFD plots indeed directly indicated a dynamic process as a large fraction of the detected molecules fell on dynamic FRET-lines (**Fig. 3d,e**). Importantly, measurements with DA1, DA2 or DA3 labeled DNA (absence of histones) as well as measurements with chromatin samples bearing only donor dyes (D1, D2 and D3; **Supplementary Table 4**) did not show comparable FRET states or dynamics (**Supplementary Fig. 8c,d**).

Step 3: Sub-ensemble Time Correlated Single Photon Counting (seTCSPC) resolved the FRET efficiency levels corresponding to chromatin structural states (**Supplementary Fig. 10**).

Step 4: Burst-ID fluorescence correlation spectroscopy (FCS) of donor-donor, donor-acceptor or cross-correlation confirmed complex sub-millisecond dynamics in a model-free approach and yielded estimates of the involved timescales (DA1-3, 0.75 mM Mg^{2+} , **Supplementary Fig. 11**).

Step 5: Photobleaching and photoblinking analysis was employed to confirm that the observed dynamic processes originate from structural transitions and did not contain contributions from photophysics of the dyes (**Supplementary Fig. 14a**).

Steps 6-11: The combined obtained data was used to **formulate kinetic models and assign states and connectivity between the states (step 6)**. Subsequently a unified kinetic model was used in dynamic PDA analysis (**step 7, Fig. 5 and Supplementary Fig. 16-18**). A global fit to the experimental data yields improved FRET efficiency levels values with corresponding population fractions and exchange rate constants. Afterwards the model was judged by applying a selection of criteria (**Supplementary Fig. 15**) including an evaluation of goodness of fit, the stability of the fit results (**step 8**) as well as by determination of the parameter uncertainties (**step 9**) and structural validation such as atomistic models (**step 9**) and coarse grained simulations (**step 10**). The procedure finally results in a complete model of chromatin dynamics (**step 11**).

Step 1. smTIRF

From donor- (F_D) and acceptor fluorescence emission intensity (F_A) traces FRET efficiency (E_{FRET}) traces were calculated, using

$$E_{FRET} = \frac{F_A - \beta F_D}{F_A - \beta F_D + \gamma F_D} \text{ and } \gamma = \frac{\Delta F_{A,bleach}}{\Delta F_{D,bleach}} \quad (0.1)$$

The values of $\beta = 0.141$ and $\gamma = 0.468$ were experimentally determined for the dye pair Alexa568/647 in our experimental setup. The bin size for all histograms was set to 0.02. E_{FRET} histograms of each trace of length > 5 s were normalized to total counts. Final histograms were calculated averaging the FRET histograms of all traces (> 100 traces) and fitted using 2 or 3 Gaussian functions $\sum_i A_i e^{-(x-c_i)^2/\sigma_i}$ (**Supplementary Table 5**).

Cross-correlation analysis was performed using

$$C_{cross}(t) = \langle \Delta F_D(0) \cdot \Delta F_A(t) \rangle / \langle \Delta F_D(0) \cdot \Delta F_A(0) \rangle \quad (0.2)$$

where ΔF_D and ΔF_A are the variances of donor and acceptor fluorescence at time 0 or t , was calculated in Matlab using a maximum lag of 10 s. Traces shorter than 10 s, as well as traces which spent less than 20% of the time at $E_{FRET} < 0.2$ were excluded from the analysis. The cross-correlation data was fitted with a bi-exponential function in OriginPro (OriginLab Corporation). To determine the fraction of dynamic traces (**Supplementary Table 6**) the individual cross-correlation decays from each trace was analyzed. Traces considered dynamic showed an amplitude < -0.1 and a decay time constant > 0.1 s.

This analysis revealed that chromatin fibers exhibit dynamics on the 50-500 ms timescale, but that such fluctuations were only observed in a subset of individual arrays. This argues for the existence of 'locked' states where tetranucleosome interactions are stable over time (**Figure 6**).

Step 2: 2D MFD plots with FRET lines and calibration of the FRET measurements

Burst selection. The bursts of all samples were identified and selected from the MFD data trace as described in ref. ¹⁶. Double-labeled chromatin arrays with the DA pair Alexa488/647 capable for FRET (FRET-active) were selected by Pulsed Interleaved Excitation (PIE) using E_{FRET} vs S (stoichiometry) 2D histograms. For subsequent analysis we selected bursts with $0.2 < S < 0.8$ to separate double-labeled species from single dye labeled molecules and $|T_{GX}-T_{RR}| < 1$ ms to remove contributions from photophysical processes ¹⁷ (**Supplementary Fig. 8a**). For PIE¹⁸, the corrected stoichiometry S is defined as

$$S = \frac{F_{D|D} + F_{A|D}}{F_{D|D} + F_{A|D} + F_{A|A}} \quad (2.1)$$

$F_{Xem|Xex}$ corresponds to a fully corrected fluorescence intensity computed from observed signal ^{obs}S considering background intensities and other experimental correction factors α , β , γ , δ defined in eq. (2.3). The meaning of the indices is as follows: (D/D) is the donor intensity if the donor was excited, (A/D) is the acceptor intensity if the donor was excited and (A/A) is the acceptor intensity if the acceptor was excited.

The stoichiometry S is computed from the observed signals ^{obs}S in two steps:

(i) The registered primary signal ^{obs}S was corrected for the mean background $\langle B \rangle$ signal contribution in the green and red channels, respectively:

$$I_{Xem|Xex} = ^{obs}S_{Xem|Xex} - \langle B_{Xem|Xex} \rangle \quad (2.2)$$

$I_{Xem|Xex}$ corresponds to a background corrected signal: $I_{G|G}$ is the background corrected signal in the donor channel (G) after donor excitation (G), $I_{R|G}$ is the background corrected signal in the acceptor channel (R) at wavelength G for donor excitation and $I_{R|R}$ is the background corrected signal in the acceptor channel after acceptor excitation, respectively.

(ii) The background corrected signals I were used together with four correction factors α , β , γ , δ to compute S according to:

$$S = \frac{\gamma \cdot I_{G|G} + (I_{R|G} - (\alpha \cdot I_{G|G} + \beta \cdot I_{R|R}))}{\gamma \cdot I_{G|G} + (I_{R|G} - (\alpha \cdot I_{G|G} + \beta \cdot I_{R|R})) + \frac{1}{\delta} \cdot I_{R|R}} \quad (2.3)$$

$$\text{with } \alpha = \frac{g_{R,D}}{g_{G,D}}; \beta = \frac{\sigma_{A|G} L_G}{\sigma_{A|R} L_R}; \gamma = \frac{g_{R,A} a \Phi_{F,A}}{g_{G,D} \Phi_{F,D(0)}}; \delta = \frac{\sigma_{A|R} L_R}{\sigma_{D|G} L_G}$$

The parameter α is a correction factor for the spectral donor fluorescence crosstalk (leakage) into the red "acceptor" detection channel. β normalizes the direct acceptor excitation rates in the FRET experiment to that in the PIE experiment defined by the acceptor excitation cross-sections $\sigma_{A|G}$ at donor excitation and

σ_{AR} , and the direct excitation irradiances [Photons/cm²] L_G and L_R for the donor and acceptor at the wavelengths G and R. γ is a correction factor for the fluorescence quantum yields $\Phi_{F,D(0)}$, $\Phi_{F,A}$, the fraction of the fluorescent trans state of Alexa647 α , and the detection efficiencies of the green donor $g_{G|D}$ and the red acceptor channel $g_{R|A}$, respectively. δ normalizes the donor excitation rate for the FRET studies to the direct acceptor excitation rate of the PIE experiment defined by the excitation cross-sections for D $\sigma_{D|G}$ and A σ_{AR} respectively, and the direct excitation irradiances [photons/cm²] L_G and L_R for the donor and acceptor at the wavelengths G and R.

For chromatin samples with the FRET pair Alexa568/647 we did not employ PIE (i.e. δ is n.a.). The direct acceptor excitation rate at the donor excitation wavelength ($\beta \gg 0$) could however be used to identify double-labeled DA species. Thus, double-labeled chromatin arrays with the DA pair Alexa568/647 capable for FRET (FRET-active) were selected by a minimal number of acceptor photons (red cut) due to direct acceptor excitation by L_G . In this way contributions from DOnly molecules were reduced. The following parameters were used for the two studied FRET pairs for given experimental setup (see **MFD measurement procedures**):

parameter	FRET pair D/A	
	Alexa488/647	Alexa568/647
α	0.016	0.146
β	0	0.131
$g_{G D}/g_{R A}$	0.95	1.45
$\Phi_{F,D(0)}$ [a]	0.8	0.69
$\alpha \Phi_{F,A}$ [a]	0.368	0.368
γ	0.5	0.38
δ	0.83	n.a.

[a] average values for the FRET pairs DA1-3. The determined values are compiled in the summary tables reported in **step 9**.

Calculation of FRET efficiencies E_{FRET} from fluorescence signals

The corrected FRET efficiency E_{FRET} is defined via fully corrected fluorescence intensities F :

$$E_{FRET} = \frac{F_{AD}}{F_{D|D} + F_{AD}} \quad (2.4)$$

In analogy to S , E_{FRET} can be computed by the observed intensities and corresponding correction parameters α , β , γ defined in eq. (2.3):

$$E_{FRET} = \frac{(I_{R|G} - (\alpha \cdot I_{G|G} + \beta \cdot I_{R|R}))}{\gamma \cdot I_{G|G} + (I_{R|G} - (\alpha \cdot I_{G|G} + \beta \cdot I_{R|R}))} \quad (2.5)$$

Expanding the dynamic range of smFRET studies. We used the FRET pairs Alexa568/647 (Förster Radius $R_0 = 82 \text{ \AA}$) and Alexa488/647 ($R_0 = 52 \text{ \AA}$) to exploit different distance sensitivities (**Fig. 3d,e**): Alexa568/647 allows for the detection of long-range dynamics beyond 120 \AA , whereas Alexa488/647 enables the investigation of sub-states and their exchange dynamics below 60 \AA .

Static and dynamic FRET lines. All MFD plots (**Fig. 3d,e**) for DA1-3 (Alexa488/647 and Alexa568/647) are presented with static and dynamic FRET lines, to demonstrate the presence of two distinct chromatin populations (register 1 and 2). Each population exhibits kinetic exchange faster than the molecular dwell time ($< 10 \text{ ms}$) within the bursts. The theoretical dependence between FRET efficiency and species weighted average donor fluorescence lifetime in presence of acceptor dye is described as

$$E_{static} = 1 - \frac{\langle \tau \rangle_x}{\tau_{D(0)}}. \quad (2.6)$$

Here we use an empirical dependence of species weighted average donor lifetime $\langle \tau \rangle_x$ on fluorescence weighted average donor lifetime $\langle \tau \rangle_F$ as a polynomial with c_i coefficients obtained by numerical simulations¹²

$$\langle \tau \rangle_x = \sum_{i=0}^n c_i (\langle \tau \rangle_F)^i. \quad (2.7)$$

Here we used the following joint parameters for DA1-3 constructs, which are common for the two FRET pairs Alexa568/647 and Alexa568/647, respectively:

Alexa568/647 labeling (**Fig. 3d**): $c_0 = -0.0083$, $c_1 = 0.0848$, $c_2 = 0.2926$, $c_3 = -0.6606$, $c_4 = 0.0085$ with $\tau_{D(0)} = 3.5 \text{ ns}$.
and

Alexa488/647 labelling (**Fig. 3e**): $c_0 = -0.0056$, $c_1 = 0.0838$, $c_2 = 0.4007$, $c_3 = -0.3806$, $c_4 = 0.00225$ with $\tau_{D(0)} = 4.0 \text{ ns}$.

The dynamic FRET line are described as

$$E_{dyn} = 1 - \frac{\tau_{F1} \cdot \tau_{F2}}{\tau_{D(0)} \cdot (\tau_{F1} + \tau_{F2} - \langle \tau \rangle_x)} \quad (2.8)$$

where τ_{F1} and τ_{F2} are the donor fluorescence lifetimes defining the limiting FRET states of the respective line. We have assumed that the limiting states of each DA sample remain the same for all Mg^{2+} concentrations.

Alexa568/647, dynamic FRET line for register 1 between A and D states with $\tau_{D(0)} = 3.5 \text{ ns}$ (**Fig. 3d**, dark blue):

DA1 between A/C and D states: $\tau_{F1} = 0.8 \text{ ns}$, $\tau_{F2} = 3.45 \text{ ns}$, $c_1 = 1.2458$, $c_2 = 0.84821$.

DA2 between A and C: $\tau_{F1} = 0.56 \text{ ns}$, $\tau_{F2} = 1.2 \text{ ns}$, $c_1 = 1.4285$, $c_2 = -0.5695$; and between C and D: $\tau_{F1} = 1.15 \text{ ns}$, $\tau_{F2} = 3.5 \text{ ns}$, $c_1 = 1.1778$, $c_2 = 0.6221$.

DA3 between A/B and C: $\tau_{F1}=0.25$ ns, $\tau_{F2}=0.8$ ns, $c_1=1.626$, $c_2=0.5523$; and between C and D: $\tau_{F1}=0.8$ ns, $\tau_{F2}=3.5$ ns, $c_1=1.2473$, $c_2=0.8655$.

Alexa568/647, dynamic FRET line for register 2 between B and D states with $\tau_{D(0)}=3.5$ ns (**Fig. 3d**, light blue):
DA1-3: $\tau_{F1}=0.25$ ns, $\tau_{F2}=3.5$ ns, $c_1=1.5198$, $c_2=1.819$.

Alexa488/647, dynamic FRET line for register 1 between A and D states with $\tau_{D(0)}=4.0$ ns (**Fig. 3e**, dark blue):

DA1: $\tau_{F1}=3.12$ ns, $\tau_{F2}=3.92$ ns, $c_1=1.0895$, $c_2=0.317$;

DA2: $\tau_{F1}=2.53$ ns, $\tau_{F2}=3.96$ ns, $c_1=1.1605$, $c_2=0.6339$;

DA3: $\tau_{F1}=2.57$ ns, $\tau_{F2}=3.96$ ns, $c_1=1.154$, $c_2=0.6082$.

Alexa488/647, dynamic FRET line for register 2 between B and D states with $\tau_{D(0)}=4.0$ ns (**Fig. 3e**, light blue):

DA1 and DA2: $\tau_{F1}=1.55$ ns, $\tau_{F2}=3.92$ ns, $c_1=1.376$, $c_2=-1.4852$;

DA3: $\tau_{F1}=1.6$ ns, $\tau_{F2}=3.95$ ns, $c_1=1.3607$, $c_2=-1.4248$.

Importantly, measurements with DA1, DA2 or DA3 double labeled DNA (absence of histones) as well as measurements with chromatin samples bearing only donor dyes (D1, D2 and D3; **Supplementary Table 4**) did not show comparable FRET states or dynamics (**Supplementary Fig. 8c,d**).

Step 3: Sub-ensemble TCSPC

For defining the limiting states for dynamic FRET lines indicated by FRET efficiency levels (**Fig. 3e** orange, wine and gray lines), we performed sub-ensemble Time Correlated Photon Counting (seTCSPC) analysis of DA1-3 (Alexa488/647), which were selected from the sample as double-labeled species by PIE (**Supplementary Fig. 8a**). Characteristic populations for each respective limiting state are analyzed for bursts with a low FRET efficiencies ($0 < E_{FRET} < 0.199$) of the low FRET population (LF) and for bursts with higher FRET efficiencies ($0.2 < E_{FRET} < 1.0$) of the dynamic FRET population (dynF). To retrieve the required information about the limiting states, we analyzed bursts of each population separately. The specific fluorescence decays were analyzed by a fit model described previously¹⁹. The fluorescence decay of the donor reference (DOnly, in the absence of FRET) was approximated by a single fluorescence lifetime, $\tau_{D(0)}$:

$$f_{D(0)}(t) = f_{D(0)}(0) \exp(-t / \tau_{D(0)}) \quad (3.1)$$

Hence, the FRET-rate (k_{FRET}) is only determined by the donor-acceptor distance and their relative orientation. In the presence of FRET, the donor fluorescence decay can be expressed using the donor-acceptor distance distribution $p(R_{DA})$:

$$f_{D(A)}(t) = f_{D(A)}(0) \int_{R_{DA}} p(R_{DA}) \exp\left(-\frac{t}{\tau_{D(0)}} \left[1 + (R_0 / R_{DA})^6\right]\right) dR_{DA} \quad (3.2)$$

Here we assumed Gaussian distribution of donor-acceptor distances ($p(R_{DA})$) with a mean of $\langle R_{DA} \rangle$ and a half-width of σ_{DA} which is expressed as:

$$p(R_{DA}) = \frac{1}{\sqrt{2\pi}\sigma_{DA}} \exp\left(-\frac{(R_{DA} - \langle R_{DA} \rangle_{\text{exp}})^2}{2\sigma_{DA,\text{exp}}^2}\right) \quad (3.3)$$

In addition, a fraction of Donor-only molecules ($x_{D\text{Only}}$) and a constant offset c was considered to describe the experimentally observed fluorescence decay $f(t)$:

$$f(t) = (1 - x_{D\text{Only}}) \cdot f_{D(A)}(t) + x_{D\text{Only}} \cdot f_{D(0)}(t) + c \quad (3.4)$$

Combining the donor fluorescence decay in the presence, $f_{D(A)}(t)$, and in the absence, $f_{D(0)}(t)$, of FRET by a time-dependent ratio a measure of FRET, $\varepsilon_D(t)$, is obtained:

$$\varepsilon_D(t) = \frac{f_{D(A)}(t)}{f_{D(0)}(t)} \quad (3.5)$$

We refer to this ratio as the FRET-induced donor decay, $\varepsilon_D(t)$, as it quantifies the quenching of the donor by FRET (see **Main Text, Fig. 3f**) with rate constant k_{FRET} . $\varepsilon_D(t)$ allows us to directly display the underlying inter-dye distances that correspond to a characteristic time for the FRET species j (where j can be the species A, B, C and D, respectively) (eq. (3.6)).

$$t_{\text{FRET},j} = \frac{1}{k_{\text{FRET}}} = \tau_{D(0),\text{ref}} \left(\frac{R_{DA,j}}{R_0(\tau_{D(0),\text{ref}})} \right)^6 \quad (3.6)$$

Note that each Förster Radius R_0 has been computed with a specific fluorescence quantum yield of the donor $\Phi_{F,D(0),\text{ref}}$ as reference which must be converted to a radiative rate constant by multiplying with the corresponding fluorescence lifetime $\tau_{D(0),\text{ref}}$. In this work $\tau_{D(0),\text{ref}}$ was 4.0 ns.

The fluorescence decays of the specific donor-only reference and the corresponding FRET samples (DA1, DA2 and DA3, respectively) were analyzed in joint fit as described in detail in ref.¹⁰ to determine the FRET species specific inter-dye distances $R_{DA,j}$. The DA1 Alexa488/647 subpopulation ($E_{FRET} > 0.065$, dynF, see also **Figure 3f**) and subpopulation with $E_{FRET} < 0.065$, LF) at 1 mM Mg^{2+} was fitted by eq. (3.1)-(3.4) with a global DOnly decay approximated by a single donor fluorescence lifetime ($\tau_{D(0)}=4.1$ ns) by a model with 3 Gaussian distributed distances and the same half-width $\sigma_{DA}=6$ Å. The fit quality is judged by χ^2_r . The fit results for the subpopulations LF and dynF are collected in the following table:

subpopulations of DA1	$R_{DA,1}$, (Å)	x_1	$R_{DA,2}$, (Å)	x_2	$R_{DA,3}$, (Å)	x_3	χ^2_r
LF	42	0.28	63	0.49	104	0.23	1.11
dynF		0.40		0.47		0.13	1.07

Further seTCSPC analysis of the fluorescence intensity decay curves for all Alexa488/647 FRET pairs, DA1-3 in 0.5 mM Mg^{2+} with corresponding fits by eq. (3.4) are shown in **Supplementary Fig. 10**. This analysis yielded a good estimate of the FRET parameters of the structural states underlying the dynamic populations (register 1 and 2). Note, that it is difficult to resolve distances of this FRET pair above 90 Å by seTCSPC.

Step 4: Burst-ID FCS

To perform an unbiased check for the presence of exchange kinetics detected by FRET³, we computed the color correlation functions (auto- (green-green (G,G) and red-red (R,R))- and cross- (green-red (G,R) and red-green (R,G)) functions, respectively) for the signal of those bursts, which were selected from the sample as double-labeled species by PIE (**Supplementary Fig. 8a**). These burst-ID cross-correlation functions $G_{G,R}$ and $G_{R,G}$ together with auto-correlation functions $G_{G,G}$ and $G_{R,R}$ were globally fitted by eq. 4.1 with three relaxation times t_{Rj} . To fit the color auto($i=m$)- and cross($i \neq m$)- correlation functions in a global approach, we have used a set of equations previously presented^{5,20}

$$\begin{aligned}
 G_{i=m}(t_c) &= 1 + \frac{1}{N_{Br}} \cdot G_{diff}^{(i)}(t_c) \cdot \left[1 - B^{(i)} + B^{(i)} \cdot \exp(-t_c/t_B) + \sum_{j=1}^n AC_{Rj}^{(i)} \cdot \left(\exp\left(-\frac{t_c}{t_{Rj}}\right) - 1 \right) \right] \\
 G_{i \neq m}(t_c) &= 1 + \frac{1}{N_{CC}} \cdot G_{diff}^{(i,m)}(t_c) \cdot \left[1 - CC^{(i,m)} \cdot \sum_{j=1}^n X_{Rj}^{(i,m)} \cdot \exp\left(-\frac{t_c}{t_{Rj}}\right) \right]
 \end{aligned} \tag{4.1}$$

where t_{Rj} are the relaxation times that correspond to the exchange times between selected color signals ($i=G,R$ and $m=G,R$) with corresponding absolute amplitudes of the auto-correlation function $AC_R^{(i)}$ and the relative normalized amplitudes of the cross-correlation function $CC^{(i,m)}$ with the fractions $X_R^{(i,m)}$. $B^{(i)}$ is the amplitude of an additional bunching term associated to photophysics with the relaxation time t_B in the

measured samples which was globally fitted for the auto-correlation functions. N_{br} is the average number of bright molecules from the color auto-correlation functions in the focus and N_{CC} of the color cross-correlations corresponds to the inverse of the initial amplitude $G_{i,m}(0)$. $G_{diff}^{(x)}(t_c)$ is the apparent diffusion term in the correlation function:

$$G_{diff}^{(x)}(t_c) = \left(1 + \frac{t_c}{t_{diff}^{(x)}}\right)^{-1} \cdot \left(1 + \left(\frac{\omega_0}{z_0}\right)^2 \cdot \frac{t_c}{t_{diff}^{(x)}}\right)^{\frac{1}{2}}. \quad (4.2)$$

A 3-dimensional Gaussian shaped volume element with parameters ω_0 and z_0 is considered. We assume that $G_{diff}(t_c) = G_{diff}^{(i)}(t_c) = G_{diff}^{(m)}(t_c)$ take the form of eq. (4.2). The selective correlation spectroscopy for the dynF population ($E_{FRET} > 0.065$) of DA1-labeled fibers (Alexa488/647) at 1 mM Mg^{2+} (see **Figure 3g**) by eq. (4.1) are compiled in the following table:

i, m	N_{Br}	z_0/w_0	t_{diff} , [ms]	$B^{(G)}$	t_B , [μs]	$AC_{R1}^{(i)}$ or $X_{R1}^{(i,m)}$	t_{R1} , [μs]	$AC_{R2}^{(i)}$ or $X_{R2}^{(i,m)}$	t_{R2} , [μs]	$AC_{R3}^{(i)}$ or $X_{R3}^{(i,m)}$	t_{R3} , [ms]	$CC^{(i,m)}$
G, G	0.69	70	5.26	0.039	0.192	0.142	2.6	0.089	27.3	0.005	3.14	-
R, R	0.26			0.256		0.183		0.259		0.080		-
G, R	0.72			0		0.168		0.271		0.561		0.42
R, G	0.74			0								0.42

Additional model-free correlation analysis from all FRET vantage points DA1-3 (488/647) at 0.75 mM Mg^{2+} revealed conformational dynamics with at least three relaxation times, thus involving at least four kinetic states (**Supplementary Fig. 11**).

Step 5: Photobleaching and photoblinking analysis

To detect possible photobleaching and photoblinking, we calculated the difference of the burst length in two PIE-channels T_{GX} and T_{RR} , where T_{GX} corresponds to the mean observation time of the photons detected in the donor or acceptor channels after donor excitation (G) and T_{RR} corresponds to mean observation time of the red photons after direct excitation of acceptor (R) (for details see ref¹⁷). In case of acceptor photobleaching and/or photoblinking the mean burst time of the acceptor fluorescence emissions is decreased and the mean burst time of donor fluorescence emission is increased simultaneously. This would lead to an increasing T_{GX} and to a decreasing T_{RR} , so that $|T_{GX} - T_{RR}|$ of the analyzed bursts would deviate significantly from zero, if photobleaching and/or photoblinking were present. However, as shown in **Supplementary Fig. 14a**, significant photobleaching and photoblinking was not present under our measurement conditions, because the $|T_{GX} - T_{RR}|$ distribution is symmetric and narrow. Additionally, we checked for the presence of potentially weak

photobleaching and photoblinking processes by applying the macro time filter $|T_{GX}-T_{RR}| < 1$ ms threshold criterion for burst selection (**Supplementary Fig. 14b, left panel**). The influence of the presence and absence of this selection criterion on the shape of the FRET efficiency distribution is demonstrated for double labeled bursts of DA1 (Alexa488/647) in 0.5 mM Mg^{2+} . We fitted two FRET efficiency E_{FRET} histograms with and without applied macro time filter (**Supplementary Fig. 14b**) by Photon Distribution Analysis (PDA, see **step 7**) for a 3 ms time window. The obtained FRET distributions and means with (left panel) and without (right panel) burst selection did not significantly differ from each other which proves the absence of marked acceptor photobleaching and photoblinking processes.

Steps 6-11. Establishing a dynamic model for chromatin dynamics

Step 6. Evaluation of kinetic networks between FRET species compatible with experimental data

The detected FRET species, which correspond to structurally meaningful chromatin conformers, form a kinetic network. Using the above presented observations from the various experiments (TIRF, seTCSPC, burst-ID FCS, MFD) kinetic and structural models for chromatin dynamics were formulated (**Supplementary Fig. 15**). The models to be evaluated involved four kinetic states (A-D) in two exchanging dynamic populations (register 1 and 2), corresponding to different tetranucleosome interactions.

In an iterative process, we used dynamic PDA (**step 7**) to refine the parameters and fit the experimental data using the developed kinetic models, followed by model validation (**step 8**). From the obtained, refined parameters, combined with structural molecular modeling (**steps 9-10**), a global model for chromatin conformational change was formulated (**step 11, Fig. 5**). The model encompasses a locally dynamic fiber which fluctuates between different tetranucleosome stacking registers on the millisecond timescale. Associations between tetranucleosomes are loose and exchange in the microsecond region. Finally, tetranucleosome open on the millisecond timescale and couple to static locked states, which persist structured over 50-500 ms. The individual **steps 7-11** for this analysis are described below.

Step 7. General description of PDA analysis

Each sample with a specific FRET dye configuration (DA1, DA2 or DA3) was measured at various Mg^{2+} concentrations under single-molecule conditions. The signals of the selected FRET bursts (**Supplementary Fig. 8a**) were split into equal time windows (TW). The FRET efficiency is calculated from the number of photons of donor and acceptor dyes in the prompt time-to-amplitude converter (TAC) channels defined by the donor excitation pulse with a repetition frequency of 32 MHz. In PIE experiments the acceptor excitation laser pulse is delayed by 15.625 ns, which defines the delayed TAC window for computation of the stoichiometry S (see

step 2, Calculation of donor acceptor distances from fluorescence signal). For each TW (only full length time windows were used and incomplete pieces at the end of bursts were excluded) the values for the FRET parameters (R_{DA} , E_{FRET}) were calculated as described in **step 2, Calculation of donor acceptor distances from fluorescence signal**, and plotted in a 1D frequency histogram with 201 bins (**Supplementary Fig. 16-18**). The fundamental idea in PDA is computing the distribution of the chosen FRET indicator for a given FRET efficiency (or FRET-averaged donor-acceptor distance, $\langle R_{DA} \rangle_E$)^{4,14} taking into account photon shot-noise. Due to the flexibility of the dye linker, FRET pairs exhibit a distribution of FRET efficiencies or apparent distances even on rigid molecules, which is caused by distinct acceptor brightnesses²¹. This distance distribution is well approximated by a Gaussian distribution with a half width $\sigma \sim 6 \text{ \AA}$.

Calculation of donor acceptor distances from fluorescence signals

The FRET-averaged distance $\langle R_{DA} \rangle_E$ between the dyes could be calculated from the mean FRET efficiency defined in eq. (2.4)

$$\langle R_{DA} \rangle_E = R_0 \left(\langle E_{FRET} \rangle - 1 \right)^{1/6} \quad (7.1)$$

In this work we calculated $\langle R_{DA} \rangle_E$ directly from the observed intensities and corresponding correction parameters α , β , γ , δ defined in **Step 2**:

$$\langle R_{DA} \rangle_E = R_0 \left(\frac{\gamma \cdot I_{G/G}}{I_{R/G} - (\alpha \cdot I_{G/G} + \beta \cdot I_{R/R})} \right)^{1/6} \quad (7.2)$$

using the following FRET pair specific Förster Radii R_0 :

parameter	FRET pair D/A	
	Alexa488/647	Alexa568/647
$R_0 [\text{\AA}]$	52	82

Dynamic PDA. Considering the sample DA1 (Alexa488/647) in 1mM Mg^{2+} , we demonstrate the effect of dynamics on the E_{FRET} histograms for two time windows of different length (TW=2ms and TW=5ms, **Supplementary Fig. 14c**). A global fit of both TWs using a joint models with static Gaussian distributions indicates that a model without dynamic exchange terms cannot describe both data sets appropriately, because the exchange dynamics influences the width of the distributions in each TW differently. Therefore we used dynamic PDA¹⁴ in the subsequent analysis, which can describe exchange dynamics comparable to NMR dispersion experiments. For each data set histograms were created for 4 different TWs (2, 3, 4 and 5 ms). All histograms created for Mg^{2+} concentrations (number of $[\text{Mg}^{2+}] \times 4$) were globally fitted by the kinetic

models described below. Each FRET species of assembled chromatin was modelled by a Gaussian distribution of distances and was approximated by 51 bins. To describe the histograms of dynamic mixing between two Gaussian distributed FRET species (e.g. species A, species B, ...), this results in $\binom{2}{51} = 50 \cdot 51 / 2 = 1275$ (all possible pairs of distances) dynamic mixing distributions. In contrast, the distributions of two FRET species undergoing dynamic mixing are approximated by 201 bins. Then, for each pair of interconverting Gaussian distributed species (e.g. dyn A-B, dyn B-C, ...), the shot-noise limited total histogram could be calculated as a sum of all $1275 \cdot 201 = 256275$ shot-noise limited FRET parameter distributions. We have shown that shot-noise limited FRET parameter histograms from Gaussian distributed distances (R_{mean}, σ) and the sum of shot-noise limited FRET parameter histograms of two fixed distances $R_{\text{mean}} - \sigma$ and $R_{\text{mean}} + \sigma$ are very similar¹⁴. Thus, in order to simulate dynamics between two Gaussian distributed species and to reduce computational cost, the model distribution can be approximated with the sum of two dynamic distributions between ($R1_{\text{mean}} - \sigma1$ and $R2_{\text{mean}} - \sigma2$) and ($R1_{\text{mean}} + \sigma1$ and $R2_{\text{mean}} + \sigma2$) (**Supplementary Fig. 14d**).

MFD data were then globally fitted using dynamic PDA and assuming a kinetic model¹⁴. To satisfy the observations of coexisting dynamic and quasi-static molecules in smTIRF experiments, each dynamic PDA model assumed the co-existence of molecules existing in a number of individual FRET species showing no dynamics on the MFD timescale ($t_R > 50$ ms, static fraction, stat A, stat B, ...), with populations of molecules which exchange between FRET species (dynamic fractions, dyn A-B, dyn B-C, ...). Secondly, we assumed the inter-dye distances in the basic FRET species (A, B, C, D) to be invariant to Mg^{2+} . Thus, a sum of Gaussian distributed FRET species (static fractions, R_{DAi}) and dynamically mixing Gaussian distributed FRET species pairs (dyn i-j) corresponding to the selected kinetic model (see list of trial models in **Supplementary Fig. 15**) was used to globally fit the group of histograms for each FRET dye configuration over all Mg^{2+} concentrations (**Fig. 5a-c** and final models in **Supplementary Fig. 16-18**). Thirdly, the dynamics of exchanging molecules was described by models with a series of two-state kinetic exchange terms connecting the quasi-static populations. Final models are shown in **Fig. 5d-f** and **Supplementary Fig. 16-18**. Importantly, global fits were employed to evaluate the Mg^{2+} dependencies, assuming a linear relationship between the logarithms of the rate constants and the ionic strength:

$$\log(k_{ij}) = m \cdot [Mg^{2+}] + k_{ij,0}, \quad (7.3)$$

similar to observations in protein folding²².

Step 8: Validation of kinetic models.

Based on the model-free FCS analysis (**Supplementary Fig. 11**), yielding 3 relaxation times, at least four kinetically relevant species are expected. As our dye configurations (DA1-3) are not equally sensitive to all structural exchanges processes and states (**Fig. 4a**) we tested models containing 3 or 4 states for each dye configuration in the dynamic PDA analysis, employing various connectivities. For each configuration DA1-3 different kinetic models were evaluated based on a number of criteria:

- i.* Physical meaningful connectivity of species,
- ii.* Minimal number of species,
- iii.* Cutoff for rate constants ($10^6 \text{ s}^{-1} > k_{ij} > 10^2 \text{ s}^{-1}$) and m-values ($-25 < m < 25$ (see equation (7.3)); assuming a change of less than ± 100 -fold in each rate constant within the tested Mg^{2+} concentrations),
- iv.* Stable fit results over the different Mg^{2+} concentration,
- v.* Acceptable goodness of fit ($\chi^2_r < 1.4$),
- vi.* Consistency with models from other FRET vantage points (DA1, DA2 and DA3),
- vii.* Transitions between FRET species which are structurally meaningful.

A number of different models were tested and based on criteria *i-vi* (**Supplementary Fig. 15**). The models shown in Fig. 3d were deemed to be the most probable to describe the experimental data. Finally, from the static and dynamic fractions, weighted by the associated rate constants, the relative populations of each state were calculated (**Fig. 5g-i**) according to $P_i = P_i^s + P_{ij}^d \cdot k_{ij} / (k_{ij} + k_{ji})$, where P_i denotes the population of state i , P_i^s is the static fraction, P_{ij}^d is the dynamic fraction between states i and j and k_{ij} , k_{ji} are the associated rate constants.

Steps 9-11. Assignment of the states

For a structural interpretation of the detected inter-dye distances from MFD and PDA, we determined the uncertainties in our analysis and subsequently applied structural modeling, using both available structures and coarse grained modeling, in combination with modeling of the conformational distributions of the dyes.

Step 9: Relating measured R_{DA} distances to structural models of compact chromatin states

Here, first we define the uncertainties in the measured parameters, followed by the construction of molecular models for the compact states.

Determination of the uncertainties for structural modeling. As a first test for the suitability of the dyes Alexa488 and Alexa647 for an accurate structural analysis based on FRET data, we checked the fluorescence lifetimes of the donor-only and acceptor samples and time-resolved anisotropies $r(t)$ using the FRET samples identified by PIE. The results (see **summaries 9.1-2** of donor dye properties, **summaries 9.3-4** of acceptor dye properties below) indicate that there is no strong quenching as compared to the free dyes in solution and that all dyes are sufficiently mobile at these positions. Anisotropy decays were analyzed by eq. (9.1).

$$r(t) = \sum_i r_i \exp(-t / \rho_i) \text{ and } \sum_i r_i = r_0 \quad (9.1)$$

Here r_i denotes the depolarization fractions related to order parameters, and ρ_i the corresponding depolarization times mainly by dye rotation. In the $r(t)$ analysis we applied the fundamental anisotropies $r_0 = 0.38$ for Alexa488 and Alexa647, respectively. We used the amplitude of the longest depolarization time r_i to approximate the residual anisotropy r_{inf} for computing the dye and position specific fraction of trapped dyes using eq. (9.2).

$$X_{trapped} = r_{inf} / r_0 \quad (9.2)$$

The fraction of trapped dyes is needed to parametrize the contact volume for improving the accuracy of the estimated spatial dye density in ACV simulations described in **step 9**, section **FRET positioning and screening calculations** below.

Summary of dye properties of the donor Alexa488. In the tables below the fluorescence lifetimes and anisotropy contributions of this donor dye are compiled.

Summary 9.1. Fluorescence lifetimes of the donor dye Alexa488

Species	τ (ns)
DA1	
Average	4.2
Std, Δ	< 0.1
DA2	
Average	4.1
Std, Δ	< 0.1
DA3	
Average	4.1
Std, Δ	< 0.1
Average of DA1-3	
Average	4.1
Std, Δ	< 0.1

Summary 9.2. Fluorescence anisotropy and rotational correlation times of the donor dye Alexa488

Species	ρ_1 (ns)	ρ_2 (ns)	ρ_3 (ns)	ρ_4 (ns)	r_1	r_2	r_3	$r_{04}=r_{inf,D}$
DA1								
Average [a]	< 0.3	1.1	4.8	> 40	0.162	0.052	0.087	0.080
Std, Δ		0.2	0.9		0.014	0.011	0.014	0.012
$X_{trapped}$								0.210
DA2								
Average [a]	< 0.3	0.6	5.0	> 40	< 0,01	0.196	0.102	0.083
Std, Δ		0.1	1.1			0.069	0.030	0.009
$X_{trapped}$								0.218
DA3								
Average [a]	< 0.3	0.6	3.3	> 40	0.032	0.199	0.092	0.057
Std, Δ		0.03	0.5		0.007	0.012	0.009	0.003
$X_{trapped}$								0.149

[a] The fit values with using eq. (9.1) are averages for measurements at 0.0, 0.5, 1.0 and 4 mM Mg²⁺.

Summary of acceptor dye properties. In the tables below the fluorescence lifetimes and anisotropy contributions of the acceptor dye Alexa647 is summarized. In practice, as all cyanine based dyes, Alexa647 can have several dye populations in distinct environments with specific brightnesses when coupled to biomolecules referred to as acceptor heterogeneity, A_{net} . This typical behavior is also seen in nucleosome arrays (see Summary 9.3). In this case a fixed DA distance is usually not sufficient to describe FRET species, and a Gaussian distance distribution with a mean apparent distance $\langle \tilde{R} \rangle$ and an apparent distribution half width (hw_{app}) has to be used instead. As shown by Kalinin and colleagues²¹ $\langle \tilde{R} \rangle$ is slightly biased towards longer distances as compared to $\langle R_{DA} \rangle_E$ (eq. (9.3)).

$$\langle \tilde{R} \rangle = \langle R_{DA} \rangle_E \langle \Phi_{FA} \rangle^{1/6} \langle \Phi_{FA}^{-1/6} \rangle \quad (9.3)$$

where Φ_{FA} is the acceptor fluorescence quantum yield. Note that the fraction of fluorescent trans states α (usually $\alpha = 0.8$) cancels out in eq. (9.3)-(9.4). In this work, the correction factors $\langle \Phi_{FA} \rangle^{1/6} \langle \Phi_{FA}^{-1/6} \rangle$ are very close to unity (Summary 9.3) and thus can be disregarded for the calculation of interdy distances (i.e. in this work $\langle \tilde{R} \rangle \cong \langle R_{DA} \rangle_E$). Applying the rules for error propagation for the function $\tilde{R}(\Phi_{FA})$, one obtains also an relation for the variance and half width (σ) of the apparent DA distance (eq. 9.4).

$$\sigma(\tilde{R}) / R_{DA} = \langle \Phi_{FA} \rangle^{1/6} [\text{var}(\Phi_{FA}^{-1/6})]^{1/2} \quad (9.5)$$

The fact that relative experimental half widths (σ/R_{DA}) (**Supplementary Figures 16-18**, $\sigma/R_{DA}(\text{DA1}) = 0.1$, $\sigma/R_{DA}(\text{DA2}) = 0.13$, $\sigma/R_{DA}(\text{DA3}) = 0.06$) are much broader than the values caused by acceptor heterogeneity

(Summary 9.4) may indicate significant heterogeneity of the nucleosome arrays which would be actually not surprising. Note that the difference is the smallest (less than factor 2) for DA3.

Summary 9.3. Fluorescence lifetimes and other dye parameters of the acceptor dye Alexa647 with $a=0.8$.

Species	τ_1 (ns)	τ_2 (ns)	x_1	x_2	$\langle \tau_A \rangle_x$ (ns)	$a \Phi_{FA}$ [a,b]	A heterogeneity, A_{het} $\langle \Phi_{FA} \rangle^{1/6} / \langle \Phi_{FA} \rangle^{-1/6}$	σ/R_{DA}
DA1								
Average [b]	1.38	1.68	0.55	0.45	1.43	0.390	1.0001	0.005
Std, Δ	0.04	0.31	0.37	0.37	0.01	0.002	< 0.0001	0.001
DA2								
Average	0.92	1.49	0.32	0.68	1.32	0.362	1.0038	0.035
Std, Δ	0.10	0.005	0.18	0.18	0.06	0.015	0.0007	0.005
DA3								
Average	0.90	1.49	0.36	0.64	1.28	0.350	1.0051	0.040
Std, Δ	0.09	0.06	0.12	0.12	0.01	0.002	0.0003	0.002
Average of DA1-3								
Average					1.34	0.368		
Std, Δ					0.06	0.017		

[a] We used the reference value of Cy5 labeled dsDNA with $\langle \tau_A \rangle_x = 1.17$ ns and $\Phi_{FA} = 0.4$ which was measured with low irradiances at a steady state fluorescence spectrometer, i.e. $a=0$.

[b] The fit values are averages for measurements at 0.0, 0.5, 1.0 and 4 mM Mg^{2+} using a fit with a series of exponentials $f_A(t) = \sum_i x_i \exp(-t/\tau_i)$ and $\sum_i x_i = 1$.

Summary 9.4. Fluorescence anisotropy and rotational correlation times of the acceptor dye (Alexa647)

Species	ρ_1 (ns)	ρ_2 (ns)	ρ_3 (ns)	r_1	r_2	$r_3=r_{inf,A}$
DA1						
Average [a]	< 0.3	1.6	10.2	0.063	0.054	0.263
Std, Δ		0.7	0.4	0.007	0.026	0.020
$X_{trapped}$						0.692
DA2						
Average [a]	< 0.3	0.9	13.7	0.072	0.056	0.252
Std, Δ		0.6	4.1	0.003	0.019	0.018
$X_{trapped}$						0.663
DA3						
Average [a]	< 0.3	1.0	9.9	0.081	0.090	0.209
Std, Δ		0.3	0.03	0.007	0.013	0.016
$X_{trapped}$						0.549

[a] The fit values with using eq. (9.1) are averages for measurements at 0.0, 0.5, 1.0 and 4 mM Mg^{2+} .

Determination of uncertainties in measured R_{DA} distances

The uncertainty in the measured R_{DA} distances, used for structural modeling, is obtained by determining the individual uncertainties of all quantities separately, and then propagating them towards an uncertainty in the distance. Considering the DA distance, R_{DA} , two main factors determine the uncertainty, ΔR_{DA} in this study: (1) the precision (noise) of the measurement, Δ_{noise} and (2) the uncertainty of the calibration, Δ_{cal} . The total uncertainty of the distance, ΔR_{DA} , is estimated by combining these error sources. With the assumption that the contributions follow a normal distribution, ΔR_{DA} is given by:

$$\Delta R_{DA} = [\Delta_{noise}^2 + \Delta_{cal}^2]^{1/2} \quad (9.6)$$

The distance, R_{DA} , can be expressed as a function of experimental observable fluorescence intensities and correction and conversion parameters (see eq. 7.2). Thus Δ_{cal}^2 can be expanded as¹⁰

$$\Delta R_{DA} = [\Delta_{noise}^2 + (\Delta_{B_{GG}}^2 + \Delta_{B_{RG}}^2 + \Delta_{\alpha}^2 + \Delta_{\beta}^2 + \Delta_{\gamma}^2 + \Delta R_0^2)]^{1/2} \quad (9.7)$$

Calibration contributions to the uncertainty, $\Delta R_{DA,cal}$. All equations used to compute the contributions $\Delta R_{DA,cal}$ were described in detail by Peulen et al. (eqs. 39-46 in ref. ¹⁰).

Contributions to the uncertainty ΔR_0 . The overall uncertainty for the Förster radius, ΔR_0 , is estimated by the uncertainties of the local refractive index, n , the exact donor fluorescence quantum yield, $\Phi_{F,D}$, spectral overlap integral, J , and the FRET orientations factor, κ^2 , ref. ¹¹ (eq. (9.8)).

$$\Delta R_0(n^{-4}, \Phi_{F,D}, J, \kappa^2) = \sqrt{\Delta R_0(n)^2 + \Delta R_0(\Phi_{F,D})^2 + \Delta R_0(J)^2 + \Delta R_0(\kappa^2)^2} \sim 0.08 - 0.09 \cdot R_0 \quad (9.8)$$

Contributions to the uncertainty $\Delta R_{DA}(R_{DA})$ by noise. We have to determine the precision of the dynamic PDA fits, $\Delta R_{DA}(R_{DA})$ caused by statistical noise. Here, we performed a subsampling analysis, where the dynamic PDA fit procedure was repeated three times using a 70% subsample of the total dataset. The standard deviations from these three fits are reported in **Supplementary Figures 16-18**, and determine the precision of our fitting procedure. The overall precision in R_{DA} , $\Delta R_{DA}(R_{DA})$, from dynamic PDA is reported in **Supplementary Table 7**: 2% (DA1 and DA3) and 3% (DA2).

Contributions to the total uncertainty $\Delta R_{DA}(R_{DA})$. The individual errors are listed in **Supplementary Table 7**. They are then propagated using eq. (9.7), to estimate the total uncertainty of the determined distances. Together, these analyses result in a total uncertainty for R_{DA} for DA1 of 9%, for R_{DA} for DA2 of 9% and R_{DA} for DA3 of 8% (**Supplementary Table 7**).

Model building. We built models using the cryo-EM structure of a 12-mer nucleosomal array with 177 bp nucleosome repeat length⁵. We then modeled the accessible contact volume (ACV) for dyes in the DA1, DA2 or DA3 configuration and employed these distance distributions to calculate an average, conformation-weighted inter-dye distance (see below, **FRET positioning and screening calculations**). Importantly, we considered two possible fiber structures: The 12-mer array could exist as a stack of three tetranucleosome (TN) units (TN1(N1-N4); TN2(N5-N8); TN3(N9-N12), 4-4-4, register 1) as observed in the cryoEM structure (see Fig. 1a). Alternatively, tetranucleosomes could stack in a different register (TN1(N3-N6); TN2(N7-N10)), with four unstacked nucleosomes at both ends, 2-4-4-2, register 2). This would put the DA1-3 dye pairs into neighboring tetranucleosomes. Finally, if the nucleosome-nucleosome interactions are local and fiber compaction is not fully cooperative, both registers are expected to be populated. We thus produced models for both registers and calculated the expected inter-dye distances for DA1-3 in register 1 and 2 (**Supplementary Fig. 12 and Supplementary Table 8**). The observed deviations for DA2 can be rationalized by rotational motions between two nucleosomes (see **Supplementary Fig. 13 e,f**). A "clamshell" motion by $\sim 10^\circ$ would be sufficient to explain the experimental data of DA2 (488/647). Note that DA1 is relatively insensitive to these motions.

FRET positioning and screening calculations. The dye distribution was modeled by the accessible contact volume approach (ACV)⁴ which is similar to the accessible volume (AV)⁶, but additionally defines an area close to the surface as contact volume. Here donor and acceptor fluorophores are approximated by an ellipsoid with an empirical radius $R_{dye(i)}$ and where central atom of the dye is connected via flexible linkage with effective length L_{link} and width w_{link} to the C₅ atom in the dT nucleotide. All geometric parameters for the dyes were: Alexa488: $L_{link} = 20 \text{ \AA}$, $w_{link} = 4.5 \text{ \AA}$, $R_{dye(1)} = 5 \text{ \AA}$, $R_{dye(2)} = 4.5 \text{ \AA}$, $R_{dye(3)} = 1.5 \text{ \AA}$, Alexa568: $L_{link} = 22 \text{ \AA}$, $w_{link} = 4.5 \text{ \AA}$, $R_{dye(1)} = 7.8 \text{ \AA}$, $R_{dye(2)} = 1.9 \text{ \AA}$, $R_{dye(3)} = 1.5 \text{ \AA}$, Alexa647: $L_{link} = 22 \text{ \AA}$, $w_{link} = 4.5 \text{ \AA}$, $R_{dye(1)} = 11 \text{ \AA}$, $R_{dye(2)} = 3 \text{ \AA}$, $R_{dye(3)} = 1.5 \text{ \AA}$ (**Supplementary Fig. 12**). In the ACV model the part of AV which is closer than 3 \AA from the macromolecular surface (referred to as contact volume) is defined to have a distinct spatial dye density ρ_{dye} . In this model, where a dye freely diffuses within the AV and its diffusion is hindered close to the surface, the spatial density ρ_{dye} along R is approximated by a step function: $\rho_{dye}(R < 3 \text{ \AA}) = \vartheta_{CV,dye} \cdot \rho_{dye}(R \geq 3 \text{ \AA})$. Here $\vartheta_{CV,dye}$ corresponds to the relative dye density in the contact volume relative to outer volume. $\vartheta_{CV,dye}$ is adjusted such that fraction of trapped dyes, determined by the residual anisotropy (see table above) is met. Note that $\vartheta_{CV,dye}$ is specific for each ACV because the shape, size, and surface area to the nucleosome varies slightly for each dye position. In the following table, we indicate the fraction of trapped dye and the dye density in the contact volume relative to the outer volume $\vartheta_{CV,dye}$ for DA1-3:

48

Summary 9.5. Parameters for modeling the contact volume in the ACV simulations

	Donor register 1	Donor register 2	Acceptor register 1	Acceptor register 2
DA1				
$X_{trapped}$ [a]	0.210		0.692	
$\vartheta_{CV,dye}$	0.1	0.3	1.6	3.1
DA2				
$X_{trapped}$	0.218		0.663	
$\vartheta_{CV,dye}$	0.3	0.1	2.1	2.3
DA3				
$X_{trapped}$	0.149		0.549	
$\vartheta_{CV,dye}$	0.2	0.2	1.6	1.6

[a] computed by eq. 9.2 with values from the Summary 9.2 (donor) and Summary 9.4 (acceptor).

Step 10: Structural models of open and dynamic states

To model the unfolded and open chromatin state, we further resorted to computational modeling. Specifically, we performed Monte Carlo simulations of an established coarse-grained model of the chromatin fiber^{7,23} (see below **Coarse grained simulations**) to generate an ensemble of open chromatin conformations in the same temperature and salt conditions as the experiments, but in the absence of inter-nucleosome stacking interactions between the H4 histone tail and the acidic patch. From this larger ensemble of conformations, a hundred relatively uncorrelated structures were picked and used to build all-atom models of the chromatin configurations (**Supplementary Fig. 13a**). We then measured inter-dye distances for all nucleosomes in these structures for DA1-3 and produced distance distribution histograms (**Supplementary Fig. 13b,c,d**). These histograms showed that expected peak inter-dye distances were 110 Å (and a smaller fraction of structures with 190 Å) for DA1, 80 Å and 120 Å for DA2 and 90 Å for DA3. These distances match distances expected for states D in the PDA (**Fig. 4a**).

Finally, to understand the intra-tetranucleosome dynamics observed for DA2 (**Fig. 4a,b**) we employed the tetranucleosome X-ray structure¹³ to test how structural distortions affect inter-dye distances for DA1 and DA2 (**Supplementary Fig. 13e,f**) and DA3 (**Supplementary Fig. 13g**). DA2 was found to be more sensitive to tetranucleosome distortions, and distances observed for state C could be modeled by a 30° change in the tetranucleosome interaction angle (**Supplementary Fig. 13e**) or by a 30° rotation of one nucleosome relative to its neighbor (**Supplementary Fig. 13f**). Importantly, these conformations still allow interactions at the H2B and H2A four-helix bundle⁵ to persist. To illustrate the effect of nucleosome structural motions on each of FRET dye configurations (DA1, DA2, DA3), we plot FRET-average inter-dye distance as a function of the motion coordinate (**Supplementary Fig. 13e,f**). We used tetranucleosome structural models¹³ as a starting point for our illustrations. First we tested, how the DA1 and DA2 inter-dye distances change with respect to the

clamshell-like opening angle between the two nucleosome units (N5, N7, **Supplementary Fig. 13e**). To define the clamshell rotation coordinate, we chose an axis going through the phosphorous atom of the unit N7, chain B, residue 55 and the phosphorous atom of the unit N7, chain A, residue -30. Thus, clamshell motion is the rotation of the unit N7 around the specified axis with the origin at the phosphorous atom of N7, chain B, residue 55. Second, we tested the DA1 and DA2 distance change with respect to the in-plane nucleosome rotation. To define this second rotational motion coordinate we chose the rotation axis between the centers of mass of the nucleosome units N5 and N7. Thus N7 is rotated around the specified axis with the origin at the center of mass of N7.

As the result we have observed that DA2 distance senses nucleosome clamshell motion while DA1 does not (**Supplementary Fig. 13e**). $\langle R_{DA} \rangle_E$ for DA2 changes from 69 Å to 48 Å in the angular range of -30° to 0° . DA1 is not sensitive to this motion and varies only from 47 to 50 Å. In the case of in-plane rotation, $\langle R_{DA} \rangle_E$ for DA2 drops from 70 Å to 50 Å, when angle ranges from -30° to 30° . $\langle R_{DA} \rangle_E$ for DA1 is also sensitive to this motion and shows an increase of $\langle R_{DA} \rangle_E$ from 45 Å to 58 Å.

Coarse grained simulations

The 12-nucleosomes chromatin fibers with 177bp repeats (~ 30 bp linker DNAs) were treated at a coarse-grained resolution using a mesoscopic model developed and validated by Arya and Schlick^{23,24}. According to this model, each nucleosome core (histone octamer plus wound DNA) is treated as a rigid body with an irregular surface described by 300 charged beads; the linker DNAs are treated as charged bead-chains with each bead representing a 3 nm-long segment of double-stranded DNA; and the histone tails (N termini of H2A, H2B, H3, and H4 and C termini of H2A) are also treated as charged bead-chains, where each bead represents five amino acid residues. The core, linker, and tail beads are assigned excluded volume potentials, to prevent them from overlapping with each other, and charges, to reproduce the electrostatic field of their corresponding atomistic counterpart at the specified salt concentration. The linker DNAs are assigned an intramolecular force field to reproduce experimentally obtained bending and torsional rigidity of DNA, and the histone tails are assigned an intramolecular force field to reproduce the configurational properties of atomistic histone tails. In this study, the nucleosome entry/exit angle was set to 130° , compatible with the trajectory of linker DNA in the tetranucleosome structure of Song et al.⁵, and the monovalent salt concentration was set to 50 mM. The effects of Mg^{2+} were treated phenomenologically, with suitably modified Debye length and persistence length of the linker DNA, as described elsewhere²³.

To generate an equilibrium ensemble of fiber conformations at 293 K, we used a tailored Monte Carlo simulation approach as described elsewhere²⁴. Briefly, the simulations employed four Monte Carlo “moves”: global pivot rotation of the end portions of the fiber about a randomly picked nucleosome core or linker DNA

bead, local translation and rotation of a randomly picked linker DNA bead or nucleosome core, and configurational bias regrowth of a randomly picked histone tail. The simulations were performed for 40 million steps, with the above four Monte Carlo moves implemented at a relative frequency of 0.2:0.1:0.1:0.6, respectively. We picked a total of 100 uncorrelated fiber conformations from the simulated ensemble, which were then used to generate the corresponding atomistic models of the fiber (**Supplementary Fig. 13a-d**).

Step 11: Final model and its validation - A unified model of chromatin dynamics

Based on the analyses presented above (**steps 1-10**) we formulated a unified model for chromatin dynamics (**Fig. 6**). The model encompasses two dynamic populations, corresponding to two tetranucleosome registers (register 1 and 2). From dynPDA of DA1 – 3, ranges for the exchange rate constants were determined and are given in Fig. 4i. The presented model is well supported by the whole of the experimental data and is corroborated by matching results from different analyses yielding FRET efficiency states, dynamics rate constants and populations (**Steps 2 - 4**) and dynamic PDA (**Step 6**).

Supplementary References

1. Robinson, P.J., Fairall, L., Huynh, V.A. & Rhodes, D. EM measurements define the dimensions of the "30-nm" chromatin fiber: evidence for a compact, interdigitated structure. *Proc. Natl. Acad. Sci. U.S.A.* **103**, 6506-11 (2006).
2. Li, F., Allahverdi, A., Yang, R., Lua, G.B.J., Zhang, X., Cao, Y., Korolev, N., Nordenskiöld, L. & Liu, C.-F. A direct method for site-specific protein acetylation. *Angew. Chem. Int. Ed. Engl.* **50**, 9611-14 (2011).
3. Felekyan, S., Sanabria, H., Kalinin, S., Kühnemuth, R. & Seidel, C.A.M. Analyzing Förster resonance energy transfer with fluctuation algorithms. *Methods Enzymol.* **519**, 39-85 (2013).
4. Dimura, M., Peulen, T.O., Hanke, C.A., Prakash, A., Gohlke, H. & Seidel, C.A.M. Quantitative FRET studies and integrative modeling unravel the structure and dynamics of biomolecular systems. *Curr. Opin. Struct. Biol.* **40**, 163-185 (2016).
5. Song, F., Chen, P., Sun, D., Wang, M., Dong, L., Liang, D., Xu, R.M., Zhu, P. & Li, G. Cryo-EM study of the chromatin fiber reveals a double helix twisted by tetranucleosomal units. *Science* **344**, 376-80 (2014).
6. Kalinin, S., Peulen, T., Sindbert, S., Rothwell, P.J., Berger, S., Restle, T., Goody, R.S., Gohlke, H. & Seidel, C.A.M. A toolkit and benchmark study for FRET-restrained high-precision structural modeling. *Nat. Methods* **9**, 1218-25 (2012).
7. Arya, G., Zhang, Q. & Schlick, T. Flexible histone tails in a new mesoscopic oligonucleosome model. *Biophys. J.* **91**, 133-50 (2006).
8. Kilic, S., Bachmann, A.L., Bryan, L.C. & Fierz, B. Multivalency governs HP1alpha association dynamics with the silent chromatin state. *Nat. Commun.* **6**, 7313 (2015).
9. Nishibuchi, G., Machida, S., Osakabe, A., Murakoshi, H., Hiragami-Hamada, K., Nakagawa, R., Fischle, W., Nishimura, Y., Kurumizaka, H., Tagami, H. & Nakayama, J. N-terminal phosphorylation of HP1alpha increases its nucleosome-binding specificity. *Nucleic Acids Res.* **42**, 12498-511 (2014).
10. Peulen, T.O., Opanasyuk, O. & Seidel, C.A.M. Combining Graphical and Analytical Methods with Molecular Simulations To Analyze Time-Resolved FRET Measurements of Labeled Macromolecules Accurately. *J. Phys. Chem. B* **121**, 8211-8241 (2017).

11. Hellenkamp, B. et al. Precision and accuracy of single-molecule FRET measurements - a worldwide benchmark study. *arXiv:1710.03807 [q-bio.QM]* (2017).
12. Sindbert, S., Kalinin, S., Nguyen, H., Kienzler, A., Clima, L., Bannwarth, W., Appel, B., Muller, S. & Seidel, C.A.M. Accurate distance determination of nucleic acids via Forster resonance energy transfer: implications of dye linker length and rigidity. *J. Am. Chem. Soc.* **133**, 2463-80 (2011).
13. Schalch, T., Duda, S., Sargent, D.F. & Richmond, T.J. X-ray structure of a tetranucleosome and its implications for the chromatin fibre. *Nature* **436**, 138-41 (2005).
14. Kalinin, S., Valeri, A., Antonik, M., Felekyan, S. & Seidel, C.A.M. Detection of structural dynamics by FRET: a photon distribution and fluorescence lifetime analysis of systems with multiple states. *J. Phys. Chem. B* **114**, 7983-95 (2010).
15. Sisamakias, E., Valeri, A., Kalinin, S., Rothwell, P.J. & Seidel, C.A.M. Accurate single-molecule FRET studies using multiparameter fluorescence detection. *Methods Enzymol.* **475**, 455-514 (2010).
16. Fries, J.R., Brand, L., Eggeling, C., Kollner, M. & Seidel, C.A.M. Quantitative identification of different single molecules by selective time-resolved confocal fluorescence spectroscopy. *J. Phys. Chem. B* **102**, 6601-6613 (1998).
17. Kudryavtsev, V., Sikor, M., Kalinin, S., Mokranjac, D., Seidel, C.A.M. & Lamb, D.C. Combining MFD and PIE for accurate single-pair Forster resonance energy transfer measurements. *ChemPhysChem* **13**, 1060-78 (2012).
18. Lee, N.K., Kapanidis, A.N., Wang, Y., Michalet, X., Mukhopadhyay, J., Ebricht, R.H. & Weiss, S. Accurate FRET measurements within single diffusing biomolecules using alternating-laser excitation. *Biophys. J.* **88**, 2939-53 (2005).
19. Vopel, T., Hengstenberg, C.S., Peulen, T.O., Ajaj, Y., Seidel, C.A.M., Herrmann, C. & Klare, J.P. Triphosphate induced dimerization of human guanylate binding protein 1 involves association of the C-terminal helices: a joint double electron-electron resonance and FRET study. *Biochemistry* **53**, 4590-600 (2014).
20. Felekyan, S., Kalinin, S., Sanabria, H., Valeri, A. & Seidel, C.A.M. Filtered FCS: species auto- and cross-correlation functions highlight binding and dynamics in biomolecules. *ChemPhysChem* **13**, 1036-53 (2012).
21. Kalinin, S., Sisamakias, E., Magennis, S.W., Felekyan, S. & Seidel, C.A.M. On the origin of broadening of single-molecule FRET efficiency distributions beyond shot noise limits. *J. Phys. Chem. B* **114**, 6197-206 (2010).
22. Song, B., Cho, J.H. & Raleigh, D.P. Ionic-strength-dependent effects in protein folding: analysis of rate equilibrium free-energy relationships and their interpretation. *Biochemistry* **46**, 14206-14 (2007).
23. Arya, G. & Schlick, T. A tale of tails: how histone tails mediate chromatin compaction in different salt and linker histone environments. *J. Phys. Chem. A* **113**, 4045-59 (2009).
24. Grigoryev, S.A., Arya, G., Correll, S., Woodcock, C.L. & Schlick, T. Evidence for heteromorphic chromatin fibers from analysis of nucleosome interactions. *Proc. Natl. Acad. Sci. U.S.A.* **106**, 13317-22 (2009).